

THIS WEEK

EDITORIALS



WORLD VIEW Greg Petsko urges saving the arts **p.1003**

HOT WATER Huge shift in amphibian breeding blamed on global warming **p.1004**

ALVIN \$40-million upgrade gives veteran submersible a new lease of life **p.1006**

Turbines and turbulence

Some legitimate questions have been raised over the green credentials of wind turbines. Politics must not block research where it is needed.

Will wind turbines wreck the environment? Last month, the *South China Morning Post* published a news story that contained a thinly veiled attack on China's wind industry. The article cited herdsmen in a village in Inner Mongolia who say rain stopped falling after the establishment of a nearby wind farm, and meteorologists who backed up the observation with a few years' data that show low precipitation. The article also quoted an engineer in the government's renewable-energy department who hastily dismissed concern over the effect of wind farms, refused to acknowledge the need for research, and asserted the overarching necessity for China to develop wind energy. The article concludes that "wind power is not completely green". There have been similar attacks on wind energy in Texas and elsewhere.

It is good to see that the newspaper, Hong Kong's most prominent English-language daily, retains a critical stance towards the Chinese government under the 'one country, two systems' policy, and is willing to put Chinese officials on the spot. But in this case, the dismissive official quoted probably has a point. There is no solid scientific evidence that wind turbines can trigger major changes in rainfall. And given *Nature's* conversations with atmospheric modellers outside China, people are not likely to find any. One expert said the idea that a wind farm could have such a dramatic and demonstrable effect was "silly".

Wind farms, however, may affect regional or global environmental systems — although to suggest this can draw rapid scorn from wind-power proponents. In 2004, the environmental engineer and atmospheric modeller Somnath Baidya Roy, then at Princeton University in New Jersey, published work showing turbulence created by turbines would, among other effects, lead to vertical mixing of energy and heat in atmospheric layers that would affect local temperatures, and possibly change evaporation patterns (S. B. Roy *et al.* *J. Geophys. Res.* **109**, D19101; 2004). Some took his study as an attack on the wind industry, and he was besieged with nasty e-mails. They questioned his sanity, threatened to get him fired from his post at Princeton, and accused him of being a pawn of the coal or oil industries. (He has never had nor sought any industrial ties.) The president of one US-based wind-farm firm told Roy to consider "how much heat is your head turning out, while you consider such thoughts?" and to ponder many other factors "while checking your navel for lint". (We know this because Roy considered the comments humorous enough to post on his webpage.)

At around the same time, other scientists used models to suggest that wind turbines could have effects on climate change and suggested that estimates of these effects should be balanced against their green benefits. Although these researchers are seen by some in the industry as overly critical, they concluded with no stronger recommendation than a call for more research.

In October, Roy, now at the University of Illinois at Urbana-Champaign, published data to back up his theoretical work (S. B. Roy and J. J. Traiteur *Proc. Natl Acad. Sci. USA* **107**, 17899–17904; 2010).

A 25-year data set showed a significant effect of wind farms on near-surface temperatures. Roy suggested in the paper that those constructing wind farms should consider low-turbulence turbines or use the results to help find the most suitable sites. It hardly constituted an attack on wind energy. In fact, he says, the main impact — a raising of

"Data showed a significant effect of wind farms on near-surface temperatures."

surface temperatures at night and lowering during the day — could benefit agriculture by decreasing frost damage and extending the growing season. Many farmers already do this with air circulators.

Roy's study was on wind farms with some 20 turbines. Local effects will be more marked in much larger farms. Roy hopes to start a field campaign that can monitor energy fluxes, evaporation, humidity and temperature on a variety of farms as they scale up.

China, developing huge wind farms and planning more, should take a prominent role in such studies. As its facilities expand, it can make solid scientific assessments, which could contribute to a more rational and beneficial use of wind. Although the Chinese official may have been right to dismiss the suggested effect on rainfall, his government should not ignore the need for wider research on the impact of its wind revolution. ■

Assessment time

Italy's proposed university reform must be linked to performance.

As Rome burned last week during anti-government riots, many of those present were focusing on the plight of Italy's underfunded and underperforming universities, which face major reform. There is no doubt that reform is needed. The question is whether the government will deliver it correctly.

Islands of excellence exist in Italian universities, particularly in the north of the country. And they survive despite such low levels of government investment that little cash remains for infrastructure or research once salaries have been paid. But malaise is widespread, and money is not the only question. University workforces are riddled with dead wood, a legacy of too little competition for academic posts or research grants. And universities are not penalized if they choose to hire staff on the basis of personal contacts instead of talent.

A controversial new law, expected to be approved this week, attempts to fix these issues. It is imperfect, but if implemented properly, it will give Italy's universities a brighter future. Critical to its implementation,

though, is the prompt creation of a long-promised evaluation agency to assess teaching and research performance and link them to university budgets. Also critical is money — just as throwing money at the problem won't solve the malaise on its own, reforms without additional funds won't be effective.

A law to reform universities was drafted in 2007 by the previous, centre-left government, which also proposed setting up an evaluation agency, known as ANVUR (National Agency for the Evaluation of the University and Research System), modelled on France's AERES agency. The current, centre-right government picked up and tweaked that draft. In doing so, it inserted the authority of its powerful finance ministry, which will directly manage some funds, and sign off annual budgets and budget proposals for each university. But the law also introduces some radical changes that could improve things. For example, it brings in mandatory peer review of all public research money, requiring that 30% of individuals who sit on peer-review committees are working abroad. This will help to avert high-profile debacles like the ministry of health's behind-closed-doors allocation in 2007 of a €3-million (US\$4-million) grant from its stem-cell research fund to scientists at a private foundation who claimed to be working more ethically than others — and the reversal of that decision following public outcry.

Changes in the system for recruiting staff may also help, but not necessarily. Traditionally, academic staff have been selected by national committees and then allocated to universities to fill relevant vacancies. Incomprehensible to many of those in other countries, where universities choose their own staff, the '*concorsi*' system was intended to challenge a tendency to recruit locally, without necessarily

choosing the best. But behind-the-scenes dealing among *concorsi* committees ensured that universities mostly got the candidates they wanted anyway, for good or bad. Extensive tinkering in the past decade or so has not yet found a better balance between quality control at a national level and local university autonomy. In the new system, all candidates who pass a national qualification exam, judged by committees similar to *concorsi* committees, will join

"Italians are familiar with fine-sounding reforms that fail to actually change things."

a national list from which a university may at any time select a candidate. The danger here is that less academically suitable people may get on the list, because — as there is no link to a concrete academic position — committees don't bear responsibility for their choices.

Italians are familiar with fine-sounding reforms, such as the attempts to improve the *concorsi* system, that fail to actually change things. They enjoy quoting Giuseppe Tomasi di Lampedusa's *The Leopard*, a novel set around the time of Italy's unification in 1861, in which a protagonist observes contemporary politics, and wryly notes how the newly empowered try to 'change everything, so that everything remains the same'. But this law has a strong chance of changing things so that they do become different — and better. A crucial foundation for such success is that the government makes ANVUR happen soon. It was, after all, founded in law in February this year. Now, Italian scientists must see it built in bricks and mortar. The system needs more money, but that money must be linked to performance. Establishing ANVUR would show that Italy has placed its university system on the road to true reform. ■

Calm in a crisis

Jane Lubchenco, *Nature's Newsmaker of the Year*, shows how scientists can help society.

For almost three months this year, a mini-volcano of oil and gas erupted into the Gulf of Mexico and disgorged nearly 5 million barrels of petroleum. Throughout the crisis, a poised scientist gave countless media interviews to explain to a scared and angry public how the US government was striving to contain the damage. Behind the scenes, with decisive leadership, she ran the National Oceanic and Atmospheric Administration (NOAA) — the agency that closed fisheries, tracked oil, protected habitats and assessed the damage to communities and the environment. For her role in the response to the crisis, Jane Lubchenco is *Nature's Newsmaker of the Year* (see page 1024).

Before becoming NOAA administrator in 2009, Lubchenco had a reputation as both a leading researcher and an environmental advocate. She made important advances in the basic science of coastal ecology and helped to raise awareness of the many threats to ocean ecosystems around the world. Lubchenco is now reorienting her US\$4.7-billion federal agency to strengthen the science and policies that protect US marine resources.

The United States could do with more scientists like Lubchenco, with the skills and the dedication to speak out on issues that matter. The need will be particularly acute next year, when the Republican Party takes over the US House of Representatives. Although Republicans have generally supported basic science, incoming House leaders have made it clear that they are hostile to certain areas of research. Some have pledged to hold hearings on climate science, which they argue is seriously flawed and has overstated the evidence for global warming. Adrian Smith (Republican, Nebraska) introduced the YouCut Citizen Review, which calls on the US public to search the National Science Foundation website list of peer-reviewed grants for those they consider wasteful. And Darrell Issa (Republican, California), the incoming head of the powerful Committee

on Oversight and Government Reform, last year led an effort to revoke funding from the National Institutes of Health for studies of substance abuse and HIV risk in other countries (see *Nature* 460, 667; 2009).

Scientific leaders in the United States must stand up against such attacks. As a first step, they should try to meet with incoming House members from both parties to voice their concerns and explain the rationale behind research in controversial areas. Recognizing that all politics is local, scientists will need to make clear why climate change or HIV research matters for the communities represented by members of Congress. They should take along science-savvy business leaders and locally elected officials to help make their case.

Beyond the scientific leadership, there is a broader need for more individual scientists to communicate with the public. Currently, that kind of activity is not particularly valued — and is even disdained — in some fields of research. And spending time meeting with elected leaders or local journalists does not help a young scientist to get tenure.

Most scientists receive no training in public communication, and will need to hone their skills. Some can learn from experienced mentors; others can benefit from programmes developed by scientific societies and other groups (see page 1032). Members of academic and government agencies can consult with public-affairs representatives, who can show them the best ways to communicate the results and implications of research. Another avenue is the Congressional Science Fellowship programme, through which scientific societies can sponsor scientists to work in congressional offices for a year, providing advice to elected officials. The societies involved should expand their programmes, and groups that do not currently sponsor fellows should consider it.

As with any endeavour, it takes time to develop the communication skills that Lubchenco and other senior scientists have acquired. Even Lubchenco floundered at times during the oil spill. She made some mistakes and was criticized for the way that her agency initially downplayed the evidence for oil spreading below the surface. Despite such slips, Lubchenco has steered her agency through the crisis with a steady hand. She is an outstanding example of how much one scientist can do to improve both society and natural ecosystems. Others would do well to follow her lead. ■

➔ **NATURE.COM**
To comment online,
click on Editorials at:
go.nature.com/xhbnq



Save university arts from the bean counters

Scientists must reach across the divide and speak up for campus colleagues in arts and humanities departments, says Gregory Petsko.

As we enter the season of goodwill, let us spare a thought for our colleagues on the other side of the two-culture divide. A number of US universities have recently drastically cut or closed their programmes in arts and the humanities. Departments of classics, French, Russian, German, American studies, theatre arts, philosophy, Italian and European literature have all suffered. To borrow a phrase from Marx (Karl, not Groucho), a spectre is haunting higher education: the spectre of the market.

Similar stories of cutbacks in non-science subjects have emerged from France, Canada, Australia, New Zealand and other countries long known for the strength of their higher-education systems. In the United Kingdom, there is deep concern that the humanities are at serious risk in the new education budget announced in October by chancellor George Osborne. Excluding research support, which, Osborne said, will remain flat “to ensure the UK remains a world leader in science and research”, the amount of money going to higher education in England will probably decline by 40% over the next four years. The government has said only that it will continue to pay for teaching in science, technology, engineering and mathematics.

If arts and humanities are to survive, we who work in the sciences need to stand up for them and alongside them. Why? We should proclaim not only our love for the humanities as educated people, but their crucial role in our lives as professional scientists. I learned to think critically, analyse deeply and write clearly in my university humanities courses, not in my science courses. I found humanities the most valuable subjects in school. They still broaden my thinking, help me to make connections and aid my ability to communicate.

The humanities are the victim of two pernicious trends that have crept into the management of universities in the past decade or two, based on the idea that market forces should control what happens in education, as they are supposed to influence the economy.

The first is that higher education is increasingly run as a business; anything that doesn't contribute positively to the bottom line of the balance sheet is reduced or eliminated. Helping to drive this trend are the disturbingly large number of institutions of higher learning that are headed by administrators recruited from the worlds of business or politics. Nothing could so undermine the mission of a university as the misguided principle that all parts of it must make a profit. Contrary to the prejudices of a number of administrators, there is evidence from recent studies, including one from the University of California, Los Angeles, that arts and humanities departments can actually make a profit. But I don't think we should use that line — it's fighting on our opponent's ground. And it is also not

clear that all science and engineering programmes make money. A better argument is that profit and loss should not be the chief basis for important academic decisions.

The second damaging trend is the growing mantra of student choice, which increasingly dictates what programmes are offered, expanded and supported. The thinking here is that students are consumers, and market forces will lead to efficiencies in education, just as they do in, say, finance. If the past two years have taught us anything, it's that markets aren't always efficient. In fact they can be manipulated, driven by emotional frenzy and subject to fads. Besides, there are things that simply shouldn't be left to the brutality of the invisible hand. Education is one.

Moreover, the idea that student choice is a good thing is wrong, whether one believes in markets or not. Students have neither the

wisdom nor the experience to know what they need to know. Left to themselves, they frequently choose subjects based on the fashion of the moment (which in the United States is currently economics, although at one time it was sociology) or on what they think will equip them best for a job. That the best and most valuable education combines breadth with depth is something that most students do not yet understand. We need less student choice, not more. We need more prescribed curricula, not less.

To reverse these trends, here are some specific suggestions for things we might do. First, we should affirm the principle that universities aren't just about discovering new knowledge or generating intellectual property; they are also supposed to preserve ideas and information that may seem out of date now, but that are bound to

become important in the future, as 'old' ideas always do.

Second, we have to fight the hegemony of the bean counters. Universities should be run by people who understand what universities are really about. Marx (still Karl) also remarked that, for the bureaucrat, the world is a mere object for him to manipulate. Bureaucrats see universities the same way. And third, we must leave the comfortable ivory towers of our laboratories and take a stand with those in higher education — be they faculty members or administrators — who oppose the tyranny of the market. There is only one market that has any place in higher education: the marketplace of ideas.

To borrow from Marx again (Groucho this time, not Karl), those who run universities have had some perfectly wonderful ideas, but to savage arts and humanities education is not one of them. If you feel the same way, please speak out. ■

Gregory Petsko is professor of biochemistry and chemistry at Brandeis University in Waltham, Massachusetts.
e-mail: petsko@brandeis.edu

**STUDENTS
HAVE NEITHER THE
WISDOM NOR THE
EXPERIENCE TO
KNOW WHAT THEY
NEED TO
KNOW.**

➔ **NATURE.COM**
Discuss this article
online at:
go.nature.com/ce41xm

RESEARCH HIGHLIGHTS

Selections from the
scientific literature

ECOLOGY

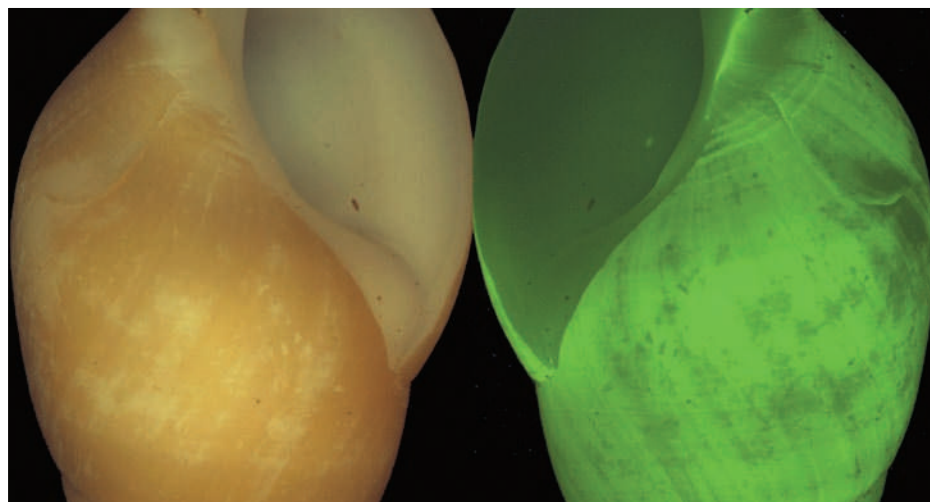
Hotter climate, altered breeding

As Earth warms, amphibians are shifting their breeding times at unprecedented rates.

Four out of ten amphibian species studied at a South Carolina wetland either delayed or advanced their breeding — depending on their breeding season — by 15.3–76.4 days over a 30-year period. For two of the species, *Ambystoma opacum* and *Eurycea quadridigitata*, this coincided with a 1.2 °C increase in overnight air temperature during their pre-breeding and breeding periods.

Brian Todd at the University of California, Davis, and his team say that the altered breeding times, which range from 5.9 to 37.2 days per decade, are among the greatest rates of change seen in ecological life-cycle events. The changes could affect the dynamics of the larger amphibian larval community, including resource availability and predation rates.

Proc. R. Soc. B doi:10.1098/rspb.2010.1768 (2010)



ZOOLOGY

Snail shells spread light around

A marine snail has a shell that is remarkably well adapted for diffusing the light that it emits to ward off predators.

Stimulating *Hinea brasiliana* snails (pictured left), by tapping them or placing them in contact with potential predators, causes them to emit a blue-green light from defined areas of their body, report Dimitri Deheyn and Nerida Wilson of the Scripps Institution of Oceanography in San Diego, California. The shell directly transmits

most wavelengths of light, with the exception of blue-green ones. These are instead spread by the shell from the limited production regions of the snail's body over a much larger area (right).

The shell produced brighter and larger areas of diffused light than a commercial diffuser. Such shells allow snails to produce visible and extensive bioluminescent signals from their protected position inside the shell.

Proc. R. Soc. B doi:10.1098/rspb.2010.2203 (2010)

R. SOC.

MATERIALS SCIENCE

Magnetic gel delivers drugs

Drugs and cells can be delivered on demand by a porous material engineered to compress in response to an applied magnetic field.

David Mooney at Harvard University in Cambridge,

Massachusetts, and his team prepared an alginate-based gel with micrometre-sized pores, and paramagnetic iron nanoparticles embedded throughout. On exposure to a magnetic field, the nanoparticles put the squeeze on the ferrogel. The authors used this to release a drug payload in *in vitro* experiments and, by implanting the gel into

mice, for localized release of dye-stained stem cells.

With a reversible volume reduction of more than 70% (pictured), such ferrogels may also find applications as actuators and sensors in biomedical applications.

Proc. Natl Acad. Sci. USA doi:10.1073/pnas.1007862108 (2010)

ANTHROPOLOGY

DNA from across the ocean

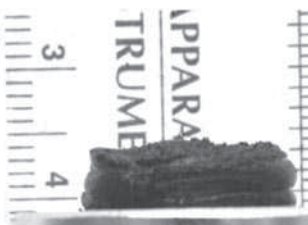
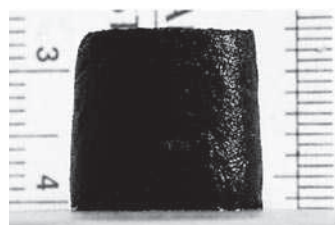
A handful of Icelanders may be descendants of a Native American woman ferried to the island hundreds of years

before Christopher Columbus reached the New World.

In a tiny proportion of the country's residents, DNA sequences from cell organelles called mitochondria (mtDNA) resemble those of some Native Americans. Unlike nuclear DNA, mtDNA is inherited only from the mother.

Sigríður Sunna Ebenesersdóttir at deCODE Genetics in Reykjavík and her colleagues traced the sequence variants back to four Icelanders born in the early 1700s. However, genetic differences between them suggest that the mtDNA derived from a woman who arrived in Iceland much earlier — possibly around

NATL ACAD. SCI.



the time the Vikings started exploring the Americas in about AD 1000. Because Native American populations were decimated after the arrival of the Europeans, the lineage may be missing from contemporary populations. DNA analysis of the remains of ancient Native Americans could provide a more definitive link.

Am. J. Phys. Anthropol. 144, 92–99 (2011)

GLACIOLOGY

Imaging grooves from glaciers

Developments in radar technology have allowed geoscientists to 'see through' a Greenland glacier and construct three-dimensional topographic maps of its bed.

Kenneth Jezek of Ohio State University in Columbus and his team used high-resolution radar tomography and synthetic-aperture radar data to measure ice thickness in a region of the Jakobshavn Glacier. They found that as the glacier slides over its bed, it cuts large-scale ridge–groove features into the bedrock that are similar to landforms found on deglaciated terrain. The orientation and dimensions of the grooves suggest that the glacier has been flowing persistently in the same direction.

Understanding past glacier movement and bedrock geomorphology helps researchers to forecast climate-driven changes in the seaward flux of ice sheets.

Geophys. Res. Lett. doi:10.1029/2010GL045519 (2010)

CANCER

Tumours aided by immune cells

Zebrafish cells with the propensity to give rise to tumours behave similarly to wounded tissue, and call for assistance from the immune system. So say Paul Martin at the University of Bristol, UK, and his colleagues, who imaged the interactions

between the cells in real time.

The authors expressed a cancer-associated mutant form of the Ras protein in zebrafish (*Danio rerio*). Because zebrafish larvae are translucent, the team was able to visualize fluorescently labelled immune cells as they responded to the transformed cells.

Cells expressing mutant Ras, and their healthy neighbours, released hydrogen peroxide, attracting immune cells called neutrophils and macrophages, which tethered themselves to the transformed cells. Blocking hydrogen peroxide synthesis — and so the recruitment of the immune cells — slowed the proliferation of transformed cells, suggesting that early immune responses may support tumour development. *PLoS Biol.* 18, e1000562 (2010)

VISION SCIENCE

Man or woman? Depends on view

Whether a face looks like that of a man or a woman depends on the part of the retina on which the image lands.



Eleven volunteers were asked to identify the gender of a series of faces (pictured) presented in one of eight possible visual-field locations relative to a central point. Arash Afraz at the Massachusetts Institute of Technology in Cambridge and his co-workers found that two identical faces were perceived to be of different gender if they were presented simultaneously in specific, different locations. Volunteers' responses became more consistent across the visual field as the images grew in size.

The researchers think that the perceptual variation may result from the small size of the stimuli relative to that of the receptive field. The small number of brain cells analysing the images at any given location

COMMUNITY CHOICE

The most viewed papers in science

NEUROSCIENCE

Better memory with less microRNA

HIGHLY READ
on jneurosci.org
in November

Learning and memory in mice seem to be enhanced by the loss of small RNA molecules called microRNAs (miRNAs) in the brain.

Witold Konopka at the German Cancer Research Center in Heidelberg and his colleagues deactivated the gene for Dicer, a key enzyme in miRNA synthesis, in forebrain neurons of adult mice. Twelve weeks later, the mice showed improved learning and memory in a behavioural test. This was mirrored by increased numbers of a type of dendritic spine in mutant neurons that is associated with learning. After 20 weeks, however, some of the neurons had degenerated, confirming the importance of microRNAs for neuronal survival.

J. Neurosci. 30, 14835–14842 (2010)

may have varying responses; these are averaged out by a larger image, which stimulates a greater number of cells.

Curr. Biol. 20, 2112–2116 (2010)

DEVELOPMENTAL BIOLOGY

Immune system emerges in layers

The human immune system develops in waves, the first of which begins even before birth. Fetal and adult T cells originate from different stem-cell populations, allowing the fetal immune system to better tolerate foreign antigens — namely the mother's.

Joseph McCune at the University of California, San Francisco, and his colleagues compared human fetal blood stem cells and T cells with those of adults. After implantation in mice that permit human blood-cell maturation, fetal stem cells were more likely than adult ones to develop into regulatory T cells. These suppress immune activity, enhancing tolerance to antigens.

Fetal stem cells and T cells also had different gene-expression profiles from the adult versions of these cells. Statistical analysis revealed that developmental stage accounted for most of these differences. *Science* 330, 1695–1699 (2010)

PALAEOANTHROPOLOGY

Neanderthal family tree

Neanderthals living 49,000 years ago may have abided in small clans banded together by their male kin.

Carles Lalueza-Fox at Pompeu Fabra University in Barcelona, Spain, Antonio Rosas at the National Museum of Natural Sciences in Madrid and their colleagues analysed the remains of 12 Neanderthals. They sequenced certain regions of the mitochondrial DNA extracted from fragments of bones and teeth.

The results showed that the group's three adult males were close relatives, but the three adult females were not. The authors further inferred that an infant and two juveniles were offspring of two of the adult females. The team suggests that the individuals represent a social unit based on patrilocality, in which individuals live with the adult male's family.

Proc. Natl Acad. Sci. USA
doi:10.1073/pnas.1011553108 (2010)

NATURE.COM

For the latest research published by Nature visit:

www.nature.com/latestresearch

SEVEN DAYS

The news in brief

POLICY

US policy flurry

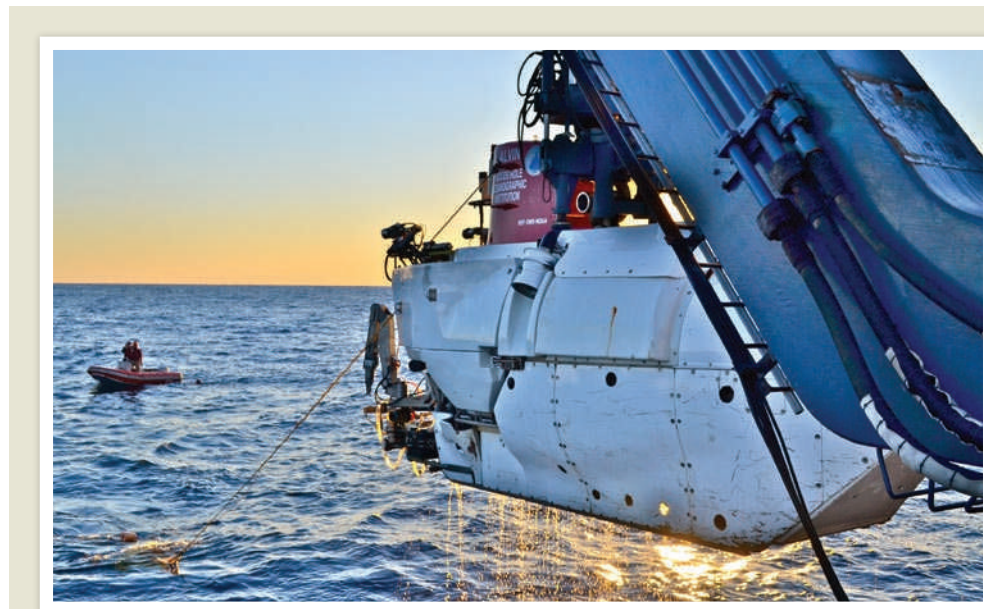
In a fit of pre-Christmas legislating, the US Senate reauthorized a version of the America COMPETES Act, which would keep on track a series of budget increases for key science funding agencies, including the National Science Foundation. If this is signed into law, money for the increases would need to be found in the 2011 budget. Last week, the Senate also passed food-safety legislation, which would give the Food and Drug Administration broad new food-policing powers. Both bills were expected to be passed by the House of Representatives as *Nature* went to press. Another bill, passed by both houses, calls for an integrated national plan to overcome Alzheimer's disease.

Haiti cholera fight

With the death toll from Haiti's cholera epidemic passing 2,400, an expert meeting convened by the Pan American Health Organization on 17 December called for the use of cholera vaccines in the country, at least as a pilot project. It also urged the creation of an international stockpile of cholera vaccine — only about 100,000 doses are currently available for shipment. Separately, the United Nations secretary-general Ban Ki-moon announced an independent investigation into the source of the outbreak.

Synthetic biology

US research in synthetic biology should be overseen at White House level, but not over-regulated, said a presidential bioethics commission in a report published on 16 December. Claiming to navigate a middle road between unbridled



M. SCHROPE

Research sub set for rebirth

The venerable *Alvin* submersible — which has enabled numerous historic discoveries since it was first launched in 1964 — is undergoing a US\$40-million transformation. During its long life, *Alvin* has been involved in the discovery of deep-sea hydrothermal vents; taken humans to the wreckage of the *Titanic* for the first time; and helped to recover a lost hydrogen

bomb. Owned by the US Navy and operated by the Woods Hole Oceanographic Institution in Massachusetts, *Alvin* had its final dive (pictured) in its current form on 14 December; it will now be upgraded to have a larger crew compartment, manipulator arms and an advanced autopilot. See go.nature.com/5adtko for more.

experimentation and a regulatory straitjacket, the commission said that the field should embrace “an ongoing process of prudent vigilance”, and did not call for new laws or changes to regulations. See go.nature.com/thidag for more.

ITER squeezed

The European Parliament has rejected a plan to close a funding gap in the budget of ITER, the €15-billion (US\$19.7-billion) fusion reactor under construction near Cadarache, France. To cover a €1.4-billion shortfall in 2012–13, the European Commission had proposed using money from elsewhere in the European Union's budget, including research

funds (see *Nature* **466**, 171; 2010). But on 15 December the parliament turned that down. Budget negotiations will now continue into 2011.

Science of security

The US Department of Defense should sponsor university research programmes in cybersecurity, according to a report by the JASON group, which advises the US government on defence science and technology. The November report — released by the Federation of American Scientists on 14 December — says cybersecurity as a discipline should be thought of as an applied science akin to medicine, which would benefit from rigorous experiments.

UN biodiversity

At its general assembly on 20 December, the United Nations gave the final go-ahead for a body that will monitor global ecology, the Intergovernmental Science-Policy Platform on Biodiversity and Ecosystem Services (IPBES). It will operate much like the Intergovernmental Panel on Climate Change, conducting periodic assessments of Earth's biodiversity and ecosystems services.

Periodic-table shift

Natural geographic variations in the abundance of a chemical element's isotopes should be noted on the periodic table, chemistry's governing body,

the International Union of Pure and Applied Chemistry, has decided. The decision means that ten common elements — including hydrogen, carbon and oxygen — will be assigned a range, rather than a single average number, for their atomic weight. Hydrogen will be [1.00784; 1.00811], for example, rather than [1.00794].

Integrity guidelines

Long-awaited guidelines on scientific integrity in government were released on 17 December by the White House Office of Science and Technology. See page 1009 for more.

PEOPLE

NIH



Zerhouni move

Elias Zerhouni (pictured), who directed the US National Institutes of Health (NIH) from 2002 to 2008, will head research and development at

French pharmaceutical giant Sanofi-aventis. The company, headquartered in Paris, announced the appointment on 16 December.

BUSINESS

Drug tug-of-war

Swiss pharmaceutical company Roche intends to challenge the US Food and Drug Administration (FDA) over its 16 December decision to withdraw approval of the drug Avastin (bevacizumab) for the treatment of advanced breast cancer. The FDA's announcement came five months after a panel of advisers decided that the drug's benefits did not outweigh its risks in patients with breast cancer. See go.nature.com/7mjlea for more.

Carbon trading

California's Air Resources Board has approved regulations to create the United States' largest market in carbon trading. From 2012, the scheme will cap greenhouse-gas emissions from the state's electric utilities and heavy industry, allowing companies to trade emissions permits to reach their targets. Transportation fuels will be included by 2015. The system may later allow firms to reduce emissions elsewhere — such as by protecting forests in Brazil — in order to meet state

requirements. California is pushing to cut emissions to 1990 levels (15% below today's levels) by 2020.

Conflicts of interest

US medical schools are quickly improving policies on conflicts of interest between faculty and pharmaceutical companies — such as restrictions on gifts and consulting relationships. According to a scorecard released on 15 December by the American Medical Student Association in Reston, Virginia (see www.amsascorecard.org), 52% of schools scored 'A' or 'B' for their policies, up from 30% in 2009 and 14% in 2008.

RESEARCH

IceCube telescope

Researchers at the South Pole have completed construction of a giant neutrino telescope that consists of an array of wires and detectors set deep in Antarctic ice. The IceCube Neutrino Observatory has been under construction since 2005; 86 wires, at depths of between 1,450 and 2,450 metres, each have 60 basketball-sized detectors that look for cosmic neutrinos hitting oxygen atoms in the water molecules of the ice. The final detector string was laid on 18 December; the full array can start taking data in May. See go.nature.com/kqqlen for more.

COMING UP

1 JANUARY

Hungary assumes a six-month presidency of the European Union.

3-7 JANUARY

The Society for Integrative and Comparative Biology meets in Salt Lake City, Utah.

www.sicb.org/meetings/2011

Carbon storage

The state of Queensland, Australia, has said it will not fund a proposed flagship demonstration project to capture carbon dioxide (CO₂) emissions from a coal-fired power station and store them underground. The ZeroGen project — on which the state had already spent A\$192 million (US\$191 million) — was intended to be a A\$4.3-billion coal-gasification plant with a 530-megawatt capacity, storing about 2 million tonnes of CO₂ per year, and in operation by 2015. But Queensland premier Anna Bligh said early research had shown that the idea was “not viable at this time on a commercial scale”. ZeroGen will now go it alone, becoming an entity owned and run by industry, Bligh said.

UK medical hub

The UK Centre for Medical Research and Innovation has received the go-ahead to begin construction. On 16 December, the London borough of Camden, which will host the £500-million (US\$778-million) facility, approved the project, which is being funded jointly by the government, Cancer Research UK, the Wellcome Trust and University College London. Construction should begin next spring and finish by 2015.

➔ NATURE.COM

For daily news updates see:

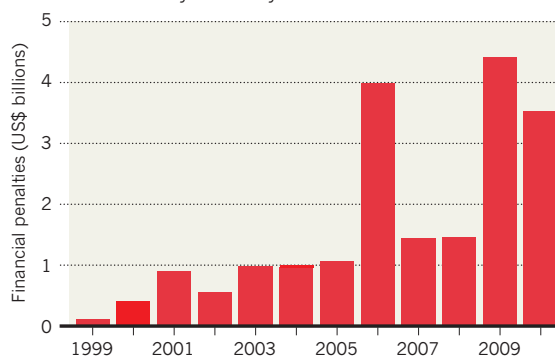
www.nature.com/news

BUSINESS WATCH

Public settlements paid by pharmaceutical companies to US governments — both state and federal — for illegal behaviour climbed to US\$14.8 billion over the past five years, according to a study released on 16 December by Public Citizen, a non-profit group in Washington DC. Illegal off-label promotion was responsible for the largest amount of federal penalties, and settlements under the False Claims Act — for activities such as inflating drug prices — now exceed those made by the defence industry.

US PHARMA FINES

The penalties paid out by US pharmaceutical companies have increased dramatically in recent years.



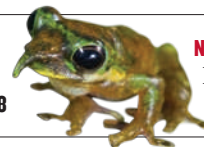
One settlement with GlaxoSmithKline for \$3.4 billion accounts for the spike in financial penalties in 2006. 2010 data include only the first 10 months of the calendar year to 1 November 2010.

NEWS IN FOCUS

BIBLIOMETRICS Harvard researchers cosy up for high-impact science **p.1011**

2010 IN REVIEW Twelve months of disasters, discoveries and disputes **p.1014**

2010 IN REVIEW A gallery of stunning science images **p.1018**



NEWMAKER OF THE YEAR Jane Lubchenco on her toughest year **p.1024**

K. SRAKOCIC/AP



demonstrate progress towards implementing the new rules.

Watchdog groups who campaign for sound science in government decision-making gave the guidelines a cautious reception. “We will just have to wait and see what the agencies do with it,” says Francesca Grifo of the Union of Concerned Scientists (UCS), headquartered in Cambridge, Massachusetts. “The jury is still out.”

The document is the product of an initiative that began soon after President Barack Obama took office. In March 2009, Obama issued a memorandum on scientific integrity that forbade the distortion of science for political ends. The move seemed to signal a clear departure from practices adopted during the administration of President George W. Bush, which faced accusations of weakening the role of science in regulatory agencies and of muzzling scientists whose views were at odds with those of the White House.

But the road to implementing Obama’s vision has been tortuous. The guidelines, expected in July 2009, became mired in unwieldy discussion as Holdren struggled to get all relevant departments and agencies to accept a common set of principles. The US Department of the Interior issued a draft policy earlier this year, only to backtrack after advocacy groups slammed it as incomplete and ambiguous. Following the oil spill in the Gulf of Mexico in summer 2010, the Obama administration was itself accused of suppressing scientific information to put a better gloss on the situation.

The White House document lays out goals for science in government but says little about how they should be achieved. It directs agencies to “ensure that the data and research used to support policy decisions undergo independent peer review”, to adopt protection for whistleblowers and to “facilitate the free flow of scientific and technological information”.

Roger Pielke of the University of Colorado, Boulder, whose research focuses on the intersection of public policy with science, questions why it has taken so long to issue such a limited document. “It sets forth discussion questions about scientific integrity in government, but I don’t think it resolves them,” he says. Pielke says that given how long it took to create the document, there may not be time for much progress before the end of Obama’s term of office in 2012. He adds that even if it had ►

Presidential adviser John Holdren drew up guidelines at Barack Obama’s request.

SCIENCE & POLITICS

Integrity policy unveiled at last

Mixed reviews greet White House guidelines for preventing political interference in US government science.

BY EUGENIE SAMUEL REICH

Four pages in 648 days. At that rate it would have taken Leo Tolstoy centuries to write *War and Peace*. But to get to this point, John Holdren, director of the White House Office of Science and Technology Policy, may have battled through the bureaucratic equivalent of the Napoleonic Wars.

On 17 December, Holdren finally released a long-promised set of guidelines for scientific integrity in US government departments and agencies. On the White House website Holdren wrote that the document includes “a clear prohibition on political interference in scientific processes and expanded assurances of transparency”. He also wrote that department and agency heads would have 120 days to

► been issued earlier it would not have prevented the issues around scientific integrity that arose during the oil spill.

Some advocates agree that the document is a disappointment. "It was a very long wait for four pages," says Jeff Ruch of Public Employees for Environmental Responsibility (PEER), based in Washington DC, which has represented several scientist whistleblowers. "We feel frustrated that this process is horribly off schedule." Ruch says that several sentences have the potential to make things worse, rather than better, for government

scientists. For example, the guidelines say that researchers can speak to the media, provided there has been "appropriate coordination" with public-affairs offices, but they fail to define what is appropriate. They also allow scientists to speak publicly about their "official work" but fail to offer protection for scientists who are judged to have spoken up in their private capacity. "Scientists are free to speak, except when they're not," says Ruch.

Grifo says that her organization is a little more positive than PEER. She points to sections that unambiguously allow government scientists to serve on the boards of scientific societies and journals, to present findings at scientific conferences and to accept awards and honours for the science they do. These are major issues, she adds, because the UCS has heard from government scientists who have been prevented from doing these things in the past because of a perceived conflict of interest.

But she agrees with Ruch that the media policy lacks specificity, and also argues that the guidelines should have taken a stronger position against scientists with financial conflicts of interest serving as advisers to the government.

James Hansen, head of the NASA Goddard Institute for Space Studies in New York City, who became well known for speaking out publicly about censorship of his scientific work by NASA press offices during the Bush administration, says that the new policy does not change either of what he sees as two central problems; the use of political appointees to run public-affairs offices, and the requirement that the White House

screen testimonies that scientists make to Congress. "A democracy cannot function well with the present approach," he says. ■

➔ **NATURE.COM**
For more on government interference see:
go.nature.com/p3g9hy

FUNDING

UK science faces facilities freeze

Four-year budget protects grants but cuts capital spending.

BY GEOFF BRUMFIEL & NATASHA GILBERT

British scientists hoping for shiny new facilities this Christmas will be disappointed by their government's research-funding plans.

On 20 December, the Department of Business Innovation and Skills, which oversees research and higher-education funding, unveiled a four-year budget which makes deep cuts to cash for large projects such as particle accelerators, research ships and university lab space (see 'Capital crunch'). Meanwhile, two of the councils that support specific areas of research announced that they will put a new emphasis on the economic impact and social benefit of the work they fund. The net effect will be a squeeze on money for new projects and blue-skies research in the coming years.

By cutting the £873-million (US\$1.3-billion) annual capital budget by roughly 40%, the government says it can maintain grant funding at the current level. Yet several key facilities will be shielded from the capital cut, including the UK Centre for Medical Research and Innovation, a new £500-million biomedical laboratory in central London. The budget also protects a handful of other planned facilities, and international subscriptions to organizations such as CERN, the European high-energy physics laboratory located near Geneva, Switzerland.

But some research councils will struggle to

cope with the cuts. The Natural Environment Research Council (NERC) said that it remained committed to a handful of key projects, including a replacement for its research vessel *Discovery*. But no new projects are likely to start in the next four years, according to Marion O'Sullivan, a NERC spokeswoman. Similarly, the Medical Research Council says the capital reductions will pose "challenges", according to a statement from John Jeans, the council's deputy chief executive.

The UK government's efforts to squeeze as much value as possible from its research spending has also led two of the research councils to announce changes to their missions. The Biotechnology and Biological Sciences Research Council (BBSRC) no longer sees itself as a science 'funder', but rather as an investor of public funding in science. Matt Goode, a spokesman for the BBSRC, says this refocus is a "subtle semantic change" and that the council is not abandoning basic research. Meanwhile, the Engineering and Physical Sciences Research Council (EPSRC) announced that it would become a "sponsor" of research. "Funding is viewed as a strategic investment and not a transfer of funds without obligations," David Delpy, the EPSRC's chief, said in a video message explaining the shift. Researchers would be asked to think about impact at every stage of the research process, Delpy said.

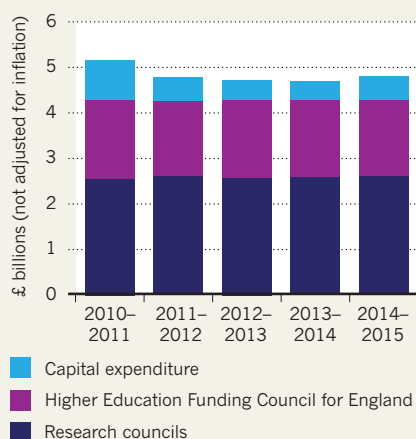
"Obviously this is sheer lunacy," says Paul Clarke, a chemist at the University of York, UK. "If I knew what the impact of the research would be, I wouldn't have to do the research."

Research funds for English universities will also be squeezed. The Higher Education Funding Council for England (HEFCE) will have its annual £1.6 billion for research grants cut by about 3% over the next four years (universities elsewhere in Britain are overseen by other bodies). But like the research councils, the biggest cuts hit the capital budget, which will be slashed by 40% from its present level of £167 million over the same period. The HEFCE will announce how it will slice up its budget between universities in March 2011.

Imran Khan, director of the Campaign for Science & Engineering in the UK, a London-based advocacy group, fears that some research councils may be forced to dip into money intended for basic research to make up for the capital shortfall. "The money will have to come from somewhere," he says. ■

CAPITAL CRUNCH

UK government funding for research has been protected, but at the expense of cash for buildings and major projects.



SOURCE: BIS

► been issued earlier it would not have prevented the issues around scientific integrity that arose during the oil spill.

Some advocates agree that the document is a disappointment. "It was a very long wait for four pages," says Jeff Ruch of Public Employees for Environmental Responsibility (PEER), based in Washington DC, which has represented several scientist whistleblowers. "We feel frustrated that this process is horribly off schedule." Ruch says that several sentences have the potential to make things worse, rather than better, for government

scientists. For example, the guidelines say that researchers can speak to the media, provided there has been "appropriate coordination" with public-affairs offices, but they fail to define what is appropriate. They also allow scientists to speak publicly about their "official work" but fail to offer protection for scientists who are judged to have spoken up in their private capacity. "Scientists are free to speak, except when they're not," says Ruch.

Grifo says that her organization is a little more positive than PEER. She points to sections that unambiguously allow government scientists to serve on the boards of scientific societies and journals, to present findings at scientific conferences and to accept awards and honours for the science they do. These are major issues, she adds, because the UCS has heard from government scientists who have been prevented from doing these things in the past because of a perceived conflict of interest.

But she agrees with Ruch that the media policy lacks specificity, and also argues that the guidelines should have taken a stronger position against scientists with financial conflicts of interest serving as advisers to the government.

James Hansen, head of the NASA Goddard Institute for Space Studies in New York City, who became well known for speaking out publicly about censorship of his scientific work by NASA press offices during the Bush administration, says that the new policy does not change either of what he sees as two central problems; the use of political appointees to run public-affairs offices, and the requirement that the White House

screen testimonies that scientists make to Congress. "A democracy cannot function well with the present approach," he says. ■

➔ **NATURE.COM**
For more on government interference see:
go.nature.com/p3g9hy

FUNDING

UK science faces facilities freeze

Four-year budget protects grants but cuts capital spending.

BY GEOFF BRUMFIEL & NATASHA GILBERT

British scientists hoping for shiny new facilities this Christmas will be disappointed by their government's research-funding plans.

On 20 December, the Department of Business Innovation and Skills, which oversees research and higher-education funding, unveiled a four-year budget which makes deep cuts to cash for large projects such as particle accelerators, research ships and university lab space (see 'Capital crunch'). Meanwhile, two of the councils that support specific areas of research announced that they will put a new emphasis on the economic impact and social benefit of the work they fund. The net effect will be a squeeze on money for new projects and blue-skies research in the coming years.

By cutting the £873-million (US\$1.3-billion) annual capital budget by roughly 40%, the government says it can maintain grant funding at the current level. Yet several key facilities will be shielded from the capital cut, including the UK Centre for Medical Research and Innovation, a new £500-million biomedical laboratory in central London. The budget also protects a handful of other planned facilities, and international subscriptions to organizations such as CERN, the European high-energy physics laboratory located near Geneva, Switzerland.

But some research councils will struggle to

cope with the cuts. The Natural Environment Research Council (NERC) said that it remained committed to a handful of key projects, including a replacement for its research vessel *Discovery*. But no new projects are likely to start in the next four years, according to Marion O'Sullivan, a NERC spokeswoman. Similarly, the Medical Research Council says the capital reductions will pose "challenges", according to a statement from John Jeans, the council's deputy chief executive.

The UK government's efforts to squeeze as much value as possible from its research spending has also led two of the research councils to announce changes to their missions. The Biotechnology and Biological Sciences Research Council (BBSRC) no longer sees itself as a science 'funder', but rather as an investor of public funding in science. Matt Goode, a spokesman for the BBSRC, says this refocus is a "subtle semantic change" and that the council is not abandoning basic research. Meanwhile, the Engineering and Physical Sciences Research Council (EPSRC) announced that it would become a "sponsor" of research. "Funding is viewed as a strategic investment and not a transfer of funds without obligations," David Delpy, the EPSRC's chief, said in a video message explaining the shift. Researchers would be asked to think about impact at every stage of the research process, Delpy said.

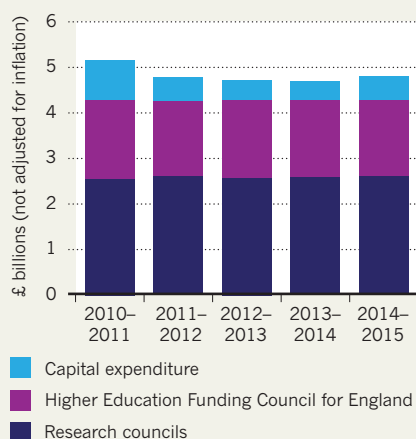
"Obviously this is sheer lunacy," says Paul Clarke, a chemist at the University of York, UK. "If I knew what the impact of the research would be, I wouldn't have to do the research."

Research funds for English universities will also be squeezed. The Higher Education Funding Council for England (HEFCE) will have its annual £1.6 billion for research grants cut by about 3% over the next four years (universities elsewhere in Britain are overseen by other bodies). But like the research councils, the biggest cuts hit the capital budget, which will be slashed by 40% from its present level of £167 million over the same period. The HEFCE will announce how it will slice up its budget between universities in March 2011.

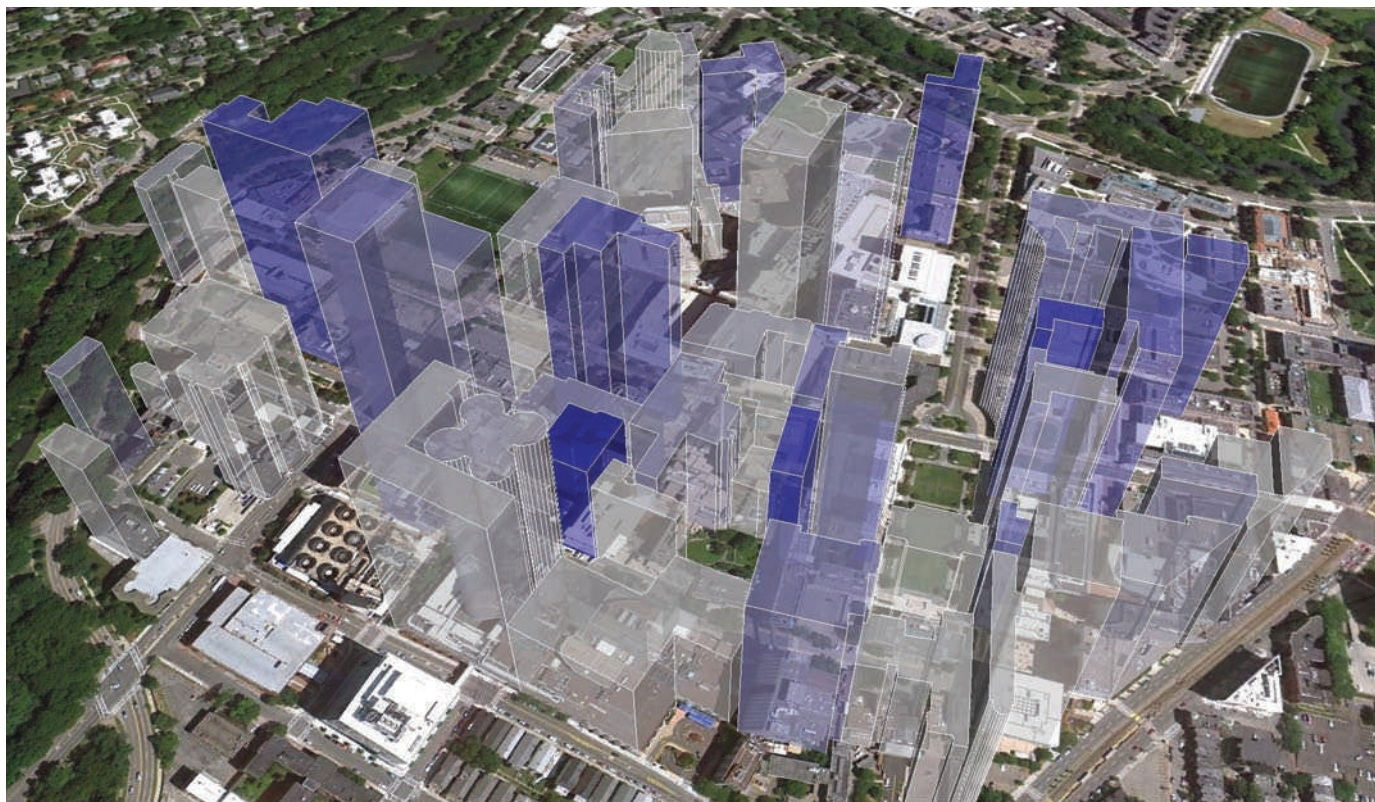
Imran Khan, director of the Campaign for Science & Engineering in the UK, a London-based advocacy group, fears that some research councils may be forced to dip into money intended for basic research to make up for the capital shortfall. "The money will have to come from somewhere," he says. ■

CAPITAL CRUNCH

UK government funding for research has been protected, but at the expense of cash for buildings and major projects.



SOURCE: BIS



A schematic of the Longwood campus of Harvard Medical School shows the mean number of publication citations originating from each building (height), and the proportion of publications in each building where first and last authors work (grey is low, blue is high). Statistically, bluer buildings are also higher.

BIBLIOMETRICS

Love thy lab neighbour

Getting closer to your collaborators boosts a paper's citations.

BY RICHARD VAN NOORDEN

Anyone who has worked in a laboratory probably feels that having key members of the group placed closer together makes for a better research project. A study linking the proximity of investigators and the impact of their research now backs up that hunch.

Isaac Kohane, co-director of the Harvard Medical School Center for Biomedical Informatics in Boston, Massachusetts, decided to put intuition to the test in 2005 after a debate with Harvard's dean of administration, Richard Mills, over the layout of the centre. "I felt this viscerally, but there was no hard evidence," says Kohane. He enlisted more than a dozen undergraduates to identify 35,000 articles published between 1999 and 2003 in biomedical sciences, each with at least one Harvard author. It took the team two years to pinpoint where individual Harvard investigators were working — right down to the level of individual offices and laboratories.

The results, published in *PLoS ONE* last week (K. Lee *et al.* *PLoS ONE* 5, e14279; 2010),

show that the shorter the geographical distance between first and last authors on a paper, the more highly cited were their research papers. First authors often bear the brunt of the work, whereas last authors tend to take the lead organizational role — and both are key players in the research project. The distance trend was not found for middle authors, who could be far removed from other collaborators without any clear effect on research impact.

Kohane and his colleagues also looked at individual buildings on the four campuses across which Harvard life-science research happens to be spread. They found that the more that researchers within a building tended to collaborate with one another rather than with people elsewhere, the more highly cited the publications that came from that building (see picture). The team does acknowledge an alternative explanation for the data: that scientists might choose to keep

NATURE.COM
See *Nature's* cities special:
go.nature.com/9233vu

potentially high-impact breakthroughs within their own laboratory, or within a close circle of researchers.

This seems to be the first empirical study of the connection between proximity and impact, says Anthony van Raan, an expert in using citation analyses to study scientific productivity and impact at Leiden University, the Netherlands. Most studies of the relationship between spatial separation and scientific impact have been done on a national and international scale, for which it has been demonstrated many times that international collaborations produce more highly cited science than local collaborations — probably a consequence of the size and scope of such efforts.

Kohane speculates that international collaborations might become even more successful if the first and last authors worked very close together, something that has not yet been tested. He certainly practises what he preaches: he and first author Kyungjoon (Joon) Lee, who coordinated the undergraduates' fact-finding, now work on the same floor. "When the study started we were on different floors," says Kohane, "and Joon told me that I became a lot more helpful when I moved to his floor." ■



A finger bone and a tooth (inset) from Denisova Cave have illuminated a mysterious strand of hominin.

PALAEOANTHROPOLOGY

Fossil genome reveals ancestral link

A distant cousin raises questions about human origins.

BY EWEN CALLAWAY

The ice-age world is starting to look cosmopolitan. While Neanderthals held sway in Europe and modern humans were beginning to populate the globe, another ancient human relative lived in Asia, according to a genome sequence recovered from a finger bone in a cave in southern Siberia. A comparative analysis of the genome with those of modern humans suggests that a trace of this poorly understood strand of hominin lineage survives today, but only in the genes of some Papuans and Pacific islanders.

Named after the cave that yielded the 30,000–50,000-year-old bone, the Denisova nuclear genome follows publication of the same individual's mitochondrial genome in March¹. From that sequence, Svante Pääbo of the Max Planck Institute for Evolutionary Anthropology in Leipzig, Germany, and his colleagues could

tell little, except that the individual, now known to be female, was part of a population long diverged from humans and Neanderthals.

Her approximately 3-billion-letter nuclear genome, reported in this issue of *Nature*², now provides a more telling glimpse into this mysterious group. It also raises previously unimagined questions about its history and relationship to Neanderthals and humans. “The whole story is incredible. It’s like a surprising Christmas present,” says Carlos Lalueza Fox, a palaeogeneticist at Pompeu Fabra University in Barcelona, Spain, who was not involved in the research.

When the ancient genome was compared to a spectrum of modern human populations, a striking relationship emerged. Unlike most groups, Melanesians — inhabitants of Papua New Guinea and islands northeast of Australia — seem to have inherited as much as one-twentieth of their DNA from Denisovan roots. This suggests that after the ancestors of today’s

Papuans split from other human populations and migrated east, they interbred with Denisovans, but precisely when, where and to what extent is unclear.

More answers could come from a closer look at Denisovan, human and even Neanderthal DNA. So far, conclusions about interbreeding have been drawn from a relatively small number of human genomes using conservative DNA-analysis methods, says David Reich, a geneticist at Harvard Medical School in Boston, Massachusetts, who led the Denisova analysis. “There may have been many more interactions,” he says. Pääbo says it may be possible to determine roughly when humans interbred with Denisovans by examining the length of DNA segments lurking in various human genomes, with shorter segments corresponding to more shuffling of genes and a longer elapsed time.

A molar discovered in the same cave also yielded mitochondrial DNA resembling that of the finger bone. But the Denisovans were probably more widespread, says Pääbo. Some fossils from China, for example, resemble neither Neanderthals nor modern humans — nor *Homo erectus*, an earlier human ancestor. Pääbo wonders whether they could be more closely related to Denisovans. His Russian collaborators plan to search for more complete Denisovan fossils that could be matched to others from China.

Chris Stringer, a palaeoanthropologist at London’s Natural History Museum, agrees that Asian fossils, such as the 200,000-year-old Dali skull from central China, could have links to the Denisovans. But he says that firm conclusions about such relationships will have to await the discovery of more complete Denisovan fossils.

Preserved DNA from other Asian fossils would also provide a clearer picture of the Denisovans, which Pääbo, to sidestep controversy, has opted not to call a new species or subspecies of hominin. The challenge will be to make sense of such discoveries and put them in the context of ancient human history, says Lalueza Fox. Palaeoanthropologists are just beginning to scrutinize the Neanderthal genome published earlier this year³ for clues to ancient human history. With the Denisova genome, “they will need to deal with another surprise”, he says. ■

SEE ALSO NEWS & VIEWS P.1044

1. Krause, J. *et al. Nature* **464**, 894–897 (2010).
2. Reich, D. *et al. Nature* **468**, 1053–1060 (2010).
3. Green, R. E. *et al. Science* **328**, 710–722 (2010).


**MORE
ONLINE**

2010 IN REVIEW



Nature looks back at a dramatic year in science
www.nature.com/2010

MORE STORIES

- Emerging nations are best innovators go.nature.com/ovv2qu
- Research in the British military soldiers on go.nature.com/5zcgwy
- Mutation-prediction software rewarded go.nature.com/87uxjq
- Digital book trove go.nature.com/wyevbv

LATEST NEWS



Fruitfly and nematode gene expression mapped
go.nature.com/vv8cmh

FACILITIES

Deep lab denied funding

Divisions within US National Science Foundation throw plans for underground science facility into crisis.

BY EUGENIE SAMUEL REICH

Ambitious plans to build one of the world's deepest underground laboratories have suffered a serious setback. The US National Science Board (NSB) has refused to continue to fund the design of the Deep Underground Science and Engineering Laboratory (DUSEL), leaving some 1,000 researchers hoping to do science there uncertain about its future.

The lab is set to be housed in Homestake, a former goldmine near Lead, South Dakota. The mine is an ideal location for sensitive experiments trying to catch sight of hard-to-detect particles such as neutrinos and dark matter. At almost 2,500 metres deep, it would shield DUSEL from the cosmic rays that would otherwise drown out signals from the lab's elusive targets.

The US National Science Foundation (NSF) and its partners, including the US Department of Energy, have already committed more than \$300 million towards DUSEL, which is expected to cost more than \$800 million in total. But Edward Seidel, assistant director for mathematical and physical sciences at the NSF, says that the \$29 million awarded to the University of California, Berkeley, in 2009 to design and prepare the mine for DUSEL has proved inadequate.

Safety concerns arose earlier this year about the mine shafts that scientists will use to access the facility. It is also proving difficult to pump groundwater from the ageing mine. As funds could not be reallocated from other parts of the project, programme managers this month requested another \$19 million now, with perhaps another \$10 million to come in the spring of 2011, to continue that preparatory work.

But the NSB, which must approve large outlays by the NSF, refused both requests on 2 December. Although the infrastructure for each of the lab's experiments will be managed by an allocated lead agency, the board was concerned by the perceived lack of a clear stewardship plan for the mine's infrastructure, raising the prospect that the NSF could face ballooning costs. Board members also believe that the energy department should contribute more than its current commitment of \$100 million.

"We don't know if this is a glitch or a death knell. I think the users feel like we're in limbo right now," says Steven Elliott, a neutron scientist at Los Alamos National

Laboratory in New Mexico and chairman of the executive committee of the DUSEL Research Association, which represents the researchers who expect to do science at the new lab.

The NSB's decision also exposes internal differences at the NSF about the best way to pay for major science infrastructure projects within a funding system more attuned to supporting research programmes. Although the decision does not mean that the NSF will not build or steward the facility, says Seidel, "it's clear that the current stewardship model will have to change". The DUSEL project team is now talking to all of its partners to formulate a plan to keep preparatory work going.

Much of that work involves designing the experiments that will be lowered into caverns

"It's clear that the current stewardship model will have to change."

near the surface, and 1,500 and 2,300 metres underground. These include the Long Baseline Neutrino Experiment — in which neutrinos will be fired at detectors in DUSEL

from 1,000 kilometres away at Fermilab in Batavia, Illinois, to find out why there is so much more matter than antimatter in our Universe — and LUX, the world's most sensitive search for dark matter. Beyond particle physics, DUSEL is expected to include a broad suite of geophysical and biological experiments, as well as a facility for testing the effects of sequestering carbon dioxide deep underground.

Building the lab would allow the United States to compete effectively with other countries that have underground facilities, such as the Super-Kamiokande neutrino observatory near Hida, Japan. "Here in the United States we are conspicuous in not having a deep underground science lab, in contrast to other countries with large science programmes," says Rick Gaitskell, a particle astrophysicist at Brown University in Providence, Rhode Island, who hopes to use DUSEL.

The Homestake mine currently houses the Sanford Underground Laboratory, which hosts smaller-scale versions of experiments intended for DUSEL. The additional funding is needed in part to transition the operations of this lab into the planned construction of DUSEL. The lab has enough funding to maintain the mine until May 2011, says its spokesman, Bill Harlan. A final NSF decision on whether to go ahead with DUSEL was expected in 2011, but may now be delayed. ■

► NATURE.COM
For a longer version
of this story, see:
go.nature.com/8p2try

2010: the year in which ...

BY ADAM MANN



REUTERS/A. SOOMRO

In a year marked by environmental disasters, Pakistan was perhaps hardest hit, as a flood affected an estimated 20 million people.

Natural disasters pummelled Earth

In January, a magnitude-7.0 earthquake struck Haiti — the most violent such event to strike the impoverished nation in a century. An estimated 230,000 people died and a further 1 million were left homeless. Other earthquakes, including a magnitude-8.8 quake in Chile in February and a magnitude 7.1 in New Zealand in September, also caused widespread damage, but smaller death tolls. Ash from the eruption of volcano Eyjafjallajökull in Iceland grounded commercial flights across Europe for a week in April, stranding thousands of travellers (see 'Quotes of the year'). And unusually intense rains related to the La Niña cooling of the Pacific Ocean flooded one-fifth of Pakistan and affected an estimated 20 million people. The weather pattern was also implicated in a drought in Russia as the country experienced the hottest summer in its recorded history, unleashing hundreds of deadly wildfires.

Ancient kissing cousins were found

Two reports suggested that modern man carries genes from extinct branches of the human family tree. The question of whether Neanderthals, which went extinct about 30,000 years ago, ever mated with humans had been hotly debated, but evidence had been sparse. Even the sequencing of the Neanderthal genome in 2009 provided no definitive evidence. On 7 May, researchers announced the results of a genetic analysis of nearly

➔ NATURE.COM
Read *Nature's*
special section
reviewing the year.
www.nature.com/2010

2,000 people from around the world, which yielded signs of gene flow between Neanderthals and *Homo sapiens* around the time that modern humans first migrated out of Africa some 50,000–60,000 years ago. Evidence of more recent mixing appears in this issue of *Nature*. A genome extracted from a 30,000–50,000 year-old finger bone found in a Siberian cave not only attests to the existence of another hominin group, but suggests that the group interbred with a particular band of human migrants that were ancestors of today's Melanesians. [SEE PP.1012, 1044 & 1053](#)

Doctors gained new weapons against HIV

In July, researchers revealed that an antiretroviral microbicide gel cut HIV infection by up to 54% in women who used it regularly. The findings, which came from a study of about 900 South African women at high risk of infection, gave hope to those seeking to bring down the rate of HIV infection in sub-Saharan Africa, where the majority of new cases occur. Another breakthrough came in November, when a study of nearly 2,500 men showed that the antiretroviral drug Truvada is an effective preventative measure. Among men who have sex with men, those who took the drug consistently lowered their risk of acquiring the virus by 73%.

Scientists unveiled a synthetic genome

In a bold step towards designer life, researchers at the J. Craig Venter Institute in Rockville, Maryland, announced on 20 May that an artificial genome inserted into a bacterium had successfully commandeered the cell and commenced replication. Using the genome from the bacterium

Mycoplasma mycoides as a blueprint, Daniel Gibson and his colleagues at the institute assembled their synthetic genome in a yeast cell and transplanted it into the closely related species *Mycoplasma capricolum*. Although the 1.1-million-base-pair sequence was a near duplicate of *M. mycoides*, it included four special 'watermark sequences' to distinguish it from the original, as well as a hidden code that, once deciphered, included a website address and several famous quotes. Some researchers considered the move to be a significant advance over conventional genetic engineering, although others argued that scientists are a long way from being able to design and construct novel bacteria from scratch. If the technology advances sufficiently, many hope that artificial life can be used for a variety of tasks, including carbon sequestration, biofuel production or the clean-up of chemicals.

Oil gushed into the Gulf of Mexico

On 20 April, an explosion on BP's Deepwater Horizon oil rig killed 11 workers and precipitated one of the worst oil spills in history. By August, the damaged well had dumped nearly 5 million barrels of oil into the Gulf of Mexico, spewing as much as 62,000 barrels a day at its peak. Engineers capped the well on 15 July, although it was not permanently sealed with cement until 19 September. During the spill, researchers detected large plumes of oil below the water's surface. In its aftermath, debate continued over where all the oil had gone. An estimate released by the US National Oceanic and Atmospheric Administration, which suggested that about half of the oil had dispersed, dissolved or evaporated, was roundly criticized as too optimistic. Later, researchers discovered a layer of precipitated oil on the sea floor. [SEE P. 1024](#)

Climate-change policy stalled

Efforts to confront climate change stumbled early on, but finished the year on a positive note. In January, the Intergovernmental Panel on Climate Change, chaired by Rajendra Pachauri, was embarrassed to learn that a 2007 report had erred when it stated that all glaciers in the central and eastern Himalayas could melt by 2035. The claim had not come from peer-reviewed scientific literature, but from a comment by Indian glaciologist Syed Hasnain in a 1999 article in *New Scientist*, and the mistake provided fodder for climate-change sceptics. Over the summer, three US senators — John Kerry (Democrat, Massachusetts), Joseph Lieberman (Independent, Connecticut) and Lindsey Graham (Republican, South Carolina) — failed to push through a bill that would have instituted a cap-and-trade system for domestic industry's carbon emissions, even though the House of Representatives had approved a similar bill. The end-of-the-year United Nations Framework Convention on ►

Quotes of the year

"The first self-replicating species we've had on the planet whose parent is a computer."

Craig Venter describes the artificial bacterium created at his lab.
Source: New York Times

"If we can turn the oil into smoke, we'll all be happy."

Ed Levine, National Oceanic and Atmospheric Administration scientific support coordinator for the Deepwater Horizon spill effort, on burning the oil in open water before it reaches land.
Source: Nature

"When I got the telephone call, I thought, 'Oh shit!' The second thought that came to my mind: 'Oh dear, I will not win many more prizes.'"

Andre Geim describes how he felt after learning he would share this year's Nobel Prize in Physics.
Source: Nature's *The Great Beyond* blog

"My own personal feeling is that the chances of life on this planet are 100%."

Astronomer Steven Vogt on his team's discovery of an extrasolar planet orbiting in the 'habitable zone' of the star Gliese 581. Other scientists have been unable to find evidence for the planet.
Source: Daily Telegraph

"We checked every option, but there were no boats and no train tickets available. That's when my fabulous assistant determined the easiest thing would be to take a taxi."

Comedian John Cleese, who made the journey from Oslo to Brussels following the eruption of Eyjafjallajökull in said taxi, at a cost of 30,000 Norwegian kroner (US\$5,000).
Source: Sky News Online

"There might be some interesting application, but frankly I don't have one now."

Physicist Andrew Cleland speaks about placing a 30-micrometre mechanical paddle into a superposition of quantum mechanical states so that it was simultaneously vibrating and not vibrating.
Source: Nature

"They have managed to reach an agreement by moving the goalposts closer to the ball."

David Victor, director of the Laboratory on International Law and Regulation at the University of California, San Diego, discusses the international climate agreement reached in Cancún.
Source: Nature

M. VILLAGRAN/GETTY IMAGES



Rajendra Pachauri felt the heat in 2010.

► Climate Change meeting in Cancún, Mexico, brought some good news when participants agreed to set a goal of limiting average warming to 2°C above preindustrial levels. Building on the ultimately unsuccessful Copenhagen Accord from last year, countries also created an international tracking system to report progress on lowering emissions.

Japan's space agency had a hit and a miss

On 16 November, researchers confirmed that micrometre-sized grains found in the Japan Aerospace Exploration Agency's Hayabusa spacecraft were authentic asteroid dust. The mission, which gently kissed the surface of the Itokawa asteroid twice in November 2005, is the first to retrieve asteroidal material and return it to Earth for study. A month later the agency experienced a setback when its Akatsuki spacecraft failed to enter orbit around Venus, instead sailing past the planet into interplanetary space. Akatsuki, which would have mapped Venus using infrared cameras that can peer beneath its dense cloud layer and search for evidence of recent volcanic activity, will have to orbit the Sun and wait six more years for another try.

Stem-cell research rode a roller coaster

US scientists were jolted on 23 August when federal district court judge Royce Lamberth placed an injunction on federally funded human embryonic stem-cell research. The move also overrode the March 2009 executive order of US President Barack Obama mandating the National Institutes of Health to develop a policy for the approval of new stem-cell lines, which had been prohibited under the administration of George W. Bush. The injunction was to remain in force until Judge Lamberth decided whether the research violates the Dickey-Wicker Amendment, which prohibits the destruction of human embryos in research. But on 9 September, the US Court of Appeals for the District of Columbia Circuit issued a stay on the injunction, allowing federal funding to continue until the court rules on whether Lamberth's injunction should stand. Some federal stem-cell research resumed, but scientists are braced for more setbacks. Unless federal law is changed, many say the argument will ultimately find its way to the Supreme Court.

Astronomers joined the dark side

In August, US astronomers released the Astro2010 Decadal Survey, a highly influential document that, once every ten years, recommends which astronomy and astrophysics projects NASA, the National Science Foundation and the Department of Energy should fund. Acknowledging the prospect of budget cuts during the economic downturn, the report recommended a few large, expensive projects — such as the US\$1.6-billion Wide Field Infrared Survey Telescope (WFIRST), a 1.5-metre space-based instrument that could investigate dark energy, the mysterious phenomenon that is causing the expansion of the Universe to accelerate. But November brought unwelcome news: a report commissioned by Senator Barbara Mikulski (Democrat, Maryland) concluded that the 6.5-metre James Webb Space Telescope, successor to the Hubble, would come in at least \$1.5 billion over budget and would be delayed for more than a year. This implicit expected drain on NASA's budget leaves funding for WFIRST an open question.

The budget crunch hit European science

Austerity measures across many European countries stricken by the financial crisis took a toll on scientists. The five member states contributing to CERN, Europe's particle-physics laboratory near Geneva, Switzerland, approved a plan in September to reduce contributions by



AP PHOTO/JANA

A Japanese capsule bearing asteroidal dust is recovered in Australia.

about \$140 million over the next five years and to slow down the pace of smaller research projects to protect the lab's flagship Large Hadron Collider, the world's largest particle accelerator. And Italy and Britain said they will temporarily reduce their contributions to the European Synchrotron Radiation Facility in Grenoble, France. Other countries, looking to slash their budgets, announced freezes or reductions in scientific investments; for example, the Spanish government's expenditure in research and development will drop by 8.37% next year. In October, UK scientists fought back against the funding cuts, rallying to protest in London. Eventually, the British government decided not to reduce science spending and agreed to protect the £4.6 billion (US\$7.3 billion) core science budget over the next four years. **SEE P. 1010**

Arsenic-based life was discovered. Or not.

A cryptic announcement from NASA in November said that the agency had important astrobiology news, leading many to speculate that it was set to unveil extraterrestrial life. Instead, during a media conference on 2 December, researchers announced the discovery of ordinary earthly bacteria from Mono Lake in California that seemed to do something extraordinary — use arsenic as a building block for DNA and proteins, in place of the phosphorus relied on by other organisms. But as soon as the unprecedented finding was made public, it drew sharp criticism from the scientific community. Biochemists took to the blogosphere, attacking the methodology and assumptions of the original research and provoking a flurry of articles in the media. Further work will be needed to settle whether the bacteria actually do use arsenic in their biochemistry as opposed to just cleverly thwarting its toxic effects.

A morality expert was accused of mischief

In August, Harvard University found that Marc Hauser, a leader in the field of animal and human cognition, had committed eight counts of scientific misconduct. Hauser studies the evolutionary origin of characteristics such as morality, language and mathematical ability, and his work has been profiled in many news outlets, such as *The New York Times* and the *Wall Street Journal*. Many scientists in the field called on Harvard to release the details of its investigation, saying that they could affect any research that uses Hauser's as a basis. As yet, Harvard has not done this. Hauser has retracted or amended at least three papers, which appeared in *Cognition*, *Proceedings of the Royal Society and Science*, respectively.

In the **EYE** *of the* **STORM**

She set out to revolutionize US ocean management — but first she faced the oil spill. Jane Lubchenco is Nature's Newsmaker of the Year.

BY RICHARD MONASTERSKY

Jane Lubchenco smiles as a dolphin leaps out of the water, arcs in the air and splashes back down just a few metres away. The 63-year-old marine ecologist is out on a boat near Pascagoula, Mississippi, with a team of researchers studying how the recent oil spill in the Gulf of Mexico has affected dolphin communities there.

On this October day, Lubchenco wears starfish-shaped earrings and a cap emblazoned with the letters 'NOAA', for National Oceanic and Atmospheric Administration. Her shirt sports a NOAA logo, as does her life vest. Rarely does she venture out in public without some symbol of the US government agency she has proudly run since March 2009. A sprawling department of 12,800 people with a budget of US\$4.7 billion, NOAA has responsibilities stretching from the bottom of the sea to the top of the atmosphere and even to the Sun, which it monitors for signs of solar storms. That mandate put Lubchenco at the centre of the government's response to the BP Deepwater Horizon oil-spill disaster — a brutal test for a scientist with little previous management experience.

On board the boat, she relishes the chance to talk about dolphin behaviour with the NOAA researchers, but seems to get the biggest kick when the pilot gives her a turn at the wheel. Gripping the throttle, Lubchenco has to be reminded to stay below the speed limit as she motors through the narrow waterway.

Going slow does not come easily to the NOAA leader. As a celebrated scientist and vocal conservationist, she made her name urging other researchers to speak out on issues of public importance, a stance that not all of her academic colleagues were comfortable with. Now, at an age when many of her cohort are easing back, she is taking on the most ambitious challenge of her career: reorienting how the nation responds to pressing environmental problems such as dwindling fish stocks, rising seas and a changing climate. She has bold plans to strengthen scientific research at NOAA, make it more relevant to society and improve the health of ecosystems and coastal communities.

But the path has not been smooth for Lubchenco, who took over the

**Lubchenco
testifies at a
Senate hearing
on the Deepwater
Horizon oil spill.**

agency in troubled times. With the economy in a nose dive and many coastal communities struggling, NOAA's policies to limit fishing have proved so contentious that members of US President Barack Obama's own party called for Lubchenco to resign. And the oil-spill disaster has severely tested her political skills. Some of her natural constituency — scientists and environmentalists — have accused her of quashing independent researchers, suppressing information and misleading the public.

Although she admits to some communications problems during the crisis, Lubchenco shakes off the broader criticisms. "I'm very proud of what we did during the heat of the moment," she says. NOAA closed down fisheries, forecast where currents would sweep the oil, monitored storms during one of the most active hurricane seasons on record, protected endangered marine species and is leading the effort to assess damage done by the oil. "I give her very high marks as a leader in what has been a difficult time for NOAA," says Michael Jackson, who was deputy director of the US



A. WONG/GETTY IMAGES



Department of Homeland Security in 2005, during Hurricane Katrina.

Throughout this day on the Gulf of Mexico, Lubchenco keeps up a hectic pace, visiting multiple sites in the Alabama and Mississippi area. This is her eleventh trip to the Gulf of Mexico region since the Deepwater Horizon oil rig exploded on 20 April, unleashing the largest single marine spill in US history.

In person, Lubchenco makes an easy connection with strangers. She looks them in the eye and asks about their jobs and how the spill affected them. Before lunch, she meets more than two dozen teachers from across the Gulf and starts by telling them how much she appreciates their work. “My sister is a middle-school science teacher. My daughter-in-law is a high-school science teacher, and I was strongly affected by teachers,” she says.

The teachers introduce themselves and talk about how the spill touched their students, many of whose parents were put out of work when the spreading oil closed fishing grounds and drove away tourists. The teachers thank

Lubchenco for all the information that NOAA posted on its website, which their classes used to find out which fishing areas were closed, where the winds were going and whether currents would carry the oil out of the Gulf. “We would check your site every day,” said one teacher. “We used so much of that data.”

CRISIS MANAGEMENT

With the well capped and the oil dispersing, Lubchenco has entered calmer waters after the tumultuous spring and summer of the crisis. She was one of the ‘principals’ — the top administration officials working on the spill, who regularly briefed President Obama and rarely rested. Two weeks after the rig exploded, she ran into an old friend at a party in Washington.

“Jane, you look really tired,” he told her.

“Yeah, I’m sleeping three or four hours a night,” she confided to him.

Such was the toll of running the lead ocean agency during one of the biggest environmental disasters in US history. The task was

complicated by a series of communications missteps, her own and those of other officials, which drew accusations that she had withheld information about the environmental toll of the spill.

The first flashpoint was the question of how much oil was leaking from the wellhead and where it was going. Days after the spill, when BP was estimating that 1,000 barrels of oil were pouring out each day, a NOAA researcher arrived at a far higher figure of 5,000–10,000 barrels — a “very rough estimate”, his e-mail warned. But that was not released to the public. Instead, a Coast Guard admiral in charge of responding to the spill said in a press conference on 28 April that “NOAA experts believe the output could be as much as 5,000 barrels”.

That figure stood as the sole government estimate for a month. At the same time, independent researchers came up with estimates in the range of 25,000–100,000 barrels a day. Months later, the government concluded that the well had gushed 62,000 barrels a day initially and then declined to 53,000 (a figure

that BP contends is too high).

Other issues also suggested to some that NOAA and the rest of the government were downplaying the magnitude of the problem. In mid-May, academic scientists working in the Gulf started finding evidence that untold amounts of oil were spreading away from the wellhead and forming vast plumes some 1,200 metres below the surface¹. NOAA initially questioned the evidence and dismissed media reports as “misleading”, even as more evidence emerged. Donald Boesch, president of the University of Maryland Center for Environmental Science in Cambridge and a member of a commission that subsequently reviewed the government’s response, says that was a mistake. “Jane was too dismissive about the fact that there could be a significant deep-water plume there,” he says. On 8 June, after analysis of more data collected by academic scientists, NOAA acknowledged the presence of diffuse plumes of oil beneath the surface.

THE FATE OF THE OIL

On 15 July, BP finally succeeded in capping the well, but there were still major questions about what had happened to all the oil that had escaped over the past three months. In early August, NOAA and other agencies released an ‘oil budget’, which tallied the fate of all the released oil. Carol Browner, director of the White House Office of Energy and Climate Change Policy, announced on television that three-quarters of the oil was “gone”. But that did not match the government’s own numbers.

Later that day, Lubchenco appeared with Browner at a White House press conference and corrected the record. “It’s important to point out that at least 50% of the oil that was released is now completely gone from the system,” said Lubchenco. Illustrating her statistics with a pie chart produced by NOAA and other agencies, Lubchenco said that containment efforts had removed roughly a quarter of the oil and another quarter had either evaporated or dissolved. The rest had dispersed as tiny subsurface droplets or as visible oil, and some of that had been collected from beaches or naturally degraded.

But in making that correction, Lubchenco made a different mistake by saying that the oil budget had been “peer reviewed”, a statement at odds with the reports of scientists who supposedly reviewed it. Academics and members of Congress also criticized NOAA’s decision to release the four-page oil budget without uncertainty ranges or the background data that justified the conclusions.

Reacting to the series of gaffes, the national commission investigating the oil spill declared in October that “the federal government created the impression that it was either not fully competent to handle the spill or not fully candid with the American people about the scope of the problem”. At the very least, those issues undermined the public’s trust in the

government, said the commission.

For Lubchenco, the judgement was both troubling and ironic. Given her record of urging scientists to speak out, she says, “I would be the last person in the world to be not valuing or promoting communication”. She says that she initially balked at the 5,000-barrel-a-day flow-rate statement. “My inclination was to correct the record, but in the grand scheme of things, since we didn’t have the accurate numbers and we were working on getting them, it didn’t seem to be that important relative to all the other stuff that was going on.” Knowing how much oil was flowing would not have helped the effort to contain it, she argues — an assertion challenged by the oil-spill commission, which says that knowledge of the true flow rate might have helped BP to avoid some problems in its attempts to cap the well. “In hindsight,” says Lubchenco, “it took far too long to come up with the eventual answer.”

During a press conference in November, she also acknowledged that she had erred in declaring that the oil budget had been peer reviewed. In a subsequent interview, she took personal responsibility for the miscommunication. “I misunderstood what kind of review it had had, so that was my mistake,” she said.

But Lubchenco defends her agency’s statements about the subsurface plumes, saying that NOAA was just insisting on careful science. “It’s frustrating to get crosswise with my academic colleagues when we thought all we were asking them to do was to be good scientists and to double check and make sure that what they were finding was in fact what they thought it was.”

Some scientists are still bothered by NOAA’s slow acknowledgement of the deep oil, but others



The Deepwater Horizon disaster posed a brutal test for a scientist with little previous management experience.

agree with her approach. “There was a lot of speculation early on,” says Richard Camilli of the Woods Hole Oceanographic Institution in Massachusetts, who led a cruise that uncovered signs of a deep plume of oil in June. “Good science requires peer review. If you’re going to say something public it should go through peer review first,” says Camilli, who published his findings in *Science* in August².

Many scientists laud NOAA’s overall performance during the spill. Boesch, although critical of Lubchenco’s initial response to reports of deep plumes, says that she and NOAA provided “very critical science support to help direct the spill response where it was needed”. And he praises the agency for doing something that gets little mention — successfully keeping the nation’s seafood safe by closing fishing areas and reopening them only after rigorous testing. “That protected the public,” he says, “and in the long run protected the industry.”

DEFYING EXPECTATIONS

By late October, the sheen of oil had disappeared from the surface of the Gulf and NOAA had shifted towards assessing the damage. “It’s far from over,” says Lubchenco. “It’s going to be years, if not decades, before we really understand the impact this massive infusion of hydrocarbons has had on this system.”

In Mississippi Sound earlier that day, Lubchenco relished the chance to spend part of her weekend on the water. As a scientist, she has studied ocean ecosystems for 40 years — an unlikely focus for a girl growing up in the 1950s in Denver, Colorado, in the middle of the continent. But the women in the Lubchenco family

C. COLE / POLARIS/EVERETT

have long challenged expectations.

In the early 1900s, her paternal grandmother left her parents' cotton farm in South Carolina to train in medicine, only to find that the dean of one of the nearest medical schools, in North Carolina, would not accept a woman. She finally wore him down, became the first female graduate in 1912 and then married a Ukrainian agricultural researcher who had visited her family's farm years earlier. (He narrowly made it to her graduation ceremony, after having missed the steamer he had originally booked to America — the *Titanic*.)

Lubchenco's parents were also doctors, and her mother worked part-time so that she could have a career and raise her six girls. In that household, everybody was expected to follow their interests. "Mom and Dad were always great about encouraging us to explore. Of the six of us, we all do completely different things," says Lubchenco.

In secondary school, young Jane was a classic overachiever: an athlete, scholar and leader, she won the school's highest award. But rather than go to a powerhouse university, she chose tiny Colorado College in Colorado Springs and enrolled in an unusual programme with no classes, no grades and no tests. She discovered that she liked biology and took a summer class at the Marine Biological Laboratory in Woods Hole, Massachusetts, where she fell in love — with invertebrates and research. "That whole summer was magical for me," she recalls. "It made me decide I was going to go to grad school and it was going to be marine science."

After getting her PhD at Harvard University in Cambridge, Massachusetts, and teaching there for two years, Lubchenco took what some considered a step down by moving to Oregon State University in Corvallis, where she and her husband, ecologist Bruce Menge, bargained to split an academic position. It was perhaps a first in the United States, and it gave them both a chance to teach, conduct research and raise their children. The two also split their research on tidal communities, with Lubchenco studying the herbivores and seaweeds and Menge the predators and prey.

At the time, ecology was largely a descriptive science, but Lubchenco was part of a group pushing to introduce experimental approaches. In graduate school, she started moving herbivorous snails around tide pools to tease apart the factors controlling the distribution of seaweeds.

Most researchers had assumed the answer had to do with physical limitations, such as how much a tide pool dries out. But Lubchenco demonstrated that the herbivores had an important role in controlling the plant populations³ — a finding that also turned out to be true in some terrestrial ecosystems. Her simple, elegant experiments became a staple in ecology courses, and her papers garnered hundreds of citations.

Lubchenco also made a name for herself by urging fellow ecologists to speak out on environmental issues. As vice-president of the Ecological Society of America in 1988–89, she chaired a panel that called for ecologists to

communicate to the public and policy-makers. "It was a coming of age for our society, to admit that relevance was not a four-letter word," recalls Lubchenco (see page 1032). Later, while serving as president of the American Association for the Advancement of Science — the premier scientific organization in the United States — in 1996–97, she continued to push scientists to become more socially relevant.

Now she has a chance to bolster science and its connection to policy-making at the highest level. NOAA has a long history of conducting some top-notch science and has nurtured pioneering researchers such as ozone specialist Susan Solomon and climate modeller Syukuro Manabe. But it has been perpetually strapped for cash, and previous administrations have at times focused less on the science than on the divisions that provide services, such as forecasting weather and managing fisheries.

When Lubchenco discussed the NOAA post with Obama soon after he was elected in 2008, she told him that one of her goals would be to renew that commitment to science. Obama's response to this proposal and others that she made, she says, was "let's do it".

Once she took office, Lubchenco set out to resurrect the chief-scientist position at NOAA, which has been vacant for 14 years. But she got a lesson in the slow ways of Washington. Much to her frustration, it took months for the Obama administration to approve her choice, Scott Doney of the Woods Hole Oceanographic Institution, and

A global reach

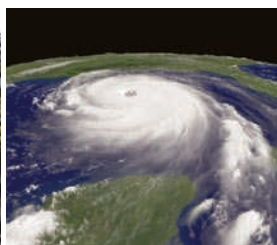
The mandate of the National Oceanic and Atmospheric Administration (NOAA) reaches from space to the sea floor. It faces challenges on all fronts.



THE NATIONAL MARINE FISHERIES SERVICE (NMFS)

What it does: Manages marine life and habitat in US federal waters, up to 370 kilometres offshore.

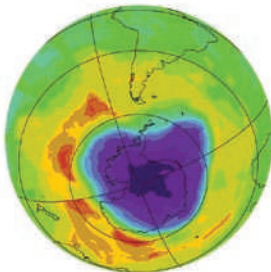
Challenge: Ending overfishing for depleted stocks by 2010 and setting catch limits for all others by 2011.



THE NATIONAL ENVIRONMENTAL, SATELLITE, AND DATA INFORMATION SERVICE (NESDIS)

What it does: Manages environmental satellites and disseminates data.

Challenge: Sorting out a satellite programme that was years late and billions of dollars over budget.



THE OFFICE OF OCEANIC AND ATMOSPHERIC RESEARCH (OAR)

What it does: Research to support services such as climate modelling and weather forecasting.

Challenge: The new Climate Service will absorb parts of OAR, which will have to reorient.



THE NATIONAL WEATHER SERVICE (NWS)

What it does: Provides forecasts and warnings for weather and climate.

Challenge: Monitoring the 2010 hurricane season, one of the most active on record, with 19 named storms, 12 hurricanes and 5 major hurricanes.



THE NATIONAL OCEAN SERVICE (NOS)

What it does: Oversees many non-fisheries aspects of marine areas, including water quality.

Challenge: Tracking the oil and assessing environmental damage from the 2010 oil spill in the Gulf of Mexico.

a senator this month put a block on Doney's nomination to protest against the administration's moratorium on offshore drilling. In the meantime, Lubchenco has increased the number of senior scientific positions at NOAA from 10 to 25, and altered the career structure within the agency so that scientists can advance in seniority and salary without having to leave research for a purely management position.

Lubchenco has made significant progress on her other priorities, say many who have watched NOAA under her leadership. "She's done the job certainly as well — and I would argue better — than anyone else," says Andrew Rosenberg, a senior vice-president at Conservation International and deputy director of NOAA's fisheries service from 1998 to 2000.

When Lubchenco arrived in Washington, one of the first problems she had to tackle was the National Polar-orbiting Operational Environmental Satellite System (NPOESS). Designed to collect weather and climate data, it was running years late and more than \$5 billion over budget. Lubchenco and her colleagues in the administration developed a plan to split the unwieldy system into a military part and a civilian part to be jointly managed by NOAA and NASA — a step that could finally get the NPOESS back on track.

Lubchenco has also pushed forward an initiative to create a NOAA division called the Climate Service, which the agency had been discussing since just after it was founded in 1970. The goal is to gather NOAA's decentralized climate expertise into a single office to enhance the science and provide an authoritative voice on climate information. The biggest reorganization in NOAA's history, this office — which awaits congressional approval — will give the public and businesses forecasts such as long-term temperature projections and flooding maps that take into account sea-level rise.

FISHING WOES

For environmentalists, one of the biggest successes of Lubchenco's tenure so far has been the administration's new ocean policy, which Obama signed on 19 July. A centrepiece of the policy is a strategy — long championed by Lubchenco — called coastal and marine spatial planning, which seeks to assess and balance human activities in particular ocean regions so that they do not conflict with each other or harm ecosystems. In the past, the government has tended to manage activities such as fishing individually, without considering how other factors, such as oil drilling and coastal development, might interact with them.

"What Jane has done is catalysed the most important transformation in ocean

management in our history," says Elliot Norse, president of the Marine Biology Conservation Institute in Bellevue, Washington.

All that change has brought some strong criticism, especially from the fishing industry. Under her leadership, NOAA has moved to implement the 2007 Magnuson–Stevens Reauthorization Act, which requires the agency to end overfishing. NOAA's actions so upset some fishermen in Gloucester, Massachusetts, that they built a life-sized model of Lubchenco hanging fishermen. The rhetoric in Congress, with the calls for her resignation, was only slightly less inflamed.

The source of the strife in New England goes back long before Lubchenco took office. Oversight of fishing in US federal waters is complicated; NOAA shares management duties with eight regional councils made up of federal and state government officials and members of the public, including the fishing



Jane Lubchenco and her husband, Bruce Menge, with students in 1997.

industry. The councils choose how they want to control fishing and propose annual limits on each type of seafood. NOAA assesses the plans and then approves or rejects them.

In the past, NOAA had given management councils more latitude, but when Lubchenco took office, she made it clear that she expected them to meet the congressional deadline to end overfishing by this year. As part of that, NOAA last year encouraged the councils to consider a strategy called catch shares. In this scheme, councils allocate fishing 'shares' to individuals or groups, usually on the basis of how much they have previously caught. The recipients of shares can use or sell them. Proponents say that catch shares give fishing communities a long-term economic incentive to rebuild stocks.

Although the strategy has been used around the world and in parts of the United States for decades, the transition to a catch-shares system can be difficult. "It has to be done very carefully. It has to involve the community, from the bottom up," says Brian Rothschild, a professor of marine science at the University of Massachusetts at Dartmouth who has close ties to

the New England fishing community. He contends that NOAA and the New England Fishery Management Council moved too quickly in May to implement a programme based on catch shares, without properly involving the local fishing community or explaining the system. Some fishing communities say that the policy has caused major job losses.

Lubchenco and others argue that New England's policy was five years in the making and the community had ample time to get involved. They also contend that fishermen in the area have been struggling economically for years — long before the management council adopted the new programme. "The reality is that this isn't about catch shares," says Lubchenco. "It really is about the economy."

Peter Baker, manager of the Pew Environment Group's New England overfishing campaign, agrees. He says that Lubchenco "has taken a stand to fix things for the future".

Those who have criticized her policy have not offered a viable alternative, he says. "I'm not sure that anything would be enough to appease her detractors."

As difficult as this year has been for Lubchenco, the next few will offer further challenges. NOAA's budget increased by 21% during the past two years, but Obama and Congress are now committed to cutting spending and the outlook for NOAA is bleak. The agency has never enjoyed the same support in Congress as some other science agencies, such as the National Institutes of Health. But Lubchenco thinks that the recent crises deliver a message on the value of NOAA's research and science-based management. "It seems NOAA's relevancy has been more obvious in the last couple of years," she says.

Nowhere is that clearer than out on the Gulf of Mexico, where signs of dead coral and other long-lasting effects of the oil spill are starting to appear. While travelling through the region, Lubchenco recalls that she turned down Obama's transition team several times when she was first offered the job. Leaving her husband and research behind in Oregon seemed too big a sacrifice. But in the end, she says, she believed in the new president and in the opportunity to achieve her lifelong goals. "I came to NOAA to lead and enable change where it would make a difference," she later explained. The rough days so far have not discouraged her. "Meaningful change is not for the timid." ■ SEE EDITORIAL P.1002

Richard Monastersky is a features editor with *Nature* in Washington DC.

1. Schrope, M. *Nature* **466**, 680–684 (2010).
2. Camilli, R. *et al. Science* **330**, 201–204 (2010).
3. Lubchenco, J. *Ecology* **64**, 1116–1123 (1983).

COMMENT

CONSERVATION Threats to Adélie penguins assessed **p.1034**

MATHEMATICS Roger Penrose reflects on 50 years and 6 volumes of work **p.1039**

REVIEWING Pool of peers grows to cope with submissions surge **p.1041**

OBITUARY Brian Marsden, keeper of comets, remembered **p.1042**



A UK crop circle, created by activists to signify uncertainty over where genetic contamination can occur.

Keep it complex

When knowledge is uncertain, experts should avoid pressures to simplify their advice. Render decision-makers accountable for decisions, says **Andy Stirling**.

Worldwide and across many fields, there lurks a hidden assumption about how scientific expertise can best serve society. Expert advice is often thought most useful to policy when it is presented as a single 'definitive' interpretation. Even when experts acknowledge uncertainty, they tend to do so in ways that reduce unknowns to measurable 'risk'. In this way, policy-makers are encouraged to pursue (and claim) 'science-based' decisions. It is also not uncommon for senior scientists to assert that there is no alternative to some scientifically contestable policy. After years researching — and participating in — science advisory processes, I have come to the conclusion that this practice is misguided.

An overly narrow focus on risk is an inadequate response to incomplete knowledge. It leaves science advice vulnerable to the social dynamics of groups — and to manipulation by political pressures seeking legitimacy, justification and blame management. When the intrinsically plural, conditional nature of knowledge is recognized, I believe that science advice can become more rigorous, robust and democratically accountable.

A rigorous definition of uncertainty can be traced back to the twentieth-century economist Frank Knight¹. For Knight, "a measurable uncertainty, or 'risk' proper ... is so far different from an unmeasurable one that it is not in effect an uncertainty at all". This is not just a matter of words, or even methods. The stakes are potentially much higher. A preoccupation with assessing risk means that policy-makers are denied exposure to dissenting interpretations and the possibility of downright surprise.

Of course, no-one can reliably foresee the unpredictable, but there are lessons to be learned from past mistakes. For example, the belated recognition that seemingly inert and benign halogenated hydrocarbons were interfering with the ozone layer. Or the slowness to acknowledge the possibility of novel transmission mechanisms for spongiform encephalopathies, in animal breeding and in the food chain. In the early stages, these sources of harm were not formally characterized as possible risks — they were 'early warnings' offered by dissenting voices. Policy recommendations that miss such warnings court overconfidence and error.

The question is how to move away ▶

G. GRAF/GREENPEACE

► from this narrow focus on risk to broader and deeper understandings of incomplete knowledge. Many practical quantitative and qualitative methods already exist (see ‘Uncertainty matrix’), but political pressure and expert practice often prevent them being used to their full potential. Choosing between these methods requires a more rigorous approach to assessing incomplete knowledge, avoiding the temptation to treat every problem as a risk nail, to be reduced by a probabilistic hammer. Instead, experts should pay more attention to neglected areas of uncertainty (in Knight’s strict sense) as well as to deeper challenges of ambiguity and ignorance². For policy-making purposes, the main difference between the ‘risk’ methods shown in the matrix and the rest is that the others discourage single ‘definitive’ policy interpretations.

ANY JUSTIFICATION

There are still times when ‘risk-based’ techniques are appropriate and can yield important information for policy. This can be so for consumer products in normal use, general road or airline-safety statistics, or the epidemiology of familiar diseases. Yet even in these seemingly familiar and straightforward areas, unforeseen possibilities, and over-reliance on aggregation, can undermine probabilistic assessments. There is a need for humility about science-based decisions.

For example, consider the risk assessment of energy technologies. The other graphic (see ‘The perils of ‘science-based’ advice’) summarizes 63 studies on the economic costs arising from health and environmental impacts of different sets of energy technologies. The aim of the studies is to help policy-makers identify the options that are likely to have the lowest impact. This is one of the most sophisticated and mature fields for quantitative risk-based comparisons. Individual policy reports commonly express their findings as if there were little room for doubt. Many of the studies present no — or tiny — uncertainty ranges. But taken together, these 63 studies tell a very different story³ — one usually hidden from policy-makers. The discrepancies between equally authoritative, peer-reviewed studies span many orders of magnitude, and the overlapping uncertainty ranges can support almost any ranking order of technologies, justifying almost any policy decision as science based.

This is not just a problem with quantitative analysis. Qualitative science advice is also usually presented in aggregated and consensual form: there is always pressure on expert committees to reach a ‘consensus’ opinion. This raises profound questions over

what is most accurate and useful for policy. Is it a picture asserting an apparent consensus, even where one does not exist? Or would it be more helpful to set out a measured array of contrasting specialist views, explaining underlying reasons for different interpretations of the evidence? Whatever the political pressures for the former, surely the latter is more consistent both with scientific rigour and with democratic accountability?

I believe that the answer lies in supporting more plural and conditional methods for science advice (the non-risk quadrants shown in ‘Uncertainty matrix’). These are plural because they even-handedly illuminate a variety of alternative reasonable interpretations. And conditional because they explore explicitly for each alternative, the associated questions, assumptions, values or intentions⁴. Under Knightian uncertainty, for instance, pessimistic and optimistic interpretations can be treated separately, each explicitly associated with assumptions, disciplines, values or interests so that these can be clearly appraised. It reminds experts that absence of evidence of harm is not the same as evidence of absence of harm. It also allows scenario analysis and the consideration of

process as a “two-way dialogue” — with a priority placed on public accountability. Great care is taken to inform the committee, not just of the results of formal analysis by the sponsoring bodies, but also of complex real-world conditions and perspectives. Reports detail contrasting recommendations by individual members and explain reasons for differences⁶. Why is this kind of thing not normal in science advice?

When scientists are faced with unmeasurable uncertainties, it is much more usual for a committee to spend hours negotiating a single interpretation across a spread of contending contexts, analyses and judgements. From my own experiences of standard-setting for toxic substances, it would often be more accurate and useful to accept these divergent expert interpretations and focus instead on documenting the reasons. In my view, concrete policy decisions could still be made — and possibly more efficiently. Moreover, the relationship between the decision and the available science would be clearer and the inherently political dimensions more honest and accountable.

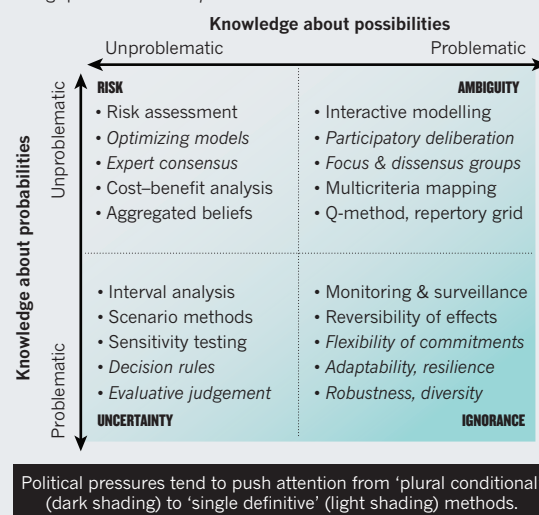
Problems of ambiguity arise when experts disagree over the framing of possible options, contexts, outcomes, benefits or harms. Like uncertainty, these cannot be reduced to risk analysis, and demand plural and conditional treatment. Such methods can highlight — rather than conceal — different regulatory questions, such as: “what is best?”, “what is safest?”, “is this safe?”, “is this tolerable?” or (as is often routine) “is this worse than what we have now?” Nobel-winning work in rational choice shows that when ambiguity rules there is no guarantee, as a matter of logic, that scientific analysis will lead to a unique policy answer⁷. Consequently, definitive science-based decisions are not just potentially misleading — they are a fundamental contradiction in terms.

METHODS THAT WORK

One practical example of ways to be plural and conditional when considering questions and options, as well as in deriving answers, is multicriteria mapping. Other participatory and deliberative procedures include interactive modelling and scenario workshops, as well as Q-method and dissensus methods. Multicriteria mapping makes use of simple but rigorous scoring and weighting procedures to reveal the ways in which overall rankings depend on divergent ways of framing the possible options. In 1999, Unilever funded me and colleagues to use multicriteria mapping to study the perspectives of different leading science advisers on genetically modified (GM) crops⁸. The backing of this transnational company helped

UNCERTAINTY MATRIX

A tool to catalyse nuanced deliberations: experts must look beyond risk (top left quadrant) to ambiguity, uncertainty and ignorance using quantitative and qualitative methods.



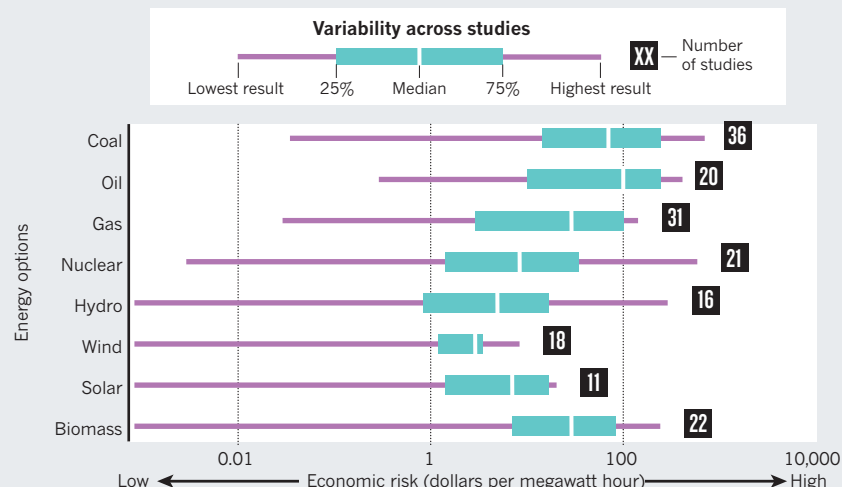
sensitivity, enabling more accountable evaluation. For example, it could allow experts to highlight conditional decision rules aimed at maximizing best or worst possible outcomes, or ‘minimizing regrets’⁵.

The few sporadic examples of the application of this approach show that it can be practical. One particularly politicized and high-stakes context for expert policy advice is the setting of financial interest rates. The Bank of England’s Monetary Policy Committee, for example, describes its expert advisory

SOURCE: REF 3

THE PERILS OF 'SCIENCE-BASED' ADVICE

A survey of 63 peer-reviewed studies of health and environmental risks associated with energy technologies. Individual studies offer conclusions with surprisingly narrow uncertainty ranges, yet together the literature offers no clear consensus for policy makers.



draw high-level UK government attention. A series of civil servants told me, in quite colourful terms, that results mapped out in plural, conditional fashion would be “absolutely no use” in practical policy-making. Yet when a chance finally emerged to present results to Mo Mowlam, the relevant cabinet minister, the reception was very positive. She immediately appreciated the value of having alternative perspectives laid out for a range of policy options. It turned out in this case, that the real block to a plural, conditional approach was not the preferences of the decision-maker herself, but of some of those around her.

In my experience, it is the single definitive representations of science that are most vulnerable to political manipulation. Plural, conditional approaches are not immune, but they can help make political pressures more visible. Indeed, this is what happened during another GM policy process in which I was involved: the 2003 UK science review of GM crops. Reporting included explicit discussion of uncertainties, gaps in knowledge and divergent views — and was described as “neither a red nor a green light” for GM technology. A benefit of this more open approach is that it helped GM proponents and critics to work more effectively together during the committee deliberations, without a high-stakes, ‘winner takes all’ dynamic. There was more space to express alternate interpretations, free from implications that one party or another was wrong. This is important in a highly-politicized area such as GM science, where there are entrenched interests on both sides. Yet this unusual attempt to acknowledge uncertainty was not universally popular. Indeed, it was also the only occasion, to my knowledge, on which the minutes of a UK science advisory committee formally

documented covert attempts to damage the career of one of its members (me, in this case)⁹. Perhaps for political — rather than scientific — reasons, this experiment towards plural and conditional advice has not been repeated.

A further argument for using more plural approaches arises from the state of ignorance, in which ‘we don’t know what we don’t know’. Ignorance typically looms in the choice of which of a range of feasible, economically viable future paths to support — either through funding or regulation — for emerging technologies. In a finite and globalizing world, no single path can be fully realized without detracting from the potential for others. Even in the most competitive

“An overly narrow focus on risk is an inadequate response to incomplete knowledge.”

consumer markets, for instance, development routinely ‘locks in’ to dominant technologies such as the QWERTY keyboard or VHS tape. The same is true of infrastructures, such as narrow-gauge rail, AC electricity or light-water reactors. This is not evidence of inevitability, but of the ‘crowding out’ of potential alternatives. Likewise, locking-in occurs in the prioritizing of certain areas of scientific enquiry over others. The paths taken by scientific and technological progress are far from inevitable. Deliberately or blindly, the direction of progress is inherently a matter of social choice¹⁰.

A move towards plural, conditional advice would help avoid erroneous ‘one-track’, ‘race to the future’ visions of progress. Such advice corrects the fallacy that scepticism over a specific technology implies a general ‘anti-science’ sentiment. It defends against

simplistic or cynical support for some particular favoured direction of change that is backed on the spurious grounds that it is somehow synonymous with ‘sound science’, or uniquely ‘pro innovation’.

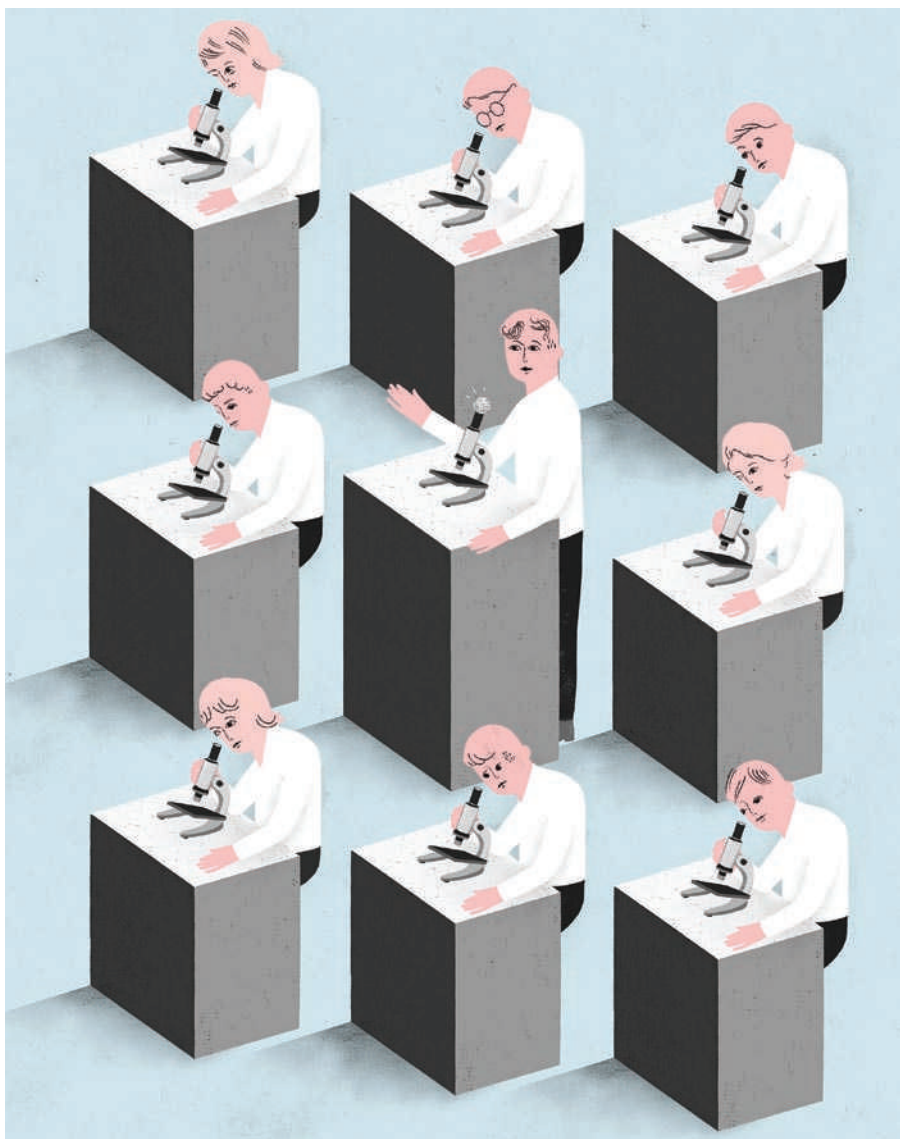
Instead, plural, conditional advice helps enable mature and sophisticated policy debate on broader questions. How reversible are the effects of a particular path, if we learn later that it was ill-advised? How flexible are the associated industrial and institutional commitments, allowing us later to shift direction? How adaptable are the innovation systems? What part might be played by the deliberate pursuit of diverse approaches — to hedge ignorance, defend against lock-in or foster innovation — in any given area?

Thus, such advice provides the basis for a more-equal partnership between social and natural science in policy advice. Plural and conditional advice may also help resolve some polarized fault-lines in current debates about science in policy. It shows how we might better: integrate quantitative and qualitative methods; articulate ‘risk assessment’ and ‘risk management’; and reconcile ‘science-based’ and ‘precautionary appraisal’ methods.

A move towards plural and conditional expert advice is not a panacea. It cannot promise escape from the deep intractabilities of uncertainty, the perils of group dynamics or the perturbing effects of power. It differs from prevailing approaches in that it makes these influences more rigorously explicit and democratically accountable. ■

Andy Stirling is research director at SPRU (Science and Technology Policy Research) and co-directs the joint Centre for Social Technological & Environmental Pathways to Sustainability at Sussex University, Falmer, Brighton BN1 9QE, UK.
e-mail: a.c.stirling@sussex.ac.uk

1. Knight, F. *Risk, Uncertainty and Profit* (Houghton Mifflin, 1921).
2. Wynne, B. *Glob. Environ. Change* **2**, 111–127 (1992).
3. Stirling, A. *Ann. NY Acad. Sci.* **1128**, 95–110 (2008).
4. Stirling, A. *Sci. Technol. Hum. Valu.* **33**, 262–294 (2008).
5. Farman, J. in *Late Lesson from Early Warnings: the precautionary principle 1898–2000* (eds Harremoës, P. et al.) 76–83 (European Environment Agency, 2001).
6. *Treasury Committee Inquiry into the Monetary Policy Committee of the Bank of England: Ten Years On* (Bank of England, 2007); available at go.nature.com/v2h4al
7. Leach, M., Scoones, I. & Stirling, A. *Dynamic Sustainabilities: Technology, Environment, Social Justice* (Earthscan, 2010).
8. Stirling, A. & Mayer, S. *Environ. Plann. C* **19**, 529–555 (2001).
9. UK GM Science Review Panel *Minutes of the Seventh Meeting* (2003); available at go.nature.com/lxbmpb
10. ESRC Centre on Social, Technological and Environmental Pathways to Sustainability, *A New Manifesto*, (Univ. Sussex, 2010); available at: go.nature.com/znqakg



Stand up for science

This year showed that good communication can make you a leader, and a better scientist, says **Nancy Baron**.

Back in 2001, I sat at the rear of a classroom with Jane Lubchenco, co-founder of the Aldo Leopold Leadership Program, while scientists stepped forward to share their fears and failures concerning communicating with the media and policy-makers. “I get a lot of calls from the press, and I don’t return most of those calls,” confessed Margaret Palmer, a restoration ecologist at the University of Maryland in College Park. A wave of sympathetic

laughter rippled through the audience.

After that two-week communications training workshop, Palmer decided to change her ways. Earlier this year, she co-authored a paper challenging US government policies that allow irreversible ecological damage through mountain-top mining in the pursuit of cheap coal¹. An avalanche of attention included an invitation to appear on the satirical television show, *The Colbert Report*. This time Palmer returned the call.

Despite Stephen Colbert’s bombastic efforts to disarm her, Palmer laughed, leaned in and scored a series of carefully prepared points while 1.2 million viewers watched.

GRACIA LAM

Palmer has become well known not just as a scientist, but as a leader. Her prominence has helped the University of Maryland become the finalist, pending formal approval by the review board, for a prestigious US National Science Foundation-funded (environmental synthesis research) centre to produce policy-relevant science with the active participation of decision-makers. In other words, science designed to make a difference.

This year, more than ever before, a chorus of voices has been summoning scientists to emerge from their laboratories and become better communicators. Little has been said about one important reason for doing so: the intrinsic link between communication and leadership. It’s no coincidence that environmental scientists who lead the pack, both within academia and beyond, are good communicators. These scientists know how to articulate a vision, focus a debate and cut to the essence of an argument. They can make a point compelling, even to those who disagree. They talk about their science in ways that make people sit up, take notice and care. After a decade of working with scientists as a communications coach and trainer, I am encouraged by the increasing number of scientists who are now chiselling doors and windows in the ivory tower to reach out. A new breed of communication-savvy researchers is emerging — albeit perhaps not fast enough.

For scientists who would be agents of change, communication is not an add-on. It is central to their enterprise. They begin with a goal in mind, frame their research questions to produce useful results and think about how they will disseminate the information. Yet learning to communicate is a critical life skill not typically taught as part of scientific training. It should be.

SPOTLIGHTS OR HEADLIGHTS?

This year, during the ‘Climategate’ affair, climate scientists froze in the face of scandal, only to become the piñatas of sceptics and deniers. Bashing these scientists continues to be a favourite pastime of the Tea Party politicians in the United States, despite those involved being cleared of wrongdoing by several independent review panels. Any vindication has been largely ignored because, as Mark Twain purportedly said: “A lie can make it half way around the world before the truth has time to put its boots on.” Now, after losing ground in the court of public opinion, climate scientists are finally rallying — stepping up to answer questions, address misconceptions and actively counter misinformation and deception². One group of scientists has set up a rapid-response team promising quick turnaround to queries from

government officials or the media³. The American Geophysical Union relaunched a climate question-and-answer service for the United Nations climate talks in Cancún, Mexico, earlier this month — to address questions of science, not policy⁴.

These are valuable steps to try to ensure scientific accuracy in the face of heated political rhetoric and wild conspiracy theories. But alone, they aren't enough. It's important to remember that not answering what policy-makers want and need to know leaves a void — one that contrarians are only too happy to fill. I concur with the late Stanford University climatologist Stephen Schneider's view: "Staying out of the fray is not taking the 'high ground'; it is just passing the buck." He believed that it is both possible and important to comment on policy without compromising scientific integrity. He would often say: "If you are asking me as a scientist, I would answer it this way ... If you are asking me as a citizen, I would say ..." In this way he made his point without overstating his science, and became extremely influential.

The Deepwater Horizon oil spill in the Gulf of Mexico illustrates how other scientists who have devoted time to thinking about communication have risen to positions to help lead policy. Lubchenco, now the administrator of the National Oceanic and Atmospheric Administration (NOAA), was an early advocate for scientists to communicate (see page 1024). In her call to arms — a 1998 paper in *Science*⁵ — she entreated scientists to be more forthcoming and share their research to benefit government, managers, policy-makers and society at large. Next she helped launch the Aldo Leopold Leadership Program and the Communication Partnership for Science and the Sea (COMPASS). Both of these initiatives help scientists connect with the media and policy-makers and deliver a bottom line to those with little time or patience.

As the first marine ecologist to lead NOAA, an agency of about 12,800 employees, Lubchenco knew her task was daunting. The oil spill provided a real test. Even this veteran communicator could not control how the media presented mixed messages and rapidly unfolding events. In August, Lubchenco was criticized for painting too rosy a picture of how fast the oil was being dispersed. Her message of "do not prematurely prejudge the impacts" was lost in the media clips. Lubchenco persevered, consistently reiterating what was and wasn't known about the oil, its effects and its final fate. By November the message was picked up. Her experience gave her the patience and persistence needed.

NATURE.COM
Communication:
Scientist as star:
go.nature.com/cjztmo

Scientists with a history of interest and practice in communication continue to have important roles in the oil

spill's ongoing saga. Donald Boesch, president of the University of Maryland Center for Environmental Science, is one of only two scientists on US President Barack Obama's seven-member commission on the Gulf of Mexico oil spill and offshore drilling. He was probably chosen from many qualified scientists because of his communication skills. Boesch is known for his ability to talk to people — from all walks of life — in a way that compels them to act. He is sympathetic, analytical and adaptive rather than superior, doctrinaire and inflexible. And he readily admits that he learns from his failures as well as from his successes.

Boesch has taken criticism from some peers for being too much in the public eye. He says the rewards of knowing that he is making a difference are worth it. On numerous occasions, a governor has told him about a recent piece of scientific work in the news, not realizing that Boesch had brought it to the media's attention in the first place. Boesch knows that the media helps to set the agenda of policy-makers and the public, and uses that system accordingly. Boesch hopes he can help guide the commission with a rigorously documented report that recommends actions to improve human and environmental safety. But

"It's important to remember that not answering what policy-makers want and need to know leaves a void."

it is his ability to communicate those recommendations, rather than his ability to help compile a report, that will ultimately make a difference. Pursuing communication as a high priority sometimes brings turbulence to academic careers. When something gets widely reported, the subsequent discussion in talk radio, television and the blogosphere can distort the facts like a funhouse mirror. Defending oneself can eat up valuable hours. Attacks can come from industry, ideologues or even colleagues.

Boris Worm, a marine ecologist from Dalhousie University in Halifax, Canada, for example, faced critiques that he had 'overreached' his results in two papers^{6,7} about fish depletion that got a lot of public attention. Instead of getting defensive, he engaged with his critics — and ultimately ended up collaborating with them⁸.

Most scientists I know who have felt such backlashes have few regrets. They dust themselves off and respond with more and better science. Their concern for the environment trumps their fear of criticism, and the progress they see in policies justifies their efforts.

Not every scientist wants to step up to the microphone — nor do they all need to. But for those who aim to change the world — and many graduate students and postdocs

do — some changes to the academic system would help. If young scientists are going to hone communication skills, they need the support of senior scientists to protect their interests and reputations at crucial junctures in their careers. In choosing an adviser, they should align themselves with scientists who have solid credentials and who share their values about outreach. Increasingly, many senior scientists are developing communication courses for their students that range from one-day workshops to accredited courses.

TIME WELL SPENT

In my work with scientists, I often hear that they cannot afford the time to work on their communication skills, with their hectic, research, publishing and teaching schedules. I see it another way: they cannot afford not to.

Many of the most prolific and accomplished scientists have risen to the top of their field by conducting significant, relevant research and working out how to communicate it within their discipline and beyond. They know the value of being quizzed by Congress or the media, even if at times it can be uncomfortable. Going public forces them to distil the essence of their work and to think harder about the questions — what is known and what is left to discover. Worm's philosophy is that engaging with thoughtful criticism — even if it seems harsh in the media spotlight — "makes everyone think more deeply and makes us push harder against the limits of the unknown".

That's why sharpening communication skills has value beyond increasing public understanding. It can breach interdisciplinary boundaries within science and help colleagues with different viewpoints catch a glimpse of a bigger picture. Articulating vision and common goals has long been a cornerstone of leadership on the battlefield. Scientists would be wise to adopt a similar strategy. Being a good communicator is not a trade-off. It makes you a better scientist. ■

Nancy Baron is science outreach director for COMPASS and lead communications trainer for the Aldo Leopold Leadership Program. She is based at the National Center for Ecological Analysis and Synthesis, Santa Barbara, California 93101, USA. Her book *Escape from the Ivory Tower: A Guide to Making Your Science Matter* was published in August.
e-mail: baron@nceas.ucsb.edu

1. Palmer, M. A. *et al. Science* **327**, 148–149 (2010).
2. Bowman, T. E. *et al. Science* **330**, 1044 (2010).
3. <http://www.climateapidresponse.org>
4. AGU Release No. 10–37 (2010); available at <http://go.nature.com/av9xng>
5. Lubchenco, J. *Science* **279**, 491–497 (1998).
6. Myers, R. A. & Worm, B. *Nature* **423**, 280–283 (2003).
7. Worm, B. *et al. Science* **314**, 787–790 (2006).
8. Worm, B. *et al. Science* **325**, 578–585 (2009).



TUI DE ROY/MINDEN PICTURES/FLPA

The future of the Adélie penguin hangs in the balance as sea-ice loss in the Antarctic threatens the supply of staple prey such as krill.

CONSERVATION

After the ice

Yvon Le Maho is moved by a powerful account of the demise of the Adélie penguin.

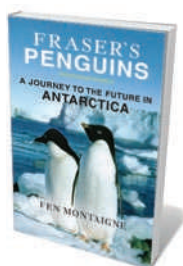
The impact of human activities on biodiversity is slow and insidious. Documenting the dramatic drop in populations of the Adélie penguin that has accompanied sea-ice loss and glacier retreat over the past three decades in the Antarctic, *Fraser's Penguins* reveals the profound environmental changes that are afoot.

Award-winning journalist Fen Montaigne spent five months in Antarctica tracking penguins with ecologist Bill Fraser and his team. Fraser, a regular visitor to the US scientific station of Palmer in the northwest Antarctic peninsula since 1974, has witnessed the site change from a polar ice habitat into a milder sub-Antarctic environment. Resisting the temptations of a quick research payoff, he began some of the first long-term studies on Antarctic seabird species, including the Adélie penguin (*Pygoscelis adeliae*). Such extended monitoring is an essential tool for assessing the health of regional ecosystems.

As a researcher who visits Antarctica regularly, I found Montaigne's account exceptionally poignant. He voices the emotions that inundate everyone who works in this

vast wilderness. And he captures details such as the fantastic scenery as the boat picks its way through broken sea ice dotted with resting seals and groups of penguins squint-eyed under a dazzling light. This was especially touching because I read the book while rolling at sea in the company of wandering albatrosses, on the way to my own penguin study site.

Montaigne reminds us why the Adélie penguins, those "smart and fussy little men in evening clothes", fascinated the first Antarctic explorers such as Fabian von Bellingshausen, Ernest Shackleton, Roald Amundsen, Robert Scott and Edward Wilson. Those men had to fight against the cold to conquer the unforgiving Terra Australis Incognita, or 'unknown southern



Fraser's Penguins:
A Journey to the Future in Antarctica
FEN MONTAIGNE
Henry Holt: 2010.
288 pp. \$26

land'. Yet the diminutive Adélie penguins thrive in these harsh conditions thanks to a unique suite of adaptations.

Penguins have evolved layers of overlapping scale-like feathers and large reserves of energy-giving body fat, which allow them to swim through the icy waters and stand through fierce storms. After heavy snow falls on their breeding colonies, their heads may be barely visible, sticking out of breathing holes as they continue incubating their eggs.

Visitors a century ago would probably have seen huge colonies of Adélie penguins. At the start of Fraser's study, in the 1970s, there were more than 30,000 breeding pairs on the seven monitored islands around Palmer station. Populations there today have dropped by 80%. Shifting weather and snow patterns, the contraction of sea ice and the retreat of glaciers have impacted ecosystems through a cascade of effects along the food web. The Adélie penguins' existence is intertwined with the presence of sea ice, as they forage on ice-dependent

NATURE.COM
Hybridization of Arctic species:
go.nature.com/zhkhul

prey such as silverfish and krill.

Sea ice serves as a grazing area for juvenile krill, who rake free the life-sustaining diatoms and phytoplankton embedded in the frozen ocean. As sea ice has declined along the western Antarctic peninsula, krill populations have dropped by up to 80% since 1976. Fisheries exacerbate the scarcity, as demand for krill in the aquaculture and pharmaceutical industries increases.

Montaigne gives an accurate portrayal of the breeding cycle and habits of the Adélie penguin. With their late maturity, low fecundity and extended generations, long-lived organisms such as penguins (and Arctic polar bears) are particularly sensitive and thus vulnerable to rapid environmental changes and extreme events. For example, my colleagues and I have shown that an increase of only 0.3 °C in sea-surface temperature in the marginal sea-ice zone leads to a 10% drop in the survival rate of king penguins.

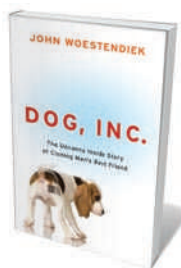
In revealing the tragic fate of the Adélie penguin, Montaigne has found an effective way to communicate the impact of human-induced global climate change. He ably explains complex climate mechanisms, such as how shifts in atmospheric circulation patterns like the Arctic Oscillation can pump warmer air into the polar regions from lower latitudes, and why some parts of the Antarctic are becoming colder when most of the peninsula's glaciers are in retreat and massive ice shelves are collapsing.

Fraser forecasts that, in the next decade, the Adélie penguins around Palmer will become memories. Rising temperatures around the Antarctic are pushing specialized polar species such as the Adélie to regional extinction. Two sub-Antarctic penguin species, gentoos and chinstraps, seem to be benefiting from climate change by expanding south. Yet they too depend on krill and winter sea ice. Although these two species might be able to shift their diet to other prey — gentoos dive deeper than the Adélie and chinstraps can feed at night — the ongoing ecosystem upheaval will jeopardize all penguins' existence in the near future.

Having worked in a more southerly part of Antarctica not yet so transformed by global warming, I found the book a piercing cry of alarm. I realize that I am lucky to have had the chance to contemplate the ecology of a pristine polar environment. As *Fraser's Penguins* shows, the beginning of the catastrophic consequences of global warming are only just visible now. The next generation of scientists may witness these changes accelerating at a dramatic pace. ■

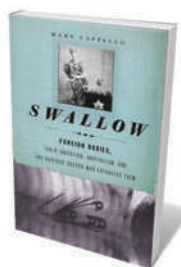
Yvon Le Maho is CNRS research director at the Department of Ecology, Physiology and Ethology, Institut Pluridisciplinaire Hubert Curien, University of Strasbourg, France. e-mail: yvon.lemaho@iphc.cnrs.fr

Books in brief



Dog, Inc.: The Uncanny Inside Story of Cloning Man's Best Friend
John Woestendiek AVERY 320 pp. \$26 (2010)

Pet cloning is big business. Investigative reporter John Woestendiek looks behind the scenes at the emerging industry of commercial dog cloning. It started in 2008 with a pitbull called Booger, whose American owner loved him so much she paid US\$50,000 to a South Korean firm to produce a litter of his identical offspring. Woestendiek suggests that the ethics of dog cloning is driven as much by our love of man's best friend as by the underlying science. He asks whether our obsession with animals makes us more likely to transgress ethical boundaries.



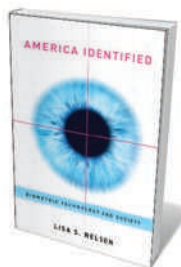
Swallow: Foreign Bodies, Their Ingestion, Inspiration, and the Curious Doctor Who Extracted Them
Mary Cappello THE NEW PRESS 336 pp. \$27.95 (2010)

Coins, jewellery, a padlock, a toy goat — people ingest the strangest things. Focusing on items rescued from patients' stomachs, award-winning writer Mary Cappello explores the psychology of why people eat non-nutritional objects. Her book centres on physician Chevalier Jackson's collection of swallowed artefacts in Philadelphia's Mutter Museum. Through the tales behind that exhibit, she unearths a history of class and poverty that compelled boys to swallow their last coins, and explores colourful characters such as sword swallows.



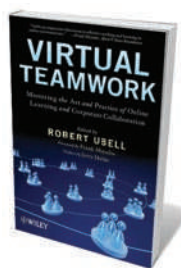
Ourselves Unborn: A History of the Fetus in Modern America
Sara Dubow OXFORD UNIVERSITY PRESS 320 pp. \$29.95 (2010)

We attach to the fetus a host of meanings — political, cultural and scientific. Historian Sara Dubow argues that these are largely based on our notions of identity, authority and sexuality, rather than fact or theology. She examines how these meanings have changed throughout history. Since the late nineteenth century, the fetus has been at the centre of a tug of war between science and religion. Although technology brought a greater understanding of embryo development in the twentieth century, social change has also made the fetus the subject of controversy.



America Identified: Biometric Technology and Society
Lisa S. Nelson THE MIT PRESS 200 pp. \$32 (2010)

Biometric technologies — such as fingerprint sensors, retina scans and handwriting analysis — are increasingly used to identify individuals. Drawing on research with focus groups, political scientist Lisa Nelson explores public attitudes to surveillance. She describes how public users of these technologies are sensitive to issues of privacy, trust and confidence in the institutions that acquire it. The expansion of these identification methods by governments through history, she explains, has bred distrust in biometrics, and highlights the need to balance harm, prevention and liberty.



Virtual Teamwork: Mastering the Art and Practice of Online Learning and Corporate Collaboration
Edited by Robert Ubell WILEY 268 pp. \$49.95 (2010)

Scientists increasingly work and teach in collaborations that have remote members. This collection of expert perspectives, edited by enterprise-learning professor Robert Ubell, offers a practical guide to virtual teamwork. It explains how to communicate across borders of geography, culture and motivational style to manage productive exchanges between participants. The essays offer advice on running online class projects and detail the latest virtual team technology.

IN RETROSPECT

Pauling's primer

Linus Pauling's book on bonding brought quantum mechanics into practical chemistry, finds **Philip Ball**.

Linus Pauling's *The Nature of the Chemical Bond* has, like Isaac Newton's *Principia* or Charles Darwin's *On the Origin of Species*, the kind of iconic status that, for some, removes any obligation to read it. Every chemist learns of Pauling's role in uniting the view of molecules as assemblies of atoms with the quantum-mechanical picture of atomic wave functions. But his book is long and mathematical, and more versatile approaches have emerged since it was published in 1939. Nevertheless, more than 70 years on, as we prepare for the International Year of Chemistry 2011, it remains a surprisingly good primer on chemical bonding that translates abstract quantum theory into the practical language of chemistry.

When Pauling's book was first published, some textbooks were still presenting an essentially nineteenth-century view of the bond. The term was introduced in 1866 by English chemist Edward Frankland, who regarded the chemical bond as a force akin to gravity. Jöns Jakob Berzelius suspected that the force was electrostatic, the attraction of oppositely charged ions. That view was encouraged by the discovery of the electron in 1897, as ions could result from an exchange of electrons between atoms.

But G. N. Lewis at the University of California, Berkeley, argued that bonding may result from sharing, not exchange, of electrons. Shared electrons give rise to what Irving Langmuir later called a covalent bond, which links neutral atoms. In 1916, Lewis suggested that atoms are stabilized by having a full 'octet' of electrons, which he saw as the corners of a cube; the octet may be completed by linking corners or edges with adjacent atoms. The model, which was popularized (or, in Lewis's bitter view, appropriated) by Langmuir, seemed vindicated when physicist Niels Bohr explained how the octets arise from quantum theory as discrete electron shells.

Yet because it considered only the individual atoms, this remained a rudimentary grafting of quantum theory on to the concepts that chemists used to rationalize molecular

formulae. Pauling, a supremely gifted young man from a poor family in Oregon who won a scholarship to the prestigious California Institute of Technology (Caltech) in 1922, was convinced that chemical bonding needed to be understood from quantum first principles. He wasn't alone — Richard Tolman at Caltech notably held the same view. But Pauling had a golden opportunity to develop it when, in 1926, he went to Europe on a Guggenheim fellowship to visit the architects of quantum theory: Bohr at Copenhagen, Arnold Sommerfeld at Munich and Erwin Schrödinger at Zurich. He also met Fritz London and his student Walter Heitler, who in 1927 published their quantum-mechanical description of the hydrogen molecule. They had found an approximate way to write the wave function of the molecule that, when inserted into the Schrödinger equation, allowed them to calculate a binding energy that was in reasonable agreement with experiment.

Pauling generalized this treatment into the valence-bond model, which considers chemical bonds to be formed by the overlap of single-atom electron orbitals. He put forward the idea of 'resonance' in molecules for which more than one valence-bond structure can be drawn; for example, in H_2^+ the single electron can be considered to reside on either hydrogen atom, and the molecule is said to resonate between the alternatives. In such cases, the mixed state has a lower energy than any of the contributing structures.

A NEW GEOMETRY

Pauling also proposed that 'hybrid' blends of atomic electron orbitals with new geometries may arise in some molecules. In methane, for example, the central carbon atom attaches to four hydrogen atoms in a tetrahedral shape; this configuration can be rationalized as the mathematical mixing of the atomic 2s and three 2p orbitals in carbon to give four tetrahedrally distributed sp^3 hybrid orbitals. These ideas on resonance and hybridization were published in a series of papers in 1928–31, which formed the core of *The Nature of the Chemical Bond*.

The book's scope is exhaustive. It brings

The Nature of the Chemical Bond

LINUS PAULING
Cornell University
Press: 1939. 429 pp.

multiple covalent bonds and ionic, metallic and hydrogen bonds all within the valence-bond framework, and explains how the ideas fit with observations of bond lengths and ionic sizes in X-ray crystallography — the technique Pauling mastered at Caltech that led to his seminal work in the early 1950s on the structure of proteins and nucleic acids.

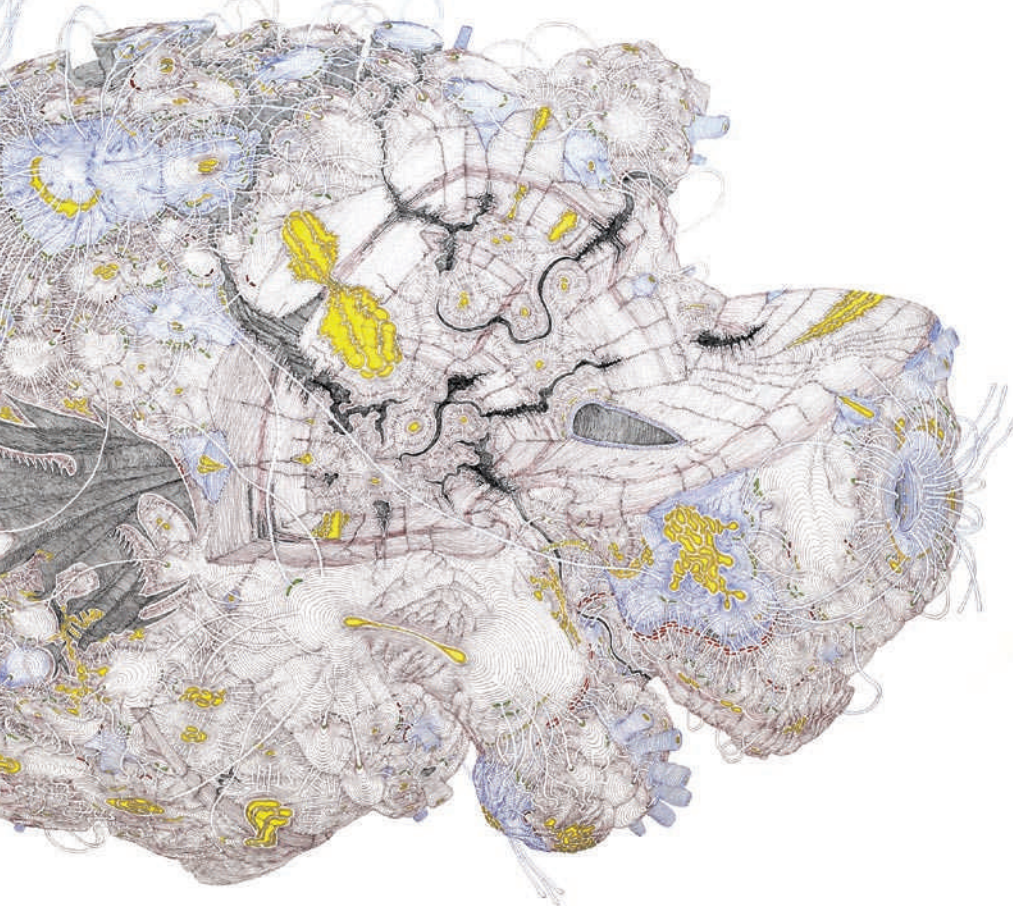
Pauling acknowledged that his treatment of chemical bonds is ultimately arbitrary — his resonating configurations of nuclei and electrons are conceptual fictions that allow us to estimate the molecule's energy. It is the wave function of the entire molecule that actually describes how the electrons are distributed in space. But he was resistant to recognizing alternative theories.

In particular, in the late 1920s, Robert Mulliken at the University of Chicago, Illinois, and Friedrich Hund at the University of Göttingen, Germany, approximated the electron wave functions in a different way to Pauling's valence-bond theory, giving rise to 'molecular orbitals' in which electrons are distributed over several nuclei. Their model offered a simpler account of the quantum energy levels as revealed by molecular electronic spectra. And it supplied a single description of some molecules for which the valence-bond approach had to invoke resonance between many structures. This was especially true for aromatic molecules such as benzene: the valence-bond model needed around 48 separate structures for naphthalene (two fused benzene rings), and no fewer than 560 for the organometallic compound ferrocene.

Although neither the valence-bond nor the molecular-orbital model could claim to be more correct than the other, the latter had practical advantages. This was known even by reviewers of Pauling's book — some criticized him for not mentioning the rival theory, and one reviewer suspected that the valence-bond method might triumph purely because of Pauling's superior presentation skills. By the 1970s, however, most chemists accepted that molecular-orbital theory was usually more convenient, although Pauling never did.

The significance of *The Nature of The Chemical Bond* was not so much that it pioneered the quantum-mechanical view of bonding, but that it made this a chemical theory: a description that chemists could understand and use, rather than a mathematical account of wave functions. It recognized that, if a model of physical phenomena is to be useful, it needs to accommodate itself to the intuitions and heuristics that enable scientists to talk coherently about the problem. Emerging from the forefront of physics, this was nevertheless a chemists' book. ■

Philip Ball is a writer based in London. His forthcoming book is *Unnatural: The Heretical Idea of Making People*.



This detail from a conceptual model of the evolution and structure of science shows emerging fields in blue, funding boosts in yellow and gaps in knowledge as black voids.

COMMUNICATION

Mapping science

Ben Shneiderman enjoys a tome full of tools for discovery.

The desire to visualize science is intense. Whereas telescopes, microscopes and magnetic resonance imaging (MRI) scans have revealed aspects of the natural world, new tools are needed to study science itself and how it changes over time. The challenge of depicting intangible processes has invigorated the growing research community dedicated to information visualization. From capturing moments of discovery to watching emerging research fronts, such tools can help us to understand the dynamics of innovation and guide its future.

In the *Atlas of Science*, information scientist Katy Börner highlights examples that summarize the evolution of research and its interlocking communities in pictorial form. The book accompanies Börner's ambitious travelling exhibitions, *Places & Spaces: Mapping Science*, an ongoing programme of well-crafted visual presentations that have conveyed aspects of science to the public in libraries and museums since 2005 (<http://scimaps.org>). Contributors to the book get bylines and photos, making the collection a collaborative effort with diverse voices. Each two-page spread is a sumptuous

**Atlas of Science:
Visualizing What
We Know**

KATY BÖRNER
MIT Press: 2010.
288 pp. \$29.95

underemphasizes the inherently interactive nature of information visualization.

Unlike in scientific visualization, which centres on three-dimensional representations of objects such as stacked MRI scans, researchers who visualize information seek patterns, clusters, relationships, gaps and anomalies in many dimensions. Such methods may be used, for example, to study financial trading patterns over time, hierarchical structures in library catalogues, networks of social relationships and medical patient attributes. In exploring these multi-dimensional spaces with bespoke software, users manipulate control panels to zoom in on desired items, filter out undesired items and select details.

The past decade has produced a steady flow of prototype software

feast of dense prose, delicious visuals and engaging quotations. Börner's use of map-making as metaphor is mostly on target, but it

for information visualization, such as Spotfire, Tableau, ILOG and Hive Group. Many of these commercial success stories have been acquired by large business-intelligence or software companies. Despite the wide impact of these programmes in drug discovery, genomic data analysis and social-network analysis, they unfortunately get little mention in the *Atlas of Science*.

These tools also support discovery by integrating rich data manipulation and statistical analyses. Data-sharing platforms such as ManyEyes or Swivel encourage discussion around visualizations, and US government sites such as data.gov and recovery.gov raise expectations of open data and cultivate policy-oriented communities. The growing interest in 'big data' has spread from the pure sciences to the social sciences and humanities. Some journalists have also become innovators in presenting graphic data, providing readers with the same opportunity to explore information and make their own discoveries.

In the *Atlas of Science*, Börner sets out the story of scientific map-making well. She shows a range of examples based on aspects of science: geographical maps, historical timelines, taxonomic hierarchies, citation networks and various forms of textual graphics. Readers will learn about the geographic concentrations of the creative class in Europe, North America and Japan; Wikipedia editing patterns; rising patent citations; and pathways to discoveries such as the structure of DNA. A recurring theme is the relative size and connectedness of disciplines, from the expected closeness of biology and ecology to the surprising linkage between computer science and social sciences.

Börner is generous in giving credit to many scientific map-makers, but her choice is subjective and some readers will favour different heroes. The book mostly lacks critiques — only one visualization is challenged for its hard-to-read labels and partially obscured links. But other displays have advantages and drawbacks that merit debate. Börner and her contributors sometimes seem more entranced by a compelling visual than by its comprehensibility.

In converting such displays to static paper, the *Atlas of Science* necessarily loses the interactive nature of information visualization. Seeing inspirational photos from Roman Vishniac's microscope or the Hubble Space Telescope can only suggest the excitement of those who operate the controls. Nevertheless, Börner's magnificent book offers provocative new maps of science that will inspire fresh thinking. ■

Ben Shneiderman is professor of computer science at the University of Maryland, College Park, Maryland 20742, USA, and co-author of *Analyzing Social Media Networks with NodeXL*. e-mail: ben@cs.umd.edu

NATURE.COM
See the Big Data
special issue:
go.nature.com/vnklyt

HISTORY

Science fit for a king

Laura Spinney visits a Versailles exhibition of curiosities.

In 1769, King Louis XV of France was given a male rhinoceros for the royal menagerie at Versailles, where it caused a sensation. The animal remained there for 22 years, until it was killed by a sabre thrust during the French Revolution. Its skin was later stretched over an oak frame and displayed at the Natural History Museum in Paris. For the next few months it is back at Versailles, welcoming visitors to the exhibition *Science and Curiosities at the Court of Versailles*.

The rhino embodies the exhibition's two main themes: science as spectacle, and science in the service of the state. King Louis XIV ushered in an era of frenetic scientific activity after his chief minister, Jean-Baptiste Colbert, persuaded him to establish a national academy of science in 1666 — as depicted in a 1680 painting by Henri Testelin (pictured). Louis XIV imposed no rules on his academicians, but he did pay them, so their projects had to be useful to him. Being invited to demonstrate your discovery or invention at court was the best way to get it known.

Scientists came to Versailles from far and wide to help create a splendid royal residence. They included astronomer Giovanni Domenico Cassini, who directed the Paris Observatory from its opening in 1671. Geometricians and astronomers laid

out the gardens (the instruments they used are on display), hydraulics experts pondered diverting the River Eure to fill the lakes — a project that was never completed — and explorers filled greenhouses and the menagerie with exotic species. The forerunner of the lift, the flying chair, was invented at Versailles to transport Louis XV's mistresses upstairs; a full-size mock-up is shown.

It wasn't all self-serving. Under Louis XIV, Cassini charted the Moon's terrain, and Louis XV paid the Cassini family to create the first map of France, parts of which are on show, revealing detail down to the most isolated windmill. Louis XV also had a passion for scientific instruments, such as an astronomical clock showing the Moon's phases and movements of the planets around the Sun according to Nicolaus Copernicus.

Louis XVI encouraged agricultural research with the hope of eradicating famine in France. He was rewarded in 1786 when Antoine-Augustin Parmentier presented him with the flowers of the potato, or 'poor bread', whose cultivation he had been perfecting. Years before Edward Jenner came up with

Science and Curiosities at the Court of Versailles

The Palace of Versailles, France.
Until 27 February 2011.

his vaccine, thousands of people, including Louis XVI himself, benefited from a crude form of inoculation against smallpox — the disease that had killed Louis XV, according to his displayed medical certificate.

Science was also entertainment at Versailles: demonstrations drew large crowds. In 1746, in the Hall of Mirrors, eyewitnesses described how Abbot Nollet literally shocked 140 hand-holding aristocrats with static electricity. Full-sized battleships were floated on the royal lakes, and in 1783, brothers Joseph and Etienne Montgolfier demonstrated their hot-air balloon in a palace courtyard.

Royal women also played a part in the scientific adventure. One of Louis XV's mistresses, Madame de Pompadour, supported the *Encyclopédie* of Denis Diderot and Jean le Rond d'Alembert, a volume of radical Enlightenment thinking that was banned by the French government. Visitors can see Marie-Antoinette's dulcimer player, a primitive robot that hammers out tunes on a stringed instrument. The queen bought it in 1784 and, realizing its scientific value, donated it to the academy a year later.

Marie-Antoinette, the rhino and the academy all met their ends in 1793 at the height of the Revolution. But the academy proved thicker-skinned than the queen and the ungulate. Realizing that they needed scientists after all, the revolutionaries recreated the academy in 1795 in its current form — as one of the five that make up the Institut de France. ■

Laura Spinney is a writer based in Lausanne, Switzerland.
e-mail: lfspinney@googlemail.com



A 1680 painting by Henri Testelin celebrates the achievements of the French national academy of sciences during the reign of Louis XIV.

CHÂTEAU DE VERSAILLES, J.-M. MANAI



Q&A Roger Penrose

Impossible thoughts

As he publishes his collected works — six volumes comprising more than 5,000 pages — the mathematical physicist muses on 50 years of groundbreaking research in general relativity, quantum mechanics, cosmology, geometry and consciousness.

Your *Collected Works* includes a diverse range of papers. Is there a theme?

Most of them involve a particular point of view on how to unify space-time structure with quantum mechanics. I believe that quantum mechanics is not the whole story. On some scales, the rules of quantum mechanics have to be violated. There has to be some other ingredient that, I suspect, has to do with gravity.

You are currently working on a book called *Fashion, Faith and Fantasy*. What is it about?

I rashly suggested that title for three lectures I gave at Princeton University in 2003. 'Fashion' refers mainly to string theory, which has many merits but is not believable. I don't see how you can make sense of all those extra dimensions. 'Faith' refers to quantum mechanics. It's a wonderful theory and works beautifully, but is self-inconsistent — in my view, when you make a measurement, you violate the Schrödinger equation. At some scale in the Universe, quantum mechanics will have to be replaced by a better theory.

And 'fantasy'?

That's largely directed at cosmic inflation, in which the Universe is supposed to have expanded by an enormous factor just after the Big Bang. I've always been against this — it can only work if you start off in a very special state. In my recent book *Cycles of*

Time, I propose my own fantastical scheme that the entire history of the Universe is just one stage in a succession. What we think of as the Big Bang is not the beginning. It's the continuation of the remote future of a previous aeon.

How might we know if that is true?

The cosmic microwave background — the radiation left over from the Big Bang — would reveal evidence of events taking place in the aeon before ours, mainly encounters between supermassive black holes. When galaxies collide, their central black holes may spiral around and swallow each other up, causing an enormous burst of gravitational radiation. Such a burst from late in the previous aeon would leave its mark as circles around which the temperature is anomalously uniform. My colleague Vahe Gurzadyan sees tentative signs of them [see go.nature.com/Lbwioiu].

What does mathematics have to say about consciousness?

In my 1989 book *The Emperor's New Mind*, I said that computers will not achieve any conscious understanding. Gödel's theorem tells us that mathematical insights fall outside any formal procedure,

Roger Penrose:
Collected Works
Oxford University
Press: 2010. 5,104 pp.
\$1,250

so understanding is not a computational process. Something else is going on. I have reason to believe it may involve the limits of quantum mechanics. Microtubules [tiny structures in cells] are the best candidate in the brain for where this might happen, as they are so small, but quantum mechanics would have to work on a huge scale to operate there.

How was your work on impossible objects taken up by the artist M. C. Escher?

When I was a graduate student at the University of Cambridge, I went to a mathematics conference in Amsterdam. One lecturer had a strange picture of birds, Escher's *Day and Night*. I decided to try something new and produced the tribar, an impossible triangle. My father also produced an impossible staircase, which goes round and round. We wrote a paper and sent a copy to Escher, crediting him. He developed the ideas into two prints: *Ascending and Descending*, with monks going around an impossible staircase; and *Waterfall*, which incorporates the tribar.

Did you meet him?

I visited Escher once. I had some angular wooden tiles, all the same shape, which I gave to him to see whether he could cover a plane without any gaps or overlaps. One of the last pictures he produced shows the arrangement using ghost shapes. Later, after both Escher and my father died, I produced the first never-repeating pair of tile shapes [Penrose tiles]. It was a shame they didn't live longer because I'm sure Escher would have done something wonderful with them, and my father would have got a great kick out of it.

Was your father a major influence?

Yes. He was a human-genetics professor at University College London and studied the inheritance of mental disease. He was interested in the question of consciousness, too. He'd cut things out of wood and make puzzles for children, and was interested in games, chess in particular. I took no interest in chess myself, but my younger brother became British champion ten times. My older brother went on to become a highly respected mathematical physicist. To my father, science was very much like a game.

Yet you were a slow learner as a child?

At school in Ontario during the Second World War, I once got moved down a class because I couldn't do mental arithmetic. I was slower than the others. Then one teacher said, "You can have as long as you like to do the tests." Given time, I did extremely well. That's always been true of me. It takes me a long time to think things through. Luckily I can get away with little sleep. I compensate by working into the night. ■

INTERVIEW BY JASCHA HOFFMAN

CORRESPONDENCE

No crisis in supply of peer reviewers

At the journal *Molecular Ecology*, we find little evidence for the common belief that the peer-review system is overburdened by the rising tide of submissions.

We analysed the number of requests required in 2001–10 to obtain a review; compared the number of submissions in 2001–07 with the number of unique reviewer names in each year; and calculated the mean number of reviews per reviewer in 2001–07 (see go.nature.com/68mh16).

The idea that it is now harder to find reviewers turns out to be true (the mean number of reviewing requests issued per review increased from 1.38 (s.e. = 0.02) in 2001 to 2.03 (s.e. = 0.05) in 2010). However, this seems to be due to changes in technology rather than to changes in reviewers' attitudes: the declining acceptance rate by invited reviewers strongly correlates with the 2008 transition from an e-mail-based editorial system to an automated one, perhaps because spam filters blocked e-mail invitations.

We also found that the reviewer pool expanded in proportion to the increased submission rate (which doubled between 2001 and 2007), yet there was no increase in the average number of reviews by individual reviewers.

The authors of the additional papers are the most likely source of the extra reviewers. Each *Molecular Ecology* submission has an average of 4.5 authors and decisions are based on an average of 2.7 reviews, so only 0.6 reviews per co-author are required to compensate for the review burden of each new article. These figures indicate that the reviewer pool still seems able to accommodate the increasing number of submissions.

Tim Vines, Loren Rieseberg
Molecular Ecology, University of British Columbia, Canada.



managing.editor@molecol.com
Harry Smith *University of Leicester, UK.*

Competing financial interests declared: see <http://dx.doi.org/10.1038/4681041a>.

Brazil's renewable energy success

Brazil's advanced energy matrix is starting to pay off: 47.3% of its primary energy is now renewable. The world average is still around 13%.

Last year, Brazil produced 244 million TOE (tonnes of oil equivalent), of which 42.6% came from oil and coal, and the rest from sugar cane (18.2%), hydropower (15.2%), biomass (13.9%), natural gas (8.7%) and uranium (1.4%).

Ethanol accounted for 18.8% of fuel usage, and natural gas and biodiesel for 3.3%. In just 2 years, Brazil has reached its target of 5% biodiesel additive in diesel. Ethanol is set to overtake petrol as fuel, thanks to flexible-fuel engines that use both at the same time. These account for 90% of small-car sales in the past 2 years.

The country is developing the technology for 'green' petrol and diesel production from sugar cane and agricultural waste, and from the castor-oil residue generated during biodiesel manufacture.

Brazil's government estimates that only about 2.5% of arable

land will be needed to meet the ethanol demand forecast for 2017 (today this is 1.4%). Burning of sugar-cane pulp (bagasse) is expected to supply 15% of Brazil's electricity by 2017, comparable to that being generated by the Itaipu hydropower plant on the Brazil–Paraguay border.
Allan Kardec Duailibe *National Agency of Petroleum, Natural Gas and Biofuels, Brazil.*
allan@anp.gov.br

Economic growth: a gross measure

Gross domestic product (GDP) is as poor a measure of the economy as it is of welfare (*Nature* 468, 370–371; 2010).

Quantifying the concept of 'the economy' is contentious because of arbitrary decisions as to what to include, and because of a drift when indexing to constant prices. For example, should the jump in price from Walkman to iPod be classed as inflation or as a 10⁹ increase in storage productivity?

And whereas economic growth theory uses a production value that is net of depreciation, GDP is a gross measure. Thus GDP looks good even when things are falling apart. Being the fastest-growing economy in the 2000s was actually a sign of economic distress, not success, for the United Kingdom.

The economy, as a complex

system, cannot logically be indexed by a single figure. In truth, GDP just reflects the perspective of the tax base, because that is how the figures are collected and presumably why the UK Treasury is keen to use it.

Force-feeding an economy's GDP index usually empties its environmental capital first, then its social capital and then whatever cash is left in the bank.

David Fisk *Imperial College London, UK.*
d.fisk@imperial.ac.uk

Misreporting: hippo stories off-target

Prevention is better than cure when it comes to the weight of ill-informed public opinion resulting from the misreporting of science by the media (*Nature* 468, 7; 2010).

Take the story of a hippopotamus coming round unexpectedly in an African national park after incomplete delivery of an immobilizer drug cocktail by a faulty dart. The animal had to be shot after attacking the attending researchers.

News of the killing spread rapidly (see go.nature.com/upkcu7), the story becoming more sensational with each rewriting (see go.nature.com/rhxx7c). It prompted a public outcry and led some people to question why the research was being performed in the first place.

Not reported was that the new drug cocktail had until then been used with 100% success on more than 20 hippos, and that previously trialled immobilization drugs had killed a quarter of the hippos tested. The real news is that this cocktail represents a breakthrough in the management and conservation of the species.

P. J. N. de Bruyn *University of Pretoria, South Africa.*
pjndebruyn@zoology.up.ac.za

Brian Marsden

(1937–2010)

The walking encyclopedia of comets.

Brian Geoffrey Marsden was the ‘go-to man’ for comets — icy bodies that release gas or dust as they travel around the Sun — as well as for the thousands of named asteroids or ‘flying rocks’.

For more than three decades, Marsden, who died aged 73 on 18 November, headed an effort to locate objects that had once been observed and named, but that could no longer be tracked because the original observations had been insufficiently precise. His favourite recovery was the comet Swift–Tuttle, first sighted in 1862 but lost a couple of years later. Conventional wisdom held that it would return around 1981, but Marsden suspected that the 1862 comet had the same properties as one seen in 1737, and this allowed him to predict, correctly, that Swift–Tuttle would not return until late in 1992.

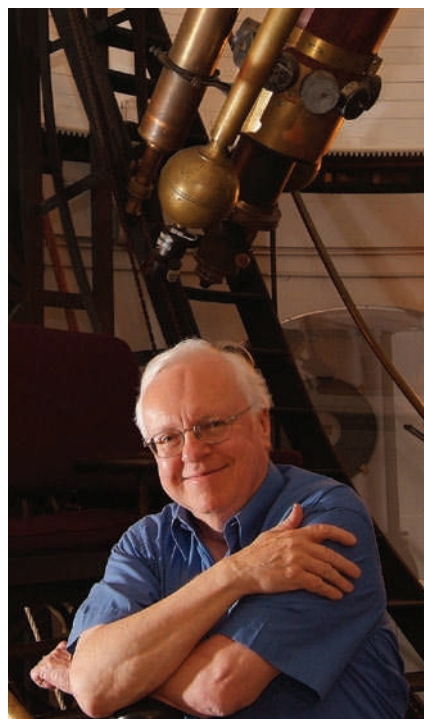
Born in Cambridge, UK, Marsden was developing primitive ways to calculate the positions of planets by the age of 11. As a teenager, he began to compute the locations of comets using logarithm tables. By the time he received his undergraduate degree from New College, Oxford, UK, he was widely known for being able to calculate comet orbits accurately.

Marsden enrolled as a graduate at Yale University in New Haven, Connecticut, in 1959, and soon programmed the university’s IBM 650 computer to calculate comet orbits. In 1965, Fred Whipple invited him to join his staff at the Smithsonian Astrophysical Observatory in Cambridge, Massachusetts. Whipple, then the director of the observatory, had recently proposed the ‘dirty snowball’ model — the idea that comets consist mostly of ice mixed with dust. The computer programs that Marsden developed to model the orbiting paths predicted by Whipple’s theory are still widely used by astronomers.

TAKING THE REINS

As the director of the Central Bureau for Astronomical Telegrams (CBAT), I had transferred it from Copenhagen to Cambridge, Massachusetts, shortly before Marsden arrived at the Smithsonian. The CBAT has, since 1920, been responsible for informing the world’s astronomers — on the behalf of the International Astronomical Union (IAU) — about comets and other objects of astronomical interest that change rapidly. It is also in charge of naming comets.

On the day before Marsden was officially to take up his staff position at the observatory,



we had a press conference to inform the public that the remarkable comet Ikeya–Seki would become bright enough to be seen near the Sun in broad daylight. Fortunately, Marsden joined us, because there were questions about historical comets that only he could answer. In the days that followed, it quickly became clear that he would prove an indispensable member of the CBAT team, and by the next IAU Congress, in 1968, I was more than happy to hand over the reins to him.

Marsden was director for 32 years. This was an onerous assignment, because he had to be on duty 24 hours a day, 7 days a week, in case a brilliant supernova burst into view. Most astronomers little appreciated the service that Marsden rendered during those decades, although in 1989 he did win the American Astronomical Society’s George Van Biesbroeck Prize ‘for service to astronomy’, and later he won a similar prize from the UK Royal Astronomical Society.

Besides directing the CBAT, Marsden took over another IAU bureau, the Minor Planet Center, in 1978. Under his leadership, all the asteroids that had been lost were located again. There are now about half a million asteroids with known orbits, more than 16,000 of which have official names. In his role in various IAU committees, Marsden became, in effect, the

chief namer of asteroids, although the full committee had to ratify his suggestions.

Because the procedures used to measure the positions of Pluto were the same as those used for minor planets, Marsden proposed, in 1999, to give it the minor planet number 10,000. He considered Pluto to be the first of the trans-Neptunian objects — icy objects that orbit the Sun but that are farther from it than Neptune.

His proposal stirred up an inordinate controversy among the public, and the IAU executive committee forbade such a move. In 1993, after three more trans-Neptunian objects were found, Marsden had been the first to suggest that they were all like Pluto in orbiting the Sun twice in the time it takes Neptune to orbit it three times.

Marsden’s wish to ‘demote’ Pluto was granted only after trans-Neptunian objects more comparable to Pluto in size were discovered in 2005. At its triennial meeting in 2006, the IAU voted to designate these objects members of a new class of ‘dwarf planet’ — which, paradoxically, are not considered simply another kind of planet. At this same IAU meeting, Marsden stepped down as director of the Minor Planet Center. He was “quite entertained by the thought that both he and Pluto had been retired on the same day”.

Brian rarely took breaks from calculating the orbits of astronomical objects, and would typically be at his desk on a Saturday afternoon. A few months ago he was diagnosed with leukaemia. In spite of his illness, he continued to come to the observatory. I saw him frequently, his office being directly across the hall from my own.

I’ve recently been working on Galileo’s discovery of the satellites of Jupiter (whose orbits had been the topic of Brian’s doctoral thesis). I told him that I needed a diagram showing what the satellite orbits would have looked like in January of 1610. He paused for a few minutes: “Try the 1941 Nautical Almanac,” he suggested. The match is amazing. Three weeks later, pneumonia took its toll on a weakened immune system. The magic will be missed. ■

Owen Gingerich is professor emeritus of astronomy and history of science at the Harvard-Smithsonian Center for Astrophysics, Cambridge, Massachusetts 02138, USA, and was a colleague of Brian Marsden’s for 45 years.
e-mail: ginger@cfa.harvard.edu

H. DORWIN

HUMAN ORIGINS

Shadows of early migrations

Analysis of ancient nuclear DNA, recovered from 40,000-year-old remains in the Denisova Cave, Siberia, hints at the multifaceted interaction of human populations following their migration out of Africa. [SEE ARTICLE P.1053](#)

CARLOS D. BUSTAMANTE & BRENNAN M. HENN

The new discipline of palaeogenetics is delivering increasing dividends, the latest news coming from Reich, Pääbo and colleagues on page 1053 of this issue¹. The authors' analysis of nuclear DNA of a human-like finger bone, found in Denisova Cave in southern Siberia, points towards a complex model of migration and colonization after anatomically modern humans moved out of Africa some 50,000–60,000 years ago.

Ever since 1925, when Raymond Dart's report of the first *Australopithecus* skull in southern Africa upended Victorian views of human origins, there has been debate over whether our species arose only once and spread throughout the world, replacing all extant species of *Homo*, or whether our ancestors interbred with the other populations and subspecies. The most extreme version of the 'candelabra' model of human origins — according to which human species arose multiple times independently of our *Homo ergaster* ancestors — has been largely discounted. But it has been difficult to assess more nuanced models, such as the possibility of genetic exchange with some archaic populations, including Neanderthals, and now perhaps ancient Siberians.

Until recently, genetic data and interpretation of the fossil record seemed to favour a complete-replacement model, in which all human species trace all of their genetic ancestry to a single origin in one or more African populations of moderate size some 200,000 years ago^{2–5}. However, the Denisovan nuclear genome sequence¹, along with that of *Homo neanderthalensis* published by some of the same authors⁶, suggest that the out-of-Africa population history of *Homo sapiens* is probably much more intertwined than previously thought, with more intertwining in some parts of the world than others.

On the basis of their analyses of ancient DNA from the Neanderthals and Denisovans, the Reich–Pääbo team proposes that limited gene flow from archaic *Homo* species to modern humans occurred in two brief episodes (Fig. 1). One episode occurred shortly after a subset of modern humans left Africa, and the second occurred only in the ancestors of Melanesian populations in Oceania. Their inference

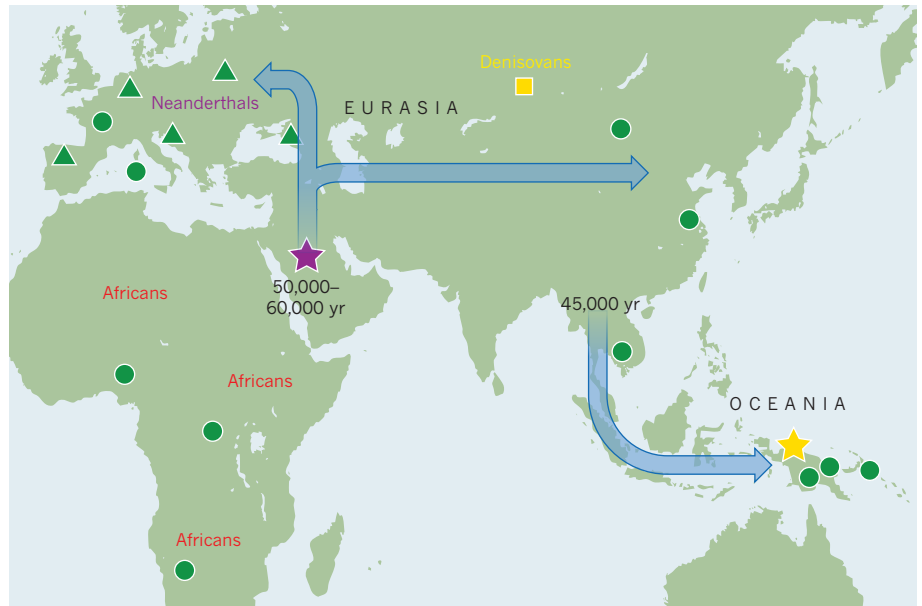


Figure 1 | New hypotheses extend the 'standard model' of modern human history. Triangles and circles respectively represent sampling locations^{1,6} of Neanderthal remains and of present-day human genomes. The blue arrows indicate generally accepted major migrations of anatomically modern humans¹¹, following their departure from Africa 50,000–60,000 years ago. At this time, there were two primary archaic species in Eurasia, Neanderthals and *Homo erectus*; Reich, Pääbo and co-workers¹ suggest that a third group was also present, represented by the ancient Denisovan genome. From ancient DNA^{1,6}, they identify additional putative events involving two episodes of limited gene flow: first, genetic admixture from Neanderthals to modern humans, shortly after the exit from Africa; second, subsequent admixture with the archaic population exemplified by the nuclear DNA extracted from the Denisova finger bone. This second event seems to affect only the ancestors of present-day Melanesians, who are thought to have colonized Papua New Guinea some 45,000 years ago. African populations, both past and present, are genetically highly diverse, as indicated by the multiple labels.

of genetic admixture does not resurrect orthodox multiregional evolution, which theorizes extensive gene flow among *Homo* species across different geographical regions for hundreds of thousands of years⁷. Nailing specific details of a 'replacement plus limited gene flow' model will require much more work. But the broad outlines from sequencing ancient DNA provide a fascinating view of our genome, and present a hypothesis that can be tested when many, more diverse, human genomes (and, one hopes, more ancient ones) are available.

The new work¹ is a follow-up to an earlier paper⁸, by a group led by Pääbo, on the deeply diverged mitochondrial DNA (mtDNA) genome recovered from the same finger fragment. Reich, Pääbo and colleagues¹ have now sequenced the bone's nuclear genome to

approximately 2× coverage — that is, on average, they have obtained sequence from two ancient DNA fragments that cover a given base in the genome. They compare these fragments with low (1–5×) coverage data from 12 modern-human genomes, as well as with the Neanderthal genome⁶ sequenced to 1.5×.

Nuclear DNA comes from the 22 pairs of autosomal chromosomes and the sex (X, Y) chromosomes. Apart from containing the vast majority of genetic information, nuclear DNA is well suited for analysis of gene flow because genetic recombination provides tens of thousands of semi-independent data points for comparing genetic relationships among present-day and ancient samples. The fragments of ancient DNA illuminate our understanding of human origins and, like the

shadows in Plato's proverbial cave, give us the broad outlines of ancient human migrations.

And what an interesting story they tell! It seems that the Denisovan was most similar genetically to Neanderthals, but not so similar as to have been sampled from the same population. The Reich–Pääbo team now demonstrates that Denisovans and Neanderthals are sister taxa, clustering, on average, slightly more often than either does with modern human samples. Compared with modern humans, the Denisovan sample clusters slightly more often (about 1–3% of time) with the present-day European or east Asian genomes as compared with the African genomes from the Yoruba, Mbuti and San. This is consistent with reported gene flow from a Neanderthal population into the ancestors of modern-day Eurasians⁶, if Denisovans and Neanderthals are close sister taxa.

What is particularly fascinating, however, is that the Denisovan sample seems to share an extra genetic affinity (beyond that for European and Asian genomes) with present-day island Melanesians. This is rather unexpected, as the earliest occupation of Papua New Guinea, an island in Oceania, by modern humans occurred only about 45,000 years ago^{9,10}, and suggests quite a complicated picture for the ancestry of the Denisovan finger fragment.

Studying ancient molecular diversity is not without its pitfalls — the molecular shadows we perceive may well have a more complex underpinning. In their Supplementary Information, Reich, Pääbo and co-workers⁶ go into exquisite detail to discount many potential sources of bias in their data, including contamination, handling of the ancient material and differences in depth-of-coverage among genomes.

Many of these problems can indeed be discounted, but some technical hurdles remain. Sequencing technology and DNA preservation may affect the interpretation of the clustering statistic for ancient genomes — for example, the finding that greater numbers of derived alleles (gene variants) are shared between Eurasians and Neanderthals than between Eurasians and Denisovans could be due to differences in sequencing technology. Nonetheless, it seems that comparison of ancient and modern genomes processed at the same time provides a consistent picture of extra allele-sharing between Denisovans and present-day Melanesians, as well as between Denisovans and Neanderthals.

Perhaps the most powerful use of ancient DNA sequencing technology is in the realm of hypothesis generation. For example, from the Denisovan remains, one can make explicit predictions about the patterns of genetic variation in modern humans who are yet to have their DNA sequenced. Specifically, if there is 5–7% extra allele-sharing in the genomes of Melanesians with an archaic *Homo* population, by sequencing modern individuals from the

region, every so often we should find oddly divergent regions of the genome in some Melanesian individuals. The same idea has been proposed to test Neanderthal admixture models (namely, looking for regions of the human genome in which the highly divergent fragments of DNA sequence are non-African and potentially inherited from an ancient population).

As this work¹ illustrates, studies of human genomic variation need to expand beyond the realm of medical interest. The study of diverse human genomes (both ancient and present-day) is the most powerful tool available for understanding our common human origins and history. The success of this research depends, of course, on proper community and individual engagement of diverse peoples (including those from isolated human populations), who may possess the genomic history of ancient human migrations across the globe. Together with the palaeoanthropological record, analyses of ancient and modern

DNA will help us to better understand our own creation myths, and illuminate the details of the molecular shadows in the cave. ■

Carlos D. Bustamante and Brenna M. Henn
are in the Department of Genetics, Stanford University School of Medicine, Stanford, California 94305, USA.
e-mail: cdbustam@stanford.edu

1. Reich, D. et al. *Nature* **468**, 1053–1060 (2010).
2. Cann, R., Stoneking, M. & Wilson, A. *Nature* **325**, 31–36 (1987).
3. Ramachandran, S. et al. *Proc. Natl Acad. Sci. USA* **102**, 15942–15947 (2005).
4. Underhill, P. et al. *Ann. Hum. Genet.* **65**, 43–62 (2001).
5. Klein, R. *The Human Career* 3rd edn (Univ. Chicago Press, 2009).
6. Green, R. E. et al. *Science* **328**, 710–722 (2010).
7. Wolpoff, M., Hawks, J. & Caspari, R. *Am. J. Phys. Anthropol.* **112**, 129–136 (2000).
8. Krause, J. et al. *Nature* **464**, 894–897 (2010).
9. O'Connell, J. & Allen, J. *J. Archaeol. Sci.* **31**, 835–853 (2004).
10. Summerhayes, G. et al. *Science* **330**, 78–81 (2010).
11. Cavalli-Sforza, L. & Feldman, M. *Nature Genet.* **33**, 266–275 (2003).

QUANTUM TECHNOLOGY

Electrons spin in the field

Nanowires are candidates for enabling the exchange of quantum information between light and matter. The rapid control of a single electron spin by solely electrical means brings this possibility closer. SEE LETTER P.1084

DAVID J. REILLY

The quest to develop ways to store and manipulate quantum information in condensed-matter systems is establishing a tool kit for controlling the nanoworld — one that promises far-reaching technological innovation. One example is the idea of encoding data, both classical¹ and quantum², in the spin orientation of a single electron (its intrinsic magnetic moment). During the past five years, this vision has largely been realized^{3–7}, and researchers are now turning to other goals, such as high-speed control of the spin orientation and the suppression of 'decoherence' processes that lead to a loss of quantum information. Innovative methods in quantum control^{8,9} and new material systems are leading the way in tackling this next generation of challenges.

On page 1084 of this issue, Kouwenhoven and co-workers¹⁰ report an experiment that exploits the unique material properties of an indium arsenide (InAs) semiconductor nanowire to rapidly control the quantum state of a single electron spin using only electric fields. Beyond just flipping the spin orientation

of a single electron, the authors tailor the precise timing of electric-field pulses to extend the spin coherence time (during which the information encoded in the quantum state of the spin is preserved).

Controlling electron and nuclear spins is central to magnetic resonance technologies such as magnetic resonance imaging. These technologies use radio- or microwave-frequency magnetic fields to manipulate some 10²³ spins in macroscopic volumes. On the nanometre scale, the application of spatially selective, oscillating magnetic fields is a formidable challenge, which makes controlling single spins difficult. Although proof-of-principle experiments have shown that nanometre-scale magnetic control is possible¹¹, the time it takes to rotate the orientation of the electron spin magnetically is long and does not allow for many rotations within a spin coherence time. This limitation inhibits the use of this technique for quantum information processing.

Kouwenhoven and colleagues' experiment¹⁰ addresses this shortcoming by moving from magnetic to all-electric fields to achieve rapid control over the spin. Although an interaction

between an electron's spin and an applied electric field is forbidden, if it is strong enough a quantum interaction known as spin-orbit coupling provides a means of controlling spins using oscillating electric fields, and is at the heart of the new field of 'spintronics'.

Special relativity requires that an electron moving through an electric field experiences an effective magnetic field that couples its spatial motion (orbit) to its spin. In the simplest picture, spin-orbit coupling is possible because, from the viewpoint of the electron, it is the electric field that is moving, and time-varying electric fields generate a magnetic field that splits the electron's spin states in energy. The detailed picture of spin-orbit coupling has played a key part in the formulation of quantum mechanics.

For semiconductors in a magnetic field, the spin-orbit interaction can be much stronger than in an atom, owing to the high electron velocities and strong electric-field gradients produced by nuclei in the semiconductor crystal lattice¹². As is the case in Kouwenhoven and colleagues' experiment, careful choice of material system and device geometry can lead to spin-orbit coupling that is so strong that the electron's spatial state and its spin cannot be considered separately: they collectively form a quantum state that preserves the long-lived spin component while allowing for manipulation through electric fields^{13,14}.

The signature of spin-orbit control has previously been identified in gallium arsenide (GaAs) semiconductor quantum devices¹⁵, but the strong coupling in the InAs nanowire devices allows both faster control and the potential for the exchange of quantum information between optical and solid-state electronic systems. Indeed, optoelectronic devices^{16,17}, such as semiconductor LEDs (light-emitting diodes), have recently been demonstrated in nanowire architectures that are similar to the authors' InAs nanowire, and the possibility of transferring the quantum state of a single spin to a single photon now seems viable. The creation of such hybrid quantum systems is pivotal because they allow the unique advantages of different quantum platforms to be combined to open up new quantum technologies. The iPhone provides the perfect example of how the tight integration of optical, mechanical and electrical devices can have a significant technological impact. In quantum mechanics, this kind of integration is not easy, owing, in part, to the nature of quantum measurement and the fragility of systems that manipulate quantum information.

For Kouwenhoven and colleagues' experiment¹⁰, an important but perhaps unexpected result is that the spin coherence lifetime, measured by a technique known as the Hahn echo pulse sequence, is significantly shorter than in GaAs. The authors' hunch is that this may result from the larger nuclear spin moment of indium compared with gallium or arsenic,

which couples uncontrollably to the electron spin. To what extent this short time presents a fundamental problem requires further research, but will undoubtedly drive fresh innovation in the science and engineering of quantum systems. ■

David J. Reilly is in the School of Physics, The University of Sydney, New South Wales 2006, Australia.
e-mail: david.reilly@sydney.edu.au

1. Datta, S. & Das, B. *Appl. Phys. Lett.* **56**, 665–667 (1990).
2. Loss, D. & DiVincenzo, D. P. *Phys. Rev. A* **57**, 120–126 (1998).
3. Elzerman, J. M. *et al. Nature* **430**, 431–435 (2004).
4. Petta, J. R. *et al. Science* **309**, 2180–2184 (2005).
5. Pioro-Ladrière, M. *et al. Nature Phys.* **4**, 776–779 (2008).
6. Barthel, C., Reilly, D. J., Marcus, C. M., Hanson,

- M. P. & Gossard, A. C. *Phys. Rev. Lett.* **103**, 160503 (2009).
7. Petta, J. R., Lu, H. & Gossard, A. C. *Science* **327**, 669–672 (2010).
8. Bluhm, H. *et al.* Preprint at <http://arxiv.org/abs/1005.2995> (2010).
9. Barthel, C., Medford, J., Marcus, C. M., Hanson, M. P. & Gossard, A. C. Preprint at <http://arxiv.org/abs/1007.4255> (2010).
10. Nadj-Perge, S., Frolov, S. M., Bakkers, E. P. A. M. & Kouwenhoven, L. P. *Nature* **468**, 1084–1087 (2010).
11. Koppens, F. H. L. *et al. Nature* **442**, 766–771 (2006).
12. Rashba, E. I. *Future Trends in Microelectronics: Up the Nano Creek* (eds Luryi, S., Xu, J. & Zaslavsky, A.) 28–40 (Wiley, 2007).
13. Golovach, V. N., Borhani, M. & Loss, D. *Phys. Rev. B* **74**, 165319 (2006).
14. Flindt, C., Sørensen, A. S. & Flensberg, K. *Phys. Rev. Lett.* **97**, 240501 (2006).
15. Nowack, K. C., Koppens, F. H. L., Nazarov, Y. V. & Vandersypen, L. M. K. *Science* **318**, 1430–1433 (2007).
16. Minot, E. D. *et al. Nano Lett.* **7**, 367–371 (2007).
17. van Weert, M. H. M. *et al. Nano Lett.* **9**, 1989–1993 (2009).

STRUCTURAL BIOLOGY

Proteins in dynamic equilibrium

Protein molecules in solution exist as an equilibrium of different conformations, but the sizes and shifts of these populations cannot be determined from static structures. A report now shows how they can be measured in solution.

PAU BERNADÓ & MARTIN BLACKLEDGE

Technologies for determining protein structure have contributed immensely to our understanding of molecular biology, providing us with three-dimensional models at atomic resolution to explain the molecular basis of physiologically important interactions between biochemically active molecules¹. But as we emerge from a decade of massive investment in structural genomic projects, it is becoming increasingly clear that a complete description of biomolecular activity also requires an understanding of the nature and role of protein conformational dynamics. Reporting in the *Proceedings of the National Academy of Sciences*, Yang *et al.*² describe a method that could provide us with just such an understanding — a combination of computational simulations and experimental X-ray scattering data enables the observation of shifts in the equilibrium population of protein conformational states.

Proteins must be able to move in order to function. Such motion can be on a small scale — involving atomic fluctuations around an average structure — or can involve large-scale reorganization of molecular machinery³. Experimental data for proteins normally represent average values for the entire ensemble of

conformations, but structural determinations routinely represent a single, static structure. The dynamic trajectories of protein movement can be invoked, by trapping and observing active or inactive conformational states and deducing the pathway that connects them. But direct access to functionally important protein motions requires new experimental and analytical tools that can accurately map conformational equilibria.

In recent years, structural biologists have risen to this challenge by developing techniques to describe dynamic systems in terms of ensembles of structures, thus providing information about the importance of molecular motion for biological function^{4,5}. For example, nuclear magnetic resonance (NMR) spectroscopy provides ensemble-averaged experimental parameters that describe the intrinsic conformational dynamics that control molecular recognition⁶. Changes in global orientations of protein domains, or in the shape and size of molecular assemblies, are more difficult to characterize using NMR alone, but these can be determined using a method known as small-angle X-ray scattering (SAXS)^{7,8}.

It is gradually becoming established that the most appropriate way to define proteins' conformational disorder is to explicitly identify the

ensembles of conformations that coexist and rapidly interconvert in dynamic equilibrium. Because of the vast number of conformations that can potentially be adopted by flexible proteins, accurate identification of these ensembles presents an ill-defined 'inverse problem' — how can the ensembles be identified from acquired data? The solution requires the development of robust statistical approaches to determine the probability that any particular multi-conformational equilibrium will exist⁹. A true statistical mechanical description of an ensemble also requires a quantitative assessment of the weighting of each conformation in the Boltzmann probability distribution of conformations. Yang *et al.* elegantly address both of these considerations in their study².

The authors used SAXS to study a multi-domain tyrosine kinase enzyme known as Hck, which belongs to the Src family of kinases. Src kinases are thought to be involved in the signalling pathways that govern cell growth and proliferation, and are implicated in many human diseases, most notably cancer. The regulation of Src kinases is known to involve large-scale reorientation of the proteins' domains.

Activation of these enzymes has been proposed to be a two-step process. In the first step, two small domains (SH2 and SH3) form intramolecular interactions with the carboxy and amino termini of a larger, catalytic domain to form a compact, inactive 'assembled' conformation. In the second step, the release of the intramolecular interactions destabilizes the compact structure, causing the formation of a more open, 'disassembled' state (the active conformation). This model of regulation has been delineated from crystal structures of different Src proteins at the end points of the activation process^{10,11}. Crucially, however, the dynamic flux between these states was poorly understood — until Yang *et al.* published their report².

The authors studied Hck in solution, both in its free form and in complex with SH2- and SH3-binding peptides. First, they used coarse-grained (low resolution) molecular dynamics simulations to extensively explore and sample accessible conformations of the protein in a physically meaningful way. Next, they used a clustering analysis on the resulting data to obtain a set of sub-states for the protein, which they used to interpret their experimentally obtained SAXS curves.

A common problem with statistical analyses is over-fitting, which occurs when a statistical model describes noise, rather than the desired underlying relationship. Yang *et al.* intelligently avoided over-fitting by evoking only the minimum number of states that could be distinguished from their SAXS data. In addition, and equally importantly, the authors used a Bayesian statistical analysis of these states to accurately determine their fractional populations under different experimental conditions that change the conformational equilibrium.

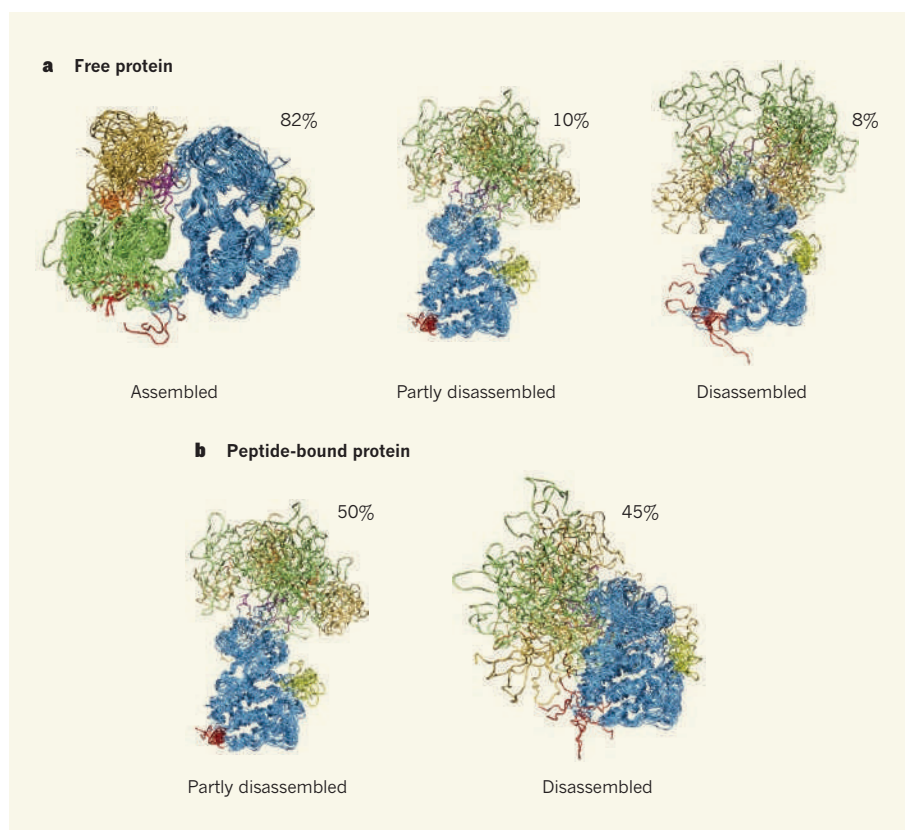


Figure 1 | Conformational states of the Hck enzyme in solution. The multidomain enzyme Hck can adopt several conformational states in solution, ranging from a compact 'assembled' state to partially assembled and disassembled states. Different domains are shown in different colours. **a**, Yang *et al.*² used a combination of molecular dynamics simulations with small-angle X-ray scattering (SAXS) data to show that, in solution, free molecules of Hck divide into different populations of these states, existing in a dynamic equilibrium with each other. The percentages indicate the fraction of the molecular population that exists in a particular state. **b**, The authors also charted major population shifts in response to the binding of peptides (not shown) to the SH2 and SH3 domains. The 5% of the population unaccounted for in the figure is divided between several other conformational states. (Figure adapted from ref. 2.)

Yang *et al.* demonstrated that several assembly states in equilibrium — not just two — must be considered to properly understand the conformational landscape that is crucial to the regulation of Hck (Fig. 1). The authors found that the enzyme is predominantly in the inactive, assembled conformation (82% of enzyme molecules), but is in dynamic equilibrium with partially and fully disassembled states. The assembled conformation predominates even in the absence of a phosphate group on the carboxy terminus of the catalytic domain. This is notable because phosphorylation of the carboxy terminus was thought to anchor Src enzymes in the assembled state, with dephosphorylation triggering disassembly to the active state.

Yang and colleagues also observed that the population equilibrium among the various states responds to the presence of signalling peptides that, on binding to the SH2 or SH3 domains, break specific intramolecular interactions in the enzyme. Taken together, their results demonstrate the link between the regulation of Hck and the complexity of its conformational-energy landscape, and exemplify

the inability of single structural images to fully describe such an intricate molecular process.

The development of quantitative approaches for characterizing highly fluctuating conformational equilibria on the basis of experimental data measured in solution is essential if we are to develop true statistical mechanical images of the potential-energy landscapes intrinsic to dynamic biomolecular systems. It is becoming clear that structural biology is experiencing a paradigm shift, with the realization that excited or partially populated states are crucial to biological function¹², and that the determination of single structures from ensemble-averaged experimental data can miss vital conformational fluctuations or population changes that may be essential for biological activity. Ensemble approaches to the interpretation of SAXS and NMR data will inevitably reveal further secrets of the role of intrinsic conformational dynamics in protein function, as structural biology continues its inexorable shift towards a richer and more dynamic equilibrium. ■

Pau Bernadó is at the Institute for Research in Biomedicine, 08028-Barcelona, Spain.

Martin Blackledge is at the *Institute de Biologie Structurale Jean-Pierre Ebel, Commissariat à l'Energie Atomique, CNRS, Université Joseph Fourier, Grenoble 38027, France.*

e-mails: pau.bernado@irbbarcelona.org; martin.blackledge@ibs.fr

1. Chandonia, J.-M. & Brenner, S. E. *Science* **311**, 347–351 (2006).

2. Yang, S., Blachowicz, L., Makowski, L. & Roux, B. *Proc. Natl Acad. Sci. USA* **107**, 15757–15762 (2010).
3. Henzler-Wildman, K. & Kern, D. *Nature* **450**, 964–972 (2007).
4. Mittermaier, A. K. & Kay, L. E. *Trends Biochem. Sci.* **34**, 601–611 (2009).
5. Zhang, Q. *et al. Nature* **450**, 1263–1267 (2007).
6. Markwick, P. R. L. *et al. J. Am. Chem. Soc.* **131**, 16968–16975 (2009).
7. Putnam, C. D., Hammel, M., Hura, G. L. & Tainer, J. A. *Q. Rev. Biophys.* **40**, 191–285 (2007).

8. Bernadó, P., Mylonas, E., Petoukhov, M. V., Blackledge, M. & Svergun, D. I. *J. Am. Chem. Soc.* **129**, 5656–5664 (2007).
9. Bertini, I. *et al. J. Am. Chem. Soc.* **132**, 13553–13558 (2010).
10. Sicheri, F., Moarefi, I. & Kuriyan, J. *Nature* **385**, 602–609 (1997).
11. Cowan-Jacob, S. W. *et al. Structure* **13**, 861–871 (2005).
12. Baldwin, A. J. & Kay, L. E. *Nature Chem. Biol.* **5**, 808–814 (2009).

EXTRASOLAR PLANETS

A giant surprise

The discovery of an inner giant planet in the unusually massive solar system around the star HR 8799 creates an ensemble of planets that is difficult to explain with prevailing theories of planet formation. SEE LETTER P.1080

LAIRD CLOSE

The solar system around the star HR 8799 should not exist. This system is unlike any other known: it is a massive system that has multiple massive planets, with each giant planet containing many times the mass of all the planets in our Solar System combined. However, on page 1080 of this issue, Marois and collaborators¹ present new images of HR 8799 in which yet another equally massive planet is visible*.

Previous work² had imaged three planets around HR 8799, and now we have the surprise discovery of a fourth, HR 8799e, an inner, massive planet (about 10 Jupiter masses) located some 14.5 astronomical units from the star (1 AU is the average distance from Earth to the Sun). One might question the importance of the discovery of another extrasolar planet when more than 500 are known. But the HR 8799 system is the only solar system known to have multiple outer planets (the other three planets, HR 8799b, HR 8799c and HR 8799d, orbit respectively at approximately 68, 38 and 24 AU from the host star, and have estimated masses of about 7, 10 and 10 Jupiters).

As HR 8799 is the only known example of a wide (greater than 25 AU) solar system with multiple giant planets, astronomers were curious to know whether the star's planets could have formed by gravitational collapse³ — one

of the most popular theories of outer-planet formation. This theory posits that outer giant planets form from the fragmentation of the disk of gas and dust that develops around stars when they are young. In a process rather like the way binary stars form, a gravitational instability in the disk fragments it and quickly (on a timescale of 10,000 years) leads to the formation of gas-giant planets³. But the discovery of

an inner planet such as HR 8799e at 14.5 AU poses a tricky puzzle. At this distance, the disk was neither cold enough nor rotating slowly enough to fragment and undergo gravitational collapse *in situ* to form HR 8799e³.

To explain the formation of this latest planet, Marois *et al.*¹ appeal to the dominant theory of giant-planet formation: a slower process than gravitational collapse (about 3.5 million years at a distance of 10 AU) in which solid dust grains conglomerate into solid cores of tens of Earth masses and then gravitationally accrete disk gas to grow to Jupiter masses. Such a 'core-accretion' process itself is only marginally fast enough at 14.5 AU to build up HR 8799e's roughly 10 Jupiter masses before the disk gas accretes onto the star in less than 10 Myr. This formation timescale problem³ becomes even more vexing if one considers that, at about 2.6 times the distance

HR 8799e is from the host star, HR 8799c would require about 20 times longer (more than about 200 Myr) to grow to the same mass at 38 AU — long after the disk has lost all its gas. What's more, at 68 AU, HR 8799b's formation is truly problematic, requiring an even longer timescale (many times the age of the star) to have formed *in situ* by core accretion. Hence, neither of the two favoured theories of giant-planet formation can explain how all the planets around HR 8799 formed: HR 8799e is too close to have formed by gravitational collapse, and HR 8799c and HR 8799b are too far out to have formed by core accretion (Fig. 1).

Perhaps all of these massive planets formed at much larger distances (more than at least 50 AU) by the gravitational collapse of an unusually massive disk and then migrated quickly inwards to their current positions, somehow sweeping into a dynamically stable set of 1:2:4 orbital resonances¹ (where, for every one orbit of planet c, there are two of d and four of e). This does not really help the situation, however, because it is unlikely

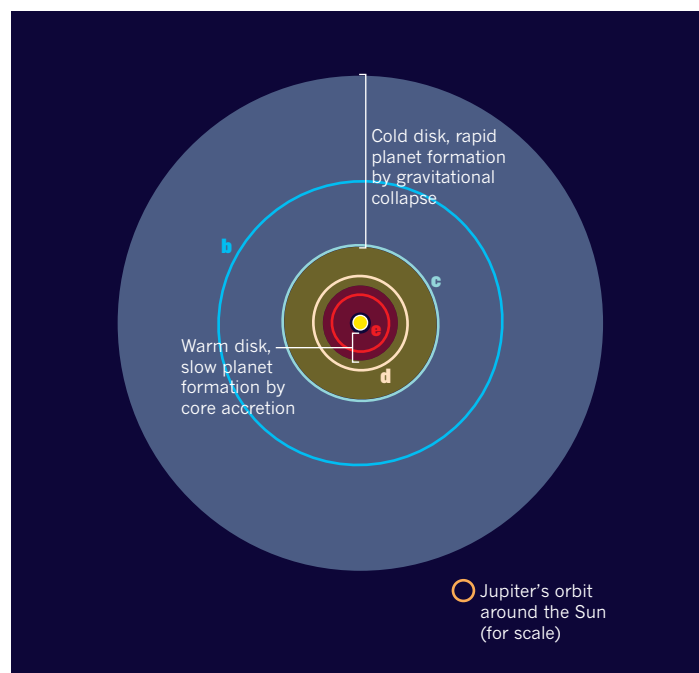


Figure 1 | The HR 8799 planetary system. When star HR 8799 formed, a massive circumstellar disk of gas and dust probably existed from which the star's four massive planets formed; the planets' approximate current orbits are overlaid and labelled b–e. The outer part of the disk was very cold and rotated slowly, and so might have collapsed through gravitational instabilities to quickly form outer planets such as 'b'. The newly discovered 'e' planet¹ is in a very different zone, where the disk was much warmer and the planet is likely to have formed in a slow, two-step 'core-accretion' process. Neither theory of planet formation — gravitational collapse or core accretion — can explain the whole family of four planets.

*This article and the paper under discussion¹ were published online on 8 December 2010.

that such a massive planet as HR 8799e could have migrated from about 50 to 14.5 AU by means of tidal torques from the residual gas that had not been used to build up the planets. The converse theory, by which the planets all form through core accretion within about 10 AU and then slowly move outwards by scattering lesser objects (planetesimals) inwards, is also problematic because there is probably too limited a reservoir of planetesimals to move a 7-Jupiter-mass object such as HR 8799b outwards some 58 AU. So, despite having a clear view of the system — thanks to the power of adaptive-optics systems and large ground-based telescopes — we cannot currently explain how all four planets formed in a coherent, coeval fashion.

A key strength of direct imaging is that photons can be collected from these self-luminous young planets as they contract, allowing the planetary spectra to be observed (to calculate temperatures and luminosities). The observed brightness of HR 8799b in direct images is much lower than would be expected from its observed temperature, given that evolutionary models indicate that HR 8799b must have a radius larger than that of Jupiter^{1,2,4}. This 'under-luminosity' problem is typical of around half of the extrasolar planets imaged to date. One possible explanation is that dusty, thick, planetary-scale high-latitude cloud 'bands' absorb/scatter light when viewing a young planet over its pole. For example, the 'under-luminous' planets in the HR 8799 system are probably being viewed close to 'pole-on'⁵, perhaps leading to less light emitted in the direction of Earth. By contrast, 'edge-on' giant planets, such as β -Pictoris b⁶, look brighter because light streams freely from the brighter equatorial regions between the dark cloud bands. Clearly, further theoretical (and direct imaging) work will be needed to identify the ultimate cause of this under-luminosity problem.

The future holds much promise for more surprises in the field of direct imaging of extrasolar planets. However, it seems unlikely that any other massive outer planets will be found around HR 8799⁷. There is always a chance, though, that low-mass terrestrial planets lie within the star's 10-AU-radius 'asteroid' belt. The next chapter in this story will soon be written by even more powerful ground-based, adaptive-optics imagers^{8,9} and, let us hope, by more powerful pathfinding, space-based planet- and disk-imaging telescopes¹⁰. These pathfinders should eventually lead to a terrestrial-planet-finding telescope even capable of taking spectra of Earth-like planets. Such an achievement could address one of the most pivotal questions in science: how common are truly Earth-like planets and life in our Universe? ■

Laird Close is in the Department of Astronomy and Steward Observatory, University of

Arizona, Tucson, Arizona 85721, USA.
e-mail lcloose@as.arizona.edu

1. Marois, C., Zuckerman, B., Konopacky, Q. M., Macintosh, B. & Barman, T. *Nature* **468**, 1080–1083 (2010).
2. Marois, C. *et al. Science* **322**, 1348–1352 (2008).
3. Nero, D. & Bjorkman, J. E. *Astrophys. J.* **702**, L163–L167 (2009).
4. Bowler, B. P., Liu, M. C., Dupuy, T. J. & Cushing, M. C. *Astrophys. J.* **723**, 850–868 (2010).

5. Moro-Martín, A., Rieke, G. H. & Su, K. Y. L. *Astrophys. J.* **721**, L199–L202 (2010).
6. Lagrange, A.-M. *et al. Science* **329**, 57–59 (2010).
7. Close, L. M. & Males, J. R. *Astrophys. J.* **709**, 342–348 (2010).
8. Beuzit, J.-L. *et al. Astron. Soc. Pacif. Conf. Ser.* **430**, 231 (2010).
9. Macintosh, B. A. *et al. Proc. SPIE* **7015**, 701518 (2008).
10. Green, T. P., Schneider, G. & EXCEDE Mission Team *Bull. Am. Astron. Soc.* **39**, 975 (2007).

BEHAVIOURAL NEUROSCIENCE

A gene for impulsivity

Impulsivity has been linked to various psychiatric disorders and forms of violent behaviour. A gene mutated in a population of violent Finnish criminal offenders provides clues to the neural basis of this trait. [SEE ARTICLE P.1061](#)

JOHN R. KELSÖE

An old adage admonishes us to look before we leap. This bit of common sense reflects a crucial and complex brain function that regulates behaviour. To act without thinking — impulsivity — is to risk leaping off a cliff. But to excessively delay an action may lead to inaction or missed opportunities. Now, using a powerful genomics approach, Bevilacqua and colleagues¹ dissect elements of the neurotransmitter system in the brain that mediates impulsivity and show that the serotonin 2B receptor (HTR2B) has a role in severe impulsivity, at least in one human population (page 1061 of this issue).

Impulsivity is generally thought to be a failure of inhibitory function in the brain². Clearly, fine-tuning of such inhibition is important for an organism to adapt to its environment. Impulsivity has been linked to a variety of behavioural and psychiatric syndromes, including attention deficit hyperactivity disorder, mania, drug addiction and borderline personality disorder (BPD)^{3,4}. It has also been associated with violent behaviour, as seen in antisocial personality disorder (ASPD) and intermittent explosive disorder (IED), and with suicide. Several neurotransmitters — serotonin and dopamine in particular — have been implicated in mediating impulsivity, but unravelling the underlying mechanisms has proved challenging.

In their search for genes predisposing to impulsivity, Bevilacqua *et al.*¹ used the well-studied 'founder' population of Finland. Because of the country's relative isolation, the current Finnish population is believed to be largely derived from two waves of immigration 4,000 and 2,000 years ago⁵. It has therefore been argued that, compared with other, more-outbred populations, there may be fewer mutations for genetic traits in this

population, and studies of various genetic disorders support this assumption. To further enhance their odds of success, Bevilacqua and co-workers focused on Finnish subjects with the most extreme manifestation of impulsivity — violent offenders whom the authors evaluated in a forensic psychiatric unit and who had strong lifetime histories of aggressive acts.

Specifically, Bevilacqua *et al.* examined 96 individuals for 14 candidate genes, using next-generation sequencing technology to identify possible disorder-causing mutations. They focused on the protein-coding regions (exons) of the genes as the regions in which mutations would most probably affect gene function. They found a variation at a single nucleotide base — dubbed *HTR2B* Q20* — in the *HTR2B* gene, which results in an erroneous stop codon, a signal that ends further protein extension. The researchers show that this mutation triggers a process called nonsense-mediated RNA decay, such that no HTR2B-receptor protein is expressed.

The *HTR2B* Q20* mutation was present in the violent offenders at three times the rate of that in matched controls (psychiatrically normal Finnish individuals). It was also inherited, along with psychiatric illnesses such as ASPD, IED and BPD, by members of their families. The 17 violent offenders who carried *HTR2B* Q20* had all committed an average of five violent crimes, 94% of which were committed under the influence of alcohol. These crimes were largely aggressive reactions to minor events that lacked premeditation or financial gain as a goal.

The authors' results are consistent with many animal and human studies that implicate serotonin in impulsive behaviour^{6,7}. Previous studies have in general supported the idea that low serotonin levels are associated with impulsive action. For instance, activation

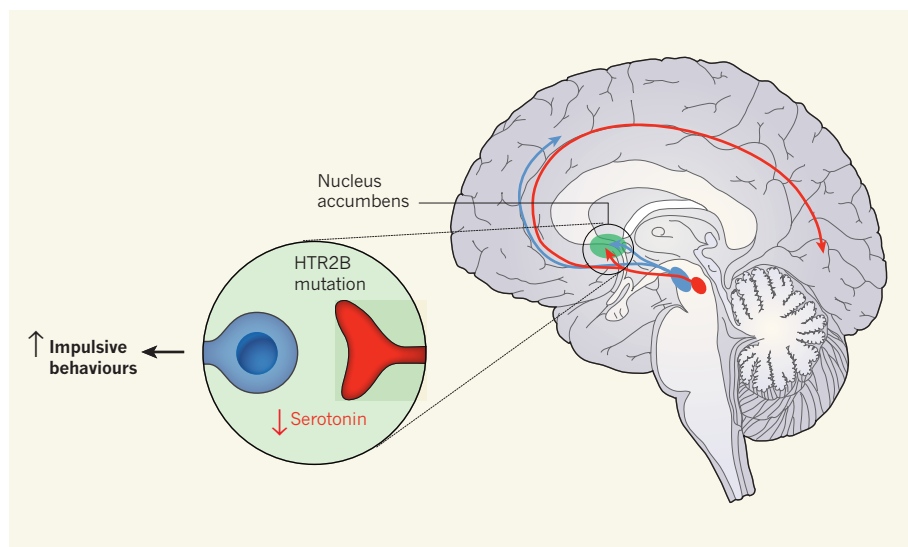


Figure 1 | HTR2B and the regulation of impulsivity. Bevilacqua *et al.*¹ find that, in a Finnish subpopulation, a mutation in the serotonin receptor HTR2B is linked to severe impulsivity. In the nucleus accumbens region (green) of the brain, projections of neurons that secrete serotonin (red) interact with those that secrete dopamine (blue). This region has been repeatedly shown to play a crucial part in choice and impulsivity. Mutations in HTR2B, which modulates the release of dopamine and serotonin in the nucleus accumbens, may reduce the release of these neurotransmitters, leading to increased impulsive behaviour.

of the 5-HT_{1A} receptor, which may inhibit serotonin release, has been linked to impulsivity in animal models⁸. Moreover, the levels of 5-hydroxyindoleacetic acid — a metabolite of serotonin — are reduced in the cerebrospinal fluid of people who are suicidal⁹. Furthermore, individuals whose serotonin levels have been experimentally lowered by diet are more likely to make impulsive choices¹⁰. Nonetheless, the role of serotonin is probably complex, not least because the serotonin system includes 14 different receptors with sometimes opposing actions.

The HTR2B receptor received little attention in earlier studies of impulsivity. So, to support their human data, Bevilacqua *et al.*¹ examined mice that lack the *Htr2b* gene. They observed increased impulsive behaviour in these animals according to several measures. How exactly HTR2B deficiency leads to this effect remains unclear, although the authors find that both male mice lacking *Htr2b* and men carrying the HTR2B Q20* mutation have elevated levels of the hormone testosterone.

Previous work² suggests that HTR2B may function by modulating both serotonin and dopamine in the nucleus accumbens — a brain region involved in impulsive behaviour (Fig. 1). For instance, the 'club drug' ecstasy has been shown¹¹ to stimulate the release of both serotonin and dopamine in the nucleus accumbens by directly activating HTR2B. It could therefore be that depletion of the HTR2B receptor results in increased impulsive behaviour by reducing the release of both serotonin and dopamine in the nucleus accumbens. However, much more work is required to elucidate how HTR2B regulates impulsive behaviour through

its modulation of the interaction between pathways involving serotonin and dopamine.

Bevilacqua and colleagues' observation¹ that the HTR2B Q20* mutation is unique to Finns serves as yet another reminder of the high level of heterogeneity likely to be seen in complex

genetic traits and the importance of population history. But although this specific mutation is absent in non-Finnish populations, different mutations in the HTR2B gene might operate in other populations.

Bevilacqua and colleagues' paper also illustrates the power of exon-based sequencing in founder populations, and suggests that exonic mutations of strong functional effect do play a part in complex behavioural traits. ■

John R. Kelsoe is in the Department of Psychiatry, University of California, San Diego, and the VA San Diego Healthcare System, La Jolla, California 92014, USA. e-mail: jkelsoe@ucsd.edu

1. Bevilacqua, L. *et al.* *Nature* **468**, 1061–1066 (2010).
2. Cardinal, R. N. *Neural Netw.* **19**, 1277–1301 (2006).
3. Moeller, F. G., Barratt, E. S., Dougherty, D. M., Schmitz, J. M. & Swann, A. C. *Am. J. Psychiatry* **158**, 1783–1793 (2001).
4. Swann, A. C., Lijffijt, M., Lane, S. D., Steinberg, J. L. & Moeller, F. G. *Bipolar Disord.* **11**, 280–288 (2009).
5. Peltonen, L., Jalanko, A. & Varilo, T. *Hum. Mol. Genet.* **8**, 1913–1923 (1999).
6. Robbins, T. W. *Psychopharmacology* **163**, 362–380 (2002).
7. Pattij, T. & Vanderschuren, L. J. M. J. *Trends Pharmacol. Sci.* **29**, 192–199 (2008).
8. Winstanley, C. A., Theobald, D. E., Dalley, J. W. & Robbins, T. W. *Neuropsychopharmacology* **30**, 669–682 (2005).
9. Traskman, L., Åsberg, M., Bertilsson, L. & Sjöstrand, L. *Arch. Gen. Psychiatry* **38**, 631–636 (1981).
10. Rogers, R. D. *et al.* *Psychopharmacology* **146**, 482–491 (1999).
11. Doly, S. *et al.* *J. Neurosci.* **28**, 2933–2940 (2008).

DRUG DISCOVERY

Reader's block

Protein factors can regulate gene expression by binding to specifically modified DNA-associated proteins. Small molecules that selectively interfere with such interaction may be of therapeutic value. SEE ARTICLE P.1067 & LETTER P.1119

SEAN D. TAVERNA & PHILIP A. COLE

Protein factors are crucial for controlling gene expression. One group of such factors affects gene activity by 'reading' epigenetic marks — reversible modifications such as the addition of phosphate, acetyl or methyl groups — on proteins after their translation from RNA. The factors' target proteins are histones, which associate with DNA to form chromatin. The reading ability of these protein factors is a result of specific, well-folded subdomains, sometimes called readers, which can distinguish between the post-translationally modified state of their binding partner and its unmodified state. Two papers^{1,2} in this issue describe highly potent and selective inhibitor molecules that compete with acetylated histones for binding to a set of such readers.

These data have therapeutic implications.

Post-translational modifications can often influence transient protein–protein interactions by creating or disrupting binding surfaces on the molecules. Among such modifications, acetylation on lysine amino-acid residues has been centre stage: originally discovered³ more than 40 years ago as a regulator of chromatin structure, this modification has now been detected in thousands of other proteins⁴. Acetyl-lysine modifications facilitate the interaction of the protein with proteins that contain bromodomains — evolutionarily conserved subdomains that can specifically bind, or read, the acetylated form of the lysine during regulatory processes⁵. Such interactions are thought to regulate transcription and to be involved in various diseases, including cancer.

A range of acetyltransferase enzymes (writers) add acetyl groups to lysine residues, and two families of deacetylase enzymes (erasers) remove these groups⁶. Two recently approved anticancer drugs⁷ — SAHA and depsipeptide — work by blocking deacetylases, and have galvanized the pharmaceutical industry's interest in targeting chromatin modifications. In fact, several start-up biotech companies have attempted to target erasers and writers of lysine acetylation. In general, however, even highly specific inhibitors of acetyltransferases and deacetylases that mediate post-translational modification can have undesired side effects, because blocking these enzymes can affect many different protein substrates and biochemical pathways.

As for targeting protein–protein interactions, with several notable exceptions the use of small-molecule drugs has been considered extremely difficult⁸ because their binding regions frequently consist of wide, shallow surfaces. For example, despite decades of work, pharmacologically practical compounds that disrupt the binding of phosphorylated proteins to their SH2-domain-containing protein partners have remained elusive. There have also been a couple of attempts to use small molecules to inhibit the interactions between proteins containing bromodomains and those carrying acetyl-lysines, but focus on this line of research has generally been limited⁹.

Using very different approaches, Filippakopoulos *et al.* (page 1067) and Nicodeme *et al.* (page 1119) now converge on a closely related set of chemical scaffolds — the triazole-diazepine-fused ring compounds JQ1 and I-BET — that inhibit the acetyl-lysine-reading ability of a specific class of bromodomain. Both sets of compounds bind tightly to bromodomains in proteins of the BET family by exploiting the unusual pockets characteristic of this protein family (Fig. 1).

The bromodomains of BET proteins show a strong preference for housing doubly modified acetyl-lysine histone tails in their wide and highly structured hydrophobic pockets¹⁰. Because of their shape and electrical properties, these pockets are also well suited for binding small molecules. Indeed, the present papers' structural data^{1,2} confirm that JQ1 and I-BET fit snugly into the acetyl-lysine pockets in a stereospecific fashion. Thermodynamic measurements further establish that both of the bromodomain–inhibitor interactions are of high affinity (with dissociation constants below 100 nM) and, compared with their interaction with other non-BET types of bromodomain, show great selectivity (at least 100-fold).

The two teams also pursue distinct biomedical applications for JQ-1 and I-BET. Filippakopoulos *et al.*¹ examine whether JQ1 can antagonize the growth of a rare but aggressive form of cancer called midline carcinoma. This cancer is defined by a gene fusion that results in the unnatural linkage of BRD4 — a BET protein

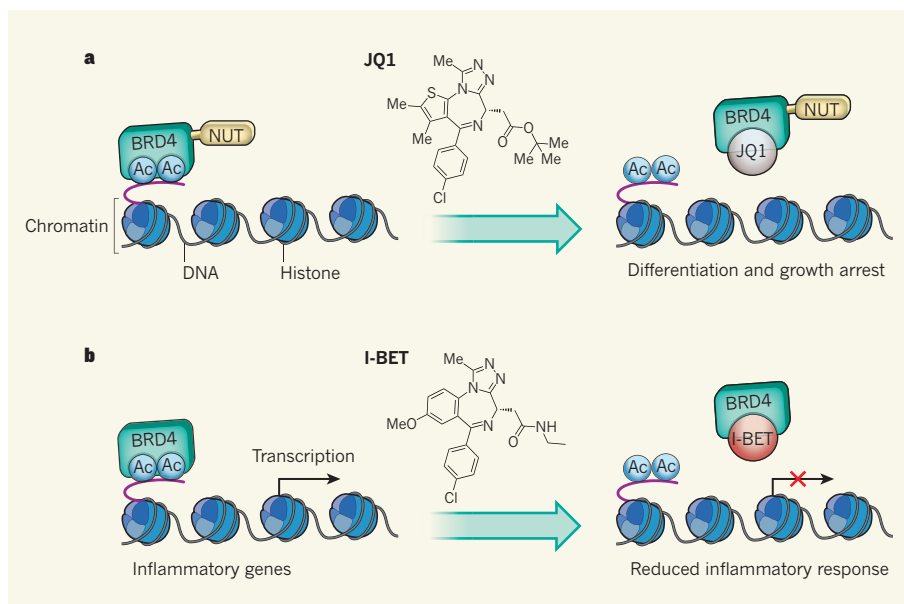


Figure 1 | Targeting the interaction between bromodomains and acetyl-lysine moieties.

a, Filippakopoulos *et al.*¹ show that JQ1 — a small-molecule competitive inhibitor that blocks the interaction of bromodomains of BET proteins with acetylated lysines (Ac) — can inhibit the proliferation of tumour cells expressing the BRD4–NUT oncoprotein. **b**, Nicodeme *et al.*² show that pretreatment of cells with another small-molecule competitive inhibitor, I-BET, which interferes with the interaction between the bromodomain of the BET protein BRD4 and Ac, can mute the transcription of genes that are induced during inflammatory responses.

containing two bromodomains — with another protein called NUT. The BRD4–NUT fusion protein mediates increased acetylation of certain chromatin domains that are normally transcriptionally inactive¹¹, and so it was predicted that inhibitors of the BRD4 bromodomains would shut down tumour growth mediated by this mechanism. Filippakopoulos and colleagues confirm this hypothesis, showing that JQ1 could blunt the growth of midline carcinoma cells in culture, as well as in mice into which the tumour cells were introduced.

Nicodeme *et al.*² investigate whether I-BET modulates genes mediating immunological and inflammatory responses. They find that it inhibits the expression of a subset of genes normally induced in response to toxic injury, with histone acetylation being reduced in the chromatin regions around these genes. In a practical application of these findings, the authors demonstrate that treating mice with I-BET protects against the excessive inflammatory response to septic shock. Such results point to the clinical potential of BET-bromodomain inhibitors in immuno-modulation therapies.

The two papers^{1,2} provide credibility for the idea of extending the pharmacology of targeting chromatin modifications beyond enzymatic activities and into the challenging arena of protein–protein interactions. One appeal of this strategy is that it avoids the promiscuity of enzyme inhibitors.

The studies further raise the prospect of identifying inhibitors of other readers, such as those that bind proteins containing methyl-lysine modifications. Nonetheless,

antagonizing a reader of post-translational modifications might also prompt unknown and unwanted alterations in biological pathways — a complication that necessitates extensive follow-up studies before such agents can move into the clinic. Moreover, the possible uniqueness of BET-bromodomain structures makes it difficult to predict whether small-molecule inhibitors would be similarly effective in antagonizing other bromodomain forms and reader modules. Nevertheless, the new tools described by these studies will undoubtedly prove attractive to biologists interested in the dynamics of chromatin and gene expression in physiology and disease. ■

Sean D. Taverna and Philip A. Cole are in the Department of Pharmacology and Molecular Sciences, Johns Hopkins University School of Medicine, Baltimore, Maryland 21205, USA.

e-mails: staverna@jhmi.edu; pcole@jhmi.edu

1. Filippakopoulos, P. *et al.* *Nature* **468**, 1067–1073 (2010).
2. Nicodeme, E. *et al.* *Nature* **468**, 1119–1123 (2010).
3. Gershey, E. L., Vidali, G. & Allfrey, V. G. *J. Biol. Chem.* **243**, 5018–5022 (1968).
4. Choudhary, C. *et al.* *Science* **325**, 834–840 (2009).
5. Taverna, S. D., Li, H., Ruthenburg, A. J., Allis, C. D. & Patel, D. J. *Nature Struct. Mol. Biol.* **14**, 1025–1040 (2007).
6. Cole, P. A. *Nature Chem. Biol.* **4**, 590–597 (2008).
7. Lemoine, M. & Younes, A. *Discov. Med.* **10**, 462–470 (2010).
8. Wells, J. A. & McClendon, C. L. *Nature* **450**, 1001–1009 (2007).
9. Sachchidanand *et al.* *Chem. Biol.* **13**, 81–90 (2006).
10. Morinier, J. *et al.* *Nature* **461**, 664–668 (2009).
11. Reynold, N. *et al.* *EMBO J.* **29**, 2943–2952 (2010).

Genetic history of an archaic hominin group from Denisova Cave in Siberia

David Reich^{1,2*}, Richard E. Green^{3,4*}, Martin Kircher^{3*}, Johannes Krause^{3,5*}, Nick Patterson^{2*}, Eric Y. Durand^{6*}, Bence Viola^{3,7*}, Adrian W. Briggs^{1,3}, Udo Stenzel³, Philip L. F. Johnson⁸, Tomislav Maricic³, Jeffrey M. Good⁹, Tomas Marques-Bonet^{10,11}, Can Alkan¹⁰, Qiaomei Fu^{3,12}, Suman Mallick^{1,2}, Heng Li², Matthias Meyer³, Evan E. Eichler¹⁰, Mark Stoneking³, Michael Richards^{7,13}, Sahra Talamo⁷, Michael V. Shunkov¹⁴, Anatoli P. Derevianko¹⁴, Jean-Jacques Hublin⁷, Janet Kelso³, Montgomery Slatkin⁶ & Svante Pääbo³

Using DNA extracted from a finger bone found in Denisova Cave in southern Siberia, we have sequenced the genome of an archaic hominin to about 1.9-fold coverage. This individual is from a group that shares a common origin with Neanderthals. This population was not involved in the putative gene flow from Neanderthals into Eurasians; however, the data suggest that it contributed 4–6% of its genetic material to the genomes of present-day Melanesians. We designate this hominin population ‘Denisovans’ and suggest that it may have been widespread in Asia during the Late Pleistocene epoch. A tooth found in Denisova Cave carries a mitochondrial genome highly similar to that of the finger bone. This tooth shares no derived morphological features with Neanderthals or modern humans, further indicating that Denisovans have an evolutionary history distinct from Neanderthals and modern humans.

Less than 200,000 years ago, anatomically modern humans (that is, humans with skeletons similar to those of present-day humans) appeared in Africa. At that time, as well as later when modern humans appeared in Eurasia, other ‘archaic’ hominins were already present in Eurasia. In Europe and western Asia, hominins defined as Neanderthals on the basis of their skeletal morphology lived from at least 230,000 years ago before disappearing from the fossil record about 30,000 years ago¹. In eastern Asia, no consensus exists about which groups were present. For example, in China, some have emphasized morphological affinities between Neanderthals and the specimen of Maba², or between *Homo heidelbergensis* and the Dali skull³. However, others classify these specimens as ‘early *Homo sapiens*’⁴. In addition, until at least 17,000 years ago, *Homo floresiensis*, a short-statured hominin that seems to represent an early divergence from the lineage leading to present-day humans^{5–7}, was present on the island of Flores in Indonesia and possibly elsewhere.

DNA sequences retrieved from hominin remains offer an approach complementary to morphology for understanding hominin relationships. For Neanderthals, the nuclear genome was recently determined to about 1.3-fold coverage⁸. This revealed that Neanderthal DNA sequences and those of present-day humans share common ancestors on average about 800,000 years ago and that the population split of Neanderthal and modern human ancestors occurred 270,000–440,000 years ago. It also showed that Neanderthals shared more genetic variants with present-day humans in Eurasia than with present-day humans in sub-Saharan Africa, indicating that gene flow from Neanderthals into the ancestors of non-Africans occurred to an extent that 1–4% of the genomes of people outside Africa are derived from Neanderthals⁸. In addition, ten partial and six complete

mitochondrial (mt)DNA sequences have been determined from Neanderthals^{9–17}. This has shown that all Neanderthals studied so far share a common mtDNA ancestor on the order of 100,000 years ago¹⁰, and in turn, share a common ancestor with the mtDNAs of present-day humans about 500,000 years ago^{10,18,19} (as expected, this is older than the Neanderthal–modern human population split time of 270,000–440,000 years ago estimated from the nuclear genome⁸). One of these mtDNA sequences has also shown that hominins carrying mtDNAs typical of Neanderthals were present as far east as the Altai Mountains in southern Siberia¹³.

In 2008, the distal manual phalanx of a juvenile hominin was excavated at Denisova Cave. This site is located in the Altai Mountains in southern Siberia, and is a reference site for the Middle to Upper Palaeolithic of the region where systematic excavations over the past 25 years have uncovered cultural layers indicating that human occupation at the site started up to 280,000 years ago²⁰. The phalanx was found in layer 11, which has been dated to 50,000 to 30,000 years ago. This layer contains microblades and body ornaments of polished stone typical of the ‘Upper Palaeolithic industry’ generally thought to be associated with modern humans, but also stone tools that are more characteristic of the earlier Middle Palaeolithic, such as side-scrapers and Levallois blanks^{21–23}.

Recently, we used a DNA capture approach¹⁰ in combination with high-throughput sequencing to determine a complete mtDNA genome from the Denisova phalanx. Surprisingly, this mtDNA diverged from the common lineage leading to modern human and Neanderthal mtDNAs about one million years ago¹⁹, that is, about twice as far back in time as the divergence between Neanderthal and modern human mtDNAs. However, mtDNA is maternally inherited as a single unit

¹Department of Genetics, Harvard Medical School, Boston, Massachusetts 02115, USA. ²Broad Institute of MIT and Harvard, Cambridge, Massachusetts 02142, USA. ³Department of Evolutionary Genetics, Max Planck Institute for Evolutionary Anthropology, Leipzig 04103, Germany. ⁴Department of Biomolecular Engineering, University of California, Santa Cruz 95064, USA. ⁵Institut für Naturwissenschaftliche Archäologie, University of Tübingen, Tübingen 72070, Germany. ⁶Department of Integrative Biology, University of California, Berkeley, California 94720, USA. ⁷Department of Human Evolution, Max Planck Institute for Evolutionary Anthropology, Leipzig 04103, Germany. ⁸Department of Biology, Emory University, Atlanta, Georgia 30322, USA. ⁹Division of Biological Sciences, University of Montana, Missoula, Montana 59812, USA. ¹⁰Howard Hughes Medical Institute, Department of Genome Sciences, University of Washington, Seattle, Washington 98195, USA. ¹¹Institute of Evolutionary Biology (UPF-CSIC), 08003 Barcelona, Spain. ¹²CAS-MPS Joint Laboratory for Human Evolution and Archeometry, Institute of Vertebrate Paleontology and Paleoanthropology of Chinese Academy of Sciences, Beijing 100044, China. ¹³Department of Anthropology, University of British Columbia, Vancouver, British Columbia V6T 1Z1, Canada. ¹⁴Palaeolithic Department, Institute of Archaeology & Ethnography, Russian Academy of Sciences, Siberian Branch, Novosibirsk 630090, Russia.

*These authors contributed equally to this work.

without recombination, and therefore is subject to chance events such as genetic drift, as well as gene flow and positive selection. In contrast, the nuclear genome comprises tens of thousands of unlinked, mostly neutrally evolving loci. This allows for analyses of genetic relationships that are robust to the stochasticity of genetic drift, and are much less affected by positive selection. To clarify the relationship of the Denisova individual to other hominin groups, we have therefore sequenced the Denisova nuclear genome and analysed its genomic relationships to Neanderthals and present-day humans. We have also attempted to clarify the chronology of hominin occupation of the cave and have identified a tooth from this group of hominins among material excavated in Denisova Cave.

DNA sequence determination

The entire internal portion of the phalanx sample was used for DNA extraction in our clean-room facility, where procedures to minimize contamination from present-day human DNA are rigorously implemented^{24,25} (Supplementary Information section 1). The DNA was treated with two enzymes: uracil-DNA-glycosylase, which removes uracil residues from DNA to leave abasic sites²⁶, and endonuclease VIII, which cuts DNA at the 5' and 3' sides of abasic sites. Subsequent incubation with *T4* polynucleotide kinase and *T4* DNA polymerase was used to generate 5'-phosphorylated blunt ends that are amenable to adaptor ligation. Because the great majority of uracil residues occur close to the ends of ancient DNA molecules, this procedure leads to only a moderate reduction in average length of the molecules in the library, but a several-fold reduction in uracil-derived nucleotide misincorporation²⁷.

Two independent sequencing libraries (SL3003 and SL3004) were created from the DNA, using a modified Illumina protocol²⁸ where a polymerase chain reaction (PCR) is used to add a 7-nucleotide index (in this case 5'-GTCGACT-3') to the library molecules. This index ensures that the libraries are not contaminated by other sequencing libraries when they are taken out of the clean room to be sequenced²⁹. The libraries were sequenced on the Illumina Genome Analyser IIx platform for 101 cycles from each end of the molecules and an additional 7 cycles for determination of the index until almost every unique sequence in the libraries had been seen multiple times, that is, almost every clone present in the libraries has been sequenced (Supplementary Information section 1). Bases were called using the machine-learning algorithm Ibis³⁰ and an overlap of at least 11 bases was required for paired-end reads to be fused to full-molecule-size DNA sequences that were further analysed. This results in a greatly reduced error rate²⁷, although it removes the few molecules that are above 191 nucleotides in length from analysis (~0.1% in SL3003 and ~0.2% in SL3004). Sequences were mapped using the program BWA³¹ to the human (hg18/NCBI 36) and the chimpanzee (panTro2/CGSC 2.1) genomes as well as to the inferred ancestral genome of these species (from the six-way Enredo-Pecan-Ortho alignment)³². PCR duplicates were identified and used to further increase sequence accuracy by calling consensus sequences.

A total of 82,227,320 sequences mapped uniquely (mapping quality ≥ 30) to the human genome, yielding about 5.2 gigabases of DNA sequences (1.9-fold genomic coverage), and 72,304,848 sequences mapped uniquely to the chimpanzee genome. When the substitutions inferred to have occurred on the Denisova and the present-day human lineages were compared, the relative numbers of different classes of nucleotide substitutions are remarkably similar, and the excess number of candidate substitutions on the Denisova lineage relative to the present-day human lineage is only 1.7-fold (Supplementary Fig. 2.2 and Supplementary Table 2.4). This reflects an improvement in error rate over the Neanderthal genome by over an order of magnitude⁸ and is mainly due to the enzymatic removal of uracil residues from the Denisova DNA²⁷. We estimate that most errors in the Denisova DNA sequences are due to low genomic coverage rather than to any features typical of ancient DNA.

Human DNA contamination estimates

Although rigorous measures to prevent contamination of the experiments by DNA from present-day humans were implemented at all laboratory steps, it is impossible to completely prevent contamination because bone samples as well as reagents may be contaminated before they enter the clean-room facility. To estimate the levels of contamination in the sequences produced we used three approaches (Supplementary Information section 3).

First, we estimated the level of mtDNA contamination using 276 sequence positions where the Denisova mtDNA differs from >99% of present-day human mtDNAs. For library SL3003, we observed 7,433 unique sequences that covered such positions and 7,421 were of the Denisova type. For library SL3004 the corresponding numbers were 5,042 and 5,036, indicating that the mtDNA contamination in the libraries is on the order of 0.2% (95% confidence interval (CI): 0.1–0.3%) and 0.1% (CI: 0.1–0.3%), respectively.

Second, we identified sequences that are unique to the Y chromosome⁸. If the individual from whom the phalanx derives is female, the number of such sequences represents the extent of male DNA contamination. We found zero and three such Y chromosomal sequences in the two libraries, respectively, whereas 1,449 and 696 are expected if the individual is male. Thus, the bone derives from a female and male DNA contamination in the two libraries is on the order of 0.00% (CI: 0.00–0.25%) and 0.43% (CI: 0.09–1.26%), respectively.

Third, to estimate the extent of nuclear DNA contamination we used one library to identify positions where the Denisova individual carries an ancestral, that is, chimpanzee-like, sequence variant that among present-day humans is derived and not known to vary. We then examined sequences that map at these positions in the other library and determined if they carry the ancestral sequence or the derived sequence. Observation of a derived sequence in the second library could be due to one of three possibilities: that the DNA fragment in question comes from present-day human contamination; that the Denisova individual is heterozygous at the position in question; or that there has been a sequencing error. We implemented a maximum likelihood method that uses the number of independent observations of ancestral and derived states across positions to co-estimate contamination along with heterozygosity and sequencing error as nuisance parameters (Supplementary Information section 3). From this analysis, both libraries are inferred to have contamination rates of less than 1%.

Ancestral features and duplications

The Denisova draft genome sequence allows features that are ancestral in the Denisova genome and derived in present-day humans to be identified. We previously described a set of 10.5 million single nucleotide differences and about half a million insertion/deletions (indels) inferred to be due to changes that occurred on the human lineage since the split from the common ancestor with the chimpanzee⁸. Of these, 4,267,431 (40.5%) single nucleotide differences and 105,372 (22.0%) indels are covered by the Denisova sequences. We identified 129 inferred amino substitutions and 14 indels in the coding sequences of genes where the Denisova individual carries the ancestral alleles at positions where present-day humans carry derived alleles and are not known to vary (Supplementary Information section 4). We also identified 90 such sites in 5' untranslated regions (UTRs), 392 in 3' UTRs, two in microRNA genes and 104 in human accelerated regions. When we compared the Denisova and Neanderthal genomes we found that they carry the same assigned state at single nucleotide differences in 87.9% of the ancestral positions and 97.7% of the derived positions. The results for indels are similar: 87.6% for ancestral states and 98.6% for the derived states (Supplementary Table 4.3).

We analysed the segmental duplication content of the Denisova genome by detecting regions with an excess read depth (Supplementary Information section 5). In a three-way comparison of Denisova, Neanderthal and present-day human genomes, we found an excess of

private Denisova duplications (2.27 megabases (Mb)) compared with duplications that were private in Neanderthals (0.60 Mb) or present-day humans (1.32 Mb). These regions were identified based on signatures of both excess read depth and increased sequence divergence, making them unlikely to be artefacts. We also identified two regions where the duplication architecture of Denisova is more similar to that of chimpanzee than to that of either Neanderthals or present-day humans, including two chromosomal regions associated with neurological disease in humans: spinal muscular atrophy on 5q13 (including *SMN2*, one of the most recent gene duplications in the human lineage) and neuropsychiatric disease on 16p12.1.

Relationship to Neanderthals and modern humans

A fundamental question is whether the Denisova individual is an outgroup to Neanderthals and modern humans, as the mtDNA suggests¹⁹, whether it is a sister group to Neanderthals or to modern humans, or whether it falls within the range of variation of either of these two groups. We addressed this by estimating the divergence between the Denisova and the human genome reference sequence as a fraction of the divergence between present-day humans and the common ancestor shared with the chimpanzee. To do this, we scored the frequency with which the Denisova genome carries the human versus the chimpanzee state at positions where the human and chimpanzee reference genomes differ; assuming constant evolutionary rates (Supplementary Information section 2). We restricted this analysis to the parts of the human reference genome that are of African ancestry³³ as gene flow from Neanderthals to non-Africans⁸ could otherwise complicate these analyses. The Denisova genome diverged from the reference human genome 11.7% (CI: 11.4–12.0%) of the way back along the lineage to the human–chimpanzee ancestor. For the Vindija Neanderthal, the divergence is 12.2% (CI: 11.9–12.5%). Thus, whereas the divergence of the Denisova mtDNA to present-day human mtDNAs is about twice as deep as that of Neanderthal mtDNA¹⁹, the average divergence of the Denisova nuclear genome from present-day humans is similar to that of Neanderthals.

A possible explanation for the similar divergence of the Denisova individual and Neanderthals from present-day Africans is that they both descend from a common ancestral population that separated earlier from ancestors of present-day humans. Such a scenario would predict a closer relationship between the Denisova individual and Neanderthals than between either of them and present-day humans. To test this prediction, we estimated the divergence between pairs of seven ancient and modern genomes (Denisova, Neanderthals, French, Han, Papuan, Yoruba and San), using an approach where we correct for error rates in each genome based on the assumption that each has the same number of true differences from chimpanzee (Supplementary Information section 6). The average divergence between Denisova and Vindija Neanderthals is estimated to be 9.84% of the way to the chimpanzee–human ancestor; that is, less than the average 12.38% divergence of both from present-day Africans. Assuming 6.5 million years for human–chimpanzee divergence, this implies that DNA sequences of Neanderthals and the Denisova individual diverged on average 640,000 years ago, and from present-day Africans 804,000 years ago.

To analyse further the relationship of the Denisova individual and Neanderthals, we aligned Denisova, Neanderthal and Yoruba sequences to the chimpanzee genome, picked a single sequence at random to represent each group, and examined sites where two copies of a derived and one copy of an ancestral allele were observed. Sequencing errors are expected to make a negligible contribution at such sites. The number of sites where the Denisova individual and Neanderthal cluster to the exclusion of the Yoruba and chimpanzee is 46,362, compared with an average of 22,012 sites for the other two possible patterns (Yoruba and Denisova, or Yoruba and Neanderthal). This excess of sites where Denisova and Neanderthal cluster supports the view that the Denisova individual and Neanderthals share a common history since separating from the ancestors of modern humans (Supplementary Information section 6).

A Neanderthal-specific bottleneck

The fact that the Denisova nuclear genome on average shares a more recent common ancestor with Neanderthal than with present-day humans raises the question of whether the overall DNA sequence divergence of the Denisova individual falls inside the group morphologically and geographically defined as Neanderthals, or if it represents a sister group to Neanderthals.

To investigate this question, we took advantage of the fact that in addition to the three individuals from Vindija Cave, Croatia, from which most of the Neanderthal genome sequences were produced, we have determined nuclear DNA sequences from three further Neanderthal individuals from Russia, Spain and Germany⁸. Of these, the 60,000–70,000-year-old skeleton of a Neanderthal child found in Mezmaiskaya Cave, Russia, is both oldest and geographically closest to the Denisova individual. Using the 56 Mb of autosomal DNA sequences determined from this specimen⁸, we estimate that the DNA sequence divergence between the Vindija and Mezmaiskaya Neanderthals corresponds to a date of $140,000 \pm 33,000$ years ago (Supplementary Information section 6) (Fig. 1). This remarkably low divergence—which is about one-third of the closest pair of present-day humans that we analysed—is in agreement with the observation that diversity among Neanderthal mtDNAs is low relative to present-day humans¹⁰ and indicates that the Vindija and Mezmaiskaya Neanderthals descend from a common ancestral population that experienced a drastic bottleneck since separating from the ancestors of the Denisova individual.

To understand further the bottleneck in the history of Vindija and Mezmaiskaya Neanderthals, we examined four-way alignments of the Vindija Neanderthal genome sequence, the Mezmaiskaya Neanderthal, the Denisova individual and the chimpanzee genome. At transversion substitutions where two copies of the derived alleles are observed, we detect 924 substitutions that cluster the Vindija and Mezmaiskaya Neanderthals, 80 that cluster Vindija and Denisova, and 81 that cluster Mezmaiskaya and Denisova. This corresponds to at least a 65% probability that the DNA sequences in the Neanderthals share a common ancestor more recently than their split from the ancestor of the Denisova individual (Supplementary Information section 7). It is much higher than the 15–20% probability associated with the ‘Out of Africa’ bottleneck common to present-day non-Africans³⁴. If we replace the Mezmaiskaya Neanderthal in this analysis with a Neanderthal from El Sidron, Spain, or from Feldhofer, Germany, results are qualitatively similar although numbers are smaller (Supplementary Information section 7). Thus, we conclude that late Neanderthals across a broad geographical range have a population history distinct from that of the Denisova individual in that they share a strong population bottleneck not experienced by the ancestors of the Denisova individual. We call

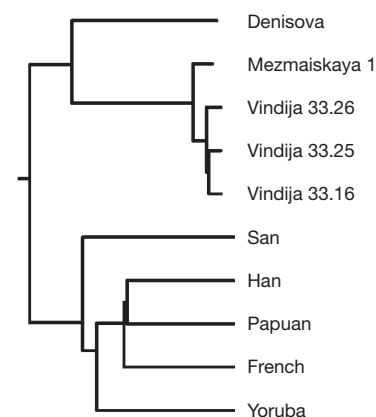


Figure 1 | A neighbour-joining tree based on pairwise autosomal DNA sequence divergences for five ancient and five present-day hominins. Vindija 33.16, Vindija 33.25 and Vindija 33.26 refer to the catalogue numbers of the Neanderthal bones.

the group to which this individual belonged Denisovans in analogy to Neanderthals, as Denisovans are described for the first time based on molecular data from Denisova Cave just as Neanderthals were first described based on skeletal remains retrieved in the Neander Valley in Germany.

No Denisovan gene flow into all Eurasians

We have previously shown that Vindija Neanderthals share more derived alleles with non-Africans than with Africans, consistent with Neanderthals contributing 1–4% of the genomes of present-day humans across Eurasia⁸. To investigate the extent to which the Denisova individual shares this pattern, we examined alignments of sets of four genomes, each consisting of an African (Yoruba or San), a Eurasian (French or Han), an archaic hominin (Neanderthal or Denisovan) and the chimpanzee. We randomly sampled one allele from each of the three hominins, and counted all transversion differences between the African and the Eurasian where the archaic individual carries the derived allele (the '*D*' statistics' of ref. 8). Neanderthals match the French genome on average $4.6 \pm 0.7\%$ more often than they match the Yoruba genome (Table 1). Although the Denisova individual also matches the French more than the Yoruba genome, this skew is significantly less strong at $1.8 \pm 0.5\%$. The estimates of *D* statistics were quantitatively consistent (within two standard deviations) for all other choices of Eurasian and African populations (Table 1). These findings indicate that the archaic component of the Eurasian gene pool is less closely related to the Denisova individual than to Neanderthals.

We also examined 13 genomic regions that we previously identified as candidates for a contribution of archaic genetic material into non-Africans, based on their deeper genetic divergences in non-Africans than in Africans⁸. Using 'tag SNPs' that are informative about whether a haplotype is from the lineage unique to non-Africans, we find that the Denisova individual matches the deeply diverged non-African haplotype in 6 cases, whereas Neanderthals do so in 11 cases (Supplementary Information section 7). Thus, both Neanderthals and Denisovans are more related than would be expected by chance to these genomic segments, but the signal in Denisovans is weaker.

These analyses indicate that Neanderthals are more closely related than Denisovans to the population that contributed to the gene pool of the ancestors of present-day Eurasians. The fact that Eurasians share some additional affinity with the Denisova individual relative to Africans is compatible with a scenario in which Denisovans shared some of their history with Neanderthals before the gene flow from Neanderthals into modern humans occurred.

Denisovan gene flow into the ancestors of Melanesians

Although the Denisova individual derives from a population that was not directly involved in the gene flow from Neanderthals to Eurasians, it is possible that Denisovans admixed with the ancestors of present-day people in some parts of the Old World. To investigate this, we analysed the relationship of the Denisova genome to the genomes of 938 present-day humans from 53 populations that have been genotyped at 642,690 single nucleotide polymorphisms (SNPs)³⁵. We

Table 1 | Sharing of derived alleles between present-day and archaic hominins

| Sample H ₁ | Sample H ₂ | Source of data for H ₁ and H ₂ | D(H ₁ , H ₂ , Neanderthal, chimpanzee) | | | | | D(H ₁ , H ₂ , Denisova, chimpanzee) | | | | |
|------------------------|-----------------------|--|--|--------------------------|--------------|----------|-----------------|---|--------------------------|--------------|----------|-----------------|
| | | | <i>n</i> _{BABA} | <i>n</i> _{ABBA} | <i>D</i> (%) | s.e. (%) | <i>Z</i> -score | <i>n</i> _{BABA} | <i>n</i> _{ABBA} | <i>D</i> (%) | s.e. (%) | <i>Z</i> -score |
| Eurasian/Eurasian* | | | | | | | | | | | | |
| French | Han | Ref. 8 | 17,214 | 17,602 | −1.1 | 0.8 | −1.4 | 27,250 | 27,265 | 0.0 | 0.6 | 0.0 |
| Karitiana | Sardinian | This study | 1,116 | 1,085 | 1.4 | 2.1 | 0.7 | 1,559 | 1,627 | −2.1 | 1.8 | −1.2 |
| Karitiana | Cambodian | This study | 1,683 | 1,707 | −0.7 | 1.8 | −0.4 | 2,371 | 2,460 | −1.8 | 1.5 | −1.2 |
| Karitiana | Mongolian | This study | 1,128 | 1,195 | −2.9 | 2.2 | −1.3 | 1,765 | 1,742 | 0.7 | 1.8 | 0.4 |
| Sardinian | Cambodian | This study | 2,592 | 2,670 | −1.5 | 1.5 | −1.0 | 3,935 | 3,925 | 0.1 | 1.2 | 0.1 |
| Sardinian | Mongolian | This study | 1,966 | 2,027 | −1.5 | 1.6 | −0.9 | 3,036 | 3,057 | −0.3 | 1.3 | −0.3 |
| Cambodian | Mongolian | This study | 2,811 | 2,804 | 0.1 | 1.4 | 0.1 | 4,442 | 4,342 | 1.1 | 1.2 | 1.0 |
| African/African* | | | | | | | | | | | | |
| San | Yoruba | Ref. 8 | 23,690 | 23,855 | −0.3 | 0.6 | −0.6 | 39,042 | 39,019 | 0.0 | 0.5 | 0.1 |
| Melanesian/Melanesian* | | | | | | | | | | | | |
| Papuan2 | Bougainville | This study | 3,351 | 3,284 | 1.0 | 1.3 | 0.8 | 5,319 | 5,140 | 1.7 | 1.1 | 1.5 |
| Eurasian/African* | | | | | | | | | | | | |
| French | San | Ref. 8 | 25,242 | 22,982 | 4.7 | 0.6 | 7.6† | 39,838 | 38,495 | 1.7 | 0.5 | 3.4† |
| French | Yoruba | Ref. 8 | 21,794 | 19,890 | 4.6 | 0.7 | 6.9† | 34,262 | 33,078 | 1.8 | 0.5 | 3.6† |
| Han | San | Ref. 8 | 25,081 | 22,470 | 5.5 | 0.6 | 8.5† | 38,815 | 37,439 | 1.8 | 0.5 | 3.4† |
| Han | Yoruba | Ref. 8 | 21,741 | 19,412 | 5.7 | 0.7 | 7.9† | 33,182 | 32,184 | 1.5 | 0.5 | 2.8 |
| Karitiana | Mbuti | This study | 1,577 | 1,473 | 3.4 | 1.9 | 1.8 | 2,368 | 2,360 | 0.2 | 1.5 | 0.1 |
| Sardinian | Mbuti | This study | 2,562 | 2,400 | 3.3 | 1.5 | 2.2 | 4,028 | 3,784 | 3.1 | 1.2 | 2.6 |
| Cambodian | Mbuti | This study | 4,235 | 3,641 | 7.5 | 1.2 | 6.5† | 6,329 | 5,850 | 3.9 | 1.0 | 4.0† |
| Mongolian | Mbuti | This study | 3,077 | 2,765 | 5.3 | 1.4 | 3.9† | 4,514 | 4,505 | 0.1 | 1.1 | 0.1 |
| Eurasian/Melanesian* | | | | | | | | | | | | |
| French | Papuan1 | Ref. 8 | 15,523 | 15,548 | −0.1 | 0.8 | −0.1 | 23,509 | 25,470 | −4.0 | 0.7 | −5.7† |
| Han | Papuan1 | Ref. 8 | 15,059 | 14,677 | 1.3 | 0.9 | 1.5 | 22,262 | 24,198 | −4.2 | 0.7 | −5.8† |
| Karitiana | Papuan2 | This study | 1,522 | 1,658 | −4.3 | 1.9 | −2.2 | 2,201 | 2,641 | −9.1 | 1.6 | −5.8† |
| Karitiana | Bougainville | This study | 1,577 | 1,717 | −4.3 | 1.8 | −2.4 | 2,229 | 2,671 | −9.0 | 1.5 | −5.9† |
| Sardinian | Papuan2 | This study | 2,447 | 2,647 | −3.9 | 1.5 | −2.6 | 3,714 | 4,150 | −5.5 | 1.2 | −4.5† |
| Sardinian | Bougainville | This study | 2,531 | 2,762 | −4.4 | 1.5 | −3.0 | 3,877 | 4,336 | −5.6 | 1.1 | −4.9† |
| Cambodian | Papuan2 | This study | 3,713 | 3,891 | −2.3 | 1.3 | −1.8 | 5,457 | 6,272 | −6.9 | 1.1 | −6.5† |
| Cambodian | Bougainville | This study | 3,847 | 3,994 | −1.9 | 1.2 | −1.6 | 5,751 | 6,333 | −4.8 | 1.0 | −4.7† |
| Mongolian | Papuan2 | This study | 2,783 | 2,852 | −1.2 | 1.5 | −0.8 | 4,192 | 4,758 | −6.3 | 1.2 | −5.3† |
| Mongolian | Bougainville | This study | 2,813 | 3,066 | −4.3 | 1.5 | −2.9 | 4,234 | 4,847 | −6.8 | 1.1 | −6.0† |
| Melanesian/African* | | | | | | | | | | | | |
| Papuan1 | San | Ref. 8 | 21,985 | 20,366 | 3.8 | 0.7 | 5.1† | 35,923 | 32,841 | 4.5 | 0.6 | 7.2† |
| Papuan1 | Yoruba | Ref. 8 | 19,107 | 17,646 | 4.0 | 0.8 | 4.9† | 30,995 | 28,186 | 4.7 | 0.6 | 7.4† |
| Papuan2 | Mbuti | This study | 3,832 | 3,324 | 7.1 | 1.3 | 5.4† | 6,124 | 5,233 | 7.8 | 1.1 | 7.2† |
| Bougainville | Mbuti | This study | 4,216 | 3,596 | 7.9 | 1.2 | 6.8† | 6,498 | 5,633 | 7.1 | 1.1 | 6.7† |

We present the *D* statistic $D(H_1, H_2, X, \text{chimpanzee})$, the normalized difference between the number of sites at which the derived allele in an archaic read from *X* matches human sample H₁ (*n*_{BABA}) and human sample H₂ (*n*_{ABBA}); thus, its value is $D = (n_{BABA} - n_{ABBA}) / (n_{BABA} + n_{ABBA})$. We restrict to autosomal transversion substitutions, compute standard errors (s.e.) from a block jackknife, and highlight (dagger symbol) the *D* statistics that are more than $Z > 3$ s.d. from zero. Both Neanderthals and Denisovans match Eurasians more than the Africans, but the signals are consistently and significantly stronger when *X* = Neanderthal than when *X* = Denisova. The slight numerical differences with Table 4 of ref. 8 are due to differences in the data filtering. Here we restrict to comparisons of present-day human samples that were sequenced by the same protocol (the five individuals sequenced in ref. 8, or the seven in this study); Supplementary Table 8.2 presents the complete set of pairwise comparisons.

* Comparison.

† *D* statistics that are more than $Z > 3$ s.d. from zero.

scored each of these present-day humans based on their relative proximity to Neanderthals and the Denisova individual at positions where we have high-quality data for both the Neanderthal and Denisova genomes (Supplementary Information section 8). Using the means of the 53 populations, the first two principal components separate the populations into three groups (Fig. 2): first, the 7 sub-Saharan African populations; second, a group of 44 non-African populations as well as one north African group; and third, Papuan and Bougainville populations from Melanesia. When individuals from selected populations are analysed separately, the Papuan and Bougainville islanders remain distinct from almost all individuals outside Africa (Supplementary Fig. 8.1b). Thus, with respect to their relationship to Neanderthals and Denisovans, the Melanesian populations stand out relative to other non-African populations.

To explore this further, we analysed the relationship of the Denisova genome to the genomes of five present-day humans that we previously sequenced to about fivefold coverage⁸ (a Yoruba and a San genome from Africa, a French genome from Europe, a Han genome from China and a Papuan genome from Melanesia), as well as seven present-day humans that we sequenced to 1–2-fold coverage for this study (a Mbuti genome from Africa, a Sardinian genome from Europe, a Mongolian genome from Central Asia, a Cambodian genome from South-East Asia, an additional Papuan genome from Melanesia, a Bougainville islander genome from Melanesia, and a Karitiana genome from South America) (Supplementary Information section 9). We used the *D* statistic⁸ to test if various pairs of present-day humans share equal numbers of derived alleles with the Denisova individual. To do this, we restricted comparisons to pairs of present-day humans sequenced at the same time to minimize the chance that differences in sample processing could affect the results. We find that the fivefold coverage Papuan individual shares $4.0 \pm 0.7\%$ more alleles with the Denisova individual than does the French individual, and we observed a similar skew in all 10 comparisons of Melanesian and other non-African populations (Table 1). When we stratified the data by base substitution class and chromosome, the *D* statistics are qualitatively unchanged (Supplementary Information section 10). Similarly, the *D* statistics

are consistent for all depths of read coverage, indicating that mapping errors, for example due to segmental duplications, are not likely to explain these results. Finally, differences in sequencing error rate across samples cannot explain the observed *D* statistics (Supplementary Information section 10).

Under the assumption that gene flow explains these observations, we determined the direction of this gene flow by asking whether Melanesians and other Eurasians share derived alleles with Africans equally often. If the gene flow was entirely into the ancestors of the Denisovan individual, we would not expect this to affect the relationship of Africans to Melanesians and other Eurasians and thus we would expect them to share derived alleles equally often with Africans. However, we find that derived alleles in Africans match Melanesians $3.4 \pm 0.4\%$ less often than other non-Africans ($Z = 10.8$). Because this skew is seen without using Denisovan data it cannot be explained by gene flow into Denisovans or, for example, by contamination of the Denisova sample by present-day Melanesian DNA. Thus, at least some of the putative gene flow must have been into Melanesians (Supplementary Information section 8).

When we compare the skew in the fraction of derived alleles shared with the two archaic hominins to what would be expected for individuals of 100% Neanderthal or Denisova ancestry, respectively (Supplementary Information section 8 and ref. 8), we estimate that $2.5 \pm 0.6\%$ of the genomes of non-African populations derive from Neanderthals, in agreement with our previous estimate of 1–4%⁸. In addition, we estimate that $4.8 \pm 0.5\%$ of the genomes of Melanesians derive from Denisovans. Altogether, as much as $7.4 \pm 0.8\%$ of the genomes of Melanesians may thus derive from recent admixture with archaic hominins.

A model of population history

To understand the implications of the relationships observed among the Denisova individual, the Neanderthals and present-day humans, we fit the *D* statistics described in the previous sections to a parameterized model of population history. The *D* statistics for the Denisova individual differ in two important ways from those for the Neanderthal. First, the Denisova individual shares fewer derived alleles with either the French or Han Chinese populations than do the Neanderthals. Second, the Denisova individual shares more derived alleles with the Papuans than do the Neanderthals. We are able to fit the data with a model that assumes the Denisovans are a sister group of Neanderthals with a population divergence time of one-half to two-thirds of the time to the common ancestor of Neanderthals and humans. After the divergence of the Denisovans from Neanderthals, there was gene flow from Neanderthals into the ancestors of all present-day non-Africans. Later there was admixture between the Denisovans and the ancestors of Melanesians that did not affect other non-African populations. This model is illustrated in Fig. 3 and is described in detail in Supplementary Information section 11.

Other, more complex models could also explain the data. For example, a model that invokes only gene flow from Denisovans to Melanesian ancestors outside Africa and assumes four subpopulations in Africa that existed between the times of the origin of Denisovan and Neanderthal ancestors and the ancestors of present-day Eurasians could also fit the data (Supplementary Fig. 11.4). However, because barriers to gene flow between such subpopulations would have to persist for hundreds of thousands of years to create the observed patterns, such a model is less plausible on biological grounds than a model that invokes two instances of gene flow outside Africa.

Discordance of mtDNA and nuclear histories

The population history indicated by the nuclear genome is different from that indicated by the mtDNA phylogeny. There are two possible explanations for this. One is that the mtDNA lineage was introduced into Denisovan ancestors by admixture from another hominin lineage for which we have no data. The other is that the discordance is the result of ‘incomplete lineage sorting’, that is, the random assortment

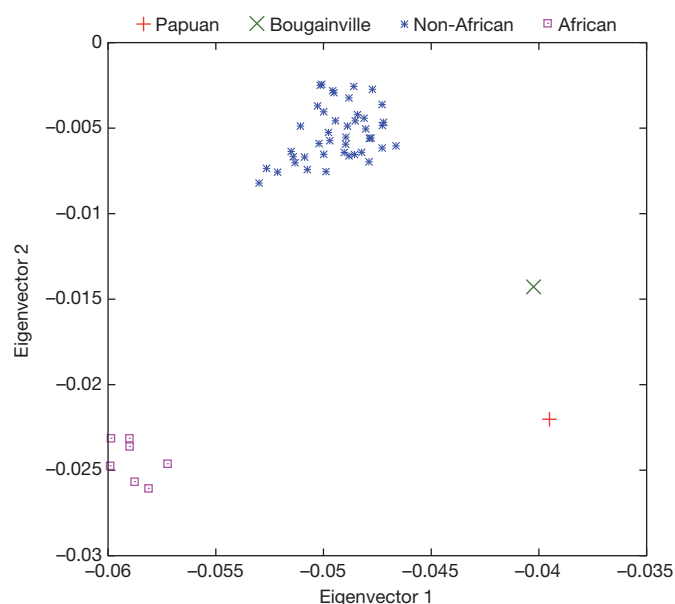


Figure 2 | Relationship of present-day populations to the Denisova individual and Neanderthals based on 255,077 SNPs. Principal component analysis of the means of 53 present-day human populations projected onto the top two principal components defined by Denisova, Neanderthal and chimpanzee. The seven ‘African’ populations are San, Mbuti, Biaka, Bantu Kenya, Bantu South Africa, Yoruba and Mandenka; the ‘Non-African’ populations are 44 diverse groups from outside Africa except for Papuan and Bougainville islanders.

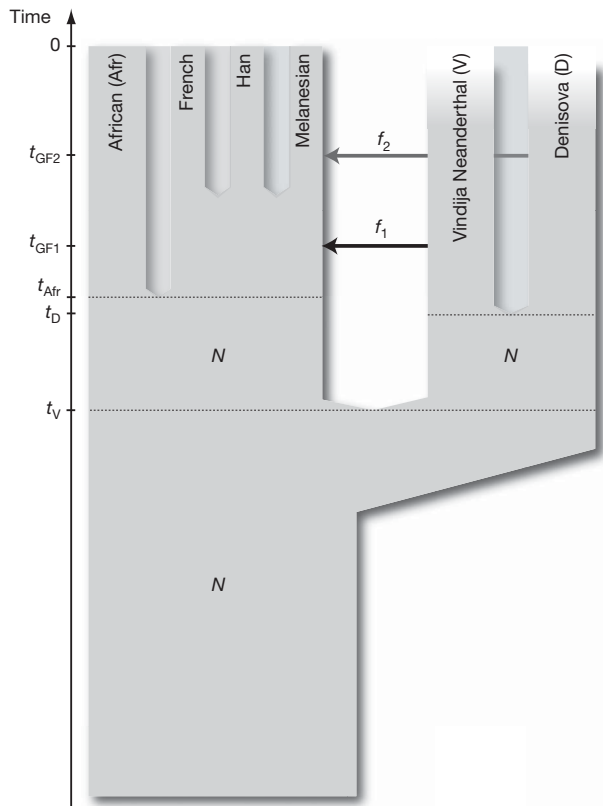


Figure 3 | A model of population history compatible with the data. N denotes effective population size, t denotes time of population separation, f denotes amount of gene flow and t_{GF} denotes time of gene flow.

of genetic lineages due to genetic drift which may have allowed a divergent mtDNA lineage to survive in Denisovans by chance while becoming lost in Neanderthals and modern humans. A large ancestral population size makes incomplete lineage sorting more likely to occur. In Supplementary Information section 11, we show that given reasonable assumptions about the size of the ancestral populations,

the discordance of the mtDNA phylogeny with that indicated by the nuclear DNA can be explained either by a small amount of admixture from another archaic hominin or by incomplete lineage sorting. Thus, the data do not allow us to favour one hypothesis over the other.

A tooth from Denisova Cave

In 2000, a hominin tooth was discovered in layer 11.1 of the south gallery of Denisova Cave (Fig. 4a, b). The tooth is from a young adult and therefore from another individual than the phalanx which stems from a juvenile (Supplementary Information section 12). To elucidate the relationship of the tooth to the individual from which the phalanx is derived, we extracted DNA from 50 mg of dentin from the root of the tooth and prepared a sequencing library (Supplementary Information section 13). About 0.17% of random DNA sequences determined from this library aligned to the human genome, whereas the rest is likely to represent microbial contamination common in ancient bones. We therefore used a novel DNA capture approach³⁶ to isolate mtDNA sequences from the sequencing library. A total of 15,094 sequences were identified which allowed the complete mtDNA genome to be assembled at an average coverage of 58-fold. This sequence differs at two positions from the mtDNA of the phalanx whereas it differs at about 380 positions from both Neanderthal and present-day humans. The time since the most recent common ancestor of the two mtDNAs from Denisova Cave is estimated to be 7,500 years, with a 95% upper bound of 16,000 years (Supplementary Information section 13). We conclude that the tooth and the phalanx derive from two different individuals that are probably from the same hominin population.

Morphology of the Denisova molar

The tooth is an almost complete left, probably third, but possibly second, upper molar (Fig. 4b). The crown is trapezoidal and tapers strongly distally, with bulging lingual and buccal walls giving the tooth an inflated appearance (Supplementary Information section 12). The roots are short but robust and strongly flaring.

Overall, the tooth is very large (mesiodistal diameter, 13.1 mm; buccolingual, 14.7 mm). As a third molar, it is outside the range of normal size variation of all fossil taxa of the genus *Homo*, with the exception of *H. habilis* and *H. rudolfensis*, and comparable to Australopithecines (Fig. 4c). Compared to second molars, it is larger

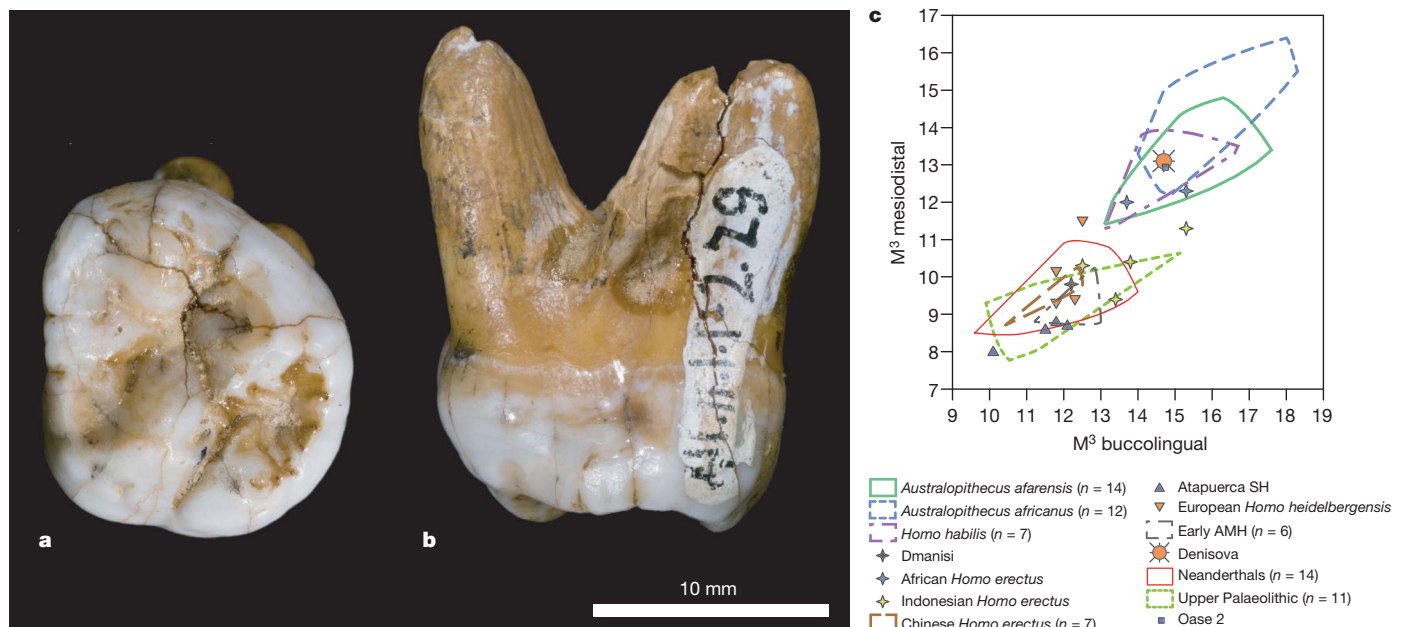


Figure 4 | Morphology of the Denisova molar. a, b, Occlusal (a) and mesial (b) views. c, Comparison of the Denisova molar to diverse third molars, in a biplot of the mesiodistal and buccolingual lengths (in mm). AMH, anatomically

modern humans; SH, Sima de los Huesos. Supplementary Fig. 12.1 presents a similar comparison to second molars.

than Neanderthals or early modern humans, but similar to *H. erectus* and *H. habilis* (Supplementary Fig. 12.1).

Besides size, it is also distinguished from most Neanderthal third molars by the absence of hypocone reduction, and from both second and third Neanderthal molars by the presence of a large talon basin and the strong flare of the crown. Furthermore, it lacks the lingual hypocone projection seen in all Neanderthal first and many second molars, and has strongly diverging roots, unlike the closely spaced and frequently fused roots of Neanderthals.

It is of particular interest to compare the Denisova molar to Middle Pleistocene hominins from China, where *H. erectus* and other archaic forms, sometimes interpreted as *H. heidelbergensis*, may have survived until recently. Unfortunately, very few of these fossils preserve third upper molars. Of the few examples that are available, most differ from the Denisova molar by their strongly reduced size. Second molars are more frequent than third molars, and most have a trapezoidal shape like Denisova, but they do not have the lingually skewed position of the hypocone and metacone and the strong basal flare of the crown.

The Denisova molar supports the DNA evidence that the Denisovan population is distinct from late Neanderthals as well as from modern humans. In fact, the primitive traits of the Denisova tooth suggest that Denisovans may have been separated from the Neanderthal lineage before Neanderthal dental features are documented in Western Eurasia (>300,000 years BP) (Supplementary Information section 12), although we cannot exclude the possibility that the Denisovan dental morphology results from a reversion.

Stratigraphy and dating

The small size of both the phalanx and the tooth precludes direct radiocarbon dating. We instead dated seven bone fragments found close to the hominin remains in layer 11 in the east and south galleries. To ensure that they were associated with human occupation of the cave we chose bones that have evidence of human modification, including a rib with regular incisions and a bone projectile point blank generally associated with Upper Palaeolithic cultural assemblages. In the south gallery, where modified bones were not available, we used herbivore bones (Supplementary Information section 12).

Four of the seven dates are infinite dates older than 50,000 years BP (uncalibrated), whereas three are finite dates between 16,000 and 30,000 years BP (Supplementary Table 12.1). The rib with incisions and the projectile point blank are about 30,000 and 23,000 years BP, respectively. Together with three previous dates²³ this shows that layer 11 contains cultural remains from at least two different time periods, one period older than 50,000 years BP and one more recent period. However, the stratigraphy is complicated by the discovery of a wedge-shaped area close to the area where the phalanx was found that is likely to be disturbed (Supplementary Information section 12). Hominin remains large enough to allow direct radiocarbon dates may eventually be discovered in the cave, but a reasonable hypothesis is that the phalanx and molar belong to the older occupation.

Discussion

The molecular preservation of the Denisova phalanx is exceptional in that the fraction of endogenous relative to microbial DNA is about 70%. By contrast, in all Neanderthal remains studied so far the relative abundance of endogenous DNA is below 5%, and typically below 1%. Furthermore, the average length of hominin DNA fragments in the Denisova phalanx is 58 base pairs (bp) (SL3003) and 74 bp (SL3004) in spite of the enzymatic treatment that removes uracil residues and decreases the average fragment size, whereas in most well-preserved Neanderthal samples it is 50 bp or smaller without this treatment. Thus, although many Neanderthals are preserved under conditions apparently similar to those in Denisova Cave, the Denisova phalanx is one of few bones found in temperate conditions that are as well preserved as many permafrost remains^{37,38}. It is not clear why this is. It is not due to some condition that affects all hominin remains in

Denisova Cave because the fraction of endogenous DNA in the tooth is 0.17%; that is, typical of other Late Pleistocene hominin remains. It is possible that a rapid desiccation of the tissue after death, which would limit degradation of the DNA by endogenous enzymes as well as microbial growth, has allowed this exceptional preservation.

The Denisova individual and the population to which it belonged carry some exceptionally archaic molecular (mtDNA) as well as morphological (dental) features. Nevertheless, the picture that emerges from analysis of the nuclear genome is one where the Denisova population is a sister group to Neanderthals. Three possibilities could account for how such archaic features have come to be present in Denisovans. One possibility is that these features were retained in Denisovans but became lost in modern humans and Neanderthals. A second, not mutually exclusive, possibility is that they entered the Denisova population through gene flow from some even more diverged hominin. Although such gene flow cannot be detected with the current mtDNA and nuclear DNA data, further sequencing of other hominin remains may in the future allow testing for it. A third possibility that could account for the apparently archaic dental morphology, but not the mtDNA, is a reversal to ancestral traits.

After they diverged from one another, Denisovans and Neanderthals had largely separate population histories as shown by a number of observations. First, patterns of allele sharing indicate that Denisovan ancestors did not contribute genes at a detectable level to present-day people all over Eurasia whereas Neanderthals did⁸. Thus, Neanderthals at some point interacted with ancestors of present-day Eurasians independently of Denisovans. Second, the genetic diversity of Neanderthals across their geographical range in the last thirty or forty thousand years of their history was extremely low, indicating that they experienced one or more strong genetic bottlenecks independently of the Denisovans. Third, our results indicate that Denisovans but not Neanderthals contributed genes to ancestors of present-day Melanesians. Fourth, the dental morphology shows no evidence of any derived features seen in Neanderthals. In fact, dental remains from the Sima de los Huesos of Atapuerca, for which ages between 350,000 and 600,000 years have been proposed^{39,40}, already carry Neanderthal-like morphological features that are not seen in the Denisova molar.

An interesting question is how widespread Denisovans were. A possibility is that they lived in large parts of East Asia at the time when Neanderthals were present in Europe and western Asia. One observation compatible with this possibility is that Denisovan relatives seem to have contributed genes to present-day Melanesians but not to present-day populations which currently live much closer to the Altai region such as Han Chinese or Mongolians (Table 1). Thus, they have at least at some point been present in an area where they interacted with the ancestors of Melanesians and this was presumably not in southern Siberia. Further studies of both molecular and morphological features of hominin remains across Asia should clarify how widespread Denisovans were and how they were related to archaic hominins other than Neanderthals.

The Denisova individual belongs to a hominin group that shares a common ancestor with Neanderthals but has a distinct population history. We define this group based on genomic evidence and call it Denisovans, but refrain from any formal Linnaean taxonomic designations that would indicate species or subspecies status for either Neanderthals or Denisovans. In our view, these results show that on the Eurasian mainland there existed at least two forms of archaic hominins in the Upper Pleistocene: a western Eurasian form with morphological features that are commonly used to define them as Neanderthals, and an eastern form to which the Denisova individuals belong. In the future, when more complete genomes from these and other archaic hominins will be sequenced from remains that allow more morphological features to be assessed, their relationships will become even better understood. This will be an important endeavour as the emerging picture of Upper Pleistocene hominin evolution is one in which gene flow among different hominin groups was common.

METHODS SUMMARY

The thirteen sections of the Supplementary Information provide a full description of the methods.

Received 15 August; accepted 30 November 2010.

- Hublin, J.J. The origin of Neandertals. *Proc. Natl Acad. Sci. USA* **106**, 16022–16027 (2009).
- Pope, G. G. Craniofacial evidence for the origin of modern humans in China. *Am. J. Phys. Anthropol.* **35**, (Suppl. 15), 243–298 (1992).
- Rightmire, G. P. Brain size and encephalization in early to Mid-Pleistocene Homo. *Am. J. Phys. Anthropol.* **124**, 109–123 (2004).
- Wu, X. & Poirier, F. E. *Human Evolution in Asia* (Oxford Univ. Press, 1995).
- Brown, P. *et al.* A new small-bodied hominin from the Late Pleistocene of Flores, Indonesia. *Nature* **431**, 1055–1061 (2004).
- Morwood, M. J. *et al.* Archaeology and age of a new hominin from Flores in eastern Indonesia. *Nature* **431**, 1087–1091 (2004).
- Morwood, M. J. *et al.* Preface: research at Liang Bua, Flores, Indonesia. *J. Hum. Evol.* **57**, 437–449 (2009).
- Green, R. E. *et al.* A draft sequence of the Neandertal genome. *Science* **328**, 710–722 (2010).
- Beauval, C. *et al.* A late Neandertal femur from Les Rochers-de-Villeneuve, France. *Proc. Natl Acad. Sci. USA* **102**, 7085–7090 (2005).
- Briggs, A. W. *et al.* Targeted retrieval and analysis of five Neandertal mtDNA genomes. *Science* **325**, 318–321 (2009).
- Caramelli, D. *et al.* A highly divergent mtDNA sequence in a Neandertal individual from Italy. *Curr. Biol.* **16**, R630–R632 (2006).
- Green, R. E. *et al.* A complete Neandertal mitochondrial genome sequence determined by high-throughput sequencing. *Cell* **134**, 416–426 (2008).
- Krause, J. *et al.* Neanderthals in central Asia and Siberia. *Nature* **449**, 902–904 (2007).
- Krings, M. *et al.* A view of Neandertal genetic diversity. *Nature Genet.* **26**, 144–146 (2000).
- Lalueza-Fox, C. *et al.* Mitochondrial DNA of an Iberian Neandertal suggests a population affinity with other European Neandertals. *Curr. Biol.* **16**, R629–R630 (2006).
- Orlando, L. *et al.* Revisiting Neandertal diversity with a 100,000 year old mtDNA sequence. *Curr. Biol.* **16**, R400–R402 (2006).
- Serre, D. *et al.* No evidence of Neandertal mtDNA contribution to early modern humans. *PLoS Biol.* **2**, e57 (2004).
- Endicott, P., Ho, S. Y. & Stringer, C. Using genetic evidence to evaluate four palaeoanthropological hypotheses for the timing of Neandertal and modern human origins. *J. Hum. Evol.* **59**, 87–95 (2010).
- Krause, J. *et al.* The complete mitochondrial DNA genome of an unknown hominin from southern Siberia. *Nature* **464**, 894–897 (2010).
- Derevianko, A. P. *et al.* *Paleoenvironment and Paleolithic Human Occupation of Gorny Altai* [in Russian] (Institute of Archeology and Ethnography SB RAS Press, 2003).
- Derevianko, A. *The Paleolithic of Siberia: New Discoveries and Interpretations* (Univ. Illinois Press, 1998).
- Derevianko, A. P. *et al.* *Archaeology, Geology, and the Pleistocene and Holocene Palaeogeography of the Mountainous Altai* [in Russian] (Nauka, 1998).
- Derevianko, A. P., Shunkov, M. V. & Volkov, P. V. A Paleolithic bracelet from Denisova cave. *Archaeol. Ethnol. Anthropol. Eurasia* **34**, 13–25 (2008).
- Green, R. E. *et al.* The Neandertal genome and ancient DNA authenticity. *EMBO J.* **28**, 2494–2502 (2009).
- Rohland, N. & Hofreiter, M. Comparison and optimization of ancient DNA extraction. *Biotechniques* **42**, 343–352 (2007).
- Lindahl, T. *et al.* DNA N-glycosidases: properties of uracil-DNA glycosidase from *Escherichia coli*. *J. Biol. Chem.* **252**, 3286–3294 (1977).
- Briggs, A. W. *et al.* Removal of deaminated cytosines and detection of *in vivo* methylation in ancient DNA. *Nucleic Acids Res.* **38**, e87 (2010).
- Meyer, M. & Kircher, M. Illumina sequencing library preparation for highly multiplexed target capture and sequencing. *Cold Spring Harb. Protoc.* 2010, doi:10.1101/pdb.prot5448 (2010).
- Briggs, A. W. *et al.* Patterns of damage in genomic DNA sequences from a Neandertal. *Proc. Natl Acad. Sci. USA* **104**, 14616–14621 (2007).
- Kircher, M., Stenzel, U. & Kelso, J. Improved base calling for the Illumina Genome Analyzer using machine learning strategies. *Genome Biol.* **10**, R83 (2009).
- Li, H. & Durbin, R. Fast and accurate short read alignment with Burrows-Wheeler transform. *Bioinformatics* **25**, 1754–1760 (2009).
- Paten, B. *et al.* Enredo and Pecan: genome-wide mammalian consistency-based multiple alignment with paralogs. *Genome Res.* **18**, 1814–1828 (2008).
- Reich, D. *et al.* Reduced neutrophil count in people of African descent is due to a regulatory variant in the Duffy antigen receptor for chemokines gene. *PLoS Genet.* **5**, e1000360 (2009).
- Keinan, A., Mullikin, J. C., Patterson, N. & Reich, D. Measurement of the human allele frequency spectrum demonstrates greater genetic drift in East Asians than in Europeans. *Nature Genet.* **39**, 1251–1255 (2007).
- Li, J. Z. *et al.* Worldwide human relationships inferred from genome-wide patterns of variation. *Science* **319**, 1100–1104 (2008).
- Maricic, T., Whitten, M. & Pääbo, S. Multiplexed DNA Sequence Capture of Mitochondrial Genomes Using PCR Products. *PLoS ONE* **5**, e14004 (2010).
- Poinar, H. N. *et al.* Metagenomics to paleogenomics: large-scale sequencing of mammoth DNA. *Science* **311**, 392–394 (2006).
- Rasmussen, M. *et al.* Ancient human genome sequence of an extinct Palaeo-Eskimo. *Nature* **463**, 757–762 (2010).
- Bischoff, J. L. *et al.* High-resolution U-series Dates from the Sima de los Huesos Hominids Yields 600[±]66 kys: Implications for the Evolution of the Early Neanderthal Lineage. *J. Archaeol. Sci.* **34**, 763–770 (2007).
- Bischoff, J. L. *et al.* The Sima de los Huesos Hominids Date to Beyond U/Th Equilibrium (>350 kyr) and Perhaps to 400–500 kyr: New Radiometric Dates. *J. Archaeol. Sci.* **30**, 275–280 (2003).

Supplementary Information is linked to the online version of the paper at www.nature.com/nature.

Acknowledgements We thank C. Bustamante, A. I. Krivoschapkin, M. Lachmann, R. Nielsen, K. Pruefer, A. Tsybankov, L. Vigilant and W. Zhai for comments; K. Finstermeier for graphics work; the MPI-EVA sequencing group, R. Schultze and S. Wehnachtsmann for technical support; and P. Fujita, A. Hinrichs and K. Learned for designing the UCSC genome browser portal to the Denisova data. The Presidential Innovation Fund of the Max Planck Society and the Krekeler Foundation provided financial support. M.S. was supported by a US National Institutes of Health grant (R01-GM40282). The National Science Foundation provided an International Postdoctoral Fellowship (OISE-0754461) to J.M.G., a Fellowship in Biological Informatics to P.L.F.J. and a HOMINID grant (1032255) to D.R.

Author Contributions J.Kr., T.M., Q.F. and M.M. performed the experiments; D.R., R.E.G., M.K., J.Kr., N.P., E.Y.D., A.W.B., U.S., P.L.F.J., T.M., J.M.G., T.B.-M., C.A., S.M., H.L., E.E.E., M.St., J.Ke., M.St. and S.P. analysed genetic data; B.V., M.R., S.T., M.V.S., A.P.D. and J.-J.H. analysed archaeological and anthropological data; D.R. and S.P. wrote and edited the manuscript.

Author Information The raw sequence data from the two Denisova fossils, the seven present-day humans, and the tooth mtDNA have been deposited in the European Nucleotide Archive at EMBL-EBI under accession numbers ERP000318, ERP000121 and FR695060, respectively. The alignments of Denisova sequence reads to the human and chimpanzee genomes are accessible for browsing and download from <http://genome.ucsc.edu/Denisova>. Reprints and permissions information is available at www.nature.com/reprints. The authors declare no competing financial interests. Readers are welcome to comment on the online version of this article at www.nature.com/nature. Correspondence and requests for materials should be addressed to D.R. (reich@genetics.med.harvard.edu), B.V. (bence.viola@eva.mpg.de) or S.P. (paabo@eva.mpg.de).

A population-specific *HTR2B* stop codon predisposes to severe impulsivity

Laura Bevilacqua¹, Stéphane Doly², Jaakko Kaprio^{3,4,5}, Qiaoping Yuan¹, Roope Tikkanen⁶, Tiina Paunio⁷, Zhifeng Zhou¹, Juho Wedenoja^{8,9}, Luc Maroteaux², Silvina Diaz², Arnaud Belmer², Colin A. Hodgkinson¹, Liliana Dell'Osso¹⁰, Jaana Suvisaari⁷, Emil Coccaro¹¹, Richard J. Rose¹², Leena Peltonen[‡], Matti Virkkunen^{6,13} & David Goldman¹

Impulsivity, describing action without foresight, is an important feature of several psychiatric diseases, suicidality and violent behaviour. The complex origins of impulsivity hinder identification of the genes influencing it and the diseases with which it is associated. Here we perform exon-focused sequencing of impulsive individuals in a founder population, targeting fourteen genes belonging to the serotonin and dopamine domain. A stop codon in *HTR2B* was identified that is common (minor allele frequency > 1%) but exclusive to Finnish people. Expression of the gene in the human brain was assessed, as well as the molecular functionality of the stop codon, which was associated with psychiatric diseases marked by impulsivity in both population and family-based analyses. Knockout of *Htr2b* increased impulsive behaviours in mice, indicative of predictive validity. Our study shows the potential for identifying and tracing effects of rare alleles in complex behavioural phenotypes using founder populations, and indicates a role for *HTR2B* in impulsivity.

Impulsivity is a broad term describing behaviour characterized by action without foresight, decreased inhibitory control and a lack of consideration of consequences¹. Cognitive function, attention and responses to reward are factors that are thought to contribute to the trait of impulsivity. Although impulsivity can be an adaptive dimension of personality, intolerance for delay, disinhibition and the inappropriate weighting of contingencies are maladaptive². The behavioural manifestations of impulsivity include suicide, addictions, attention deficit hyperactivity disorder (ADHD) and violent criminality³, as well as antisocial personality disorder (ASPD), borderline personality disorder (BPD) and intermittent explosive disorder (IED). These behaviours and diagnoses, including impulsivity itself, are moderately heritable^{4,5}, indicating that it should be feasible to identify genes influencing them. Gene identification would also validate the idea that it is possible to deconstruct the multi-process origins of impulsivity. Still, studies demonstrating that genetic variation predicts impulsivity have been relatively sparse^{6–11}. The fact that few genes influencing impulsivity have been discovered could reflect the complexity of the phenotype, the nature of the samples or the methodologies used.

To detect novel alleles that influence impulsivity, we studied severely impulsive Finnish criminal offenders and matched controls. This study had six components (as charted in Supplementary Fig. 1): resequencing and identification of putatively functional variants in severe impulsive probands from a founder population; association and linkage with impulsive behaviour; population genetics; evaluation of cognitive effects of the identified variant; gene expression and functionality; and animal studies.

Exon-centric sequencing was performed on fourteen genes involved in dopamine or serotonin function (the genes are listed in Supplementary Methods). Dysregulated activity of the monoamine neurotransmitters

has been implicated in impulsivity both on a neuropharmacological basis and a genetic basis via gene knockouts and/or association studies with common functional variants. In rats, serotonin and dopamine interact in the control of impulsive choice, with differential actions in regions of the prefrontal cortex involved¹². The spontaneous impulsivity of rats correlates with lower levels of dopamine D2 receptors in the nucleus accumbens, predicting liability to compulsive drug seeking and addiction¹³; also, in humans a reduction in D2 receptors, as well as a decrease in dopamine release, has been described in the ventral tegmental area of cocaine abusers¹⁴. The serotonin system has long been implicated in impulsivity^{15,16} and, in particular, impulsive aggression and suicide. *Maoa* knockout mice have higher levels of monoamines and increased aggressive behaviour¹⁷, and a functional variable number tandem repeat (VNTR) in the MAOA regulatory region (*MAOA-LPR*) moderates the effect of maltreatment on vulnerability to develop antisocial behaviour in humans^{8,18}. It has been shown that a stop codon variant that produces complete deficiency of MAOA activity co-segregates with severe impulsivity⁶. Stress-modified associations with suicidality have been reported also for a polymorphism in the serotonin transporter (degenerate repeat polymorphic region 5-HTTLPR in *SLC6A4*)^{19,20}.

Deep sequencing was recently successfully applied to gene identification in rare Mendelian disorders²¹. In the domain of complex disorders, sequencing revealed putatively functional alleles at a gene previously implicated by genome-wide association studies of type I diabetes²². Here we attempted to use sequencing to identify novel loci contributing to a non-Mendelian phenotype.

Sequencing Finnish impulsive subjects

Founder populations can increase power to detect effects of rare alleles. At autosomal loci, Finns are equally as diverse as other Europeans, yet a

¹Laboratory of Neurogenetics, National Institute on Alcohol Abuse and Alcoholism, NIH, Rockville, Maryland 20852, USA. ²INSERM UMR-S 839 and Université Pierre et Marie Curie, Institut du Fer à Moulins, Paris 75654, France. ³Department of Public Health, University of Helsinki, Helsinki FI-00014, Finland. ⁴Institute for Molecular Medicine, Helsinki FI-00014, Finland. ⁵Unit for Child and Adolescent Psychiatry, National Institute for Health and Welfare, Helsinki FI-00271, Finland. ⁶Institute of Clinical Medicine, Department of Psychiatry, University of Helsinki, Helsinki FI-00014, Finland. ⁷Department of Psychiatry, Helsinki University Central Hospital, Helsinki FI-00014, Finland. ⁸Department of Medical Genetics, University of Helsinki, Helsinki FI-00014, Finland. ⁹Institute for Molecular Medicine Finland FIMM, University of Helsinki and National Institute for Health and Welfare, Helsinki FI-00014, Finland. ¹⁰Department of Psychiatry, University of Pisa, Pisa 56100, Italy. ¹¹Department of Psychiatry, The Pritzker School of Medicine, University of Chicago, Chicago, Illinois 60637, USA. ¹²Department of Psychological and Brain Sciences, Indiana University, Bloomington, Indiana 47405, USA. ¹³Kellokoski Psychiatric Hospital, Kellokoski FI-04500, Finland.

‡Deceased.

restricted number of founders and isolation have moulded the Finnish gene pool²³. Many disease alleles are more abundant or unique to Finland and conversely some disease alleles common in other European populations are rare or nonexistent²³. From the standpoint of identifying rare or uncommon alleles with roles in complex phenotypes, it is perhaps most important that Finnish ancestry seems to have reduced the genetic heterogeneity of various diseases. For seventeen Finnish disease alleles, 70% of disease chromosomes (and as many as 98% for some diseases) were attributable to a single allele²³.

Sequencing was conducted in 96 unrelated Finnish males with impulsive behaviour and an equal number of unrelated Finnish males free of psychiatric diagnoses (Supplementary Table 1 and Methods). Proband had ASPD, BPD or IED and were all violent offenders and arsonists who, because of the extreme nature of their crimes, underwent inpatient forensic psychiatric examination at the University of Helsinki at the time of their initial incarceration. ASPD and BPD share genetic risk for impulsive aggression⁴, which is a central characteristic of both of these personality disorders. Impulsivity is also key to IED, described in the Diagnostic and Statistical Manual of Mental Disorders III-R (DSM-III-R) as a failure to resist aggressive impulses.

The 96 cases were selected for resequencing from a larger cohort of Finnish violent offenders comprising 228 cases on the basis that they had the highest Brown–Goodwin Lifetime Aggression scores: 23.7 (standard deviation (s.d.) \pm 4.9) as compared to 8.1 (s.d. \pm 4.9) in controls. Their higher scores were indicators of a life history of aggressive, violent and impulsive behaviour as behavioural manifestations of impulsive temperament. The 96 male controls were free of DSM-III-R Axis I and II diagnoses and matched for age, and were selected for sequencing for single nucleotide polymorphism (SNP) discovery from a larger control cohort comprising 295 individuals. As compared to controls, cases also had significantly higher impulsivity (action on the spur of the moment) scores on the Karolinska Scales of Personality ($P < 0.0001$)²⁴. However, analysis was conducted on a behaviourally based phenotype, rather than a measure of temperament, because behaviour has repeatedly shown the strongest relationship to biological predictors, including genes. Genetic loci previously implicated in impulsivity include the *MAOA* stop codon linked to impulsive behaviour in one Dutch family⁶, *5-HTTLPR* at the serotonin transporter, which predicts suicidality^{19,20}, and the dopamine transporter *VNTR*, which has been associated with ADHD¹¹. Impulsive behaviour also can be predicted by neurotransmitters and endocrine factors, as illustrated by associations with brain serotonin turnover²⁵, testosterone levels and a gene–testosterone interaction⁹. Animal behavioural pharmacology, gene knockout and strain-difference studies all primarily rely on measured behaviour. By selecting the most phenotypically extreme probands for sequencing, we increased the probability that we would detect functional variants altering impulsivity. Clinical and criminal records, including evaluation of premeditation and spontaneity of crimes, were available for all cases.

Exonic and promoter regions (comprising 82 kb) were amplified in pools of 12 genomic DNAs and sequenced simultaneously at 80× coverage on an Illumina Genome Analyser, as described in Methods. Sequencing allowed us to identify and accurately estimate frequencies of alleles (Supplementary Fig. 8 compares frequencies determined by sequencing and genotyping; correlation coefficient $r = 0.94$). Of 360 SNPs identified, 44% were known (National Center for Biotechnology Information (NCBI) Build128). Frequencies of novel SNPs ranged as high as 0.2. Within 37 kb of protein-coding DNA, 25 synonymous SNPs, of which 9 were novel, and 26 nonsynonymous SNPs (nsSNPs), were detected. Of a total of 22 nsSNPs confirmed by Sanger sequencing, 10 were novel.

Association of putatively functional SNPs

Four nsSNPs were predicted to be functional according to both SIFT (sorting intolerant from tolerant) and PolyPhen (polymorphism phenotyping): *TPH2* Pro206Ser (rs17110563), *DRD1* Ser259Tyr, *HTR2B*

Arg388Trp and *HTR2B* Q20*, a stop codon (Supplementary Table 5). These four nsSNPs were genotyped in male Finnish cases and controls. In a global test of association with an aggregate of potential susceptibility variants, these four putatively functional variants were twice as common in cases (13.0%) compared to controls (6.5%, $\chi^2 = 6.76$, $P = 0.009$; Supplementary Table 6). However, this global association was driven by *HTR2B* Q20*. Seventeen out of two-hundred and twenty-eight cases were heterozygous for *HTR2B* Q20* compared to 7/295 controls ($\chi^2 = 7.26$, $P = 0.007$; Supplementary Table 6), with an allele frequency in controls of 0.012. Eighty-nine pedigrees comprising family members of the violent offenders were collected and all were genotyped without pre-selection for phenotype or genotype, identifying eight *HTR2B* Q20* carrier families (Fig. 1 and Methods). Affected status was defined as presence of ASPD, BPD, or IED. The transmission disequilibrium test detected over-transmission of Q20* to affected offspring (McNemar $\chi^2 = 5.0$, $P = 0.025$). Similarly, among affected individuals, 6/7 had Q20* transmitted, and among unaffected individuals 10/14 did not have Q20* transmitted (Supplementary Table 7). From the cumulative binomial distribution, previously proposed for linkage of functional loci in families²⁶, the likelihood of 16/21 or more linked outcomes was 0.013.

The *HTR2B* gene is on 2q36.3–q37.1, a location implicated in early-onset obsessive compulsive disorder²⁷ and illicit substance abuse²⁸. However, resequencing of *HTR2B* in these two studies yielded no functional variants^{27,28}. 5-HT_{2B} receptor function in the brain is mainly unknown; however, it has been shown that 3,4-methylenedioxymethamphetamine (MDMA, commonly known as ecstasy) selectively binds and activates 5-HT_{2B} receptors, inducing serotonin release in mouse raphe nuclei, leading to dopamine release in the nucleus accumbens and ventral tegmentum²⁹, and 5-HT_{2B} agonists increase serotonin transporter phosphorylation³⁰.

HTR2B Q20* in humans

We assessed molecular functionality of *HTR2B* Q20* by using RNA and proteins extracted from lymphoblastoid cell lines, and in addition *HTR2B* expression was measured in multiple brain regions, including the frontal cortex, by quantitative polymerase chain reaction (qPCR; Methods). Q20* led to variable nonsense-mediated RNA decay and blocked expression of the 5-HT_{2B} receptor protein (Fig. 2 and Methods). *HTR2B* is widely expressed in the adult human brain, and the frontal lobe is one of the regions where it is most highly expressed (Methods and Supplementary Fig. 13).

HTR2B Q20* is apparently exclusive to Finns. In >3,100 individuals representative of worldwide diversity, including the Human Genome Diversity Panel (Supplementary Table 8), one additional Q20* carrier was observed: a female with a Finnish surname and with alcoholism. Indicative of a common origin and founder population effect, Q20* was found on a single haplotype background (Supplementary Fig. 9), and in Finns who were likely to be non-admixed (Supplementary Fig. 2). Genetic subisolates have been identified within Finland, including families in Eastern Finland. Also, the Finnish population apparently was founded by two waves of migration: Eastern Uralic founders arrived 4,000 years ago, followed by Indo-European speakers 2,000 years later²³. However, it is unlikely that the Q20* association is an occult admixture artefact because Q20* carriers are common across Finland (in Middle, Western and Eastern regions) (Supplementary Fig. 3), and cases and controls did not differ in Finnish ancestry (Supplementary Fig. 4 and Methods).

In the 17 violent offenders (from the case–control study) who carried Q20*, impulsivity had a strong role in their crimes. Although convicted for a variety of offences including homicide, attempted homicide, arson, battery and assault, 94% of their crimes were committed under the influence of alcohol. The crimes of the Q20* carrier probands occurred as disproportionate reactions to minor irritations and were unpremeditated, without potential for financial gain and recurrent. From court records up to an average age of 43, Q20* carriers had

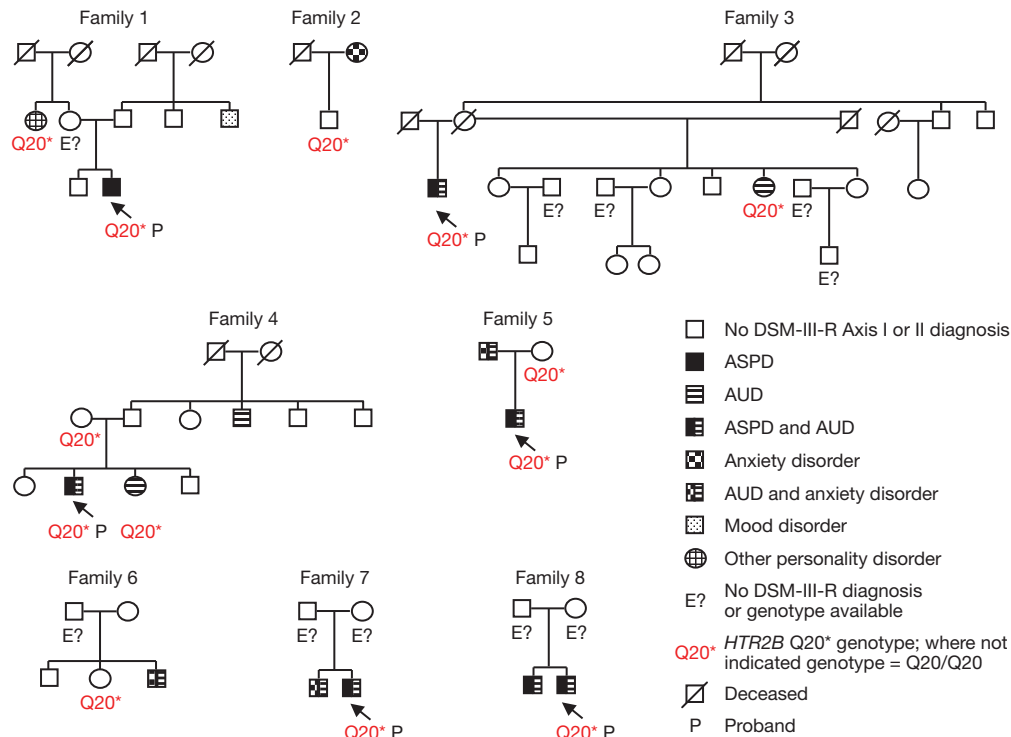


Figure 1 | *HTR2B* Q20* co-segregates with impulsivity. Co-segregation of *HTR2B* Q20* with ASPD and alcohol use disorder (AUD) in eight informative families.

committed an average of 5 violent crimes (range 2–12). The Q20* cases tended to fulfil the criteria for ASPD (82%) and IED (57% meeting 3 out of 4 IED criteria), except that alcoholism, ASPD and BPD are exclusionary for IED. Overall, Q20* carriers were cognitively normal (mean IQ, 98; s.d., 14.9; range 75–124; two with IQ <87, Wechsler Adult Intelligence Scale).

In temperament—as measured by the Tridimensional Personality Questionnaire—Q20* carriers, like others with ASPD, score more highly in ‘novelty seeking’ and ‘harm avoidance’, but are otherwise more socially attached, empathic and dependent than the other violent offenders within the study group (Supplementary Data). Extrapolating from the Q20* frequency of 0.012 (and with 174 Q20* carriers directly

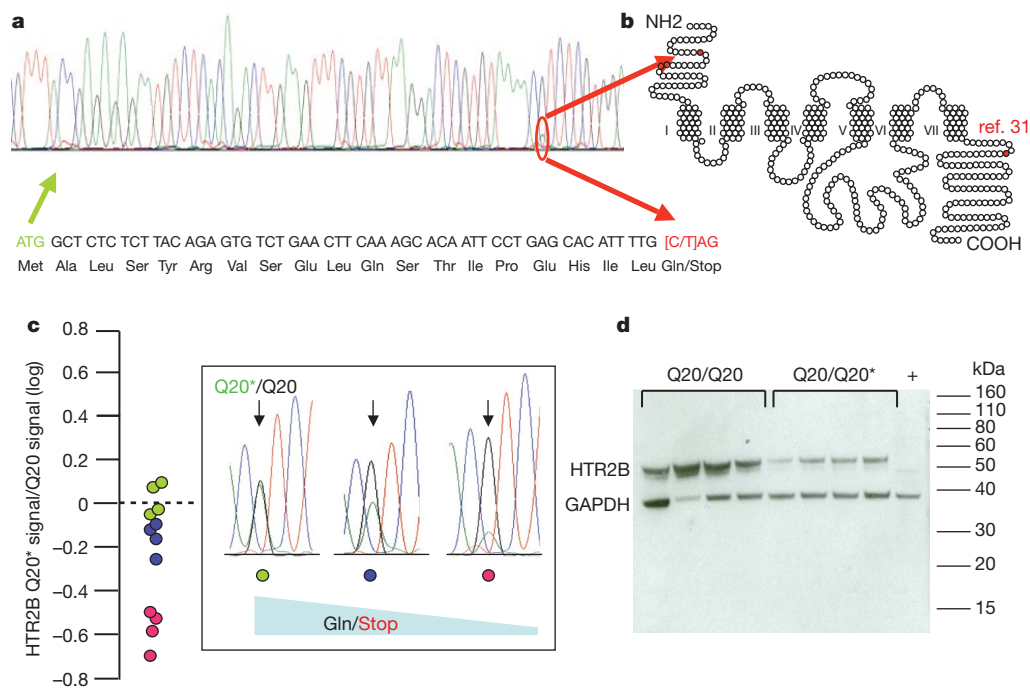


Figure 2 | *HTR2B* Q20* blocks protein expression. a, b, cDNA (a) and protein locations (b) of *HTR2B* Q20*. b, Labels I, II, III, IV, V, VI and VII refer to the seven transmembrane domains of the 5-HT_{2B} protein and ref. 31 indicates the position in the 5-HT_{2B} protein of a known, previously identified, *HTR2B* stop codon. c, Variable stop-codon-mediated RNA decay determined

by cDNA sequencing of 12 Q20* heterozygotes. d, Q20*-mediated blockade of 5-HT_{2B} protein expression in western blots (validated with three anti-5-HT_{2B} antibodies; described in Methods). The 5-HT_{2B} protein ratio was 1.93:1 in 14 Q20/Q20 homozygotes (mean, 1.78; s.d., 2.24) compared to 14 Q20/Q20* heterozygotes (mean, 0.92; s.d., 1.14) ($P = 0.03$) (Methods).

genotyped), 53,000 Finnish males (and as many females) are heterozygous. However, although few Q20* carriers are criminals, violent criminals with Q20* seem to represent some of the most impulsive individuals within our violent offender cohort. Among 100–155 homicides annually in the Finnish population of 5.3 million, there are few instances of multiple homicide. In our sample, only three individuals were convicted of multiple homicide, and all three carried the Q20* allele.

In our sample, the influence of Q20* was not due to interaction with MAOA or serotonin transporter genotypes (data not shown). However, it was not possible to rule out other gene interactions, or a modifying role of stress. Cerebrospinal fluid monoamine metabolite levels, another potential confounding factor, did not differ in Q20* carriers (Supplementary Data). Therefore, it is unlikely that their impulsivity was due to low turnover of serotonin, dopamine or norepinephrine or that Q20* substantially affects monoamine metabolism, as does the MAOA stop codon⁶.

Risk conferred by Q20* seems to be modulated by sex and alcohol. Worldwide, suicide accounts for 1.5% of deaths, and Finland has a very high suicide rate, especially among men³². In our study, 70% of the Q20* male cases showed impulsive suicidal behaviour (for example, slashings, hanging attempts, drug overdoses) usually while intoxicated, for an average of 3.2 suicide attempts. At age 33.5 (s.d. \pm 11), 66% had at least one life-threatening suicide attempt. It is unknown if suicide risk conferred by Q20* extends to the general population, whose members are at lower risk. Males are more likely to commit suicide³² and to have ASPD and aggression, with a tenfold higher preponderance for the early-onset life-course-persistent variant of ASPD³³. Moreover, alcohol-related violence is known to be higher among males, and the serotonin system is thought to contribute to individual differences in alcohol-facilitated impulsive aggression³⁴.

In the violent offender cohort, Q20* carriers were cognitively normal and in almost every instance acted out on their impulsivity only when inebriated. Having found the association of Q20* with impulsivity in a phenotypically extreme sample, it was important to define Q20* frequency and relationship to behaviour in the wider population, even though the only possible follow-up was in Finland. In >6,000 Finns ascertained epidemiologically (rather than from the criminal population), the Q20* allele frequency was 0.012 (the same as the frequency in controls) (Supplementary Table 9). We identified one Q20* homozygote, a young male adult with no major medical illness but with a history of violent behaviour while under the influence of alcohol (Supplementary Methods).

We followed up the cognitive effects of Q20* in 933 individuals in the FinnTwin12 and FinnTwin16 studies (22 with the stop codon) (Supplementary Methods). Overall, Q20* carriers were again cognitively normal. However, male (but not female) Q20* carriers had significantly lower Digit Span Forward ($P = 0.002$) and Backward ($P < 0.001$) scores, possibly indicating selective impairment in working memory (Supplementary Fig. 12), a specific measure of frontal cortical function.

Htr2b^{-/-} mice

Although severe developmental consequences have been observed in *Htr2b* knockout mice, approximately 50% of the mice that survive the first postnatal week are apparently normal as adults³⁵. These mice were reported to be impulsive in an open field novelty test²⁹. We assessed *Htr2b* knockout mice for five separate measures of impulsivity and novelty seeking: delay discounting, activity in a novel environment, exposure to a novel object, motor activity after a dopamine D1 receptor agonist, and decreased latency to eat in the novelty suppressed feeding test (hyponeophagia). The *Htr2b*^{-/-} mice were more impulsive and more responsive to novelty in all of these tests (Fig. 3). In rats, both impulsivity and response to novelty are predictors for the development of addiction-like behaviours³⁶. In addition to their differences in behaviour, *Htr2b*^{-/-} males had a threefold elevation in plasma testosterone (Fig. 3 and Supplementary Methods). Testosterone (measured in the

cerebrospinal fluid of nine heterozygous violent offenders) also seemed to be higher in human males carrying Q20* (Supplementary Fig. 11). This raises the possibility of an interaction between Q20* and testosterone contributing to impulsive behaviours, as was reported between MAOA and testosterone in the same population of Finns that we studied here⁹.

Discussion

The aim of this study was to identify genetic variation associated with impulsivity, an intermediate phenotype thought to contribute to several psychiatric disorders including addictions¹². The goal is to track shared genetic factors in these diseases and to contribute to their reconceptualization on a neurobiological basis. Another purpose of identifying genes influencing impulsivity is to determine which of the potential aetiologies and types of impulsivity, for example novelty seeking versus executive dysfunction³⁶, are important in human populations. The discovery of genes influencing impulsive behaviour would validate the idea that it is possible to deconstruct the multi-process origins of impulsive behaviour.

HTR2B Q20* is associated and co-segregates with disorders characterized by impulsivity, reflected in severe crimes committed on the spur of the moment—as documented by criminal and clinical records—and under alcohol intoxication, a condition where impulse control is impaired. Thus, the Q20* allele can be regarded as one determinant of behavioural variation. However, the presence of Q20* was not in itself sufficient: male sex, testosterone level, the decision to drink alcohol, and probably other factors such as stress exposure, all have important roles. Although relatively common in Finland, *HTR2B* Q20* is unlikely to explain a large fraction of the overall variance in impulsive behaviours. There are likely to be many pathways to impulsivity in its various manifestations, and the genetic association may be present only in the most phenotypically extreme.

It is unsurprising that a stop codon variant discovered by sequencing within a founder population is common only in it, and even restricted to it. However, this observation is also in line with the significance of Q20* as a complete loss of function variant, and with the behavioural consequences in some heterozygous carriers. The relatively high frequency of Q20* in Finns would thus reflect its status as a founder mutation, in contrast with MAOA, COMT and SLC6A4 (previously known as *HTT*) alleles that are common worldwide, more modestly affect molecular function, and may have counterbalancing selective advantages. However, it is highly unlikely that Finns are unique in possessing a severe genetic variation leading to impulsivity. There is the previous example of the MAOA stop codon found in one Dutch family. On average, ten or more heterozygous stop codons reside in the genomes of each individual of European ancestry²¹, but perhaps because the source populations from which the probands were sequenced did not have founder characteristics, no common stop codon had yet been reported for a neurotransmitter gene. Although rare variants identified in founder populations are more likely to be confined to those populations, analyses of the relationship between gene variation and phenotype can be conducted within the founder population, identifying new candidate genes and pathways influencing behaviour or other aetiologically complex phenotypes.

As has often been illustrated, the availability of mouse genetic models, including gene knockouts, offers an opportunity to test the predictive validity of genetic discoveries and to define effects in contexts where genetic background and environment are better controlled. The *Htr2b* mouse knockout reveals more general effects of 5-HT_{2B} deficiency on behaviour, including effects on novelty seeking. This could be explained by pleiotropic actions of the serotonin 2B receptor. On the other hand, the effect of the *Htr2b* knockout on delay discounting seems to validate the effect of the Q20* stop codon on impulsivity in people. In people, we observed a significant association between the *HTR2B* Q20* variant and impairment in working memory, a neurocognitive process contributing or predictive of executive cognitive function. The ability to store and

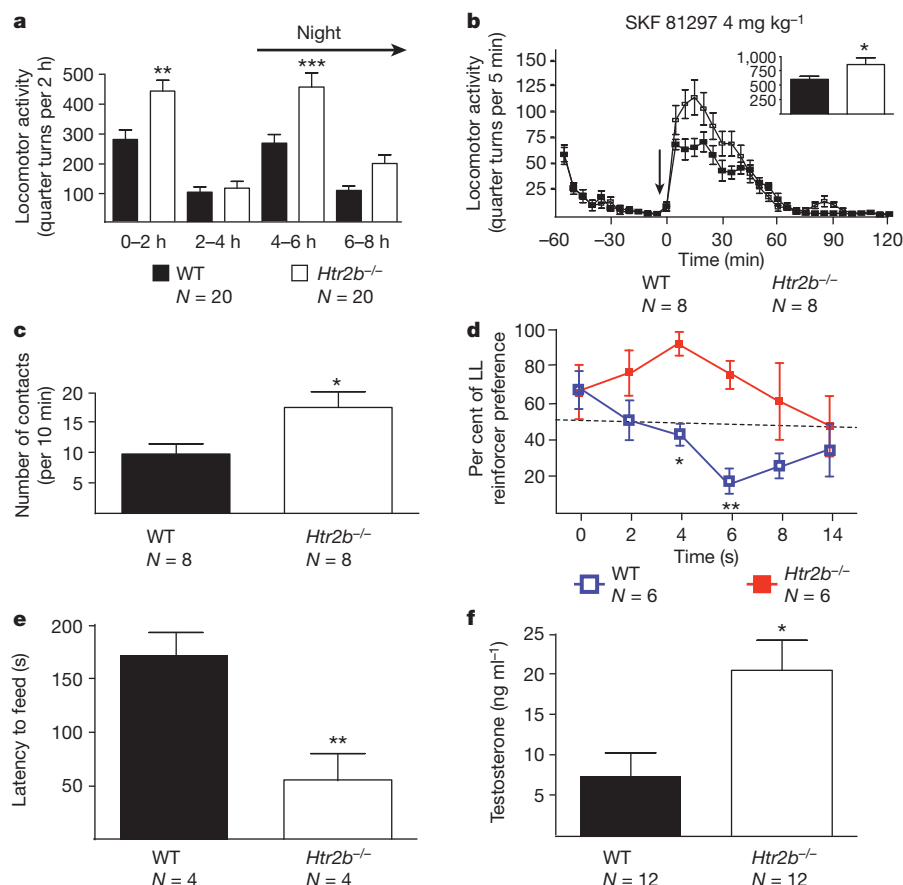


Figure 3 | Increased impulsivity and novelty seeking in *Htr2b*^{-/-} mice. **a, b,** Increased locomotor response of *Htr2b*^{-/-} mice to environmental novelty (**a**) and to a dopamine D1 receptor agonist (SKR 81297) (**b**). WT, wild type. **c,** Increased number of contacts of *Htr2b*^{-/-} mice with a novel object. **d,** Increased delay discounting of *Htr2b*^{-/-} mice. LL, large and late hole, nose

pokes leading to delivery of a larger but later reward. **e,** Reduced hyponeophagia in 18-h starved *Htr2b*^{-/-} mice. **f,** Male *Htr2b*^{-/-} mice have threefold higher plasma testosterone levels as compared to control mice. **P* < 0.05, ***P* < 0.01, ****P* < 0.001. Error bars are data ± standard error.

integrate knowledge about possible choices with the current context enables the individual to select appropriate cognitive strategies and generate optimal reactions. This is coherent with the impulsivity observed in *HTR2B* Q20* cases, who seemed deficient in the ability to weigh the consequences of their acts.

The use of deep sequencing to detect a stop codon associated with impulsivity in a founder population reveals a role for the *HTR2B* gene in behaviour. It also indicates that this approach may be applicable to other complex behavioural traits, including those diseases for which impulsivity is itself an intermediate phenotype.

METHODS SUMMARY

Fourteen serotonergic and dopaminergic genes were resequenced (Solexa GA2) in 96 Finnish Caucasian male violent offenders and 96 matched controls free of psychiatric diagnoses. Exon-centric sequencing was performed by amplifying 108 regions, for a total of 82 kb, in pools of 12 subjects. *HTR2B* Q20* was genotyped in a Finnish sample of 228 cases and 295 controls, in 89 Finnish families, and in 5,684 individuals belonging to either a Finnish family data set (*N* = 1,885), the Older Finnish Twin cohort (*N* = 2,388) or the FinnTwin16 and FinnTwin12 studies (*N* = 1,411), as described in detail in Supplementary Methods, and in >3,100 samples representing worldwide diversity. Genotyping was performed with a custom 5' exonuclease assay (Applied Biosystems 7900) using these primers and probes: forward primer, 5'-AGAGTGTCTGAACCTCAAGACACAA-3'; reverse primer, 5'-TCCAGACCAGTTAGAAGAGATAACGT-3'; probe 1, 5'-AGGTGCTCTGCAAAAT-3'; probe 2, 5'-AGGTGCTCTACAAAAT-3'.

One-hundred and eight-six ancestry informative markers were genotyped on 1536-SNP arrays (Illumina). qPCR for *HTR2B* expression in 13 human brain regions was determined by ABI Taqman gene expression assays (Hs01118766 and Hs00168362). β -actin was the internal control. Total protein and total RNA

were extracted from lymphoblastoid cell lines using the TRIzol LS reagent protocol (Invitrogen). Nonsense-mediated RNA decay was detected by sequencing on a 3700ABI capillary sequencer complementary DNA from *HTR2B* Q20/Q20* heterozygotes. HT2B protein was measured in 12 Finnish Q20/Q20 homozygotes and 14 Finnish Q20/Q20* heterozygotes. Blots were probed with antisera raised against the amino-terminal (mouse monoclonal antibody; Novus Biologicals), internal (goat polyclonal antibody; Santa Cruz Biotechnology), or carboxy-terminal (rabbit polyclonal antibody; Santa Cruz Biotechnology) regions of the HT2B receptor, and GAPDH antibody (Millipore). Densitometry was performed using National Institutes of Health (NIH) Image]. *Htr2b*^{-/-} knockout mice were made in a pure 129Sv/PAS background and compared to 129/SvPAS control mice (8–10 weeks old) for four measures of response to novelty and for delay discounting.

Full Methods and any associated references are available in the online version of the paper at www.nature.com/nature.

Received 25 August; accepted 27 October 2010.

- Winstanley, C. A., Eagle, D. M. & Robbins, T. W. Behavioral models of impulsivity in relation to ADHD: translation between clinical and preclinical studies. *Clin. Psychol. Rev.* **26**, 379–395 (2006).
- Eysenck, S. B. & Eysenck, H. J. The place of impulsiveness in a dimensional system of personality description. *Br. J. Soc. Clin. Psychol.* **16**, 57–68 (1977).
- DeJong, J., Virkkunen, M. & Linnoila, M. Factors associated with recidivism in a criminal population. *J. Nerv. Ment. Dis.* **180**, 543–550 (1992).
- Kendler, K. S. *et al.* The structure of genetic and environmental risk factors for DSM-IV personality disorders. *Arch. Gen. Psychiatry* **65**, 1438–1446 (2008).
- Coccaro, E. F., Bergeman, C. S. & McClearn, G. E. Heritability of irritable impulsiveness: a study of twins reared together and apart. *Psychiatry Res.* **48**, 229–242 (1993).
- Brunner, H. G., Nelen, M., Breakefield, X. O., Ropers, H. H. & van Oost, B. A. Abnormal behavior associated with a point mutation in the structural gene for monoamine oxidase A. *Science* **262**, 578–580 (1993).

7. Sabol, S. Z., Hu, S. & Harner, D. A functional polymorphism in the monoamine oxidase A gene promoter. *Hum. Genet.* **103**, 273–279 (1998).
8. Caspi, A. *et al.* Role of genotype in the cycle of violence in maltreated children. *Science* **297**, 851–854 (2002).
9. Sjöberg, R. L. *et al.* A non-additive interaction of a functional MAO-A VNTR and testosterone predicts antisocial behavior. *Neuropsychopharmacology* **33**, 425–430 (2008).
10. Misener, V. L. *et al.* Linkage of the dopamine receptor D1 gene to attention deficit/hyperactivity disorder. *Mol. Psychiatry* **9**, 500–509 (2004).
11. Faraone, S. V. *et al.* Molecular genetics of attention deficit/hyperactivity disorder. *Biol. Psychiatry* **57**, 1313–1323 (2005).
12. Winstanley, C. A. *et al.* Double dissociation between serotonergic and dopaminergic modulation of medial prefrontal and orbitofrontal cortex during a test of impulsive choice. *Cereb. Cortex* **16**, 106–114 (2006).
13. Everitt, B. J. *et al.* Neural mechanisms underlying the vulnerability to develop compulsive drug-seeking habits and addiction. *Phil. Trans. R. Soc. Lond. B* **363**, 3125–3135 (2008).
14. Volkow, N. D., Fowler, J. S. & Wang, G. J. Role of dopamine in drug reinforcement and addiction in humans: results from imaging studies. *Behav. Pharmacol.* **13**, 355–366 (2002).
15. Virkkunen, M. & Linnoila, M. Brain serotonin, type II alcoholism and impulsive violence. *J. Stud. Alcohol, Suppl.* **11**, 163–169 (1993).
16. Chiavegatto, S. *et al.* Brain serotonin dysfunction accounts for aggression in male mice lacking neuronal nitric oxide synthase. *Proc. Natl Acad. Sci. USA* **98**, 1277–1281 (2001).
17. Cases, O. *et al.* Plasma membrane transporters of serotonin, dopamine, and norepinephrine mediate serotonin accumulation in atypical locations in the developing brain of monoamine oxidase A knock-outs. *J. Neurosci.* **18**, 6914–6927 (1998).
18. Ducci, F. *et al.* Interaction between a functional MAOA locus and childhood sexual abuse predicts alcoholism and antisocial personality disorder in adult women. *Mol. Psychiatry* **13**, 334–347 (2007).
19. Roy, A., Hu, X. Z., Janal, M. N. & Goldman, D. Interaction between childhood trauma and serotonin transporter gene variation in suicide. *Neuropsychopharmacology* **32**, 2046–2052 (2007).
20. Caspi, A. *et al.* Influence of life stress on depression: moderation by a polymorphism in the 5-HTT gene. *Science* **301**, 386–389 (2003).
21. Ng, S. B. *et al.* Targeted capture and massively parallel sequencing of 12 human exomes. *Nature* **461**, 272–276 (2009).
22. Nejantsev, S., Walker, N., Riches, D., Egholm, M. & Todd, J. A. Rare variants of *IFIH1*, a gene implicated in antiviral responses, protect against type 1 diabetes. *Science* **324**, 387–389 (2009).
23. Peltonen, L., Jalanko, A. & Varilo, T. Molecular genetics of the Finnish disease heritage. *Hum. Mol. Genet.* **8**, 1913–1923 (1999).
24. Gustavsson, J. P. Swedish universities Scales of Personality (SSP): construction, internal consistency and normative data. *Acta Psychiatr. Scand.* **102**, 217–225 (2000).
25. Virkkunen, M. *et al.* CSF biochemistries, glucose metabolism, and diurnal activity rhythms in alcoholic, violent offenders, fire setters, and healthy volunteers. *Arch. Gen. Psychiatry* **51**, 20–27 (1994).
26. Abel, L., Alcais, A. & Mallet, A. Comparison of four sib-pair linkage methods for analyzing sibships with more than two affecteds: interest of the binomial maximum likelihood approach. *Genet. Epidemiol.* **15**, 371–390 (1998).
27. Kim, S. J. *et al.* Mutation screening of human 5-HT_{2B} receptor gene in early-onset obsessive-compulsive disorder. *Mol. Cell. Probes* **14**, 47–52 (2000).
28. Lin, Z., Walther, D., Yu, X. Y., Drgon, T. & Uhl, G. R. The human serotonin receptor 2B: coding region polymorphisms and association with vulnerability to illegal drug abuse. *Pharmacogenetics* **14**, 805–811 (2004).
29. Doly, S. *et al.* Serotonin 5-HT_{2B} receptors are required for 3,4-methylenedioxymethamphetamine-induced hyperlocomotion and 5-HT release *in vivo* and *in vitro*. *J. Neurosci.* **28**, 2933–2940 (2008).
30. Launay, J. M., Schneider, B., Loric, S., Da Prada, M. & Kellermann, O. Serotonin transport and serotonin transporter-mediated antidepressant recognition are controlled by 5-HT_{2B} receptor signaling in serotonergic neuronal cells. *FASEB J.* **20**, 1843–1854 (2006).
31. Blanpain, C. *et al.* Serotonin 5-HT_{2B} receptor loss of function mutation in a patient with fenfluramine-associated primary pulmonary hypertension. *Cardiovasc. Res.* **60**, 518–528 (2003).
32. Hawton, K. & van Heeringen, K. Suicide. *Lancet* **373**, 1372–1381 (2009).
33. Rutter, M., Caspi, A. & Moffitt, T. E. Using sex differences in psychopathology to study causal mechanisms: unifying issues and research strategies. *J. Child Psychol. Psychiatry* **44**, 1092–1115 (2003).
34. Chiavegatto, S., Quadros, I. M., Ambar, G. & Miczek, K. A. Individual vulnerability to escalated aggressive behavior by a low dose of alcohol: decreased serotonin receptor mRNA in the prefrontal cortex of male mice. *Genes Brain Behav.* **9**, 110–119 (2010).
35. Jaffré, F. *et al.* Serotonin and angiotensin receptors in cardiac fibroblasts coregulate adrenergic-dependent cardiac hypertrophy. *Circ. Res.* **104**, 113–123 (2009).
36. Belin, D., Mar, A. C., Dalley, J. W., Robbins, T. W. & Everitt, B. J. High impulsivity predicts the switch to compulsive cocaine-taking. *Science* **320**, 1352–1355 (2008).

Supplementary Information is linked to the online version of the paper at www.nature.com/nature.

Acknowledgements This study is dedicated to the memory of L.P. and M. Linnoila. We thank L. Akhtar for assistance with tissue culture, C. Marietta for assistance with measurement of receptor protein levels, V. Srivastava and G. Yamini for discussions, and P.-H. Shen for contributions to ancestry analyses. M. Eggert and L. Brown assisted with clinical ascertainment and assessment of the University of Helsinki sample. We thank M. Linnoila for his contributions to the collection of the University of Helsinki sample. E. Kempas assisted with genotyping. J.-M. Launay measured plasma testosterone levels in *Htr2b*^{-/-} mice. We also thank A. Tuulio-Henriksson, E. Vuoksimaa, A. Häppölä and L. Arala. This work was supported by the Intramural Research Program of the National Institute on Alcohol Abuse and Alcoholism, NIH and the Academy of Finland Centre of Excellence in Complex Disease Genetics. The FinnTwin12 and FinnTwin16 studies were supported by the National Institute on Alcohol Abuse and Alcoholism (AA-12502 and AA-09203 to R.J.R.), and by the Academy of Finland (100499, 205585 and 118555 to J.K.). The studies on *Htr2b*^{-/-} mice were supported by the Centre National de la Recherche Scientifique, the Institut National de la Santé et de la Recherche Médicale, the Université Pierre et Marie Curie, and by grants from the Fondation de France, the Fondation pour la Recherche Médicale, the French Ministry of Research (Agence Nationale pour la Recherche), and the European Union. L.M.'s team is an "Equipe Fondation pour la Recherche Médicale". S. Diaz is supported by a fellowship from IBRO and Region Ile de France DIM STEM.

Author Contributions L.B. and D.G. drafted and revised the manuscript, conceptualized the study, and performed molecular, clinical and statistical analyses. L.M., S. Doly, S. Diaz and A.B. performed behavioural analyses in mice and statistical analyses. J.K. performed clinical and statistical analyses. Q.Y. performed statistical analyses. R.T., M.V. and J.S. performed clinical analyses. T.P. directed molecular analyses. J.W. performed molecular analyses. C.A.H. and Z.Z. helped direct molecular analyses. L.P. helped direct clinical analyses. C.A.H., Z.Z., J.K., T.P., J.S., M.V. and E.C. revised the manuscript. D.G., L.M., J.K., C.A.H., L.P., L.D., E.C., R.J.R. and M.V. also helped with organization and support.

Author Information: The NCBI accession number for the *HTR2B* stop codon is rs79874540. For all newly discovered SNPs, NCBI accession numbers are listed in Supplementary Table 4. Reprints and permissions information is available at www.nature.com/reprints. The authors declare no competing financial interests. Readers are welcome to comment on the online version of this article at www.nature.com/nature. Correspondence and requests for materials should be addressed to D.G. (davidgoldman@mail.nih.gov).

METHODS

Human studies. Written informed consent was obtained from each participant. Protocols were approved by the Institutional Review Board (IRB) of the NIH and the National Institute of Mental Health (NIMH), by the Office for Protection from Research Risks (OPRR), Indiana University IRB, by the University of Helsinki Department of Psychiatry IRB, by the University of Helsinki Central Hospital IRB, the University of Turku Central Hospital IRB, and by the Ministry of Social Affairs and Health and the Ethics Committee of the National Public Health Institute of Finland.

Animal studies. Mice were housed under controlled environmental conditions. Behavioural tests and animal care were conducted in accordance with standard ethical guidelines (NIH's "Guide for the Care and Use of Laboratory animals", and the European Communities Council European Communities Directive 86/609 EEC). All experiments involving mice were approved by the Ile de France Regional Ethics Committee for Animal Experiments.

Finnish violent offenders' cohort and controls. Cases were 228 unrelated Finnish male violent offenders and arsonists (Supplementary Table 1) who, because of the extreme nature of their crimes, underwent forensic psychiatric examination at the time of their initial incarceration. They were studied as inpatients at the University of Helsinki^{25,37}. These subjects were diagnosed with the Structural Clinical Interview for DSM (SCID) according to DSM-III-R criteria for ASPD, BPD and IED. Excluded were subjects with schizophrenia or a history of psychosis. Ninety-six cases were selected for resequencing from the larger Finnish case cohort, comprising 228 individuals with diagnoses of ASPD, BPD and IED, on the basis that they had the highest Brown–Goodwin Lifetime Aggression (BGLAS) scores³⁸, with scores of 23.7 (s.d. \pm 4.9) out of a theoretical maximum of 36. Controls (N = 295) were unrelated, nonimpulsive Finnish volunteers recruited by advertisements in local newspapers, paid for their participation and psychiatrically interviewed by trained psychiatrists. Cases and controls were independently blind-rated from interview data by two research psychiatrists under the supervision of a senior research psychiatrist. Inter-rater reliability was high, and differences were resolved by the senior psychiatrist. Controls were free of ASPD, BPD, IED, psychosis or schizophrenia but some had mood or anxiety disorders or alcohol use disorder (Supplementary Table 1). Ninety-six male controls free of Axis I and II diagnoses and matched for age were selected for sequencing for SNP discovery from a cohort of 295 controls. Controls had a BGLAS score of 8.1 (s.d. \pm 4.9).

A total of 89 pedigrees were collected. Family members were interviewed using the SCID and diagnosed using DSM-III-R criteria. DNA and data were available for 397 subjects in families. Genomic DNA was prepared from lymphoblastoid cell lines.

Resequencing. For the exon-centric targeting of 14 candidate genes, we custom-designed or used Applied Biosystem oligonucleotide primers to amplify 108 target regions that covered exons, flanking regions and \sim 800–1,000 bp of the upstream regions of 14 genes, for a total of 82 kb (Supplementary Table 2).

DNA samples were individually quantified in three replicates by RT-PCR, using TaqMan RNase P Detection Reagent kits (FAM) and Roche human DNA standards, and were normalized to 10 ng μ l⁻¹. Eight DNA pools (12 subjects per pool) were made with equal amounts of DNA from 96 Finnish cases and in parallel fashion eight pools were made from 96 Finnish controls. Average sequencing coverage per individual per nucleotide was 80 \times .

For DNA amplification, DNA pools were amplified in 108 separate PCR reactions (Supplementary Methods).

Before DNA sequencing, amplicon concentrations were normalized using SequalPrep Normalization Plate kits (Invitrogen). All amplicons from the same DNA pool were combined. The DNA was sheared by sonication and purified with QIAquick PCR purification kits (QIAGEN). Genomic DNA preparation kits and protocol (Illumina) were used to prepare sequencing libraries.

Analysis of sequence data was carried out by calling sequences from image files with the Illumina Genome Analyser Pipeline and aligning them to human reference sequences from NCBI build 36.3 using the Illumina Eland software. Each 36-base read was uniquely mapped to the human reference genome. Sequence reads with more than two mismatches were excluded. Sequence reads with alternative alleles that did not exactly match the reference genome did not uniquely map to the corresponding location in the reference sequence. Additional results are described in Supplementary Data.

Capillary electrophoresis sequencing. nsSNPs were validated by Sanger sequencing using the BigDye Terminator Sequencing Mix (Applied Biosystems) and analysed on the Applied Biosystems 3730 DNA Analyser. Of 26 nsSNPs, 22 were validated, and overall 30/34 SNPs tested in this way were validated.

Predicted functionality. Missense, nonsense and synonymous variants were predicted to be probably damaging or damaging for protein function via PolyPhen and SIFT amino acid substitution prediction methods. Four variants

(*DRD1* S259Y, *HTR2B* R388W, *HTR2B* Q20* and *TPH2* P206S—rs17110563) scored as damaging or intolerant by both methods were used in a global test of proportion of rare functional variants in cases (ASPD, BPD or IED) and controls. Genotypes of the four SNPs were collapsed so that an individual was coded as 1 if a rare allele was present and otherwise as 0. Frequencies of putatively functional variants were globally compared between cases and controls, with the null hypothesis being a lack of difference between cases and controls in the proportion carrying the putatively functional variants. A case–control association test was also performed for *HTR2B* Q20* alone. Pearson χ^2 test was used to test the null hypothesis. All analyses were conducted using JMP software v7.0 (SAS Institute). The criterion for statistical significance was set at 0.05.

Genotyping. *HTR2B* Q20* was genotyped in 228 Finnish cases and 295 Finnish controls and in 89 pedigrees belonging to the Finnish cohort for a total of 352 subjects. Taking into account the fact that some families had affected probands, we genotyped a total of 872 Finnish DNAs. In addition to the Finnish case/control and family data set and over 3,100 samples representing worldwide diversity, we also genotyped a total of 5,684 individuals belonging to either a Finnish family data set (N = 1,885), or to the Older Finnish Twin cohort (N = 2,388) and the FinnTwin16 and FinnTwin12 studies (N = 1,411), as described in Supplementary Methods.

Genotyping of Q20* was performed with a custom 5' exonuclease assay (Applied Biosystems 7900) using these primers and probes: forward primer, 5'-AGAGTGTCTGAACCTCAAAGCACAA-3'; reverse primer, 5'-TCCAGAC CAGTTAGAAGAGATAACGT-3'; probe 1, 5'-AGGTGCTCTGCAAAAT-3'; probe 2, 5'-AGGTGCTCTACAAAAT-3'.

Ancestry informative markers. A panel of 186 ancestry informative markers were genotyped on 1536-SNP arrays (Illumina)³⁹. No difference was detected between cases (ASPD, BPD and IED) and controls in proportions of ancestries. The pattern of measured ancestry for seven ancestry factors derived separately for each subject was compared between controls (N = 279) and cases (N = 220) with reference to the Human Genome Diversity Panel (HGDP) (1,051 DNAs representing 51 populations worldwide).

Finnish ancestry was measured using 177 ancestry informative markers in 29 Q20* carriers, 580 other Finns, and 200 individuals representing 10 European populations in HGDP. Principal component analysis was performed with EIGENSTRAT.

For *HTR2B* RNA and protein expression studies, total protein and RNA were extracted from lymphoblastoid cell lines using the TRIzol LS reagent protocol (Invitrogen).

***HTR2B* cDNA sequencing for nonsense-mediated decay.** Nonsense-mediated RNA decay was detected by sequencing cDNA from *HTR2B* Q20/Q20* heterozygotes on a 3700ABI capillary sequencer (Fig. 2 and Supplementary Methods). The sequences of the upstream and downstream oligonucleotides were as follows: 5'-gagtggttggcaggttaca-3' and 3'-accaggcaggacatagaaca-5' (Supplementary Methods). *HTR2B* Q20 and Q20* transcripts were quantified by comparing the relative intensities of the Q20 and Q20* sequencing peaks within each heterozygous individual (Supplementary Methods).

Western blots. HT2B protein was measured in 12 Finnish Q20/Q20 homozygotes and 14 Finnish Q20/Q20* heterozygotes. Western blots were prepared using 50 μ g of protein per lane on a 10% Bis-Tris gel (Invitrogen). Separated proteins were transferred to nitrocellulose using the iBlot transfer system (NuPage; Invitrogen). Blots were probed with antisera raised against the amino-terminal (mouse monoclonal antibody; Novus Biologicals), internal (goat polyclonal antibody; Santa Cruz Biotechnology) or carboxy-terminal (rabbit polyclonal antibody; Santa Cruz Biotechnology) regions of the HT2B receptor, and GAPDH antibody (Millipore).

Antibody binding was visualized on X-ray film (Kodak XAR) using chemiluminescence (ECL Plus, GE Healthcare). Densitometry was performed using NIH ImageJ. Ratios between the 5-HT2B receptor and the housekeeping protein GAPDH were calculated to normalize 5-HT2B protein quantity.

qPCR for *HTR2B* in human brain. qPCR for *HTR2B* expression in 13 human brain regions was determined by ABI Taqman gene expression assays (Hs01118766 and Hs00168362). β -actin was the internal control.

Neuropsychological assessment. Neuropsychological assessment was conducted on both the combined FinnTwin16 and FinnTwin12 cohorts (described in Supplementary Methods) for measures of verbal intellectual ability, working memory and executive function. Working memory was assessed with the Digit Span Forward and Backward subtests of the Wechsler Memory Scale-Revised (WMS-R). We analysed the combined FinnTwin16 and FinnTwin12 data sets. A linear regression model was constructed using performance on the working memory test as the dependent variable and sex and genotype as independent variables. Sex was a significant predictor, so the sample was stratified into male and female. Male heterozygotes performed significantly worse on the Digit Span

Backward and Forward tests, and combined score (Supplementary Table 12 and Supplementary Fig. 12). All statistical analyses were conducted using Stata (version 11, Stata Corp, College Station, Texas, USA). The criterion for statistical significance was set at 0.05. Bonferroni correction for multiple testing was applied, as presented in Supplementary Table 12.

Htr2b knockout mice. *Htr2b*^{-/-} knockout mice (50% males and 50% females) were made in a pure 129Sv/PAS background. Wild-type 129/SvPAS mice (8–10 weeks old), bred in-house, were used as controls.

Novelty seeking and impulsive behaviour in *Htr2b*^{-/-} knockout mice were investigated using five experimental measures: novelty-induced locomotion;

locomotor reactivity in response to a dopamine D1 receptor agonist; exposure to a novel object; delay discounting; and novelty-suppressed feeding. Plasma testosterone levels were measured.

37. Linnoila, M. *et al.* Low cerebrospinal fluid 5-hydroxyindoleacetic acid concentration differentiates impulsive from nonimpulsive violent behavior. *Life Sci.* **33**, 2609–2614 (1983).
38. Brown, G. L. *et al.* Aggression in humans correlates with cerebrospinal fluid amine metabolites. *Psychol. Res.* **1**, 131–139 (1979).
39. Hodgkinson, C. A. *et al.* Addictions biology: haplotype-based analysis for 130 candidate genes on a single array. *Alcohol Alcohol.* **43**, 505–515 (2008).

Selective inhibition of BET bromodomains

Panagis Filippakopoulos^{1*}, Jun Qi^{2*}, Sarah Picaud^{1*}, Yao Shen³, William B. Smith², Oleg Fedorov¹, Elizabeth M. Morse², Tracey Keates¹, Tyler T. Hickman⁴, Ildiko Felletar¹, Martin Philpott¹, Shonagh Munro⁵, Michael R. McKeown^{2,6}, Yuchuan Wang⁷, Amanda L. Christie⁸, Nathan West², Michael J. Cameron⁴, Brian Schwartz⁴, Tom D. Heightman¹, Nicholas La Thangue⁵, Christopher A. French⁴, Olaf Wiest³, Andrew L. Kung^{8,9}, Stefan Knapp^{1,5} & James E. Bradner^{2,6}

Epigenetic proteins are intently pursued targets in ligand discovery. So far, successful efforts have been limited to chromatin modifying enzymes, or so-called epigenetic ‘writers’ and ‘erasers’. Potent inhibitors of histone binding modules have not yet been described. Here we report a cell-permeable small molecule (JQ1) that binds competitively to acetyl-lysine recognition motifs, or bromodomains. High potency and specificity towards a subset of human bromodomains is explained by co-crystal structures with bromodomain and extra-terminal (BET) family member BRD4, revealing excellent shape complementarity with the acetyl-lysine binding cavity. Recurrent translocation of BRD4 is observed in a genetically-defined, incurable subtype of human squamous carcinoma. Competitive binding by JQ1 displaces the BRD4 fusion oncoprotein from chromatin, prompting squamous differentiation and specific antiproliferative effects in BRD4-dependent cell lines and patient-derived xenograft models. These data establish proof-of-concept for targeting protein–protein interactions of epigenetic ‘readers’, and provide a versatile chemical scaffold for the development of chemical probes more broadly throughout the bromodomain family.

Gene regulation is fundamentally governed by reversible, non-covalent assembly of macromolecules¹. Signal transduction to RNA polymerase requires higher-ordered protein complexes, spatially regulated by assembly factors capable of interpreting the post-translational modification states of chromatin². Readers of epigenetic marks are structurally diverse proteins each possessing one or more evolutionarily conserved effector modules, which recognize covalent modifications of histone proteins or DNA. The ϵ -N-acetylation of lysine residues (Kac) on histone tails is associated with an open chromatin architecture and transcriptional activation³. Context-specific molecular recognition of acetyl-lysine is principally mediated by bromodomains.

Bromodomain-containing proteins are of substantial biological interest, as components of transcription factor complexes and determinants of epigenetic memory⁴. There are 41 diverse human proteins containing a total of 57 bromodomains. Despite large sequence variations, all bromodomain modules share a conserved fold comprising a left-handed bundle of four α helices (α_Z , α_A , α_B , α_C), linked by diverse loop regions (ZA and BC loops) that contribute to substrate specificity. Co-crystal structures with peptidic substrates showed that the acetyl-lysine is recognized by a central hydrophobic cavity and is anchored by a hydrogen bond with an asparagine residue present in most bromodomains⁵. The BET family (BRD2, BRD3, BRD4 and BRDT) shares a common domain architecture featuring two amino-terminal bromodomains that exhibit high levels of sequence conservation, and a more divergent carboxy-terminal recruitment domain (Supplementary Fig. 1)⁶.

Recent research has established a compelling rationale for targeting BRD4 in cancer. BRD4 remains bound to transcriptional start sites of genes expressed during the M/G1 transition, influencing mitotic progression⁴. BRD4 is also a critical mediator of transcriptional elongation,

functioning to recruit the positive transcription elongation factor complex (P-TEFb)^{7,8}. Cyclin-dependent kinase-9, a core component of P-TEFb^{9–11}, is a validated target in chronic lymphocytic leukaemia¹², and has recently been linked to c-Myc-dependent transcription¹³. Thus, BRD4 recruits P-TEFb to mitotic chromosomes resulting in increased expression of growth-promoting genes¹⁴.

Importantly, BRD4 has recently been identified as a component of a recurrent t(15;19) chromosomal translocation in an aggressive form of human squamous carcinoma^{15,16}. Such translocations express the tandem N-terminal bromodomains of BRD4 as an in-frame chimera with the NUT (nuclear protein in testis) protein, genetically defining the so-called NUT midline carcinoma (NMC). Functional studies in patient-derived NMC cell lines have validated the essential role of the BRD4–NUT oncoprotein in maintaining the characteristic proliferation advantage and differentiation block of this uniformly fatal malignancy¹⁷. Notably, RNA silencing of BRD4–NUT arrests proliferation and prompts terminal squamous differentiation. These observations underscore the broad utility and immediate therapeutic potential of a direct-acting inhibitor of human bromodomain proteins.

A selective and potent inhibitor of BET family bromodomains

A major collaborative focus of our research groups concerns the development of chemical probes^{18,19} and the optimization of therapeutic leads for the translation of small-molecule modulators of epigenetic targets as cancer therapeutics. Motivated by the above rationale, we have developed biochemical platforms for the identification of new inhibitors of bromodomain isoforms using high-throughput screening, as well as the annotation of putative ligands emerging from collaborative and published research. In the course of these studies, we learned of an

¹Department of Clinical Medicine, Structural Genomics Consortium, University of Oxford, Old Road Campus, Roosevelt Drive, Oxford OX3 7DQ, UK. ²Department of Medical Oncology, Dana-Farber Cancer Institute, Harvard Medical School, 44 Binney Street, Boston, Massachusetts 02115, USA. ³Walther Cancer Research Center and Department of Chemistry and Biochemistry, University of Notre Dame, Notre Dame, Indiana 46556, USA. ⁴Department of Pathology, Brigham & Women's Hospital, Harvard Medical School, 75 Francis Street, Boston, Massachusetts 02115, USA. ⁵Department of Clinical Pharmacology, University of Oxford, Old Road Campus, Roosevelt Drive, Oxford OX3 7DQ, UK. ⁶Department of Medicine, Harvard Medical School, 25 Shattuck Street, Boston, Massachusetts 02115, USA. ⁷Department of Imaging, Dana-Farber Cancer Institute, Harvard Medical School, 44 Binney Street, Boston, Massachusetts 02115, USA. ⁸Lurie Family Imaging Center, Dana-Farber Cancer Institute, Harvard Medical School, 44 Binney Street, Boston, Massachusetts 02115, USA. ⁹Department of Pediatric Oncology, Dana-Farber Cancer Institute and Children's Hospital, Boston, Harvard Medical School, 44 Binney Street, Boston, Massachusetts 02115, USA.

*These authors contributed equally to this work.

observation by Mitsubishi Pharmaceuticals that simple thienodiazepines possessed binding activity for BRD4 (ref. 20). Previous research from this group indicates that these compounds emerged from anti-inflammatory phenotypic studies, such as inhibition of CD28 co-stimulation as a means of treating autoimmune diseases^{21,22}. A rich literature has established the synthetic accessibility and favourable pharmacological properties of this privileged class of drug-like small molecules²³. Indeed, the core scaffold described appears in FDA-approved substances such as alprazolam and triazolam.

Inferring structure–activity relationships also derived from molecular modelling of candidate ligands within the binding pocket of the apo crystal structure of the first bromodomain of BRD4 (hereafter referred to as BRD4(1); Protein Data Bank code 2OSS), we designed a prototype ligand, JQ1 (Fig. 1a). JQ1 is a novel thieno-triazolo-1,4-diazepine, possessing an appended, bulky *t*-butyl ester functional group at C6 in order to (1) allow for additional pendant group diversity, as needed, and (2) to mitigate binding to the central benzodiazepine receptor as predicted by published structure–activity relationships²³. We first established a high-yielding, seven-step synthetic route to access racemic JQ1 (hereafter referred to as JQ1) and derivatives (scheme 1 in Supplementary

Methods). We have also identified a route to synthesize each enantiomer, (+)-JQ1 and (–)-JQ1 (scheme 2 in Supplementary Methods).

To establish a biochemical platform for comprehensive selectivity screening, all human bromodomains were subcloned into bacterial expression vectors. Testing of an average of 15 expression constructs per bromodomain resulted in the identification of 37 expression systems that yielded soluble protein suitable for specificity screening and covered all bromodomain subfamilies (Supplementary Table 1). Because the specific substrates of most bromodomains are unknown, a general binding assay based on differential scanning fluorimetry (DSF) was implemented²⁴. Binding of (+)-JQ1 significantly increased the thermal stability of all bromodomains of the BET family (Fig. 1b and Supplementary Table 2) with ΔT_m^{obs} values between 4.2 °C (BRDT(1)) and 10.1 °C (BRD4(1)). No significant stability shifts were detected for bromodomains outside the BET family, indicating that this ligand is highly selective. In contrast, the stereoisomer (–)-JQ1 showed no significant interaction with any bromodomain present in our panel.

Within a family of proteins a linear correlation between DSF ΔT_m^{obs} values and binding constants has been observed, with temperature shifts larger than 6 °C corresponding to compounds with nanomolar

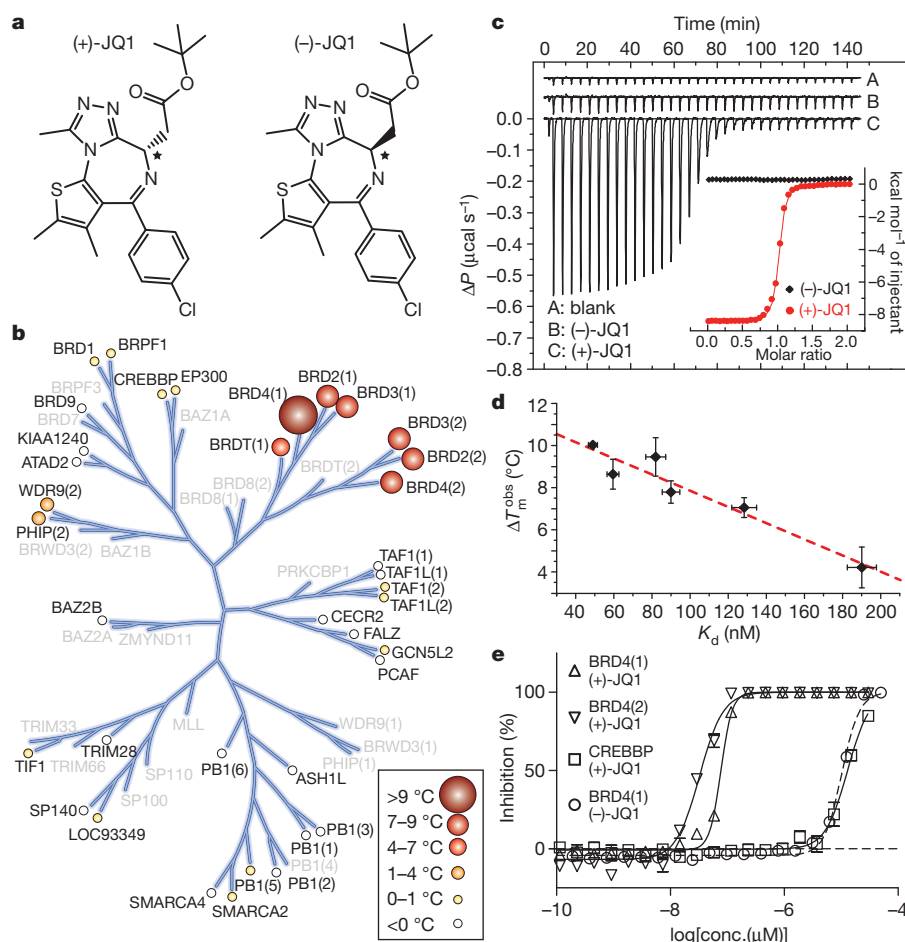


Figure 1 | Structure and selectivity of JQ1. **a**, Structure of the two JQ1 stereoisomers. The stereocenter at C6 is indicated by an asterisk. **b**, Assessment of inhibitor selectivity using differential scanning fluorimetry (DSF). Shown are averaged temperature shifts (ΔT_m^{obs}) in degrees Celsius upon binding of 10 μM (+)-JQ1. The temperature shifts are represented by spheres as indicated in the inset. Screened bromodomains are labelled and proteins not included in the selectivity panel are shown in grey. (–)-JQ1 did not reveal any significant temperature shifts to any of the screened bromodomains. **c**, Isothermal titration calorimetry (ITC). Differential power (ΔP) data time course of raw injection heats are shown for a blank titration of BRD4(1) into buffer (A), and reverse titrations using the inactive isomer (–)-JQ1 (B) and the active isomer (+)-JQ1 (C). The inset shows normalized binding enthalpies corrected for the heat of

dilution as a function of binding site saturation (symbols as indicated in the inset). Solid lines represent a nonlinear least squares fit using a single-site binding model. **d**, Thermal shifts (ΔT_m^{obs}) show good correlation to dissociation constants (K_d) determined by ITC for the BET bromodomains. The dotted red line represents a least squares fit with an R of 96%. The ΔT_m^{obs} data represent the mean \pm s.d. ($n = 3$). Error for ITC data was based on deviations to least squares fit described in **c**. **e**, Competitive displacement of a histone peptide from human bromodomains is exhibited by JQ1 using a bead-based proximity assay. Alpha-screen titrations monitoring the displacement of a tetra-acetylated histone H4 peptide by JQ1 isomers using the bromodomains BRD4(1), BRD4(2) or of an acetylated H3 peptide using CREBBP are shown.

dissociation constants (K_d)^{25,26}. Because the sensitivity of this assay may vary between different protein families, isothermal titration calorimetry (ITC) was used to determine binding constants precisely. Enantiomerically pure (+)-JQ1 bound with a K_d of about 50 nM and 90 nM to the first and second bromodomains of BRD4, respectively (Fig. 1c and Supplementary Table 3). Comparable binding to both domains of BRD3 was observed, whereas the first bromodomains of BRD2 and BRD2 revealed about threefold weaker binding. Affinities determined by ITC and ΔT_m^{obs} values showed very good correlation (Fig. 1d). Importantly, (+)-JQ1 showed no detectable binding to bromodomains that exhibited minimal temperature shifts, such as WDR9(2) and CREBBP.

To assess whether (+)-JQ1 binding was competitive with acetyllysine, we adapted a luminescence proximity homogeneous assay (alpha-screen)²⁷ to the BET bromodomains. Binding of a tetra-acetylated histone H4 peptide to BRD4 was strongly inhibited by (+)-JQ1, with half-maximum inhibitory concentration (IC_{50}) values of 77 nM and 33 nM for the first and second bromodomain, respectively (Fig. 1e). The IC_{50} for the (–)-JQ1 stereoisomer against BRD4(1) and for (+)-JQ1 against CREBBP were both estimated to be above 10,000 nM (Fig. 1e). Thus, (+)-JQ1 represents a potent, highly specific and Kac-competitive inhibitor for the BET family of bromodomains.

(+)-JQ1 binds to the Kac binding site of BET bromodomains

To establish the binding mode of JQ1 we determined co-crystal structures using racemic material and purified, recombinant BRD4(1) and BRD2(2) (for data collection and refinement statistics see Supplementary Table 4). The determined high-resolution structures revealed that only the (+)-JQ1 enantiomer bound directly into the Kac binding site (Figs 2 and 3a, b). Similar to interactions observed in acetyl-lysine complexes²⁸, the triazole ring formed a hydrogen bond with the evolutionarily conserved asparagine (Asn 140 in BRD4(1) and Asn 429 in

BRD2(2); Fig. 2a). The inhibitor showed an extraordinary shape complementarity with the Kac binding site, occupying the entire binding pocket (Fig. 2c, d). In both complexes, ligand binding was stabilized by hydrophobic interactions with conserved BET residues in the ZA- and BC-loop regions (Fig. 3a, b). Structural and sequence comparison showed high conservation of the BET Kac binding pocket, but revealed a number of differences in loop regions lining the binding cavity that could be explored for future development of isoform-specific inhibitors (Fig. 3a–c).

Docking of either isomer of JQ1 to BRD4(1) resulted in excellent fit of (+)-JQ1 in a position of perfect overlap to the crystallographically determined binding mode, whereas (–)-JQ1 resulted in an energetically unfavourable conformation with significant distortion of the diazepine ring system due to steric clashes with residues of the ZA-loop region (Fig. 3d). To explore the dynamic features of BET bromodomains, we carried out 20-ns molecular dynamics simulations of BRD4(1) in the absence and presence of (+)-JQ1. The simulations revealed little displacement of the protein helices, but the loop regions surrounding the acetyl-lysine binding site showed significant conformational

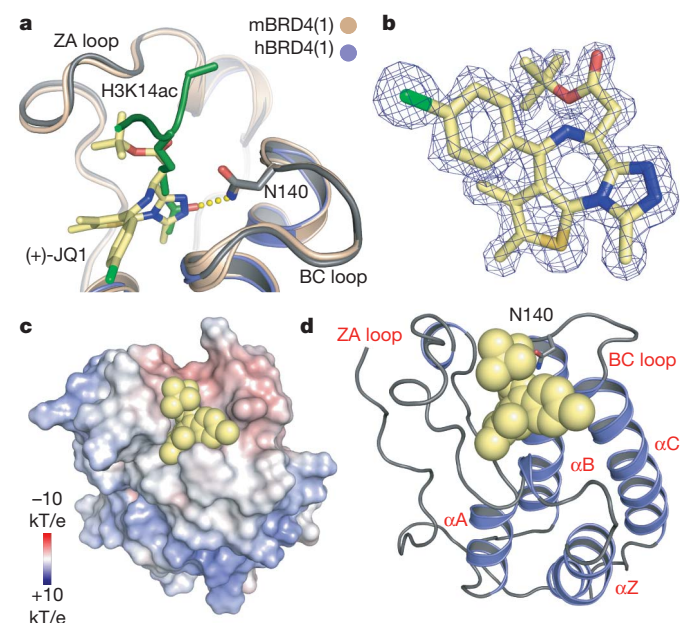


Figure 2 | Characterization of BET complexes with (+)-JQ1.

a, Superimposition of the mouse BRD4(1)–H3K14ac peptide complex²⁸ with the human BRD4(1)–(+)-JQ1 complex structure. The hydrogen bond formed to the conserved asparagine (N140) in the peptide complex is shown as yellow dots. **b**, $2F_o - F_c$ map of (+)-JQ1 in complex with BRD4(1) contoured at 2σ . **c**, Electrostatic surface of BRD4(1) in complex with (+)-JQ1. The ligand is shown as a Corey–Pauling–Koltun (CPK) model demonstrating the excellent shape complementarity with the protein acetylated lysine receptor site. **d**, Ribbon diagram of the complex of human BRD4(1) with (+)-JQ1 in CPK representation. The main secondary structural elements and the conserved active site asparagine side chain (N140) are labelled.

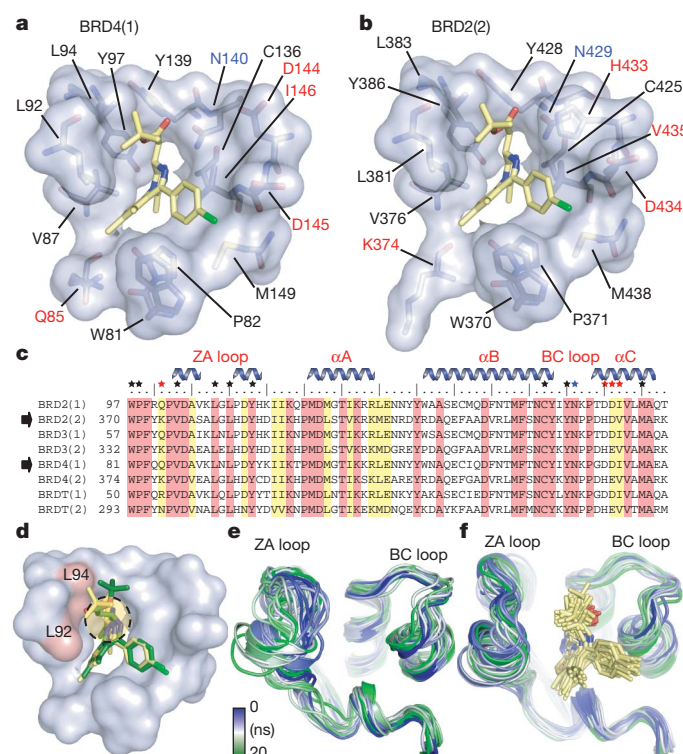


Figure 3 | Binding site comparison between N- and C-terminal bromodomains in complex with (+)-JQ1.

a, The acetyl-lysine binding pocket of BRD4(1) is shown as a semi-transparent surface with contact residues labelled and depicted in stick representation. Carbon atoms in (+)-JQ1 are coloured yellow to distinguish them from protein residues. Distinguishing surface residues are shown in red; the family conserved asparagine is shown in blue. **b**, The acetyl-lysine binding pocket of BRD2(2) is shown in identical representation and orientation as described in **a**. **c**, Protein sequence alignment of the human BET sub-family highlighting conserved (red) and similar (yellow) residues. Major bromodomain structural elements are shown. The side-chain contacts with (+)-JQ1 are annotated with a black star. Contacts which differ between the N- and C-terminal BET bromodomains (red star) are highlighted. The conserved asparagine is indicated by a blue star. **d**, Models of (+)-JQ1 (in yellow) and (–)-JQ1 (in green) docked into the BRD4(1) binding site. The steric clashes of the (–)-JQ1 stereoisomer with Leu 92 and Leu 94 are highlighted in red. **e**, Molecular dynamics simulation demonstrating the flexibility of the ZA and BC loops of the BRD4(1) apo-structure. Shown is the backbone of BRD4(1) during a 20-ns simulation as snapshots separated by 1-ns intervals. The different structures are distinguished by colours changing from blue to green as indicated in the inset. **f**, Molecular dynamics simulation of the BRD4(1)–(+)-JQ1 complex depicted in 1-ns snapshots as described in **e**.

flexibility. Furthermore, these loops were much more flexible in the absence (Fig. 3e) than in the presence (Fig. 3f) of the inhibitor, indicating that (+)-JQ1 stabilized the Kac binding cavity. In all cases, molecular dynamics simulation energies converged (Supplementary Fig. 2).

JQ1 displaces BRD4 from nuclear chromatin in cells

To establish whether JQ1 binds bromodomains competitively with chromatin in a cellular environment, we performed fluorescence recovery after photobleaching (FRAP) experiments. Previous research has demonstrated the utility of FRAP in assessing the pace of lateral redistribution of human bromodomains^{17,29}. Human osteosarcoma cells (U2OS) transfected with GFP-BRD4 show a time-dependent recovery of fluorescence intensity (Fig. 4a, b). In the presence of JQ1 (500 nM), the observed recovery is immediate, indicating displaced and freely diffusing nuclear BRD4 (Fig. 4a, b). Cellular FRAP studies confirmed that the effects on the mobile fraction of BRD4 are limited to the biochemically active (+)-JQ1 stereoisomer (Supplementary Fig. 3).

Having demonstrated potent, selective binding to BRD4 in homogeneous and cell-based assays, we became interested to explore the effects of JQ1 on disease-relevant phenotypes. Previous studies have established that the pathogenic BRD4-NUT fusion protein arising

from the t(15;19) translocation in NMC binds avidly to discrete foci of acetylated chromatin, conferring a proliferative advantage and differentiation block¹⁷. Using FRAP, we assessed the ability of JQ1 to target directly the BRD4-NUT oncoprotein. Compared to a vehicle control, JQ1 (500 nM) markedly accelerated time to half fluorescence recovery in photobleached regions of cells transfected with GFP-BRD4-NUT (Fig. 4c, d). Notably, no effect was observed on redistribution of GFP-NUT (Supplementary Fig. 3). These data are consistent with competitive binding of JQ1 to BRD4 in cultured cells.

JQ1 induces differentiation and growth arrest in NMC

Direct inhibition of gene products expressed from recurrent, oncogenic translocations is a validated therapeutic approach in cancer^{30,31}. We thus endeavoured to establish the consequences of competitive inhibition of BRD4-NUT in NMC. A characteristic feature of NMC is the appearance of discrete nuclear speckles of the BRD4-NUT oncoprotein by NUT-directed immunohistochemistry³². Treatment of the patient-derived 797 NMC cell line for 48 h with JQ1 (500 nM) effaces nuclear foci, producing diffuse nuclear NUT staining by immunohistochemistry (Supplementary Fig. 3e). In a dose- and time-dependent manner, JQ1 provokes a differentiation phenotype in NMC cell lines,

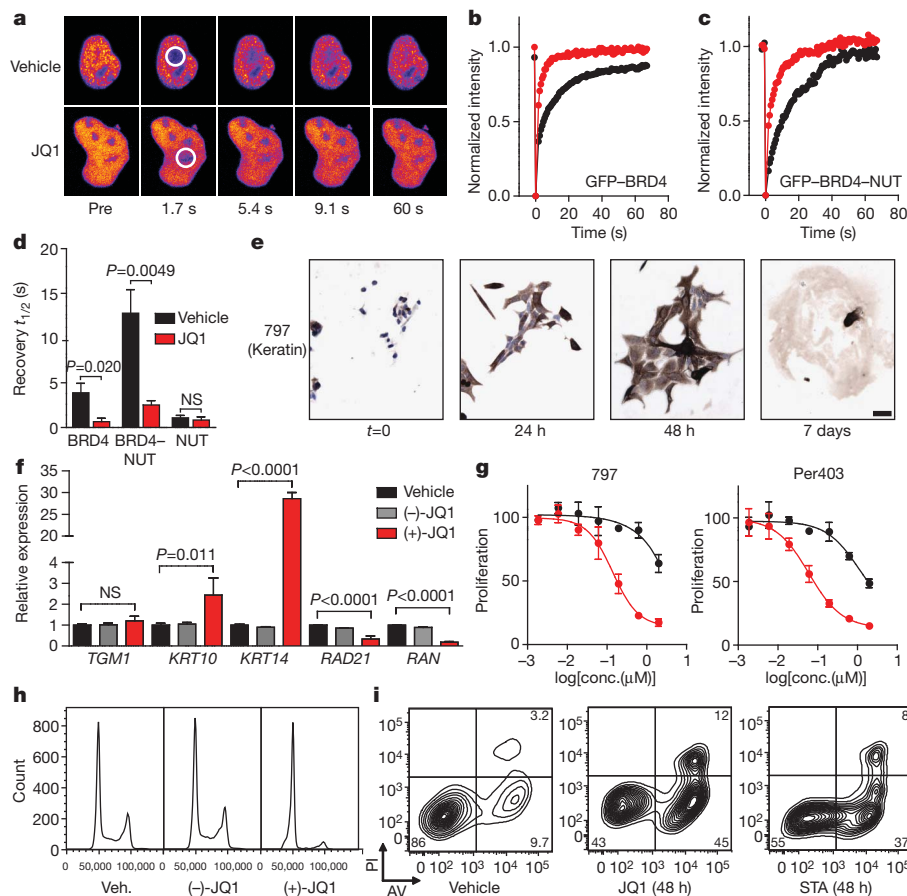


Figure 4 | JQ1 binds BRD4 competitively with chromatin resulting in differentiation and growth arrest of NMC cells. **a**, Fluorescence recovery after photobleaching (FRAP) of GFP-BRD4 demonstrates enhanced recovery in the presence of JQ1. Nuclei are false-coloured in proportion to fluorescence intensity. White circles indicate target regions of photobleaching. **b**, **c**, JQ1 accelerates fluorescence recovery in FRAP experiments performed with transfected GFP-BRD4 (**b**) and GFP-BRD4-NUT (**c**). **d**, Quantitative comparison of time to half-maximal fluorescence recovery for FRAP studies (**b**, **c**, Supplementary Fig. 3a). Data represent the mean \pm s.d. ($n = 5$), and are annotated with P -values as obtained from a two-tailed t -test. NS, not significant. **e**, Differentiation of NMC cells by JQ1 (500 nM) is prompt and characterized by a marked increase in cytokeratin expression (mouse anti-cytokeratin clone AE1/AE3; $\times 10$, scale bar is 50 μ m). **f**, Comparative gene

expression studies of (+)-JQ1 (red; 250 nM, 48 h) versus (-)-JQ1 (grey; 250 nM, 48 h) and vehicle (black) confirm squamous differentiation. Data represent the mean \pm s.d. ($n = 3$), and are annotated with P -values as obtained from a two-tailed t -test. **g**, Growth effects of BRD4 inhibition on BRD4-NUT-dependent cell lines. Cells were incubated with (+)-JQ1 (red circles) or (-)-JQ1 (black circles) and monitored for proliferation after 72 h. (+)-JQ1 uniquely attenuates proliferation by NMC cell lines. Data are presented as mean \pm s.d. ($n = 3$). Curve fit was calculated by logistical regression. **h**, Flow cytometry for DNA content in NMC 797 cells. (+)-JQ1 (250 nM, 48 h) induces a G1 arrest compared to (-)-JQ1 (250 nM) and vehicle control. Data are presented as a histogram of nuclear fluorescence intensity. **i**, Flow cytometric analysis of NMC 797 squamous carcinoma cells treated with vehicle, JQ1 or staurosporine (STA), as indicated. AV, annexin-V; PI, propidium iodide.

featuring cell spreading and flattening, open chromatin and striking spindle morphology (Fig. 4e and Supplementary Fig. 4). Differentiation is prompt (<24 h) and characterized by marked changes in cell shape accompanied by markedly augmented expression of cytokeratin, a hallmark of squamous differentiation (Fig. 4e). After 7 days in culture with submicromolar exposures to JQ1, terminal differentiation is observed. In this manner, JQ1 phenocopies the morphological changes and increased keratin expression observed with BRD4–NUT silencing by RNA interference (Supplementary Fig. 5)¹⁷. Corroborating these studies, expression analysis of three canonical squamous tissue genes by RT–PCR identified marked (30-fold) induction of keratin-14 by (+)-JQ1 in NMC 797 cells (Fig. 4f). The modest induction of keratin-10 without affecting epidermal transglutaminase (TGM1) may indicate differentiation towards thoracic squamous epithelium, consistent with the mediastinal primary tumour from which NMC 797 cells derive³³. Induction of differentiation with intense keratin staining is progressive over 72 h, as determined by quantitative immunohistochemistry analysis (Supplementary Fig. 6). Supporting an on-target mechanism-of-action, the (–)-JQ1 enantiomer is comparatively inactive in NMC, and a non-BRD4-dependent squamous carcinoma cell line (TE10) fails to exhibit differentiation effects of active JQ1 (Supplementary Fig. 4c).

In BRD4-dependent NMC cells, differentiation is expectedly accompanied by growth arrest, as demonstrated by reduced Ki67 staining (Supplementary Fig. 7), sustained inhibition of proliferation (Fig. 4g; Supplementary Fig. 8) and G1 cell-cycle arrest (Fig. 4h). To understand further the observed G1 arrest and to confirm an effect of JQ1 on known BRD4-dependent genes, we performed quantitative RT–PCR for *RAD21* and *RAN* (ref. 4). (+)-JQ1 potently decreased expression of both BRD4 target genes, whereas (–)-JQ1 had no effect (Fig. 4f). Early and late apoptosis were assessed with annexin-V and propidium iodide staining to ascertain whether the antiproliferative effect and irreversible differentiation was accompanied by cell death. Indeed, JQ1 induces immediate and progressive apoptosis in BRD4-dependent human carcinoma cells, without triggering significant growth arrest or cell death in cell lines lacking the BRD–NUT fusion (Supplementary Figs 8 and 9).

Antitumour efficacy of JQ1 in xenograft models of NMC

To determine whether JQ1 could attenuate the growth of BRD4-dependent carcinoma as a single agent *in vivo*, we developed three xenograft models of NMC in mice. First, short-term treatment studies were performed in NMC 797 xenografts with positron-emission tomography (PET) imaging of ¹⁸F-fluorodeoxyglucose (FDG) uptake as a primary endpoint to explore whether activity of JQ1 could be demonstrated by non-invasive imaging. Matched cohorts of mice with established tumours were randomized to treatment with JQ1 (50 mg kg^{–1}) or vehicle, administered by daily intraperitoneal injection. Before randomization, and after 4 days of therapy, mice were evaluated by FDG-PET imaging. A marked reduction in FDG uptake was observed with JQ1 treatment, whereas vehicle-treated mice demonstrated progressive disease (Fig. 5a). Tumour-volume measurements confirmed a reduction in tumour growth with JQ1 treatment (Fig. 5b and Supplementary Fig. 10). JQ1 was well tolerated at this dose and schedule without overt signs of toxicity or weight loss (Supplementary Fig. 10b).

To confirm that the antineoplastic effect observed with JQ1 treatment was associated with target engagement, sectioned tumour tissue was examined for the BRD4–NUT oncoprotein. As presented in Supplementary Fig. 11, JQ1 treatment resulted in effacement of NUT nuclear speckles, consistent with competitive binding to nuclear chromatin. Cell spreading and increased keratin expression confirmed induction of squamous differentiation (Fig. 5c). Decreased nuclear Ki67 and increased TUNEL staining in treated animals confirmed an ongoing antiproliferative, pro-apoptotic effect (Supplementary Fig. 11). To quantify the pharmacodynamic biomarker of tumour keratin expression, we established protocols for automated immunohistochemistry image acquisition

and analysis. Paired samples from treated and untreated animals were prepared and analysed using standardized protocols and commercially available software (ImageScope; Aperio Technologies), demonstrating that JQ1 induced strong (grade 3+) keratin expression in NMC 797 xenografts (Supplementary Fig. 12).

In parallel with these studies, we had occasion to care for a 29-year-old patient with widely metastatic BRD4–NUT-positive NMC arising from the mediastinum. With the goal of developing a more clinically relevant disease model, we established short-term cultures (11060 cells) using discarded clinical material obtained from pleural fluid draining from a palliative chest tube. As presented in Supplementary Fig. 13, *in vitro* studies confirmed the stereospecific, potent effect of (+)-JQ1 on cellular viability (IC₅₀ = 4 nM), growth and cell cycle progression. Four animals engrafted with patient-derived tumour material developed measurable disease, which was strongly FDG-avid by PET imaging (Fig. 5d). Animals were randomly assigned to vehicle or (+)-JQ1 treatment. Before treatment and after 4 days of therapy, mice were evaluated by PET imaging. A marked response in FDG uptake was observed with (+)-JQ1 treatment, whereas vehicle-treated animals demonstrated progressive disease (Fig. 5e). Tumour material prepared for quantitative immunohistochemistry analysis demonstrated induction of keratin expression after (+)-JQ1 treatment (Fig. 5f, g and Supplementary Fig. 14) in this minimally passaged NMC xenograft model.

To confirm the translational potential of direct-acting BRD4 inhibition in NMC, we further adapted the patient-derived 11060 cells to expansion *in vivo*, and performed definitive efficacy studies. Marked tumour regression and prolonged overall survival were observed, after only 18 days of well-tolerated therapy with (+)-JQ1 (Fig. 5h, i). These results were recapitulated in a third NMC xenograft model, using Per403 cells (Fig. 5j, k and Supplementary Fig. 15). Together, these data establish *in vivo* proof-of-concept for targeting BRD4 with JQ1 in NMC.

Discussion

Across the complex landscape of the cancer genome, recurrent chromosomal rearrangements comprise a compelling subset of clear, genetic targets in cancer. As evidenced by the successful development of first- and second-generation kinase inhibitors targeting BCR–ABL in chronic myelogenous leukaemia, well-characterized probe compounds^{34,35}, high-resolution crystallographic data³⁶, translational research studies³⁷, and informative murine models³⁸, where available, provide an optimal platform for ligand discovery and target validation. Herein, we provide comparable evidence supporting the BRD4–NUT fusion as a therapeutic target in an incurable, genetically-defined human squamous carcinoma, using a novel BRD4-directed small-molecule inhibitor.

Beyond NUT-midline carcinoma, BET-family bromodomains contribute to other neoplastic and non-neoplastic diseases. BRD4 targets the P-TEFb complex to mitotic chromosomes, resulting in the expression of growth-promoting genes such as *c-Myc*^{12,14} and the well-established cancer target Aurora B³⁹. BET family members have been recognized as essential genes for the replication of viruses^{40,41} and in mediating inflammatory responses⁴². Thus, the availability of (+)-JQ1 will prompt informative research broadly in developmental and disease biology. JQ1 possesses many desirable qualities of a chemical probe, such as high target potency in homogeneous and cellular assays, a well-characterized profile of selectivity, synthetic accessibility and herein proven utility in experimental biology^{18,19}. We have also found JQ1 to exhibit few off-target effects on cellular receptors and excellent pharmacokinetic properties including 49% oral bioavailability (Supplementary Figs 16 and 17 and Supplementary Table 5), establishing the plausibility of developing drug-like derivatives for therapeutic application.

The discovery and optimization of small-molecule inhibitors of epigenetic targets is a major focus of current biomedical research⁴³. We sought to meet the challenge of developing potent, selective inhibitors of epigenetic readers. Here we present a first, thoroughly characterized

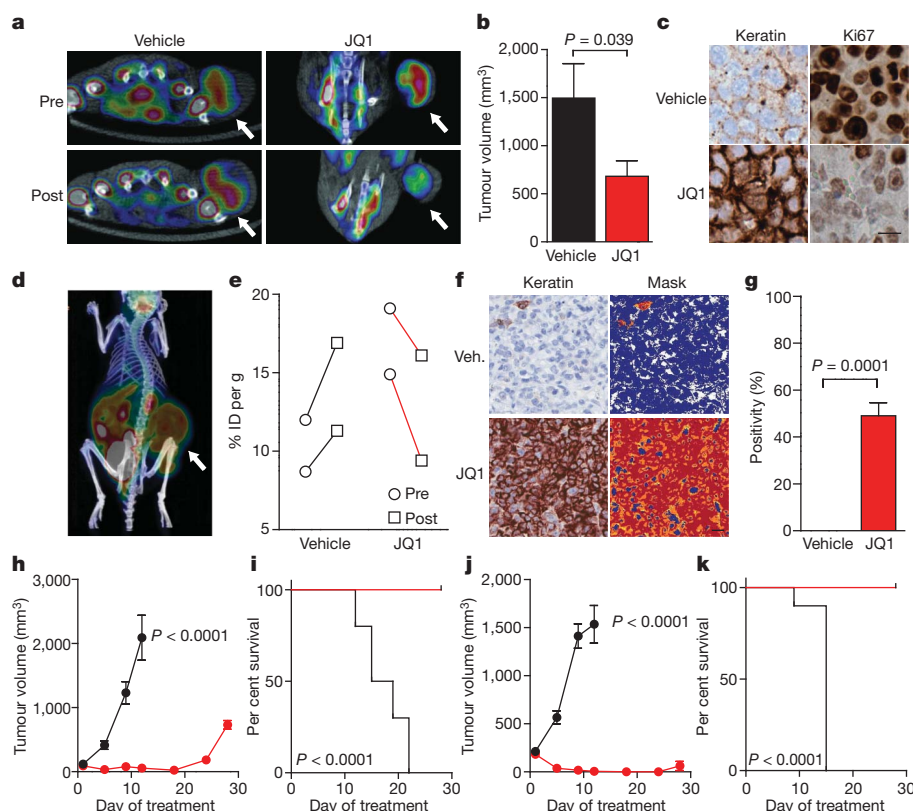


Figure 5 | JQ1 promotes differentiation, tumour regression and prolonged survival in murine models of NMC. **a**, PET imaging of murine NMC 797 xenografts. FDG uptake in xenograft tumours is reduced by 50 mg kg⁻¹ JQ1 treatment compared to vehicle control. Arrows indicate the anatomical location of tumour xenograft. **b**, Tumour volume is reduced in mice with established disease (NMC 797 xenografts) treated daily with 50 mg kg⁻¹ JQ1 compared to vehicle control. A significant response to therapy is observed by a two-tailed *t*-test at 14 days ($P = 0.039$). Data represent the mean \pm s.d. ($n = 7$). **c**, Histopathological analysis of NMC 797 tumours excised from animals treated with JQ1 reveals induction of keratin expression (mouse anti-cytokeratin clone AE1/AE3, $\times 40$) and impaired proliferation (Ki67, $\times 40$), as compared to vehicle-treated animals (scale bar is 20 μ m). **d**, Viability of patient-derived NMC 11060 xenografts was confirmed by PET imaging. Arrow indicates the anatomical location of tumour xenograft. **e**, Therapeutic response of primary 11060 NMC xenografts to (+)-JQ1 (50 mg kg⁻¹ daily for 4 days) was demonstrated by PET imaging. Integrated signal encompassed within the

tumour volume is presented as the per cent injected dose per gram (% ID per g). **f**, Histopathological analysis of primary NMC 11060 tumours excised from animals treated with (+)-JQ1 reveals induction of keratin expression (mouse anti-cytokeratin clone AE1/AE3, $\times 20$; scale bar is 20 μ m), compared to vehicle-treated animals. Quantitative analysis of keratin induction was performed using image masking (**f**, right panel) and pixel positivity analysis (**g**). A significant response to therapy is observed by a two-tailed *t*-test ($P = 0.0001$). Data represent the mean \pm s.d. of three independent wide microscopic fields. Comparative images of stained excised tumours and quantitative masks are provided in Supplementary Fig. 14. **h–k**, (+)-JQ1 (red circles and lines; 50 mg kg⁻¹ daily for 18 days) produces a decrease in tumour volume (**h**, **j**) and promotes prolonged survival (**i**, **k**) in patient-derived 11060 (**h**, **i**) and Per403 (**j**, **k**) NMC xenograft models ($n = 10$ in all groups). A significant response to therapy is observed for tumour volume by a two-tailed *t*-test ($P < 0.0001$) and for overall survival by a log-rank test ($P < 0.0001$). Black circles and lines, vehicle.

inhibitor of the BET-family of bromodomains. The approach outlined herein further establishes the feasibility of abrogating protein–protein interactions with small molecules, and targeting additional epigenetic readers for ligand discovery.

METHODS SUMMARY

The inhibitor JQ1 was synthesized in both racemic and enantiomerically pure format using the synthetic route outlined in scheme 1 and scheme 2 (Supplementary Methods) and its structure was fully characterized. Human bromodomains were expressed in bacteria as His-tagged proteins and were purified by nickel-affinity and gel-filtration chromatography. Protein integrity was assessed by SDS-PAGE and electro-spray mass spectrometry on an Agilent 1100 Series LC/MSD TOF. All crystallizations were carried out at 4 °C using the sitting-drop vapour-diffusion method. X-ray diffraction data were collected at the Swiss Light source beamline X10SA, or using a Rigaku FR-E generator. Structures were determined by molecular replacement. Isothermal titration calorimetry experiments were performed at 15 °C on a VP-ITC titration microcalorimeter (MicroCal). Thermal melting experiments were carried out on an Mx3005p RT-PCR machine (Stratagene) using SYPRO Orange as a fluorescence probe. Dose-ranging small-molecule studies of proliferation were performed in white, 384-well plates (Corning) in DMEM media containing 10% FBS. Compounds

were delivered with a JANUS pin-transfer robot and proliferation measurements were made on an Envision multilabel plate-reader (PerkinElmer). Murine xenografts were established by injecting NMC cells in 30% Matrigel (BD Biosciences) into the flank of 6-week-old female NCr nude mice (Charles River Laboratories). Tumour measurements were assessed by caliper measurements, and volume was calculated using the formula $Vol = 0.5 \times L \times W^2$. All mice were humanely killed, and tumours were fixed in 10% formalin for histopathological examination. Quantitative immunohistochemistry was performed using the Aperio Digital Pathology Environment (Aperio Technologies) at the DF/HCC Core Laboratory at the Brigham and Women's Hospital.

Received 5 May; accepted 17 September 2010.

Published online 24 September 2010.

1. Ptashne, M. Binding reactions: epigenetic switches, signal transduction and cancer. *Curr. Biol.* **19**, R234–R241 (2009).
2. Schreiber, S. L. & Bernstein, B. E. Signaling network model of chromatin. *Cell* **111**, 771–778 (2002).
3. Marushige, K. Activation of chromatin by acetylation of histone side chains. *Proc. Natl Acad. Sci. USA* **73**, 3937–3941 (1976).
4. Dey, A., Nishiyama, A., Karpova, T., McNally, J. & Ozato, K. Brd4 marks select genes on mitotic chromatin and directs postmitotic transcription. *Mol. Biol. Cell* **20**, 4899–4909 (2009).

5. Owen, D. J. *et al.* The structural basis for the recognition of acetylated histone H4 by the bromodomain of histone acetyltransferase gcn5p. *EMBO J.* **19**, 6141–6149 (2000).
6. Zeng, L. & Zhou, M. M. Bromodomain: an acetyl-lysine binding domain. *FEBS Lett.* **513**, 124–128 (2002).
7. Yang, X. J. Multisite protein modification and intramolecular signaling. *Oncogene* **24**, 1653–1662 (2005).
8. Yang, Z. *et al.* Recruitment of P-TEFb for stimulation of transcriptional elongation by the bromodomain protein Brd4. *Mol. Cell* **19**, 535–545 (2005).
9. Peng, J., Zhu, Y., Milton, J. T. & Price, D. H. Identification of multiple cyclin subunits of human P-TEFb. *Genes Dev.* **12**, 755–762 (1998).
10. Marshall, N. F. & Price, D. H. Purification of P-TEFb, a transcription factor required for the transition into productive elongation. *J. Biol. Chem.* **270**, 12335–12338 (1995).
11. Marshall, N. F., Peng, J., Xie, Z. & Price, D. H. Control of RNA polymerase II elongation potential by a novel carboxyl-terminal domain kinase. *J. Biol. Chem.* **271**, 27176–27183 (1996).
12. Phelps, M. A. *et al.* Clinical response and pharmacokinetics from a phase 1 study of an active dosing schedule of flavopiridol in relapsed chronic lymphocytic leukemia. *Blood* **113**, 2637–2645 (2009).
13. Rahl, P. B. *et al.* c-Myc regulates transcriptional pause release. *Cell* **141**, 432–445 (2010).
14. Yang, Z., He, N. & Zhou, Q. Brd4 recruits P-TEFb to chromosomes at late mitosis to promote G1 gene expression and cell cycle progression. *Mol. Cell. Biol.* **28**, 967–976 (2008).
15. French, C. A. *et al.* BRD4 bromodomain gene rearrangement in aggressive carcinoma with translocation t(15;19). *Am. J. Pathol.* **159**, 1987–1992 (2001).
16. French, C. A. *et al.* BRD4-NUT fusion oncogene: a novel mechanism in aggressive carcinoma. *Cancer Res.* **63**, 304–307 (2003).
17. French, C. A. *et al.* BRD-NUT oncoproteins: a family of closely related nuclear proteins that block epithelial differentiation and maintain the growth of carcinoma cells. *Oncogene* **27**, 2237–2242 (2008).
18. Frye, S. V. The art of the chemical probe. *Nature Chem. Biol.* **6**, 159–161 (2010).
19. Oprea, T. I. *et al.* A crowdsourcing evaluation of the NIH chemical probes. *Nature Chem. Biol.* **5**, 441–447 (2009).
20. Miyoshi, S., Ooike, S., Iwata, K., Hikawa, H. & Sugarah, K. Antitumor agent. International Patent No. PCT/JP2008/073864 (WO/2009/084693) (2009).
21. Adachi, K. *et al.* Thienotriazolodiazepine compound and a medicinal use thereof. International Patent No. PCT/JP2006/310709 (WO/2006/129623) (2006).
22. Sueoka, H., Komatsu, H., Kobayashi, H. & Ehara, S. *Thienotriazolodiazepine Compounds and Medicinal Uses Thereof* 1–50 (Yoshitomi Pharmaceutical Industries, Ltd, 1998).
23. VonVoigtlander, P. F. & Straw, R. N. Alprazolam: Review of pharmacological, pharmacokinetic and clinical data. *Drug Dev. Res.* **6**, 1–12 (1985).
24. Niesen, F. H., Berglund, H. & Vedadi, M. The use of differential scanning fluorimetry to detect ligand interactions that promote protein stability. *Nature Protocols* **2**, 2212–2221 (2007).
25. Fedorov, O. *et al.* A systematic interaction map of validated kinase inhibitors with Ser/Thr kinases. *Proc. Natl Acad. Sci. USA* **104**, 20523–20528 (2007).
26. Bullock, A. N. *et al.* Structural basis of inhibitor specificity of the human protooncogene proviral insertion site in moloney murine leukemia virus (PIM-1) kinase. *J. Med. Chem.* **48**, 7604–7614 (2005).
27. Quinn, A. M. *et al.* A homogeneous method for investigation of methylation-dependent protein-protein interactions in epigenetics. *Nucleic Acids Res.* **38**, e11 (2010).
28. Vollmuth, F., Blankenfeldt, W. & Geyer, M. Structures of the dual bromodomains of the P-TEFb-activating protein Brd4 at atomic resolution. *J. Biol. Chem.* **284**, 36547–36556 (2009).
29. Dey, A. *et al.* A bromodomain protein, MCAP, associates with mitotic chromosomes and affects G₂-to-M transition. *Mol. Cell. Biol.* **20**, 6537–6549 (2000).
30. Huang, M. E. *et al.* Use of all-trans retinoic acid in the treatment of acute promyelocytic leukemia. *Blood* **72**, 567–572 (1988).
31. Druker, B. J. *et al.* Efficacy and safety of a specific inhibitor of the BCR-ABL tyrosine kinase in chronic myeloid leukemia. *N. Engl. J. Med.* **344**, 1031–1037 (2001).
32. Haack, H. *et al.* Diagnosis of NUT midline carcinoma using a NUT-specific monoclonal antibody. *Am. J. Surg. Pathol.* **33**, 984–991 (2009).
33. Toretsky, J. A. *et al.* Translocation (11;15;19): a highly specific chromosome rearrangement associated with poorly differentiated thymic carcinoma in young patients. *Am. J. Clin. Oncol.* **26**, 300–306 (2003).
34. Buchdunger, E. *et al.* Selective inhibition of the platelet-derived growth factor signal transduction pathway by a protein-tyrosine kinase inhibitor of the 2-phenylaminopyrimidine class. *Proc. Natl Acad. Sci. USA* **92**, 2558–2562 (1995).
35. Buchdunger, E. *et al.* Inhibition of the Abl protein-tyrosine kinase *in vitro* and *in vivo* by a 2-phenylaminopyrimidine derivative. *Cancer Res.* **56**, 100–104 (1996).
36. Schindler, T. *et al.* Structural mechanism for STI-571 inhibition of abelson tyrosine kinase. *Science* **289**, 1938–1942 (2000).
37. Druker, B. J. *et al.* Effects of a selective inhibitor of the Abl tyrosine kinase on the growth of Bcr-Abl positive cells. *Nature Med.* **2**, 561–566 (1996).
38. le Coutre, P. *et al.* *In vivo* eradication of human BCR/ABL-positive leukemia cells with an ABL kinase inhibitor. *J. Natl Cancer Inst.* **91**, 163–168 (1999).
39. You, J. *et al.* Regulation of aurora B expression by the bromodomain protein Brd4. *Mol. Cell. Biol.* **29**, 5094–5103 (2009).
40. You, J. *et al.* Kaposi's sarcoma-associated herpesvirus latency-associated nuclear antigen interacts with bromodomain protein Brd4 on host mitotic chromosomes. *J. Virol.* **80**, 8909–8919 (2006).
41. Abbate, E. A., Voitenleitner, C. & Botchan, M. R. Structure of the papillomavirus DNA-tethering complex E2:Brd4 and a peptide that ablates HPV chromosomal association. *Mol. Cell* **24**, 877–889 (2006).
42. Huang, B., Yang, X. D., Zhou, M. M., Ozato, K. & Chen, L. F. Brd4 coactivates transcriptional activation of NF- κ B via specific binding to acetylated RelA. *Mol. Cell. Biol.* **29**, 1375–1387 (2009).
43. Cole, P. A. Chemical probes for histone-modifying enzymes. *Nature Chem. Biol.* **4**, 590–597 (2008).

Supplementary Information is linked to the online version of the paper at www.nature.com/nature.

Acknowledgements We are grateful to U. Oppermann, S. Müller, S. Sallan, C. Lathan, P. Rahl, R. Young, K. Lee and K. Shaw for discussions and sharing unpublished information; K. Agu, S. Johnston and L. Li for analytical chemistry support; J. Daley for flow cytometry support; T. Bowman, T. Caron, C. Marvin and S. Rodig for immunohistochemistry; and A. Bass for sharing cell lines. The Structural Genomics Consortium is a registered charity (number 1097737) that receives funds from the Canadian Institutes for Health Research, the Canadian Foundation for Innovation, Genome Canada through the Ontario Genomics Institute, GlaxoSmithKline, Karolinska Institutet, the Knut and Alice Wallenberg Foundation, the Ontario Innovation Trust, the Ontario Ministry for Research and Innovation, Merck & Co., Inc., the Novartis Research Foundation, the Swedish Agency for Innovation Systems, the Swedish Foundation for Strategic Research and the Wellcome Trust. This research was supported by a Graduate Fellowship from the Chemistry-Biochemistry-Biology Interface Program at the University of Notre Dame, NIGMS T32-075762 (to Y.S.), the DF/HCC (to C.A.F. and J.E.B.), the National Institutes of Health, the Burroughs Wellcome Fund, and the Leukemia & Lymphoma Society (to J.E.B.).

Author Contributions P.F., J.Q., S.K. and J.E.B. designed the study, analysed data and wrote the manuscript. P.F. and S.P. performed and analysed biophysical studies. J.Q. and J.E.B. designed JQ1 and established the synthetic routes. Y.S. and O.W. completed docking and molecular dynamics studies. O.F. performed and analysed DSF. S.M. and N.L.T. contributed biochemical assays. M.R.M., M.P. and T.D.H. performed and analysed alpha-screen assays. W.B.S., M.J.C. and J.E.B. performed *in vitro* NMC studies and immunohistochemistry. E.M.M. performed flow cytometry studies. E.M.M. and N.W. performed proliferation studies. T.T.H., M.J.C., C.A.F. and J.E.B. completed FRAP studies. M.R.M. and B.S. performed expression analysis. Y.W., A.L.C. and A.L.K. completed *in vivo* efficacy studies. T.K. and I.F. expressed and purified proteins. S.K. and J.E.B. supervised the research.

Author Information Atomic coordinates and structure factors for the reported crystal structures have been deposited with the Protein Data Bank under accession codes 2OSS (BRD4(1)), 3MXF (BRD4(1)-(+)JQ1) and 3ONI (BRD2(2)-(+)JQ1). Reprints and permissions information is available at www.nature.com/reprints. The authors declare no competing financial interests. Readers are welcome to comment on the online version of this article at www.nature.com/nature. Correspondence and requests for materials should be addressed to S.K. (stefan.knapp@sgc.ox.ac.uk) or J.E.B. (james_bradner@dfci.harvard.edu).

Driving the cell cycle with a minimal CDK control network

Damien Coudreuse¹ & Paul Nurse¹

Control of eukaryotic cell proliferation involves an extended regulatory network, the complexity of which has made it difficult to understand the basic principles of the cell cycle. To investigate the core engine of the mitotic cycle we have generated a minimal control network in fission yeast that efficiently sustains cellular reproduction. Here we demonstrate that orderly progression through the major events of the cell cycle can be driven by oscillation of an engineered monomolecular cyclin-dependent protein kinase (CDK) module lacking much of the canonical regulation. We show further that the CDK oscillator acts as the primary organizer of the cell cycle, imposing timing and directionality to a system of two CDK activity thresholds that define independent cell cycle phases. We propose that this simple core architecture forms the basic control of the eukaryotic cell cycle.

Progression through the eukaryotic cell cycle is driven by CDKs, which form bipartite complexes with different cyclins¹. Changes in activity of these complexes depend on oscillations in levels of the cyclins, the synthesis and degradation of which are regulated throughout the cell cycle, while combinatorial associations of CDKs and cyclins are thought to generate the distinct substrate specificities required to bring about the different cell cycle transitions^{2,3}. Control of the respective expression and subcellular localization of central CDK machinery subunits constitutes a primary layer of cell cycle regulation⁴. In addition, CDK activity is modulated by specific inhibitors and by changes in phosphorylation of the catalytic subunit in response to inputs such as nutrient availability, cell size, and activation of checkpoint mechanisms¹. Some of these controls form feedback loops that generate sharp changes in activity with hysteretic properties, contributing to the unidirectionality of the cell cycle^{5–9}. Integration of all these parameters ensures orderly progression through the mitotic cycle and appropriate responses to perturbations.

The complexity of eukaryotic cell cycle control has made it difficult to fully understand its basic principles, as demonstrated by the plasticity reported for certain key cell cycle effectors^{10–13}. To investigate the core engine of the mitotic cycle, we have generated a minimal control network in the fission yeast *Schizosaccharomyces pombe*. We show that oscillation of a single monomolecular CDK module in the absence of many of the known regulatory inputs and feedbacks is sufficient to sequentially trigger the major cell cycle events. We demonstrate further that the core cycle can be built on a circuit of two CDK activity thresholds defining independent states with no inherent directionality, upon which sequence and timing are imposed by a single CDK oscillator.

A minimal cell cycle in fission yeast

The fission yeast cell cycle is controlled by a single CDK, Cdc2, required for both the G1/S and G2/M transitions^{14,15}. DNA replication and mitosis are triggered by association of Cdc2 with the B-type cyclins Cig2 and Cdc13^{16–20}, respectively, with two additional cyclins, Cig1 and Puc1, having more minor roles in G1^{17,21–25}. In addition, Cdc13/Cdc2 activity in G2 blocks reinitiation of DNA replication^{26,27}.

To simplify the cell cycle control machinery, a cassette expressing a fusion of *cdc13* and *cdc2* under the control of the *cdc13* regulatory

elements was integrated into the genome (*cdc13-L-cdc2*; Fig. 1a). This minimal CDK system differs from that operative in wild-type cells in several ways: (1) the regulatory and catalytic subunits are subject to the same transcriptional, translational and degradation programs, are always present in a 1:1 ratio, and always co-localize; (2) the rise in CDK activity is not triggered by a separate cyclin concentration threshold; (3) fusing the kinase with a specific cyclin is likely to prevent association with other cyclins and renders modulators of binding between the two subunits irrelevant. The fusion protein was active and additive to the function of the endogenous CDK machinery (Supplementary Fig. 1). We next deleted the genomic copies of *cdc2*

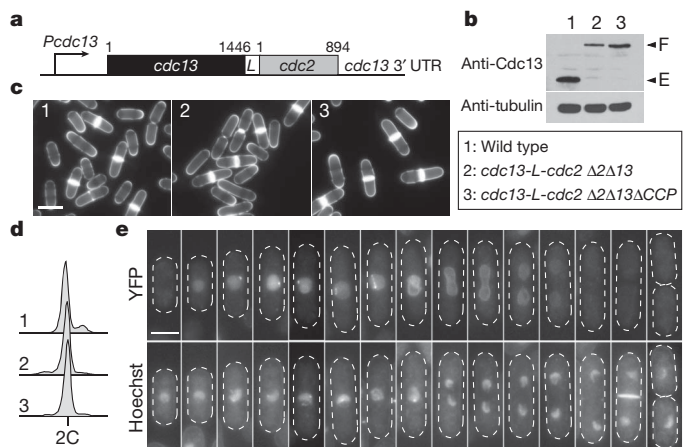


Figure 1 | A Cdc13-L-Cdc2 fusion in fission yeast. **a**, Schematic representation of the *cdc13-L-cdc2* fusion. Numbers are open reading frame coordinates. *L*, linker. *Pcdc13*, *cdc13* promoter and 5' untranslated region (UTR). **b–d**, Labels are indicated in box. **b**, Western blots probed for Cdc13 and tubulin. **c**, Blankophor staining of exponentially growing cells. Scale bar, 10 μ m. **d**, DNA content analysis of cells in **c** (see Methods). **e**, Exponentially growing *cdc13-L-cdc2-YFP Δ2Δ13ΔCCP* cells at 25 °C. YFP and DNA imaging (Hoechst) of individual cells arranged according to their cell cycle stage. Dashed lines show cell outlines. Scale bar, 5 μ m.

¹Laboratory of Yeast Genetics and Cell Biology, The Rockefeller University, 1230 York Avenue, New York, New York 10065, USA.

and *cdc13* ($\Delta 2A13$). In this background, Cdc13-L-Cdc2 was detected as a single full-length protein (Fig. 1b) and *cdc13-L-cdc2* $\Delta 2A13$ cells were almost identical to wild type, having a normal generation time and only a small increase in cell length at division (Fig. 1c and Table 1). DNA content analysis showed the same profile as wild type (Fig. 1d and Methods), indicating that the relative durations of the different cell cycle phases were maintained.

To demonstrate that this minimal machinery autonomously drives cell cycle progression, two alterations were introduced within the fusion protein (Supplementary Fig. 2a): (1) Cdc13(C379Y) (here referred to as Cdc13_{ts}), generating a temperature-sensitive protein¹⁴; and (2) Cdc2(F84G) (here referred to as Cdc2_{as}; as, analogue sensitive), rendering the kinase sensitive to chemical inhibition^{28,29}. Treatment with inhibitor (ATP analogue NmPP1) or shift to restrictive temperature arrested *cdc13_{ts}-L-cdc2_{as}* $\Delta 2A13$ cells in G2 (Supplementary Fig. 2b). Next, we additionally deleted *cig2*, which encodes the major S-phase cyclin. Absence of Cig2 had no effect on the timing of DNA replication (Supplementary Fig. 3a), but impairing function of either moiety of the fusion protein in G1 cells delayed S-phase onset (Supplementary Fig. 3b–e). These data show that both kinase and cyclin moieties of the CDK module are required to trigger the G1/S and G2/M transitions.

The fission yeast genome contains 13 cyclin-like genes. Protein sequence comparisons showed that Cig1, Cig2 and Puc1, the only other cyclins known to have mitotic cell cycle functions in complexes with Cdc2, were the only mitotic cyclins that clustered with Cdc13 (Supplementary Fig. 4). To simplify the network further, we therefore deleted *cig1*, *cig2* and *puc1* (ΔCCP) in *cdc13-L-cdc2* $\Delta 2A13$ cells. This strain had no apparent cell cycle defects (Fig. 1b–d and Table 1). In this background, the CDK module oscillated in abundance, peaking at the end of G2 and disappearing at mitotic exit, and recapitulated the normal cell cycle changes in Cdc13 subcellular localization³⁰ (Fig. 1e and Supplementary Fig. 5).

These results demonstrate that a single monomolecular CDK module lacking several regulatory features of the endogenous machinery is sufficient to trigger the two major cell cycle transitions and sustains an effective mitotic cycle. Other endogenous cyclin/CDK complexes that may have more peripheral roles in cell cycle regulation, including Mcs2/Mcs3³¹ and Pas1/Pef1³², cannot substitute for the CDK fusion and so do not have direct roles in driving the onsets of S and M phases.

Oscillations in CDK activity

Next we investigated how a single CDK module distinguishes between G1/S and G2/M. Using *cdc13-L-cdc2_{as}* $\Delta 2A13$ ΔCCP cells (Table 1 and Supplementary Fig. 6), we asked whether progression through S and M in the absence of much of the canonical regulation is primarily mediated by distinct thresholds of a single CDK activity.

First, different inhibitor concentrations were added to synchronized cells in early G2. Timing of mitosis was delayed in a dose-dependent manner, with concentrations of 300 nM and above preventing mitosis

(Fig. 2a and Supplementary Fig. 7a–d). Cells delayed in G2 elongated and accumulated the fusion protein (Supplementary Fig. 8a, b). We surmised that a critical ratio of CDK module to inhibitor concentration must be reached to allow mitotic onset. Consistent with this, a population of large cells incubated with inhibitor in early G2 entered mitosis earlier than similarly treated small cells, but at the same size (Supplementary Fig. 8c–g). Moreover, cells of asynchronous cultures treated for 8 h with different NmPP1 concentrations had longer sizes at division, proportional to the amount of inhibitor (Supplementary Fig. 7e).

Second, entry into S phase was monitored when synchronized cells were exposed to inhibitor in G1 (Supplementary Fig. 9a). None of the concentrations that affected G2/M had any effect on S phase (data not shown), even though G1 cells have lower levels of fusion protein (Supplementary Fig. 5). However, a dose-dependent delay in S-phase onset was observed when 1–5 μ M NmPP1 was used (Fig. 2b and Supplementary Fig. 9b–e). The difference in inhibitor concentration required to delay G1/S and G2/M supports the view that these transitions are associated with low and high kinase activities, respectively.

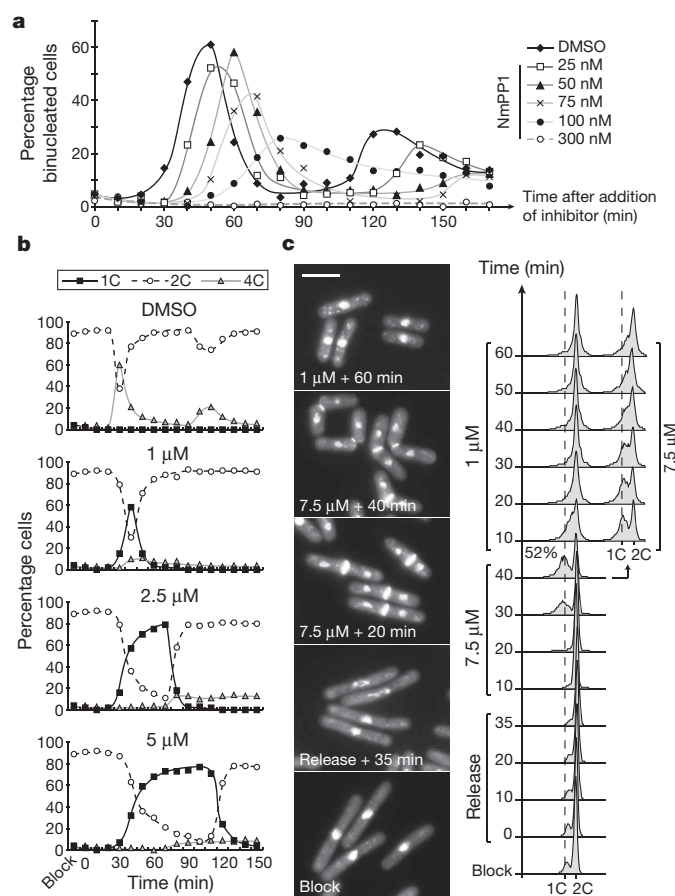


Figure 2 | Oscillation of a single CDK activity between two thresholds.

a, Percentage of binucleated cells (includes septated cells; $n = 400$) in synchronized *cdc13-L-cdc2_{as}* $\Delta 2A13$ ΔCCP cultures incubated with NmPP1 (added in early G2; $T = 0$ in Supplementary Fig. 7a). Concentrations above 300 nM also prevented mitosis (data not shown). **b**, DNA content analysis of synchronized *cdc13-L-cdc2_{as}* $\Delta 2A13$ ΔCCP cells treated with NmPP1 after mitotic onset ($T = 0$ in Supplementary Fig. 9a; flow cytometry profiles are in Supplementary Fig. 9c). Inhibitor-treated cells arrested in the next G2 and became elongated (data not shown). Block: 1 μ M NmPP1 for 2 h 45 min at 32 °C. **c**, Inhibitor-mediated oscillation in activity using *cdc13 Δ DB-L-cdc2_{as}* *cdc2-33_{ts}* $\Delta cig2$ cells (see Supplementary Figs 10 and 11 for protocol and description of the entire experiment). DAPI/Blankophor staining (left panel) and DNA content analysis (right panel) at representative times during the first artificial cycle. Scale bar, 10 μ m. The percentage of cells with a 1C DNA content after 40 min in 7.5 μ M NmPP1 is indicated.

Table 1 | Characterization of cells operating with the minimal CDK module

| Genotype | Size at division (μ m) | Generation time (min) | Dead cells (%) |
|---|-----------------------------|-----------------------|----------------|
| Wild type | 14 \pm 0.1 | 160 \pm 3 | 1.3 \pm 0.8 |
| <i>cdc13-L-cdc2</i> $\Delta 2A13$ | 15.6 \pm 0.3 | 163 \pm 2 | ND |
| <i>cdc13-L-cdc2</i> $\Delta 2A13$ ΔCCP | 15.9 \pm 0.2 | 162 \pm 6 | 0.2 \pm 0.2 |
| <i>cdc13-L-cdc2_{as}</i> $\Delta 2A13$ ΔCCP | 14.7 \pm 0.2 | 158 \pm 6 | ND |
| <i>cdc13-L-cdc2</i> $\Delta 2A13$ ΔCCP <i>Arum1</i> * | 15.9 \pm 0.1 | 155 \pm 3 | ND |
| <i>cdc13-L-cdc2AF</i> $\Delta 2A13$ ΔCCP * | 13.9 \pm 0.2 | 248 \pm 0 | 5.3 \pm 0.9 |
| <i>cdc13-L-cdc2</i> $\Delta 2A13$ ΔCCP <i>Awee1</i> | 13.7 \pm 0 | 217 \pm 0 | 6.2 \pm 1.3 |
| <i>Amik1</i> | | | |
| <i>wee1-50_{ts}</i> † | 6.9 \pm 0.1 | ND | ND |

Numbers are averages of three independent experiments with standard errors ($n \geq 50$ for cell size determination and ≥ 400 for dead cells). ND, not determined.

* Similar sizes were obtained using NmPP1 sensitive strains.

† Cell size at division was measured after 6 h at restrictive temperature (36 °C).

These data indicate that oscillation of qualitatively the same CDK activity between two thresholds may be the sole requirement to drive the minimal cell cycle. This interpretation predicts that substituting the oscillation in protein levels with an inhibitor-mediated oscillation in activity using a constantly present and non-degradable form of the CDK module should be sufficient to artificially drive the entire cycle. To test this, we deleted the Cdc13 destruction box within the fusion protein (*cdc13 Δ DB-L-cdc2_{as}*) and drove its expression by the inducible *urg1* regulatory elements³³ (Fig. 2c and Supplementary Figs 10 and 11). *cdc13 Δ DB-L-cdc2_{as} cdc2-33_{ts} Δ cig2* cells (see Methods) maintained at restrictive temperature entered mitosis when expression of the fusion cassette was induced. Impaired degradation of the protein prevented mitotic exit, but addition of 7.5 μ M NmPP1 allowed completion of mitosis and cytokinesis with cells arresting in G1. Subsequent reduction to 1 μ M inhibitor resulted in rapid DNA replication. Finally, another cycle of inhibitor oscillation allowed cells to proceed through the next mitosis.

These results show that artificial modulation of the activity of a single stable CDK module enables progression through S and M, supporting the idea of a quantitative CDK model of the cell cycle^{10,34,35}. We propose that changes in protein levels and cyclin/CDK ratios are not essential to cell cycle regulation and that a simple oscillation in activity generated by a minimal control system is sufficient to drive the mitotic cycle.

Resetting the cell cycle

Next we asked whether the oscillator itself constitutes the primary system that sets the order and separation of cell cycle events. CDK activity was manipulated in *cdc13-L-cdc2_{as} Δ 2113 Δ CCP* cells to determine if this alone could change cell cycle architecture.

First, G2-arrested cells were released into medium with varying concentrations of inhibitor (Fig. 3a and Supplementary Fig. 12a–d). Cells released in dimethylsulphoxide (DMSO) resumed cycling, whereas 1 or 2.5 μ M NmPP1 maintained the G2 block (data not shown). In contrast, treatments with 5 μ M NmPP1 and more led to replication without an intervening mitosis, after delays reflecting the concentrations of inhibitor used and with increased amounts of fusion protein. These data demonstrate that when CDK activity is reduced to a low level, G2 cells bypass mitosis and enter a G1/S-like program. This is consistent with earlier studies showing that loss of *cdc13*, overexpression of the CDK inhibitor Rum1 or chemical inhibition of Cdc2 induces re-replication^{10,27,29,36,37}. In these cases, however, Cig1 and Cig2 are required, indicating that the minimal CDK network used here renders cells independent of additional regulation present in wild-type cells. Finally, G2-arrested *cdc13-L-cdc2_{as} Δ 2113 Δ CCP* cells were subjected to a pulse of 10 μ M NmPP1. Subsequent release into 1 μ M inhibitor resulted in rapid entry into S phase without an intervening mitosis, showing that re-replication does not require persistence of low CDK activity (Supplementary Fig. 12e–g).

Next we investigated how G1 cells respond to an abrupt switch to high CDK activity. G2-arrested *cdc13-L-cdc2_{as} Δ 2113 Δ CCP* cells were reset in G1 as in Supplementary Fig. 12e, bypassing mitotic degradation of the fusion protein, but released into inhibitor-free medium. An overlap between S and M was observed in most cells, resulting in aberrant nuclei and ‘cut’ phenotypes (G1 reset; Fig. 3b–d). Similar results were obtained when synchronized cells were maintained in G1 to allow accumulation of the fusion protein and then released into inhibitor-free medium (G1 arrest; Fig. 3b–d and Supplementary Fig. 13b). In this latter case, although bulk DNA synthesis appeared complete shortly after release, labelling of newly synthesized DNA showed that replication was still occurring when mitotic phenotypes were apparent (Supplementary Fig. 13c). Moreover, the presence of aberrant nuclei reflected late stages of the mitotic process. In both experiments, release into 1 μ M NmPP1 suppressed the mitotic phenotype but allowed DNA replication (data not shown), indicating that these effects are due to early induction of high

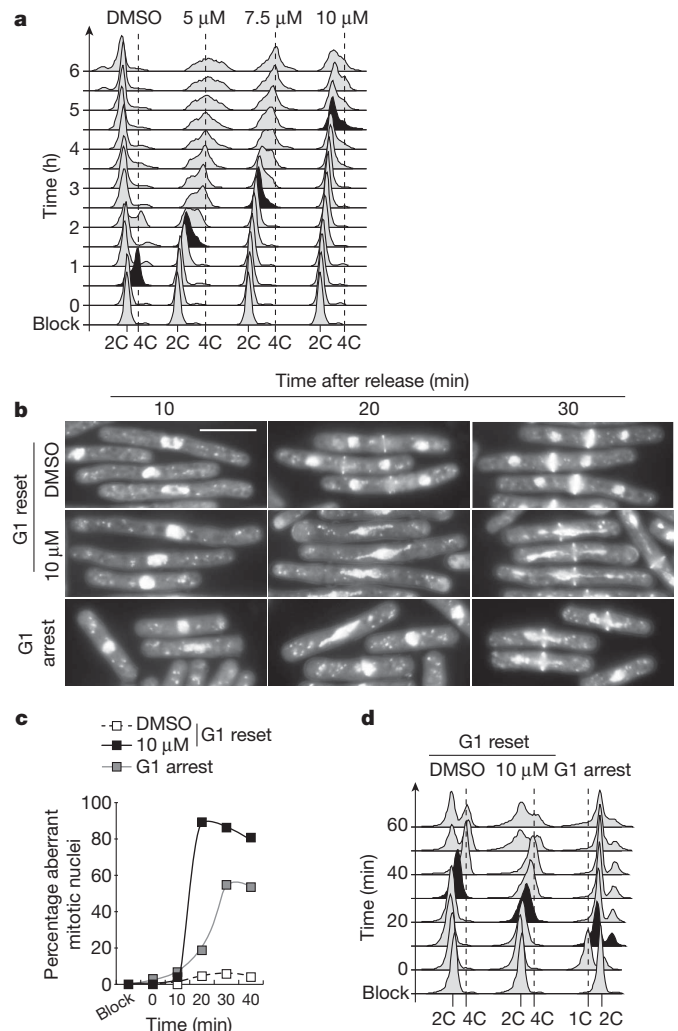


Figure 3 | Resetting the cell cycle. **a**, DNA content analysis of G2-arrested *cdc13-L-cdc2_{as} Δ 2113 Δ CCP* cells released in various concentrations of NmPP1 ($T = 0$). Block: 1 μ M NmPP1 for 2 h 45 min at 32 °C. Black profiles show S-phase onset. Cells treated with inhibitor did not undergo mitosis (Supplementary Fig. 12a). **b–d**, G1 reset: *cdc13-L-cdc2_{as} Δ 2113 Δ CCP* cells were treated as in Supplementary Fig. 12e but released into inhibitor-free medium ($T = 0$). G1 arrest: Synchronized *cdc13-L-cdc2_{as} Δ 2113 Δ CCP* cells as in Supplementary Fig. 9a were arrested in G1 for 2 h with 10 μ M NmPP1 before release ($T = 0$). **b**, DAPI/Blankophor staining (see Supplementary Fig. 13a for the entire time course). Scale bar, 10 μ m. **c**, Percentage of aberrant mitotic nuclei, including elongated, fragmented, asymmetrically divided and ‘cut’ nuclei ($n = 400$). **d**, DNA content analysis. Black profiles show first detection of significant DNA synthesis.

CDK activity which simultaneously brings about S and M. Furthermore, this shows that S phase can proceed with high CDK activity as long as cells have previously experienced low activity. Finally, when S-phase progression was blocked using hydroxyurea in these experiments, cells entered S and M simultaneously but failed to segregate distinct DNA masses (Fig. 4a and Supplementary Fig. 14), supporting the interpretation that the observed phenotype is a consequence of the mitotic machinery attempting to segregate incompletely replicated DNA. These data establish that cells with sufficient CDK activity can enter mitosis from inappropriate points in the cell cycle regardless of their previous state.

The apparent independency of S and M conflicts with models that link mitosis with completion of DNA replication through the S-phase checkpoint. Surprisingly, we found that the checkpoint remained inactive (Fig. 4b and Supplementary Fig. 15a), indicating that it did not sense this overlap between S and M as a pathological situation.

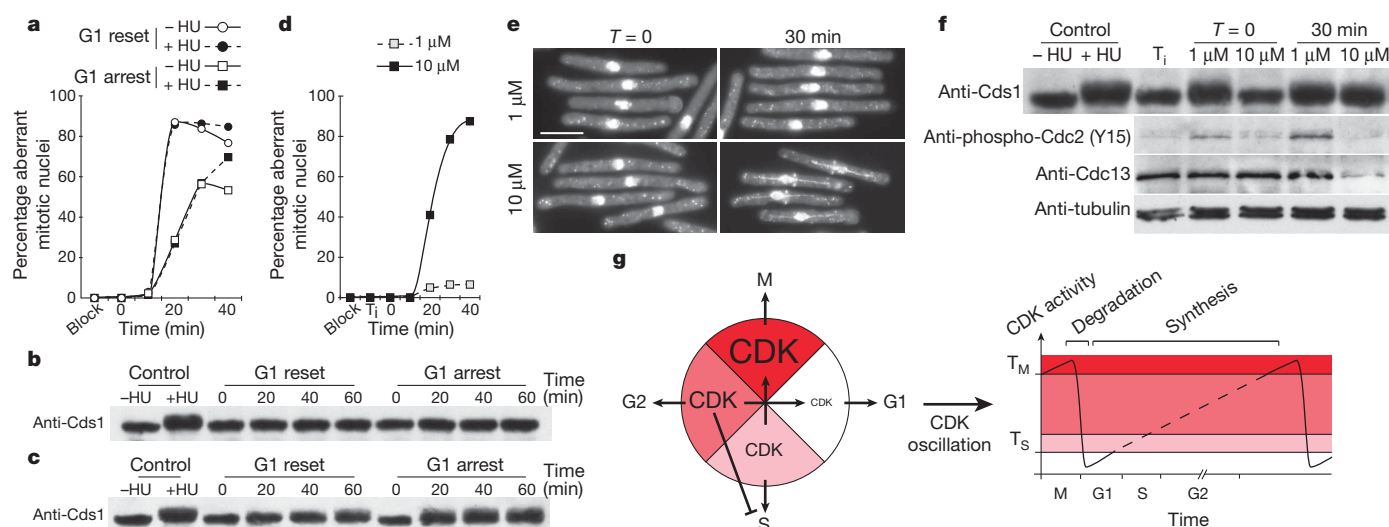


Figure 4 | Timing and directionality of the minimal cell cycle. **a**, Percentage of aberrant mitotic nuclei in cells treated as in Fig. 3b–d but released in normal medium or in 12 mM hydroxyurea (HU) ($n = 200$). **b**, Western blot as in Fig. 3b–d probed for the checkpoint effector Cds1. Controls are G2-arrested *cdc13-L-cdc2_{as} Δ2A13ΔCCP* cells (1 μ M NmPP1 for 2 h 45 min at 32 °C) that were released in 12 mM hydroxyurea, and proteins were extracted 2 h after release. Phosphorylation of Cds1 upon checkpoint activation results in a mobility shift (Methods). **c**, Western blot for the hydroxyurea-treated cells in **a** probed for Cds1. Despite the rapid activation of the S-phase checkpoint, S and M phases occurred simultaneously (**a** and Supplementary Fig. 14a). Controls are as in **b**. **d–f**, Ectopic activation of the checkpoint using hydroxyurea prevents mitosis when the onsets of S and M are separated (modified G1 reset protocol, Supplementary Fig. 15b). **d**, Percentage of aberrant mitotic nuclei

($n = 200$). Similar results were obtained using a G1 arrest-derived protocol (data not shown). **e**, DAPI/Blankophor staining. Scale bar, 10 μ m. **f**, Western blots probed for Cds1, phospho-Cdc2(Y15), Cdc13 and tubulin. Controls are as in **b**. Cells incubated for 40 min with 1 μ M inhibitor entered S phase before release (Supplementary Fig. 15c), resulting in checkpoint activation and inhibition of mitosis. Note that proper mitotic exit is set up in cells undergoing simultaneous S and M as shown by the degradation of the fusion protein (10 μ M, $T = 30$ min). **g**, The core cell cycle solely relies on changes in qualitatively the same CDK activity and lacks global timing and directionality (left panel). A temporal sequence is imposed on the critical independent cell cycle events by the characteristic oscillation of CDK activity between two thresholds (right panel: T_s , S-phase threshold; T_M , M-phase threshold). The precise kinetics of CDK activity accumulation are unknown (dashed line).

Furthermore, ectopic activation of the checkpoint using hydroxyurea only prevented mitosis when entry into M phase was separated from the onset of S phase by temporary incubation in 1 μ M inhibitor before release (Fig. 4c–f and Supplementary Fig. 15d). This demonstrates that the S-phase checkpoint can only have a role when the basic sequence of cell cycle events is pre-established by proper kinetics of CDK oscillation.

We propose that the different phases of the mitotic cycle, defined by specific CDK activity thresholds, can operate independently of each other, establishing that the core cell cycle lacks inherent directionality. The oscillation of a single CDK activity can form the basic engine that provides directionality to this circuit and imposes the temporal order of S and M (Fig. 4g).

CDK regulatory loops and size control

The major systems directly regulating CDK activity in fission yeast involve the CDK inhibitor Rum1^{22,36,38} and control of Cdc2 phosphorylation by Wee1, Mik1 and Cdc25^{39–42}. We asked if these mechanisms are part of the core regulation or if they are only relevant in normal cells with a more complex CDK machinery.

Neither deregulation of Rum1 through deletion of *cig1* and *puc1*^{23,25}, nor deletion of *rum1* in *cdc13-L-cdc2 Δ2A13ΔCCP* cells had any effect on vegetative growth and checkpoint responses, but *Arum1* cells did not arrest in G1 after nitrogen starvation, consistent with previous observations¹⁷ (Table 1 and Supplementary Figs 16 and 18).

Cdc2 phosphorylation has central roles in the control of cell size at division⁴³, the S-phase and DNA-damage checkpoints^{44,45}, and the response to changes in nutrient availability^{46,47}. To determine the importance of this regulation in the minimal cell cycle, Thr 14 (which can be phosphorylated by Wee1⁴⁸) and Tyr 15 (ref. 41) were altered (*cdc13-L-cdc2AF* cassette producing a Cdc13-L-Cdc2(T14A, Y15F) fusion protein; Supplementary Fig. 17). Whereas cells operating with a Cdc2(Y15F) protein showed poor viability⁴¹, *cdc13-L-cdc2AF Δ2A13ΔCCP* cells were surprisingly healthy, although with a longer

generation time (Fig. 5a and Table 1). Confirming these results, *cdc13-L-cdc2 Δ2A13ΔCCP Awee1 Δmik1* cells had similar characteristics (Fig. 5a, Table 1 and Supplementary Fig. 17), despite the co-lethality of *wee1* and *mik1* in a normal background⁴². As expected, the S-phase and DNA-damage checkpoints, which are operative in *cdc13-L-cdc2 Δ2A13ΔCCP* cells, were impaired in the *AF* mutant (Supplementary Fig. 18). Although an imbalance in this regulatory loop affects the functioning of the wild-type fusion protein (Supplementary Fig. 19), these data show that simplifying the cell cycle network relieves cells from tight regulation by Wee1, Mik1 and Cdc25.

In contrast to *wee1* mutants, which divide at 50% of wild-type size, *cdc13-L-cdc2AF Δ2A13ΔCCP* cells divided only 15% smaller than *cdc13-L-cdc2 Δ2A13ΔCCP* cells (Table 1). Nevertheless, G1 was elongated as in *wee1* cells⁴³ (Fig. 5b). *cdc13-L-cdc2AF Δ2A13ΔCCP* cells also showed a higher variability in size at division (Fig. 5c). However, the majority of cells (67%) divided at a size within the range of variation observed for the control strain. Furthermore, despite this increased heterogeneity, G2-arrested *cdc13-L-cdc2AF_{as} Δ2A13ΔCCP* cells returned to their normal average size efficiently upon release (Fig. 5d and Supplementary Fig. 20). These data indicate that a Wee1-independent size control system is operative in these cells and that Wee1 may integrate additional pathways that render this control more accurate.

Discussion

We have shown that a minimal control network based on a single monomolecular CDK module can autonomously drive the fission yeast cell cycle, indicating that differential expression, degradation and subcellular localization of CDK subunits, attainment of specific ratios of cyclin to CDK, and cyclin-mediated changes in substrate specificity are not essential for cell cycle progression. We demonstrate that the CDK oscillator provides timing and directionality to a simple circuit of two activity thresholds that define independent cell cycle phases, and prevails over the S-phase checkpoint in organizing the

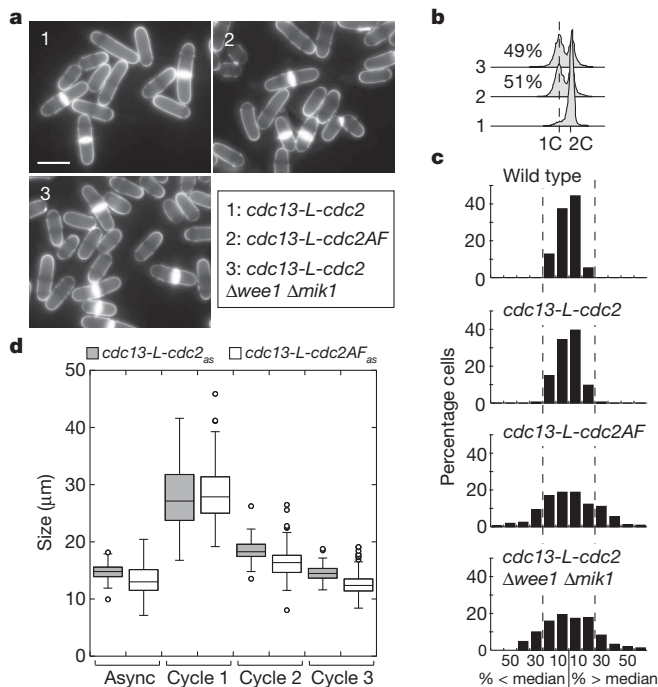


Figure 5 | Role of Cdc2 T14 and Y15 phosphorylation. **a–d**, All strains carried deletions of the endogenous copies of *cdc2*, *cdc13*, *cig1*, *cig2* and *puc1*. **a**, **b**, Labels are indicated in box. **a**, Blankophor staining of exponentially growing cells. Scale bar, 10 μ m. **b**, DNA content analysis. The percentages of 1C cells are indicated. **c**, Distribution of cell size at division in exponentially growing cultures presented as a percentage of the median size ($n \geq 150$). **d**, G2-arrested cells (1 μ M NmPPI for 3 h 30 min at 32 $^{\circ}$ C) were released and cell size at division determined at the peak of binucleated cells for the following three cycles ($n \geq 50$; Supplementary Fig. 20). Box and whisker plot. Async, asynchronous cultures.

mitotic cycle (Fig. 4g). We propose that this minimal architecture reveals the core control of the eukaryotic cell cycle. Although cell cycle regulation is more elaborate in multicellular eukaryotes, the redundancy observed for metazoan CDK subunits^{11–13} indicates that our conclusions may also be relevant for more complex cells.

We show also that regulation by Wee1, Mik1 and Cdc25 is dispensable for the minimal cell cycle. Interestingly, *cdc13-L-cdc2AF Δ 2A13ACCP* cells divide at a length close to wild type, indicating that the Pom1 gradient operating through Wee1^{49,50} cannot be the only system that prevents short cells from dividing. Cell-to-cell variation in size at division is higher in this strain. This could result from increased heterogeneity in the timing and degree of CDK activation that may perturb the Wee1-independent size control. Feedback signalling through CDK phosphorylation may promote size homogeneity by reducing potential noise in core CDK expression, stability or activation. In other systems, CDK activation shows Wee1/Cdc25-dependent stepwise and hysteretic properties^{5–9}, which provide sharp transitions and directionality to the cell cycle. In *cdc13-L-cdc2AF Δ 2A13ACCP* cells, CDK activity may therefore rise more progressively, altering the kinetics of substrate phosphorylation and resulting in the observed phenotypes.

It is unclear how a single CDK activity can sequentially trigger DNA replication and mitosis, as the possible overlap between S and M establishes the simultaneous presence of G1/S and G2/M substrates. The CDK may have higher affinity for G1/S substrates. Coupled with periodic cyclin degradation, this would allow temporal separation of S and M. Alternatively, activity-dependent changes in subcellular localization of the whole CDK machinery may provide substrate specificity. It is also possible that specific phosphatases target G2/M substrates more readily. In G1, the significant CDK activity differential—from close to zero to a low level—coupled to a lower phosphorylation turnover would allow accumulation only of phosphorylated G1/S

substrates. G2/M substrate-specific phosphatases would establish a futile cycle with Cdc2, allowing the more modest differential in CDK activity at the end of G2 to produce a significant increase in net phosphorylation of G2/M substrates.

The results presented here may have evolutionary implications. A single oscillating CDK module could be the way primitive eukaryotes regulated their cell cycle. Subsequent selection would have introduced other regulatory layers to improve and fine-tune the core system. Cells may have become dependent on these additional elements, rendering them essential in modern cells and making it more difficult to fully appreciate the core processes involved.

METHODS SUMMARY

Standard methods for molecular biology, genetics and microscopy are detailed in Methods. Strains are listed in Supplementary Table 1. Experiments were carried out in supplemented minimal medium at 32 $^{\circ}$ C, except where otherwise noted, with various concentrations of NmPPI inhibitor (TRC). Cell size measurements were made from images of blankophor-stained cells. DNA was visualized in heat-fixed cells using 4',6-diamidino-2-phenylindole (DAPI) and in live cells using Hoechst. Western analyses were performed using total protein extracts normalized by amounts of proteins except where otherwise noted. DNA content was analysed using a BD FACSCalibur.

Full Methods and any associated references are available in the online version of the paper at www.nature.com/nature.

Received 23 April; accepted 28 September 2010.

- Morgan, D. O. Cyclin-dependent kinases: engines, clocks, and microprocessors. *Annu. Rev. Cell Dev. Biol.* **13**, 261–291 (1997).
- Loog, M. & Morgan, D. O. Cyclin specificity in the phosphorylation of cyclin-dependent kinase substrates. *Nature* **434**, 104–108 (2005).
- Bloom, J. & Cross, F. R. Multiple levels of cyclin specificity in cell-cycle control. *Nature Rev. Mol. Cell Biol.* **8**, 149–160 (2007).
- Yang, J. & Kornbluth, S. All aboard the cyclin train: subcellular trafficking of cyclins and their CDK partners. *Trends Cell Biol.* **9**, 207–210 (1999).
- Sha, W. *et al.* Hysteresis drives cell-cycle transitions in *Xenopus laevis* egg extracts. *Proc. Natl Acad. Sci. USA* **100**, 975–980 (2003).
- Pomeroy, J. R., Sontag, E. D. & Ferrell, J. E. Building a cell cycle oscillator: hysteresis and bistability in the activation of Cdc2. *Nature Cell Biol.* **5**, 346–351 (2003).
- Kim, S. Y. & Ferrell, J. E. Substrate competition as a source of ultrasensitivity in the inactivation of Wee1. *Cell* **128**, 1133–1145 (2007).
- Novak, B., Tyson, J. J., Gyorffy, B. & Csikasz-Nagy, A. Irreversible cell-cycle transitions are due to systems-level feedback. *Nature Cell Biol.* **9**, 724–728 (2007).
- Deibler, R. W. & Kirschner, M. W. Quantitative reconstitution of mitotic CDK1 activation in somatic cell extracts. *Mol. Cell* **37**, 753–767 (2010).
- Fisher, D. L. & Nurse, P. A single fission yeast mitotic cyclin B p34cdc2 kinase promotes both S-phase and mitosis in the absence of G1 cyclins. *EMBO J.* **15**, 850–860 (1996).
- Kozar, K. *et al.* Mouse development and cell proliferation in the absence of D-cyclins. *Cell* **118**, 477–491 (2004).
- Santamaria, D. *et al.* Cdk1 is sufficient to drive the mammalian cell cycle. *Nature* **448**, 811–815 (2007).
- Hochegger, H., Takeda, S. & Hunt, T. Cyclin-dependent kinases and cell-cycle transitions: does one fit all? *Nature Rev. Mol. Cell Biol.* **9**, 910–916 (2008).
- Nurse, P., Thuriaux, P. & Nasmyth, K. Genetic control of the cell division cycle in the fission yeast *Schizosaccharomyces pombe*. *Mol. Gen. Genet.* **146**, 167–178 (1976).
- Nurse, P. & Bissett, Y. Gene required in G1 for commitment to cell cycle and in G2 for control of mitosis in fission yeast. *Nature* **292**, 558–560 (1981).
- Mondesert, O., McGowan, C. H. & Russell, P. Cig2, a B-type cyclin, promotes the onset of S in *Schizosaccharomyces pombe*. *Mol. Cell Biol.* **16**, 1527–1533 (1996).
- Martin-Castellanos, C., Labib, K. & Moreno, S. B-type cyclins regulate G1 progression in fission yeast in opposition to the p25rum1 cdk inhibitor. *EMBO J.* **15**, 839–849 (1996).
- Boher, R. & Beach, D. Involvement of *cdc13+* in mitotic control in *Schizosaccharomyces pombe*: possible interaction of the gene product with microtubules. *EMBO J.* **7**, 2321–2327 (1988).
- Boher, R. N., Alfa, C. E., Hyams, J. S. & Beach, D. H. The fission yeast *cdc2/cdc13/suc1* protein kinase: regulation of catalytic activity and nuclear localization. *Cell* **58**, 485–497 (1989).
- Moreno, S., Hayles, J. & Nurse, P. Regulation of p34^{cdc2} protein kinase during mitosis. *Cell* **58**, 361–372 (1989).
- Bueno, A., Richardson, H., Reed, S. I. & Russell, P. A fission yeast B-type cyclin functioning early in the cell cycle. *Cell* **66**, 149–159 (1991).
- Correa-Bordes, J., Gulli, M. P. & Nurse, P. p25^{rum1} promotes proteolysis of the mitotic B-cyclin p56^{cdc13} during G1 of the fission yeast cell cycle. *EMBO J.* **16**, 4657–4664 (1997).

23. Benito, J., Martín-Castellanos, C. & Moreno, S. Regulation of the G₁ phase of the cell cycle by periodic stabilization and degradation of the p25^{rum1} CDK inhibitor. *EMBO J.* **17**, 482–497 (1998).
24. Forsburg, S. L. & Nurse, P. Identification of a G₁-type cyclin *puc1*⁺ in the fission yeast *Schizosaccharomyces pombe*. *Nature* **351**, 245–248 (1991).
25. Martín-Castellanos, C., Blanco, M. A., de Prada, J. M. & Moreno, S. The *puc1* cyclin regulates the G₁ phase of the fission yeast cell cycle in response to cell size. *Mol. Biol. Cell* **11**, 543–554 (2000).
26. Broek, D., Bartlett, R., Crawford, K. & Nurse, P. Involvement of p34^{cdc2} in establishing the dependency of S phase on mitosis. *Nature* **349**, 388–393 (1991).
27. Hayles, J., Fisher, D., Woollard, A. & Nurse, P. Temporal order of S phase and mitosis in fission yeast is determined by the state of the p34^{cdc2}-mitotic B cyclin complex. *Cell* **78**, 813–822 (1994).
28. Bishop, A. C. *et al.* A chemical switch for inhibitor-sensitive alleles of any protein kinase. *Nature* **407**, 395–401 (2000).
29. Dischinger, S., Krapp, A., Xie, L., Paulson, J. R. & Simanis, V. Chemical genetic analysis of the regulatory role of Cdc2p in the *S. pombe* septation initiation network. *J. Cell Sci.* **121**, 843–853 (2008).
30. Decottignies, A., Zarzov, P. & Nurse, P. *In vivo* localisation of fission yeast cyclin-dependent kinase cdc2p and cyclin B cdc13p during mitosis and meiosis. *J. Cell Sci.* **114**, 2627–2640 (2001).
31. Buck, V., Russell, P. & Millar, J. B. Identification of a cdk-activating kinase in fission yeast. *EMBO J.* **14**, 6173–6183 (1995).
32. Tanaka, K. & Okayama, H. A *pcl*-like cyclin activates the Res2p-Cdc10p cell cycle “start” transcriptional factor complex in fission yeast. *Mol. Biol. Cell* **11**, 2845–2862 (2000).
33. Watt, S. *et al.* *urg1*: a uracil-regulatable promoter system for fission yeast with short induction and repression times. *PLoS ONE* **3**, e1428 (2008).
34. Stern, B. & Nurse, P. A quantitative model for the cdc2 control of S phase and mitosis in fission yeast. *Trends Genet.* **12**, 345–350 (1996).
35. Murray, A. W. Recycling the cell cycle: cyclins revisited. *Cell* **116**, 221–234 (2004).
36. Moreno, S. & Nurse, P. Regulation of progression through the G₁ phase of the cell cycle by the *rum1*⁺ gene. *Nature* **367**, 236–242 (1994).
37. Snaith, H. A. & Forsburg, S. L. Rereplication phenomenon in fission yeast requires MCM proteins and other S phase genes. *Genetics* **152**, 839–851 (1999).
38. Correa-Bordes, J. & Nurse, P. p25^{rum1} orders S phase and mitosis by acting as an inhibitor of the p34^{cdc2} mitotic kinase. *Cell* **83**, 1001–1009 (1995).
39. Russell, P. & Nurse, P. *cdc25*⁺ functions as an inducer in the mitotic control of fission yeast. *Cell* **45**, 145–153 (1986).
40. Russell, P. & Nurse, P. Negative regulation of mitosis by *wee1*⁺, a gene encoding a protein kinase homolog. *Cell* **49**, 559–567 (1987).
41. Gould, K. L. & Nurse, P. Tyrosine phosphorylation of the fission yeast *cdc2*⁺ protein kinase regulates entry into mitosis. *Nature* **342**, 39–45 (1989).
42. Lundgren, K. *et al.* *mik1* and *wee1* cooperate in the inhibitory tyrosine phosphorylation of *cdc2*. *Cell* **64**, 1111–1122 (1991).
43. Fantes, P. A. & Nurse, P. Control of the timing of cell division in fission yeast. Cell size mutants reveal a second control pathway. *Exp. Cell Res.* **115**, 317–329 (1978).
44. Rhind, N., Furnari, B. & Russell, P. Cdc2 tyrosine phosphorylation is required for the DNA damage checkpoint in fission yeast. *Genes Dev.* **11**, 504–511 (1997).
45. Rhind, N. & Russell, P. Tyrosine phosphorylation of *cdc2* is required for the replication checkpoint in *Schizosaccharomyces pombe*. *Mol. Cell. Biol.* **18**, 3782–3787 (1998).
46. Fantes, P. & Nurse, P. Control of cell size at division in fission yeast by a growth-modulated size control over nuclear division. *Exp. Cell Res.* **107**, 377–386 (1977).
47. Petersen, J. & Nurse, P. TOR signalling regulates mitotic commitment through the stress MAP kinase pathway and the Polo and Cdc2 kinases. *Nature Cell Biol.* **9**, 1263–1272 (2007).
48. Den Haese, G. J., Walworth, N., Carr, A. M. & Gould, K. L. The Wee1 protein kinase regulates T14 phosphorylation of fission yeast Cdc2. *Mol. Biol. Cell* **6**, 371–385 (1995).
49. Martin, S. G. & Berthelot-Grosjean, M. Polar gradients of the DYRK-family kinase Pom1 couple cell length with the cell cycle. *Nature* **459**, 852–856 (2009).
50. Moseley, J. B., Mayeux, A., Paoletti, A. & Nurse, P. A spatial gradient coordinates cell size and mitotic entry in fission yeast. *Nature* **459**, 857–860 (2009).

Supplementary Information is linked to the online version of the paper at www.nature.com/nature.

Acknowledgements We thank J. Hayles, P.-Y. Wu and F. Navarro for critically reading the manuscript, and N. Rhind for the anti-Cds1 antibody. D.C. was supported by post-doctoral fellowships from EMBO (ALTF 899-2007) and the Human Frontier Science Program (LT00623/2008) and P.N. by the Breast Cancer Research Foundation, The Rockefeller University and the Anderson Cancer Center Research at Rockefeller University.

Author Contributions D.C. designed and performed the experiments and wrote the manuscript. Both authors discussed the experiments and edited the manuscript.

Author Information Reprints and permissions information is available at www.nature.com/reprints. The authors declare no competing financial interests. Readers are welcome to comment on the online version of this article at www.nature.com/nature. Correspondence and requests for materials should be addressed to D.C. (dcoudreuse@rockefeller.edu).

METHODS

Strains and growth conditions. Standard media and methods were used^{51,52}. Strains used in this study are listed in Supplementary Table 1. All experiments were carried out in minimal medium plus supplements (EMM4S) at 32 °C except where otherwise noted. The CDK module is a fusion of *cdc13* and *cdc2* open reading frames without introns. The fusion cassettes were cloned in a vector adjacent to the *ura4⁺* cassette; flanking regions allowed a restriction fragment to replace the *leu1* gene by homologous recombination. The NmPP1 inhibitor (A603003; TRC) was dissolved in DMSO at a stock concentration of 10 mM and added to the cultures at the indicated concentrations. The first 67 amino-terminal residues of Cdc13 were deleted in the Cdc13ΔDB-L-Cdc2_{as} protein⁵³. Expression of the *cdc13ΔDB-L-cdc2_{as}* cassette was induced by addition of 250 mg l⁻¹ uracil to the medium. For hydroxyurea treatments in Fig. 4 and Supplementary Figs 14 and 15, hydroxyurea was added 10 min before release from the inhibitor. The alteration in *cdc13-117_{ts}* cells (Cdc13(C379Y)) was determined by sequencing. The *cig1Δ::ura4⁺*, *cig2Δ::ura4⁺*, *puc1Δ::ura4⁺*, *mik1Δ::leu2⁺* deletions and the *cdc2-33_{ts}*, *wee1-50_{ts}* and *cdc25-22_{ts}* alleles have been previously described^{14,21,54–58}. The *rad3Δ::ura4⁺* deletion was a gift from R. Daga. The *cdc2Δ::kanMX6*, *cdc13Δ::natMX6*, *rum1Δ::hphMX6* and *cig2Δ::natMX6* deletions were exact replacements of the open reading frames as described^{59,60}.

Cell size measurement and DNA staining. For size measurement, live cells were stained with Blankophor (MP Biochemicals). For DNA staining, cells were either heat-fixed on microscope slides and stained with DAPI (with 1:4 blankophor where indicated) or stained live with 50 μg ml⁻¹ Hoechst DNA stain. Images were acquired in Metamorph (MDS Analytical Technologies) using an Axioplan 2 (Carl Zeiss) epifluorescence microscope and a CoolSNAP HQ camera (Roper Scientific). Cell size was determined in ImageJ (National Institutes of Health) using the Pointpicker plug-in.

Protein extracts and western blots. Western blots were performed on total protein extracts. Protein extracts in Fig. 1 and Supplementary Figs 6, 16 and 17 were prepared using NaOH extraction⁶¹. In all other cases, cells were frozen in liquid nitrogen, broken with glass beads in the presence of protease and phosphatase inhibitors (Roche) and resuspended in SDS buffer. Samples were normalized by amounts of proteins except where otherwise noted. Antibodies used: Cdc13 polyclonal (SP4 (ref. 20); 1:2,500), Cds1 polyclonal (1:3,000, a gift from N. Rhind⁶²), phospho-Cdc2(Y15) polyclonal (Cell Signaling; 1:300) and tubulin monoclonal (1:10,000, a gift from K. Gull⁶³). Activation of the S-phase checkpoint was monitored by the phosphorylation-dependent shift in Cds1 mobility⁶⁴ by 8% SDS–polyacrylamide gel electrophoresis.

Flow cytometry profile interpretation. DNA content analysis was performed by flow cytometry using ethanol-fixed and propidium-iodide-stained cells (2 μg ml⁻¹ propidium iodide in 50 mM sodium citrate) and a BD FACSCalibur. The fission yeast cell cycle has a very short G1, and cells undergo DNA replication before cytokinesis. As a result, fission yeast cells spend most of their cell cycle with a 2C DNA content. In synchronized cultures, a transient 4C peak appears as S phase occurs in post-mitotic binucleated cells. This is resolved upon cytokinesis, producing mononucleated 2C cells. This phase only represents a small fraction of the population in an asynchronous culture; a larger 4C peak corresponds either to binucleated cells that have completed S phase but show a cytokinesis defect or to mononucleated G2 cells that have undergone an additional round of DNA replication without intervening mitosis. The appearance of a 1C peak reflects an elongation of G1 resulting in cytokinesis taking place before completion of DNA replication. Intermediate, non-discrete profiles occur when cells divide although mitosis is not complete, resulting in the septum cutting through the DNA mass and subsequent aberrant distribution of the DNA; this is referred to as 'cut' cells⁶⁵. Finally, cell size has an effect on the position of the flow cytometry profiles as non-nuclear staining increases with size: profiles are shifted to the right in long cells and to the left in newly divided cells, despite identical DNA contents⁶⁶.

Nuclear YFP quantification. Cells were imaged on agar pads under a coverslip and Z stacks were acquired using a DeltaVision RT microscope (Applied Precision). Quantification was performed on maximum projections using ImageJ (National Institutes of Health) as follows. Fluorescence intensity of equivalent areas within the nucleus (N), the cytoplasm (C) and outside (B) of each *cdc13-L-cdc2-YFP Δ2A13ACCP* cell was measured (strongly stained structures such as the spindle or spindle pole body were excluded) as well as cell size. Similar measurements were performed in *cdc13-L-cdc2 Δ2A13ACCP* cells as a control. C

was not significantly different than in the control cells and therefore was used as a normalization value. Using the *cdc13-L-cdc2 Δ2A13ACCP* cells, we estimated the average auto-fluorescence (A) in the nucleus as a constant percentage of B. The value reflecting nuclear fluorescence for each cell was calculated as $[N - B - (A \times B)] / C$. For binucleated and septated cells, N was calculated as the average fluorescence of both nuclei. Values were then sorted by cell size. The rare cells showing a negative value were considered as negative for the YFP signal.

Total YFP quantification by flow cytometry. The fluorescence (FL1-H) of *cdc13-L-cdc2-YFP Δ2A13ACCP* and *cdc13-L-cdc2 Δ2A13ACCP* cells in minimal medium at 25 °C was measured as a function of size (FSC-H) by flow cytometry using a BD FACSCalibur. YFP measurements were averaged in size bins of 250 cells. The equation of the linear regression obtained in the control strain was used to subtract the auto-fluorescence background from the *cdc13-L-cdc2-YFP Δ2A13ACCP* measurements.

Percentage of dead cells in liquid cultures. Liquid cultures were exponentially grown for 36 h at the appropriate temperatures in the presence of 25 mg l⁻¹ of the dye phloxin B (phloxin B stains dead cells in pink). The percentage of dead cells was estimated by microscopy.

Nitrogen starvation. Cells were exponentially grown at 28 °C in minimal medium with supplements, washed with water and inoculated at approximately 1.5×10^6 cells ml⁻¹ into non-supplemented minimal medium without nitrogen at 28 °C.

EdU incorporation and detection. *cdc13-L-cdc2_{as} Δ2A13ACCP* cells expressing the human ENT1 transporter and herpes simplex virus thymidine kinase⁶⁷ were incubated with 2 μM EdU (Invitrogen) for 5 min and fixed in 3.7% formaldehyde. After permeabilization (A. Kaykov, manuscript in preparation), EdU detection was performed according to manufacturer's instructions (Invitrogen, Click-iT EdU Alexa Fluor 594 Imaging Kit) and imaged in Metamorph (MDS Analytical Technologies) using an Axioplan 2 (Carl Zeiss) epifluorescence microscope and a CoolSNAP HQ camera (Roper Scientific).

51. Hayles, J. & Nurse, P. Genetics of the fission yeast *Schizosaccharomyces pombe*. *Annu. Rev. Genet.* **26**, 373–402 (1992).
52. Moreno, S., Klar, A. & Nurse, P. Molecular genetic analysis of fission yeast *Schizosaccharomyces pombe*. *Methods Enzymol.* **194**, 795–823 (1991).
53. Yamano, H., Gannon, J. & Hunt, T. The role of proteolysis in cell cycle progression in *Schizosaccharomyces pombe*. *EMBO J.* **15**, 5268–5279 (1996).
54. Obara-Ishihara, T. & Okayama, H. A B-type cyclin negatively regulates conjugation via interacting with cell cycle 'start' genes in fission yeast. *EMBO J.* **13**, 1863–1872 (1994).
55. Forsburg, S. L. & Nurse, P. Analysis of the *Schizosaccharomyces pombe* cyclin *puc1*: evidence for a role in cell cycle exit. *J. Cell Sci.* **107**, 601–613 (1994).
56. Zarrov, P., Decottignies, A., Baldacci, G. & Nurse, P. G₁/S CDK is inhibited to restrain mitotic onset when DNA replication is blocked in fission yeast. *EMBO J.* **21**, 3370–3376 (2002).
57. Nurse, P. Genetic control of cell size at cell division in yeast. *Nature* **256**, 547–551 (1975).
58. Thuriaux, P., Sipiczki, M. & Fantès, P. A. Genetical analysis of a sterile mutant by protoplast fusion in the fission yeast *Schizosaccharomyces pombe*. *J. Gen. Microbiol.* **116**, 525–528 (1980).
59. Bähler, J. et al. Heterologous modules for efficient and versatile PCR-based gene targeting in *Schizosaccharomyces pombe*. *Yeast* **14**, 943–951 (1998).
60. Hentges, P., Van Driessche, B., Tafforeau, L., Vandenhaute, J. & Carr, A. M. Three novel antibiotic marker cassettes for gene disruption and marker switching in *Schizosaccharomyces pombe*. *Yeast* **22**, 1013–1019 (2005).
61. Matsuo, Y., Asakawa, K., Toda, T. & Katayama, S. A rapid method for protein extraction from fission yeast. *Biosci. Biotechnol. Biochem.* **70**, 1992–1994 (2006).
62. Bhaumik, D. & Wang, T. S. Mutational effect of fission yeast *polα* on cell cycle events. *Mol. Biol. Cell* **9**, 2107–2123 (1998).
63. Woods, A. et al. Definition of individual components within the cytoskeleton of *Trypanosoma brucei* by a library of monoclonal antibodies. *J. Cell Sci.* **93**, 491–500 (1989).
64. Lindsay, H. D. et al. S-phase-specific activation of Cds1 kinase defines a subpathway of the checkpoint response in *Schizosaccharomyces pombe*. *Genes Dev.* **12**, 382–395 (1998).
65. Uemura, T. & Yanagida, M. Isolation of type I and II DNA topoisomerase mutants from fission yeast: single and double mutants show different phenotypes in cell growth and chromatin organization. *EMBO J.* **3**, 1737–1744 (1984).
66. Sazer, S. & Sherwood, S. W. Mitochondrial growth and DNA synthesis occur in the absence of nuclear DNA replication in fission yeast. *J. Cell Sci.* **97**, 509–516 (1990).
67. Sivakumar, S., Porter-Goff, M., Patel, P. K., Benoit, K. & Rhind, N. *In vivo* labeling of fission yeast DNA with thymidine and thymidine analogs. *Methods* **33**, 213–219 (2004).

Images of a fourth planet orbiting HR 8799

Christian Marois¹, B. Zuckerman², Quinn M. Konopacky³, Bruce Macintosh³ & Travis Barman⁴

High-contrast near-infrared imaging of the nearby star HR 8799 has shown three giant planets¹. Such images were possible because of the wide orbits (>25 astronomical units, where 1 AU is the Earth–Sun distance) and youth (<100 Myr) of the imaged planets, which are still hot and bright as they radiate away gravitational energy acquired during their formation. An important area of contention in the exoplanet community is whether outer planets (>10 AU) more massive than Jupiter form by way of one-step gravitational instabilities² or, rather, through a two-step process involving accretion of a core followed by accumulation of a massive outer envelope composed primarily of hydrogen and helium³. Here we report the presence of a fourth planet, interior to and of about the same mass as the other three. The system, with this additional planet, represents a challenge for current planet formation models as none of them can explain the *in situ* formation of all four planets. With its four young giant planets and known cold/warm debris belts⁴, the HR 8799 planetary system is a unique laboratory in which to study the formation and evolution of giant planets at wide (>10 AU) separations.

New near-infrared observations of HR 8799, optimized for detecting close-in planets, were made at the Keck II telescope in 2009 and 2010. (See Table 1 for a summary.) A subset of the images is presented in Fig. 1. A fourth planet, designated HR 8799e, is detected at six different epochs at an averaged projected separation of $0.368'' \pm 0.003''$ (14.5 ± 0.4 AU). Planet e is bound to the star and is orbiting anticlockwise (see Fig. 2), as are the three other known planets in the system. The measured orbital motion, 46 ± 10 mas yr^{-1} , is consistent with a roughly circular orbit of semimajor axis (a) 14.5 AU with a ~ 50 -year period.

Knowledge of the age and luminosity of the planets is critical for deriving their fundamental properties, including mass. In 2008 we used various techniques to estimate an age of 60 Myr with a plausible

range between 30 and 160 Myr (here we represent this as 60^{+100}_{-30} Myr), consistent with an earlier estimate of 20–150 Myr (ref. 5). Two recent analyses (R. Doyon *et al.*, and B. Zuckerman *et al.*, manuscripts in preparation) independently deduce that HR 8799 is very likely to be a member of the 30 Myr Columba association⁶. This conclusion is based on common Galactic space motions and age indicators for stars located between the previously-known Columba members and HR 8799. The younger age suggests smaller planet masses, but to be conservative, we use both age ranges (30^{+20}_{-10} Myr (Columba association) and 60^{+100}_{-30} Myr¹) to derive the physical properties of planet e.

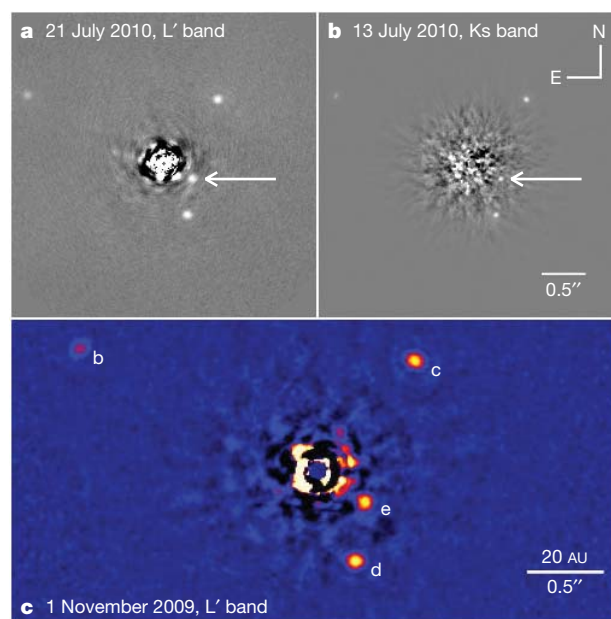


Figure 1 | HR 8799e discovery images. Images of HR 8799 (a star at 39.4 ± 1.0 pc and located in the Pegasus constellation) were acquired at the Keck II telescope with the Angular Differential Imaging technique (ADI)²² to allow a stable quasi-static point spread function (PSF) while leaving the field-of-view to rotate with time while tracking the star in the sky. The ADI/LOCI^{22,23} SOSIE software²⁴ was used to subtract the stellar flux, and to combine and flux-calibrate the images. Our SOSIE software²⁴ iteratively fits the planet PSF to derive relative astrometry and photometry (the star position and its photometry were obtained from unsaturated data or from its PSF core that was detectable through a flux-calibrated focal plane mask). **a**, An L'-band image acquired on 21 July 2010; **b**, a Ks-band image acquired on 13 July 2010 (arrows in **a** and **b** point towards planet e); **c**, an L'-band image acquired on 1 November 2009. All three sequences were ~ 1 h long. No coronagraphic focal plane mask was used on 1 November 2009, but a 400-mas-diameter mask was used on 13 July and 21 July 2010. HR 8799e is located southwest of the star. Planets b, c and d are seen at respective projected separations of 68, 38 and 24 AU from the central star, consistent with roughly circular orbits at inclinations of $<40^\circ$ (refs 11–13). Their masses (7, 10 and 10 M_{Jup} for b, c and d for 60 Myr age¹; 5, 7 and 7 M_{Jup} for 30 Myr age) were estimated from their luminosities using age-dependent evolutionary models²⁵. North is up and east is left.

Table 1 | HR 8799e astrometry, photometry and physical characteristics

| Epoch, band, wavelength | Separation [E, N] from the host star |
|---|--------------------------------------|
| 2009 Jul. 31, Kp band $2.124 \mu\text{m}$ ($\pm 0.019''$) | $[-0.299'', -0.217'']$ |
| 2009 Aug. 1, L' band $3.776 \mu\text{m}$ ($\pm 0.013''$) | $[-0.303'', -0.209'']$ |
| 2009 Nov. 1, L' band $3.776 \mu\text{m}$ ($\pm 0.010''$) | $[-0.304'', -0.196'']$ |
| 2010 Jul. 13, Ks band $2.146 \mu\text{m}$ ($\pm 0.008''$) | $[-0.325'', -0.173'']$ |
| 2010 Jul. 21, L' band $3.776 \mu\text{m}$ ($\pm 0.011''$) | $[-0.324'', -0.175'']$ |
| 2010 Oct. 30, L' band $3.776 \mu\text{m}$ ($\pm 0.010''$) | $[-0.334'', -0.162'']$ |
| Parameter | Value |
| Projected separation, avg. from all epochs* (AU) | 14.5 ± 0.4 |
| Orbital motion (arcsec yr^{-1}) | 0.046 ± 0.010 |
| Period for a face-on circular orbit (yr) | ~ 50 |
| ΔK_s $2.146 \mu\text{m}$ † (mag) | 10.67 ± 0.22 |
| $\Delta L'$ $3.776 \mu\text{m}$ † (mag) | 9.37 ± 0.12 |
| Absolute magnitude at $2.146 \mu\text{m}$, M_{Ks} (mag) | 12.93 ± 0.22 |
| Absolute magnitude at $3.776 \mu\text{m}$, $M_{L'}$ (mag) | 11.61 ± 0.12 |
| Luminosity ($\log L_\odot$) | -4.7 ± 0.2 |
| Mass for 30^{+20}_{-10} Myr (M_{Jup}) | 7^{+3}_{-2} |
| Mass for 60^{+100}_{-30} Myr (M_{Jup}) | 10^{+3}_{-3} |

* The projected separation error (in AU) also accounts for the uncertainty in the distance to the star.

† Planet-to-star flux ratios, expressed as difference of magnitude. No reliable photometry was derived for the Kp-band 2009 Jul. 31 data.

¹National Research Council Canada, Herzberg Institute of Astrophysics, 5071 West Saanich Road, Victoria, British Columbia V9E 2E7, Canada. ²Physics & Astronomy Department, University of California, Los Angeles, California 90095, USA. ³Lawrence Livermore National Laboratory, 7000 East Avenue, Livermore, California 94550, USA. ⁴Lowell Observatory, 1400 West Mars Hill Road, Flagstaff, Arizona 86001, USA.

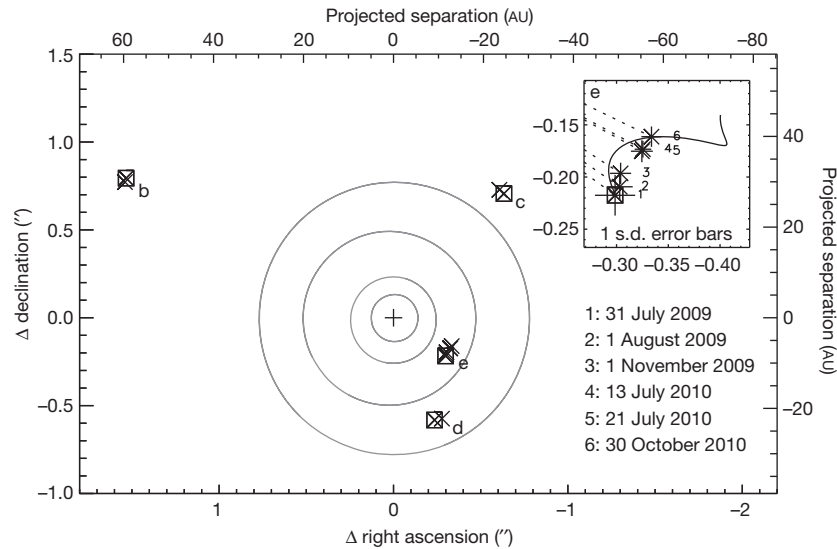


Figure 2 | HR 8799e 2009–10 astrometry. Main figure, the 2009–10 orbital motions of the four planets—b, c, d, e. Crosses denote the positions for 2009 and 2010 first and last epochs for b, c and d, and for all six epochs for e. A square is drawn over the cross symbol of each planet's first epoch. Inset, a zoomed version of planet e's astrometry, including the expected motion (curved solid line) if it is an unrelated background object; each epoch is labelled by a number 1–6; a dashed line connects the star to each epoch data point; error bars, ± 1 s.d.

HR 8799e is located very near planets c and d in a K_s versus $K_s - L'$ colour–magnitude diagram, suggesting that all three planets have similar spectral shapes and bolometric luminosities. We, therefore, adopt the same luminosity for these three planets; however, given the larger photometric error-bars and sparse wavelength coverage associated with planet e, we have conservatively assigned to it a luminosity error (Table 1) twice as large as those for planets b, c and d¹. This luminosity estimate is consistent with empirically calibrated bolometric corrections for brown dwarfs⁷, although such corrections may be ill-suited

Planet e is confirmed as bound to HR 8799, and it is moving at 46 ± 10 mas yr⁻¹ anticlockwise. In the main figure, the orbits of the giant planets of our Solar System (Jupiter, Saturn, Uranus and Neptune) are drawn to scale (light grey circles). With a period of ~ 50 years, the orbit of HR 8799e will be rapidly constrained by future observations; at our current measurement accuracy, it will be possible to measure orbital curvature after only 2 years.

for young planets with distinct spectra and colours. Using the two overlapping age ranges outlined above and the evolutionary models described in the HR 8799bcd discovery article¹, we estimate the mass of planet e to be $7^{+3}_{-2} M_{\text{Jup}}$ (30 Myr) and $10^{+3}_{-3} M_{\text{Jup}}$ (60 Myr), where M_{Jup} is the mass of Jupiter; see Fig. 3. The broadband photometry of planets b, c, and d provide strong evidence for significant atmospheric cloud coverage, while recent spectroscopy of planets b and c show evidence for non-equilibrium CO/CH₄ chemistry^{8–10}. Given the limited wavelength coverage of the discovery images for planet e, it is too early to

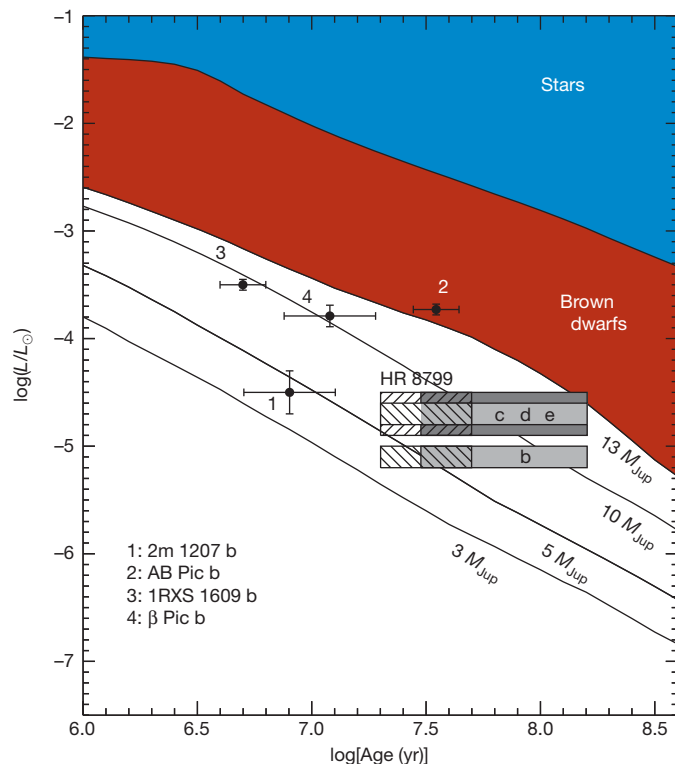


Figure 3 | The mass of HR 8799e from the age–luminosity relationship.

Solid lines are luminosity-versus-age tracks for planet evolution models²⁵ (luminosities are normalized to the solar luminosity, L_{\odot}). Objects above $13 M_{\text{Jup}}$ are typically considered to be outside the planet-mass regime; however, the tail end of the planet distribution found by radial velocity surveys extends above this IAU-defined mass limit²⁶. Boxed areas show adopted luminosity ranges (± 1 s.d.) and estimated age ranges for the four HR 8799 planets: cross-hatched boxes show age range 30^{+100}_{-10} Myr; grey boxes show age range 60^{+20}_{-30} Myr; planets c, d and e have similar luminosities, but the luminosity uncertainty for e is larger and indicated by the darker box/opposite hatch. For comparison, the ages and luminosities of four recently imaged planet-mass companions near other stars are indicated (numbered 1–4; see key on figure) showing 1 s.d. error bars for the luminosity and estimated age ranges). An asteroseismology study suggested that the HR 8799 system might be as old as ~ 1 Gyr (ref. 27), but it is highly unlikely that such an old star would have very massive debris belts^{21,28}; such an age would also require planetary masses far too high for long-term stability¹³. The older age also requires an inclination of the stellar pole relative to the line of sight of $\sim 50^\circ$, inconsistent with the nearly face-on planetary system and the $\sim 25^\circ$ inclination upper limit measured from Spitzer images of the outer dust halo⁴. Mass estimates based on any existing evolutionary model at ages as young as 20–30 Myr suffer from unconstrained initial formation conditions; the masses presented here could be underestimated if the planets formed by core-accretion, though ‘cold start’ core-accretion models²⁹ do not reproduce the observed luminosity for any combination of mass and age. While this additional uncertainty can lead temporarily to ambiguity about the planets’ masses and formation history (core-accretion or gravitation instability), it does highlight the importance of discovering and following in orbit planet-mass companions at ages when formation processes are important.

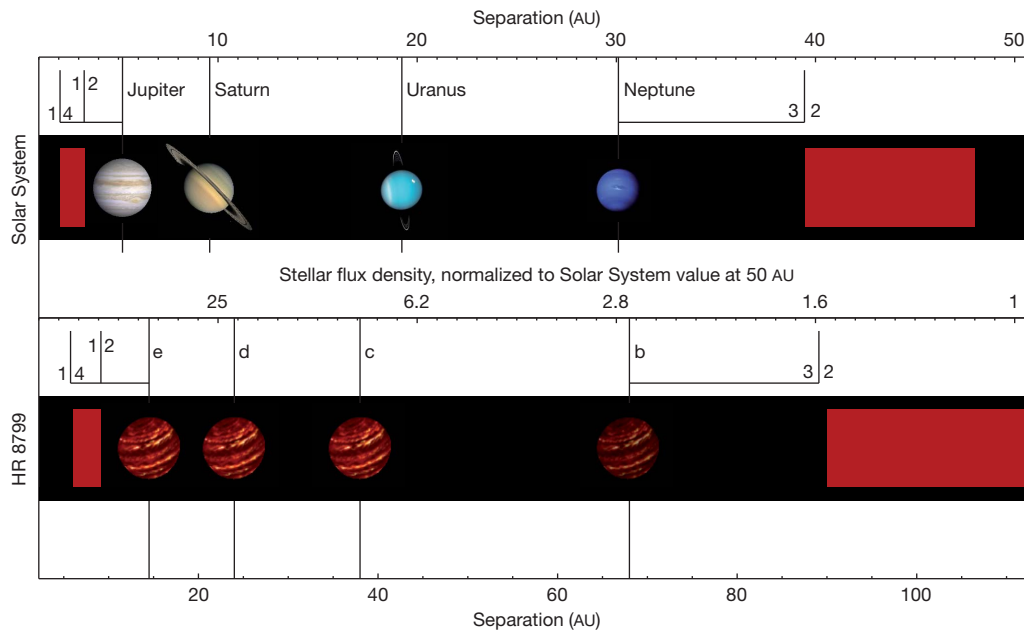


Figure 4 | Comparison of HR 8799 and our Solar System. Top, Solar System; bottom, the HR 8799 system. HR 8799 infrared data indicate the existence of an asteroid belt analogue located at 6–15 AU (we have moved the estimated outer edge of this belt to 10 AU because of planet e's estimated chaotic region³⁰), a Edgeworth-Kuiper-belt-like debris disk at >90 AU and a small particle halo extending up to 1,000 AU (ref. 4). The red shaded regions represent the locations of the inner and outer debris belts in both systems (the Solar System Oort comet cloud and the HR 8799 halo are not shown). The horizontal axis of the HR 8799 plot is compressed by the square root of the ratio of the luminosity of HR 8799 ($4.92 \pm 0.41 L_{\odot}$) to that of the Sun to show both systems over the same equilibrium temperature range. Given the current apparent separations of the

four planets of HR 8799 and the preferred locations of the inner warm debris disk and the inner edge of the outer cold disk (90 AU)⁴, then (1) the indicated 4:1 and 2:1 period resonances between the inner/outer edge of the warm debris belt and planet e, and (2) a 3:2 mean motion resonance of b with the inner edge of the outer cold disk, are both consistent with the observations. By analogy, the inner and outer edges of the main asteroid belt of our Solar System are, respectively, in 4:1 and 2:1 mean motion resonances with Jupiter. Many members of the Edgeworth-Kuiper belt, including Pluto, are in a 3:2 mean motion orbital resonance with Neptune. Solar System planet images are from NASA; HR 8799 artwork is from Gemini Observatory and L. Cook. Planet diameters are not to scale.

say much about the atmospheric properties of this particular planet; however, given that its near-infrared colour is similar to those of the other three planets, we can anticipate similar cloud structure and chemistry for planet e.

Stability analyses^{11–13} have shown that the original three-planet system may be in a mean motion period resonance with an upper limit on planetary masses of $\sim 20 M_{\text{Jup}}$ assuming an age of up to 100 Myr. With the discovery of a fourth planet, we revisit the stability of this system. We searched for stable orbital configurations with the HYBRID/Mercury package¹⁴ using the 30-Myr (5, 7, 7 and 7 M_{Jup} for b, c, d and e respectively) and 60-Myr (7, 10, 10 and 10 M_{Jup}) masses. In our preliminary search, we held the parameters for b, c and d fixed to those matching either the single resonance (1:2 resonance between planets c and d only) or double resonance (1:2:4 resonance between planets b, c, and d) stable solutions found to date¹³, but allowed the parameters for e to vary within the regime allowed by our observations. On the basis of the single-resonance configuration and using the 30-Myr masses, in 100,000 trials seven solutions for e were found that are stable for at least 160 Myr (the maximum estimated age of the system), and an additional five solutions were found that are stable for over 100 Myr. All maximally stable solutions have a semimajor axis of ~ 14.5 AU, with planets c, d and e in a 1:2:4 resonance (planet b not in resonance). A set of 100,000 trials was also performed using the 60-Myr masses, but only two solutions were found that are stable for over 100 Myr, each of which requires a semimajor axis of ~ 12.5 AU, 4σ away from our astrometry. This is suggestive that a younger system age and lower planet masses are preferred, although a much more thorough search of parameter space is required (see the Supplementary Information for tables of stable solutions).

The mechanism for the formation of this system is unclear. It is challenging for gravitational-instability fragmentation to occur at $a < 20$ –40 AU (refs 15,16)—ruling that mechanism out for *in situ*

formation of planet e. In addition, disk instability mechanisms preferentially form objects more massive than these planets^{16,17}. If the HR 8799 system represented low-mass examples of such a population, brown-dwarf companions to young massive stars would be plentiful. Nearby young star surveys^{18–20} and our nearly complete survey of 80 stars with similar masses and ages to HR 8799 have discovered no such population of brown dwarf companions. HR 8799e and possibly d are close enough to the primary star to have formed by bottom-up accretion *in situ*¹⁵, but planets b and c are located where the collisional timescale is conventionally thought to be too low for core accretion to form giant planets before the system's gas is depleted. A hybrid process with different planets forming through different mechanisms cannot be ruled out, but seems unlikely with the similar masses and dynamical properties of the four planets. It is possible that one mechanism dominated the other and the planets later migrated to their current positions. The HR 8799 debris disk is especially massive for a star of its age (or for any older main sequence star²¹), which could indicate an extremely dense protoplanetary disk. Such a disk could have induced significant migration, moving planets formed by disk-instability inward, or the disk could have damped the residual eccentricity from multi-planet gravitational interactions that moved core-accretion planets outward. The massive debris disk and the lack of higher-mass analogues to this system do suggest that HR 8799 represents the high-mass end of planet formation.

The HR 8799 system does show interesting similarities with our Solar System; all giant planets are located past the estimated snow line of each system (~ 2.7 AU for the Solar System, ~ 6 AU for HR 8799), and the debris belts of each system are located at similar equilibrium temperatures (Fig. 4). With its four massive planets, massive debris belts and large scale, the HR 8799 planetary system is an amazing example of extreme systems that can form around stars.

Received 5 November; accepted 18 November 2010.

Published online 8 December 2010.

1. Marois, C. *et al.* Direct imaging of multiple planets orbiting the star HR 8799. *Science* **322**, 1348–1352 (2008).
2. Kuiper, G. P. On the origin of the Solar System. *Proc. Natl Acad. Sci. USA* **37**, 1–14 (1951).
3. Mizuno, H. Formation of the giant planets. *Prog. Theor. Phys.* **64**, 544–557 (1980).
4. Su, K. Y. L. *et al.* The debris disk around HR 8799. *Astrophys. J.* **705**, 314–327 (2009).
5. Moór, A. *et al.* Nearby debris disk systems with high fractional luminosity reconsidered. *Astrophys. J.* **644**, 525–542 (2006).
6. Torres, C. A. O., Quast, G. R., Melo, C. H. F. & Sterzik, M. F. in *Handbook of Star Forming Regions Vol. II, The Southern Sky* (ed. Reipurth, B.) 757–812 (ASP Monograph Publications, MP 005, 2008).
7. Golimowsky, D. A. *et al.* L' and M' photometry of ultracool dwarfs. *Astrophys. J.* **127**, 3516–3536 (2004).
8. Hinz, P. M. *et al.* Thermal infrared MMTAO observations of the HR 8799 planetary system. *Astrophys. J.* **716**, 417–426 (2010).
9. Janson, M., Bergfors, C., Goto, M., Brandner, W. & Lafrenière, D. Spatially resolved spectroscopy of the exoplanet HR 8799 c. *Astrophys. J.* **710**, L35–L38 (2010).
10. Bowler, B. P., Liu, M. C., Dupuy, T. J. & Cushing, M. C. Near-infrared spectroscopy of the extrasolar planet HR 8799 b. *Astrophys. J.* **723**, 850–868 (2010).
11. Goździewski, K. & Migaszewski, C. Is the HR 8799 extrasolar system destined for planetary scattering? *Mon. Not. R. Astron. Soc.* **397**, L16–L20 (2009).
12. Reidemeister, M. *et al.* A possible architecture of the planetary system HR 8799. *Astron. Astrophys.* **503**, 247–258 (2009).
13. Fabrycky, D. C. & Murray-Clay, R. A. Stability of the directly imaged multiplanet system HR 8799: resonance and masses. *Astrophys. J.* **710**, 1408–1421 (2010).
14. Chambers, J. E. A hybrid symplectic integrator that permits close encounters between massive bodies. *Mon. Not. R. Astron. Soc.* **304**, 793–799 (1999).
15. Dodson-Robinson, S. E., Veras, D., Ford, E. B. & Beichman, C. A. The formation mechanism of gas giants on wide orbits. *Astrophys. J.* **707**, 79–88 (2009).
16. Kratter, K. M., Murray-Clay, R. A. & Youdin, A. N. The runts of the litter: why planets formed through gravitational instability can only be failed binary stars. *Astrophys. J.* **710**, 1375–1386 (2010).
17. Stamatellos, D. & Whitworth, A. P. The properties of brown dwarfs and low-mass hydrogen-burning stars formed by disc fragmentation. *Mon. Not. R. Astron. Soc.* **392**, 413–427 (2009).
18. Lafrenière, D. *et al.* The Gemini Deep Planet Survey. *Astrophys. J.* **670**, 1367–1390 (2007).
19. Nielsen, E. & Close, L. M. A uniform analysis of 118 stars with high-contrast imaging: long-period extrasolar giant planets are rare around Sun-like stars. *Astrophys. J.* **717**, 878–896 (2010).
20. Chauvin, G. *et al.* Deep imaging survey of young, nearby austral stars. VLT/NACO near-infrared Lyot-coronagraphic observations. *Astron. Astrophys.* **509**, A52–A68 (2010).
21. Rhee, J. H., Song, I., Zuckerman, B. & McElwain, M. Characterization of dusty debris disks: the IRAS and Hipparcos catalogs. *Astrophys. J.* **660**, 1556–1571 (2007).
22. Marois, C., Lafrenière, D., Doyon, R., Macintosh, B. & Nadeau, D. Angular differential imaging: a powerful high-contrast imaging technique. *Astrophys. J.* **641**, 556–564 (2006).
23. Lafrenière, D., Marois, C., Doyon, R., Nadeau, D. & Artigau, É. A new algorithm for point-spread function subtraction in high-contrast imaging: a demonstration with angular differential imaging. *Astrophys. J.* **660**, 770–780 (2007).
24. Marois, C., Macintosh, B. & Véran, J.-P. Exoplanet imaging with LOCI processing: photometry and astrometry with the new SOSIE pipeline. *Proc. SPIE* **7736**, 77361J–77361J-12 (2010).
25. Baraffe, I., Chabrier, G., Barman, T. S., Allard, F. & Hauschildt, P. H. Evolutionary models for cool brown dwarfs and extrasolar giant planets. The case of HD 209458. *Astron. Astrophys.* **402**, 701–712 (2003).
26. Eggenberger, A. & Udry, S. Detection and characterization of extrasolar planets through Doppler spectroscopy. *EAS Publ. Ser.* **41**, 27–75 (2010).
27. Moya, A. *et al.* Age determination of the HR8799 planetary system using asteroseismology. *Mon. Not. R. Astron. Soc.* **405**, L81–L85 (2010).
28. Gáspár, A. *et al.* The low level of debris disk activity at the time of the late heavy bombardment: a Spitzer study of Praesepe. *Astrophys. J.* **697**, 1578–1596 (2009).
29. Marley, M. S., Fortney, J., Hubickyj, O., Bodenheimer, P. & Lissauer, J. J. On the luminosity of young Jupiters. *Astrophys. J.* **655**, 541–549 (2007).
30. Malhotra, R. in *Solar System Formation and Evolution* (eds Lazzaro, D., Vieira Martins, R., Ferraz-Mello, S. & Fernandez, J.) 37–63 (ASP Conf. Ser. Vol. 149, 1998).

Supplementary Information is linked to the online version of the paper at www.nature.com/nature.

Acknowledgements We thank the Keck staff, particularly H. Lewis, B. Goodrich and J. Lyke, for support with the follow-up observations. We thank G. Laughlin and D.C. Fabrycky for discussions. Portions of this research were performed under the auspices of the US Department of Energy by LLNL and also supported in part by the NSF Center for Adaptive Optics. We acknowledge support by NASA grants to UCLA, LLNL and Lowell Observatory. The data were obtained at the W.M. Keck Observatory. This publication makes use of data products from the Two Micron All Sky Survey and the SIMBAD database.

Author Contributions The authors contributed equally to this work.

Author Information Reprints and permissions information is available at www.nature.com/reprints. The authors declare no competing financial interests. Readers are welcome to comment on the online version of this article at www.nature.com/nature. Correspondence and requests for materials should be addressed to C.M. (christian.marois@nrc-cnrc.gc.ca).

Spin-orbit qubit in a semiconductor nanowire

S. Nadj-Perge¹*, S. M. Frolov¹*, E. P. A. M. Bakkers^{1,2} & L. P. Kouwenhoven¹

Motion of electrons can influence their spins through a fundamental effect called spin-orbit interaction. This interaction provides a way to control spins electrically and thus lies at the foundation of spintronics¹. Even at the level of single electrons, the spin-orbit interaction has proven promising for coherent spin rotations². Here we implement a spin-orbit quantum bit (qubit) in an indium arsenide nanowire, where the spin-orbit interaction is so strong that spin and motion can no longer be separated^{3,4}. In this regime, we realize fast qubit rotations and universal single-qubit control using only electric fields; the qubits are hosted in single-electron quantum dots that are individually addressable. We enhance coherence by dynamically decoupling the qubits from the environment. Nanowires offer various advantages for quantum computing: they can serve as one-dimensional templates for scalable qubit registers, and it is possible to vary the material even during wire growth⁵. Such flexibility can be used to design wires with suppressed decoherence and to push semiconductor qubit fidelities towards error correction levels. Furthermore, electrical dots can be integrated with optical dots in p-n junction nanowires⁶. The coherence times achieved here are sufficient for the conversion of an electronic qubit into a photon, which can serve as a flying qubit for long-distance quantum communication.

Figure 1a shows a scanning electron microscope image of our nanowire device. Two electrodes, source and drain, are used to apply a voltage bias of 6 mV across the InAs nanowire. Voltages applied to five closely spaced, narrow gates underneath the nanowire create a confinement potential for two electrons separated by a tunnelling barrier. The defined structure is known as a double quantum dot in the (1, 1) charge configuration⁷.

Each of the two electrons represents a spin-orbit qubit (Fig. 1b). In the presence of strong spin-orbit coupling, neither spin nor orbital number is separately well defined. Instead, each qubit state is a spin-orbit doublet, $\uparrow\uparrow$ and $\downarrow\downarrow$. Similar to pure spin states, a magnetic field, B , controls the energy splitting, $E_Z = g\mu_B B$, between spin-orbit states, where g is the Landé g -factor in a quantum dot and μ_B is the Bohr magneton. The crucial difference from a spin qubit is that in a spin-orbit qubit the orbital part of the spin-orbit wavefunction is used for qubit manipulation^{2,8}.

The qubit read-out and initialization rely on the effect of spin blockade^{9,10}. A source-drain bias induces a current of electrons passing one by one through the double dot. The process of electron transfer between the dots can be allowed energetically but blocked by a spin selection rule. For instance, a (1, 1) triplet state cannot change into a (0, 2) singlet state. This stops the left-hand electron from tunnelling into the right-hand dot, and thereby blocks the current. In practice, the double dot becomes blocked only in a parallel configuration, that is, in either a ($\uparrow\uparrow$, $\uparrow\uparrow$) or a ($\downarrow\downarrow$, $\downarrow\downarrow$) state, because antiparallel states decay quickly to a non-blocked singlet state^{11,12}. By idling the qubits in the parameter range of spin blockade, they will be initialized in one of the two parallel states with equal probability. We note that spin-orbit and hyperfine interactions also mediate a slower decay of parallel states into (0, 2)^{7,9,10}. This reduces the read-out fidelity to 70–80% (Supplementary Information, section 5.1).

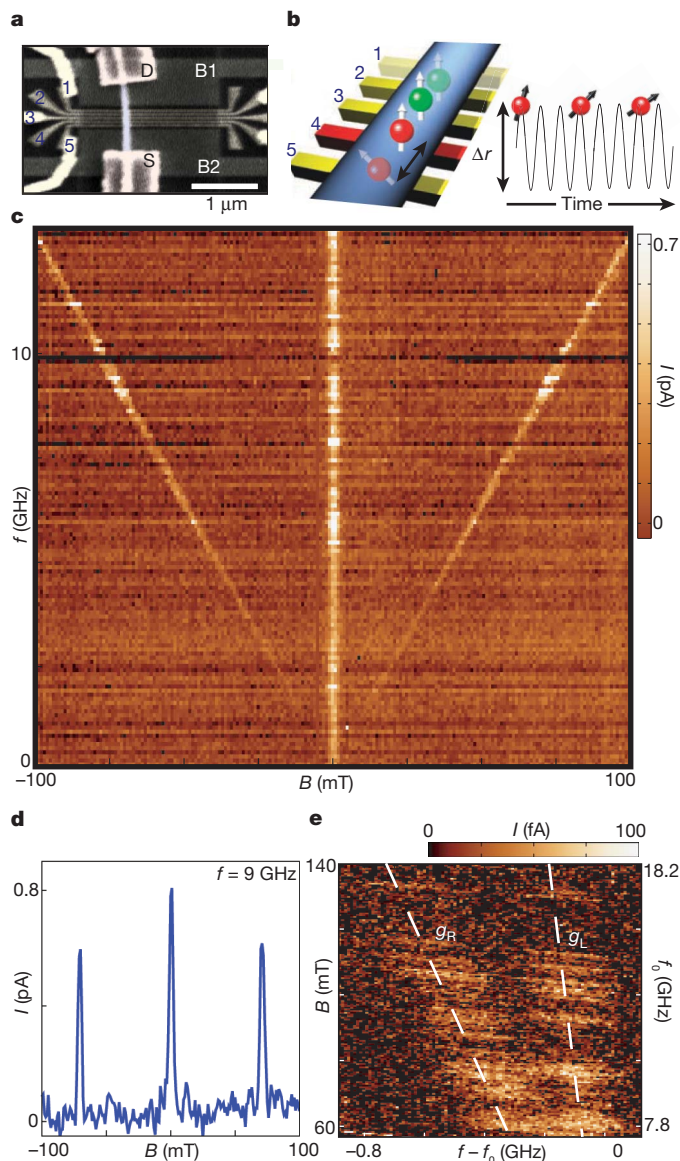


Figure 1 | Electric-dipole spin resonance. **a**, Scanning electron microscope image of a prototype device showing source (S) and drain (D) contacts, narrow gates one to five and wide gates B1 and B2. **b**, Left-hand (red) and right-hand (green) quantum dots are formed between gates two and five. A microwave electric field applied to gate four oscillates both electrons with amplitude $\sim \Delta r$, inducing EDSR. **c**, Spin blockade is lifted near $B = 0$ and on resonance when $f = g\mu_B B/h$. Here the microwave power is $P = -42$ dBm. I , current. **d**, Trace extracted from **c** at $f = 9$ GHz. **e**, Magnified view of the EDSR line, which is split at high B values owing to the difference between g_L and g_R . At each B value, the frequency is swept in a fixed range around $f_0 = g\mu_B B/h$ ($g = 9.28$). The current at resonance varies owing to non-monotonic microwave transmission.

¹Kavli Institute of Nanoscience, Delft University of Technology, 2600 GA Delft, The Netherlands. ²Department of Applied Physics, Eindhoven University of Technology, 5600 MB Eindhoven, The Netherlands.

*These authors contributed equally to this work.

A microwave-frequency electric field applied to gate four oscillates electrons inside the nanowire (Fig. 1b). This motion can induce resonant transitions between spin-orbit states by means of an effect called electric-dipole spin resonance^{2,8,13–16} (EDSR). Such transitions are expected when the frequency of the a.c. electric field is equal to the Larmor frequency, $f_0 = g\mu_B B/h$ (h , Planck's constant). At resonance, the spin-orbit state of the double dot rapidly changes from parallel to antiparallel. The antiparallel state does not experience spin blockade, so the left-hand electron tunnels to the right, thereby contributing to the current. Figure 1c shows the resonance as a V shape that maps out the Larmor frequency in the plane of microwave frequency and magnetic field.

The V-shaped resonance signal vanishes in the vicinity of zero magnetic field. This behaviour is consistent with spin-orbit mediated EDSR: the effect of spin-orbit interaction must cancel at zero field owing to time-reversal symmetry^{2,16}. The field-dependent EDSR strength rules out a.c. magnetic field and hyperfine field gradient as possible mechanisms. A g -tensor modulation in our nanowires is estimated to be too weak to drive EDSR (Supplementary Information, section 2). The current peak near zero magnetic field arises from the hyperfine interaction between electron spin and the nuclear spin bath^{11,12}. From the width of this hyperfine-induced peak, we extract the root mean squared magnetic field generated by the fluctuating nuclear spins, $B_N = 0.66 \pm 0.1$ mT (ref. 17). The width of the EDSR line at low microwave power is also consistent with broadening due to fluctuating nuclear spins¹⁸ (that is, the side EDSR peaks and the central hyperfine peak have comparable widths in Fig. 1d).

At higher magnetic field, the resonance line splits (Fig. 1e), indicating that the g -factors in the left- and right-hand dots, g_L and g_R , are different. This is expected for quantum dots of different sizes because confinement changes the effective g -factor¹⁹. We measured the confinement as the orbital excitation energy at the $(1, 0) \leftrightarrow (0, 1)$ transition and found 7.5 ± 0.1 meV for the left-hand dot and 9.0 ± 0.2 meV for the right-hand dot. A smaller orbital excitation energy should correspond to a larger g -factor in InAs; therefore, we assign the values obtained from Fig. 1e to the left- and right-hand dots as follows: $|g_L| = 9.2 \pm 0.1$ and $|g_R| = 8.9 \pm 0.1$. At frequencies above 10 GHz, the two resonances are more than a linewidth apart, allowing us to control the left- and right-hand qubits separately⁸.

Coherent control over spin-orbit states is demonstrated in a time-resolved measurement of Rabi oscillations^{2,18,20}, explained in Fig. 2a, b. Periodic square pulses shift the relative positions of the energy levels in the two dots between spin blockade and Coulomb blockade. First, the double dot is initialized in a parallel state by idling in spin blockade. This is followed by a shift to Coulomb blockade, from which electrons cannot escape. While in Coulomb blockade, a resonant microwave burst is applied for a time τ_{burst} to induce qubit rotation. Finally, the double dot is brought back into spin blockade for read-out. At the read-out stage, the probability of the left-hand electron tunnelling out is proportional to the probability of projecting the final state onto the $(1, 1)$ singlet. This cycle is repeated continuously.

The singlet component in the final state is measured as the d.c. current. The current oscillates as τ_{burst} is varied, reflecting Rabi oscillations of the driven qubit (Fig. 2c). Rabi oscillations are observed for driving frequencies in the range $f \approx 9$ –19 GHz. Rabi oscillations are not observed at lower frequencies (and lower magnetic fields) because the effective spin-orbit field, B_{SO} , is less than B_N , such that nuclear fluctuations average out the coherent qubit dynamics. We note that the observation of incoherent EDSR (Fig. 1c) requires a much smaller B_{SO} , because even qubit rotations with a random phase contribute to extra current near resonance.

Our highest Rabi frequency is $f_R = 58 \pm 2$ MHz (Fig. 2d), achieved at $f = 13$ GHz. The field B_{SO} is expected to grow with B (ref. 16); however, at higher driving frequencies the Rabi frequency is limited by the maximum microwave source power and by the reduced transmission of the microwave circuit. With the strongest driving, the

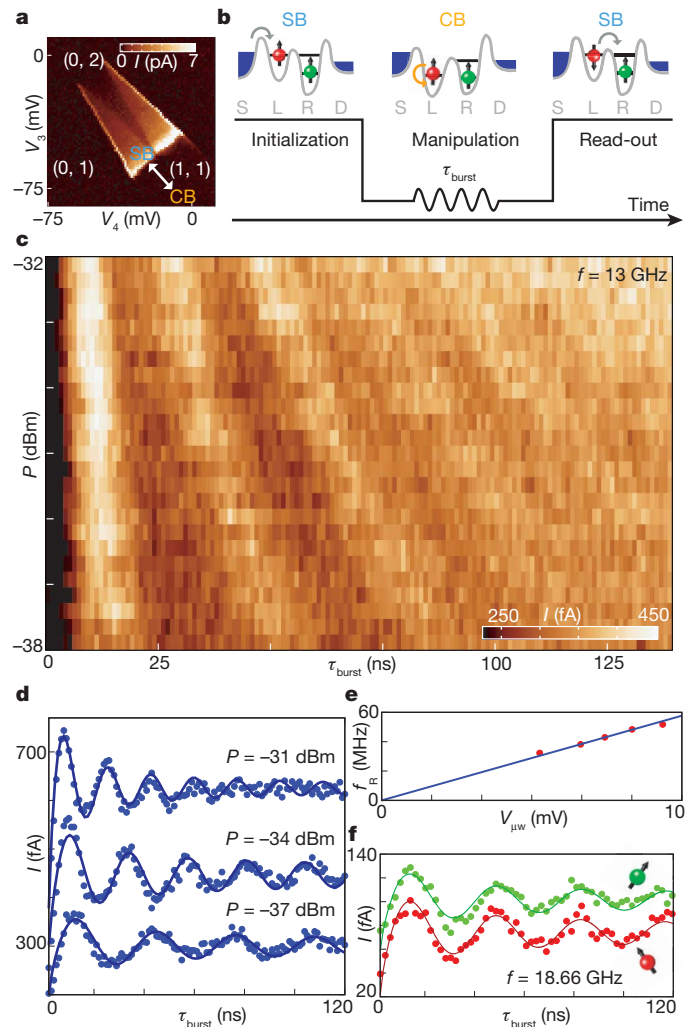


Figure 2 | Rabi oscillations. **a**, Charge stability diagram obtained by sweeping the voltages, V_3 and V_4 , on gates three and four. CB, Coulomb blockade; SB, spin blockade. **b**, Measurement cycle with diagrams showing electrochemical potentials of the source (S), drain (D), left-hand dot (L) and right-hand dot (R) for each stage. **c**, Rabi oscillations for a range of microwave powers at $f = 13$ GHz and $B = 102$ mT. **d**, Rabi oscillations at $f = 13$ GHz, with fits to $a \cos(f_R \tau_{\text{burst}} + \varphi) / \tau^d + b$ ($d = 0.8$ for top trace and $d = 0.5$ for the bottom two traces). Rabi frequencies are 58 ± 2 , 43 ± 2 and 32 ± 2 MHz (top to bottom). Linear slopes of 2 fA ns^{-1} , 1 fA ns^{-1} and 0.3 fA ns^{-1} (top to bottom) are subtracted to flatten the average. They are attributed to photon-assisted tunnelling. Traces are offset vertically for clarity. **e**, Dependence of f_R on driving amplitude, $V_{\mu w} = 2(P \times 50 \Omega)^{0.5}$, with a linear fit. **f**, Rabi oscillations with separated addressing of the left- and right-hand qubits at $f = 18.66$ GHz and $B = 144$ mT (red) and 149 mT (green), with $f_R = 29 \pm 2$ MHz fitted to the expression used in **d**.

amplitude of the orbital oscillation is estimated to reach 1 nm. The qubit state is flipped in ~ 110 microwave periods, and thus rotated by $\sim 1.6^\circ$ per cycle of the orbital motion.

We can resolve up to five Rabi oscillation periods. The damping of the oscillations at a microwave power of $P < -32$ dBm is consistent with a $\sim \tau_{\text{burst}}^{-0.5}$ decay envelope observed previously for rotations of a single spin interacting with a slow nuclear bath²¹. We have verified that the relaxation time, T_1 , does not limit coherent evolution on timescales up to $1 \mu\text{s}$ (Supplementary Information, section 3). The qubit manipulation fidelity is $48 \pm 2\%$, estimated by comparing the values of B_{SO} and B_N (ref. 18; Supplementary Information, section 5.3). As expected, the Rabi frequency is proportional to the square root of the microwave power, P , applied to the gate (Fig. 2e). Absorption of microwave photons allows interdot tunnelling regardless of the qubit state. This

effect probably accelerates the decay of Rabi oscillations near the highest power^{2,18} (Fig. 2d, top trace). However, the apparent photon-assisted tunnelling is substantially reduced for $P < -32$ dBm, although Rabi frequencies remain high.

In Fig. 2c, d only the left qubit is rotated. Figure 2f shows data from coherent rotations of either the left- or the right-hand qubit induced at the same microwave frequency but at two different magnetic fields, which correspond to the two EDSR resonance conditions shown in Fig. 1e (ref. 22; Supplementary information, section 4).

In the Rabi experiment, the qubit state is rotated around only one axis. This is not enough for full qubit operation, which ultimately requires the preparation of an arbitrary superposition of \uparrow and \downarrow , known as universal control^{23–25}. Such ability is demonstrated in a Ramsey experiment (Fig. 3a, b). Here two short bursts with different microwave phases are applied during the manipulation stage. In the reference frame that rotates at the Larmor frequency, the qubit is initially rotated from $|+z\rangle$ to $|-y\rangle$ on the Bloch sphere by applying a $\pi/2$ rotation around the x axis. After a delay time, τ , we apply a $3\pi/2$ pulse. The tunable phase of the microwave signal, ϕ , sets the axis of the second rotation ($\phi = 0$ corresponds to a rotation around x and $\phi = \pi/2$ corresponds to a rotation around y). The final z component depends on the axis of the second rotation as well as on dephasing. The double-dot current oscillates with ϕ , revealing Ramsey fringes (Fig. 3a). The contrast of the Ramsey fringes decreases with increasing τ , allowing us to determine the inhomogeneous dephasing time, $T_2^* = 8 \pm 1$ ns (Fig. 3b).

Coherence can be extended by a Hahn echo technique, which partly cancels dephasing coming from a slowly varying nuclear magnetic field (Fig. 3c, d). In the echo sequence, a π pulse is applied halfway between the two $\pi/2$ pulses. The contrast of the Ramsey fringes is

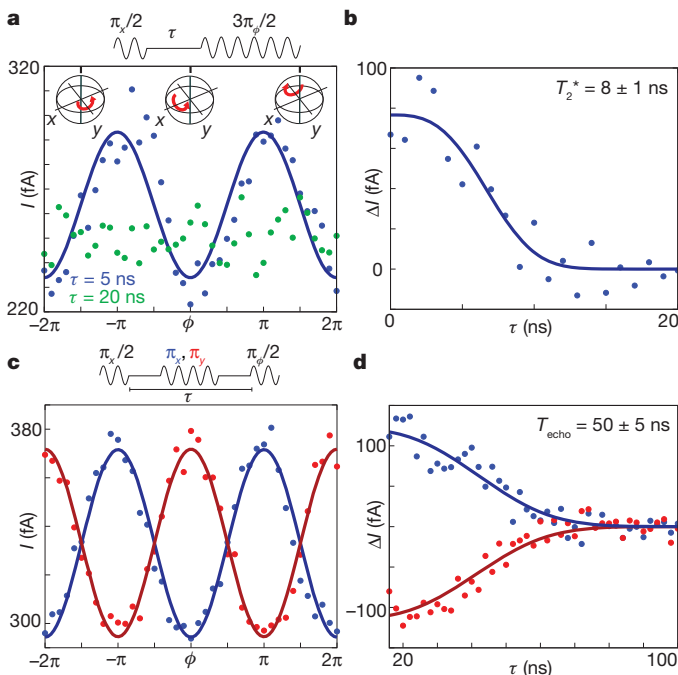


Figure 3 | Universal qubit control and coherence times. **a**, Ramsey experiment sequence (top) and measurement of fringes $I(\phi)$ for $\tau = 5$ and 20 ns. The axes of the second rotation are indicated with red arrows on the Bloch spheres for three values of ϕ . **b**, Decay of the Ramsey fringe contrast, $\Delta I = I(\phi = \pi) - I(\phi = 0)$, fitted to $\exp[-(\tau/T_2^*)^2]$. **c**, Hahn echo sequence (top) extends fringe contrast beyond $\tau = 34$ ns. Fringes for two orthogonal phases of the π pulse (π_x , blue; π_y , red) are out of phase. **d**, Decay of the fringe contrast obtained for the two Hahn echo sequences (π_x , blue; π_y , red) is used to extract T_{echo} from a fit to $\exp[-(\tau/T_{\text{echo}})^3]$. A fit to $\exp[-(\tau/T_{\text{echo}})^4]$ gives a similar value of T_{echo} . In this figure, the duration of a π pulse is 14 ns, with $P = -35$ dBm, $f = 13$ GHz and $B = 102$ mT.

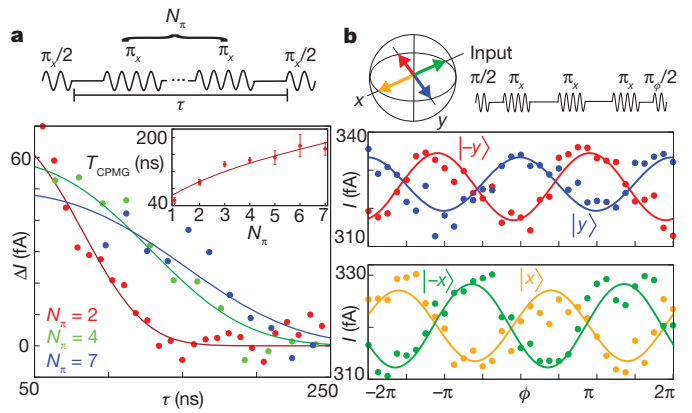


Figure 4 | Dynamical decoupling. **a**, Decay of the contrast of the Ramsey fringes for CPMG sequences (top) with an increasing number of π pulses, N_π . Solid lines are fits to $\exp[-(\tau/T_{\text{CPMG}})^3]$. Inset, coherence times T_{CPMG} versus N_π are fitted to N_π^d with $d = 0.53 \pm 0.1$. Error bars are standard deviations of $\Delta I(\tau)$ fits. **b**, Ramsey fringes for four different phases of the initial $\pi/2$ pulse obtained for an $N_\pi = 3$ CPMG sequence (shown above the panel) with $\tau = 150$ ns. The input states are indicated with arrows on the Bloch sphere. In this figure, the duration of a π pulse is 8 ns with $P = -32$ dBm, $f = 13$ GHz and $B = 102$ mT.

extended to longer coherent evolution times by performing Hahn echo (Fig. 3c). The phase of the fringes can be flipped depending on whether the π rotation is around the x axis (π_x) or around the y axis (π_y). Hahn echoes of both these types increase the coherence time to $T_{\text{echo}} = 50 \pm 5$ ns (Fig. 3d).

Gate-defined spin qubits were previously only realized in lateral quantum dots in GaAs–AlGaAs two-dimensional electron gases⁹. Owing to the much stronger spin–orbit interaction in InAs, the Rabi frequencies in our nanowire spin–orbit qubits are more than an order of magnitude higher than in GaAs dots². Dephasing times, T_2^* , are of the same order in InAs and GaAs quantum dots^{23,26}. The relatively low T_{echo} found in the present work encourages further study. A likely reason is faster nuclear spin fluctuations caused by the large nuclear spin of indium, $I = 9/2$. However, charge noise and nearby paramagnetic impurities cannot be ruled out as significant dephasing sources (Supplementary Information, section 6). Nanowires offer future solutions for suppressing the effects of nuclear spins, such as nanowires with sections of nuclear-spin-free silicon. The qubit can be stored in a silicon section of the nanowire and moved to an InAs section only for manipulation using spin–orbit interaction.

In the present qubit, longer coherence times can already be achieved by Carr–Purcell–Meiboom–Gill (CPMG) dynamical-decoupling pulse sequences^{27,28} (Fig. 4a). Here a single echo π pulse is replaced with an array of equidistant π pulses, each of which refocuses the qubit state. The total time of coherent evolution grows as the number of π pulses is increased (Fig. 4a, inset). Importantly, an arbitrarily prepared qubit state in the x – y plane is preserved during the decoupling sequence. This is verified in Fig. 4b, which shows that the phase of the initial $\pi/2$ pulse determines the phase of the Ramsey fringes. Similar evaluation was carried out for CPMG sequences of up to seven π pulses. In future, more efficient dynamical decoupling can be achieved using nuclear spin state preparation^{27,29} in combination with faster π pulses or adiabatic pulse techniques³⁰.

METHODS SUMMARY

We fabricate devices on undoped silicon substrates. Instead of a global back gate, two wide gates, B1 and B2, are located underneath the nanowire contacts (Fig. 1a). They are set to constant positive voltages to enhance conductance through the nanowire. The wide gates are covered by a 50-nm layer of Si_3N_4 dielectric; on top of this layer narrow gates and a 25-nm layer of Si_3N_4 are deposited. InAs nanowires with diameters between 50 and 80 nm are grown nearly free of stacking faults using metal-organic vapour phase epitaxy. The wires have the wurtzite crystal symmetry

with the c axis along the long nanowire axis. Nanowires are transferred in air from the mother chip to the device substrates, which already contain Ti–Au gates. Selected wires are contacted with ohmic Ti–Al electrodes, and during the same step contacts are made to the gates. We make measurements in a He^3 refrigerator at $T = 300$ mK. A magnetic field is applied in the plane of the substrate at an angle of $45^\circ \pm 5^\circ$ with respect to the nanowire. We create high-frequency pulses using two arbitrary waveform generators (one gigasample per second) and a 20-GHz, 23-dBm microwave vector source. Pulses are delivered to the sample through silver-plated CuNi coaxial lines with 36-dB attenuators followed by coplanar striplines printed on the sample holder. Square pulses are applied synchronously to gates two and four. Microwave bursts are applied to gate four. A measurement cycle lasts 2 μs in the coherent rotations detailed in Fig. 2f. In the rest of the paper, a cycle lasts 600 ns and each data point is averaged over 5–40 million cycles. The pulse period should remain less than 2 μs to detect the double-dot current, which is limited by the noise floor of the d.c. current amplifier.

Received 29 September; accepted 10 November 2010.

- Datta, S. & Das, B. Electronic analog of the electrooptic modulator. *Appl. Phys. Lett.* **56**, 665–667 (1990).
- Nowack, K. C., Koppens, F. H. L., Nazarov, Y. V. & Vandersypen, L. M. K. Coherent control of a single electron spin with electric fields. *Science* **318**, 1430–1433 (2007).
- Fasth, C., Fuhrer, A., Samuelson, L., Golovach, V. N. & Loss, D. Direct measurement of the spin-orbit interaction in a two-electron InAs nanowire quantum dot. *Phys. Rev. Lett.* **98**, 266801 (2007).
- Pfund, A., Shorubalko, I., Ensslin, K. & Leturcq, R. Spin-state mixing in InAs double quantum dots. *Phys. Rev. B* **76**, 161308 (2007).
- Minot, E. D. *et al.* Single quantum dot nanowire LEDs. *Nano Lett.* **7**, 367–371 (2007).
- van Weert, M. H. M. *et al.* Selective excitation and detection of spin states in a single nanowire quantum dot. *Nano Lett.* **9**, 1989–1993 (2009).
- Nadj-Perge, S. *et al.* Disentangling the effects of spin-orbit and hyperfine interactions on spin blockade. *Phys. Rev. B* **81**, 201305 (2010).
- Pioro-Ladriere, M. *et al.* Electrically driven single-electron spin resonance in a slanting Zeeman field. *Nature Phys.* **4**, 776–779 (2008).
- Hanson, R., Kouwenhoven, L. P., Petta, J. R., Tarucha, S. & Vandersypen, L. M. K. Spins in few-electron quantum dots. *Rev. Mod. Phys.* **79**, 1217–1265 (2007).
- Pfund, A., Shorubalko, I., Ensslin, K. & Leturcq, R. Suppression of spin relaxation in an InAs nanowire double quantum dot. *Phys. Rev. Lett.* **99**, 036801 (2007).
- Koppens, F. H. L. *et al.* Control and detection of singlet-triplet mixing in a random nuclear field. *Science* **309**, 1346–1350 (2005).
- Johnson, A. C. *et al.* Triplet-singlet spin relaxation via nuclei in a double quantum dot. *Nature* **435**, 925–928 (2005).
- Rashba, E. I. & Efros, A. L. Orbital mechanisms of electron-spin manipulation by an electric field. *Phys. Rev. Lett.* **91**, 126405 (2003).
- Kato, Y. *et al.* Gigahertz electron spin manipulation using voltage-controlled g -tensor modulation. *Science* **299**, 1201–1204 (2003).
- Laird, E. A. *et al.* Hyperfine-mediated gate-driven electron spin resonance. *Phys. Rev. Lett.* **99**, 246601 (2007).
- Golovach, V. N., Borhani, M. & Loss, D. Electric-dipole-induced spin resonance in quantum dots. *Phys. Rev. B* **74**, 165319 (2006).
- Danon, J. & Nazarov, Y. V. Pauli spin blockade in the presence of strong spin-orbit coupling. *Phys. Rev. B* **80**, 041301 (2009).
18. Koppens, F. H. L. *et al.* Driven coherent oscillations of a single electron spin in a quantum dot. *Nature* **442**, 766–771 (2006).
19. Pryor, C. E. & Flatte, M. E. Lande g factors and orbital momentum quenching in semiconductor quantum dots. *Phys. Rev. Lett.* **96**, 026804 (2006).
20. Berezovsky, J., Mikkelsen, M. H., Stoltz, N. G., Coldren, L. A. & Awschalom, D. D. Picosecond coherent optical manipulation of a single electron spin in a quantum dot. *Science* **320**, 349–352 (2008).
21. Koppens, F. H. L. *et al.* Universal phase shift and nonexponential decay of driven single-spin oscillations. *Phys. Rev. Lett.* **99**, 106803 (2007).
22. Obata, T. *et al.* Coherent manipulation of individual electron spin in a double quantum dot integrated with a micromagnet. *Phys. Rev. B* **81**, 085317 (2010).
23. Koppens, F. H. L., Nowack, K. C. & Vandersypen, L. M. K. Spin echo of a single electron spin in a quantum dot. *Phys. Rev. Lett.* **100**, 236802 (2008).
24. Press, D., Ladd, T. D., Zhang, B. Y. & Yamamoto, Y. Complete quantum control of a single quantum dot spin using ultrafast optical pulses. *Nature* **456**, 218–221 (2008).
25. Foletti, S., Bluhm, H., Mahalu, D., Umansky, V. & Yacoby, A. Universal quantum control of two-electron spin quantum bits using dynamic nuclear polarization. *Nature Phys.* **5**, 903–908 (2009).
26. Petta, J. R. *et al.* Coherent manipulation of coupled electron spins in semiconductor quantum dots. *Science* **309**, 2180–2184 (2005).
27. Bluhm, H. *et al.* Long coherence of electron spins coupled to a nuclear spin bath. Preprint at (<http://arxiv.org/abs/1005.2995>) (2010).
28. Barthel, C., Medford, J., Marcus, C. M., Hanson, M. P. & Gossard, A. C. Interlaced dynamical decoupling and coherent operation of a singlet-triplet qubit. Preprint at (<http://arxiv.org/abs/1007.4255>) (2010).
29. Reilly, D. J. *et al.* Suppressing spin qubit dephasing by nuclear state preparation. *Science* **321**, 817–821 (2008).
30. Fuchs, G. D., Dobrovitski, V. V., Toyli, D. M., Heremans, F. J. & Awschalom, D. D. Gigahertz dynamics of a strongly driven single quantum spin. *Science* **326**, 1520–1522 (2009).

Supplementary Information is linked to the online version of the paper at www.nature.com/nature.

Acknowledgements We thank K. Nowack, R. Schouten, M. Laforest, K. Zuo, M. Hocevar, R. Algra, J. van Tilburg, M. Scheffler, G. de Lange, V. Dobrovitski, J. Danon, R. Hanson, R. Liu, Yu. V. Nazarov and L. Vandersypen for their help. This work has been supported by NWO/FOM (the Netherlands Organization for Scientific Research), an ERC Advanced Grant and through the DARPA program QUEST.

Author Contributions S.N.-P., S.M.F. and L.P.K. designed the experiments. S.N.-P. and S.M.F. performed the measurements and analysed the data. E.P.A.M.B. provided nanowires. All authors wrote the manuscript.

Author Information Reprints and permissions information is available at www.nature.com/reprints. The authors declare no competing financial interests. Readers are welcome to comment on the online version of this article at www.nature.com/nature. Correspondence and requests for materials should be addressed to L.P.K. (l.p.kouwenhoven@tudelft.nl).

Atom-by-atom spectroscopy at graphene edge

Kazu Suenaga¹ & Masanori Koshino¹

The properties of many nanoscale devices are sensitive to local atomic configurations, and so elemental identification and electronic state analysis at the scale of individual atoms is becoming increasingly important. For example, graphene is regarded as a promising candidate for future devices, and the electronic properties of nanodevices constructed from this material are in large part governed by the edge structures¹. The atomic configurations at graphene boundaries have been investigated by transmission electron microscopy and scanning tunnelling microscopy^{2–4}, but the electronic properties of these edge states have not yet been determined with atomic resolution. Whereas simple elemental analysis at the level of single atoms can now be achieved by means of annular dark field imaging⁵ or electron energy-loss spectroscopy^{6,7}, obtaining fine-structure spectroscopic information about individual light atoms such as those of carbon has been hampered by a combination of extremely weak signals and specimen damage by the electron beam. Here we overcome these difficulties to demonstrate site-specific single-atom spectroscopy at a graphene boundary, enabling direct investigation of the electronic and bonding structures of the edge atoms—in particular, discrimination of single-, double- and triple-coordinated carbon atoms is achieved with atomic resolution. By demonstrating how rich chemical information can be obtained from single atoms through energy-loss near-edge fine-structure analysis⁸, our results should open the way to exploring the local electronic structures of various nanodevices and individual molecules.

A low-voltage scanning transmission electron microscope (STEM) was used for the single-atom spectroscopy⁹. Flakes were cleaved from the synthetic highly oriented pyrolytic graphite (HOPG) and put onto the microgrids for energy-loss near-edge fine structure (ELNES)

analysis. STEM annular dark field (ADF) images indicate that the graphene flakes have open and active edges³ and that the edges are steadily etched by the incident electron beam when the probe-scanning is repeated at the same region (Supplementary Fig. 1). The accelerating voltage used here (60 kV) is below the critical energy predicted for severe knock-on damage¹⁰ and therefore the carbon atoms in bulk are mostly stable. Only the edge atoms are mobile during the observation, as indicated by the wiggling contrast frequently observed at the edge regions. The fast Fourier transformation of an ADF image of few-layer graphene shows that the spatial resolution of the experimental set-up is better than 0.106 nm (inset to Supplementary Fig. 1a) and so the hexagonal network of carbon atoms, separated by about 0.14 nm, is clearly visible in a monolayer region (Supplementary Fig. 1b). A probe of the same size and brightness was used for the following ELNES analysis.

Figure 1a shows a typical ADF image of the edge region of a single graphene layer. The hexagonal network of carbon atoms in bulk is visible on the right-hand side of the image and the vacuum region appears in black on the left-hand side. The possible carbon atom positions derived from the local intensity maxima of ADF signals are marked by yellow circles after an image-smoothing process in Fig. 1b. There is strong wiggle contrast at the edge regions and some of the atom positions cannot be completely identified. We note that some of the hexagonal networks are imperfect and considerably reconstructed at the edge region.

The typical ELNES spectra of carbon *K* (1s)-edge are displayed with their corresponding atomic positions in Fig. 1c. Figure 1d shows three characteristic carbon *K*-edge fine structures extracted using sequential electron energy-loss spectroscopy (EELS) with probe-scanning (known as the spectrum-image mode)¹¹. The spectrum in green was recorded at an atomic position in bulk (indicated by a green circle and arrow in

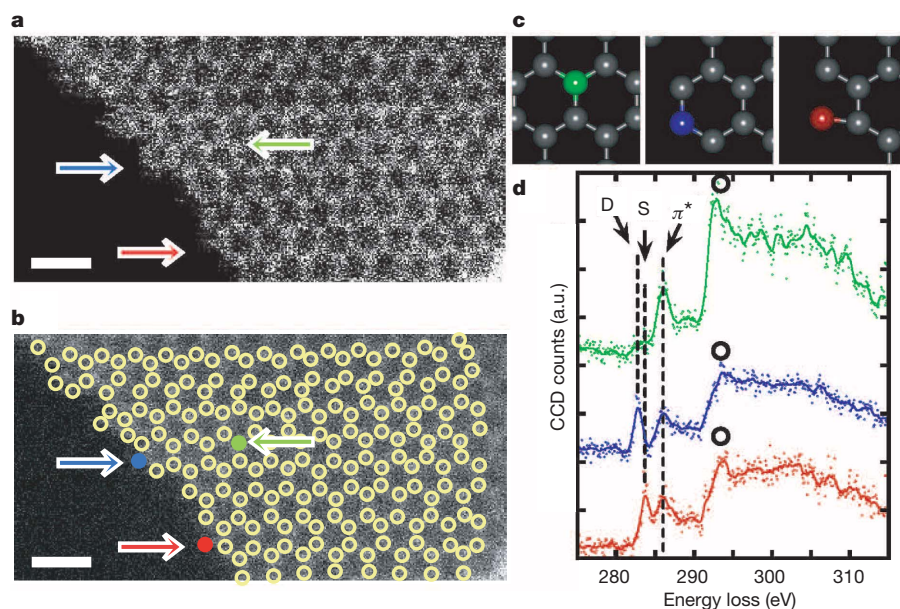


Figure 1 | Graphene edge spectroscopy. **a**, ADF image of single graphene layer at the edge region. No image-processing has been done. Atomic positions are marked by circles in a smoothed image (**b**). Scale bars, 0.5 nm. **c**, ELNES of carbon *K* (1s) spectra taken at the colour-coded atoms indicated in **b**. Green, blue and red spectra correspond to the normal sp^2 carbon atom, a double-coordinated atom and a single-coordinated atom, respectively. These different states of atomic coordination are marked by coloured arrows in **a** and **b** and illustrated in **c**. CCD, charge-coupled device.

¹Nanotube Research Center, National Institute of Advanced Industrial Science and Technology (AIST), AIST Central 5, Tsukuba 305-8565, Japan.

Fig. 1b) as a reference. This spectrum exhibits the features of typical sp^2 coordinated carbon atoms, such as the sharp π^* peak around 286 eV and the exciton peak of σ^* at 292 eV. These features are in good agreement with the previously reported spectra recorded from a bulk graphite specimen¹². The spectrum in blue was recorded from an edge atom located at the border of the hexagonal network with two-coordination, as illustrated in Fig. 1c. Remarkably, this spectrum has an extra peak around 282.6 ± 0.2 eV (labelled D in Fig. 1d), with the π^* peak having reduced intensity. Also the exciton peak intensity is considerably reduced and broadened compared to the bulk spectrum (marked by open circles).

The spectrum in red shows similar features, also with weaker π^* peak and broadened σ^* peak. Its extra peak occurs at a different energy position of 283.6 ± 0.2 eV (labelled S in Fig. 1d). It is extremely difficult to assign the atomic position completely for this red spectrum because the spectrum disappears quickly and is not fully reproducible. The edge region of the specimen tends to be strongly damaged and the edge morphology frequently changes after recording the spectrum image. Therefore, we can reasonably infer that this energy state must be somehow damage-related. One of the possible models for this edge structure is the Klein edge^{13,14}. The edge atom indicated in red in Fig. 1b is indeed single-bonded to its neighbour. The structure should be very unstable under the incident electron beam and so it may also explain the wiggling contrast often observed at the graphene edge.

These spectral features involving peaks D and S have not previously been reported, to our knowledge. No fingerprinting method, comparing against the reference spectra of the existing polymorphic carbon, is able to explain them. We therefore performed ELNES simulations to correlate the experimental features with different atomic configurations (Fig. 2). The π^* peak shift to the lower energy is well reproduced for the edge atoms in the Klein, zigzag and armchair edge configurations (Fig. 2a, b and c), in comparison with the bulk carbon atom (Fig. 2d). The diminished excitonic effect can be confirmed for the Klein edge (Fig. 2a). The peak shift around 2 eV is well reproduced for the zigzag edge (Fig. 2b). In the spectrum of the armchair edge a sharp peak between π^* and σ^* is expected (Fig. 2c).

To show an atom-by-atom spectroscopy, we also performed EELS in the spectrum-line mode across a graphene edge. The probe scanned across the protruded carbon atom—the Klein edge—from the vacuum to the bulk region along the dotted line in Fig. 3a. A series of 100 spectra were sequentially recorded by scanning the electron probe with a constant step of about 0.02 nm. The total acquisition time was as small as 50 s. The illustrated model in Fig. 3b shows that eight carbon atoms were investigated in the spectrum line. Figure 3c shows a profile of ADF signals (in red) that was simultaneously recorded with the ELNES spectra. It shows good agreement with the simulated profile (in blue) showing eight maxima sequentially corresponding to the eight carbon atoms. Although the experimental profile is rather scattered owing to specimen instability or a possible inclination of the specimen to the incident electron beam, which should produce a slight asymmetry in the profile of the carbon doublets, we can deduce the carbon atomic positions reasonably well from the line profile and extract the ELNES spectra corresponding to each atom. Figure 3d shows ELNES fine structures obtained in this way, with the corresponding atoms numbered in Fig. 3c (each spectrum presented consists of four spectra in total).

The delocalization effect at the carbon K-edge (~ 290 eV) with an incident electron probe of 60 kV is estimated as 0.20–0.25 nm in classical theory⁸ and as ~ 0.12 nm at 300 kV more recently¹⁵. Therefore the EELS signals, if combined with the probe size (~ 0.1 nm), may not be completely localized at the single atoms on which the probe is exactly positioned. However the series of ELNES spectra in Fig. 3d strongly suggest that site-specific spectroscopy is indeed possible with atomic resolution at the graphene edge. The spectrum from atom 1 clearly shows peak S at 283.6 eV (indicated by a dotted circle), which is related to the Klein edge, but spectrum 2 does not show peak S (it may be a minor feature). Spectrum 5 shows a small trace of peak D, which can reasonably be explained by a possible introduction of the bond-breakage

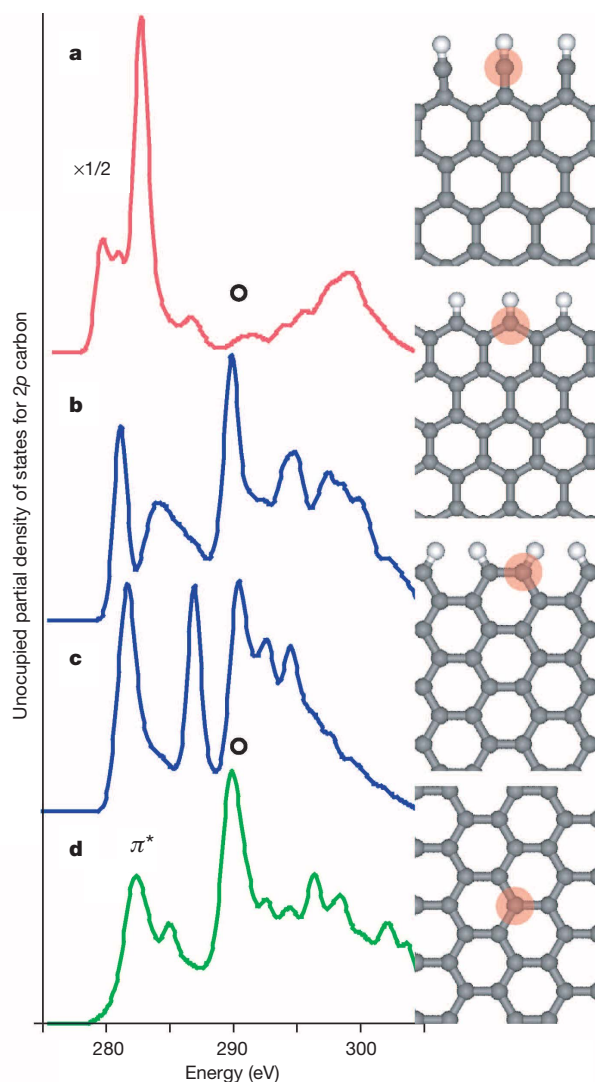


Figure 2 | ELNES simulations for three graphene edge structures. Carbon K-edge spectra simulated for the Klein edge (a), zigzag edge (b), armchair edge (c) and bulk (three-coordinated) atom (d). A core-hole was introduced by partially removing a 1s electron from the carbon atoms (indicated by pink shading) to estimate the relative peak shift of the spectra. The reduced exciton peak found experimentally is well reproduced. The simulated ELNES from the zigzag and armchair edges show at least a qualitative match with experiments, although the absolute value for the energy shift cannot be fully confirmed.

during the probe-scanning across the atom. Spectrum 8 from an atom 1.5 nm away from the edge shows normal sp^2 features with the sharp π^* and excitonic σ^* peaks, which is very close to the bulk spectrum¹².

We performed intensity mapping of peaks D and S to estimate the delocalization effects further. A number of experiments, involving one set of spectrum-image and seven sets of spectrum-line on the graphene edges, are summarized in Supplementary Figs 3, 4 and 5. Results confirm that single-atom spectroscopy at specific sites of the graphene edge is indeed feasible with the reduced delocalization effect.

We found no trace of oxygen at the investigated edges. This may contradict a generally accepted concept in which the graphene edge can be terminated by -OH or -COOH groups and the edge carbon atoms cannot be bared¹. In this experiment, *in situ* etching with continuous removal of the carbon edge atoms in vacuum always takes place and therefore the edge structures are always kept fresh.

From this study, we have picked up some practical information about the graphene edge engineering. The open edges involve both single- and double-coordinated carbon atoms but their specific edge

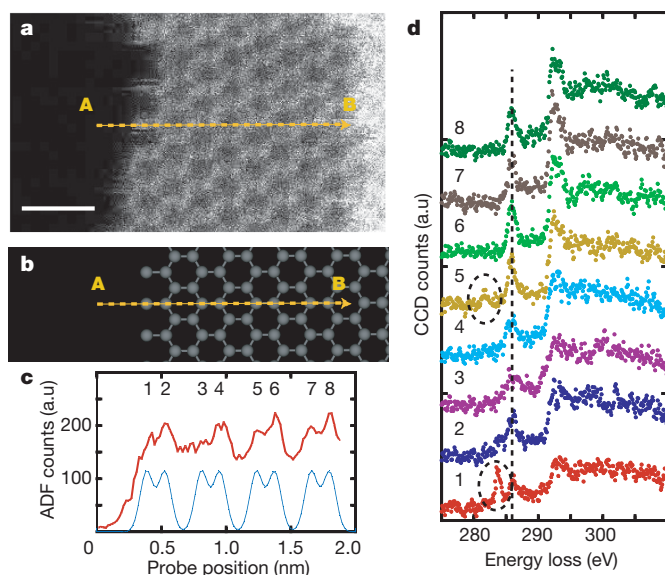


Figure 3 | Atom-by-atom spectroscopy across the Klein edge. **a**, ADF image of graphene edge (no image-processing). The dotted arrow indicates where the spectrum-line was made (A to B). Scale bar, 0.5 nm. **b**, An atomic model of the investigated edge. **c**, Line-profile of the ADF counts (in red) recorded simultaneously with the spectrum-line. For comparison with the simulated ADF counts (blue), the number of each atom is indicated (from 1 to 8). **d**, The carbon K-edge ELNES obtained from each atom across the Klein edge. The single-coordinated carbon atom (numbered 1) clearly shows peak S.

states are completely localized at the atomic level. Even for triple-coordinated carbon atoms, slight electronic structure modification, as indicated by the restricted excitonic effect (or the reduced σ^* peak), may exist near the edge region but it vanishes after 1.5 nm from the edge front. The properties of graphene nanoribbons with smaller widths might be governed by the edge effects¹⁶.

It is very surprising that the EELS signal delocalization has turned out not to be very important for atom-by-atom spectroscopy in the present experiment. The EELS signal delocalization should be substantially decreased when a lower accelerating voltage is used for the incident electron probe⁸. The delocalization effect with a 30–60 kV incident probe is only a fraction of that for the normal STEM operation voltage at 200–300 kV. Lowering the accelerating voltage of the electron microscope is therefore very beneficial, reducing the delocalization effect in addition to contrast enhancement and damage reduction.

ELNES analysis from single atoms is highly desirable because the rich information it supplies will become accessible from individual atoms at any local area. The ELNES fingerprinting method has been widely used to determine the electronic/bonding states of unknown materials by comparison with the reference spectra of known materials. For example, the chemical state of Ce^{3+} or Ce^{4+} in metallofullerene molecules has been clearly discriminated at the single-atom level simply by measuring the energy shift¹⁷. Here we have demonstrated the possibilities of ELNES spectra analysis beyond the simple fingerprinting method. Non-bulk atoms provide peculiar electronic structures and therefore their ELNES should be completely new (or previously unknown) and cannot be compared with any existing reference. Further efforts should be made to obtain the electronic state information from new ELNES spectra by combining atomic resolution imaging with theoretical calculations.

METHODS SUMMARY

STEM-EELS experiments. A JEOL 2100F transmission electron microscope with the DELTA corrector was operated at 60 kV (ref. 9). The energy resolution was around 0.4 eV. We used a probe of 0.1 nm diameter with 20 pA for experiments. For spectroscopy, we used GIF Quantum¹⁸, designed for low-voltage operations. The convergence angle for incident probe was set to 30 mrad, while the inner angle for ADF imaging was around 45–50 mrad, which is equal to the EELS collection angle. ELNES analysis was performed at each pixel while the incident probe

digitally scanned¹¹. The spectrum-image mode, consisting of a two-dimensional set of ELNES spectra, takes longer for total acquisition and easily leads to the destruction of the specimen. Therefore we frequently used the spectrum-line mode, consisting of a one-dimensional set of ELNES spectra, in this study. Typical acquisition time is around 0.1 to 1.0 s for each spectrum. A spectrum line consists of 100 spectra, while an image spectrum consists of typically 12×12 spectra (see also Supplementary Fig. 3).

Specimen preparation. Commercially available synthetic HOPG (NT-MDT Company) was used for experiments. Some of the flakes were cleaved using Scotch tapes and then transferred to transmission electron microscope microgrids following the method developed by Meyer and co-workers¹⁹.

ELNES simulations. The first-principles calculation based on DFT theory was used to estimate energy levels and partial density of states on carbon atoms of graphene structures. In the discrete variance- $X\alpha$ method, the energy levels and partial density of states of unoccupied carbon 2p orbitals are estimated from the self-consistent charge calculation. To estimate the threshold energy of the carbon K-edge, the core-hole effect was considered by employing the transition-state approximation method, which configures a half-electron removed from the carbon 1s orbital and added to an unoccupied orbital^{20,21}. See also Supplementary Fig. 2.

Received 23 July; accepted 9 November 2010.

Published online 15 December 2010.

- Kobayashi, Y., Fukui, K., Enoki, T. & Kusakabe, K. Edge state on hydrogen-terminated graphite edges investigated by scanning tunneling microscopy. *Phys. Rev. B* **73**, 125415 (2006).
- Gass, M. H. et al. Free-standing graphene at atomic resolution. *Nature Nanotechnol.* **3**, 676–681 (2008).
- Liu, Z., Suenaga, K., Harris, P. & Iijima, S. Open and closed edges of graphene layers. *Phys. Rev. Lett.* **102**, 015501 (2009).
- Girit, C. O. et al. Graphene at the edge: stability and dynamics. *Science* **323**, 1705–1708 (2009).
- Krivanek, O. L. et al. Atom-by-atom structural and chemical analysis by annular dark-field electron microscopy. *Nature* **464**, 571–574 (2010).
- Suenaga, K. et al. Element selective single atom imaging. *Science* **290**, 2280–2282 (2000).
- Krivanek, O. L. et al. Gentle STEM: ADF imaging and EELS at low primary energies. *Ultramicroscopy* **110**, 935–945 (2010).
- Egerton, R. F. *Electron Energy-Loss Spectroscopy in the Electron Microscope* 2nd edn, 363–369 (Plenum, 1996).
- Sasaki, T. et al. Performance of low-voltage STEM/TEM with delta corrector and cold field emission gun. *J. Electron Microsc.* **59**, s7–s13 (2010).
- Zobelli, A., Gloter, A., Ewels, C. P., Seifert, G. & Colliex, C. Electron knock-on cross section of carbon and boron nitride nanotubes. *Phys. Rev. B* **75**, 245402 (2007).
- Jeanguillaume, C. & Colliex, C. Spectrum-image: the next step in EELS digital acquisition and processing. *Ultramicroscopy* **28**, 252–257 (1989).
- Garvie, L. A., Craven, A. J. & Brydson, R. Use of electron-energy loss near-edge fine structure in the study of minerals. *Am. Mineral.* **79**, 411–425 (1994).
- Klein, D. J. Graphitic polymer strips with edge states. *Chem. Phys. Lett.* **217**, 261–265 (1994).
- Kusakabe, K. & Maruyama, M. Magnetic nanographite. *Phys. Rev. B* **67**, 092406 (2003).
- Cosgriff, E. C., Oxley, M. P., Allen, L. J. & Pennycook, S. J. The spatial resolution of imaging using core-loss spectroscopy in the scanning transmission electron microscope. *Ultramicroscopy* **102**, 317–326 (2005).
- Jiao, L. et al. Facile synthesis of high-quality graphene nanoribbons. *Nature Nanotechnol.* **5**, 321–325 (2010).
- Suenaga, K. et al. Visualising and identifying single atoms using electron energy-loss spectroscopy with low accelerating voltage. *Nature Chem.* **1**, 415–418 (2009).
- Gubbens, A. et al. The GIF Quantum, a next generation post-column imaging energy filter. *Ultramicroscopy* **110**, 962–970 (2010).
- Pacile, D., Meyer, J. C., Girit, C. O. & Zettl, A. The two-dimensional phase of boron nitride: few-atomic-layer sheets and suspended membranes. *Appl. Phys. Lett.* **92**, 133107 (2008).
- Mizoguchi, T. et al. Core-hole effects on theoretical ELNES/NEXAFS of MgO. *Phys. Rev. B* **61**, 2180–2187 (2000).
- Koshino, M., Kurata, H. & Isoda, S. Study of structures at the boundary and defects in organic thin films of perchlorocoronene by high-resolution and analytical transmission electron microscopy. *Ultramicroscopy* **110**, 1465–1474 (2010).

Supplementary Information is linked to the online version of the paper at www.nature.com/nature.

Acknowledgements This work is partially supported by the JST-CREST programme. We thank C. Jin for discussions and H. Kobayashi for specimen preparations.

Author Contributions K.S. designed and performed experiments. K.S. and M.K. analysed data. M.K. performed simulations. K.S. and M.K. co-wrote the paper.

Author Information Reprints and permissions information is available at www.nature.com/reprints. The authors declare no competing financial interests. Readers are welcome to comment on the online version of this article at www.nature.com/nature. Correspondence and requests for materials should be addressed to K.S. (suenaga-kazu@aist.go.jp).

Mantle superplasticity and its self-made demise

Takehiko Hiraga¹, Tomonori Miyazaki¹, Miki Tasaka¹ & Hidehiro Yoshida²

The unusual capability of solid crystalline materials to deform plastically, known as superplasticity, has been found in metals and even in ceramics¹. Such superplastic behaviour has been speculated for decades to take place in geological materials, ranging from surface ice sheets to the Earth's lower mantle^{2–8}. In materials science, superplasticity is confirmed when the material deforms with large tensile strain without failure; however, no experimental studies have yet shown this characteristic in geomaterials. Here we show that polycrystalline forsterite + periclase (9:1) and forsterite + enstatite + diopside (7:2.5:0.5), which are good analogues for Earth's mantle, undergo homogeneous elongation of up to 500 per cent under subsolidus conditions. Such superplastic deformation is accompanied by strain hardening, which is well explained by the grain size sensitivity of superplasticity and grain growth under grain switching conditions (that is, grain boundary sliding); grain boundary sliding is the main deformation mechanism for superplasticity. We apply the observed strain–grain size–viscosity relationship to portions of the mantle where superplasticity has been presumed to take place, such as localized shear zones in the upper mantle and within subducting slabs penetrating into the transition zone and lower mantle after a phase transformation. Calculations show that superplastic flow in the mantle is inevitably accompanied by significant grain growth that can bring fine grained ($\leq 1\ \mu\text{m}$) rocks to coarse-grained (1–10 mm) aggregates, resulting in increasing mantle viscosity and finally termination of superplastic flow.

Microstructures of some deformed rocks (such as ultramylonite) resemble those of experimental superplastic materials. Further, synthetic mineral aggregates that are analogues of rocks often exhibit a dependence of flow rate on stress and grain size similar to that found during superplastic deformation. On the basis of these results, superplasticity has been speculated to occur in geological materials, including glaciers², lower crust^{3,4}, upper mantle^{3,5}, transition zone⁶ and lower mantle^{7,8}. The term 'superplasticity' refers to tensile deformation to large strain without failure; however, no experimental studies have shown this characteristic in geomaterials. Thus, Earth scientists have been compelled to use superplasticity to describe creep accommodated mainly by grain boundary sliding (GBS)^{2,9}, which is considered to be the primary deformation mechanism for superplasticity¹⁰. Grain switching as a result of GBS is expected to leave little evidence of its operation. Grains with random crystallographic orientations and equant shapes are characteristic of superplastically deformed samples. Thus, geologists have identified superplasticity (or GBS) in their collected rocks simply by eliminating other possible deformation mechanisms, such as dislocation and diffusion creep.

Two types of polycrystalline aggregates—consisting of 90 vol.% forsterite (Mg_2SiO_4) and 10 vol.% periclase (MgO) (Fo+Per) and of 70 vol.% forsterite, 25 vol.% enstatite (MgSiO_3) and 5 vol.% diopside ($\text{CaMgSi}_2\text{O}_6$) (Fo+En+Di), which are good analogues for lower and upper mantle composites—were prepared by sintering of nanosized mineral powders (see details in Methods and ref. 11). Minimizing the particle size of the initial powders and introducing secondary phases, such as periclase and pyroxenes, facilitated the maintenance of a fine grain size ($<500\ \text{nm}$) with a porosity of $<0.1\ \text{vol.}\%$ for both samples.

Tensile tests at a constant displacement rate ($\dot{\nu} = 10^{-3}$ – $10^{-4}\ \text{mm s}^{-1}$) were performed on the blade-shaped sintered aggregates with an Instron-type testing machine at 1,350–1,450 °C in air. A few compression tests were also carried out on cylinder-shaped samples to explore the effect of deformation conditions such as temperature and loading type on the strain–grain size relationship, as discussed later. A piece of the same starting material was placed next to the creep sample in all tests to see how the microstructure changed simply through static annealing (we refer to this sample as a reference sample).

Typical displacement–stress curves for our materials exhibited strain hardening in the initial to middle stages of the deformation and weakening in the final stage before failure (Supplementary Fig. 1). Samples with and without failure both exhibited almost homogeneous strain (Fig. 1). The largest elongation of 515% was achieved for a sample of Fo+Per at $\dot{\nu} = 1.2 \times 10^{-3}\ \text{mm s}^{-1}$ (corresponding to an initial strain rate ($\dot{\epsilon}$) of $1.0 \times 10^{-4}\ \text{s}^{-1}$) at 1,450 °C. A maximum elongation of 315% for a sample of Fo+En+Di was reached at the same displacement speed and at 1,350 °C. Both samples clearly demonstrate superplasticity, which is defined by a tensile strain of $\gg 100\%$ (ref. 12).

Superplasticity in the Fo+Per system occurred over a wider range of temperature and strain rate than in the Fo+En+Di system; thus, we primarily describe deformation behaviour and microstructure of the Fo+Per samples in this study. Microstructures of starting, deformed and reference samples were observed by field-emission-gun scanning electron microscopy (FEG-SEM) (Fig. 2a–c). Both starting and reference samples exhibited homogeneous (random) distribution of grains of secondary phase (periclase; Fig. 2a); however, static grain growth was detected in the reference samples, following the relationship

$$d_{\text{st}}^4 - d_0^4 = kt \quad (1)$$

where d_{st} and d_0 are grain size under static annealing conditions and initial grain size, respectively, t is time and k is the growth coefficient (Supplementary Fig. 2). The relationship is expected to hold when an intergranular secondary phase effectively pins the growth of the first phase, and the growth of the secondary phase is rate-limited by grain boundary diffusion of the slowest ions^{13,14}. The presence of periclase grains at intergranular regions between forsterite grains indicates the operation of such a process (Fig. 2a). Grains are equigranular in the

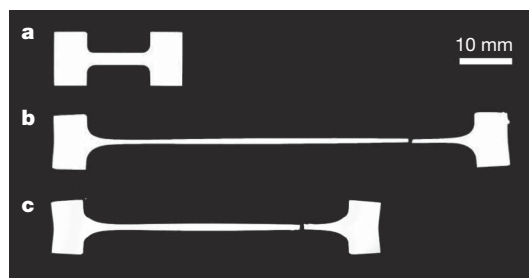


Figure 1 | Specimens before and after tensile deformation experiments. **a**, Starting sample of Fo+Per. **b**, Fo+Per sample after 515% elongation ($\dot{\nu} = 1.2 \times 10^{-3}\ \text{mm s}^{-1}$ and $T = 1,450\ ^\circ\text{C}$). **c**, Fo+En+Di sample after 315% elongation ($\dot{\nu} = 1.2 \times 10^{-3}\ \text{mm s}^{-1}$ and $T = 1,350\ ^\circ\text{C}$).

¹Earthquake Research Institute, University of Tokyo, 1-1-1 Yayoi, Bunkyo-ku, Tokyo 113-0032, Japan. ²Nano Ceramics Center, National Institute for Materials Science, 1-2-1 Sengen, Tsukuba, Ibaraki 305-0047, Japan.

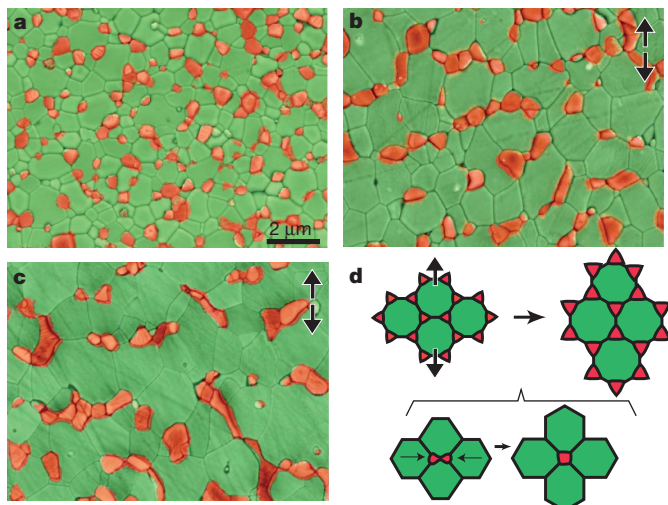


Figure 2 | Microstructures of reference and deformed samples, and schematic illustration of the deformation process. Sample surfaces were thermally etched at 1,250 °C for 0.5 h in air. Pairs of arrows indicate the tensile directions. False colours: green, forsterite; red, periclase. **a**, Reference sample for Fo+Per shown in **c**. **b**, Fo+Per sample with 84% elongation at $\dot{\nu} = 6.0 \times 10^{-4} \text{ mm s}^{-1}$. Total experimental time is 16,876 s. **c**, Fo+Per sample with 399% elongation at $\dot{\nu} = 6.0 \times 10^{-3} \text{ mm s}^{-1}$. Total experimental time is 7,984 s. **d**, Model of grain switching accompanied by grain coalescence (modified after ref. 15).

starting and reference samples, whereas grains in the deformed samples were weakly elongated in the direction of tension (Fig. 2b, c). Further, a very weak lattice-preferred orientation (*a*-axis concentration parallel to the tensile direction) and few dislocations were detected under SEM-EBSD (electron back scattered diffraction) and transmission electron microscopy, respectively (Supplementary Figs 3 and 4); these observations correspond to deformation characteristics expected from the model of superplasticity¹⁰. Deformed samples always exhibit larger grain size than their reference samples (Fig. 2a, c). Further, a sample with larger strain but deformed for a shorter period of time exhibited a larger grain size than a sample with less strain deformed for longer time (Fig. 2b, c).

Randomly distributed grains of secondary phase (=Per) in starting materials coalesced perpendicular to the tensile direction in deformed samples, and such structure is readily recognized in the samples deformed under larger strain and strain rate. The coalescence is well explained by grain switching of the primary phase accompanied by movement of grains of the secondary phase, as illustrated in Fig. 2d (refs 10, 15). When grain switching is fast relative to grain boundary migration, a coalesced structure composed of multiple grains can be preserved. A similar structure is identified in natural ultramylonite (see, for example, ref. 16). Here, we assume that grains of both phases can grow until they encounter grains of a different phase. As grains of secondary phase are isolated from one another, their growth is essentially controlled by their coalescence due to grain switching (Fig. 2d). In the deformed samples, the grain size of the primary phase (d_i^e) is expected to increase parallel to the grain size of the secondary phase (d_{ii}^e) (that is, $d_i^e/d_{ii}^e = \text{constant}$); thus, grain sizes of both phases are expected to follow the relationship (see details in Supplementary Discussions)¹⁷

$$\ln(d^e/d_0) = \alpha \varepsilon \quad (2)$$

where α is a coefficient determined by the fraction of secondary phase grains coalesced in a single grain switching event. Here we use d as an average grain size without distinguishing between phases. It has been shown that d_0 can be replaced by the grain size from the reference samples, d_{ref} , when static grain growth is not significant¹⁸. The $\ln(d^e/d_{\text{ref}})$ versus ε data from the Fo+Per samples are well fitted by equation (2)

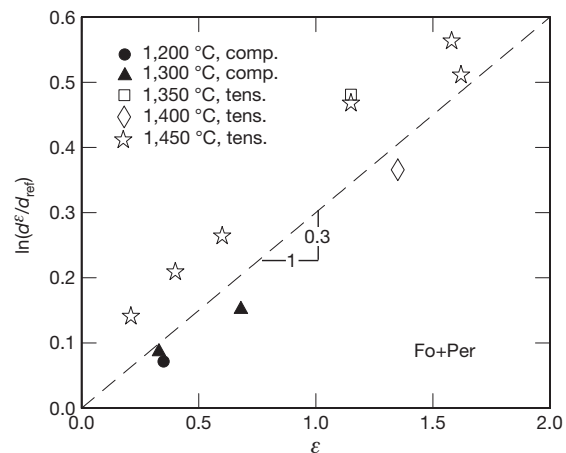


Figure 3 | Experimental data ($\ln(d^e/d_{\text{ref}})$ versus ε) for Fo+Per samples. See text for details of model. Comp., compression; tens., tension.

with $\alpha \approx 0.3$ (Fig. 3), the value commonly reported for metals and ceramics¹⁸. Overall, under deformation via the GBS dominant creep mechanism, we are able to predict grain growth by combining equations (1) and (2) (Supplementary Table 1).

Rheological data were analysed on the basis of the power-law relationship

$$\dot{\varepsilon} = A(\sigma^n/d^p) \quad (3)$$

where $\dot{\varepsilon}$ is strain rate, A is a constant, σ is stress, n is the stress exponent, d is grain size and p is the grain size exponent. To determine flow parameters, the value of p was derived first. As grain growth inevitably occurred during the experiments, we attribute strain hardening of the sample to grain growth and attribute weakening to cavity formation. To obtain flow strength free from the effect of cavities, we analysed flow data only for $\varepsilon \leq 1.0$ before cavity formation. As described above, we explain the change of grain size during the tests through a combination of static and dynamic grain growth laws, which allow us to attribute the hardening to grain growth with $p \approx 1.5$. Using this value to normalize grain size to 1 μm , we find a linear relationship between $\log \sigma$ and $\log \dot{\varepsilon}$, resulting in a value of $n = 2.3$ (see details in Methods and Supplementary Fig. 5), which corresponds to the value commonly reported from superplastic ceramic materials (that is, $n \approx 2$)¹⁹.

Although true tensile elongation is not likely to be important under geologic conditions, grain-scale deformation processes during laboratory tensile tests should be the same as those during mantle flow. Geological settings at probable temperatures where superplasticity has been proposed to take place are considered here: that is, in localized shear zones in the upper mantle at $T \approx 700$ °C (ref. 5), and in subducting slabs penetrating into the transition zone at $T \approx 1,500$ °C (ref. 6) and into the top of the lower mantle at $T \approx 1,600$ °C (refs 7, 8). Here we assume grain growth of the major phase (70 vol.%) in the upper mantle, the transition zone, and the lower mantle to be pinned by secondary phases (30 vol.%); the major and secondary phases are respectively olivine and pyroxene in the upper mantle, ringwoodite and majorite in the transition zone, and Mg-perovskite and magnesiowustite (and/or Ca-perovskite) in the lower mantle. Under static conditions, grain growth can be predicted by equation (1) by estimating k from numerous parameters, including grain boundary diffusivity of the slowest ions (Supplementary Discussions)^{13,14}. On the basis of Si diffusivities for each mineral and temperature^{20–22}, the value of k for the three mantle settings varies by only one order of magnitude. For the sake of simplicity, we use $k = 10^{-31} \text{ m}^4 \text{ s}^{-1}$ as a representative value for all three settings. If we start the aggregates with a grain size of 1 μm , corresponding to the minimum grain size observed in the shear zone⁵ and the predicted value after a phase transformation during subduction²³, grain size will follow the black solid line in Fig. 4; this gives $\sim 30 \mu\text{m}$ and $\sim 200 \mu\text{m}$ after

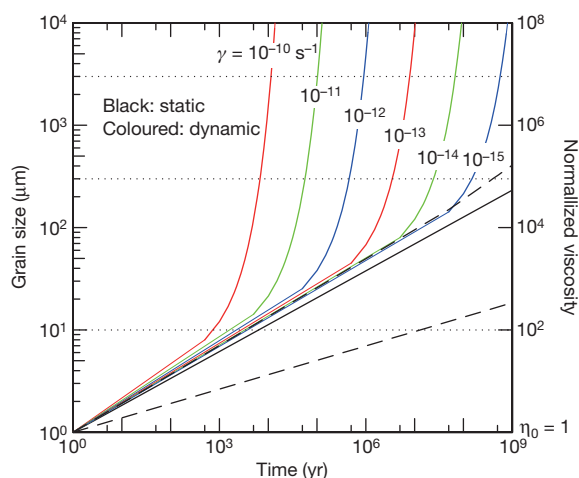


Figure 4 | Predicted grain size and normalized viscosity as a function of time under static and dynamic conditions applicable to three different mantle settings. Settings are: localized shear zone in upper mantle; subducting slab penetrating into transition zone; and subducting slab penetrating into the top of lower mantle. We assume $d_0 = 1 \mu\text{m}$, $\ln d^2/d_{st} = 0.3\gamma/2$ and $p = 2$ (equation (1)). Black solid line, static grain growth; coloured solid lines, dynamic grain growth with different strain rates from 10^{-10} to 10^{-15} s^{-1} . Dashed lines, previously predicted static grain growth at the top of lower mantle^{24,25}. η_0 , viscosity when $d = 1 \mu\text{m}$. See details in text and Supplementary Information.

10 Myr and 1 Gyr, respectively. For the case of the top of the lower mantle, the experimental result²⁴ and previous estimates using a grain growth law for a volume diffusion mechanism²⁵, both of which are represented by dashed lines in the figure, predict $\sim 20 \mu\text{m}$ and $\sim 400 \mu\text{m}$, respectively, after 1 Gyr. Although estimation of static grain growth contains significant uncertainties, pinning due to the secondary phase is so effective overall that grain growth under static conditions is too slow to reach a realistic grain size of 1–10 mm in the mantle settings considered here. Under dynamic conditions, grain growth can be predicted by a combination of equations (1) and (2) by imposing $\dot{\epsilon}$. When the rocks deform at an $\dot{\epsilon}$ of 10^{-15} – 10^{-10} s^{-1} , the strain effect on growth rate becomes significant between 10^3 and 10^8 years, depending on strain rate (coloured lines in Fig. 4). Accordingly, mantle viscosity increases dramatically.

Microstructures of a peridotite mylonite from a shear zone, as compared to the deformation mechanism map for olivine aggregates, indicate that diffusion, GBS and dislocation creep took place in domains with grain sizes of 1–10 μm , 10–300 μm and $> 300 \mu\text{m}$, respectively^{5,26}. Displacement at the shear zone does not contribute to a change in creep regime from diffusion to GBS creep, whereas a change from GBS to dislocation creep can occur through deformation-induced grain growth (Fig. 4). Assuming a shear strain rate ($\dot{\gamma}$) of 10^{-12} s^{-1} , the change from GBS to dislocation creep can occur after $\sim 5 \times 10^5$ years corresponding to a shear strain of ~ 15 , indicating that the domain deforming via a grain-size sensitive mechanism cannot survive after such deformation in the shear zone.

When a subducting slab of thickness 200 km penetrates into the transition zone or lower mantle at 5 cm yr^{-1} , the shear strain rate inside the slab will be $\sim 10^{-14} \text{ s}^{-1}$, assuming simple shear geometry. Although numerous assumptions are involved, the boundary between diffusion and dislocation creep is considered to lie at a grain size of the order of $1 \mu\text{m}$ in the transition zone²¹. In this case, the slab deforms via dislocation creep immediately after the transformation. A grain size of $\sim 3 \text{ mm}$ in the top of the lower mantle is required to explain geophysically estimated viscosity with experimentally obtained Si diffusivity²⁷. As shown, such a large grain size is never attained under static conditions; however, under dynamic conditions, this size can be attained in $\sim 6 \times 10^7$ years following the transformation, which corresponds to

$\sim 3,000 \text{ km}$ horizontal movement of the slab. Our calculation demonstrates that deformation-induced grain growth controls grain size, viscosity and the extent (in space and time) of superplasticity in the mantle.

METHODS SUMMARY

Mineral powders for sintering were prepared through solid state reactions between nanosized powders of $\text{Mg}(\text{OH})_2$ and colloidal SiO_2 with and without CaCO_3 . Such powders were then cold pressed under isostatic pressure into bars. Subsequently, they were vacuum sintered to obtain very dense fine-grained materials. The blade-shaped sintered aggregates for tensile experiments were machined to a gauge length of 12 mm, a width of 2 mm, and a thickness of 2 mm (Fig. 1a). For creep experiments, we used an Instron 5580 uniaxial mechanical testing machine with a furnace to heat the samples. The samples were held by SiC rods, and testing temperatures were established by raising the temperature at $650^\circ \text{C h}^{-1}$. All tests were conducted in a temperature range of 1,350–1,450 $^\circ \text{C}$ and under atmospheric conditions. Constant displacement rates were established in all the tests. Tensile strain was determined from the crosshead displacement, assuming uniform elongation in the gauge portion. After the tests, all samples were polished in the plane parallel to the tension direction and thermally etched to expose grain and interphase boundaries. The diameter of each grain was measured by approximating the grain shape to a circle with imaging software. More than 170 grains were measured in each sample to obtain the mean diameter of the circles, which should represent grain size in the sample.

Full Methods and any associated references are available in the online version of the paper at www.nature.com/nature.

Received 20 May; accepted 18 November 2010.

- Wakai, F., Sakaguchi, S. & Matsuno, Y. Superplasticity of yttria-stabilized tetragonal ZrO_2 polycrystals. *Adv. Ceram. Mater.* **1**, 259–263 (1986).
- Goldsby, D. L. & Kohlstedt, D. L. Superplastic deformation of ice: experimental observations. *J. Geophys. Res.* **106** (B6), 11017–11030 (2001).
- Boullier, A. M. & Gueguen, Y. SP-Mylonites: origin of some mylonites by superplastic flow. *Contrib. Mineral. Petrol.* **50**, 93–104 (1975).
- Behrmann, J. H. & Mainprice, D. Deformation mechanisms in a high-temperature quartz-feldspar mylonite: evidence for superplastic flow in the lower continental crust. *Tectonophysics* **140**, 297–305 (1987).
- Warren, J. M. & Hirth, G. Grain size sensitive deformation mechanisms in naturally deformed peridotites. *Earth Planet. Sci. Lett.* **248**, 423–435 (2006).
- Karato, S., Dupas-Bruzek, C. & Rubie, D. C. Plastic deformation of silicate spinel under the transition-zone conditions of the Earth's mantle. *Nature* **395**, 266–269 (1998).
- Ito, E. & Sato, H. Aseismicity in the lower mantle by superplasticity of the descending slab. *Nature* **351**, 140–141 (1991).
- Karato, S., Zhang, S. & Wenk, H. R. Superplasticity in Earth's lower mantle: evidence from seismic anisotropy and rock physics. *Science* **270**, 458–461 (1995).
- Karato, S. *Deformation of Earth Materials: an Introduction to the Rheology of Solid Earth* (Cambridge Univ. Press, 2008).
- Ashby, M. F. & Verrall, R. A. Diffusion-accommodated flow and superplasticity. *Acta Metall.* **21**, 149–163 (1973).
- Koizumi, S. et al. Synthesis of highly dense and fine-grained aggregates of mantle composites by vacuum sintering of mineral nano-powders. *Phys. Chem. Miner.* **37**, 505–518 (2010).
- Hiraga, K., Kim, B.-N., Morita, K., Suzuki, T. S. & Sakka, Y. Microstructural design for high-strain-rate superplastic oxide ceramics. *J. Ceram. Soc. Jpn* **113**, 191–197 (2005).
- Ardell, A. J. On the coarsening of grain boundary precipitates. *Acta Metall.* **20**, 601–609 (1972).
- Speight, M. V. Grain growth kinetics of grain-boundary precipitates. *Acta Metall.* **16**, 133–135 (1968).
- Wilkinson, D. S. & Cáceres, C. H. On the mechanism of strain-enhanced grain growth during superplastic deformation. *Acta Metall.* **32**, 1335–1345 (1984).
- Ishii, K., Kanagawa, K., Shigematsu, N. & Okudaira, T. High ductility of K-feldspar and development of granitic banded ultramylonite in the Ryoke metamorphic belt. *SW Jpn J. Struct. Geol.* **29**, 1083–1098 (2007).
- Holm, K., Embury, J. D. & Purdy, G. R. Structure and properties of microduplex Zr-Nb alloys. *Acta Metall.* **25**, 1191–1200 (1977).
- Sato, E., Kuribayashi, K. & Horiuchi, R. in *Superplasticity and Superplastic Forming* (eds Hamilton, C. H. & Paton, N. E.) 115–119 (Minerals, Metals and Materials Society, 1988).
- Nieh, T. G., Wadsworth, J. & Wakai, F. Recent advances in superplastic ceramics and ceramic composites. *Int. Mater. Rev.* **36**, 146–161 (1991).
- Farver, J. R. & Yund, R. A. Silicon diffusion in forsterite aggregates: implications for diffusion accommodated creep. *Geophys. Res. Lett.* **27**, 2337–2340 (2000).
- Shimojuku, A. et al. Si and O diffusion in $(\text{Mg,Fe})_2\text{SiO}_4$ wadsleyite and ringwoodite and its implications for the rheology of the mantle transition zone. *Earth Planet. Sci. Lett.* **284**, 103–112 (2009).
- Yamazaki, D., Kato, T., Yurimoto, H., Ohtani, E. & Toriumi, M. Silicon self-diffusion in MgSiO_3 perovskite at 25 GPa. *Phys. Earth Planet. Inter.* **119**, 299–309 (2000).

23. Kubo, T., Kaneshima, S., Torii, Y. & Yoshioka, S. Seismological and experimental constraints on metastable phase transformations and rheology of the Mariana slab. *Earth Planet. Sci. Lett.* **287**, 12–23 (2009).
24. Yamazaki, D., Kato, T., Ohtani, E. & Toriumi, M. Grain growth rates of MgSiO₃-perovskite and periclase under lower mantle conditions. *Science* **274**, 2052–2054 (1996).
25. Solomatov, V. S., El-Khonzondar, R. & Tikare, V. Grain size in the lower mantle: constraints from numerical modeling of grain growth in two-phase systems. *Phys. Earth Planet. Inter.* **129**, 265–282 (2002).
26. Hirth, G. & Kohlstedt, D. L. in *The Subduction Factory* (ed. Eiler, J.) 83–105 (Geophys. Monogr. 138, American Geophysical Union, 2003).
27. Yamazaki, D. & Karato, S. Some mineral physics constraints on the rheology and geothermal structure of Earth's lower mantle. *Am. Mineral.* **86**, 385–391 (2001).

Supplementary Information is linked to the online version of the paper at www.nature.com/nature.

Acknowledgements Technical support from S. Sano, N. Ohashi, S. Ohtsuka, K. Ibe, M. Uchida, H. Yoshida and A. Yasuda is appreciated. Scientific discussions with T. Kubo, S. Honda, T. Takei and D. L. Kohlstedt were valuable. Part of the synthesis of the specimens was supported by S. Sano, Ube Materials. Scientific and editorial comments from C. McCarthy were valuable. This research was supported by the JSPS through a Grant-in-Aid for Young Scientists (A 20684024), by the Earthquake Research Institute's cooperative research programme (to T.H.) and by a Grant-in-Aid for Young Scientists (A 19686042), a Grant-in-Aid for Scientific Research (B 21360328) and a Grant-in-Aid for Scientific Research on Priority Areas (474-19053008) (to H.Y.).

Author Contributions T.H., T.M. and H.Y. organized the project, and T.H. drafted the manuscript. TEM and SEM-EBSD were carried out by M.T.

Author Information Reprints and permissions information is available at www.nature.com/reprints. The authors declare no competing financial interests. Readers are welcome to comment on the online version of this article at www.nature.com/nature. Correspondence and requests for materials should be addressed to T.H. (hiraga@eri.u-tokyo.ac.jp).

METHODS

Mineral powders for sintering were prepared through solid state reactions among nano-sized powders of $\text{Mg}(\text{OH})_2$, colloidal SiO_2 and $\pm\text{CaCO}_3$ at $\sim 1,000^\circ\text{C}$. Calcined powders were cold pressed under an isostatic pressure of 200 MPa into bars of $\sim 5 \times 10 \times 30$ mm. Subsequently, they were vacuum sintered at 1,330–1,350 $^\circ\text{C}$ to obtain very dense fine-grained materials. We have reported the details of these procedures elsewhere^{11,28}. Average grain sizes before deformation experiments were 280 and 480 nm for the samples of Fo+Per and Fo+En+Di, respectively. The blade-shaped sintered aggregates for tensile experiments were machined to a gauge length of 12 mm, a width of 2 mm, and a thickness of 2 mm (Fig. 1a). A cylindrical furnace with heating elements of Kanthal Super was used to heat the samples. The furnace was attached to an Instron 5580 uniaxial mechanical testing machine. The samples were held by SiC rods consisting of 2 to 3 parts with flexible joints so that the sample could be adjusted to tensile geometry after a small amount of displacement. Testing temperatures were established by raising the temperature at 650°C h^{-1} . All tests were conducted under constant displacement rate ($\dot{\nu} = 10^{-4}$ – 10^{-3} mm s⁻¹). Tensile strain was determined from the crosshead displacement by considering the compliance of the apparatus and by assuming uniform elongation in the gauge portion. As achievable displacement was so large, nominal strain can be significantly different from true strain. Thus, we use true strain (ϵ) instead of nominal strain when discussing the strain effect on creep characteristics. We collected one force–displacement–time datum per 1,000–2,000 ms using a load cell attached to the crosshead of the Instron machine. We read stress and strain rate at $0.2 \leq \epsilon < 1$ (Supplementary Table 1). Within this range, we are able to obtain reliable stress and strain rate data, which are free from the effects of frictional and elastic behaviours of the samples and sample holders and from the effect of cavitation on sample strength. Half of the tests were conducted until sample failure. Experiments at higher temperature and slower displacement rate tended to achieve larger strain before failure. Compression tests were conducted on cylinder-shaped samples (~ 5 mm radius, 10 mm length) at $\dot{\nu} = (1.7 \times 10^{-4})$ – (1.3×10^{-3}) mm s⁻¹ at 1,200 and 1,300 $^\circ\text{C}$. All samples were quenched by $\sim 20^\circ\text{C min}^{-1}$ to preserve deformation microstructure.

After the tests, all the samples were polished in the plane parallel to the tension direction and thermally etched at temperatures more than 100 $^\circ\text{C}$ lower than that used for the experiments for < 0.5 h in air to expose grain and interphase boundaries^{11,28} (Fig. 2 and Supplementary Fig 6). Microstructural change during the thermal etching was confirmed to be negligible by microstructural observations of the samples that were chemically etched with dilute HCl + HNO₃. We did not apply any etching techniques to the samples for TEM observations. We measured the diameter of each grain by approximating the grain shape to a circle with imaging software. The mean diameter of the circles should represent grain size in the sample, when grain shape is essentially equiaxed. More than 170 grains were measured in each sample.

As we are able to reproduce grain growth with grain growth laws for both static and dynamic conditions (equations (1) and (2)), we can estimate grain size at any point of the deformation when experimental time and strain are known (we refer to this grain size as d^e) (Supplementary Table 1). Such grain size is used to extract flow parameters such as grain size and stress exponents in equation (1) from mechanical data. Details of this procedure follow. Final (total) strain of the samples, ϵ^{fin} , and final grain size, d^{fin} , are substituted into equation (2) to obtain α for each sample. Grain size versus time for reference samples of Fo+Per annealed at 1,450 $^\circ\text{C}$ is shown in Supplementary Fig. 2. The best fit indicates a grain growth exponent of ~ 4 , which corresponds to the predicted exponent in equation (1). The best fit relationship of static grain growth allows us to predict the grain size d_{ref} at t which corresponds to the time when the deformed sample reached ϵ . With calculated α and d_{ref} , we are able to predict grain size in the deformed samples (d^e) using equation (2). Values used for ϵ , t and d^e are all listed in Supplementary Table 1. Within a small range of strain, $\dot{\epsilon}$ can be approximated as a constant so that grain size exponent p is obtained from strain hardening (that is, analysis of $\partial \ln \sigma / \partial \ln d^e$), giving $p \approx 1.5$. Once p is fixed, $\dot{\epsilon}$ is normalized to the value for a grain size of $d = 1 \mu\text{m}$ by $\dot{\epsilon} \times (d^e/d)^{1.5}$. Finally, we plot stress ($\log \sigma$) versus normalized strain rate ($\log \dot{\epsilon} \times (d^e)^{1.5}$) as shown in Supplementary Fig. 5. Linear relationships between $\log \sigma$ and $\log \dot{\epsilon}$ were found, resulting in values of $n = 2.3$ (Supplementary Fig. 5).

28. Hiraga, T., Tachibana, C., Ohashi, N. & Sano, S. Grain growth systematics for forsterite \pm enstatite aggregates: effect of lithology on grain size in the upper mantle. *Earth Planet. Sci. Lett.* **291**, 10–20 (2010).

Subtypes of medulloblastoma have distinct developmental origins

Paul Gibson¹, Yiai Tong¹, Giles Robinson^{1,2}, Margaret C. Thompson⁹, D. Spencer Currell¹, Christopher Eden¹, Tanya A. Kranenburg¹, Twala Hogg¹, Helen Poppleton¹, Julie Martin¹, David Finkelstein³, Stanley Pounds⁴, Aaron Weiss¹⁰, Zoltan Patay⁵, Matthew Scoggins⁵, Robert Ogg⁵, Yanxin Pei¹¹, Zeng-Jie Yang¹¹, Sonja Brun¹¹, Youngsoo Lee⁶, Frederique Zindy⁶, Janet C. Lindsey¹², Makoto M. Taketo¹³, Frederick A. Boop⁷, Robert A. Sanford⁷, Amar Gajjar², Steven C. Clifford¹², Martine F. Roussel⁶, Peter J. McKinnon⁶, David H. Gutmann¹⁴, David W. Ellison⁸, Robert Wechsler-Reya¹¹ & Richard J. Gilbertson^{1,2}

Medulloblastoma encompasses a collection of clinically and molecularly diverse tumour subtypes that together comprise the most common malignant childhood brain tumour^{1–4}. These tumours are thought to arise within the cerebellum, with approximately 25% originating from granule neuron precursor cells (GNPCs) after aberrant activation of the Sonic Hedgehog pathway (hereafter, SHH subtype)^{3–8}. The pathological processes that drive heterogeneity among the other medulloblastoma subtypes are not known, hindering the development of much needed new therapies. Here we provide evidence that a discrete subtype of medulloblastoma that contains activating mutations in the WNT pathway effector *CTNNB1* (hereafter, WNT subtype)^{1,3,4} arises outside the cerebellum from cells of the dorsal brainstem. We found that genes marking human WNT-subtype medulloblastomas are more frequently expressed in the lower rhombic lip (LRL) and embryonic dorsal brainstem than in the upper rhombic lip (URL) and developing cerebellum. Magnetic resonance imaging (MRI) and intra-operative reports showed that human WNT-subtype tumours infiltrate the dorsal brainstem, whereas SHH-subtype tumours are located within the cerebellar hemispheres. Activating mutations in *Ctnnb1* had little impact on progenitor cell populations in the cerebellum, but caused the abnormal accumulation of cells on the embryonic dorsal brainstem which included aberrantly proliferating *Zic1*⁺ precursor cells. These lesions persisted in all mutant adult mice; moreover, in 15% of cases in which *Tp53* was concurrently deleted, they progressed to form medulloblastomas that recapitulated the anatomy and gene expression profiles of human WNT-subtype medulloblastoma. We provide the first evidence, to our knowledge, that subtypes of medulloblastoma have distinct cellular origins. Our data provide an explanation for the marked molecular and clinical differences between SHH- and WNT-subtype medulloblastomas and have profound implications for future research and treatment of this important childhood cancer.

SHH-subtype medulloblastoma is characterized by aberrant SHH signalling that is often driven by inactivating mutations in *PTCH1*^{3,4}. These medulloblastomas tend to arise in very young children, display a 'large cell-anaplastic' or 'desmoplastic' histology and have a relatively poor prognosis^{2–4}. WNT-subtype medulloblastomas are strikingly different. Arising in much older children, these highly curable tumours have 'classic' morphology and activating mutations in *CTNNB1*^{1–4}. Mouse models have shown that SHH-subtype medulloblastomas arise

from committed GNPCs of the cerebellum^{7,8} and enabled the development of new therapies that suppress the oncogenic SHH-signal^{9,10}. It has been suggested that the other medulloblastoma subtypes might have a different cellular origin^{5,11,12}, but little is known about their biology and there are no mouse models of these tumours.

Recently, we showed that subtypes of the brain tumour ependymoma arise from discrete populations of neural progenitor cells with which they share similar gene expression profiles¹³. Therefore, to determine if medulloblastoma subtypes also arise from discrete cell populations, we first used four online gene expression databases to chart the regional expression of 110 genes that mark human SHH- or WNT-subtype medulloblastomas³. Twenty-four WNT-subtype and 25 SHH-subtype medulloblastoma signature genes are contained within 'Brain Explorer 2', which generates three-dimensional gene expression maps across the mouse brain (www.brain-map.org, Supplementary Methods and Supplementary Data set 1). As expected¹⁴, these data revealed the URL at embryonic day (E) 11.5 and the cerebellum at E15.5 to be the most common sites of SHH-subtype signature gene expression (Fig. 1a, b and Supplementary Data Set 1). In contrast, WNT-subtype medulloblastoma signature genes were predominantly expressed within the LRL at E11.5 (rhombomeres (r) 2–r8) and the dorsal brainstem at E15.5. Expression of an additional 61 medulloblastoma signature genes, reported by three other online databases, confirmed this differential pattern (Supplementary Fig. 1 and Supplementary Table 1). These data suggest that SHH- and WNT-subtype medulloblastomas arise from distinct regions of the hindbrain and identify the dorsal brainstem as a potential source of WNT-subtype tumours.

If SHH- and WNT-subtype medulloblastomas have different origins, we reasoned that these tumours should demonstrate anatomical differences at diagnosis. Remarkably, all validated WNT-subtype medulloblastomas examined ($n = 6/6$, Supplementary Fig. 2) were located within the IV ventricle and infiltrated the dorsal surface of the brainstem, whereas all SHH-subtype tumours ($n = 6/6$) were distributed away from the brainstem within the cerebellar hemispheres (Fig. 1c, d and Supplementary Fig. 3, exact Mann–Whitney $P < 0.005$). Five of the six WNT-subtype, but no SHH-subtype, tumours were adherent to the dorsal brainstem at surgery (Fisher's exact test, $P < 0.005$). Thus WNT-subtype medulloblastomas are anatomically distinct from SHH tumours and are intimately related to the IV ventricle and dorsal brainstem.

We noted various cell types surrounding the IV ventricle that could give rise to WNT-subtype medulloblastomas, including dorsal

¹Department of Developmental Neurobiology, St Jude Children's Research Hospital, 262 Danny Thomas Place, Memphis, Tennessee 38105, USA. ²Department of Oncology, St Jude Children's Research Hospital, 262 Danny Thomas Place, Memphis, Tennessee 38105, USA. ³Hartwell Center for Bioinformatics and Biotechnology, St Jude Children's Research Hospital, 262 Danny Thomas Place, Memphis, Tennessee 38105, USA. ⁴Department of Biostatistics, St Jude Children's Research Hospital, 262 Danny Thomas Place, Memphis, Tennessee 38105, USA. ⁵Department of Radiological Sciences, St Jude Children's Research Hospital, 262 Danny Thomas Place, Memphis, Tennessee 38105, USA. ⁶Department of Genetics and Tumor Cell Biology, St Jude Children's Research Hospital, 262 Danny Thomas Place, Memphis, Tennessee 38105, USA. ⁷Department of Surgery, St Jude Children's Research Hospital, 262 Danny Thomas Place, Memphis, Tennessee 38105, USA. ⁸Department of Pathology, St Jude Children's Research Hospital, 262 Danny Thomas Place, Memphis, Tennessee 38105, USA. ⁹Department of Pediatric Hematology/Oncology, The Cleveland Clinic, 9500 Euclid Avenue/S20, Cleveland, Ohio 44195, USA. ¹⁰Robert Wood Johnson Medical School, 195 Little Albany Street, New Brunswick, New Jersey 08903, USA. ¹¹Department of Pharmacology and Cancer Biology, Duke University Medical Center, Durham, North Carolina 27710, USA. ¹²Northern Institute for Cancer Research, Newcastle University, Newcastle upon Tyne NE2 4HH, UK. ¹³Graduate School of Medicine, Kyoto University, Yoshida-Konoé-cho, Sakyo, Kyoto 606-8501, Japan. ¹⁴Department of Neurology, Washington University School of Medicine, St Louis, Missouri 63110, USA.

brainstem progenitors of cochlear, mossy-fibre and climbing-fibre neurons (Fig. 1a, b and Supplementary Fig. 4)¹⁵. But it remained possible that cerebellar ventricular-zone radial glia^{12,16} or GNPCs generate WNT-subtype medulloblastomas. To identify hindbrain cells that are susceptible to transformation by *Ctnnb1*, we generated mice carrying a cre-dependent mutant allele of *Ctnnb1* (*Ctnnb1*^{lox(ex3)})¹⁷ and the *Blbp-Cre* transgene¹⁸. *Blbp-Cre* induces efficient recombination in progenitor cell populations across the hindbrain including the cerebellar ventricular zone, GNPCs of the external germinal layer (EGL) and Olig3⁺ progenitor cells in the LRL¹⁹ (Supplementary Fig. 5). We also generated *Blbp-Cre*^{+/−};*Ctnnb1*^{+/lox(ex3)} (hereafter, *Ctnnb1*-mutant) mice that were homozygous for a cre-dependent mutant allele of *Tp53* (*Tp53*^{flx})²⁰ because loss of this tumour suppressor accelerates medulloblastoma formation in *Ptch1*^{+/−} mice²¹. As expected, *Ctnnb1*-mutant embryos expressed mutant nuclear-Ctnnb1 in all hindbrain germinal zones, regardless of *Tp53* status (Supplementary Figs 5k and 6). Surprisingly, mutation of *Ctnnb1* did not affect significantly the proliferation or

apoptosis of ventricular-zone cells or GNPCs in the cerebellum (Fig. 2a and Supplementary Fig. 7).

Because GNPCs generate SHH-subtype medulloblastomas^{7,8}, we sought additional evidence that these cells are not impacted by mutant *Ctnnb1*. First, we generated *Atoh1-Cre*^{+/−};*Ctnnb1*^{+/lox(ex3)} mice because *Atoh1-Cre* drives efficient recombination in GNPCs, generating medulloblastomas in conditional *Ptch1* mice (see Supplementary Fig. 8a–j and ref. 7). We also used the *Atoh1* enhancer element present in the *Atoh1-Cre* allele to drive expression of a constitutively active Ctnnb1-green fluorescence fusion protein (GFP) in GNPCs (*Atoh1-Ctnnb1*^{ΔN90GFP}, Supplementary Fig. 8k–o)²². Neither *Atoh1-Cre*^{+/−};*Ctnnb1*^{+/lox(ex3)} nor *Atoh1-Ctnnb1*^{ΔN90GFP} mice (more than 20 mice examined each) developed hyperplasia or masses within the URL or EGL. Concordantly, aberrant Ctnnb1 signalling did not impact the proliferation of GNPCs *ex vivo* (Supplementary Fig. 8p). Thus, in contrast to aberrant Shh signalling, mutant Ctnnb1 does not appear to disrupt cell-cycle or differentiation control in GNPCs.

In stark contrast to the cerebellum, by E16.5 all *Ctnnb1*-mutant mice developed aberrant cell collections in the dorsal brainstem that persisted into adulthood (exact Mann–Whitney $P < 0.005$, Fig. 2a–f). These cells were marked by Olig3 and Pax6, which suggested they may be derived from progenitor cells within the LRL^{19,23} (Fig. 2d, e). This abnormality was independent of *Tp53* status and did not involve the floor plate that is not targeted by *Blbp-Cre* (Supplementary Fig. 9). Progenitors within the embryonic dorsal brainstem proliferate to produce daughter cells that express specific marker proteins and follow complex migration streams to their respective nuclei in the developing brainstem (Supplementary Fig. 4)¹⁵. We observed no significant differences in the overall proliferation (Ki67 labelling), apoptosis (TdT-mediated dUTP nick end labelling) or cell-cycle duration (5-bromo-2-deoxyuridine pulse-chase) of progenitors in the dorsal brainstem of *Ctnnb1*-mutant versus control mice (Fig. 2c, data not shown). However, a significant fraction of proliferating cells within *Ctnnb1*-mutant dorsal brainstems expressed Zic1 (37% Zic1⁺/Ki67⁺ = 122/322; Fig. 2c, f–h). This expression is aberrant because Zic1 normally marks postmitotic mossy-fibre neuron precursors as they exit the dorsal brainstem to form nuclei in the ventral brainstem^{23,24} (Fig. 2g). Thus mutant Ctnnb1 might stall the dorso-ventral migration of brainstem neuron precursors, resulting in aberrant dorsal cell collections²⁵. To test this, we used *in utero* GFP electroporation to track the fate of embryonic dorsal brainstem precursors (Fig. 2i–q and Supplementary Figs 10 and 11). GFP-labelled Zic1⁺ mossy-fibre neuron precursors underwent normal migration from the dorsal brainstem to the pontine grey nucleus and other brainstem nuclei in control mice (Fig. 2k–n and Supplementary Fig. 11). In contrast, mutation of *Ctnnb1* markedly reduced the numbers of precursors transiting from the dorsal brainstem to the pontine grey nucleus (Fig. 2o–q; exact Mann–Whitney, $P < 0.05$). Together, these data demonstrate that mutant Ctnnb1 disrupts the normal differentiation and migration of progenitor cells on the dorsal brainstem, resulting in the accumulation of aberrant cell collections. These cells may include stalled mossy-fibre neuron precursors, but further work is required to determine their precise lineage.

Aberrant cell collections in the dorsal brainstem of *Ctnnb1*-mutant mice are reminiscent of the EGL hyperplasia that precedes formation of SHH-subtype medulloblastoma in the cerebellum of *Ptch1*-deficient mice²⁶. Therefore we aged *Ctnnb1*-mutant mice harbouring *Tp53*^{+/flx}, *Tp53*^{+/flx} or *Tp53*^{flx/flx} alleles to test if WNT-subtype medulloblastomas might arise from the dorsal brainstem (n more than 54 mice per genotype). Aberrant cell collections persisted throughout adulthood on the dorsal brainstem of all *Ctnnb1*-mutant;*Tp53*^{+/flx} mice, but these animals did not develop medulloblastoma or tumours in any part of the hindbrain (median follow up 365 days). In contrast, 2 out of 10 *Ctnnb1*-mutant;*Tp53*^{flx/flx} mice aged older than 6 months harboured asymptomatic tumours that were confined to the dorsal brainstem (Supplementary Fig. 12). When aged for longer periods, 15% ($n = 8/55$) of *Ctnnb1*-mutant;*Tp53*^{flx/flx} and 4% ($n = 2/54$) *Ctnnb1*-mutant;*Tp53*^{+/flx}

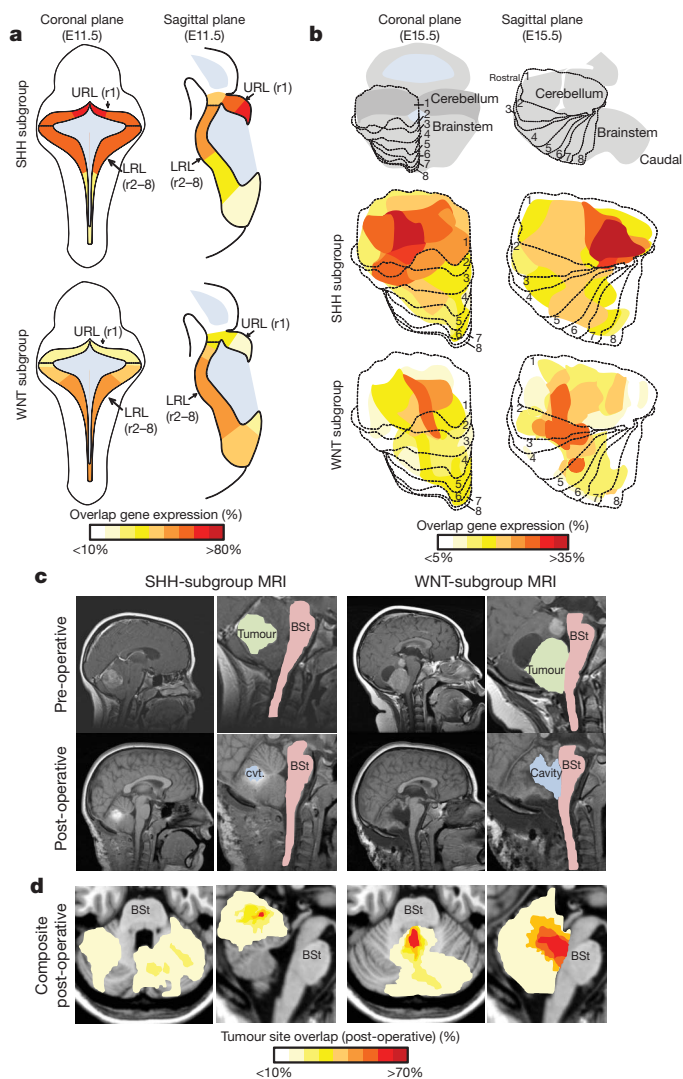


Figure 1 | WNT and SHH subtypes of medulloblastoma are anatomically distinct. **a, b**, Expression distribution in (a) E11.5 and (b) E15.5 mouse hindbrain of orthologues that distinguish human WNT- and SHH-subtype medulloblastoma (Supplementary Data Set 1). Cartoons in **b** denote the position of rhombomeres relative to the cerebellum and brainstem. **c**, Top, pre-operative, and bottom, post-operative, MRI scans of exemplary SHH- and WNT-subtype medulloblastomas. Right panels show close-up views of left panels. Brainstem (BSt), post-operative tumour cavity (cvt). **d**, Frequency and site of post-operative surgical cavities of SHH- ($n = 6$) and WNT- ($n = 6$) subtype medulloblastomas. Axial (left) and sagittal (right) views are shown.

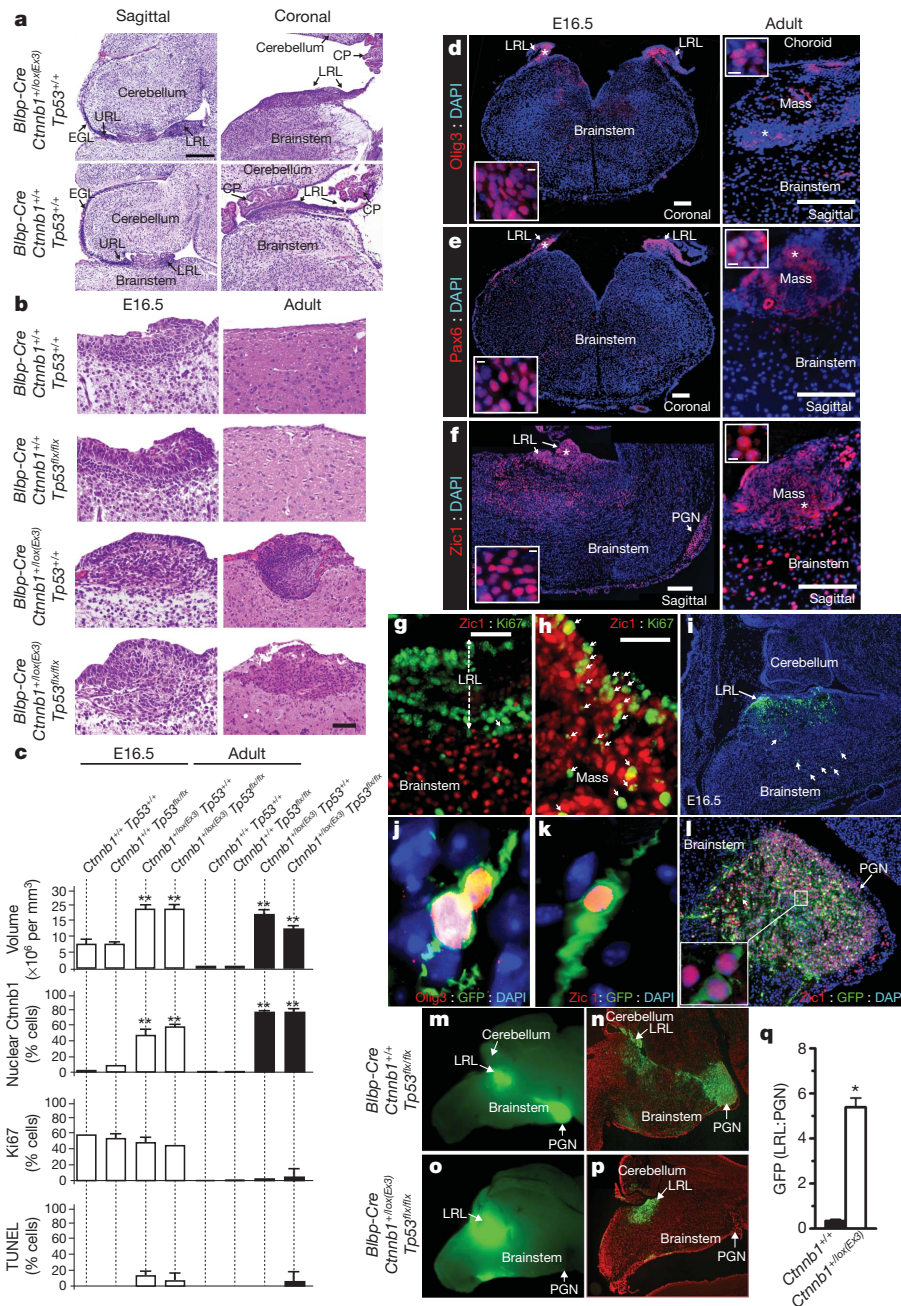


Figure 2 | Mutant-*Ctnnb1* causes aberrant accumulation of LRL cells.

a, Low- (scale bar, 180 μm) and **b**, high- (scale bar, 50 μm) power views of LRL/dorsal brainstem in *Ctnnb1* mutant and wild-type E16.5 embryos; **b** includes the corresponding adult brainstem region. **c**, Volume and indicated immunoreactivity differences between *Ctnnb1*-mutant and wild-type LRL ($n \geq 3$ mice per group; bars, mean \pm s.d.). Immunofluorescence of Olig3 (**d**), Pax6 (**e**) and Zic1 (**f**) in *Ctnnb1*-mutant E16.5 LRL (left) and aberrant adult dorsal brainstem masses (right) (scale bar, 180 μm). Inset, high-power views of '*' (scale bar, 5 μm). **g**, Postmitotic mossy-fibre precursor neurons

mice developed 'classic' medulloblastomas that were Zic1⁺ and contained populations of nuclear-Ctnnb1⁺/Olig3⁺ cells (median follow up 290 and 287 days, respectively; Fig. 3a–d). These mouse medulloblastomas displayed an immunoprofile similar to human WNT-subtype tumours and were invariably connected with the brainstem (Fig. 3d, e and Supplementary Fig. 13). In contrast, mouse models of human SHH-subtype medulloblastoma^{21,27,28} are nuclear-Ctnnb1 negative, arise within the cerebellum and do not invade the brainstem (Fig. 3d, e). Together, these data support the hypothesis that progenitor cells within the dorsal brainstem are susceptible to transformation by concurrent

(Zic1⁺/Ki67[−]) exit the proliferating E16.5 control LRL. **h**, *Ctnnb1*-mutant LRL contains aberrant proliferating Zic1⁺ precursors (arrows; scale bar, 50 μm). **i**, GFP-electroporated wild-type LRL marks Olig3⁺ cells (**j**) and migrating precursors (arrows in **i**) that include Zic1⁺ mossy-fibre neurons (**k**) that form the pontine grey nucleus (**l**). GFP-fluorescence of whole (**m**, **o**) and sectioned (**n**, **p**) *Ctnnb1*-mutant and wild-type P0 hindbrains electroporated at E12.5. **q**, Mean \pm s.d. of LRL/pontine grey nucleus GFP fluorescence in whole hindbrains of three *Blbp-Cre*; *Ctnnb1*^{+/+} and five *Blbp-Cre*; *Ctnnb1*^{+/lox(Ex3)} mice (graphs; * $P \leq 0.05$, ** $P \leq 0.005$, exact Mann–Whitney).

mutation in *Ctnnb1* and *Tp53*, resulting in the formation of tumours that mimic the anatomical features of human WNT-subtype medulloblastoma. Deletion of *Tp53* is presumably required to allow key second mutations during transformation of the LRL in *Ctnnb1*-mutant mice. Notably, we have observed two cases of TP53-mutant human WNT-subtype medulloblastoma, suggesting this gene also suppresses these tumours in humans (Supplementary Fig. 14).

To test further the fidelity of *Ctnnb1*-mutant mouse medulloblastoma as a model of human WNT-subtype disease, we compared the tumour transcriptomes in the two species using an algorithm we have

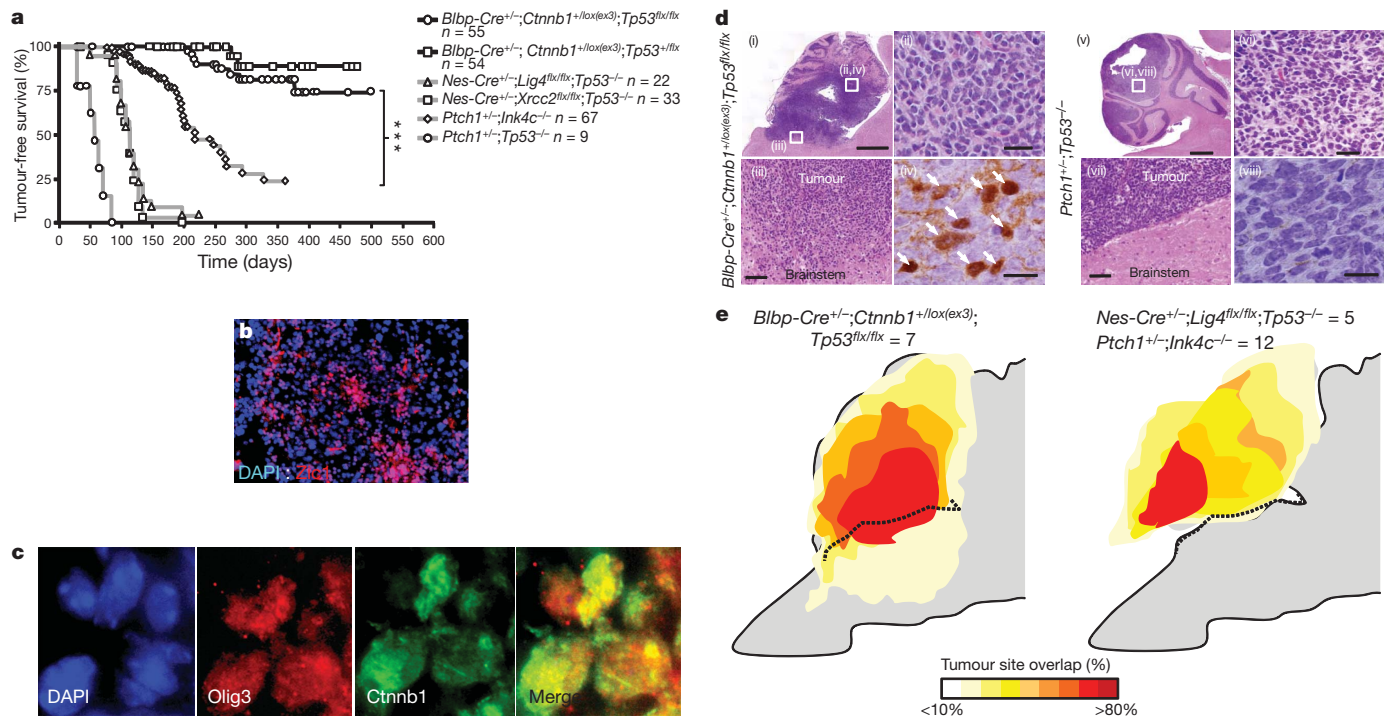


Figure 3 | Mutant-*Ctnnb1* and SHH-subtype mouse medulloblastomas are anatomically distinct. **a**, Tumour-free survival of SHH-subtype medulloblastoma mouse models (*Nes-Cre^{+/+};Lig4^{flx/flx};Tp53^{-/-}*, *Nes-Cre^{+/+};Xrcc2^{flx/flx};Tp53^{-/-}*, *Ptch1^{+/+};Ink4c^{-/-};Tp53^{-/-}*, data from refs 14, 27, 28) and *Ctnnb1*-mutant;*Tp53^{flx/flx}* and *Ctnnb1*-mutant;*Tp53^{+/flx}* mice. ***Log rank $P < 0.0001$. Immunofluorescence of (b) Zic1 and (c) Olig3 and

Ctnnb1 expression in a *Ctnnb1*-mutant;*Tp53^{flx/flx}* medulloblastoma. **d**, Haematoxylin and eosin-stained low- (i, v; scale bar, 800 μ m) and high- (ii, vi; scale bar, 25 μ m) power views of mouse medulloblastomas and tumour-brainstem interface (iii, vii; scale bar, 50 μ m). *Ctnnb1* immunostaining (iv, viii; scale bar, 10 μ m, arrows indicate nuclear immunoreactivity). Boxes indicate location of high-power views. **e**, Frequency and anatomical site of mouse medulloblastomas.

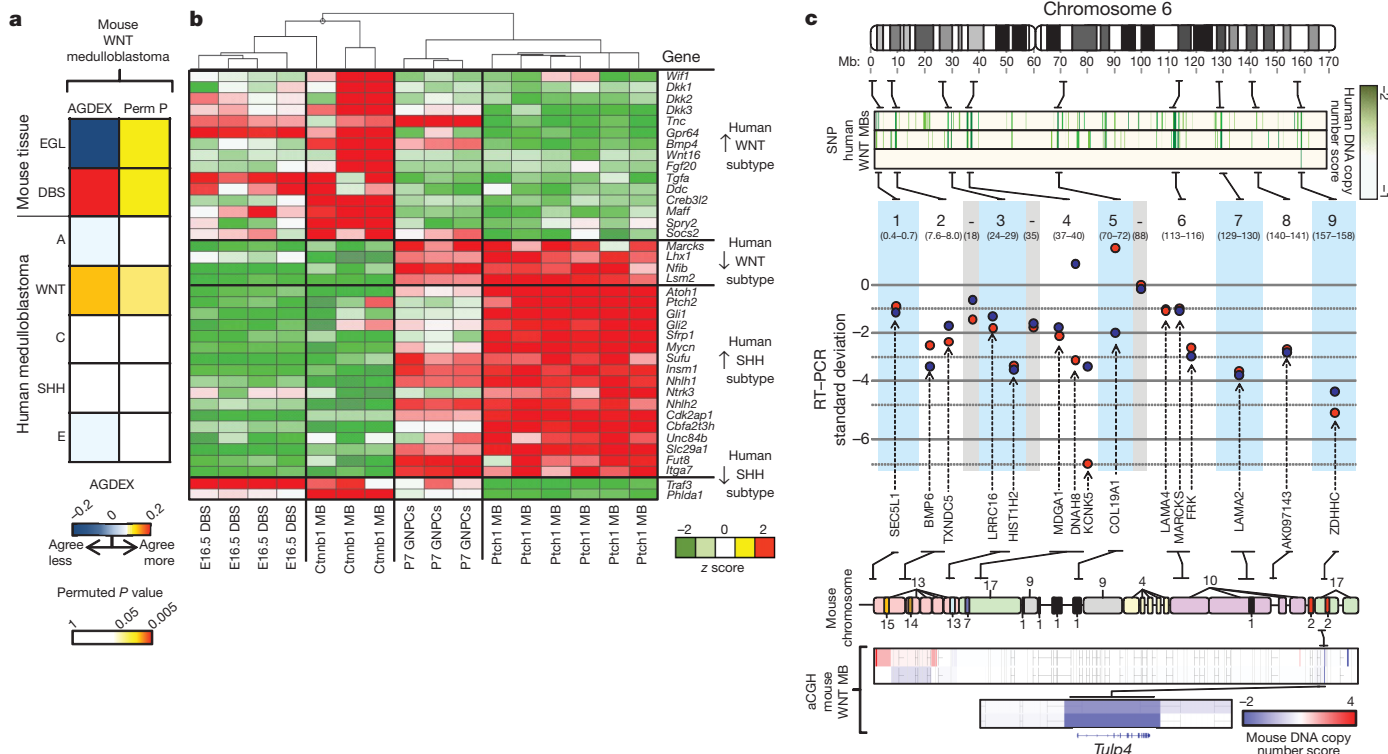


Figure 4 | Mutant-*Ctnnb1* mouse medulloblastomas recapitulate the molecular characteristics of human WNT-subtype disease. **a**, AGDEX comparison of *Ctnnb1*-mutant;*Tp53^{flx/flx}* mouse medulloblastoma, and mouse EGL, E16.5 dorsal brainstem (DBS) and human medulloblastoma subgroups. **b**, Unsupervised clustering of human WNT- and SHH-subtype medulloblastoma signature orthologue expression in E16.5 DBS, *Ctnnb1*-mutant;*Tp53^{flx/flx}* mouse medulloblastoma (*Ctnnb1* MB), P7 GNPCs and

Ptch1^{+/+};Tp53^{-/-} medulloblastoma (*Ptch1* MB). **c**, Top-bottom: nine single nucleotide polymorphism-inferred homozygous deletions in three human WNT-subtype medulloblastomas; real-time PCR validation of deletions in the human tumours (s.d. below the mean diploid copy number); mouse chromosomal regions syntenic for human chromosome 6; array comparative genomic hybridization-inferred copy number in *Ctnnb1*-mutant;*Tp53^{flx/flx}* mouse medulloblastomas identifies common syntenic deletion of *TULP4*.

developed for cross-species genomic comparisons¹³. Remarkably, the transcriptome ($n = 11,049$ orthologues) of *Ctnnb1*-mutant;*Tp53*^{flx/flx} medulloblastomas matched only human WNT-subtype medulloblastoma and the cells of the embryonic dorsal brainstem (both permuted $P < 0.05$), validating it as a model of this human tumour subtype and further pinpointing the brainstem as the source of WNT-subtype medulloblastomas (Fig. 4a, b). Finally, because human WNT-subtype medulloblastomas selectively delete chromosome 6 (ref. 3), we looked in *Ctnnb1*-mutant mouse medulloblastomas to see if syntenic regions of this chromosome are deleted (Fig. 4c). DNA microarray analysis identified a single common deletion of mouse chromosome 17 3.2 cM/human 6q25.3 in tumours in the two species. This locus encodes a single gene, *TULP4*, that is a distant member of the tubby-gene family implicated in regulating neuronal cell apoptosis²⁹. Thus *Ctnnb1*-mutant;*Tp53*^{flx/flx} mouse medulloblastomas accurately model the molecular characteristics of human WNT-subtype tumours and pinpoint *TULP4* as a novel candidate suppressor gene of these tumours. By demonstrating that subtypes of medulloblastoma have distinct cellular origins, our data should significantly accelerate the hunt for curative treatments of these diseases, which must now account for the different developmental origins of these tumours.

METHODS SUMMARY

MRI analysis. MRI images of patients were spatially normalized into a standard stereotaxic space for quantitative comparison of tumour location (SPM5; www.fil.ion.ucl.ac.uk/spm). Radiologists masked to patient subtype determined the three-dimensional location of the tumour or surgical cavity relative to pre-defined anatomical landmarks.

Expression mapping. The expression of mouse orthologues of key signature genes of human WNT- and SHH-subtype medulloblastoma (Supplementary Data Set 1 and Supplementary Table) were mapped in the developing mouse hindbrain using four publicly accessible data sets (see Supplementary Methods).

Mouse studies. *Blbp-Cre*, *Ctnnb1*^{lox(ex3)/lox(ex3)}, *Atoh1-Cre* and *Tp53*^{flx/flx} mice were bred to generate appropriate genotypes and subjected to clinical surveillance for signs of tumour development. *RosaYFP* and *RosaLacZ* reporter strains traced the lineage of Cre-recombined cells. Mouse tumours comprised at least 85% tumour cells. *Atoh1-Ctnnb1*^{Δ90} transgenic mice were generated by pro-nuclear injection. *In utero* electroporation and cell tracking were performed by anaesthetizing pregnant mice of the appropriate genotype. The uterus was externalized and the dorsal brainstem of E12.5 embryos electroporated with CMV-eGFP plasmid DNA. GNPCs for culture studies were isolated from postnatal day 7 *Atoh1-GFP* transgenic mice. GFP⁺ cells (2×10^5 per well) were cultured in poly-D-lysine-coated 96-well plates and challenged with mutant *Ctnnb1-GFP*, control *GFP* virus, Wnt1 protein (50 ng ml^{-1}) or Shh supernatant ($3 \mu\text{g ml}^{-1}$) before pulsing with [methyl-3H]thymidine and scintillation counting.

Histology, messenger RNA and DNA microarray profiling. Immunohistochemistry was performed using routine techniques and primary antibodies of the appropriate tissues as described (Supplementary Methods). Cells undergoing apoptosis were detected with the Apoptag kit (Millipore, S7100). Messenger RNA expression (GEO accession number GSE24628) and DNA copy number profiles (available at <http://stjuderesearch.org/site/authors/gilbertson>) were generated from mouse and human tissues using appropriate microarray platforms as detailed (Supplementary Methods). Reverse transcriptase real-time PCR and gene re-sequencing of human medulloblastomas were performed as described previously³. Messenger RNA expression and DNA microarray profiles of human and mouse medulloblastomas were integrated using established and novel bioinformatic and statistical approaches.

Received 26 September 2009; accepted 15 October 2010.

Published online 8 December 2010.

1. Ellison, D. W. *et al.* β -Catenin status predicts a favorable outcome in childhood medulloblastoma: the United Kingdom Children's Cancer Study Group Brain Tumour Committee. *J. Clin. Oncol.* **23**, 7951–7957 (2005).
2. Gajjar, A. *et al.* Risk-adapted craniospinal radiotherapy followed by high-dose chemotherapy and stem-cell rescue in children with newly diagnosed medulloblastoma (St Jude Medulloblastoma-96): long-term results from a prospective, multicentre trial. *Lancet Oncol.* **7**, 813–820 (2006).
3. Thompson, M. C. *et al.* Genomics identifies medulloblastoma subgroups that are enriched for specific genetic alterations. *J. Clin. Oncol.* **24**, 1924–1931 (2006).
4. Kool, M. *et al.* Integrated genomics identifies five medulloblastoma subtypes with distinct genetic profiles, pathway signatures and clinicopathological features. *PLoS ONE* **3**, e3088 (2008).

5. Gilbertson, R. J. & Ellison, D. W. The origins of medulloblastoma subtypes. *Annu. Rev. Pathol.* **3**, 341–365 (2008).
6. Goodrich, L. V., Milenkovic, L., Higgins, K. M. & Scott, M. P. Altered neural cell fates and medulloblastoma in mouse patched mutants. *Science* **277**, 1109–1113 (1997).
7. Schuller, U. *et al.* Acquisition of granule neuron precursor identity is a critical determinant of progenitor cell competence to form Shh-induced medulloblastoma. *Cancer Cell* **14**, 123–134 (2008).
8. Yang, Z. J. *et al.* Medulloblastoma can be initiated by deletion of Patched in lineage-restricted progenitors or stem cells. *Cancer Cell* **14**, 135–145 (2008).
9. Romer, J. T. *et al.* Suppression of the Shh pathway using a small molecule inhibitor eliminates medulloblastoma in *Ptc1*^{+/-}*p53*^{-/-} mice. *Cancer Cell* **6**, 229–240 (2004).
10. Rudin, C. M. *et al.* Treatment of medulloblastoma with Hedgehog pathway inhibitor GDC-0449. *N. Engl. J. Med.* **2**, 1173–1178 (2009).
11. Louis, D., Ohgaki, H., Wiestler, O. & Cavenee, W. (eds) *World Health Organization Classification of Tumours of the Central Nervous System* (International Agency for Research on Cancer, 2007).
12. Huang, X. *et al.* Transventricular delivery of Sonic hedgehog is essential to cerebellar ventricular zone development. *Proc Natl Acad. Sci. USA* **107**, 8422–8427 (2010).
13. Johnson, R. A. *et al.* Cross-species genomics matches driver mutations and cell compartments to model ependymoma. *Nature* **466**, 632–636 (2010).
14. Lee, Y. *et al.* A molecular fingerprint for medulloblastoma. *Cancer Res.* **63**, 5428–5437 (2003).
15. Ray, R. S. & Dymecki, S. M. Rautenlippe Redux—toward a unified view of the precerebellar rhombic lip. *Curr. Opin. Cell Biol.* **21**, 741–747 (2009).
16. Morales, D. & Hatten, M. E. Molecular markers of neuronal progenitors in the embryonic cerebellar anlage. *J. Neurosci.* **26**, 12226–12236 (2006).
17. Harada, N. *et al.* Intestinal polyposis in mice with a dominant stable mutation of the beta-catenin gene. *EMBO J.* **18**, 5931–5942 (1999).
18. Hegedus, B. *et al.* Neurofibromatosis-1 regulates neuronal and glial cell differentiation from neuroglial progenitors *in vivo* by both cAMP- and Ras-dependent mechanisms. *Cell Stem Cell* **1**, 443–457 (2007).
19. Storm, R. *et al.* The bHLH transcription factor Olig3 marks the dorsal neuroepithelium of the hindbrain and is essential for the development of brainstem nuclei. *Development* **136**, 295–305 (2009).
20. Jonkers, J. *et al.* Synergistic tumor suppressor activity of BRCA2 and p53 in a conditional mouse model for breast cancer. *Nature Genet.* **29**, 418–425 (2001).
21. Wetmore, C., Eberhart, D. E. & Curran, T. Loss of p53 but not ARF accelerates medulloblastoma in mice heterozygous for patched. *Cancer Res.* **61**, 513–516 (2001).
22. Chenn, A. & Walsh, C. A. Regulation of cerebral cortical size by control of cell cycle exit in neural precursors. *Science* **297**, 365–369 (2002).
23. Landsberg, R. L. *et al.* Hindbrain rhombic lip is comprised of discrete progenitor cell populations allocated by Pax6. *Neuron* **48**, 933–947 (2005).
24. DiPietrantonio, H. J. & Dymecki, S. M. Zic1 levels regulate mossy fiber neuron position and axon laterality choice in the ventral brain stem. *Neuroscience* **162**, 560–573 (2009).
25. Farago, A. F., Awatramani, R. B. & Dymecki, S. M. Assembly of the brainstem cochlear nuclear complex is revealed by intersectional and subtractive genetic fate maps. *Neuron* **50**, 205–218 (2006).
26. Oliver, T. G. *et al.* Loss of patched and disruption of granule cell development in a pre-neoplastic stage of medulloblastoma. *Development* **132**, 2425–2439 (2005).
27. Uziel, T. *et al.* The tumor suppressors Ink4c and p53 collaborate independently with Patched to suppress medulloblastoma formation. *Genes Dev.* **19**, 2656–2667 (2005).
28. Frappart, P. O. *et al.* Recurrent genomic alterations characterize medulloblastoma arising from DNA double-strand break repair deficiency. *Proc. Natl Acad. Sci. USA* **106**, 1880–1885 (2009).
29. Ikeda, A., Ikeda, S., Gridley, T., Nishina, P. M. & Naggert, J. K. Neural tube defects and neuroepithelial cell death in *Tulp3* knockout mice. *Hum. Mol. Genet.* **10**, 1325–1334 (2001).

Supplementary Information is linked to the online version of the paper at www.nature.com/nature.

Acknowledgements R.J.G. holds the Howard C. Schott Research Chair from the Malia's Cord Foundation, and is supported by grants from the National Institutes of Health (R01CA129541, P01CA96832 and P30CA021765), the Collaborative Ependymoma Research Network and by the American Lebanese Syrian Associated Charities. We are grateful to A. Chenn, J. Johnson and C. Birchmeier for their gifts of reagents and the staff of the Hartwell Center for Bioinformatics and Biotechnology and ARC at St Jude Children's Research Hospital for technical assistance.

Author Contributions R.J.G. conceived the research and planned experiments. P.G. also planned and conducted most of the experiments. Y.T., G.R., D.S.C., M.C.T., T.H., H.P., J.M., J.C.L., Y.L., F.Z., C.E., S.C.C., M.F.R., P.J.M. and R.W.-R. conducted experiments. D.F. and S.P. provided bioinformatic expertise. A.G., F.A.B. and R.A.S. provided clinical advice and tumour samples. D.H.G. provided the *Blbp-Cre* mouse and data. M.M.T. provided the *Ctnnb1*^{lox(ex3)/lox(ex3)} mouse. Z.P. and R.O. reviewed and analysed the human MRI scans. D.W.E. provided pathology review. All authors contributed to writing the manuscript.

Author Information Reprints and permissions information is available at www.nature.com/reprints. The authors declare no competing financial interests. Readers are welcome to comment on the online version of this article at www.nature.com/nature. Correspondence and requests for materials should be addressed to R.J.G. (Richard.Gilbertson@stjude.org).

mTORC1 controls fasting-induced ketogenesis and its modulation by ageing

Shomit Sengupta^{1,2,3}, Timothy R. Peterson^{1,2,3}, Mathieu Laplante^{1,2,3}, Stephanie Oh^{1,2,3} & David M. Sabatini^{1,2,3}

The multi-component mechanistic target of rapamycin complex 1 (mTORC1) kinase is the central node of a mammalian pathway that coordinates cell growth with the availability of nutrients, energy and growth factors¹. Progress has been made in the identification of mTORC1 pathway components and in understanding their functions in cells, but there is relatively little known about the role of the pathway *in vivo*. Specifically, we have little knowledge regarding the role mTORC1 has in liver physiology. In fasted animals, the liver performs numerous functions that maintain whole-body homeostasis, including the production of ketone bodies for peripheral tissues to use as energy sources. Here we show that mTORC1 controls ketogenesis in mice in response to fasting. We find that liver-specific loss of TSC1 (tuberous sclerosis 1), an mTORC1 inhibitor¹, leads to a fasting-resistant increase in liver size, and to a pronounced defect in ketone body production and ketogenic gene expression on fasting. The loss of raptor (regulatory associated protein of mTOR, complex 1) an essential mTORC1 component¹, has the opposite effects. In addition, we find that the inhibition of mTORC1 is required for the fasting-induced activation of PPAR α (peroxisome proliferator activated receptor α), the master transcriptional activator of ketogenic genes², and that suppression of NCoR1 (nuclear receptor co-repressor 1), a co-repressor of PPAR α ³, reactivates ketogenesis in cells and livers with hyperactive mTORC1 signalling. Like livers with activated mTORC1, livers from aged mice have a defect in ketogenesis^{4,5}, which correlates with an increase in mTORC1 signalling. Moreover, we show that the suppressive effects of mTORC1 activation and ageing on PPAR α activity and ketone production are not additive, and that mTORC1 inhibition is sufficient to prevent the ageing-induced defect in ketogenesis. Thus, our findings reveal that mTORC1 is a key regulator of PPAR α function and hepatic ketogenesis and suggest a role for mTORC1 activity in promoting the ageing of the liver.

Whereas mice lacking the mTORC1 components mTOR or raptor die in early embryogenesis⁶, mice treated with pharmacological inhibitors of mTORC1 or with tissue-specific deletions of raptor or mTOR are viable, and are beginning to reveal diverse roles for mTORC1 in adult physiology⁶. To begin the study of mTORC1 in liver physiology, we determined the effects of fasting and feeding on hepatic mTORC1 activity. In fasted mice, mTORC1 activity in the liver was low (Fig. 1a, Supplementary Fig. 1a), as detected by the phosphorylation of the ribosomal S6 protein, an established marker of mTORC1 pathway activity. Refeeding led to an increase in phospho-S6 levels that was blocked by rapamycin, an mTORC1 inhibitor. mTORC1 activation preceded that of Akt (Fig. 1b), an effector of the insulin-activated PI3K pathway, which is consistent with mTORC1 responding not only to insulin but also to other food-triggered signals, such as nutrients.

We examined the functions of mTORC1 in the liver using genetically engineered mice with the liver-specific deletion of the gene for raptor, or TSC1, a negative regulator of mTORC1 (Fig. 1c) (Methods). We refer to mice lacking hepatic TSC1 or raptor as Li-Tsc1^{KO} or Li-Rap^{KO} mice, respectively. In Li-Tsc1^{KO} mice, the mTORC1 pathway was

constitutively active and not affected by fasting or feeding, while the loss of raptor eliminated mTORC1 activity irrespective of feeding status (Fig. 1d). Compared to controls, TSC1 or raptor deletion led to an ~40% increase or decrease, respectively, in liver mass, hepatocyte size, and protein content (Fig. 1e; Supplementary Fig. 1b, c). Whereas in control animals a 24-h fast caused a ~25% reduction in liver mass, the livers of Li-Tsc1^{KO} mice were largely refractory to the shrinking effects of fasting. In addition, fasting did not further decrease the size of the already small livers of Li-Rap^{KO} mice (Fig. 1e). Thus, mTORC1 is strongly regulated by fasting and feeding and plays a major role in setting liver size in response to the nutritional state.

We measured the levels of several serum and liver metabolites in control, Li-Tsc1^{KO} and Li-Rap^{KO} mice that were fasted or given *ad libitum* access to food (Supplementary Fig. 1d). Because mTORC1 activation suppresses Akt signalling⁷ (Supplementary Fig. 1e), we also examined Li-Ir^{KO} (also known as LIRKO; ref. 8) mice that lack the Insulin Receptor in the liver and thus have attenuated Akt signalling⁸. Levels of most serum and hepatic metabolites were not significantly affected by TSC1 loss, except that fasted Li-Tsc1^{KO} mice had markedly low serum ketones, a phenotype not shared by Li-Ir^{KO} mice (Fig. 2a; Supplementary Fig. 1d, f, g). Compared to control animals, Li-Tsc1^{KO} mice had decreased locomotor activity and body temperature upon fasting (Supplementary Fig. 1h, i), phenotypes also observed in other mutant mice with defective ketogenesis⁹.

The ketone bodies, acetoacetate and β -hydroxybutyrate, are produced by the liver primarily from fatty acids released by adipose tissue and are used by tissues to generate acetyl-CoA for energy production during fasting. The defect in ketone production in Li-Tsc1^{KO} mice is not due to an impairment in fatty acid uptake by the liver, as they were unable to generate ketones even when given sodium octanoate, a fatty acid that freely diffuses into liver mitochondria and serves as a ketogenic substrate¹⁰ (Supplementary Fig. 2a).

As Li-Tsc1^{KO} mice have a defect in ketone production when fasted, we asked if Li-Rap^{KO} mice could produce ketones when fed. Li-Rap^{KO} mice given food *ad libitum* do not have elevated levels of ketones (Fig. 2a), perhaps because the serum fatty acids that are ketogenic substrates are at low levels in fed mice¹¹. Indeed, when Li-Rap^{KO} mice were administered the ketogenic substrate sodium octanoate upon refeeding after a fast, they did produce ketones for several hours after feeding, even at times when ketone levels had dropped precipitously in control animals (Supplementary Fig. 2b). Furthermore, Li-Rap^{KO} or rapamycin-treated mice do have elevated serum ketones at the short times after refeeding when the control animals already have baseline ketone levels (Supplementary Fig. 2c, d).

The defect in ketogenesis in the Li-Tsc1^{KO} mice is liver-autonomous, as liver tissue from these mice failed to oxidize fatty acids or produce ketones *ex vivo* (Fig. 2b). To confirm these results in cells *in vitro*, we developed a ketogenic media containing the PPAR α agonist WY-14643 (Methods) that induces ketone production in murine AML12 hepatocytes (Fig. 2c). Consistent with the *in vivo* and *ex vivo* findings, the suppression of TSC1 or TSC2 inhibited, in a rapamycin-sensitive

¹Whitehead Institute for Biomedical Research, Nine Cambridge Center, Cambridge, Massachusetts 02142, USA. ²Howard Hughes Medical Institute, Department of Biology, Massachusetts Institute of Technology, Cambridge, Massachusetts 02139, USA. ³The David H. Koch Institute for Integrative Cancer Research at MIT, 77 Massachusetts Avenue, Cambridge, Massachusetts 02139, USA.

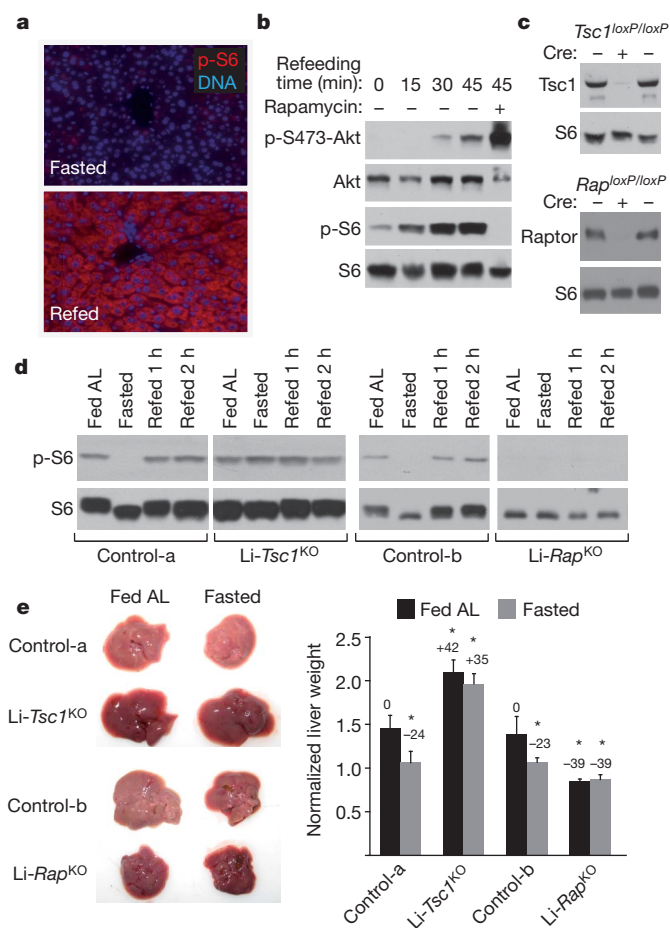


Figure 1 | In the liver, mTORC1 activity is sensitive to fasting and feeding and regulates organ size. **a**, Images of liver sections from mice fasted for 24 h or fasted and refed for 45 min, and co-stained for serine 240/244 phosphorylated-S6 (p-S6; red) and DNA (blue). **b**, Mice were fasted for 24 h or fasted and then refed for 15, 30 or 45 min, or injected with rapamycin 2 h before refeeding for 45 min. Liver lysates were analysed by immunoblotting for the indicated proteins and phosphorylation states. **c**, Immunoblot analyses for TSC1 or raptor protein in liver lysates from indicated mouse strains that have or do not have Cre recombinase expression in the liver. **d**, Indicated mice were killed after being given food *ad libitum* (fed AL), fasted for 24 h (fasted), or fasted and refed for 1 or 2 h. Liver lysates were analysed by immunoblotting for the levels of S6 and serine 240/244 phosphorylated-S6. Control-a are *Tsc1^{loxP/loxP}* mice administered the empty adenovirus, and control-b are *Rap^{loxP/loxP}* mice not carrying the Albumin-Cre transgene. The same nomenclature is used in the subsequent figures. **e**, Gross images of livers from *Li-Tsc1^{KO}* or *Li-Rap^{KO}* mice that were fed *ad libitum* or fasted for 24 h (fasted). Bar graph shows mean \pm s.d. normalized liver weight for $n \geq 5$. The percentage changes in liver weight compared to respective fed control mice are indicated. * $P < 0.05$ compared to respective fed control mice.

fashion, ketone production by AML12 cells (Fig. 2c; Supplementary Fig. 3a). Taken together, our loss of function data indicate that mTORC1, in a liver-autonomous fashion, is a key regulator of ketone production in response to fasting.

Because the nuclear hormone receptor PPAR α is a master activator of the hepatic ketogenic gene expression program in response to fasting², we asked if mTORC1 controls ketogenesis by modulating PPAR α function. PPAR α transactivates its own gene as well as those for enzymes required for fatty acid oxidation and ketogenesis, such as *Cpt1a*, *AOX*, *HMGCS2* and *HMGCL*¹². Fasting increased the mRNA levels of PPAR α and its target genes in control, but not TSC1-null, livers (Fig. 2d). In contrast, loss of TSC1 did not block the fasting-induced increase in the mRNA for PEPCK, which is not a target of PPAR α (Fig. 2d). In *Li-Tsc1^{KO}* mice, WY-14643, the synthetic PPAR α

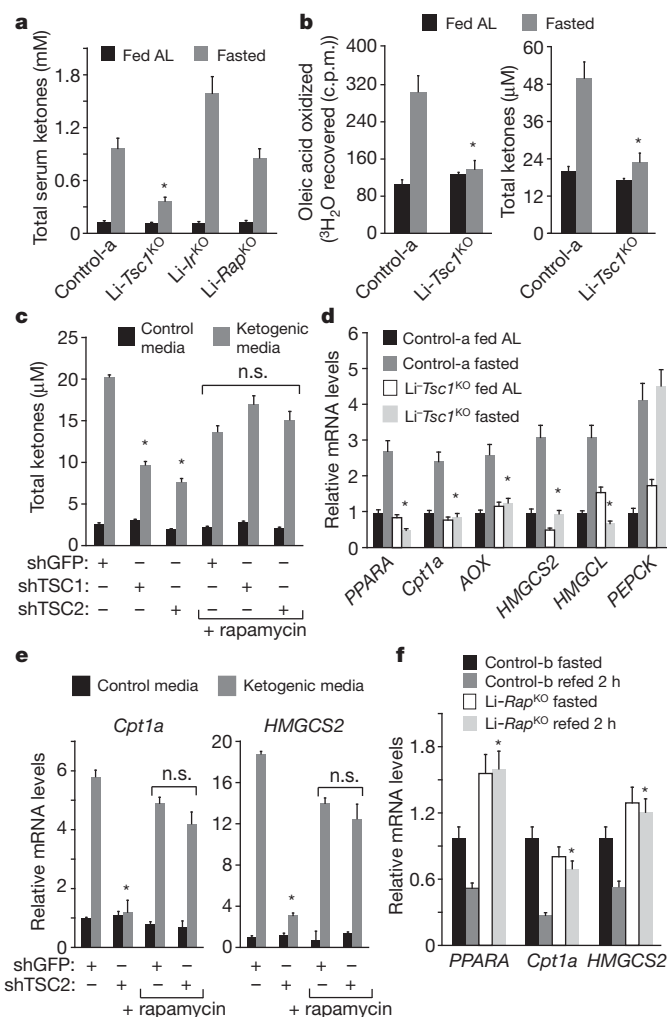


Figure 2 | mTORC1 inhibits ketogenesis and PPAR α activity in a liver autonomous fashion. **a**, Fed mice were given *ad libitum* access to food and killed at the beginning of the day. Fasted mice were denied food for 24 h and killed at the same time of day as the fed mice. Indicated values are mean \pm s.d. for $n \geq 6$; * $P < 0.05$ compared to fasted control mice. **b**, Indicated measurements were made as described in Methods using liver tissue isolated from control or *Li-Tsc1^{KO}* mice that had *ad libitum* access to food (fed) or had been fasted for 24 h. Values are mean \pm s.d. for $n = 4$. * $P < 0.05$ compared to fasted control mice. **c**, AML12 cells stably expressing validated lentiviral shRNAs targeting GFP, TSC1 or TSC2 were placed in control or ketogenic media with or without 20 nM rapamycin. Total ketones in the culture media were determined after a 3-day incubation. Values are mean \pm s.d. for $n = 6$. * $P < 0.05$ compared to shGFP-expressing cells cultured in ketogenic media. n.s., no significant differences between bracketed values. **d**, mRNA levels were quantified by qRT-PCR in total RNA isolated from indicated liver samples. Values are mean \pm s.d. for $n \geq 8$. * $P < 0.05$ compared to fasted control mice. **e**, mTORC1 activation inhibits, in a rapamycin-sensitive fashion, PPAR α -target gene expression in cells in culture. mRNA levels were determined as in **d** from the AML12 cells used in **c**. Values are mean \pm s.d. for $n = 6$. * $P < 0.05$ compared to shGFP-expressing cells growing in ketogenic media. **f**, Control and *Li-Rap^{KO}* mice were fasted for 24 h and then refed for 2 h. Levels of indicated mRNAs were measured as in **d**. Values are mean \pm s.d. for $n \geq 4$. * $P < 0.05$ compared to refed control mice.

agonist³, did not increase serum ketones or PPAR α -target gene expression in the liver (Supplementary Fig. 2e, f), but did activate PPAR α in the small intestine (a secondary site of ketogenesis), confirming that *Li-Tsc1^{KO}* mice have liver-specific defects in PPAR α function (Supplementary Fig. 2f). In accord with the *in vivo* findings, a knockdown of TSC2 in AML12 cells inhibited PPAR α in a rapamycin-sensitive fashion (Fig. 2e). Lastly, as suggested by the capacity of *Li-Rap^{KO}* mice to produce ketones in the fed state (Supplementary

Fig. 2b), feeding did not downregulate the expression of PPAR α and its target genes in the livers of Li-Rap^{KO} mice (Fig. 2f) or in mice treated with rapamycin before feeding (Supplementary Fig. 2g). Because PPAR α overexpression did not restore PPAR α -target gene expression in livers or AML12 cells with activated mTORC1 (Supplementary Fig. 4a–f), these results are consistent with mTORC1 negatively regulating ketogenesis by preventing the activation of PPAR α . Unlike mice lacking PPAR α ¹³, those without TSC1 do not have hepatic steatosis upon fasting, perhaps because plasma triglyceride and hepatic microsomal triglyceride transfer protein (MTTP) levels are increased in these mice (Supplementary Fig. 1d and data not shown), suggesting that mTORC1 promotes very low density lipoprotein assembly and secretion.

In the fed state, PPAR α interacts with the NCoR1 and SMRT corepressors, which suppress ketogenic gene expression by recruiting histone deacetylases¹⁴. Upon fasting, ligand-binding to PPAR α initiates corepressor release and the association of coactivators, like p300 or CBP, which activate ketogenic genes by recruiting histone acetylases¹⁵. In the livers of control animals, fasting led to an increase in histone acetylation at PPAR α response element (PPRE)-containing promoters, which correlated with the loss and gain of NCoR1 and p300, respectively, from the promoters (Fig. 3a–c). In contrast, in TSC1-null livers, NCoR1 did not exit the PPRE-containing promoters upon fasting, and p300 occupancy and histone acetylation remained in a fed-like state (Figs 3a–c). Raptor-null livers had the opposite phenotypes (Supplementary Fig. 5a, b) and TSC1 loss did not affect the binding of PPAR α to promoters (Supplementary Fig. 5c). In AML12 cells, the knockdown of TSC2 repressed the disassociation of NCoR1 from PPRE-containing promoters, even when the cells were treated with the PPAR α ligand (Supplementary Fig. 5d). The suppression of NCoR1 restored ketone production and PPAR α -target gene expression in TSC2-deficient AML12 cells and livers (Fig. 3d, e, Supplementary Fig. 6a–c), while the histone deacetylase inhibitor trichostatin A reversed the defect in ketone production in AML12 cells caused by mTORC1 activation (Supplementary Fig. 6d).

As these results suggested an active role for NCoR1 in the inhibition of ketogenesis and PPAR α by mTORC1, we asked if mTORC1 regulates NCoR1 function. Because mTORC1 did not affect NCoR1 protein levels (data not shown), we considered the possibility that fasting and feeding control the nuclear localization of NCoR1 in an mTORC1-dependent fashion. Quantitative imaging assays using an antibody that recognizes endogenous NCoR1 (Supplementary Fig. 7a) showed that NCoR1 was present in both the cytoplasm and nuclei of hepatocytes in fed animals but only in the cytoplasm in fasted mice (Supplementary Fig. 8a). The loss of TSC1 led to the presence of NCoR1 in the nucleus even in fasted mice (Supplementary Fig. 8a), while that of raptor prevented the feeding-induced movement of NCoR1 into the nucleus (Supplementary Fig. 8b). Analogous results were obtained with endogenous or epitope-tagged recombinant NCoR1 in cultured AML12 cells (Supplementary Figs 7b, 8c). Thus, mTORC1 regulates the subcellular localization of NCoR1, providing a potential mechanism for how mTORC1 might control PPAR α and ketogenesis.

Given that mTORC1 regulates ketogenesis and previous work showing that ageing blunts PPAR α -target gene expression and ketone production in rodents^{4,5}, we asked if mTORC1 mediates the effects of ageing on ketogenesis. If this were the case, the inhibitory effects on ketogenesis of mTORC1 activation and ageing should not be additive. Indeed, while the loss of TSC1 in young mice reduced serum ketones and hepatic PPAR α -target gene expression, the deletion of TSC1 in aged mice (Supplementary Fig. 3c) did not further reduce the already low levels of serum ketones and PPAR α and Cpt1a mRNAs observed in old animals (Fig. 4a, b). Furthermore, in aged mice, fasting did not inhibit liver mTORC1 activity to nearly the same degree as in young mice (Fig. 4c). Consistent with this defect in mTORC1 inhibition, ageing greatly impaired the fasting-induced exit of NCoR1 from the nucleus and the release of NCoR1 from PPRE-containing promoters

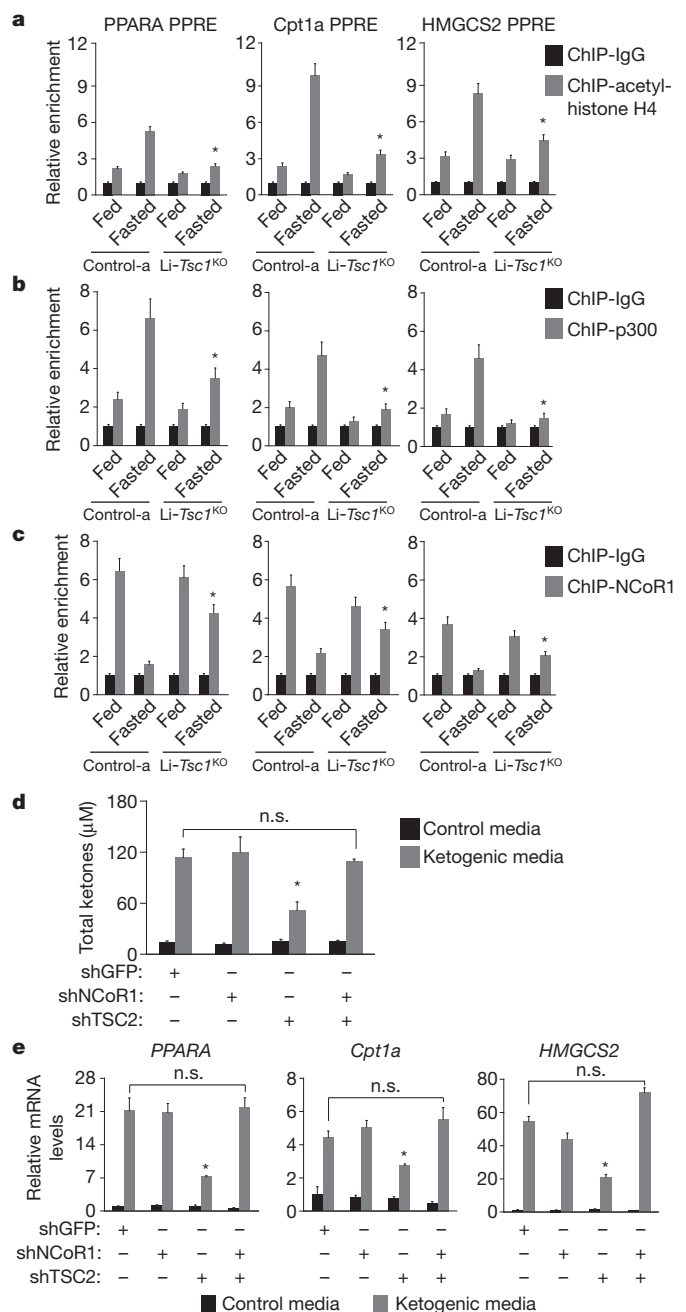
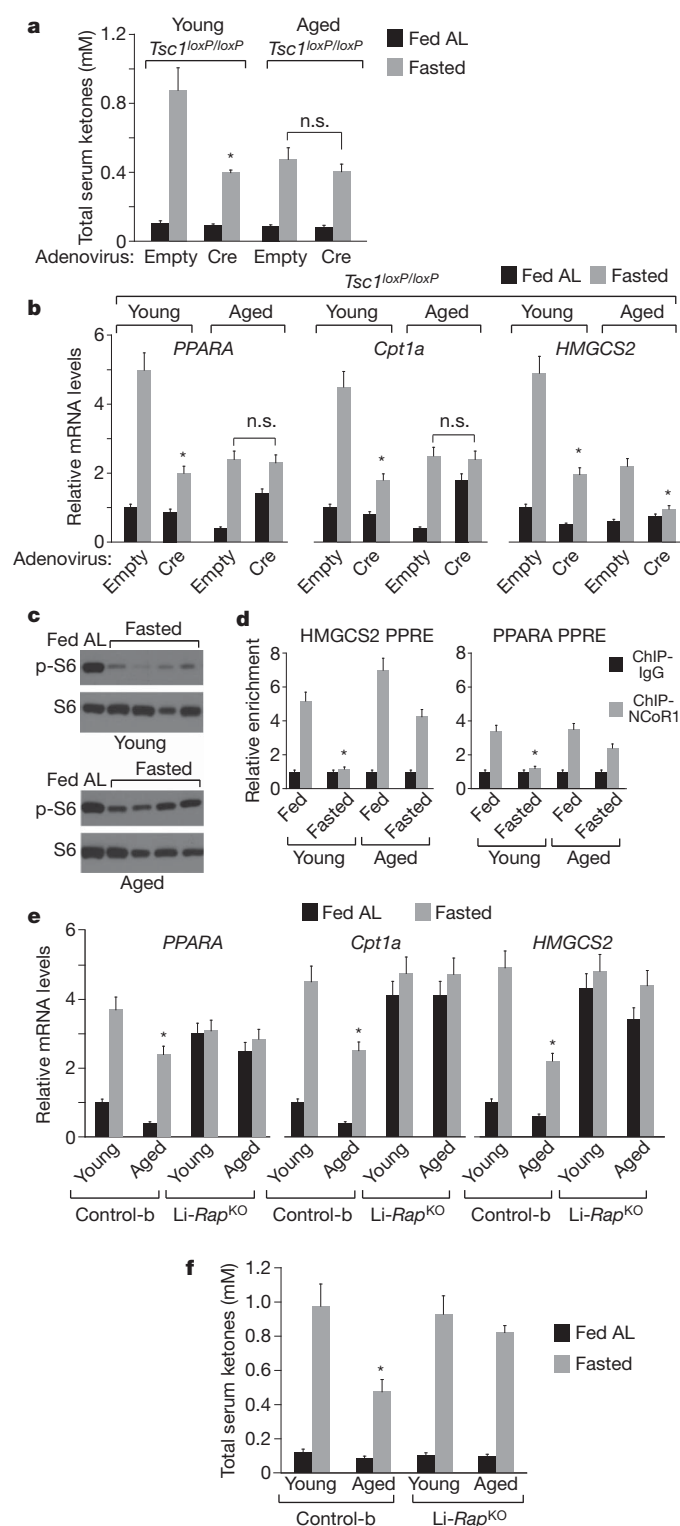


Figure 3 | mTORC1 requires the NCoR1 corepressor to inhibit PPAR α function.

a–c, At PPRE-containing promoters, mTORC1 activation in the liver prevents fasting-induced histone H4 acetylation (**a**), p300 occupancy (**b**), and release of NCoR1 (**c**). Liver extracts from control or Li-Tsc1^{KO} mice that were fed or fasted as in Fig. 2a were subjected to ChIP assays (Methods). Values are mean \pm s.d. relative enrichment values for *n* = 4. **P* < 0.05 compared to fasted control mice. **d**, **e**, AML12 cells stably expressing lentiviral shRNAs targeting GFP, NCoR1, TSC2, or NCoR1 and TSC2 were incubated in control or ketogenic media for 3 days and total media ketones (**d**) and indicated mRNA levels were determined as in Fig. 2d (**e**). Values are mean \pm s.d. for *n* \geq 5. **P* < 0.05 compared to shGFP-expressing cells cultured in ketogenic media (**d**, **e**).

(Fig. 4d, Supplementary Fig. 9a). In contrast, in Li-Rap^{KO} mice, NCoR1 remained cytoplasmic in the livers of both young and aged animals (Supplementary Figs 8b, 9a). Remarkably, aged Li-Rap^{KO} mice did not suffer (unlike aged control mice) a reduction in ketone production or PPAR α -target gene expression during fasting (Fig. 4e, f; Supplementary Figs 3d, 9b). Collectively, these findings establish that mTORC1 activity mediates the suppression of hepatic ketogenesis induced by ageing.



In conclusion, mTORC1 regulates ketogenesis and PPAR α activity in response to fasting and feeding as well as ageing. The control of NCoR1 subcellular localization by mTORC1 may be how mTORC1 regulates PPAR α and ketogenesis. Because activated mTORC1 inhibits PPAR α function in cells treated with a PPAR α agonist, mTORC1 may also regulate PPAR α through additional mechanisms, such as by preventing PPAR α from responding appropriately to ligand binding or by inhibiting PPAR α coactivators. The finding that mTORC1 promotes an ageing phenotype in the liver is consistent with substantial evidence showing that inhibition of the TORC1 pathway elongates lifespan in diverse organisms^{16,17}. If mTORC1 regulates PPAR α in

Figure 4 | mTORC1 mediates the ageing-induced inhibition of PPAR α function and ketone production. **a, b,** Young (2–8 months) or aged (20–24 months) mice having the conditional null allele of TSC1 (*Tsc1^{loxP/loxP}*) were injected with an empty adenovirus or a Cre recombinase-expressing adenovirus. Two weeks later, total serum ketones (**a**) and indicated liver mRNA levels (**b**) were measured in fed or fasted mice. Values are mean \pm s.d. for $n = 4$. $*P < 0.05$ compared to fasted young mice administered an empty adenovirus. **c,** Immunoblotting was used to measure the levels of serine 240/244 phosphorylated and total S6 in the livers of fed or fasted control mice that were young or aged. **d,** ChIP assays were performed on indicated liver extracts (Methods). Values are mean \pm s.d. for $n = 5$. $*P < 0.05$ compared to fasted young mice. **e, f,** Indicated liver mRNA levels (**e**) and total serum ketones (**f**) were measured in fed or fasted control or Li-Rap^{KO} mice that were young (2–8 months) or aged (20–24 months). Values are mean \pm s.d. for $n \geq 5$. $*P < 0.05$ compared to fasted young control mice.

other organs besides the liver, our findings may be relevant to the ageing-induced decline in PPAR α function that is known to occur in organs besides the liver¹⁸.

METHODS SUMMARY

All animal studies and procedures were approved by the MIT Institutional Animal Care and Use Committee. Mice were given chow *ad libitum*, fasted or refed for the indicated times and indicated serum metabolites were measured. Hepatic metabolite measurements (20), *ex vivo* fatty acid oxidation (19) and ketogenesis assays (19), and sodium octanoate (10), rapamycin (21) and WY 14643 (3) administrations were performed as previously described^{3,10,19–21}. Chromatin immunoprecipitation assays were performed using a kit from Millipore according to the manufacturer's instructions. Significance P values were obtained by performing non-paired, two-tailed Student's t -tests to compare two groups.

Full Methods and any associated references are available in the online version of the paper at www.nature.com/nature.

Received 28 February; accepted 13 October 2010.

1. Sarbassov, D. D., Ali, S. M. & Sabatini, D. M. Growing roles for the mTOR pathway. *Curr. Opin. Cell Biol.* **17**, 596–603 (2005).
2. Desvergne, B. & Wahli, W. Peroxisome proliferator-activated receptors: nuclear control of metabolism. *Endocr. Rev.* **20**, 649–688 (1999).
3. Dowell, P. et al. Identification of nuclear receptor corepressor as a peroxisome proliferator-activated receptor α interacting protein. *J. Biol. Chem.* **274**, 15901–15907 (1999).
4. Sanguino, E. et al. Lack of hypotriglyceridemic effect of gemfibrozil as a consequence of age-related changes in rat liver PPAR α . *Biochem. Pharmacol.* **67**, 157–166 (2004).
5. Sastre, J. et al. Aging of the liver: age-associated mitochondrial damage in intact hepatocytes. *Hepatology* **24**, 1199–1205 (1996).
6. Polak, P. & Hall, M. N. mTOR and the control of whole body metabolism. *Curr. Opin. Cell Biol.* **21**, 209–218 (2009).
7. Huang, J. & Manning, B. D. A complex interplay between Akt, TSC2 and the two mTOR complexes. *Biochem. Soc. Trans.* **37**, 217–222 (2009).
8. Michael, M. D. et al. Loss of insulin signaling in hepatocytes leads to severe insulin resistance and progressive hepatic dysfunction. *Mol. Cell* **6**, 87–97 (2000).
9. Gavrilova, O. et al. Torpor in mice is induced by both leptin-dependent and -independent mechanisms. *Proc. Natl Acad. Sci. USA* **96**, 14623–14628 (1999).
10. McGarry, J. D. & Foster, D. W. The regulation of ketogenesis from octanoic acid. The role of the tricarboxylic acid cycle and fatty acid synthesis. *J. Biol. Chem.* **246**, 1149–1159 (1971).
11. McGarry, J. D., Meier, J. M. & Foster, D. W. The effects of starvation and refeeding on carbohydrate and lipid metabolism *in vivo* and in the perfused rat liver. The relationship between fatty acid oxidation and esterification in the regulation of ketogenesis. *J. Biol. Chem.* **248**, 270–278 (1973).
12. Hsu, M. H., Savas, U., Griffin, K. J. & Johnson, E. F. Identification of peroxisome proliferator-responsive human genes by elevated expression of the peroxisome proliferator-activated receptor α in HepG2 cells. *J. Biol. Chem.* **276**, 27950–27958 (2001).
13. Hashimoto, T. et al. Defect in peroxisome proliferator-activated receptor α -inducible fatty acid oxidation determines the severity of hepatic steatosis in response to fasting. *J. Biol. Chem.* **275**, 28918–28928 (2000).
14. Guan, H. P., Ishizuka, T., Chui, P. C., Lehrke, M. & Lazar, M. A. Corepressors selectively control the transcriptional activity of PPAR γ in adipocytes. *Genes Dev.* **19**, 453–461 (2005).
15. Glass, C. K. & Rosenfeld, M. G. The coregulator exchange in transcriptional functions of nuclear receptors. *Genes Dev.* **14**, 121–141 (2000).
16. Stanfel, M. N., Shamieh, L. S., Kaeblerlein, M. & Kennedy, B. K. The TOR pathway comes of age. *Biochim. Biophys. Acta* **1790**, 1067–1074 (2009).
17. Harrison, D. E. et al. Rapamycin fed late in life extends lifespan in genetically heterogeneous mice. *Nature* **460**, 392–395 (2009).

18. Iemitsu, M. *et al.* Aging-induced decrease in the PPAR- α level in hearts is improved by exercise training. *Am. J. Physiol. Heart Circ. Physiol.* **283**, H1750–H1760 (2002).
19. Faraj, M. & Cianflone, K. Differential regulation of fatty acid trapping in mouse adipose tissue and muscle by ASP. *Am. J. Physiol. Endocrinol. Metab.* **287**, E150–E159 (2004).
20. Folch, J., Lees, M. & Sloane Stanley, G. H. A simple method for the isolation and purification of total lipides from animal tissues. *J. Biol. Chem.* **226**, 497–509 (1957).
21. Cunningham, J. T. *et al.* mTOR controls mitochondrial oxidative function through a YY1-PGC-1 α transcriptional complex. *Nature* **450**, 736–740 (2007).

Supplementary Information is linked to the online version of the paper at www.nature.com/nature.

Acknowledgements We thank S. Biddinger and C.R. Kahn for providing the $Il^{loxP/loxP}$ and $Li-Il^{KO}$ mice; D. Kwiatkowski for the $Tsc1^{loxP/loxP}$ mice; R. Zoncu for assistance with imaging experiments and image analysis; F. Reinhardt for assistance in animal virus

injections; and T. Jacks, L. Guarente, V. Mootha and members of the Sabatini laboratory for support and discussions. This research was supported by fellowships from the American Diabetes Association and Ludwig Cancer Fund to T.R.P.; a fellowship from the Canadian Institutes of Health Research to M.L.; and NIH grants CA103866 and CA129105 to D.M.S. D.M.S. is an investigator of the Howard Hughes Medical Institute.

Author Contributions S.S. and D.M.S. conceived the project and designed the experiments, S.S. performed the experiments, and T.R.P. aided in generating the $Li-Rap^{KO}$ mice and adenovirus preparations. M.L. assisted in metabolite measurements and animal dissections. S.O. assisted with animal dissections and husbandry. S.S. wrote and D.M.S. edited the manuscript.

Author Information Reprints and permissions information is available at www.nature.com/reprints. The authors declare no competing financial interests. Readers are welcome to comment on the online version of this article at www.nature.com/nature. Correspondence and requests for materials should be addressed to D.M.S. (sabatini@wi.mit.edu).

METHODS

Materials. TSC1^{loxP/loxP} mice and Li-Ir^{KO} mice were gifts from D. Kwiatkowski (Harvard Medical School) and C.R. Kahn (Joslin Diabetes Center), respectively. Antibodies to TSC1, raptor, phospho-S235/236 S6, phospho-240/244 S6, and S6 were purchased from Cell Signaling Technology; the antibody to NCoR1 for ChIP experiments and immunofluorescence assays from Abcam (ab24552); the antibody to NCoR1 for immunofluorescence studies from Thermo Scientific (PA1-844A); the p300 (sc-585x) and PPAR α (sc-9000x) antibodies from Santa Cruz Biotechnology; antibodies to the acetyl-histone H4 (06-866) from Millipore; and the Cy3-conjugated secondary antibody from Invitrogen. WY-14643 was purchased from Cayman chemicals; rapamycin from LC Labs; dexamethasone, transferrin, insulin, sodium octanoate, selenium, trichostatin A, and oleic acid from Sigma; radiolabelled oleic acid from Perkin Elmer; PPAR α -expressing adenovirus from Vector Biolabs; high-titre empty adenovirus and Cre recombinase-expressing adenovirus from the Gene Transfer Vector Core at the University of Iowa; and AML12 cells from ATCC. Lentiviral shRNAs targeting murine TSC1, TSC2 and NCoR1 were obtained from The RNAi Consortium (TRC) collection of the Broad Institute²² and from Sigma-Aldrich. The sequences for each shRNA are as follows. shNCoR1, CCGGCCTCTAATACAGCAGCTTCAACTCGAGTTGAAGTGCC TGTATTAGAGGTTTTTGT; shTsc1, CCGGGCCAGTGTATTATGCCCTCTTTTC TCGAGAAAGAGGGCATAAACAAGTGGCTTTTTTGT; shTsc2, CCGGGCCCCGA TATGTGTTCTCCAATCTCGAGATTGGAGAACACATATCGGGCTTTTTTGT; shGFP, CCGGTACAACAGCCACAACGTCTATCTCGAGATAGACGTTGTG GCTGTGTGTTTTT.

Generation of Li-Tsc1^{KO} and Li-Rap^{KO} mice. Mice carrying a floxed allele of TSC1 (*Tsc1*^{loxP/loxP})²³ were backcrossed to C57BL/6 mice for three generations, and then bred to homozygosity. For liver-specific recombination of the floxed TSC1 allele, 100 μ l of high-titre adenoviral-Cre ((3–6) $\times 10^{10}$ p.f.u. ml⁻¹) was administered via retro-orbital injection under isoflurane anaesthesia to mice ranging from 2 to 20 months in age, and subsequent experiments were performed within a month. PCR genotyping for the floxed and recombined allele was performed as previously described²³. For generation of Li-Rap^{KO} mice, a BAC clone (identifier: RP24-125C11, strain: C57BL/6J) containing raptor exon 6 was obtained from the RP24-24 mouse genomic DNA library²⁴. Standard PCR and cloning procedures were used to generate fragments spanning 4.3 kb upstream of raptor exon 6 and 2.6 kb downstream of and including raptor exon 6 (as well as a 3' LoxP site downstream of raptor exon 6) that were subsequently assembled together into the PGKneoF2L2DTA vector²⁵. In the final targeting construct, the neomycin resistance (neo) cassette was flanked by one 5' LoxP site and 5' and 3' FLP recognition target (Frt) recombination sites. Raptor exon 6 was flanked by a 5' and 3' LoxP site located 111 bp upstream and 547 bp downstream, respectively. The targeting vector was linearized and electroporated into embryonic stem cells derived from 129/SvEv mice²⁶. Clones were analysed for correct integration by Southern blot and PCR analysis. Chimaeric mice were obtained by microinjection of the correctly targeted clones into BALB/C blastocysts and crossed with C57BL/6 mice to obtain offspring with germline transmission. Mice analysed in this study were backcrossed to C57BL/6 for four generations. Some of the backcrosses involved mice constitutively expressing the FLP recombinase so as to excise the neomycin cassette from the targeted allele²⁷. Mice were bred to homozygosity for the floxed raptor allele (*Rap*^{loxP/loxP}), and then crossed to mice expressing the Cre-recombinase transgene from the liver-specific albumin promoter²⁸. PCR genotyping of *Rap*^{loxP/loxP} and Li-Rap^{KO} mice was performed with the following primers that detect the following. 3' LoxP site of targeted raptor allele: forward, CTCAGTAGTGGTATGTGCTCAG; reverse, GGGTACAGTATGTC AGCACAG. This PCR reaction generates an amplicon of 174 bp when the 3' LoxP site is present and of 140 bp when the wild-type allele is present.

Albumin Cre recombinase: forward, GTTAATGATCTACAGTTATTGG; reverse, CGCATAACCAAGTGAACAGCATTGC. This PCR reaction generates an amplicon of ~500 bp and indicates the presence of the transgene.

In all experiments involving the Li-Tsc1^{KO} mice, the control mice were *Tsc1*^{loxP/loxP} mice that were administered 'empty' adenovirus of a similar titre as the Cre-expressing adenovirus (called 'control-a' mice in figures). For all experiments involving Li-Rap^{KO} mice, the control mice were *Rap*^{loxP/loxP} mice that did not have the Albumin Cre transgene ('control-b' mice in figures). For the experiment involving Li-Ir^{KO} mice, the control mice were *Ir*^{loxP/loxP} mice that did not have the Albumin Cre transgene ('control-c' mice in figures). No significant changes in body weight, adiposity or satiety were observed in Li-Tsc1^{KO} and Li-Rap^{KO} mice compared to their respective controls. The increased liver size of Li-Tsc1^{KO} mice did not affect the sizes of other organs.

Animal experiments. WY-14643 was suspended in 10% DMSO, 90% corn oil at 1.5 mg ml⁻¹ and was administered via oral gavage to mice for 5 consecutive days at a dose of 25 mg kg⁻¹ (ref. 29). 500 mM sodium octanoate in 0.9% sodium chloride was given to mice via intra-peritoneal injections at a dose of 6 μ l per gram of body

weight (ref. 30). Rapamycin was given to mice via intra-peritoneal injections at a dose of 10 mg per kg body weight (ref. 31). For hepatic overexpression of GFP and PPAR α , mice were administered high-titre adenovirus expressing either cDNA via retro-orbital injection under isoflurane anaesthesia and killed 5 days later. For depletion of NCoR1 in the liver, mice were administered high-titre adenovirus expressing shRNAs targeted to NCoR1 or lacZ via retro-orbital injection under isoflurane anaesthesia and killed 6 days later. Low titre adenovirus expressing shRNAs were constructed using the Block-iT Adenoviral RNAi Expression System (Invitrogen) per manufacturer's instructions. High-titre virus was generated by infecting HEK-293T cells with low-titre virus (10¹⁰ p.f.u. ml⁻¹), waiting until some cell death was observed, and then concentrating 200 ml of the culture media into 1 ml using the Vivapure AdenoPACK 100 (Sartorius Stedim Biotech). Fasting experiments began at lights out and ended after the times indicated in the figures. Activity measurements were performed in cages where infrared light beams were placed every 1.5 inches along the length of the cage and beam breaks were measured using a digital counter. Body temperature was measured using an anal probe accurate to 0.1 °C. All experiments were carried out with approval from the Committee for Animal Care at MIT and under supervision of the Department of Comparative Medicine at MIT.

Immunofluorescence assays. Immunofluorescence-based imaging of NCoR1 was performed as follows: fixed liver tissue was embedded in paraffin and 3–5 μ m thick sections placed on microscope slides. Paraffin-coated sections were then de-waxed using EZ-DeWax deparaffinization solution (BioGenex), placed in boiling citrate buffer, pH 6.0 for ten minutes, and then blocked in PBS with 0.1% Tween-20 and 5% goat serum. Sections were stained overnight with the primary antibody in blocking solution at 4 °C, washed 3 times in PBS/Tween and then incubated at room temperature with Cy3-conjugated secondary antibody in blocking solution for 45 min. Sections were incubated in Hoechst solution for 10 min to stain the DNA, and then coverslipped. Immunofluorescence assays in AML12 cells were performed as previously described³². Tiled images were obtained from an inverted epifluorescence microscope (Zeiss) and the exposure time for each channel was kept constant for all slides on a given day. Signal intensity was quantified using ImageJ (NIH) as described below. The PA1-844A antibody (Thermo Scientific) was used for the NCoR1 immunofluorescence studies shown in the figures. Equivalent results were also obtained with the ab24552 (Abcam) antibody.

Image analysis. Quantification of fluorescence intensity, pixel location, and hepatocyte size were performed using the NIH software ImageJ. Greyscale 1,048 \times 792 pixel images acquired at 63 \times magnification of cells immunostained with the anti-NCoR1 antibody were used for measuring cellular NCoR1 localization. For each condition, 6 cells from 2 individual images from each liver were measured for a total of 12 cells per liver and thus 60 cells per condition. A line 90 pixels in length, which was sufficiently long to span the nucleus and some of the surrounding cytoplasmic area of all cells, was placed over each cell, such that the midpoint of the line was over the centre of the circle defined by the nucleus. The pixel intensity along the line was then recorded. Given the variability in nuclei size, the width of multiple nuclei per experimental group was also measured. A shaded area, whose width equals the mean diameter of the nuclei plus one standard deviation, was then superimposed upon the plots of pixel intensity of the NCoR1 staining to indicate the cellular location of the pixel intensity measurements.

Serum metabolite and hepatic measurements. Tail blood or blood obtained from retro-orbital bleeds at the time of death was centrifuged at low speed at 4 °C for 30 min and serum isolated for metabolite measurements. Total ketones were measured using a colorimetric assay from Wako Chemicals according to manufacturer's protocol. Total glucagon levels were measured using an ELISA kit from Wako Chemicals. True serum triglycerides were measured using a kit from Sigma, and values represent total triglycerides minus serum glycerol. Non-esterified free fatty acids were measured with a colorimetric assay from Roche, while serum insulin was measured using an ELISA kit from DSLabs. Serum glucose measurements were taken from tail blood using an instant glucometer (Ascensia Elite). Hepatic triglycerides were extracted as previously described³³, and measured as above.

Quantitative RT-PCR. Total RNA was isolated from cells and tissues using the RNeasy kit from Qiagen. Equal amounts of total RNA for each sample was used for oligo-d(T) (Invitrogen) primed reverse transcription into cDNA using SuperScript II (Invitrogen). Primers for real-time PCR were obtained from Integrated DNA Technologies. Reactions were run on an Applied Biosystems Prism machine using Sybr Green Master Mix (Applied Biosystems). The amount of β -actin cDNA was used to normalize results from gene-specific reactions. Primer sequences used to produce gene-specific amplicons are as follows. NCOR1: forward, GAAGCCACA GCAGAAGAACC; reverse, ACGACCATGTTCTACCAGGC. HMGS2: forward, ATACCACCAACGCCTGTGTTATGG; reverse, CAATGTCACCACAGA CCACCAG. PPARA: forward, AGAGCCCCATCTGTCTCTC; reverse,

ACTGGTAGTCTGCAAAACCAAA. CPT1a: forward, CCATGAAGCCCTCA AACAGATC; reverse: ATCACACCCACCACCAGATA. TSC1: forward, ATGGCCAGTTAGCCAACATT; reverse, GCTGAGAATTGGTTTCCAGGT. β -Actin: forward, GGCTGTATTCCCTCCATCG; reverse: CCAGTTGGTAA CGCCATGT. HMGCL: forward, ACTACCCAGTCTGACTCCAA; reverse: TAGAGCAGTTCCGCTTCTTCC. PEPC: forward, CGATGACATCGCTGG ATGA; reverse, TCTTGCCCTTGTGTTCTGCA. ACOX: forward, GCCTGAG CTTTCATGCCCTCA; reverse, ACCAGAGTTGGCCAGACTGC.

Ex vivo liver measurements. The hepatic *ex vivo* fatty-acid oxidation assay was performed as previously described³⁴. Briefly, livers were removed from mice and three ~40 mg portions were placed in individual wells of a 24-well plate along with 1 ml of Krebs-Ringer saline and 1 mM ³H-oleic acid-BSA (final concentration was 1 μ Ci per mM ³H-oleic acid). Livers were incubated at 37 °C and 5% oxygen for 2 h. After two hours, the medium was removed, 10 μ l was retained for ketone measurements, and the rest transferred to an Eppendorf tube with no cap. Tubes were placed in scintillation vials that contained 2 ml of water, wrapped in aluminium foil, and incubated overnight at 65 °C. The next day the vials were cooled at 4 °C for 30 min, the Eppendorf tube was removed, scintillation fluid was added, and the levels of ³H₂O were measured using a scintillation counter.

In vitro ketogenesis in AML12 cells. For passaging, AML12 cells were cultured in medium prescribed by ATCC that contains insulin and serum. For induction of ketogenesis, cells were first grown to confluence, washed once with PBS, and then incubated in media devoid of serum and insulin and containing 50 μ M WY-14643 and 2 mM sodium octanoate. At indicated times, aliquots of the media were removed and total ketone levels measured. Total RNA was also isolated from each well and used to normalize media ketone levels between wells. When employed, lentiviral shRNAs were used as described³². Using qRT-PCR, all shRNAs were validated to knockdown their respective targets by at least 70% (Supplementary Fig. 2a, b).

Chromatin immunoprecipitation assays. Chromatin immunoprecipitation assays were performed using a kit from Millipore according to the manufacturer's instructions. Liver portions were crosslinked in 1.5% formaldehyde in PBS for 15 min at room temperature, and the reaction was quenched with 0.125 M glycine. Liver cells were disaggregated using 20 gauge syringe needles. Resulting cells were then lysed in 1% SDS lysis buffer for 10 min, and sonicated at 30 s intervals for a total of 5 min. Resulting lysates were diluted in buffer containing 0.01% SDS, 1.1% Triton, 1.2 mM EDTA, 167 mM NaCl and 16.7 mM Tris-HCl. Diluted lysates were pre-cleared with protein-A agarose/salmon sperm and then incubated overnight at 4 °C with 3 μ l of NCoR1 antibody, 5 μ l of acetyl-histone H4 antibody, and 4 μ g of p300 antibody or 4 μ g IgG per 10⁶ cells. The next day, the antibodies were captured with protein-A agarose/salmon sperm for 1 h, pelleted, and subjected to washes in low salt, high salt, LiCl and TE buffers contained in the Millipore kit.

The chromatin was eluted from antibodies with 1% SDS and 0.1 M NaHCO₃, and the crosslinks reversed by heating at 65 °C for 4 h. The chromatin was treated with proteinase K, purified using the High Pure PCR Template Preparation Kit from Roche, and used for PCR analysis. AML12 cells were processed with the same protocol except beginning at the step in which cells are lysed in 1% SDS lysis buffer. The primers below were used to amplify a 150–200 bp amplicon encompassing the PPPE of the indicated genes. As both a negative control and to ensure that proper shearing length was achieved for genomic DNA, PCR was also performed for an amplicon within the second intron of Cpt1a. PPARA PPPE: forward, TTCCGAACCATTCTTCCAG; reverse, GCTGCCTTCTTTGCAGAGT. HMGCS2 PPPE: forward, TGAGCCACTCAGCAGAGGAATCAG; reverse: CTGGGTTGGGCTTTATAAGACTCC. CPT1a PPPE: forward, CTTTCCTA CTGAGGCCAGATAG; reverse: TACAGCCTAGAACCCTGACTGC. CPT1a Intron: forward, CTGGTTGGAATAGGTGTGTCAGT; reverse, ATTGGGGC TGCTTACAGGTTT.

22. Moffat, J. *et al.* A lentiviral RNAi library for human and mouse genes applied to an arrayed viral high-content screen. *Cell* **124**, 1283–1298 (2006).
23. Uhlmann, E. J. *et al.* Astrocyte-specific TSC1 conditional knockout mice exhibit abnormal neuronal organization and seizures. *Ann. Neurol.* **52**, 285–296 (2002).
24. Osoegawa, K. *et al.* Bacterial artificial chromosome libraries for mouse sequencing and functional analysis. *Genome Res.* **10**, 116–128 (2000).
25. Hoch, R. V. & Soriano, P. Context-specific requirements for Fgfr1 signaling through Frs2 and Frs3 during mouse development. *Development* **133**, 663–673 (2006).
26. Nagy, A., Rossant, J., Nagy, R., Abramow-Newerly, W. & Roder, J. C. Derivation of completely cell culture-derived mice from early-passage embryonic stem cells. *Proc. Natl Acad. Sci. USA* **90**, 8424–8428 (1993).
27. Rodríguez, C. I. *et al.* High-efficiency deleter mice show that FLPe is an alternative to Cre-loxP. *Nature Genet.* **25**, 139–140 (2000).
28. Postic, C. & Magnuson, M. A. DNA excision in liver by an albumin-Cre transgene occurs progressively with age. *Genesis* **26**, 149–150 (2000).
29. Issemann, I. & Green, S. Activation of a member of the steroid hormone receptor superfamily by peroxisome proliferators. *Nature* **347**, 645–650 (1990).
30. McGarry, J. D. & Foster, D. W. The regulation of ketogenesis from octanoic acid. The role of the tricarboxylic acid cycle and fatty acid synthesis. *J. Biol. Chem.* **246**, 1149–1159 (1971).
31. Cunningham, J. T. *et al.* mTOR controls mitochondrial oxidative function through a YY1-PGC-1 α transcriptional complex. *Nature* **450**, 736–740 (2007).
32. Sancak, Y. *et al.* The Rag GTPases bind raptor and mediate amino acid signaling to mTORC1. *Science* **320**, 1496–1501 (2008).
33. Folch, J., Lees, M. & Sloane Stanley, G. H. A simple method for the isolation and purification of total lipides from animal tissues. *J. Biol. Chem.* **226**, 497–509 (1957).
34. Faraj, M. & Cianflone, K. Differential regulation of fatty acid trapping in mouse adipose tissue and muscle by ASP. *Am. J. Physiol. Endocrinol. Metab.* **287**, E150–E159 (2004).

The histone variant macroH2A suppresses melanoma progression through regulation of CDK8

Avnish Kapoor^{1,2}, Matthew S. Goldberg^{1,2}, Lara K. Cumberland^{1,2*}, Kajan Ratnakumar^{1,2*}, Miguel F. Segura^{4,6}, Patrick O. Emanuel^{2,3}, Silvia Menendez^{4,6}, Chiara Vardabasso^{1,2}, Gary LeRoy⁷, Claudia I. Vidal^{2,3†}, David Polsky^{4,5,6}, Iman Osman^{5,6}, Benjamin A. Garcia⁷, Eva Hernando^{4,6} & Emily Bernstein^{1,2}

Cancer is a disease consisting of both genetic and epigenetic changes. Although increasing evidence demonstrates that tumour progression entails chromatin-mediated changes such as DNA methylation, the role of histone variants in cancer initiation and progression currently remains unclear. Histone variants replace conventional histones within the nucleosome and confer unique biological functions to chromatin^{1–3}. Here we report that the histone variant macroH2A (mH2A) suppresses tumour progression of malignant melanoma. Loss of mH2A isoforms, histone variants generally associated with condensed chromatin and fine-tuning of developmental gene expression programs^{1,4–6}, is positively correlated with increasing malignant phenotype of melanoma cells in culture and human tissue samples. Knockdown of mH2A isoforms in melanoma cells of low malignancy results in significantly increased proliferation and migration *in vitro* and growth and metastasis *in vivo*. Restored expression of mH2A isoforms rescues these malignant phenotypes *in vitro* and *in vivo*. We demonstrate that the tumour-promoting function of mH2A loss is mediated, at least in part, through direct transcriptional upregulation of CDK8. Suppression of CDK8, a colorectal cancer oncogene^{7,8}, inhibits proliferation of melanoma cells, and knockdown of CDK8 in cells depleted of mH2A suppresses the proliferative advantage induced by mH2A loss. Moreover, a significant inverse correlation between mH2A and CDK8 expression levels exists in melanoma patient samples. Taken together, our results demonstrate that mH2A is a critical component of chromatin that suppresses the development of malignant melanoma, a highly intractable cutaneous neoplasm.

The H2A family is the largest and most diverse histone family, and includes vertebrate-specific mH2A1 (splice variants mH2A1.1 and 1.2) and mH2A2 (refs 1,3,9–11), which are generally associated with transcriptionally repressed chromatin^{12,13}. However, mH2A is widely distributed throughout chromatin^{4–6} and exists in post-translationally modified forms^{3,14}, suggesting additional unidentified functions for this variant.

Given increasing evidence for variant-mediated transcriptional control^{1–3} and recent reports describing variants as prognostic markers in cancer^{15,16}, we hypothesized that global alteration of variants could contribute to malignant melanoma, the most lethal form of skin cancer with rising incidence^{17,18}. Its radial growth phase (RGP) is characterized by lateral melanocyte growth and its vertical growth phase (VGP) by spread of melanoma cells into the dermis and subcutis, upon which metastasis can occur¹⁹.

Using well characterized, paired series of murine and human melanoma cells lines, we probed the H2A variant profile. The murine B16 series represents cells of increasing metastatic potential²⁰, and the human series of a primary melanoma (WM115) and two subsequent

skin metastases derived from this same patient (WM266-4 and WM165-1)²¹. In highly malignant cells of the murine and human series, a global decrease of mH2A1 and mH2A2 protein and messenger RNA (mRNA) was observed (Fig. 1a and Supplementary Figs 1 and 2). Analysis of histones from both series using multiplexed quantitative mass spectrometry²² confirmed these findings (Supplementary Fig. 1). Furthermore, mH2A1 and mH2A2 loss was observed in a panel of primary and metastatic melanoma cells (Supplementary Fig. 1). Interestingly, a 1.5- to threefold increase in H2A.Z levels (often associated with promoters of active genes)^{1,3} was also observed (Fig. 1a and Supplementary Fig. 3), implicating possible H2A variant exchange during melanoma progression. Consistent with a global loss of mH2A and increased H2A.Z levels, we observed highly decondensed chromatin in B16-F10 cells by micrococcal nuclease digestion (Supplementary Fig. 2).

Next, we performed immunohistochemistry (IHC) on approximately 115 human tissues ranging from benign nevi to metastatic melanoma (tissue set 1, Supplementary Fig. 4). mH2A2 antibody was used for IHC, as it produced clear nuclear staining, and tissues were independently scored (0–3) by two blinded dermatopathologists with excellent interobserver consistency ($\kappa = 0.80$). IHC demonstrated that although mH2A2 is abundant in melanocytes of benign nevi and RGP lesions, its expression is dramatically lost in more than 80% of VGP and metastatic melanomas ($P < 0.001$) (Fig. 1b and Supplementary Fig. 4). This suggests mH2A loss occurs during the critical RGP to VGP transition. IHC was also performed on 25 melanomas with known BRAF status (D.P., unpublished observations)²³. An activating mutation of BRAF, V600E, is present in approximately 65% of melanomas²⁴. Although this data set did not reveal a significant correlation between mH2A2 loss and V600E mutation, it produced similar mH2A2 results as the first cohort, as did a tissue microarray (Supplementary Fig. 4). Using fresh tissues, we observed significantly reduced levels of mH2A1 and mH2A2 mRNA in metastatic melanoma specimens compared with nevi and primary melanocytes (Fig. 1c).

Owing to the transcriptional downregulation of mH2A in human melanoma, combined with its re-expression in metastatic melanoma cells upon 5-Aza-2'-deoxycytidine treatment (Supplementary Fig. 5), we hypothesized that DNA methylation may enable silencing of mH2A. Indeed, through extensive bisulphite sequencing analysis, we identified a region of the mH2A2 promoter that is significantly methylated in metastatic melanoma tissues and cell lines, but not in primary melanocytes, WM115 cells or benign nevi (Fig. 1d and Supplementary Fig. 5).

Collectively, these findings prompted us to examine the functional consequences of mH2A loss. We established multiple stable short hairpin RNA (shRNA) lines in murine B16-F0 and F1 and human WM115 melanoma cells, targeting mH2A1, mH2A2 and control

¹Department of Oncological Sciences, Mount Sinai School of Medicine, 1425 Madison Avenue, New York, New York 10029, USA. ²Department of Dermatology, Mount Sinai School of Medicine, 1425 Madison Avenue, New York, New York 10029, USA. ³Department of Pathology, Mount Sinai School of Medicine, 1425 Madison Avenue, New York, New York 10029, USA. ⁴Department of Pathology, New York University Langone Medical Center, New York, New York 10016, USA. ⁵Department of Dermatology, New York University Langone Medical Center, New York, New York 10016, USA. ⁶Interdisciplinary Melanoma Cooperative Group, New York University Langone Medical Center, New York, New York 10016, USA. ⁷Department of Molecular Biology, Princeton University, 415 Schultz Laboratory, Princeton, New Jersey 08544, USA. [†]Present address: Department of Dermatology, Saint Louis University School of Medicine, St Louis, Missouri 63104, USA.

*These authors contributed equally to this work.

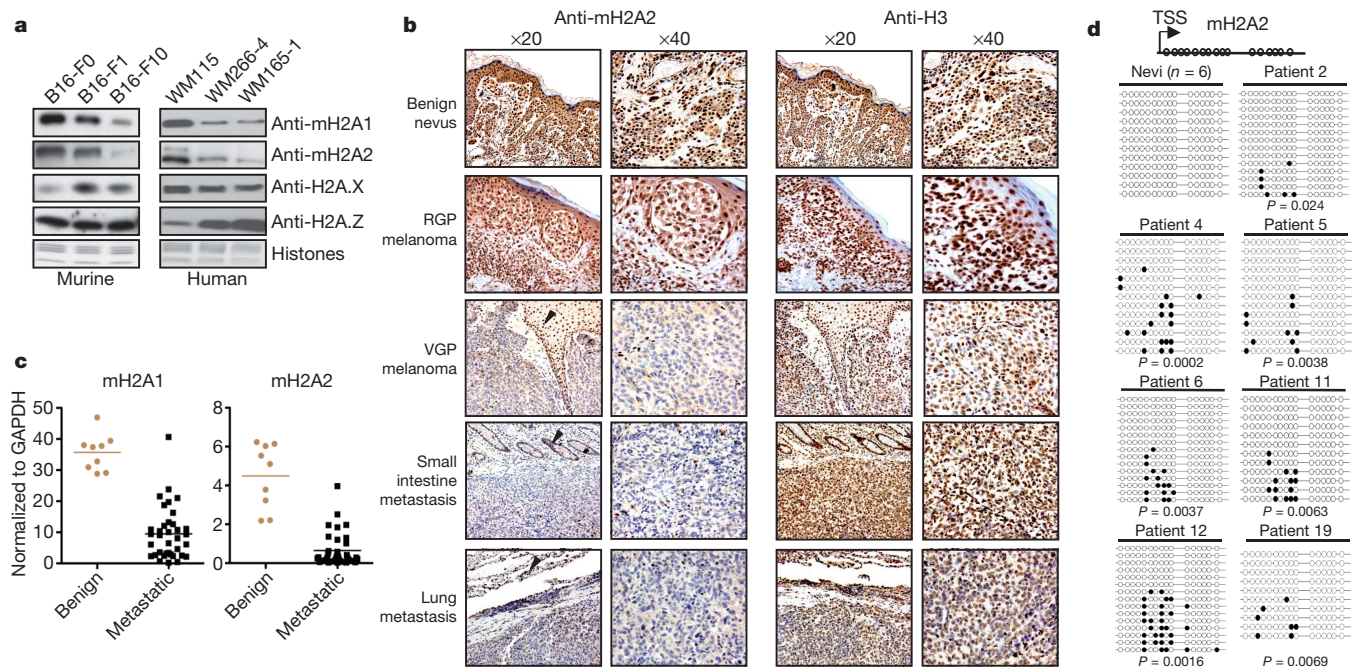


Figure 1 | mH2A loss correlates with increasing melanoma malignancy. **a**, Melanoma cells probed for H2A variants; core histones used for loading. **b**, IHC of human tissue with mH2A2 (left) and histone H3 (right). Original magnifications $\times 20$ and $\times 40$ are shown. mH2A2 visualized using DAB (brown) and haematoxylin (blue). Arrows depict mH2A2 staining in non-melanocytic cells. **c**, qRT-PCR of mH2A1 and mH2A2 in benign nevi and

melanocytes (brown circles) and metastatic melanoma (black squares); $P < 0.0001$. **d**, DNA methylation of mH2A2 promoter in nevi ($n = 6$, 10–12 clones per nevus) and metastatic melanoma tissues ($n = 7$, 10–14 clones per tissue); 16 CpG sites shown. Open circles (unmethylated), black circles (methylated); P values determined by Mann–Whitney U test.

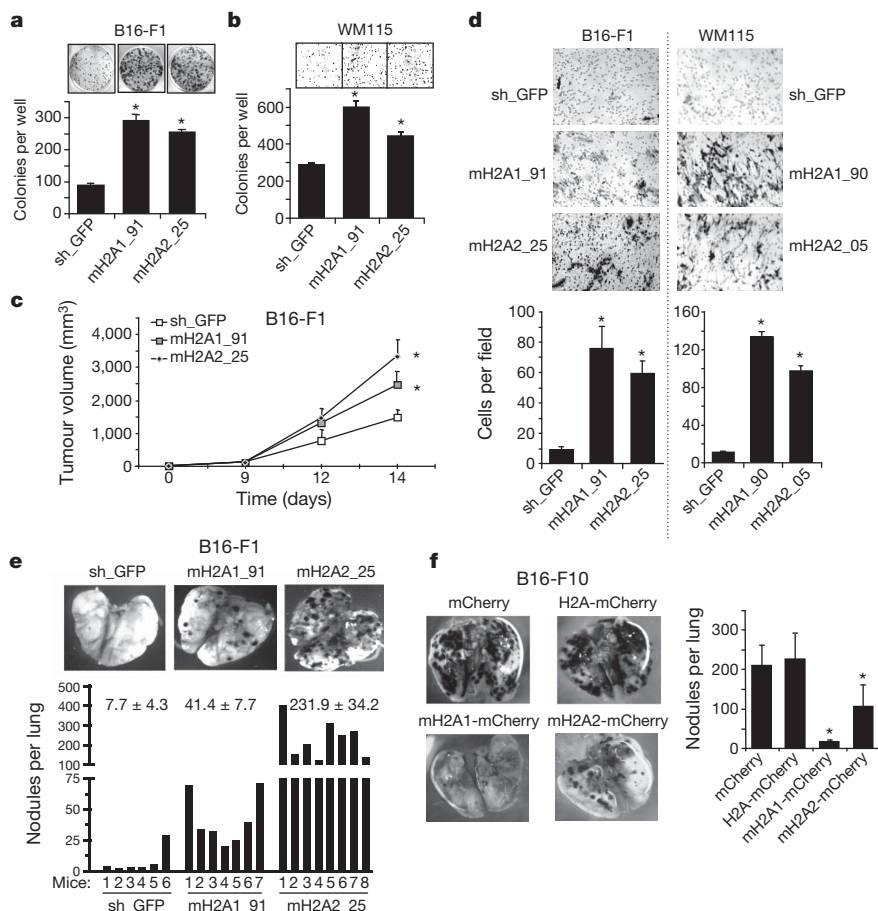


Figure 2 | mH2A depletion and ectopic expression alter malignant properties of melanoma cells *in vitro* and *in vivo*. **a**, Colony assay of B16-F1 shRNA-expressing cells. Quantified (below); $*P < 0.0000005$; mean \pm s.e.m. ($n = 4$). **b**, Soft agar assay of WM115 shRNA-expressing cells. Quantified (below); $*P < 0.0005$; mean \pm s.d. ($n = 4$). **c**, Tumour volume (in cubic millimetres) after subcutaneous injections of B16-F1 shRNA cells; $*P < 0.05$ at day 14; mean \pm s.e.m. ($n = 10$ mice per group). **d**, Trans-well migration assay in B16-F1 and WM115. Quantification below; $*P < 0.0001$; mean \pm s.d. ($n = 5$). **e**, Representative lungs of B16-F1 cells injected intravenously, 14 days after injection; mean \pm s.e.m.; nodules/lung/mouse shown ($n = 6$ –8 mice per group). **f**, Representative lungs of B16-F10 cells injected intravenously, 10 days after injection. Quantified (right); $*P < 0.005$; mean \pm s.e.m. ($n = 6$ –9 mice per group).

green fluorescent protein (GFP) (Supplementary Figs 6 and 7). Two shRNA-transduced cell lines from mouse and human were used for in-depth analysis: B16-F1 mH2A1_91 and mH2A2_25 and WM115 mH2A1_90 and mH2A2_05 (Supplementary Figs 6 and 7 for additional shRNA lines and isoform-specific knockdown).

Proliferation was examined in shRNA-expressing cells by colony formation and MTS cell viability assays. The loss of mH2A increases proliferation of murine and human melanoma cells (Fig. 2a and Supplementary Figs 6 and 7), as well as anchorage-independent growth of WM115 cells (Fig. 2b and Supplementary Fig. 7). To examine growth potential *in vivo*, B16-F1 shRNA cell lines were injected subcutaneously into mice; mH2A-deficient cells exhibited significantly enhanced tumour growth compared with controls (Fig. 2c). mH2A knockdown was confirmed by immunoblotting lysates from tumours (Supplementary Fig. 8).

Because cell motility contributes to metastasis and melanocytes originate from migratory neural crest cells, shRNA lines were analysed for migratory behaviour. Loss of mH2A in murine and human cells enhanced migration through an 8- μ m Transwell and the ability to close an artificial wound, compared with control cells (Fig. 2d and Supplementary Figs 6 and 7). Next, murine shRNA cell lines were injected into the lateral tail veins of mice to assay metastatic potential. Fourteen days after injection, mice were killed and lungs dissected for macro- and microscopic histology (Fig. 2e). Lungs of mice injected with mH2A1_91 and mH2A2_25 cells showed a five- and 30-fold increase, respectively, in the number of macroscopic metastases compared with lungs from control mice (Fig. 2e). Haematoxylin and eosin and Ki-67 staining revealed metastatic disease with proliferation, respectively, in mH2A shRNA-expressing tumours; mH2A knockdown in lungs was confirmed by IHC (Supplementary Fig. 8).

Next, mH2A expression was stably restored in malignant B16-F10 and human WM266-4 and A375 cells. The core histones H2A, mH2A1 (1.2) and mH2A2 were fused to mCherry and functional stable lines generated (Supplementary Figs 9, 11 and 13). Ectopic expression of mH2A1.2 and mH2A2, but not H2A or mCherry alone, resulted in reduced proliferation (without evidence of apoptosis) and migration (Supplementary Figs 10, 12 and 14). Human A375 cells expressing the mCherry series were injected subcutaneously into the flanks of immunocompromised mice; expression of mH2A1.2 and mH2A2 suppressed growth (Supplementary Fig. 14). Furthermore, B16-F10 cells expressing mCherry fusions were injected into tail veins of mice; mH2A1.2 and mH2A2 significantly suppressed metastasis to the lungs (Fig. 2f and Supplementary Fig. 10).

Given the striking phenotypes of mH2A manipulation in melanoma cells, we hypothesized that loss of mH2A may alter the transcriptional state of proliferation- and metastasis-related genes. We performed gene expression profiling using Affymetrix microarrays with B16-F1 cells (mH2A1_91, mH2A2_25 and sh_GFP). As expected for mH2A's role in fine-tuning of gene expression⁴, many genes showed a less than twofold change (Supplementary Figs 15, 16 and 17 for Venn diagrams, heatmaps and gene ontology). Fifteen genes showed at least a twofold change, common to both shRNA lines in two independent experiments, including Integrin alpha 4 (Itga4), transcriptional regulators CDK8 (Mediator complex component) and Cited1 (CBP/p300 transactivator) (Fig. 3a). In concordance with our data, Itga4 expression is inversely correlated with invasive potential of B16 cells²⁵ and expression profiling of human melanoma cells identified Cited1 loss in metastatic cells²⁶. CDK8, however, is a new player in melanoma malignancy.

In concordance, CDK8 mRNA and protein levels were elevated both in murine and human cells depleted of mH2A (Fig. 3a–c), as well as subcutaneous tumours and lung metastases derived from mH2A-deficient lines (Supplementary Fig. 18). Next we stably expressed RNA interference (RNAi)-resistant mH2A2 and H2A in the B16-F1 mH2A2_24 shRNA line, which targets the 3' untranslated region of mH2A2. Although CDK8 levels remained high in mH2A2_24 cells expressing H2A-mCherry, addition of mH2A2-mCherry rescued

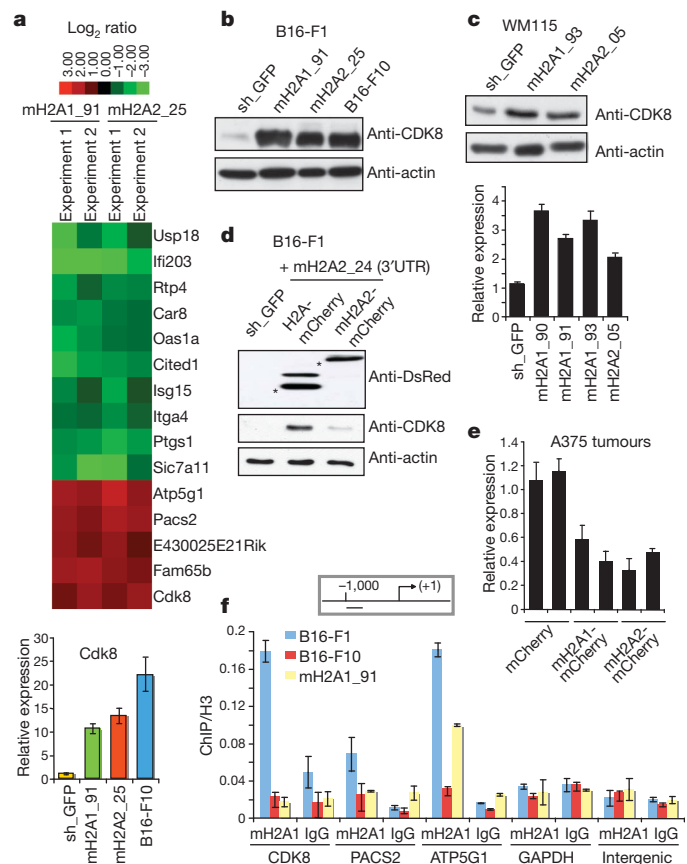


Figure 3 | Microarray and ChIP analyses identify CDK8 as a direct mH2A-regulated gene in melanoma. **a**, Heat map representing gene expression changes (at least twofold) in B16-F1 mH2A-deficient cells. qRT-PCR of CDK8 (bottom); mean \pm s.d. ($n = 3$). **b**, Immunoblots of CDK8 in murine shRNA lines; actin for loading. **c**, Immunoblot and qRT-PCR of CDK8 in human shRNA lines; mean \pm s.d. ($n = 3$). **d**, CDK8 and DsRed immunoblots of mH2A2_24 line expressing H2A- and mH2A2-mCherry; asterisk depicts fusion proteins. **e**, CDK8 qRT-PCR analysis in A375 subcutaneous tumours; mean \pm s.d. ($n = 3$). **f**, mH2A1 ChIP analysis of the -1 kb position from TSS for CDK8, PACS2, ATP5G1 and GAPDH; intergenic control. IgG used as control antibody; mean \pm s.d. ($n = 3$).

CDK8 expression to B16-F1 levels (Fig. 3d). Moreover, CDK8 was downregulated in subcutaneous tumours derived from A375 cells expressing mH2A1- and mH2A2-mCherry (Fig. 3e and Supplementary Fig. 14).

Intrigued by transcriptional upregulation of CDK8, a colorectal cancer oncogene^{7,8}, we enquired if CDK8 is a direct target of mH2A. Chromatin immunoprecipitation (ChIP) analysis demonstrated that the CDK8 promoter is enriched in mH2A1-containing nucleosomes in B16-F1, but absent in B16-F10 cells and a control shRNA line (Fig. 3f and Supplementary Fig. 18). ChIP analysis of additional mH2A target genes (but not an intergenic locus or GAPDH) also revealed enrichment, and demonstrated that CDK8 is a highly enriched mH2A target gene (Fig. 3f).

By examining a panel of human cell lines, we observed high CDK8 protein levels in metastatic melanoma cells, comparable to that of colon cancer cells (Fig. 4a). We used shRNAs to deplete CDK8 from B16-F10 and human A375 and WM165-1 cells, which contain high levels of CDK8 (Fig. 4b, Supplementary Figs 19 and 20). The loss of CDK8 significantly reduced proliferation (Fig. 4b) mediated by G2/M arrest in human cells (Supplementary Fig. 20). Conversely, ectopic expression of CDK8 (and a kinase-defective mutant, D173A)⁷ in B16-F1 cells resulted in significantly increased proliferation (Supplementary Fig. 21). Although proliferation in murine melanoma cells appears independent of the kinase activity of CDK8, it may be

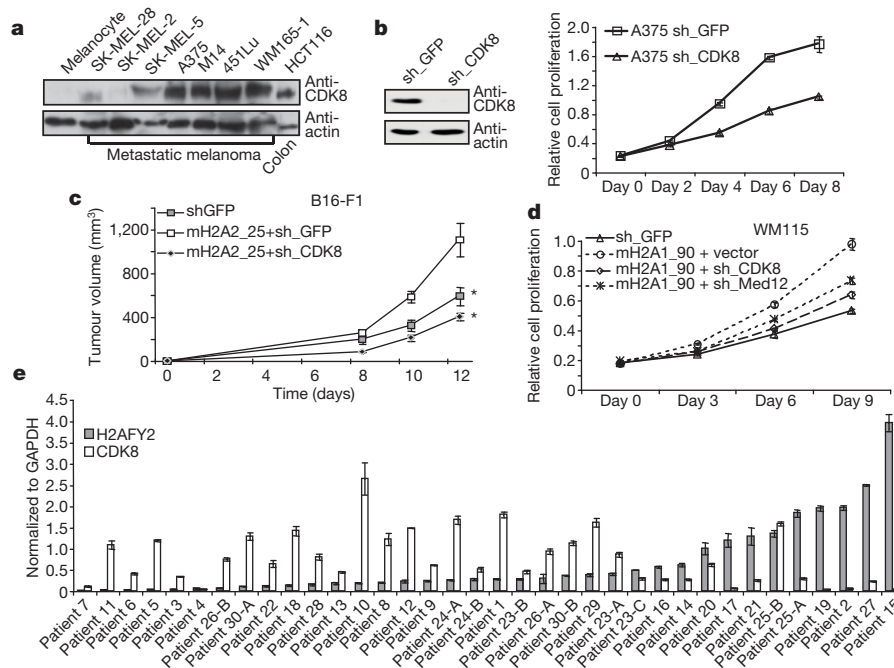


Figure 4 | CDK8 is a major effector of mH2A loss. **a**, Melanocytes, metastatic melanoma and colon cancer cells probed for CDK8; actin for loading. **b**, Immunoblot of A375 cells expressing CDK8 shRNA (left), MTS assay (right); mean \pm s.d. ($n = 5$). **c**, Tumour volume (in cubic millimetres) after subcutaneous injections; $*P < 0.05$ at day 12; mean \pm s.e.m. ($n = 9$ mice per

group). **d**, MTS assay of WM115 mH2A1_90 line co-expressing CDK8 or Med12 shRNAs; mean \pm s.d. ($n = 5$). **e**, qRT-PCR of mH2A2 and CDK8 in 36 melanoma tissues (from 30 patients; Supplementary Table 4); Pearson's $r = -0.406$ with $P = 0.014$; mean \pm s.d. ($n = 3$).

consistent with recent studies demonstrating a kinase-independent role of CDK8 (ref. 27).

To dissect the relationship between mH2A and CDK8, we first depleted CDK8 in mH2A shRNA-expressing cells (B16-F1 and WM115 lines). Knockdown of CDK8 was able to suppress the enhanced proliferation induced by mH2A loss *in vitro* and *in vivo* (Fig. 4c, d and Supplementary Figs 21 and 22). Knockdown of Med12, a subunit of the CDK8 submodule of Mediator²⁷, showed a similar effect (Fig. 4d and Supplementary Fig. 22), suggesting that CDK8 functions within the Mediator subcomplex in melanoma.

Next, we performed quantitative PCR with reverse transcription (qRT-PCR) of mH2A and CDK8 in 36 fresh melanoma specimens. This analysis demonstrated a statistically significant inverse correlation of mH2A2 and CDK8 at the mRNA level (Pearson's $r = -0.406$; $P = 0.014$; Fig. 4e). We performed IHC for CDK8 ($\kappa = 0.58$) in human tissues previously scored for mH2A2, and observed strong CDK8 staining (scored 2–3) in a large fraction of mH2A2 negative (scored 0) melanomas (29/38 = 76%; Supplementary Fig. 23). A similar inverse trend was observed in a panel of human melanoma cell lines (Supplementary Fig. 23). Finally, by probing fresh benign nevus tissues, we observed high mH2A and low CDK8 protein levels (Supplementary Fig. 23). Collectively, these results strongly suggest that CDK8 is a major effector of mH2A-mediated melanoma progression.

Here we demonstrate that mH2A is globally lost during melanoma progression. Similar findings have recently been described in lung cancer; mH2A1.1 is enriched in pre-cancerous senescent cells, but lost upon bypass of senescence¹⁶. However, the mechanism by which this occurs and its biological consequences remain unclear. Our study suggests mH2A loss in melanoma, mediated in part by DNA methylation, occurs after a potential senescence bypass (that is, in a nevus), but rather during the critical RGP to VGP transition. Nevertheless, mH2A isoforms may serve as important biomarkers for melanoma, and/or other cancers.

The data presented here point towards a novel mechanism whereby CDK8 is regulated by the unique histone variant mH2A. We look forward to future studies focused on CDK8 function and its inhibition

in melanoma. Our findings support emerging links between chromatin structure and cancer, and, for the first time to our knowledge, demonstrate a direct role of mH2A in this process.

METHODS SUMMARY

Cell culture, plasmids, infections and RNAi. Detailed information is described in Methods.

Chromatin fractionation, acid extraction of histones and immunoblotting. Chromatin fractionation and acid extraction of histones was performed as described¹⁴. Antibodies used for immunoblotting can be found in Methods.

Quantitative mass spectrometry. Quantitative mass spectrometry was performed as described²².

Immunohistochemistry, pathology and statistical analysis. Specimens were obtained from Mount Sinai School of Medicine's Division of Dermatopathology (project number HSD08-00565), New York University (IRB number 10362) and melanoma tissue microarray (Imgenex number IMH-369). Details on staining, pathology and statistical analyses are described in Methods.

Clinical specimens. Human specimens were collected at the time of surgery. Approval to collect melanoma specimens was granted by Mount Sinai Biorepository Cooperative and the New York University Interdisciplinary Melanoma Cooperative Group (project numbers above). Approval to collect benign nevi was granted by Mount Sinai School of Medicine's Division of Dermatopathology (project number 08-0964).

Bisulphite sequencing. This was performed according to the manufacturer's instructions (Zymo Research). Details are described in Methods.

Cell proliferation, migration and mouse injections. MTS was performed according to the manufacturer's instructions (Promega). Colony formation and soft agar assays were performed as described²⁸. The Transwell migration assay is described in Methods. *In vivo* metastasis assays were performed as described²⁸. For subcutaneous injections, 2.5×10^5 B16-F1 cells were injected into 6-week-old C57BL/6J mice and 2×10^6 A375 cells injected into NOG mice (Jackson Laboratories); tumour volume measured over 14- and 20-day periods, respectively.

Microarray hybridization, data analysis and hierarchical clustering. Microarray was performed using two biological replicates according to Affymetrix GeneChip protocol. Initial data extraction was performed at the Microarray Shared Research Facility at Mount Sinai School of Medicine. Heatmaps were generated using Cluster and Tree View programs.

Quantitative PCR and ChIP. qPCR was performed in triplicate on Stratagene Opticon 2 using FastStart SYBR Green Mix (Roche). Expression levels were

normalized to TATA binding protein or GAPDH. ChIP assays were performed using a Magna ChIP Kit (Millipore) as per the manufacturer's instructions.

Full Methods and any associated references are available in the online version of the paper at www.nature.com/nature.

Received 15 November 2009; accepted 13 October 2010.

- Bernstein, E. & Hake, S. B. The nucleosome: a little variation goes a long way. *Biochem. Cell Biol.* **84**, 505–517 (2006).
- Sarma, K. & Reinberg, D. Histone variants meet their match. *Nature Rev. Mol. Cell Biol.* **6**, 139–149 (2005).
- Thambirajah, A. A., Li, A., Ishibashi, T. & Ausió, J. New developments in post-translational modifications and functions of histone H2A variants. *Biochem. Cell Biol.* **87**, 7–17 (2009).
- Changolkar, L. N. *et al.* Developmental changes in histone macroH2A1-mediated gene regulation. *Mol. Cell. Biol.* **27**, 2758–2764 (2007).
- Buschbeck, M. *et al.* The histone variant macroH2A is an epigenetic regulator of key developmental genes. *Nature Struct. Mol. Biol.* **16**, 1074–1079 (2009).
- Gamble, M. J., Frizzell, K. M., Yang, C., Krishnakumar, R. & Kraus, W. L. The histone variant macroH2A1 marks repressed autosomal chromatin, but protects a subset of its target genes from silencing. *Genes Dev.* **24**, 21–32 (2010).
- Firestein, R. *et al.* CDK8 is a colorectal cancer oncogene that regulates beta-catenin activity. *Nature* **455**, 547–551 (2008).
- Morris, E. J. *et al.* E2F1 represses beta-catenin transcription and is antagonized by both pRB and CDK8. *Nature* **455**, 552–556 (2008).
- Pehrson, J. R. & Fried, V. A. MacroH2A, a core histone containing a large nonhistone region. *Science* **257**, 1398–1400 (1992).
- Pehrson, J. R., Costanzi, C. & Dharia, C. Developmental and tissue expression patterns of histone macroH2A1 subtypes. *J. Cell. Biochem.* **65**, 107–113 (1997).
- Costanzi, C. & Pehrson, J. R. MacroH2A2, a new member of the MacroH2A core histone family. *J. Biol. Chem.* **276**, 21776–21784 (2001).
- Costanzi, C. & Pehrson, J. R. Histone macroH2A1 is concentrated in the inactive X chromosome of female mammals. *Nature* **393**, 599–601 (1998).
- Zhang, R. *et al.* Formation of MacroH2A-containing senescence-associated heterochromatin foci and senescence driven by ASF1a and HIRA. *Dev. Cell* **8**, 19–30 (2005).
- Bernstein, E. *et al.* A phosphorylated sub-population of the histone variant macroH2A1 is enriched during mitosis and excluded from the inactive X chromosome. *Proc. Natl Acad. Sci. USA* **105**, 1533–1538 (2008).
- Hua, S. *et al.* Genomic analysis of estrogen cascade reveals histone variant H2A.Z associated with breast cancer progression. *Mol. Syst. Biol.* **4**, 188 (2008).
- Sporn, J. C. *et al.* Histone macroH2A isoforms predict the risk of lung cancer recurrence. *Oncogene* **28**, 3423–3428 (2009).
- Hocker, T. L., Singh, M. K. & Tsao, H. Melanoma genetics and therapeutic approaches in the 21st century: moving from the bedside to the bedside. *J. Invest. Dermatol.* **128**, 2575–2595 (2008).
- Jemal, A. *et al.* Cancer Statistics, 2009. *CA Cancer J. Clin.* **59**, 225–249 (2009).
- Clark, W. H. Jr *et al.* Model predicting survival in stage I melanoma based on tumor progression. *J. Natl Cancer Inst.* **81**, 1893–1904 (1989).
- Fidler, I. J. Selection of successive tumor lines for metastasis. *Nature* **242**, 148–149 (1973).
- Satyamoorthy, K. *et al.* Melanoma cell lines from different stages of progression and their biological and molecular analyses. *Melanoma Res.* **7**, S35–S42 (1997).
- Plazas-Mayorca, M. D. *et al.* One-pot shotgun quantitative mass spectrometry characterization of histones. *J. Proteome Res.* **8**, 5367–5374 (2009).
- Yancovitz, M. *et al.* Detection of mutant BRAF alleles in the plasma of patients with metastatic melanoma. *J. Mol. Diagn.* **9**, 178–183 (2007).
- Davies, H. *et al.* Mutations of the BRAF gene in human cancer. *Nature* **417**, 949–954 (2002).
- Qian, F., Vaux, D. L. & Weissman, I. L. Expression of the integrin $\alpha 4 \beta 1$ on melanoma cells can inhibit the invasive stage of metastasis formation. *Cell* **77**, 335–347 (1994).
- Ryu, B., Kim, D. S., Deluca, A. M. & Alani, R. M. Comprehensive expression profiling of tumor cell lines identifies molecular signatures of melanoma progression. *PLoS ONE* **2**, e594 (2007).
- Knuesel, M. T., Meyer, K. D., Bernecky, C. & Taatjes, D. J. The human CDK8 subcomplex is a molecular switch that controls Mediator coactivator function. *Genes Dev.* **23**, 439–451 (2009).
- Segura, M. F. *et al.* Aberrant miR-182 expression promotes melanoma metastasis by repressing FOXO3 and microphthalmia-associated transcription factor. *Proc. Natl Acad. Sci. USA* **106**, 1814–1819 (2009).

Supplementary Information is linked to the online version of the paper at www.nature.com/nature.

Acknowledgements We thank G. Hannon, S. Hake and M. Wirtz for reading this manuscript; J. Doucette for statistical support; the laboratories of S. Aaronson, J. Aguirre-Ghiso, D. Burstein and M. O'Connell for discussions and advice; M. Lebwohl, S. Mercer, J. Emer and G. Singer for dermatology and pathology support. We also thank N. Mall, L. Murray, S. Malu and S. Mungamuri for technical assistance; J. Pehrson, M. Narita, A. Aplin, H. Wei, A. Ting, S. Young Kim, M. Herlyn and J. Espinosa for reagents; T. Chu (Mount Sinai School of Medicine Microarray SRF) for data analysis; Q. Yu, the New York University Interdisciplinary Melanoma Cooperative Group and Mount Sinai Biorepository Cooperative for melanoma specimens. This work was supported by an American Skin Association Medical Student Grant to M.S.G., American Society for Mass Spectrometry Award, New Jersey Commission on Cancer Research Seed Grant, and National Science Foundation CBET-0941143 to B.A.G., National Institutes of Health CA109388 and the Sergei S. Zlinkoff Fund for Medical Education to D.P., New York University Cancer Institute Cancer Center Support Grant (5P30CA016087-27) and Marc Jacobs Campaign to I.O., NYSTEM IDEA C024291 and Harry L. Lloyd Charitable Trust to E.H., and an American Skin Association Research Scholar Award, Ellison Medical Foundation New Scholar Award, Tisch Cancer Institute Developmental Funds and NCI R21CA150117 to E.B.

Author Contributions A.K., M.S.G., K.R. and E.B. conceived ideas and experimental design. A.K. generated shRNA and overexpression cell lines and performed all *in vitro* and *in vivo* studies, DNA methylation analysis, microarray studies, qPCR and ChIP. M.S.G. performed immunoblots, IHC and statistical analysis. L.K.C. performed IHC, immunoblots and *in vivo* studies, and K.R. performed MNase studies. C.V. performed ChIP, and P.O.E. and C.I.V. scored and evaluated all human and mouse tissues. S.M., M.F.S. and E.H. designed and performed mouse studies, G.L. and B.A.G. performed and analysed quantitative mass spectrometry studies, and D.P. and I.O. contributed critical reagents. E.B. wrote the manuscript with contributions from all other authors.

Author Information Microarray data are deposited in National Center for Biotechnical Information Gene Expression Omnibus under accession number GSE19181. Reprints and permissions information is available at www.nature.com/reprints. The authors declare no competing financial interests. Readers are welcome to comment on the online version of this article at www.nature.com/nature. Correspondence and requests for materials should be addressed to E.B. (emily.bernstein@mssm.edu).

METHODS

Cell culture, plasmids and infections. Murine B16 and human WM266-4, A375 and HCT116 cells were maintained in DMEM supplemented with 10% fetal bovine serum (FBS) and 1% antibiotics. All other melanoma cells were grown in Tu2% media (80% MCDB 153 media, 20% Leibovitz's L-15 media, 2% FBS, 5 $\mu\text{g ml}^{-1}$ bovine insulin, 1.68 mM CaCl_2). Human melanocytes were grown in Medium 254 (Invitrogen). Lentiviral plasmids encoding shRNAs against murine and human mH2A1, mH2A2, GFP (control) and murine CDK8 were obtained from Open Biosystems (Thermo Fisher Scientific). Med12 and CDK8 shRNAs were provided by J. Espinosa and Addgene (CDK8 (ref. 7)). RNAi sequences are listed in Supplementary Table 1. Complementary DNA (cDNAs) encoding human H2A, rat mH2A1.2 and human mH2A2 were amplified and cloned into the retroviral vector N-Cherry-LPC (gift of M. Narita). Plasmids expressing CDK8 (pBabe.puro.CDK8 and CDK8-KD⁷) were obtained from Addgene. Infections were performed using standard procedures.

Chromatin fractionation, acid extraction of histones and immunoblotting. Chromatin fractionation and acid extraction of histones performed as described¹⁴. Whole-cell extracts were generated by lysing cells directly in Laemmli loading buffer, followed by sonication (for tumour tissue), and boiled extensively. The following antibodies were used for immunoblotting: mH2A1 (Millipore 07-219); mH2A2 (ref. 11); H3 C-terminal (Abcam ab1791 or Millipore 05-928); H4 (Millipore 05-858); H2A.X (Millipore 07-627); H2A.Z (Millipore 07-594); CDK8 (Santa Cruz sc-1521); Cited1 (Abcam ab15096); DsRed (Clontech 632496); and Actin (Sigma A5441).

Quantitative mass spectrometry. Bulk acid extracted histones were derivatized by treatment with propionyl anhydride as described²². Histones were labelled with stable isotope using d_{10} -propionic anhydride (Cambridge Isotope Laboratories). Online high-performance liquid chromatography separation of peptides was followed by liquid chromatography-mass spectrometry (LC-MS/MS) using an LTQ-Orbitrap mass spectrometer (ThermoFisher Scientific) as described²². All data were manually inspected for quantification and MS/MS interpretation. Two independent experiments using biological replicates were performed.

Immunohistochemistry, pathology and statistical analysis. Specimens were obtained from Mount Sinai School of Medicine's Division of Dermatopathology by Institutional Review Board approval (project number HSD08-00565) and New York University (Institutional Review Board number 10362). Primary RGP melanoma (Breslow thickness less than 1.0 mm) and VGP melanoma (Breslow thickness greater than 1.0 mm) were examined. IHC was also performed on BRAF-genotyped melanoma (New York University) and melanoma tissue microarray (Imgenex IMH-369). IHC was performed as per the manufacturer's instructions (Vector Laboratories). In brief, 5- μm sections from formalin-fixed paraffin-embedded specimens were deparaffinized, incubated for antigen retrieval with Vector Citrate-Based Antigen Unmasking Solution (Vector Laboratories H-3300) in microwave for 10 min, exposed to 0.3% hydrogen peroxide to block endogenous peroxidase activity, blocked with Vector Normal Horse Serum (2.5%) for 20 min, incubated with mH2A2 (ref. 11) (1:350–1:500) prepared in 0.1% BSA and incubated at 4 °C overnight. Slides were subsequently developed using Vector imPRESS Universal Kits anti-mouse/rabbit Ig or anti-goat Ig (Vector Laboratories MP-7500 or MP-7405), Vector DAB Peroxidase Substrate Kit as the chromagen (Vector Laboratories SK-4100) and Harris Hematoxylin (Sigma HHS32) for counterstaining. Slides were then sealed and mounted with Permount (Sigma SP15) and randomized for subsequent blinded review. Two independent dermatopathologists (P.O.E. and C.I.V.) scored specimens for extent of melanocyte nuclear staining (0–3). Slides were compared with haematoxylin and eosin sections and all slides stained with H3 (Abcam ab1791 or Millipore 05-928; both at 1:200) for tissue quality control. For CDK8 staining, mH2A negative melanomas were stained (Santa Cruz sc-1521, 1:200, and sc-13155, 1:15), followed by randomization and scoring. All statistical analyses were conducted using SPSS 14 software (SPSS). Average staining score was used for analyses, and inter-observer consistency between dermatopathologists was assessed with the κ coefficient. Statistical significance of mH2A2 scores was first assessed using the non-parametric Kruskal–Wallis one-way analysis of variance test, followed by two-sided Mann–Whitney *U* tests.

Micrococcal nuclease assays. Cells were counted (Beckman Coulter particle counter) and evenly aliquoted (2.5×10^6 cells per MNase time point). Each sample treated with 1/150 unit of micrococcal nuclease (Sigma) for 2, 5, 7 or 10 min at 37 °C, and stopped with 1 mM EGTA. Samples were centrifuged at 10,000g (for 10 min) and DNA extracted using a DNeasy Blood and Tissue Kit (Qiagen). Equal amounts of DNA were resolved on 1% agarose gel and stained with ethidium bromide.

Azacytidine treatment and bisulphite DNA methylation analysis. Cells were treated with 10 μM 5-aza-2'-deoxycytidine and collected at days 2 and 4. Fresh medium containing 5-aza-2'-deoxycytidine was added at day 2 for collecting at day 4. For bisulphite DNA methylation analysis, DNA from cells and tissues was

prepared with a DNeasy Blood and Tissue Kit (Qiagen). Bisulphite treatment was performed with an EZ DNA Methylation Kit (Zymo Research) according to the manufacturer's instructions (2 μg of DNA was used in the bisulphite reaction). After bisulphite conversion, DNA was amplified by PCR in triplicate, pooled, cloned into pGEMT (Promega) and sequenced using SP6 universal primer. Primers used for amplifying mH2A2 promoter were as follows: M2-CG2-F: GTTTAGTTTGGGGAAAGTTTATGT; M2-CG2-R: TAAAAAAATTACTCAACCTCATCC. The online tool QUMA (<http://quma.cdb.riken.jp/>) was used for bisulphite sequencing analysis²⁹.

Cell proliferation, soft agar and migration assays. An MTS proliferation kit was used according to the manufacturer's instructions (Promega). Absorbance values (490 nm) were recorded on at least triplicate samples using a BIOTEK Microplate Reader. Colony assays performed by seeding cells at low density and allowing growth for 10 days. Colonies were fixed, stained with crystal violet and counted. Soft agar was performed essentially as described²⁸. Briefly, cells were plated in Tu2% media with 0.33% (w/v) noble agar on top of a 0.5% noble agar layer. After 3 weeks, colonies were stained, photographed and counted in five different fields using an inverted microscope. Cell migration was measured by trans-well assay (8- μm pores from Corning). Cells were suspended in serum-free medium, and DMEM supplemented with 10% FBS used as chemoattractant. For assays with WM115 cells, the lower surface of the Transwell was pre-coated with fibronectin (Sigma, 100 $\mu\text{g ml}^{-1}$ for 30 min at 37 °C). Cells that migrated after 18 h were stained with Diff-Quick Stain Kit (Dade Behring) and counted in five different fields using an inverted microscope. Wound healing assays were performed as described²⁸.

Statistics. All results are presented as the mean \pm s.d. or s.e.m. as indicated. Statistical analyses were performed by calculating *P* values using an unpaired Student's *t*-test (two tailed), unless indicated otherwise.

Flow cytometry. Cells were collected, washed in phosphate-buffered saline (PBS), and fixed in ice-cold 70% ethanol. Propidium iodide staining was performed using a Cycletest Plus Staining Kit following the manufacturer's instructions (Becton Dickinson). For apoptosis studies, cells were analysed by flow cytometry by Annexin V staining using an Apoptosis Detection Kit (R&D Systems).

In vivo metastasis assay and subcutaneous injections. *In vivo* metastasis assays were performed as described²⁸. Briefly, 2×10^5 B16-F1 cells (stably transduced with sh_GFP, mH2A1_91 and mH2A2_25 shRNA) and 1.5×10^5 B16-F10 cells (stably transduced with mCherry, H2A-mCherry, mH2A1.2- and mH2A2-mCherry) were injected intravenously into BALB/c mice. Mice injected with B16-F1 cells were killed 14 or 21 days after infection (performed in duplicate with similar results; 6–8 mice per group). Mice injected with B16-F10 cells were killed 10 days after injection ($n = 6$ –9 per group). Lungs were removed and fixed, isolated and discrete pigmented lung surface lesions were counted. For subcutaneous injections, 2.5×10^5 B16-F1 cells stably infected with shRNAs were injected in the flanks of 6-week-old C57BL/6J mice (Jackson Laboratories). Mice were injected ($n = 6$ –9 per group) and measurements taken over 12–14 days. Two million A375 cells expressing mCherry series were injected into NOG mice (NOD/Shi-scid/IL-2R⁰ null, Jackson Laboratories), and measurements taken over 21 days. Tumour volume was estimated by $V = (a^2 \times b)/2$, where *a* is the short axis and *b* is the long axis of the tumour. Tissues from all assays were paraffin-embedded and 5- μm sections stained with haematoxylin and eosin. Experiments were conducted under protocol number 080901-01 approved by the New York University Institutional Animal Care and Use Committee.

Microarray hybridization and data analysis. Microarray samples were processed in the Microarray Shared Research Facility at Mount Sinai School of Medicine and performed on two biological replicates. Total RNA was isolated from cells using RNeasy column purification per manufacturer's protocol (Qiagen). The quality of the RNA was evaluated using the Agilent BioAnalyser RNA nano assay. Briefly, 150 ng of total RNA was reverse transcribed using T7-poly(dT) primer and converted into double-stranded cDNA. The cDNA was used as a template for subsequent *in vitro* transcription with biotin-labelled uridine triphosphate at 37 °C for 16 h using a Genechip 3' IVT Express Kit (Affymetrix). The resulting biotin-labelled cDNA was chemically fragmented, made into hybridization cocktail and hybridized to the Mouse Genome 430 Plus 2.0 arrays (Affymetrix) according to the Affymetrix GeneChip protocol. The array images were generated through a high-resolution GeneChip Scanner 3000 7G (Affymetrix), then converted to digitized data based on MAS 5.0 within the GeneChip Operating Software. Spike-in controls and percentage of present ('P') call generated were used for data quality control.

Data were analysed as follows. For normalization, all chip data were scaled to have an average signal intensity of 150. Comparison analysis based on MAS 5.0 was performed for each pair (sh_GFP compared with mH2A1_91, and sh_GFP compared with mH2A2_25) on both data sets. The compared data were subjected to the following arbitrary filters to improve data reliability: (1) detection call—only

probes that had at least one 'P' call in the pair were retained; (2) signal intensity—only probes that showed signal intensity of at least 100 in at least one of the pairs were retained; (3) fold change—probes that showed a log-fold change of at least 2 in at least one data set were retained for further analysis; (4) concordance analysis was performed to reduce false-positive selection between shRNA lines and the two independent microarray experiments: direction and fold-change in gene regulation had to be a 100% match to qualify as altered genes. Gene list was annotated by submission to Netaffx annotation centre within the Affymetrix website (<http://www.affymetrix.com>), which periodically updates the integrated information for each gene across multiple public genome databases.

Hierarchical clustering, generation of heat maps and gene ontology analysis. A portion of the filtered subset of data was used for additional analysis. Cluster analysis was performed by unsupervised hierarchical clustering on the log-transformed data with Gene Cluster 3.0 (<http://bonsai.ims.u-tokyo.ac.jp/~mdehoon/software/cluster/index.html>) by using the correlation (uncentred) similarity metric and centeroid linkage clustering method. The resulting tree-images were visualized using Java TreeView. Gene ontology analysis was performed using DAVID Bioinformatics Resources³⁰ (<http://david.abcc.ncifcrf.gov/home.jsp>).

Quantitative PCR and ChIP. Total RNA was extracted using RNeasy Kit (Qiagen). Reverse transcription was performed with SuperScript II (Invitrogen) using oligo dT. qPCR reactions were performed in triplicate on Stratagene Opticon 2 using FastStart SYBR Green Master Mix (Roche). Expression levels were normalized to TATA binding protein in mouse cells and GAPDH in human cells, or relative to B16-F1 sh_GFP for gene target expression. Each qPCR used two independent biological replicates. Primer sets used for qRT-PCR are listed in Supplementary Table 2. ChIP assays were performed using a Magna ChIP Kit (Protein G; Millipore) as per the manufacturer's instructions. Immunoprecipitations were performed with antibodies against mH2A1 (Millipore 07-219), H3 (Abcam ab1791) and control IgG (Millipore 12-370). ChIP signals were represented as the percentage of H3, calculated by $100 \times 2^{(C_{H3} - C_{Antibody})}$. Primers used for ChIP-qPCR are listed in Supplementary Table 3.

29. Kumaki, Y., Oda, M. & Okano, M. QUMA: quantification tool for methylation analysis. *Nucleic Acids Res.* **36**, W170–175 (2008).
30. Huang, D. W., Sherman, B. T. & Lempicki, R. A. Systematic and integrative analysis of large gene lists using DAVID Bioinformatics Resources. *Nature Protocols* **4**, 44–57 (2009).

Planar polarized actomyosin contractile flows control epithelial junction remodelling

Matteo Rauzi^{1,†}, Pierre-François Lenne¹ & Thomas Lecuit¹

Force generation by Myosin-II motors on actin filaments drives cell and tissue morphogenesis^{1–15}. In epithelia, contractile forces are resisted at apical junctions by adhesive forces dependent on E-cadherin¹⁶, which also transmits tension^{6,17–19}. During *Drosophila* embryonic germband extension, tissue elongation is driven by cell intercalation²⁰, which requires an irreversible and planar polarized remodelling of epithelial cell junctions^{4,5}. We investigate how cell deformations emerge from the interplay between force generation and cortical force transmission during this remodelling in *Drosophila melanogaster*. The shrinkage of dorsal–ventral-oriented (‘vertical’) junctions during this process is known to require planar polarized junctional contractility by Myosin II (refs 4, 5, 7, 12). Here we show that this shrinkage is not produced by junctional Myosin II itself, but by the polarized flow of medial actomyosin pulses towards ‘vertical’ junctions. This anisotropic flow is oriented by the planar polarized distribution of E-cadherin complexes, in that medial Myosin II flows towards ‘vertical’ junctions, which have relatively less E-cadherin than transverse junctions. Our evidence suggests that the medial flow pattern reflects equilibrium properties of force transmission and coupling to E-cadherin by α -Catenin. Thus, epithelial morphogenesis is not properly reflected by Myosin II steady state distribution but by polarized contractile actomyosin flows that emerge from interactions between E-cadherin and actomyosin networks.

The planar polarized remodelling of cell junctions^{4,5} that occurs during germband extension (GBE) is shown in Fig. 1a. Myosin II (Myo-II) is concentrated in ‘vertical’ junctions^{4,21} and directs junction shrinkage by increasing junctional tension^{7,12}. To understand how Myo-II planar polarity is established, we investigated changes in Myo-II distribution at the onset of GBE. We used a fusion between Myo-II regulatory light chain (MRLC, called Sqh in *Drosophila*) and Cherry (MRLC–Cherry)¹⁵ together with E-cad–GFP to mark adherens junctions (AJs). When the epithelium is formed, MRLC–Cherry is visible in aggregates in the medial region of AJs (Fig. 1b). Subsequently, MRLC–Cherry is also detected at the cortex of AJs of intercalating cells (Fig. 1b). An MRLC–GFP fusion rescuing a null *sqh*^{AX3} mutant (Fig. 1c) and an antibody against endogenous Myo-II heavy chain (not shown) displayed the same features. Thus two Myo-II populations exist during cell intercalation: a medial and a junctional pool (Supplementary Fig. 1). Labelling of F-actin with Utrophin–GFP (Utr–GFP) shows a network spanning the AJs (Fig. 1d, Supplementary Fig. 1, Supplementary Movie 1a). This network is thin (<500 nm), and contains filaments at low density (mesh size 0.5–2 μ m) that overlap and intersect in the form of brighter puncta, which are more apparent in a slightly less apical focal plane intersecting the AJs (Supplementary Movie 1b, Supplementary Fig. 1). Thus, both Myo-II pools are part of a large-scale actomyosin network, spanning multiple cells, which contrasts with previous descriptions focused on junctional actin and Myo-II (refs 4, 5, 7, 12, 18, 21–23).

Live imaging of Utr–GFP and MRLC–GFP indicated complex dynamics (Supplementary Movies 1a, b and 2). The F-actin mesh fluctuated, with the mesh changing size in a few tens of seconds (Fig. 1d and Supplementary Movie 1a, b). Myo-II formed small clusters

(presumably Myo-II minifilaments), which coalesced into large (~1 μ m) medial aggregates on similar timescales (Fig. 1e, Supplementary Movie 2). Co-imaging of Utr–GFP and MRCL–Cherry revealed

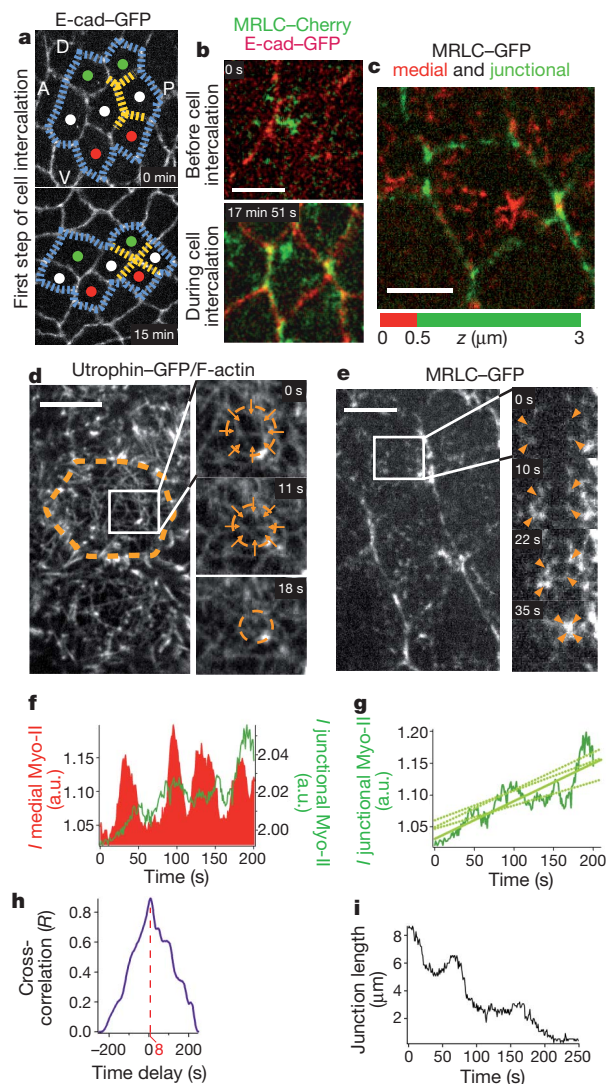


Figure 1 | Two pulsating pools of acto-myosin in intercalating cells.

a, Polarized junction shrinkage during cell intercalation. A, P, D and V denote respectively dorsal, ventral, anterior and posterior. **b**, Localization of Myo-II and E-cad before and during intercalation. **c**, Respective distribution of medial (red) and junctional (green) Myo-II along the apico-basal (z) axis. **d**, **e**, Apical F-actin coalesces locally (**d**, magnified in right panels, arrows), while medial Myo-II clusters (**e**, magnified in right panels, arrowheads). **f**, Myo-II pulses in the medial (red) and junctional (green) regions. **g**, Average junctional Myo-II (dark green) and linear fits for different junctions. **h**, Temporal cross-correlation of the curves in **f**. R is the correlation coefficient. **i**, Evolution of junctional length. Scale bars, 5 μ m.

¹IBDML, UMR6216 CNRS-Université de la Méditerranée, Campus de Luminy, case 907, 13288 Marseille Cedex 09, France. [†]Present address: EMBL, Meyerhofstrasse 1, 69126 Heidelberg, Germany.

that actin and Myo-II coalesce together during aggregation (Supplementary Fig. 2a, Supplementary Movie 3; Methods), reflecting local and transient contractions within the actomyosin network, as also reported in the *Drosophila* mesoderm and the one-cell stage *Caenorhabditis elegans* cortex^{15,24}.

To further investigate the functions of the medial and junctional Myo-II networks, we monitored their temporal evolution during intercalation (Fig. 1f–i). Both medial and junctional Myo-II, respectively in the vicinity of and at shrinking junctions, fluctuated in intensity (Fig. 1f). In addition to being pulsed, the intensity of junctional Myo-II gradually increased (Fig. 1g). Meanwhile, the changes in ‘vertical’ junction length are irregular, showing successive steps of shrinkage and arrest (Fig. 1i). In some cases, however, transient relaxation was observed (17.6%, $N = 17$).

To disentangle this complex behaviour and relate contractile dynamics of medial and junctional networks with junction shrinkage, we conducted temporal cross-correlation of fluorescence intensity (Online Methods). Correlation between temporal profiles of MRLC–GFP intensity at the junctions and in the medial regions is high (mean $\langle R \rangle = 0.86$, Fig. 1h), indicative of similar overall dynamics. Moreover, medial pulses precede junctional pulses by 8 ± 4 s (mean \pm s.d. hereafter, Fig. 1h and Supplementary Fig. 3).

We then compared rates of junction shrinkage with rates of MRLC–GFP intensity changes (Fig. 2a left), which correspond to local accumulations of Myo-II by contraction (Fig. 1e). The maximum of the MRLC–GFP contraction rate in the medial region precedes that of junctional MRCL–GFP by an average of 10.5 ± 2.5 s (Fig. 2b left). Thus contraction of Myo-II occurs in the medial region first and subsequently at junctions (Fig. 2b left, right). Each step of junction shrinkage was associated with

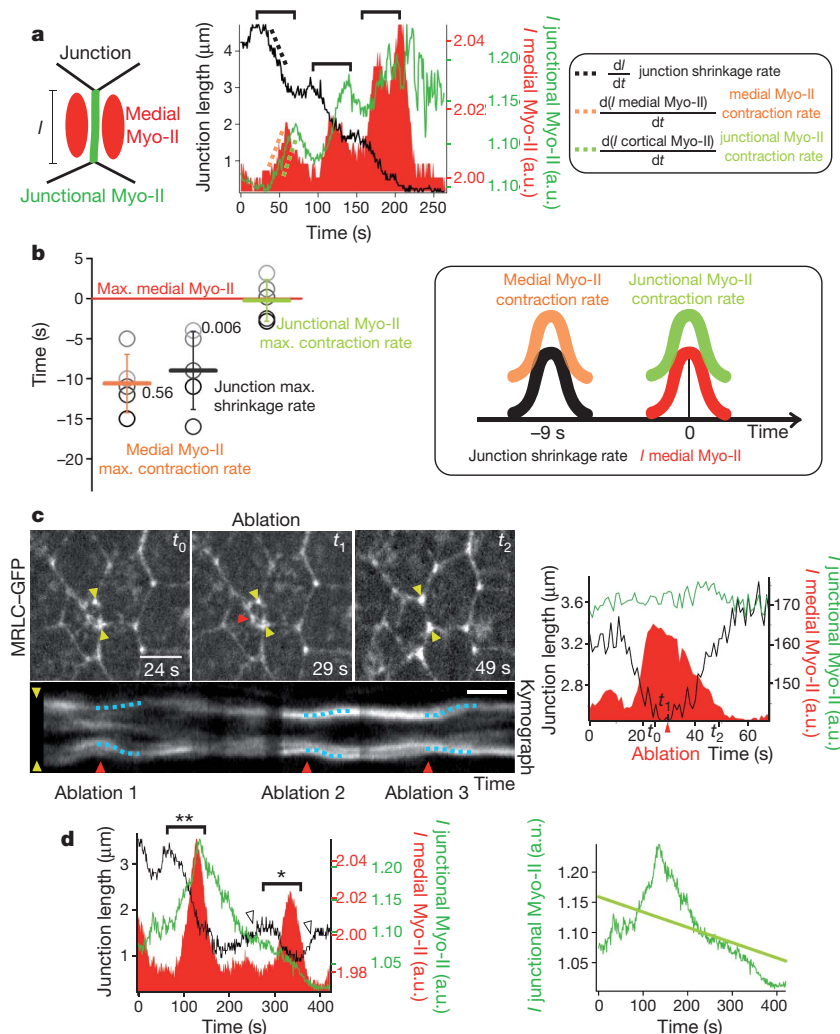
tandem medial and junctional Myo-II pulses (Fig. 2a right, horizontal braces). Temporal cross-correlation indicated that the peak rate of junction shrinkage precedes that of junctional Myo-II accumulation by 9 ± 3 s (Fig. 2b left), indicating that junctional Myo-II accumulation cannot cause the shrinkage steps. However, peak junction shrinkage rate temporally coincided with the peak rate of medial Myo-II contraction (Fig. 2b left, right) suggesting a mechanical contribution to shrinkage increments.

To test this, we used laser nanodissection¹² to locally disrupt medial Myo-II clusters at the vicinity of shrinking junctions. Each ablation pulse produced a collapse of the Myo-II pulse and a transient and reversible relaxation of junction length without affecting junctional Myo-II (Fig. 2c left, right, Supplementary Movie 4). Thus, medial Myo-II mechanically causes junction shrinkage. This led us to investigate the function of junctional Myo-II pulses, as previous studies showed it was essential for global junction shrinkage^{4,7,12}. Close inspection reveals two situations: (1) in most cases (88%, $N = 17$), medial Myo-II pulses are followed by junctional pulses, and shrinkage steps proceed successfully without relaxation (14/15 cases, Fig. 2a right); (2) occasionally, (12%) medial pulses are not followed by junctional pulses and shrinkage steps relax in all cases (Fig. 2d). Relaxation correlates with failure to sustain junctional Myo-II and with an overall decrease of Myo-II at junctions (Fig. 2d left, right). This suggests that junctional Myo-II stabilizes junction length.

Together these observations point to a mechanical ‘division of labour’, where medial Myo-II pulses shrink, and sustained junctional Myo-II accumulation stabilizes, junction length. This iterative cycle ensures persistent shrinkage.

Figure 2 | Medial and junctional Myo-II pools have different mechanical roles.

a, Left: cartoon depicting a vertical junction (length l) and regions where medial and junctional Myo-II are measured. Right: evolution of junction length and Myo-II intensities (I). Brackets show clusters of events and dashed lines represent the rates of changes. **b**, Time delays using medial Myo-II intensity maximum as a reference. Mean and s.d. are shown in the left panel. **c**, Left: evolution of a junction (between yellow arrowheads) before (t_0), during (t_1) and after (t_2) focal ablation of a Myo-II pulse (red arrowhead). Bottom, kymograph of the same junction with three ablation events (red arrowheads). Blue dashed lines mark junction relaxation. Scale bar, 25 s. Right: length of junction (from **c**, left) and medial and junctional Myo-II intensity as a function of time. The red arrowhead marks the ablation. **d**, Left: junction relaxation (arrowheads) when a medial pulse is not followed by a junctional pulse (*) or when junctional Myo-II is not sustained (**). Right: junctional Myo-II intensity (dark green) and linear fit (light green). Scale bars in **c**, 5 μ m.



These observations suggested that both processes may be spatially coordinated. Indeed, medial pulses show a planar polarized distribution like junctional Myo-II. Defining four quadrants (anterior, A; posterior, P; dorsal, D; and ventral, V; diagram in Fig. 3a right) in the medial region of cells, we determined the integrated intensity ratio of $(A+P)/(D+V)$ MRLC-GFP in time series (Fig. 3a left). Intercalating germband cells exhibit a significant medial Myo-II polarity compared to non-intercalating head cells or to germband cells of *Krüppel* (*Kr*) RNAi embryos where planar cell polarization is affected^{4,20} (Fig. 3a left, Supplementary Movie 6).

We next investigated the spatial dynamics of medial and junctional actomyosin networks. Co-imaging of Utr-GFP and MRLC-Cherry and particle imaging velocimetry (PIV) indicated that F-actin and Myo-II have very similar dynamics and that actomyosin clusters flow in the plane of the medial region (Fig. 3b, Supplementary Movie 3). Myo-II was moving slightly (22%) but consistently faster than F-actin (Supplementary Fig. 5), in agreement with the idea that Myo-II is responsible for flow.

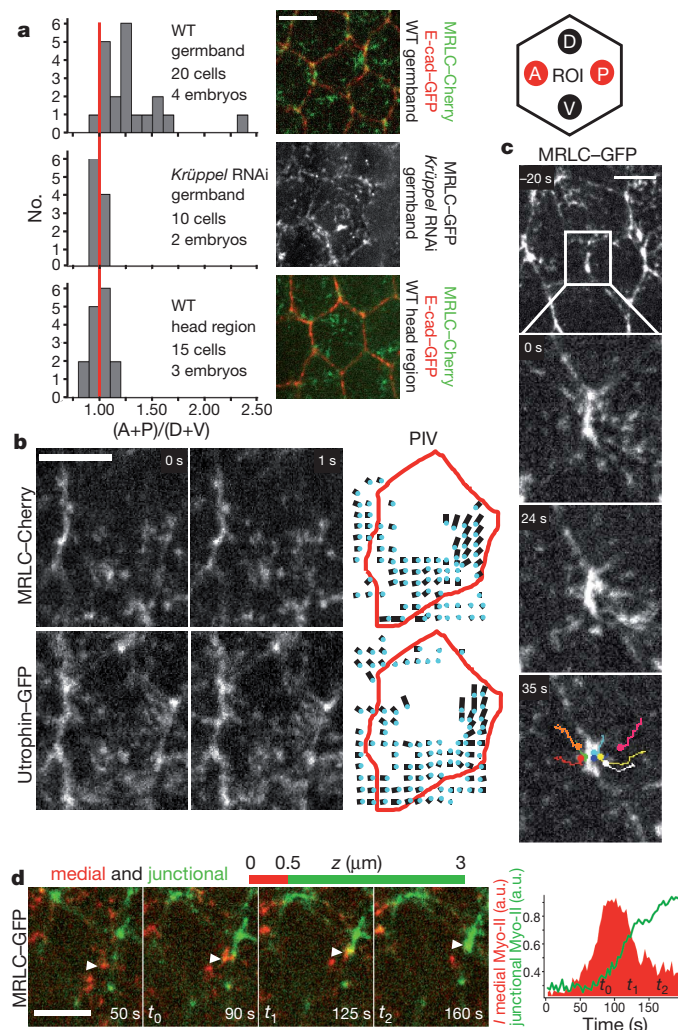


Figure 3 | Medial Myosin-II displays anisotropic flow and feeds 'vertical' junctions. **a**, Left: histograms of medial Myo-II relative intensities in $(A+P)$ regions over $(D+V)$ regions (see diagram at right for nomenclature) in the germband of wild-type (WT) and *Krüppel* (*Kr*) RNAi embryos, and the head of WT embryos. WT/*Kr*RNAi: $P = 0.0007$, WT(germband)/WT(head): $P = 0.001$ (T-student). Right: representative images of cells with MRLC-Cherry and E-cad-GFP. **b**, Comparative PIV of Utr-GFP and MRLC-Cherry in a cell outlined in red. Blue dots mark vector tips. **c**, Medial Myo-II flowing to a vertical junction. Tracking of speckles is shown in coloured lines (right). **d**, Left: a medial cluster (red, arrowhead) flows and fuses to the junctional Myo-II pool (green); right: corresponding quantification. Scale bars, 5 μ m.

Tracking of Myo-II speckles (Fig. 3c, Supplementary Movies 2, 5) or of F-actin with Myo-II (Supplementary Fig. 2b) indicated that the polarized distribution of medial Myo-II results from the lateral flow of medial pulses towards 'vertical' junctions. In *Kr*RNAi embryos, this movement occurred randomly (Supplementary Movie 6), consistent with the loss of medial Myo-II polarity (Fig. 3a left).

The polarized flow of Myo-II ($0.11 \pm 0.03 \mu\text{m s}^{-1}$) could either reflect a movement of Myo-II minifilaments or the propagation of contractile waves. We tested these alternatives by photobleaching medial MRLC-GFP clusters. The fluorescence recovery in the bleached area (recovery fractions $34 \pm 10\%$ ($N = 5$), $\tau_{1/2} = 4 \pm 1$ s, Supplementary Fig. 6a, b, d) was low compared to the junctions (recovery fractions $\sim 70\%$ (ref. 8), not shown). Moreover, no new cluster appears in the vicinity of bleached pulses, as would be expected for contractile waves (Supplementary Fig. 6a). Together this indicates that medial flows correspond to the movement of relatively stable Myo-II filaments. Fluorescence recovery after photobleaching (FRAP) experiments with Utr-GFP show extensive ($83 \pm 22\%$, $N = 5$) turnover within < 3 s (Supplementary Fig. 6c, d), suggesting that the actomyosin flow is mainly determined by Myo-II contractility on a fast-recycling, 'permissive' actin substrate.

We then addressed whether medial pulses are transferred to the junctional cortex and cause the formation of junctional pulses. As medial MRLC-GFP is slightly (500–1,000 nm) more apical than junctional MRLC-GFP, confocal sections distinguished the two pools and showed fusion of medial Myo-II (red) to the cortex and formation of a junctional pulse (green) (Fig. 3d left, right; Supplementary Movie 7). No transfer of medial pulses occurred to the adjacent junction following their ablation (Fig. 2c right). Moreover, photobleaching of MRLC-GFP along a junction (Supplementary Fig. 7a, b; Supplementary Movie 8) indicates two sources of exchange: pre-existing Myo-II patches are rapidly and strongly recovered ($72 \pm 6\%$), consistent with previous reports⁷; new junctional patches form *de novo* where medial Myo-II clusters fuse with junctions.

Junctional Myo-II pulses are delayed by ~ 8 s relative to medial ones (Supplementary Fig. 3), reflecting a speed of transfer of $\sim 0.125 \mu\text{m s}^{-1}$, which is similar to the direct flow speed measurements ($0.11 \pm 0.03 \mu\text{m s}^{-1}$).

Thus, medial and junctional actomyosin networks have tightly coordinated and hierarchically organized mechanical functions. Medial pulses flow to and produce steps of shrinkage of the adjacent 'vertical' junctions. They subsequently fuse with junctions and sustain junctional Myo-II accumulation, which stabilizes junction length. This flow and transfer are planar polarized, and drive junctional planar polarity and cell intercalation.

What controls the planar polarized flow of medial Myo-II pulses to vertical junctions? Mechanical anchoring of actomyosin networks at AJs is essential for force production during cell morphogenesis^{6,17–19,25}. The medial network is also potentially connected to the apical plasma membrane given its tight apposition (Supplementary Fig. 8). Imaging of the apical plasma membrane with palmitoylated YFP (GAP43-Venus) revealed however a flat apical surface in the medial part of intercalating cells with few, small protrusions (Supplementary Fig. 9, Supplementary Movie 9), unlike apically constricting mesoderm cells where the plasma membrane is strongly ruffled (Supplementary Movie 10). These protrusions display local jitter but no aggregation or flow patterns characteristic of the underlying actomyosin network, suggesting moderate coupling (Supplementary Fig. 9, Supplementary Movie 9). Co-imaging of GAP43-Cherry and Utr-GFP shows that small protrusions and F-actin had un-correlated trajectories (Supplementary Movie 11) or moved at different speeds (Supplementary Movie 12; 3.7-fold reduced lateral dynamics ($0.03 \pm 0.015 \mu\text{m s}^{-1}$, Supplementary Fig. 9) compared to MRLC-GFP or Utr-GFP ($0.11 \pm 0.03 \mu\text{m s}^{-1}$, Fig. 3c)). Therefore, the apical surface and the medial actomyosin network are in contact but moderately coupled.

This suggested that the anisotropic actomyosin flow may largely depend on the distribution of junctional anchoring points. This requires E-cadherin/ β -Catenin complexes at AJs and depends on α -Catenin^{18,26}. E-cadherin/ β -Catenin/ α -Catenin complexes are planar polarized⁵ (not shown), such that medial pulses flow towards regions with lower amounts of E-cadherin complexes. The level of E-cadherin along 'vertical' relative to adjacent junctions (E-cadherin anisotropy, Fig. 4a left) is also fluctuating (Fig. 4a middle). Moreover, the onset of medial pulses coincided with the time when E-cadherin anisotropy reached a local maximum (Fig. 4a middle, right) raising the possibility that E-cadherin anisotropy may orient the actomyosin flow. Reduction of E-cadherin by RNAi causes the disappearance of medial Myo-II (Fig. 4b top, c top; Supplementary Movies 13, 14). The junctional Myo-II level is consequently strongly reduced and no longer planar polarized (Fig. 4b bottom, c bottom). We reasoned that reducing the levels of α -Catenin by RNAi should attenuate coupling more subtly. α -Catenin RNAi reduces the number of E-cadherin clusters at AJs and disrupts interactions with junctional F-actin¹⁸. Moreover, the distribution of E-cadherin is no longer planar polarized in α -CateninRNAi embryos (Fig. 4e, Supplementary Fig. 10). This is associated with a loss of medial (Fig. 4f, Supplementary Movie 15) and junctional (Fig. 4d

top, bottom) Myo-II planar polarity. Thus, the planar polarized distribution of E-cadherin/ β -Catenin/ α -Catenin complexes biases the flow of medial Myo-II and junctional polarization.

In addition to Myo-II contractility, flow requires (1) crosslinkers between filaments to transmit tension within the medial meshwork, and (2) coupling at the cortex to E-cadherin/ β -Catenin/ α -Catenin complexes. Increased levels of E-cadherin in 'transverse' junctions may change properties of the actin network (for example, crosslinking/viscosity) and inhibit internal transmission of contractile forces and hence prevent D–V oriented flow. To test this, we disrupted the force balance within the medial actomyosin network by focal ablation (Fig. 4g top, bottom), and imaged the redistribution of medial clusters. If increased E-cadherin levels at transverse junctions inhibit tension transmission along the D–V axis, then medial pulses should not flow in this direction following ablation. However, we observed that Myo-II medial clusters flowed radially and away from the point of ablation towards the junctions (velocity $v = 0.05 \pm 0.01 \mu\text{m s}^{-1}$) in 100% of cases ($N = 25$), even towards transverse junctions (12/25 cases, Fig. 4g top, bottom; Supplementary Fig. 11; Supplementary Movie 16). Focal ablation of the actin meshwork produces a local hole, which expands radially (Supplementary Movie 17). This argues that transverse

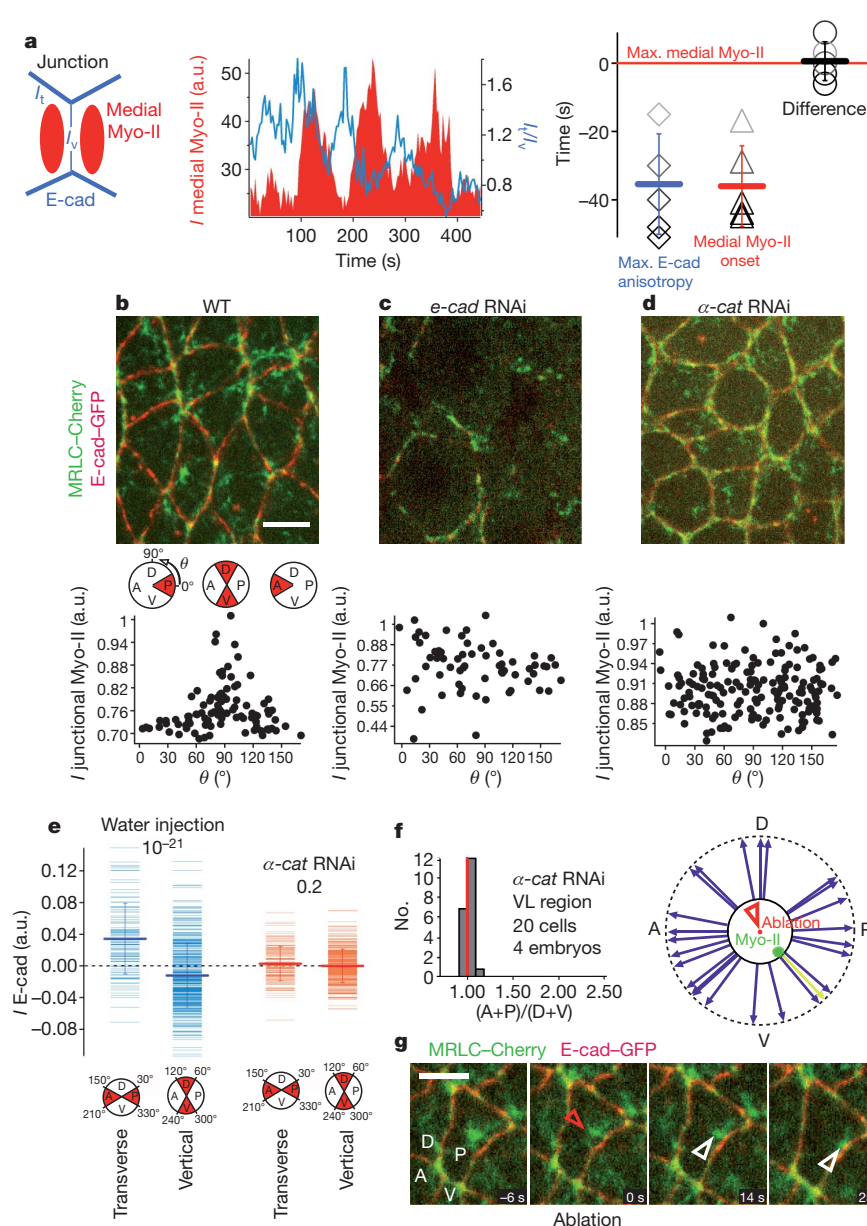


Figure 4 | E-cadherin planar polarity orients medial Myosin-II flow. **a**, Left and middle: medial MRLC-Cherry average intensity (red) and E-cad-GFP polarity (blue) as a function of time. E-cad-GFP polarity is the ratio of its mean intensity in transverse (I_t) and vertical (I_v) junctions. Right: chronology of events taking as a reference medial Myo-II intensity maximum. Delays between events are obtained by correlation; shown are mean and s.d. The difference is in black. **b–d**, Top row: Myo-II and E-cad in control (**b**), *e-cad* RNAi (**c**) and α -cat RNAi (**d**) embryos. Bottom row: average intensity of junctional Myo-II as a function of the angle (θ) of the junctions with respect to the A/P axis. **e**, Top: Comparison between normalized E-cad-GFP average intensity ($= (I_t - I_v)/I_t$) of transverse versus vertical junctions for water injected (blue) and α -cat RNAi embryos (orange); P values are shown (Student's T test). I_t , mean intensity at a junction; I_v , mean intensity of all junctions in a cell. Diagram at bottom indicates the angles of vertical and transverse junctions with respect to the A–P axis. **f**, Histogram of average medial Myo-II intensity as in Fig. 2a, right, for α -cat RNAi embryos. WT/ α -cat RNAi: $P = 0.0006$ (Student's T test). **g**, Bottom: movement of a Myo-II cluster (white arrowhead) following nearby focal ablation (red arrowhead). Top right: diagram showing the centrifugal directions of the trajectories followed by Myo-II clusters ($N = 25$). Scale bars, 5 μm .

junctions do not inhibit flow *per se* and that flow directionality emerges from the properties of the actomyosin meshwork integrated over the entire apical surface.

The mechanical properties of the medial actomyosin network are locally defined by Myo-II contractility (concentration, affinity, duty cycle), tension transmission within the network (crosslinking), and viscous resistance to deformations (interactions between filaments)^{27,28}. Moreover, these properties fluctuate owing to protein turnover and interactions. E-cadherin is known to anchor^{18,26} and modify actin dynamics^{29,30}. Our results suggest that the polarized distribution of E-cadherin may control the actomyosin flow pattern by spatially modulating mechanical properties of the actin network.

Current models of epithelial morphogenesis centre on Myo-II steady state distribution and associated contractile forces^{1,2,4,5,7,10,12,14,15}. Our data show however that cell deformations cannot be simply derived from the Myo-II distribution itself, but from two central features of actomyosin dynamics, namely concentration (pulses) and movement (flow). Pulsed dynamics defines the rhythm and possibly the speed of deformation. Flow pattern, which in the case of intercalation is anisotropic, dictates the orientation of cell deformation (Supplementary Fig. 12). Flows of Myo-II foci have been reported in the one-cell stage *C. elegans* embryo^{22,24}, pointing to a more general property of actomyosin networks^{15,23}. An important future avenue of research will be to investigate what properties of actin networks control Myo-II flow dynamics in different systems.

METHODS SUMMARY

Mutants and constructs. To visualize Myosin-II we used MRLC fused to eGFP or mCherry and rescuing a protein null *sqh*^{AX3} mutant. The following stocks were used: *sqh*^{AX3}; *sqh*-MRLC::GFP (II) and *sqh*^{AX3}; *ubi-e-cad::GFP*, *sqh*-MRLC::mCherry. The plasmid coding for the fusion of eGFP and the actin binding domain of human Utrophin was obtained from W. Bement. The Utr-GFP clone was cloned by PCR in a pUASp destination vector (Fig. 1, Supplementary Fig. 1, Supplementary Movies 1a, b) or under the *sqh* promoter (Fig. 3, Supplementary Fig. 2, Supplementary Movie 3). The construct were verified by sequencing. To label the plasma membrane, we used a fusion between the palmitoylated GAP43 protein and YFP/Venus expressed by the GAL4/UAS system with the maternal tubGAL4VP16 driver line. GAP43-Cherry was expressed under the *sqh* promoter.

RNA interference. We generated by PCR dsRNA probes directed against *Krippel*, α -catenin and *e-cadherin* as described in refs 4, 18.

Time-lapse imaging. Embryos were prepared and imaged using a spinning disc confocal system (Perkin Elmer) on an inverted Nikon microscope with 100 \times oil immersion objective. Nano-ablation was performed using a home-built set-up¹². Fluorescence recovery after photobleaching (FRAP) measurements were performed as in Supplementary Fig. 6 using a confocal LSM510 (Zeiss) with a Plan-Apochromat 100 \times oil objective and an argon laser (488 nm).

Image analysis and quantifications. Intensity measurements, cross-correlation analysis, time-delays analysis and PIV analysis are detailed in Online Methods and in Supplementary Figs 3, 4.

Full Methods and any associated references are available in the online version of the paper at www.nature.com/nature.

Received 2 April; accepted 8 October 2010.

Published online 10 November 2010.

1. Lecuit, T. & Lenne, P. F. Cell surface mechanics and the control of cell shape, tissue patterns and morphogenesis. *Nature Rev. Mol. Cell Biol.* **8**, 633–644 (2007).
2. Montell, D. J. Morphogenetic cell movements: diversity from modular mechanical properties. *Science* **322**, 1502–1505 (2008).
3. Hutson, M. S. *et al.* Forces for morphogenesis investigated with laser microsurgery and quantitative modeling. *Science* **300**, 145–149 (2003).
4. Bertet, C., Sulak, L. & Lecuit, T. Myosin-dependent junction remodelling controls planar cell intercalation and axis elongation. *Nature* **429**, 667–671 (2004).
5. Blankenship, J. T., Backovic, S. T., Sanny, J. S., Weitz, O. & Zallen, J. A. Multicellular rosette formation links planar cell polarity to tissue morphogenesis. *Dev. Cell* **11**, 459–470 (2006).
6. Dawes-Hoang, R. E. *et al.* Folded gastrulation, cell shape change and the control of myosin localization. *Development* **132**, 4165–4178 (2005).
7. Fernandez-Gonzalez, R., Simoes Sde, M., Roper, J. C., Eaton, S. & Zallen, J. A. Myosin II dynamics are regulated by tension in intercalating cells. *Dev. Cell* **17**, 736–743 (2009).

8. Hildebrand, J. D. Shroom regulates epithelial cell shape via the apical positioning of an actomyosin network. *J. Cell Sci.* **118**, 5191–5203 (2005).
9. Krieg, M. *et al.* Tensile forces govern germ-layer organization in zebrafish. *Nature Cell Biol.* **10**, 429–436 (2008).
10. Monier, B., Pelissier-Monier, A., Brand, A. H. & Sanson, B. An actomyosin-based barrier inhibits cell mixing at compartmental boundaries in *Drosophila* embryos. *Nature Cell Biol.* **12**, 60–65 (2010).
11. Nishimura, T. & Takeichi, M. Shroom3-mediated recruitment of Rho kinases to the apical cell junctions regulates epithelial and neuroepithelial planar remodeling. *Development* **135**, 1493–1502 (2008).
12. Rauzi, M., Verant, P., Lecuit, T. & Lenne, P. F. Nature and anisotropy of cortical forces orienting *Drosophila* tissue morphogenesis. *Nature Cell Biol.* **10**, 1401–1410 (2008).
13. Skoglund, P., Rolo, A., Chen, X., Gumbiner, B. M. & Keller, R. Convergence and extension at gastrulation require a myosin IIB-dependent cortical actin network. *Development* **135**, 2435–2444 (2008).
14. Landsberg, K. P. *et al.* Increased cell bond tension governs cell sorting at the *Drosophila* anteroposterior compartment boundary. *Curr. Biol.* **19**, 1950–1955 (2009).
15. Martin, A. C., Kaschube, M. & Wieschaus, E. F. Pulsed contractions of an actin-myosin network drive apical constriction. *Nature* **457**, 495–499 (2009).
16. Nishimura, T. & Takeichi, M. Remodeling of the adherens junctions during morphogenesis. *Curr. Top. Dev. Biol.* **89**, 33–54 (2009).
17. Gorfinkel, N. & Arias, A. M. Requirements for adherens junction components in the interaction between epithelial tissues during dorsal closure in *Drosophila*. *J. Cell Sci.* **120**, 3289–3298 (2007).
18. Cavey, M., Rauzi, M., Lenne, P. F. & Lecuit, T. A two-tiered mechanism for stabilization and immobilization of E-cadherin. *Nature* **453**, 751–756 (2008).
19. Sawyer, J. K., Harris, N. J., Slep, K. C., Gaul, U. & Peifer, M. The *Drosophila* afadin homologue Canoe regulates linkage of the actin cytoskeleton to adherens junctions during apical constriction. *J. Cell Biol.* **186**, 57–73 (2009).
20. Irvine, K. D. & Wieschaus, E. Cell intercalation during *Drosophila* germband extension and its regulation by pair-rule segmentation genes. *Development* **120**, 827–841 (1994).
21. Zallen, J. A. & Wieschaus, E. Patterned gene expression directs bipolar planar polarity in *Drosophila*. *Dev. Cell* **6**, 343–355 (2004).
22. Hird, S. N. & White, J. G. Cortical and cytoplasmic flow polarity in early embryonic cells of *Caenorhabditis elegans*. *J. Cell Biol.* **121**, 1343–1355 (1993).
23. Bertet, C., Rauzi, M. & Lecuit, T. Repression of Wasp by JAK/STAT signalling inhibits medial actomyosin network assembly and apical cell constriction in intercalating epithelial cells. *Development* **136**, 4199–4212 (2009).
24. Munro, E., Nance, J. & Priess, J. R. Cortical flows powered by asymmetrical contraction transport PAR proteins to establish and maintain anterior-posterior polarity in the early *C. elegans* embryo. *Dev. Cell* **7**, 413–424 (2004).
25. Martin, A. C., Gelbart, M., Fernandez-Gonzalez, R., Kaschube, M. & Wieschaus, E. F. Integration of contractile forces during tissue invagination. *J. Cell Biol.* **188**, 735–749 (2010).
26. Yonemura, S., Wada, Y., Watanabe, T., Nagafuchi, A. & Shibata, M. α -Catenin as a tension transducer that induces adherens junction development. *Nature Cell Biol.* **12**, 533–542 (2010).
27. Bendix, P. M. *et al.* A quantitative analysis of contractility in active cytoskeletal protein networks. *Biophys. J.* **94**, 3126–3136 (2008).
28. Koenderink, G. H. *et al.* An active biopolymer network controlled by molecular motors. *Proc. Natl Acad. Sci. USA* **106**, 15192–15197 (2009).
29. Kobiak, A., Pasolunghi, H. A. & Fuchs, E. Mammalian formin-1 participates in adherens junctions and polymerization of linear actin cables. *Nature Cell Biol.* **6**, 21–30 (2004).
30. Drees, F., Pokutta, S., Yamada, S., Nelson, W. J. & Weis, W. I. α -Catenin is a molecular switch that binds E-cadherin- β -catenin and regulates actin-filament assembly. *Cell* **123**, 903–915 (2005).

Supplementary Information is linked to the online version of the paper at www.nature.com/nature.

Acknowledgements We thank R. Levayer, M. Mavrikis and J.-M. Philippe for making and sharing respectively the utrophin-GFP, GAP43-Venus and GAP43-Cherry transgenic lines. We are grateful to our colleagues for their gifts of reagents: B. Bement, R. Karsenti, H. Oda, A. Martin and E. Wieschaus. We thank E. Munro and all members of the Lecuit and Lenne groups for discussions, and comments on the manuscript. This work was supported by a Programme Grant from HFSP to T.L., P.-F.L. and E. Munro, by the CNRS, the Fondation pour la Recherche Médicale (to T.L.), the ANR-Blanc 2005 (to T.L. and P.-F.L.), Région PACA and ANR-PCV 2008 (to P.-F.L. and T.L.). M.R. was supported by a PhD fellowship by the Région PACA and Amplitude Systems.

Author Contributions M.R. made the original observations of pulsed contractility and flow. M.R. and T.L. planned the project, and analysed the data together with P.-F.L.; M.R. conducted the experiments except for FRAP experiments on MRLC-GFP, which were performed by P.-F.L. and T.L.; P.-F.L. and M.R. developed the nano-ablation system. T.L. and P.-F.L. wrote the manuscript together with M.R. All authors commented on the manuscript.

Author Information Reprints and permissions information is available at www.nature.com/reprints. The authors declare no competing financial interests. Readers are welcome to comment on the online version of this article at www.nature.com/nature. Correspondence and requests for materials should be addressed to T.L. (lecuit@ibdm.univ-mrs.fr) or P.-F.L. (lenne@ibdm.univ-mrs.fr).

METHODS

Fly stocks and constructs. *Drosophila* MRLC is encoded by *spaghetti-squash* (*sqh*). All experiments visualizing dynamics of MRLC were looking at MRLC fused to either eGFP or mCherry under the *sqh* promoter and rescuing a protein null *sqh*^{AX3} mutant³¹. E-cad-GFP was expressed under the ubiquitin promoter *ubi-Ecad::GFP* and rescues a null *e-cad/shotgun* mutant³².

The following fly stocks were used. Figure 1, Supplementary Fig. 1 and Supplementary Movies 1a, b: matGAL4(67) UASp-Utr-GFP (recombinant on II). *sqh*^{AX3}; *sqh-MRLC::GFP* (II) (generous gift of R. Karess) and *sqh*^{AX3}; *ubi-Ecad::GFP*; *sqh-sqh::mCherry* (recombinant on II). Figure 3, Supplementary Fig. 2, Supplementary Movie 3: *sqh*^{AX3}; *sqh-MRLC::mCherry*; *sqh-Utr::GFP* (recombinant on II). *sqh-MRLC::mCherry* (on II) is a gift from A. Martin and E. Wieschaus.

The plasmid coding for the fusion of eGFP and the actin binding domain of human Utraphin was obtained from W. Bement³³. The Utr-GFP fusion was PCR amplified and inserted in the p221DONR GATEWAY plasmid (Invitrogen). The fusion was recombined in a pUASp GATEWAY destination vector (pPW, from T. Murphy, Carnegie Institute) for expression under the maternal tubGAL4VP16 driver line (67Gal4) in Fig. 1, Supplementary Fig. 1 and Supplementary Movies 1a, b, or expression under the *sqh* promoter in Fig. 3, Supplementary Fig. 2 and Supplementary Movie 3. In the latter case, Utr-GFP expression is lower than under the Gal4 system, hence only reveals brighter structures (puncta) also visible in Supplementary Movie 1a and b and Fig. 1d and not individual filaments contrary to Fig. 1d.

To label the plasma membrane we used a fusion between the palmitoylated GAP43 protein and the YFP variant Venus³⁴ expressed by the GAL4 UAS system with the maternal tubGAL4VP16 driver line. GAP43-Cherry was constructed similarly and expressed under the *sqh* promoter as in ref. 31.

RNAi interference. We generated by PCR dsRNA probes directed against *Krüppel*, *α-catenin*, and *e-cadherin* using the following primers. The underlined sequence is the T7 promoter. The sequence not underlined corresponds to the template sequence. *e-cadherin*: 533 nucleotides, between +1475 to +2008 from ATG. E-cad-T7-F, taatacgaactcactataggagaccagctcttctgataatggcgagc. E-cad-T7-R, taatacgaactcactataggagaccagcgttccatcgttctggtgaac. *α-catenin*: 728 nucleotides, between +81 to +808 from ATG. *α-Cat-T7-F*, taatacgaactcactataggagc aatgtcagttgaataaaccttg. *α-Cat-T7-R*, taatacgaactcactataggagcgttggatgactttcttgggc aac. *Krüppel*: 775 nucleotides, between +491 to +1266 from ATG. Kr-T7-F, taatacgaactcactataggagaccagcgaggttccagacgagatcagca. Kr-T7-R, taatacgaactcactataggagaccagcgttccatcttcagaca. Embryos were injected as described in ref. 35.

Time lapse imaging. Embryos were prepared and imaged as detailed in ref. 36, using a spinning disc confocal system (Perkin Elmer) on an inverted Nikon microscope with 100×/1.4 oil immersion objective.

Nano-ablation experiments. We performed nano-dissection experiments with a home-built system. A near-infrared (NIR, 1,030 nm) femtosecond (fs) laser at 50 MHz repetition rate (t-Pulse, Amplitude Systems) was coupled to an inverted microscope (Eclipse TE 2000-E, Nikon). A fast multicolour confocal imaging system, based on the Yokogawa spinning disk (Ultraview ERS, Perkin Elmer), was also mounted at a side port of the microscope. Local ablation and fast fluorescence imaging were thus possible simultaneously. The NIR-fs laser beam is expanded through a ×5 telescope and is aligned with the microscope optical path with a dichroic mirror (FF01-750/SP, Semrock) immediately below the objective lens (×60/1.2, water immersion, Plan Apo VC, Nikon). The collimated beam fills the back aperture of the objective lens which transmits 68% of the incoming NIR light. Nano-dissections of medial Myo-II were performed by exposing this structure to the tightly focused laser during 1–3 ms with an average power of 360 mW at the back aperture of the objective. Exposure time was controlled by an automated 1.5-mm-diameter mechanical shutter (LS2, Uniblitz). The sample was positioned over the tightly focused laser beam thanks to a computer-controlled mechanical stage (Scan IM with a Tango2-Desktop controller, Marzhauser). A very similar set-up has already been shown to allow sub-cellular ablations¹².

Fluorescence intensity measurements. The intensity of the medial Myo-II is defined as the sum of average intensities of two regions of interest (ROIs) close to the junction (the centre of the elliptical ROIs were ~1 μm away from the junction, Fig. 2a in red). The intensity of the junctional Myo-II is defined as the average intensity of a 500-nm-wide stripe along the junction (Fig. 2a in green). The E-cad anisotropy is the average intensity of a 500-nm-wide stripe along transverse junctions divided by the average intensity measured along the vertical junction (Fig. 4a in blue). Intensity measurements were made by using ImageJ (1.39p version). Analysis were done on time lapse movies (one frame every 1–3 s). For

each frame, 6–10 z-planes were imaged over 3 μm. For long time lapse imaging (>200 s), bleach correction was performed by using ImageJ.

Cross-correlation analysis. Cross-correlation was performed applying Igor Pro (Wavemetrics) cross-correlation function. This function is given by:

$$C(\tau) = \frac{\int_0^T f(t)g(t+\tau)dt}{\int_0^T f(t)dt \int_0^T g(t)dt}$$

where T represents the overall time over which measurements were made, $f(t)$ and $g(t)$ the two cross-correlated functions (taking f as reference), and τ the time delay.

The basal signal f_{\min} and g_{\min} were subtracted from f and g functions respectively before cross-correlation. The final cross-correlation function was normalized as follows:

$$C_N(\tau) = \frac{\int_0^T (f(t) - f_{\min})(g(t + \tau) - g_{\min})dt}{\sqrt{\int_0^T (f(t) - f_{\min})^2 dt} \sqrt{\int_0^T (g(t) - g_{\min})^2 dt}}$$

Time delay measurements. In Fig. 2b all time delays were measured by cross-correlation. Cross-correlation analysis was assessed by performing a measure of delays between peaks for each cluster of events (for example, Fig. 2 shows three clusters of events) (see Supplementary Figs 1 and 2 top middle panel). When correlating with contraction rate functions, curves were smoothed by using a binomial algorithm implemented in Igor Pro software. For this analysis five cases of fully intercalating cells (corresponding to 15 clusters of events) were taken from five different wild-type MRLC-GFP embryos. Time lapse movies were taken at a rate of 1 frame s⁻¹. Each frame consisted in a z-stack of 3 μm (images spaced by 500 nm). Time lapse ranged between 200 and 500 s. Time delays in Fig. 4a, right, were determined as follows. The delay between the E-cad anisotropy peak and the medial Myo-II intensity peak was measured by cross-correlation (the medial Myo-II intensity curve was taken as reference). The time onset of medial Myo-II intensity pulses with respect to medial Myo-II intensity peak maxima was determined from the autocorrelation of the medial Myo-II intensity, which provides a measure of the average pulse duration, and therefore a measure of the average delay between pulse onset and pulse intensity peak. Auto-correlation analysis was assessed by performing a measure of delays for each cluster of events (see Supplementary Fig. 2 bottom) as for cross-correlation analysis. For this analysis five cases of intercalating cells were taken from five different wild-type MRLC-Cherry / E-cad-GFP embryos. Time lapse movies (one frame every 3 s) of both MRLC-Cherry and E-cad-GFP were taken. Each frame consisted of a z-stack of 3 μm (images spaced by 500 nm). Time lapse ranged between 200 and 500 s. Igor Pro software was used for all time delay measurements.

PIV analysis. PIV was determined with the Matlab toolbox (procedure MatPIV) developed by J. K. Sveen.

Fluorescence recovery after photobleaching. Fluorescence recovery after photobleaching (FRAP) measurements were performed as in Supplementary Fig. 6 using a confocal LSM510 (Zeiss) with a Plan-Apochromat 100×/1.3 oil objective and an argon laser (488 nm). Before and after photobleaching, images were acquired at low laser power (0.1% AOTF, Acousto Optic Tunable Filter) to avoid bleaching and with a pixel size of 40 nm. Photobleaching was performed for 0.9 s at full laser power over an ROI with 1 μm diameter. Fluorescence recovery was then recorded for 50 s. In Supplementary Fig. 7, we used the photokinesis unit of a Perkin Elmer confocal system for FRAP and the region of interest is a line 5 μm long.

- Royou, A., Field, C., Sisson, J. C., Sullivan, W. & Karess, R. Reassessing the role and dynamics of nonmuscle myosin II during furrow formation in early *Drosophila* embryos. *Mol. Biol. Cell* **15**, 838–850 (2004).
- Oda, H. & Tsukita, S. Real-time imaging of cell-cell adherens junctions reveals that *Drosophila* mesoderm invagination begins with two phases of apical constriction of cells. *J. Cell Sci.* **114**, 493–501 (2001).
- Burkel, B. M., von Dassow, G. & Bement, W. M. Versatile fluorescent probes for actin filaments based on the actin-binding domain of utrophin. *Cell Motil. Cytoskeleton* **64**, 822–832 (2007).
- Mavrikakis, M., Rikhy, R. & Lippincott-Schwartz, J. Plasma membrane polarity and compartmentalization are established before cellularization in the fly embryo. *Dev. Cell* **16**, 93–104 (2009).
- Pilot, F., Philippe, J. M., Lemmers, C. & Lecuit, T. Spatial control of actin organization at adherens junctions by a synaptotagmin like protein Btsz. *Nature* **442**, 580–584 (2006).
- Cavey, M. & Lecuit, T. Imaging cellular and molecular dynamics in live embryos using fluorescent proteins. *Methods Mol. Biol.* **420**, 219–238 (2008).

S-glutathionylation uncouples eNOS and regulates its cellular and vascular function

Chun-An Chen¹, Tse-Yao Wang¹, Saradhadevi Varadharaj¹, Levy A. Reyes¹, Craig Hemann¹, M. A. Hassan Talukder¹, Yeong-Renn Chen^{1†}, Lawrence J. Druhan^{1†} & Jay L. Zweier¹

Endothelial nitric oxide synthase (eNOS) is critical in the regulation of vascular function, and can generate both nitric oxide (NO) and superoxide ($O_2^{\bullet-}$), which are key mediators of cellular signalling. In the presence of Ca^{2+} /calmodulin, eNOS produces NO, endothelial-derived relaxing factor, from L-arginine (L-Arg) by means of electron transfer from NADPH through a flavin containing reductase domain to oxygen bound at the haem of an oxygenase domain, which also contains binding sites for tetrahydrobiopterin (BH_4) and L-Arg^{1–3}. In the absence of BH_4 , NO synthesis is abrogated and instead $O_2^{\bullet-}$ is generated^{4–7}. While NOS dysfunction occurs in diseases with redox stress, BH_4 repletion only partly restores NOS activity and NOS-dependent vasodilation⁷. This suggests that there is an as yet unidentified redox-regulated mechanism controlling NOS function. Protein thiols can undergo S-glutathionylation, a reversible protein modification involved in cellular signalling and adaptation^{8,9}. Under oxidative stress, S-glutathionylation occurs through thiol–disulphide exchange with oxidized glutathione or reaction of oxidant-induced protein thiol radicals with reduced glutathione^{10,11}. Cysteine residues are critical for the maintenance of eNOS function^{12,13}; we therefore speculated that oxidative stress could alter eNOS activity through S-glutathionylation. Here we show that S-glutathionylation of eNOS reversibly decreases NOS activity with an increase in $O_2^{\bullet-}$ generation primarily from the reductase, in which two highly conserved cysteine residues are identified as sites of S-glutathionylation and found to be critical for redox-regulation of eNOS function. We show that eNOS S-glutathionylation in endothelial cells, with loss of NO and gain of $O_2^{\bullet-}$ generation, is associated with impaired endothelium-dependent vasodilation. In hypertensive vessels, eNOS S-glutathionylation is increased with impaired endothelium-dependent vasodilation that is restored by thiol-specific reducing agents, which reverse this S-glutathionylation. Thus, S-glutathionylation of eNOS is a pivotal switch providing redox regulation of cellular signalling, endothelial function and vascular tone.

We observed that oxidized glutathione (GSSG) induces dose-dependent S-glutathionylation of human eNOS (heNOS) that was reversed by reducing agents, such as 2-mercaptoethanol or dithiothreitol (DTT) (Fig. 1a). S-Glutathionylation greatly decreased NOS activity (Fig. 1b) in a dose-dependent manner (Supplementary Fig. 1), but this was reversed by DTT with more than 80% recovery. When accessible thiols were alkylated by *N*-ethylmaleimide (NEM), NOS activity was abolished (more than 95% decrease; Fig. 1b). As expected, the NOS activity of control, S-glutathionylated or S-alkylated heNOS was totally inhibited by the NOS inhibitor *L*-N^G-nitroarginine methyl ester (*L*-NAME). In contrast to the marked (more than 70%) loss of NOS activity with S-glutathionylation, only a 56% decrease in NADPH consumption was seen that was only partly inhibited by *L*-NAME or the Ca^{2+} chelator EGTA (Supplementary Fig. 2). Although thiol-alkylation abolished NOS activity, it decreased NADPH consumption by only

about 50%, and this was not inhibited by *L*-NAME or EGTA. Thus, thiol modification uncouples eNOS with electron leakage from the reductase.

Because electron leakage could trigger $O_2^{\bullet-}$ generation, electron paramagnetic resonance (EPR) spin trapping was performed to demonstrate

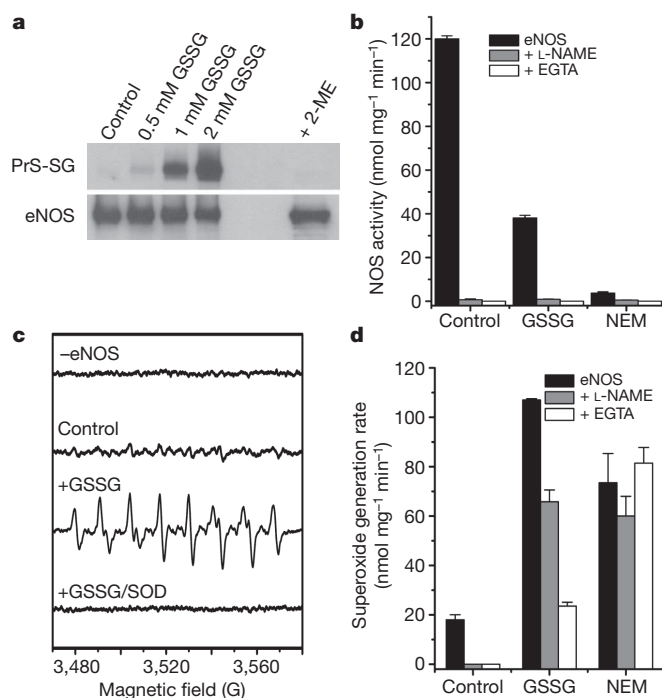


Figure 1 | S-glutathionylation of heNOS occurs and inhibits NOS activity.

a, Immunoblotting of heNOS S-glutathionylation. Top: immunoblotting of protein S-glutathionylation (PrS-SG) with anti-GSH antibody. Control non-S-glutathionylated heNOS (1 μ g in 20 μ l) or heNOS S-glutathionylated by 0.5, 1 or 2 mM GSSG at room temperature (23 °C) for 1 h. Treatment with 2-mercaptoethanol (ME) after S-glutathionylation with 2 mM GSSG reversed the S-glutathionylation. Bottom: immunoblotting with anti-eNOS antibody. **b**, Effect of S-glutathionylation and S-alkylation on heNOS activity. NOS activity was measured from control, S-glutathionylated (2 mM GSSG for 20 min) or alkylated (1 mM NEM for 20 min) heNOS. NOS activity of treated or untreated heNOS was fully inhibited by *L*-NAME (1 mM) or EGTA (1 mM). **c**, **d**, Effects of S-glutathionylation on $O_2^{\bullet-}$ generation from heNOS. $O_2^{\bullet-}$ generation was measured from control, S-glutathionylated (as in **b**) or alkylated (as in **b**) BH_4 -bound heNOS by EPR spin trapping with 25 mM 5-diethoxyphosphoryl-5-methyl-1-pyrroline *N*-oxide (DEPMPO). **c**, Spin-trapping showed no signal in the absence of heNOS and only trace signal from control enzyme; S-glutathionylation triggered a marked increase in $O_2^{\bullet-}$ generation with a $O_2^{\bullet-}$ -adduct spectrum that was quenched by Cu,Zn superoxide dismutase (SOD) (200 U ml⁻¹). **d**, Effect of *L*-NAME (1 mM) and EGTA (1 mM) on $O_2^{\bullet-}$ generation from control, S-glutathionylated and alkylated BH_4 -bound heNOS. Results in **b** and **d** are shown as means and s.e.m. ($n = 3-5$).

¹Davis Heart and Lung Research Institute and Division of Cardiovascular Medicine, Department of Internal Medicine, College of Medicine, Ohio State University, Columbus, Ohio 43210, USA. [†]Present addresses: Northeastern Ohio Universities College of Medicine Department of Integrative Medical Sciences, Rootstown, Ohio 44272, USA (Y.-R.C.); Department of Anesthesiology, College of Medicine, Ohio State University, Columbus, Ohio 43210, USA (L.J.D.).

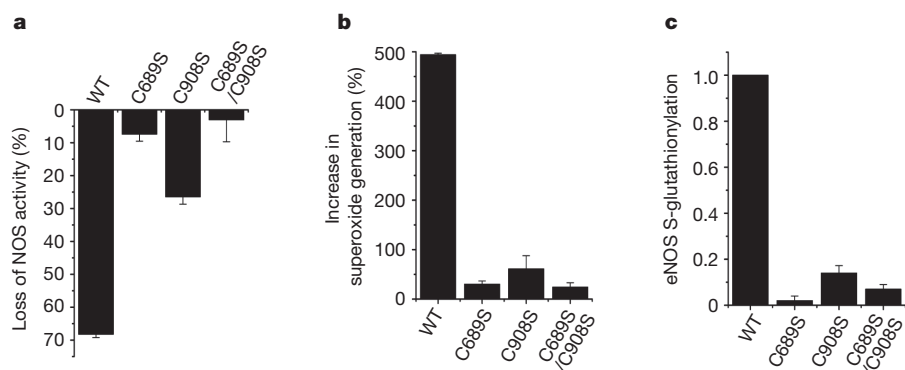


Figure 2 | Cysteine mutants (C689S, C908S and C689S/C908S) of heNOS resist S-glutathionylation and secondary uncoupling. WT heNOS and heNOS C689S, C908S and C689S/C908S mutants were treated with 2 mM GSSG. **a**, Percentage loss of NOS activity after treatment of heNOS with GSSG. **b**, Percentage increase in $O_2^{\bullet-}$ generation after treatment of heNOS with GSSG. **c**, Ratio of relative eNOS S-glutathionylation to eNOS protein. The relative intensity of eNOS S-glutathionylation/eNOS protein was normalized to the wild-type value. The Cys→Ser mutants maintained a NOS activity similar to that of the wild type ($120 \pm 12 \text{ nmol min}^{-1} \text{ mg}^{-1}$). Results are shown as means and s.e.m. ($n = 3$).

this S-glutathionylation-dependent $O_2^{\bullet-}$ generation from heNOS. S-Glutathionylation greatly increased $O_2^{\bullet-}$ generation (more than five-fold) with a prominent $O_2^{\bullet-}$ -adduct signal that was quenched by Cu,Zn superoxide dismutase (Fig. 1c). The NOS inhibitor L-NAME, which blocks $O_2^{\bullet-}$ generation from the oxygenase, only partly blocked this $O_2^{\bullet-}$ generation (Fig. 1d), and it was also incompletely blocked by EGTA. S-Alkylation of heNOS increased $O_2^{\bullet-}$ generation (about four-fold), and this was not blocked by L-NAME or EGTA. In contrast, the low-level $O_2^{\bullet-}$ production from control heNOS was fully quenched by L-NAME or EGTA. Thus, S-glutathionylation and S-alkylation uncouple heNOS, greatly increasing $O_2^{\bullet-}$ generation, and the partial or complete lack of inhibition by L-NAME suggests that the observed $O_2^{\bullet-}$ is largely derived from the reductase domain.

To investigate the mechanism of S-glutathionylation-induced heNOS uncoupling, we sought to determine the specific residues modified. We therefore subjected S-glutathionylated heNOS to proteolytic digestion and liquid chromatography–tandem mass spectrometry (LC–MS/MS) analysis. Peptides with a mass difference of 305 Da, representing one glutathione moiety, were detected by LC–MS and their primary sequence was determined by MS/MS. We identified two glutathionylated cysteine residues within the reductase domain,

namely Cys 689 and Cys 908, from both trypsin and chymotrypsin digestions (Supplementary Fig. 3a, b). Using molecular modelling to predict the three-dimensional structure of the heNOS reductase domain (Supplementary Fig. 4), we found that Cys 689 and Cys 908 are located on the domain surface surrounded by several positively charged residues, and thus would probably be deprotonated at physiological pH, making them good candidates for S-glutathionylation.

S-Glutathionylation results in the formation of a mixed disulphide bond between the reactive Cys-thiol and reduced glutathione (GSH), a tripeptide consisting of glycine, cysteine and glutamate. The addition of this bulky negatively charged group can alter protein structure and function in a similar manner to the addition of a phosphate^{14,15}. Our molecular modelling reveals that both Cys 689 and Cys 908 are located at the interface of the FAD-binding and FMN-binding domains. Modification of these residues would therefore disrupt FAD–FMN alignment, interrupting electron transfer between the flavins and enhancing their solvent accessibility¹⁶ (Supplementary Fig. 4), so that O_2 could gain access and accept an electron from the reduced flavin, with the formation of $O_2^{\bullet-}$.

Mutagenesis of Cys 689 or Cys 908 to Ser was used to test the importance of these residues on the redox regulation of eNOS.

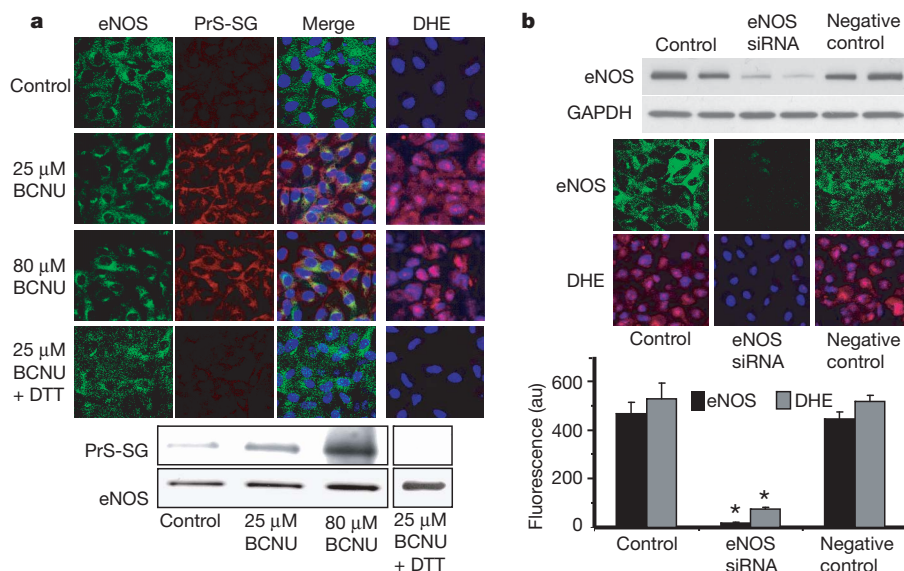


Figure 3 | Effect of redox stress on eNOS S-glutathionylation and function in endothelial cells. **a**, Immunostaining of eNOS (left column, green fluorescence) and S-glutathionylation (second column, red fluorescence) in control BAECs and cells preincubated with BCNU. The third column shows the merged S-glutathionylation/eNOS image along with 4',6-diamidino-2-phenylindole (DAPI) staining of the nucleus (blue). eNOS staining and S-glutathionylation seem to co-localize. The right-hand column shows $O_2^{\bullet-}$ detection with dihydroethidine (DHE), which is oxidized by $O_2^{\bullet-}$ to a product with red fluorescence, and the cell nuclei were counterstained with DAPI (blue). Increased $O_2^{\bullet-}$ generation was seen in the BCNU-treated cells. Bottom:

immunoprecipitation of eNOS from the BCNU-treated cells shows that eNOS S-glutathionylation occurs but is reversed by 1 mM DTT. The upper row shows immunoblotting with anti-GSH antibody; the lower row shows immunoblotting with anti-eNOS antibody. **b**, Effects of eNOS silencing from BAECs on BCNU-induced $O_2^{\bullet-}$ generation. Top: immunoblotting against eNOS to determine the efficiency of eNOS silencing. Middle: confocal microscopy of eNOS (upper row) and $O_2^{\bullet-}$ measurements with DHE (lower row). NOS3 short interfering RNA (siRNA) greatly decreases eNOS expression in BAECs (middle column). Bottom: graph of the effect of eNOS silencing on BCNU-induced $O_2^{\bullet-}$ generation. Results are shown as means and s.e.m. ($n = 5$). Asterisk, $P < 0.001$.

Whereas wild-type (WT) eNOS is S-glutathionylated by GSSG with a roughly 70% loss of NOS activity, Cys→Ser mutants resist glutathionylation, with no loss of NOS activity in the double mutant and only modest loss in the single mutants (Fig. 2a–c). These mutants also resist GSSG-induced eNOS uncoupling with $O_2^{\bullet-}$ generation. Thus, both Cys 689 and Cys 908 are critical for the redox regulation of eNOS.

Next we sought to determine the consequences of eNOS S-glutathionylation in endothelial cells. Inhibition of glutathione reductase by 1,3-bis(2-chloroethyl)-1-nitrosourea (BCNU) decreases the cellular GSH/GSSG ratio, leading to protein S-glutathionylation^{17,18}. Previous studies of bovine aortic endothelial cells (BAECs) treated with BCNU reported eNOS inhibition with glutaredoxin or thioredoxin inactivation^{19,20}; however, the molecular mechanism of this process and alterations in eNOS were not investigated. In our current study of BAECs treated with BCNU, confocal microscopy demonstrated marked cellular S-glutathionylation that co-localized with eNOS (Fig. 3a, left column). Immunoprecipitation of eNOS followed by immunoblotting confirmed that the BCNU-induced increase in GSSG led to eNOS S-glutathionylation (Fig. 3a, bottom). This was further confirmed by mass spectrometry, in which Cys 689 was more than 50% S-glutathionylated (Supplementary Fig. 5). BCNU-treated BAECs showed increased $O_2^{\bullet-}$ generation that was blocked by DTT, which reversed the eNOS S-glutathionylation (Fig. 3a, right column, and Supplementary Fig. 6). BCNU also dose-dependently decreased cellular eNOS-derived NO production (Supplementary Fig. 7). Thus, alterations in the cellular GSH/GSSG ratio led to the S-glutathionylation of eNOS, and this resulted in decreased NO and increased $O_2^{\bullet-}$ generation. eNOS gene silencing from BAECs abolished BCNU-induced $O_2^{\bullet-}$ generation (Fig. 3b). Experiments in COS7 cells transfected with WT or C689A/C908A eNOS confirmed that glutathionylation at Cys 689/Cys 908 is critical for the triggering of BCNU-induced $O_2^{\bullet-}$ generation (Supplementary Fig. 8).

To further determine whether redox stress leading to S-glutathionylation alters endothelial function in vessels, aortic segments were pre-exposed to BCNU and then measurements of endothelium-dependent or endothelium-independent relaxation were performed. In BCNU-exposed vessels, a marked decrease in endothelium-dependent vasodilation was seen (Fig. 4a, left panel), whereas endothelium-independent vasodilation elicited by exogenous NO was unaffected (Fig. 4a, right panel). Furthermore, DTT, which reverses eNOS S-glutathionylation, restored endothelium-dependent vasodilation in BCNU-treated vessels.

Oxidant-stress-induced disruption of endothelium-dependent vasodilation is involved in the pathogenesis of hypertension, atherosclerosis and other cardiovascular disease²¹. Because eNOS S-glutathionylation profoundly impaired endothelium-dependent vasodilation, we speculated that there might be an increase in eNOS S-glutathionylation in hypertension. Indeed, in the vessels of spontaneously hypertensive (SHR) rats *en face* immunohistology showed marked S-glutathionylation with prominent endothelial co-localization with eNOS (Supplementary Fig. 9), whereas control normotensive vessels (from WKY rats) had little S-glutathionylation. Immunoprecipitation of eNOS confirmed these results, showing much higher eNOS S-glutathionylation in vessels from SHR rats in comparison with vessels from WKY rats (Fig. 4c). The marked decrease in endothelium-dependent vasodilation of aortic rings from SHR rats was reversed by thiol-specific reducing agents that concurrently reverse eNOS S-glutathionylation (Fig. 4b, c). Thus, just as in the *in vitro* and *ex vivo* settings, eNOS S-glutathionylation occurs in vessels *in vivo* and increases with oxidative stress, resulting in a loss of endothelium-dependent relaxation, leading to hypertension. Other redox modifications of critical thiols on eNOS or other important regulatory proteins could further contribute to vascular dysfunction and the pathogenesis of hypertension^{22,23}.

There is extensive evidence that thiols potentiate eNOS activity and alleviate oxidant stress^{24,25}. NOS uncoupling induces oxidant stress and has previously been shown to occur with depletion of L-Arg or BH₄ and

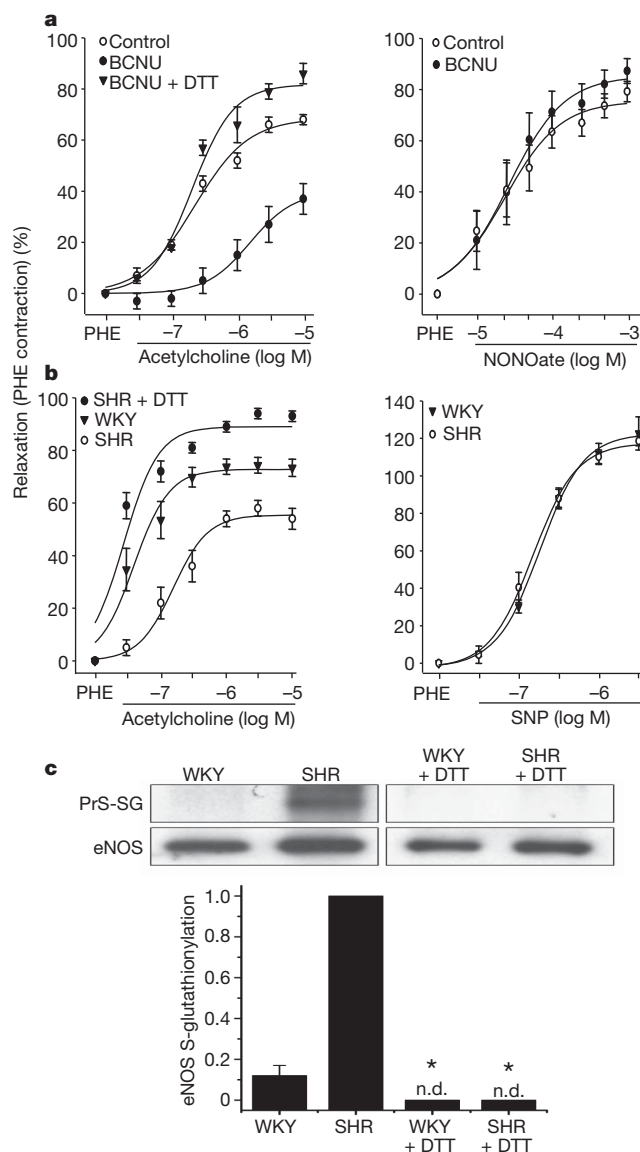


Figure 4 | Effect of redox stress on eNOS S-glutathionylation and function in vessels. **a**, Endothelium-dependent and endothelium-independent vasorelaxation in control and BCNU (80 μ M)-treated rat aortic rings. BCNU markedly decreased endothelium-dependent relaxation to acetylcholine (left panel) but not endothelium-independent relaxation by the NO donor NONOate (right panel). DTT (1 mM for 20 min) reversed the BCNU-induced inhibition of relaxation (left panel). Aortic relaxation is plotted as the percentage decrease in phenylephrine (PHE)-induced contraction against agonist concentration on a logarithmic scale. Results are shown as means \pm s.e.m.; $P < 0.05$, BCNU versus control or BCNU + DTT ($n = 4$). **b**, Endothelium-dependent vasorelaxation in spontaneously hypertensive (SHR) and control (WKY) aortic rings. SHR rings showed a marked decrease in relaxation to acetylcholine; however, DTT (as above) re-established the acetylcholine response. Endothelium-independent relaxation (right) was similar for both SHR and WKY rings. Aortic relaxation is expressed as in **a**. $P < 0.05$, SHR versus WKY or SHR + DTT ($n = 4$). See also Supplementary Fig. 10. **c**, eNOS S-glutathionylation of SHR and WKY aortae. Top: WKY and SHR aortae, either untreated or DTT-pretreated as in **b**, were homogenized. This was followed by immunoprecipitation with anti-eNOS antibody. The immunoprecipitation products were separated by SDS-PAGE followed by immunoblotting against anti-GSH and anti-eNOS antibodies. In SHR aortae, eNOS S-glutathionylation was markedly increased compared with WKY aortae and was abolished by pretreatment with DTT. Bottom: ratio of relative intensity of eNOS S-glutathionylation/eNOS, normalized to SHR aortae. There is only trace eNOS S-glutathionylation in WKY aortae, whereas high levels are seen in SHR aortae. There was no detectable (n.d.) NOS S-glutathionylation in DTT-pretreated WKY or SHR aortae. Asterisk, $P < 0.001$ versus SHR ($n = 5$).

elevation of methylarginine levels^{4,26–28}. Here we show that eNOS possesses specific redox-sensitive thiols that are readily S-glutathionylated in endothelial cells and vessels with marked endothelial dysfunction and hypertension. This oxidative modification switches eNOS from its classical NO synthase function to that of an NADPH-dependent oxidase generating $O_2^{\bullet-}$, which occurs primarily from the reductase domain and, in contrast to other uncoupling mechanisms, is not inhibited by typical NOS inhibitors. Because NO and $O_2^{\bullet-}$ have many opposing roles in cell signalling and vascular function²⁹, S-glutathionylation of eNOS will trigger profound changes in cellular and vascular function and will mediate redox-signalling under oxidative stress. This mechanism of eNOS uncoupling could be triggered by other uncoupling processes such as BH₄ depletion, but could also further enhance BH₄ depletion. Further studies will be needed to elucidate these interactions.

These observations provide a new molecular understanding of how oxidant stress alters endothelial function and vascular tone and how the restoration or supplementation of reducing equivalents can restore endothelial function and normalize vascular tone. Therapeutics with thiol-reducing properties can therefore now be developed and refined as potent drugs for reversing endothelial dysfunction and ameliorating hypertension and other cardiovascular disease. Recently, hydrogen sulphide, a potent reducing agent, has been identified as a critical endogenous signalling molecule conferring potent cardiac protection in diseases with oxidant stress³⁰; however, its mechanism of action is unknown. Our present observations provide a mechanism by which it might confer protection.

S-Glutathionylation thus uncouples eNOS, switching it from NO to $O_2^{\bullet-}$ generation. This process is induced by oxidant stress and is reversible. Two highly conserved cysteine residues at the interface between the FMN-binding and FAD-binding domains are S-glutathionylated, leading to uncoupling with $O_2^{\bullet-}$ generation. Oxidant stress triggers eNOS S-glutathionylation in endothelial cells and intact vessels. Furthermore, S-glutathionylation is increased in hypertensive vessels, resulting in impaired endothelium-dependent vasodilation. In view of the central importance of NO and eNOS-mediated endothelial dysfunction in diseases including heart attack, stroke, diabetes and cancer, identification of this novel redox-signalling pathway provides new insights into therapeutic approaches for the prevention or amelioration of many of the most prevalent diseases afflicting mankind.

METHODS SUMMARY

heNOS was expressed, purified and characterized as described¹⁵. EPR spin-trapping and fluorescence were used to measure NO and $O_2^{\bullet-}$ generation. Immunofluorescence microscopy and immunoprecipitation were applied to detect eNOS S-glutathionylation in BAECs and aortae. Specific cysteine residues of eNOS that are S-glutathionylated were identified by mass spectrometry, and site-directed mutagenesis was performed to determine their role in enzyme function *in vitro* and *in vivo*. Acetylcholine-dependent relaxation of aortic rings was used to determine endothelium-dependent vasodilator function.

Full Methods and any associated references are available in the online version of the paper at www.nature.com/nature.

Received 25 February; accepted 12 October 2010.

- Bredt, D. S. *et al.* Cloned and expressed nitric oxide synthase structurally resembles cytochrome P-450 reductase. *Nature* **351**, 714–718 (1991).
- Palmer, R. M., Ashton, D. S. & Moncada, S. Vascular endothelial cells synthesize nitric oxide from L-arginine. *Nature* **333**, 664–666 (1988).
- Rapoport, R. M., Draznin, M. B. & Murad, F. Endothelium-dependent relaxation in rat aorta may be mediated through cyclic GMP-dependent protein phosphorylation. *Nature* **306**, 174–176 (1983).
- Xia, Y., Tsai, A. L., Berk, V. & Zweier, J. L. Superoxide generation from endothelial nitric-oxide synthase. A Ca^{2+} /calmodulin-dependent and tetrahydrobiopterin regulatory process. *J. Biol. Chem.* **273**, 25804–25808 (1998).
- Vasquez-Vivar, J. *et al.* Superoxide generation by endothelial nitric oxide synthase: the influence of cofactors. *Proc. Natl Acad. Sci. USA* **95**, 9220–9225 (1998).
- Stuehr, D. J., Santolini, J., Wang, Z. Q., Wei, C. C. & Adak, S. Update on mechanism and catalytic regulation in the NO synthases. *J. Biol. Chem.* **279**, 36167–36170 (2004).

- Dumitrescu, C. *et al.* Myocardial ischemia results in tetrahydrobiopterin (BH₄) oxidation with impaired endothelial function ameliorated by BH₄. *Proc. Natl Acad. Sci. USA* **104**, 15081–15086 (2007).
- Giustarini, D., Rossi, R., Milzani, A., Colombo, R. & Dalle-Donne, I. S-glutathionylation: from redox regulation of protein functions to human diseases. *J. Cell. Mol. Med.* **8**, 201–212 (2004).
- Biswas, S., Chida, A. S. & Rahman, I. Redox modifications of protein-thiols: emerging roles in cell signaling. *Biochem. Pharmacol.* **71**, 551–564 (2006).
- Ying, J., Clavreul, N., Sethuraman, M., Adachi, T. & Cohen, R. A. Thiol oxidation in signaling and response to stress: detection and quantification of physiological and pathophysiological thiol modifications. *Free Radic. Biol. Med.* **43**, 1099–1108 (2007).
- Hill, B. G. & Bhatnagar, A. Role of glutathionylation in preservation, restoration and regulation of protein function. *IUBMB Life* **59**, 21–26 (2007).
- Hofmann, H. & Schmidt, H. H. Thiol dependence of nitric oxide synthase. *Biochemistry* **34**, 13443–13452 (1995).
- Harbrecht, B. G. *et al.* Glutathione regulates nitric oxide synthase in cultured hepatocytes. *Ann. Surg.* **225**, 76–87 (1997).
- Fulton, D. *et al.* Regulation of endothelium-derived nitric oxide production by the protein kinase Akt. *Nature* **399**, 597–601 (1999).
- Chen, C. A., Druhan, L. J., Varadharaj, S., Chen, Y. R. & Zweier, J. L. Phosphorylation of endothelial nitric-oxide synthase regulates superoxide generation from the enzyme. *J. Biol. Chem.* **283**, 27038–27047 (2008).
- Garcin, E. D. *et al.* Structural basis for isozyme-specific regulation of electron transfer in nitric-oxide synthase. *J. Biol. Chem.* **279**, 37918–37927 (2004).
- Caruso, R. L., Upham, B. L., Harris, C. & Trosko, J. E. Biphasic lindane-induced oxidation of glutathione and inhibition of gap junctions in myometrial cells. *Toxicol. Sci.* **86**, 417–426 (2005).
- Wang, Y., Qiao, M., Miesal, J. J., Asmis, L. M. & Asmis, R. Molecular mechanism of glutathione-mediated protection from oxidized low-density lipoprotein-induced cell injury in human macrophages: role of glutathione reductase and glutaredoxin. *Free Radic. Biol. Med.* **41**, 775–785 (2006).
- Wang, J., Pan, S. & Berk, B. C. Glutaredoxin mediates Akt and eNOS activation by flow in a glutathione reductase-dependent manner. *Arterioscler. Thromb. Vasc. Biol.* **27**, 1283–1288 (2007).
- Sugiyama, T. & Michel, T. Thiol-metabolizing proteins and endothelial redox state: differential modulation of eNOS and biopterin pathways. *Am. J. Physiol. Heart Circ. Physiol.* **298**, H194–H201 (2010).
- Muscoli, C. *et al.* On the selectivity of superoxide dismutase mimetics and its importance in pharmacological studies. *Br. J. Pharmacol.* **140**, 445–460 (2003).
- Huang, A., Xiao, H., Samii, J. M., Vita, J. A. & Kearney, J. F. Jr. Contrasting effects of thiol-modulating agents on endothelial NO bioactivity. *Am. J. Physiol. Cell Physiol.* **281**, C719–C725 (2001).
- Sayed, N., Baskaran, P., Ma, X., van den Akker, F. & Beuve, A. Desensitization of soluble guanylyl cyclase, the NO receptor, by S-nitrosylation. *Proc. Natl Acad. Sci. USA* **104**, 12312–12317 (2007).
- Vita, J. A. *et al.* L-2-Oxothiazolidine-4-carboxylic acid reverses endothelial dysfunction in patients with coronary artery disease. *J. Clin. Invest.* **101**, 1408–1414 (1998).
- Kugiyama, K. *et al.* Intracoronary infusion of reduced glutathione improves endothelial vasomotor response to acetylcholine in human coronary circulation. *Circulation* **97**, 2299–2301 (1998).
- Xia, Y., Dawson, V. L., Dawson, T. M., Snyder, S. H. & Zweier, J. L. Nitric oxide synthase generates superoxide and nitric oxide in arginine-depleted cells leading to peroxynitrite-mediated cellular injury. *Proc. Natl Acad. Sci. USA* **93**, 6770–6774 (1996).
- Cardounel, A. J., Xia, Y. & Zweier, J. L. Endogenous methylarginines modulate superoxide as well as nitric oxide generation from neuronal nitric-oxide synthase: differences in the effects of monomethyl- and dimethylarginines in the presence and absence of tetrahydrobiopterin. *J. Biol. Chem.* **280**, 7540–7549 (2005).
- Druhan, L. J. *et al.* Regulation of eNOS-derived superoxide by endogenous methylarginines. *Biochemistry* **47**, 7256–7263 (2008).
- Pryor, W. A. *et al.* Free radical biology and medicine: it's a gas, man! *Am. J. Physiol. Regul. Integr. Comp. Physiol.* **291**, R491–R511 (2006).
- Szabo, C. Hydrogen sulphide and its therapeutic potential. *Nature Rev. Drug Discov.* **6**, 917–935 (2007).

Supplementary Information is linked to the online version of the paper at www.nature.com/nature.

Acknowledgements We thank L. Zhang and K. Green-Church for support with mass spectrometric analysis. This work was supported by R01 grants HL63744, HL65608, HL83234 (J.L.Z.), HL83237 (Y.-R.C.) and HL103846 (C.-A.C.) from the National Institutes of Health.

Author Contributions C.-A.C., the primary author, performed most of the experiments and data analysis with assistance from T.-Y.W., S.V. and L.J.D. L.R. and T.-Y.W. performed the vessel studies. S.V. performed the confocal microscopy and immunohistology work. C.H. performed molecular modelling and protein expression and purification. Y.-R.C. provided mass spectrometry expertise and guidance. M.A.H.T. coordinated physiology experiments and data analysis. J.L.Z. envisioned, directed, guided and fully supported all of the work and prepared the final manuscript with input from all the authors. All authors discussed the results and commented on the manuscript.

Author Information Reprints and permissions information is available at www.nature.com/reprints. The authors declare no competing financial interests. Readers are welcome to comment on the online version of this article at www.nature.com/nature. Correspondence and requests for materials should be addressed to J.L.Z. (jay.zweier@osumc.edu).

METHODS

heNOS purification. heNOS was purified from an *Escherichia coli* overexpression system in which plasmids expressing heNOS (pCwheNOS or pDEST17heNOS) and calmodulin (pCaM) were co-transformed into BL21(DE3). The detailed expression procedures have been described previously^{15,31}.

Determination of protein and haem content. Protein concentration of purified heNOS was determined by the Bradford protein assay (Bio-Rad), with BSA as a standard. The haem content of heNOS was determined by pyridine haemochromogen assay. heNOS (50 µg) was added to a solution containing 0.15 M NaOH and 1.8 M pyridine, and the difference spectrum (reduced minus oxidized bispyridine haem) was recorded and quantified by using $\Delta\epsilon = 24 \text{ mM}^{-1} \text{ cm}^{-1}$ at 556–538 nm. Reduction of the bispyridine haem was achieved by the addition of a few grains of dithionite^{15,32}.

Thiol modification of heNOS. To induce protein S-glutathionylation *in vitro*, purified heNOS was incubated for 20 min with the specified GSSG concentration in 50 mM Tris-HCl pH 7.4 at room temperature³³. To alkylate all accessible thiols on heNOS, the purified heNOS was incubated for 20 min with 1 mM NEM in 50 mM Tris pH 7.4 at room temperature. Thiol modified enzyme preparations were then subjected to further analysis: immunoblotting, NO activity assay, and NO and $\text{O}_2^{\bullet-}$ measurement^{4,15,26,34–37}. For mass spectrometric identification of sites of S-glutathionylation, heNOS was incubated for 1 h with 2 mM GSSG at room temperature and then subjected to SDS-PAGE separation under non-reducing conditions. The molar ratio of eNOS to GSSG was 1:250 when 2 mM GSSG was used for the reaction.

Measurement of NOS activity. NOS activity was measured by the conversion of L-[¹⁴C]arginine to L-[¹⁴C]citrulline in a total volume of 200 µl of buffer containing 50 mM Tris-HCl pH 7.4, 100 µM L-Arg, 1 µM L-[¹⁴C]arginine, 0.5 mM NADPH, 0.5 mM Ca^{2+} , 10 µg ml⁻¹ calmodulin, 10 µM BH₄ and 5 µg ml⁻¹ purified eNOS. After incubation for 10 min at 37 °C, the reaction was terminated by the addition of 3 ml of ice-cold stop buffer (20 mM HEPES pH 5.5, 2 mM EDTA, 2 mM EGTA). L-[¹⁴C]citrulline was separated by passing reaction mixtures through Dowex AG 50W-X8 (Na⁺ form; Sigma) cation-exchange columns and quantified by liquid scintillation counting³⁴.

Measurement of NADPH consumption. NADPH oxidation²⁸ was followed spectrophotometrically at 340 nm with a Varian Cary 300 UV-Vis spectrophotometer. The reaction mixture (total volume 500 µl) contained 10 µg of CaM, 100 µM L-Arg, 200 µM NADPH, 10 µM BH₄ and 500 µM CaCl₂ in 50 mM Tris-HCl pH 7.4. heNOS (2–5 µg) was used in the NADPH consumption assay. The reaction was initiated by the addition of 10 µl of 10 mM NADPH, and all experiments were run at room temperature. The rate of NADPH oxidation during the first 10 min was followed and the initial rate was calculated from the linear portion and an extinction coefficient of $6.22 \text{ mM}^{-1} \text{ cm}^{-1}$.

Measurement of $\text{O}_2^{\bullet-}$ generation by EPR spin trapping. Spin-trapping measurements of oxygen radical production from heNOS were performed in 50 mM Tris-HCl buffer pH 7.4 containing 0.5 mM NADPH, 0.5 mM Ca^{2+} , 10 µg ml⁻¹ calmodulin, 15 µg ml⁻¹ purified heNOS and 25 mM DEPMPO^{15,37}. For these measurements the binding of BH₄ to heNOS was reconstituted in advance by incubation of the enzyme with 100 µM BH₄ for 3 h; the unbound BH₄ was then removed to prevent superoxide scavenging. EPR spectra were recorded in a 50-µl capillary at room temperature with a Bruker EMX spectrometer operating at 9.86 GHz with 100 kHz modulation frequency at room temperature, as described¹⁵. Spectra were measured by using the following parameters: centre field 3,510 G; sweep width 140 G; power 20 mW; receiver gain 2×10^5 ; modulation amplitude 0.5 G; conversion time 41 ms; time constant 328 ms.

SDS-PAGE and immunoblotting. The standard procedures for SDS-PAGE and immunoblotting were followed as described previously¹⁵. The reaction mixture was separated on a 4–20% Tris-glycine polyacrylamide gradient gel. Samples were run at room temperature for 1.5 h at 125 V. Protein bands were transferred electrophoretically to a nitrocellulose membrane in 12 mM Tris-HCl, 96 mM glycine, 20% methanol with an Xcell II Blot Module (Invitrogen) with 25 V constant for 90 min. Membranes were blocked for 1 h at room temperature in Tris-buffered saline (TBS) containing 0.05% Tween 20 (TTBS), with 5% dried milk (Bio-Rad). Membranes were then incubated overnight with anti-glutathione monoclonal antibody (ViroGen) or anti-eNOS polyclonal antibody (Santa Cruz) at 4 °C. Membranes were then washed three times in TTBS and incubated for 1 h with horseradish peroxidase-conjugated anti-mouse or anti-rabbit IgG in TTBS at room temperature. Membranes were again washed three times in TTBS and were then detected with ECL Western Blotting detection reagents (Amersham Biosciences). The signal intensity of blotting was digitized and quantified with ImageJ from the National Institutes of Health.

Mass spectrometry. The protein sample was subjected to SDS-PAGE on a 4–20% gradient polyacrylamide gel. Protein bands on the gel were then stained with Coomassie blue. The band containing S-glutathionylation of heNOS, which was confirmed by immunoblotting against anti-GSH antibody, was cut and digested

in-gel with trypsin, chymotrypsin, or trypsin and chymotrypsin before mass spectrometric measurement³³.

The S-glutathionylation of heNOS was determined with capillary-liquid chromatography tandem mass spectrometry (Nano-LC-MS/MS), which was performed on a LTQ or LTQ Orbitrap mass spectrometer (Thermo). The detailed parameters used in the MS measurements have been described in our previous study³³. Sequence information from MS/MS data was processed with Mascot Distiller software, by using standard data processing parameters. Database searches were performed with the MASCOT (Matrix Science) program.

Modelling. The three-dimensional structure of heNOS reductase domain was predicted by use of the Swiss-Model First Approach Mode³⁸. The input sequence of heNOS starts from Ala 515 to Ser 1177 of heNOS. The lower Blast P(N) limit for template selection was set to 0.0001. The three-dimensional structure of the reductase domain of rat neuronal NOS (PDB ID 1F20) was also used as the self-input template file for the tertiary structure prediction of the heNOS reductase domain. The final model output was a Swiss-PDB viewer project file. PyMOL (DeLano Scientific LLC) was used to construct and view the three-dimensional structure of the heNOS reductase domain.

Site-directed mutagenesis of heNOS. For bacterial expression, the human NOS3 gene was subcloned into pDEST17 vector (Invitrogen). It contains a His tag at the amino terminus of heNOS. The reading frame and heNOS sequence were confirmed by DNA sequencing. QuikChange site-directed mutagenesis (Stratagene) was used for heNOS Cys→Ser mutations. Primers for each mutation were as follows: Cys 689→Ser, 5'-GGCGACGAGCTGAGCGGCCAGGAGG-3' (sense) and 5'-CCTCCTGGCCGCTCAGCTCGTCCG-3' (antisense); Cys 908→Ser, 5'-GAAGTGTTCCGACGCCACGCTGC-3' (sense) and 5'-GCAGCGTGGGGCTGCGGAACCACTTC-3' (antisense). The sequence of each heNOS mutant was further confirmed by DNA sequencing. The detailed procedures of protein expression and purification have been described previously^{15,31}.

For mammalian expression, the human NOS3 gene was subcloned into pcDNA-DEST40 gateway vector (pc40heNOS) (Invitrogen). It contains the V5 epitope and a His tag at the carboxy terminus of heNOS. The reading frame and heNOS sequence were confirmed by DNA sequencing. QuikChange site-directed mutagenesis (Stratagene) was used for heNOS Cys→Ala mutations. Primers for each mutation were as follows: Cys 689→Ala, 5'-GGCGACGAGCTGGCCGCCAGGAGG-3' (sense) and 5'-CCTCCTGGCCGCGCCAGCTCGTCCG-3' (antisense); Cys 908→Ala, 5'-GAAGTGTTCCGCGCCCCACGCTGCTG-3' (sense) and 5'-CAGCAGCGTGGGGCGCGGAACCACTTC-3' (antisense). The sequence of the heNOS double mutant (C689A/C908A) from pc40heNOS was further confirmed by DNA sequencing. For mammalian expression, COS-7 was used for heNOS overexpression for cellular assays, because there is no eNOS in COS-7, as reported previously³⁹.

Fluorescence and immunofluorescence microscopy. BAECs cultured on 22-mm² sterile coverslips (Harvard Apparatus) in 35-mm sterile dishes at a density of 10^4 cells per dish were subjected to treatment with BCNU for 4 h. BCNU, an inhibitor of glutathione reductase, has been shown to alter cellular redox environment, leading to an increased GSSG/GSH ratio. The increase in oxidized GSH leads to increased cellular S-glutathiolation. At the end of the experiment, cells attached to coverslips were washed with PBS, fixed for 10 min with 3.7% paraformaldehyde and permeabilized for 5 min with 0.25% Triton X-100 in Tris-buffered saline containing 0.01% Tween 20 (TBST), washed three times, and then blocked for 30 min with 1% BSA in TBST. Permeabilization is required to provide access for the antibody to the antigen throughout the cell. Permeabilization and washing is also critical for the detection of protein-bound GSH adducts, because it clears the free GSH that would otherwise bind the antibody. For detection of S-glutathionylation and eNOS, the fixed and permeabilized cells were incubated at room temperature for 1 h with mouse anti-GSH and rabbit anti-eNOS primary antibodies at a dilution of 1:2,000 in TBST containing 1% BSA, followed by secondary anti-mouse Alexa fluor-568 and anti-rabbit Alexa fluor-488-conjugated antibody (1:1,000 dilution) for 1 h at room temperature. The coverslips with cells were then mounted on a glass slide with Fluoromount G mounting medium and viewed with a Olympus FluoView-1000 confocal microscope at $\times 60$ magnification, and data were captured digitally and analysed.

To detect $\text{O}_2^{\bullet-}$ generation from S-glutathionylated eNOS in BAECs, cells were then incubated with the $\text{O}_2^{\bullet-}$ indicator 10 µM DHE to detect $\text{O}_2^{\bullet-}$ in live cells. DHE fluoresces when oxidized by $\text{O}_2^{\bullet-}$. Nuclei were stained with blue-fluorescent DAPI (1 µM) for 10 min in the incubator. After incubation, cells were washed with PBS and mounted; images were captured and analysed at $\times 60$ magnification by confocal fluorescence microscopy, and overlaid with LSM software¹⁵.

En face sections. After surgery the aortae from WKY and SHR rats were cleaned and washed with ice-cold PBS. A slit was made longitudinally and the opened aortae were fixed in 3.7% paraformaldehyde for 3 h at room temperature. The fixed aortae were washed for 2–3 h in 0.1 M cacodylate buffer and then incubated

overnight with 2.3 M sucrose gradients titrated for 10 min each with 5% sucrose in cacodylate buffer (2:1, 1:1, 1:2 and 1:3) and 2.3 M sucrose at 4 °C. The samples were then mounted in OCT medium and frozen in liquid nitrogen⁴⁰. Tissues were cryosectioned *en face* from anterior to posterior and the sections were probed for eNOS and PrS-SG. The sections were permeabilized with 0.25% Triton X-100 for 10 min and washed, followed by immunostaining for eNOS/PrS-SG as described above. High-magnification images were obtained and analysed with an Olympus FluoView-1000 confocal microscope at $\times 100$ original magnification.

EPR spin-trapping measurement of NO production. Spin-trapping measurements of NO from BAECs were performed with a Bruker EMX spectrometer with Fe-*N*-methyl-D-glucamine dithiocarbamate (Fe-MGD) as the spin trap^{35,36}. Spin-trapping experiments were performed on cells grown in six-well plates (10^6 cells per well). Before EPR spin-trapping measurements, control cells or cells treated with BCNU were washed twice with PBS (without CaCl_2 or MgCl_2). Next, 0.8 ml of PBS containing glucose (1 g l^{-1}), CaCl_2 , MgCl_2 , the NO spin-trap Fe-MGD (0.5 mM Fe^{2+} , 5.0 mM MGD) and calcium ionophore ($1 \mu\text{M}$) was added to each well, and the plates were incubated for 20 min at 37 °C in a humidified environment containing 5% CO_2 /95% O_2 . After incubation, the medium from each well was removed, and the trapped NO in the supernatants was quantified by EPR. Spectra recorded from these cellular preparations were obtained with the following parameters: microwave power 20 mW; modulation amplitude 4.0 G; modulation frequency 100 kHz.

Aortic preparations and functional measurements. Aortae were excised from anaesthetized and heparinized rats, placed in ice-cold buffer, cleaned of loosely adhering fat and connective tissue and cut into rings 5 mm in length for measurements of vascular tone as described previously, with minor modification⁴¹.

In brief, aortic rings were mounted horizontally and connected to an isometric force transducer in organ chambers (Multi Wire Myograph, Model 610M; DMT) filled with 5 ml of Krebs–Henseleit (K-H) buffer (37 °C, pH 7.4) consisting of 118 mM NaCl, 4.6 mM KCl, 1.2 mM CaCl_2 , 1.2 mM NaH_2PO_4 , 24 mM NaHCO_3 , 18 mM glucose, $10 \mu\text{M}$ indomethacin and 4.6 mM HEPES bubbled with 95% O_2 /5% CO_2 . The aortic segments were allowed to equilibrate for 60 min with an initial tension of 1 g. The stability of each ring was checked by the successive administration of 4 M KCl. Preparations were then washed three times with drug-free oxygenated K-H buffer and allowed to relax fully for 15 min before the experimental protocol began. Then the aortic rings were contracted with phenylephrine ($10 \mu\text{M}$) and, after stable contraction, the vasorelaxant effects of cumulative addition of acetylcholine, NONOate or sodium nitroprusside (SNP) were determined by measuring the tension and expressing this as the percentage relaxation with respect to the maximal phenylephrine contraction. To induce S-glutathionylation, rings were pretreated with $80 \mu\text{M}$ BCNU during the 60 min equilibration period, and to reverse S-glutathionylation the rings were treated with 1 mM DTT for 20 min. Similarly, to reverse the intrinsic S-glutathionylation present, SHR or WKY aortae or aortic rings were treated with 1 mM DTT for 20 min at 37 °C. For immunoprecipitation studies measuring the effect of DTT in reversing eNOS glutathionylation in aortae, DTT was added to the bioassay blood vessels, taking care to employ exactly the same conditions with the same duration of incubation and concentration of DTT as in the experiments measuring endothelial function. We then washed out the DTT and immunoprecipitated eNOS from the vessel homogenates.

For the BCNU studies, male Sprague–Dawley rats (Harlan) were used. Male SHR and WKY rats were supplied by Harlan or Charles River.

NOS3 gene silencing in bovine aortic endothelial cells. NOS3 gene silencing from BAECs was used to confirm eNOS S-glutathionylation induced by BCNU contributing to increased cellular superoxide generation. The sequence of NOS3 siRNA was based on a previous study⁴². The sense siRNA strand of eNOS is 5'-GA GUUACAAGAUCCGCUUCTT-3' and the antisense siRNA is 3'-TTCUCAU

GUUCUAGGCGAAG-5'. These siRNAs were custom synthesized by Invitrogen. BLOCK-iT transfection kit (Invitrogen) was used to deliver NOS3 siRNAs to BAECs. Scrambled siRNA was used as a negative control. After 48 h, eNOS immunoblotting was used to determine the eNOS knockdown efficiency. The same set of BAECs was further treated with $80 \mu\text{M}$ BCNU for 4 h, and confocal microscopy with DHE was used to determine BCNU-induced superoxide generation.

Homogenization of cells and tissues. Cells or tissues were homogenized in lysis buffer (50 mM Tris-HCl pH 7.4, 500 mM NaCl, 1% Nonidet P40, 0.5% sodium deoxycholate, 0.1% SDS, 50 mM NEM, and protease inhibitors) with a tissue grinder. After homogenization, cell or tissue debris was removed by centrifugation at 4 °C for 1 h. The supernatant was further used for immunoblotting analysis or immunoprecipitation assay.

Immunoprecipitation assay. Supernatant of cell or tissue lysate was used for the immunoprecipitation assay. Agarose-conjugated anti-eNOS (Santa Cruz) antibody was first incubated overnight with cell or tissue lysate at 4 °C. After incubation, eNOS immunoprecipitation product was washed three times with cold PBS buffer. $1 \times$ SDS loading buffer was used to elute eNOS for immunoblotting analysis of eNOS glutathionylation.

Statistical analysis. All data are expressed as means and s.e.m. All experiments were repeated at least three times. Microsoft Excel and Origin were used for data analysis. Student's *t*-test was used for statistical analysis, with $P < 0.05$ being considered significant.

- Rodriguez-Crespo, I., Gerber, N. C. & Ortiz de Montellano, P. R. Endothelial nitric-oxide synthase. Expression in *Escherichia coli*, spectroscopic characterization, and role of tetrahydrobiopterin in dimer formation. *J. Biol. Chem.* **271**, 11462–11467 (1996).
- Berka, V., Palmer, G., Chen, P. F. & Tsai, A. L. Effects of various imidazole ligands on heme conformation in endothelial nitric oxide synthase. *Biochemistry* **37**, 6136–6144 (1998).
- Chen, C. L. *et al.* Site-specific S-glutathionylation of mitochondrial NADH ubiquinone reductase. *Biochemistry* **46**, 5754–5765 (2007).
- Giraldez, R. R., Panda, A., Xia, Y., Sanders, S. P. & Zweier, J. L. Decreased nitric-oxide synthase activity causes impaired endothelium-dependent relaxation in the postischemic heart. *J. Biol. Chem.* **272**, 21420–21426 (1997).
- Xia, Y., Cardounel, A. J., Vanin, A. F. & Zweier, J. L. Electron paramagnetic resonance spectroscopy with *N*-methyl-D-glucamine dithiocarbamate iron complexes distinguishes nitric oxide and nitroxyl anion in a redox-dependent manner: applications in identifying nitrogen monoxide products from nitric oxide synthase. *Free Radic. Biol. Med.* **29**, 793–797 (2000).
- Vanin, A. F., Liu, X., Samouilov, A., Stukan, R. A. & Zweier, J. L. Redox properties of iron-dithiocarbamates and their nitrosyl derivatives: implications for their use as traps of nitric oxide in biological systems. *Biochim. Biophys. Acta* **1474**, 365–377 (2000).
- Roubaud, V., Sankarapandi, S., Kuppusamy, P., Tordo, P. & Zweier, J. L. Quantitative measurement of superoxide generation using the spin trap 5-(diethoxyphosphoryl)-5-methyl-1-pyrroline-*N*-oxide. *Anal. Biochem.* **247**, 404–411 (1997).
- Chen, C. A. & Cowan, J. A. Characterization of *Saccharomyces cerevisiae* Atm1p: functional studies of an ABC7 type transporter. *Biochim. Biophys. Acta* **1760**, 1857–1865 (2006).
- Shaul, P. W. *et al.* Acylation targets endothelial nitric-oxide synthase to plasmalemmal caveolae. *J. Biol. Chem.* **271**, 6518–6522 (1996).
- Takizawa, T. & Robinson, J. M. Ultrathin cryosections: an important tool for immunofluorescence and correlative microscopy. *J. Histochem. Cytochem.* **51**, 707–714 (2003).
- Alzawhra, W. F., Talukder, M. A., Liu, X., Samouilov, A. & Zweier, J. L. Heme proteins mediate the conversion of nitrite to nitric oxide in the vascular wall. *Am. J. Physiol. Heart Circ. Physiol.* **295**, H499–H508 (2008).
- Kang-Decker, N. *et al.* Nitric oxide promotes endothelial cell survival signaling through S-nitrosylation and activation of dynamin-2. *J. Cell Sci.* **120**, 492–501 (2007).

Suppression of inflammation by a synthetic histone mimic

Edwige Nicodeme^{1*}, Kate L. Jeffrey^{2*}, Uwe Schaefer^{2*}, Soren Beinke^{3*}, Scott Dewell⁴, Chun-wa Chung⁵, Rohit Chandwani², Ivan Marazzi², Paul Wilson⁵, Hervé Coste¹, Julia White⁵, Jorge Kirilovsky¹, Charles M. Rice⁶, Jose M. Lora³, Rab K. Prinjha³, Kevin Lee³ & Alexander Tarakhovskiy²

Interaction of pathogens with cells of the immune system results in activation of inflammatory gene expression. This response, although vital for immune defence, is frequently deleterious to the host due to the exaggerated production of inflammatory proteins. The scope of inflammatory responses reflects the activation state of signalling proteins upstream of inflammatory genes as well as signal-induced assembly of nuclear chromatin complexes that support mRNA expression^{1–4}. Recognition of post-translationally modified histones by nuclear proteins that initiate mRNA transcription and support mRNA elongation is a critical step in the regulation of gene expression^{5–10}. Here we present a novel pharmacological approach that targets inflammatory gene expression by interfering with the recognition of acetylated histones by the bromodomain and extra terminal domain (BET) family of proteins. We describe a synthetic compound (I-BET) that by ‘mimicking’ acetylated histones disrupts chromatin complexes responsible for the expression of key inflammatory genes in activated macrophages, and confers protection against lipopolysaccharide-induced endotoxic shock and bacteria-induced sepsis. Our findings suggest that synthetic compounds specifically targeting proteins that recognize post-translationally modified histones can serve as a new generation of immunomodulatory drugs.

BET proteins BRD2, BRD3 and BRD4 (hereafter defined as BET) govern the assembly of histone acetylation-dependent chromatin complexes that regulate inflammatory gene expression^{5–8}. This function of BET suggests the possibility of intervention with inflammatory gene expression by disrupting chromatin complexes essential for mRNA transcription, elongation and splicing.

The diversity of binding surfaces, created by differences in sequences surrounding the bromodomain acetyl-binding pocket of BET, and other bromodomain-containing proteins, provided a foundation for selective pharmacological targeting of BET^{9,11–14}. Using an approach that uses the ability of synthetic compounds to bind selectively to individual proteins in cell lysates (see Supplementary Material), we identified compounds that interact with BET. One of these compounds, GSK525762A (Fig. 1a), henceforth referred to as I-BET, showed the highest affinity interaction with BET (Fig. 1). The crystal structure of I-BET bound to BRD4-bromodomain 1 (BD1) showed I-BET positioned at the acetyl-lysine (AcK)-binding pocket (Fig. 1b and Supplementary Fig. 1a, b). Hydrogen bonding interactions essential for binding of AcK to asparagine 140 and tyrosine 97 within the bromodomain was mimicked by the triazolyl ring of I-BET (Fig. 1b). The selectivity of I-BET interaction with BET was determined by the ZA hydrophobic channel and WPF shelf outside of the AcK binding pocket, where a conserved isoleucine or valine impose spatial constraints on the size of molecules that can gain access to the WPF shelf (Fig. 1b and Supplementary Fig. 1b, c). Indeed, an enantiomer

compound of I-BET (GSK525768A) had no activity towards BET (Fig. 1c, far right panel). The structural features of I-BET allow two molecules of I-BET to bind to the tandem bromodomains of BET with high affinity (dissociation constant K_d of 50.5–61.3 nM; Fig. 1c and Supplementary Fig. 1d, e). Moreover, I-BET could successfully compete with AcK within the recognition pocket of BET. Fluorescence resonance energy transfer (FRET) analysis demonstrated that I-BET displaced, with high efficacy (half-maximum inhibitory concentration IC_{50} of 32.5–42.5 nM), a tetra-acetylated H4 peptide that had been pre-bound to tandem bromodomains of BET (Fig. 1d and Supplementary Fig. 1e). I-BET is highly selective as it did not interact with other bromodomain-containing proteins from each arm of the phylogeny tree (Supplementary Fig. 1f) and had no activity towards a panel of 38 unrelated proteins (Supplementary Table 1).

Stimulation of bone marrow-derived macrophages (BMDMs) with lipopolysaccharide (LPS) upregulated numerous inflammatory genes (Fig. 2a). Pre-treatment of BMDMs with I-BET shortly before LPS stimulation resulted in the downregulation of 38 and 151 of the LPS-inducible genes at 1 and 4 h, respectively (Fig. 2a, b and Supplementary Table 2). I-BET suppressed the expression of key LPS-inducible cytokines and chemokines, including *Il6*, *Ifnb1*, *Il1b*, *Il12a*, *Cxcl9* and *Ccl12*. The inhibitory effect of I-BET on the expression of the IL-1 β processing enzyme *Mefv*¹⁵ underscored the potential of I-BET to control the IL-1 β inflammatory circuit. Furthermore, diminished expression of transcription factors *Rel*, *Irf4* and *Irf8* point to the ability of I-BET to curtail the initial wave of inflammatory gene expression (Fig. 2b and Supplementary Table 2). In the absence of LPS stimulation, treatment of BMDMs with I-BET had a marginal effect on gene transcription (Supplementary Fig. 3 and Supplementary Table 3) and did not have an impact on the expression of *Thrl–13*, *Myd88*, *Ticam1*, *Cd14*, *Mapk*, *Mapk2k*, *Map3k* and *Map4k* family members, *Ikbkb*, *Ikbke* and *Ikbkg* and *Aoah*¹⁶, in unstimulated or LPS-treated macrophages at 1 h, that control LPS sensing and signalling (Supplementary Fig. 4). Furthermore, an unaltered pattern of LPS-induced ERK phosphorylation and I κ B α degradation in I-BET-treated cells excluded the impact of I-BET on gene expression through dysregulation of Toll-like receptor 4 (TLR4)-dependent signalling (Supplementary Fig. 5). I-BET also had no effect on the expression of housekeeping genes or the viability of BMDMs (Supplementary Figs 4 and 5). The impact of I-BET on LPS-inducible gene expression is highly selective. The cytokine *Tnf* as well as chemokines *Ccl2–5*, *Cxcl1/2* were not affected by I-BET (Supplementary Table 2 and Supplementary Fig. 6). This specificity and anti-inflammatory potential of I-BET has been validated by the similarity between the effects of I-BET treatment and siRNA-mediated BET knockdown on inflammatory gene expression (Supplementary Fig. 7). Notably, knockdown of BET suppressed the expression of *Tnf* that was resistant to I-BET (Supplementary Figs 6 and 7). This

¹Centre de Recherche GSK, 27 Avenue du Québec, 91140 Villebon Sur Yvette, France. ²Laboratory of Lymphocyte Signaling, The Rockefeller University, 1230 York Avenue, New York, New York 10065, USA.

³Epinova DPU, Immuno-Inflammation Centre of Excellence for Drug Discovery, GlaxoSmithKline, Medicines Research Centre, Gunnels Wood Road, Stevenage SG1 2NY, UK. ⁴Genomics Resource Center, The Rockefeller University, 1230 York Avenue, New York, New York 10065, USA. ⁵GlaxoSmithKline R&D, Medicines Research Centre, Gunnels Wood Road, Stevenage SG1 2NY, UK. ⁶Laboratory of Virology and Infectious Disease, The Rockefeller University, 1230 York Avenue, New York, New York 10065, USA.

*These authors contributed equally to this work.

result points to the existence of BET-recruiting mechanisms that are independent of BET interaction with acetylated histones. The existence of such a mechanism is supported by findings that show recruitment of BET to acetylated Rela or mediator complex^{7,8,17,18}. Certain genes were upregulated by I-BET treatment but none of these have a well-established role in inflammation (Supplementary Table 2). The upregulation of *Brd2* and histone-encoding genes (Supplementary Table 2) may reflect the existence of a positive feedback mechanism where suppression of BET leads to a compensatory increase in the expression of chromatin proteins. The activating effect of I-BET on gene expression may also reflect the ability of BET to function not only as transcriptional co-activators but also as co-repressors¹⁹.

The genome-wide analysis of the epigenetic states of LPS-inducible genes that were significantly suppressed or not affected by I-BET (si-BET and naI-BET genes, respectively) provided a clue for the selective effect of I-BET on gene expression. Elevated basal levels of histone H3 and H4 acetylation (H3ac and H4ac) at the naI-BET gene promoters

indicated that naI-BET genes were already primed or actively involved in transcription (Fig. 3 and Supplementary Fig. 8). Indeed, the naI-BET gene promoters were associated with higher basal levels of H3K4me3 and RNA polymerase (Pol) II, including the elongation competent RNA Pol II, phosphorylated at serine 2 (RNA Pol II S2; Fig. 3). The important role of the primed/active state in defining the sensitivity to I-BET was underscored by the lack of I-BET effect on expression of housekeeping genes such as *Gapdh*, *Tubb5* and *Hprt* (Supplementary Fig. 4) that are characterized by high levels of H3ac, H4ac, H3K4me3 and RNA Pol II at their promoters⁵. Furthermore, an increase in overall histone acetylation levels caused by BMDM treatment with the histone deacetylase (HDAC) inhibitor trichostatin A (TSA) was able to 'convert' si-BET into naI-BET genes (Supplementary Fig. 9).

The primed and/or active transcription state of naI-BET genes before LPS stimulation was accomplished without recruitment of significant amounts of BET, thus reducing the likelihood of suppression of these genes by I-BET (Fig. 3). Furthermore, treatment with I-BET has less impact on BET association with naI-BET compared to si-BET gene promoters in LPS-treated cells (Fig. 3). The mechanism of this

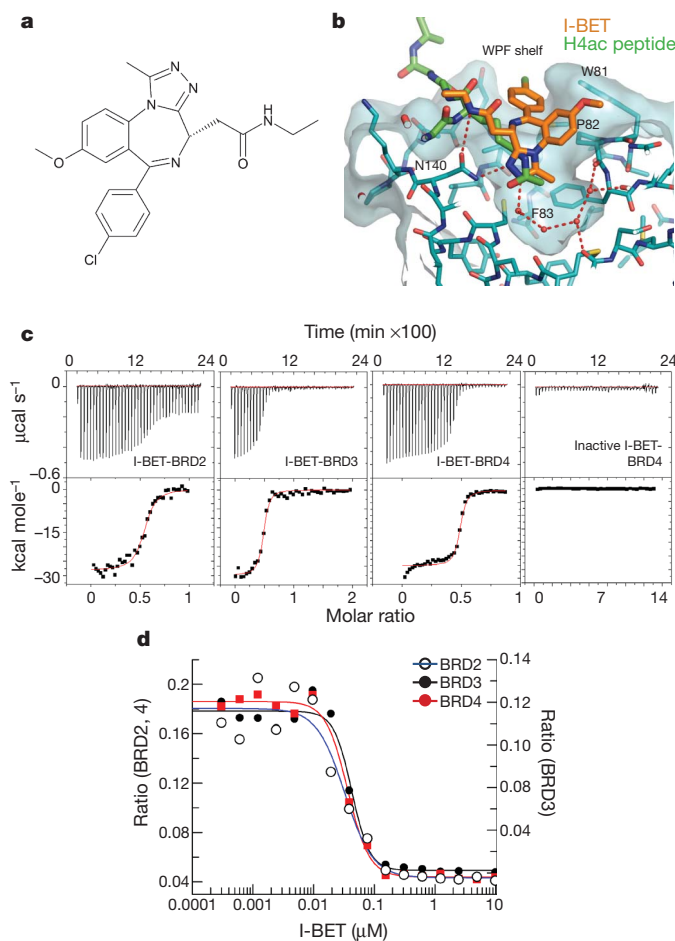


Figure 1 | I-BET is a selective antagonist of BET proteins. **a**, Chemical structure of GSK525762A (I-BET). **b**, Structure of I-BET (orange) bound to the acetyl-binding pocket of BRD4-BD1 overlaid with acetylated histone H4 peptide (H4ac, green). The 'WPF shelf' (W81, P82, F83) as well as the asparagine N140 essential for acetylated lysine (Kac) binding are indicated. **c**, I-BET binds with high affinity to BET proteins as determined by isothermal titration calorimetry (ITC) of tandem bromodomain fragments of BRD2 (1–473), BRD3 (1–434), BRD4 (1–477) interaction with I-BET or BRD4 (1–477) interaction with an inactive enantiomer of I-BET (inactive I-BET). Time courses of raw injection heats (upper panel) and normalized binding enthalpies, calculated using a single site binding model (Origin software, Microcal, lower panel), are shown. **d**, I-BET competes with H4ac peptide for bromodomain binding. Displacement of tetra-acetylated histone H4 peptide from bromodomains of BRD2 (blue), BRD3 (black) and BRD4 (red) by I-BET was determined by FRET analysis.

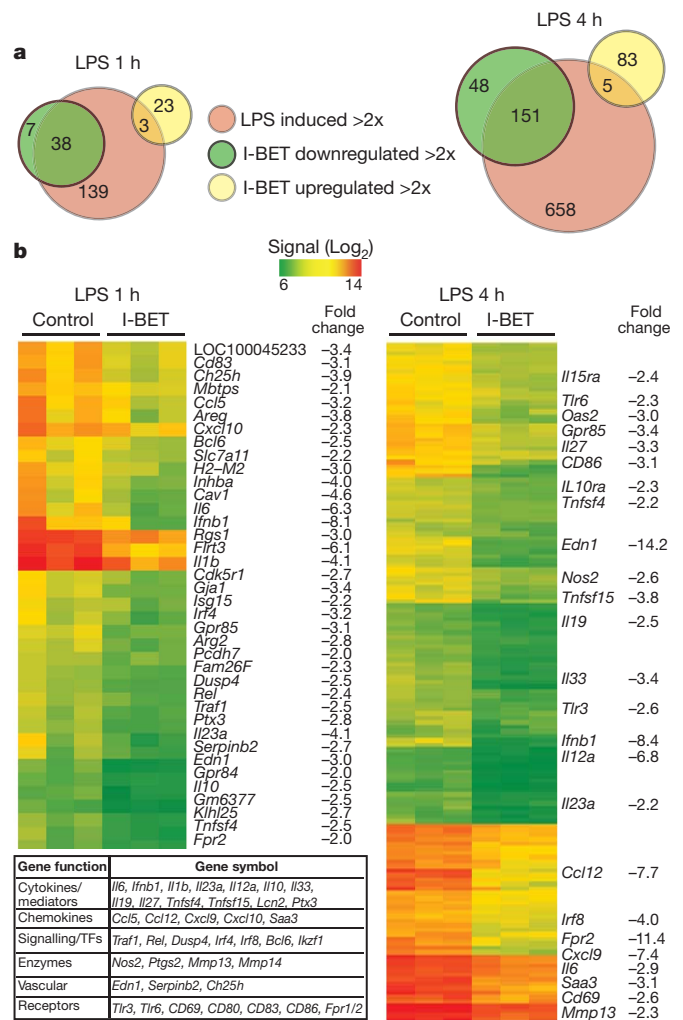


Figure 2 | I-BET suppresses a specific subset of LPS-inducible genes. **a**, Venn diagrams display the number of LPS-inducible (>twofold, red circles) genes that were suppressed (>twofold, green circles) or upregulated (>twofold, yellow circles) by I-BET (1 μ M) treatment at 1 or 4 h after LPS stimulation (left and right panels) of BMDMs. **b**, Heat map representation of expression levels of genes that were downregulated by I-BET at 1 h (left panel) and 4 h (right panel) after LPS stimulation of three independent macrophage cultures. Scale ranges from a signal value of 2^6 (64, green) to 2^{14} (16,384, red). Fold-change values are listed. Table shows the distribution of downregulated genes into functional categories.

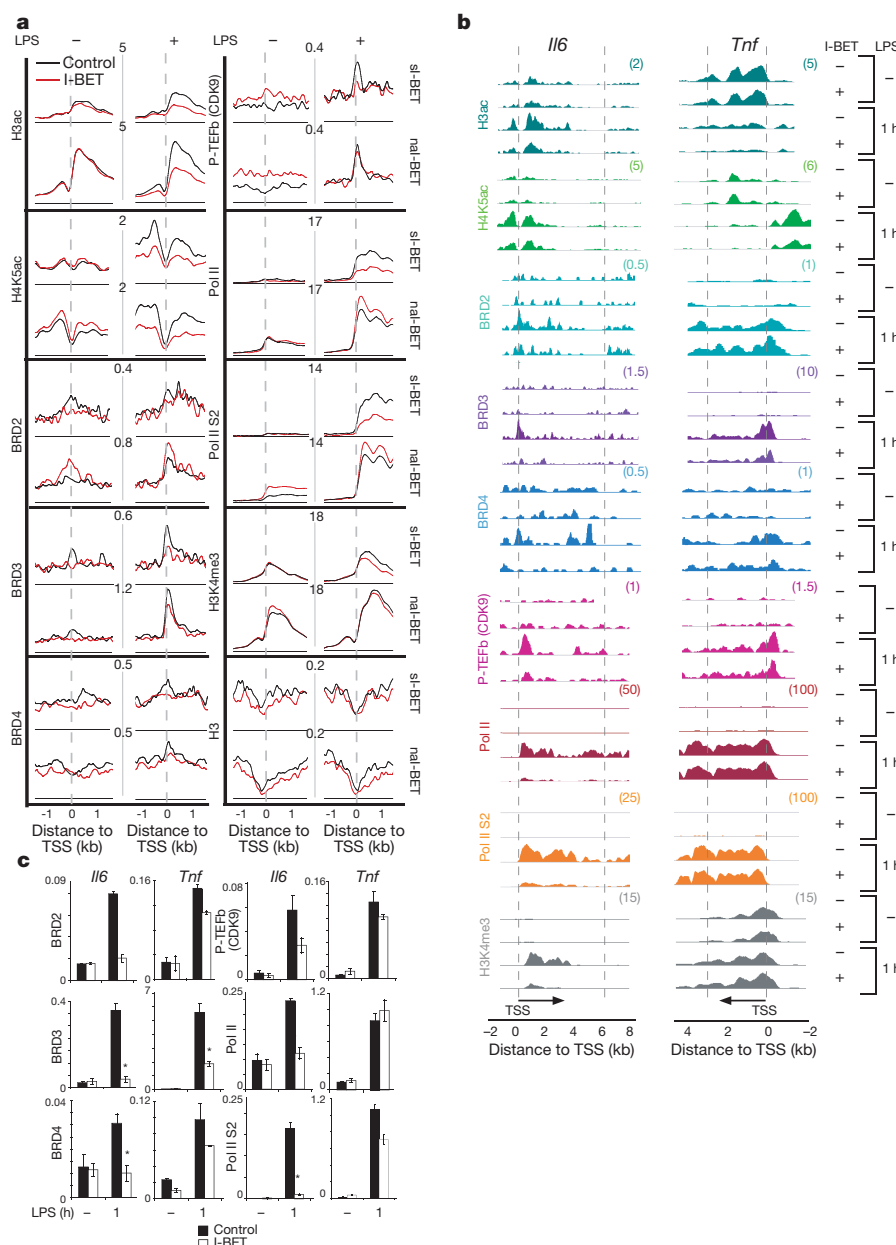


Figure 3 | Epigenetic profiles of genes suppressed or unaffected by I-BET in LPS-stimulated macrophages. **a**, Genome-wide epigenetic profiles of si-BET or naI-BET genes in unstimulated or LPS-stimulated (1 h) macrophages pretreated with 5 μ M of I-BET or a DMSO control. Analysed epigenetic marks are indicated. *y*-Axes represent the number of reads per million mapped reads. **b**, Epigenetic profiles of *Il6* and *Tnf*. The *y*-axes represent the average number of tags per gene per 25 base pairs per 1,000,000 mapped reads. Scale values are

indicated in parentheses. **c**, The abundance of epigenetic marks on *Il6* and *Tnf* gene promoters was quantified by ChIP qPCR from four (BRD3, BRD4, Pol II and Pol II S2) or two (BRD2 and P-TEFb) independent experiments performed in triplicate. Error bars are s.e.m. of independent experiments or s.d. of representative experiments, respectively. Asterisks indicate $P < 0.05$ as determined by an unpaired *t*-test.

phenomenon may reflect higher LPS-induced H3ac and H4ac levels at naI-BET compared to si-BET gene promoters before and after I-BET treatment (Fig. 3 and Supplementary Fig. 8). Additionally, some of the naI-BET genes may recruit BET via histone acetylation-independent mechanisms¹⁷.

Treatment of BMDMs with I-BET affected not only the promoter-bound BET but also the levels of H3ac, H4K5ac, H4K8ac, H4K12ac and total H4ac on LPS-induced gene promoters (Fig. 3 and Supplementary Fig. 8). The mechanism of the negative impact of I-BET on histone H3 and H4 acetylation might be twofold. First, by preventing BET from binding to H3ac/H4ac, I-BET increases the accessibility of exposed H3ac/H4ac to HDACs. This model is supported by a non-enzymatic role of BRD4 in H4ac preservation in embryonic stem (ES) cells²⁰. It is also possible that I-BET binding to BET prevents the

formation of multi-molecular complexes that contain histone acetyltransferases (HATs), other histone modifying enzymes, including lysine H3K4me3 methyltransferases, as well as the positive transcriptional elongation factor b (P-TEFb) and RNA Pol II^{7,8,18,19}. This model is consistent with diminished levels of P-TEFb, that contributes to mRNA elongation by RNA Pol II phosphorylation^{5,21,22}, and reduced amounts of H3K4me3 and RNA Pol II at si-BET genes (Fig. 3). The possible direct impact of I-BET on H3ac/H4ac through inhibition of bromodomain-containing HATs was excluded by the inability of I-BET to suppress the activity of the most common HATs such as pCAF, p300, GCN5 and CBP (also known as Kat2b, Ep300, Kat2a and Crebbp, respectively; Supplementary Fig. 10).

The features of si-BET and naI-BET genes assessed by the genome-wide analysis were mirrored by the epigenetic states of selected si-BET

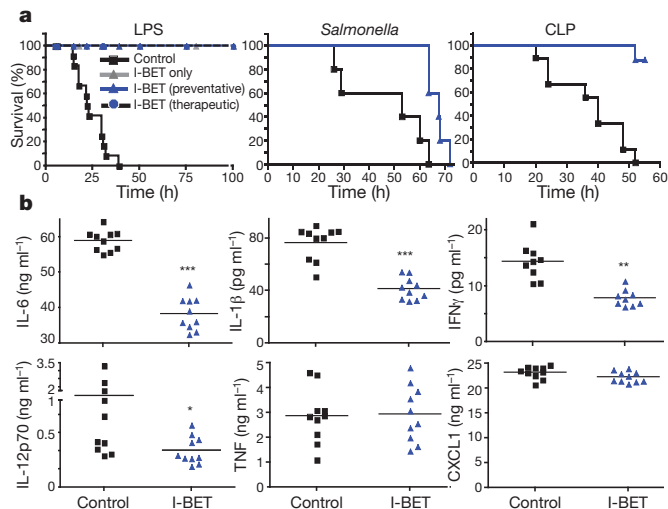


Figure 4 | I-BET suppresses inflammation *in vivo*. **a**, Kaplan–Meier survival curves of: LPS-treated C57BL/6 mice (5 mg per kg, i.p., $n = 12$ per group) that were injected i.v. with a solvent control (black squares) or 30 mg per kg of I-BET 1 h before (blue triangles) or 1.5 h after (blue circles) LPS administration (left panel); mice injected i.v. with heat-killed *Salmonella typhimurium*, strain IR71 (5×10^9 per kg, $n = 10$ per group) (middle panel); or mice subjected to caecal ligation puncture (CLP) procedure that were administered a solvent control or 30 mg per kg of I-BET twice a day for 2 days ($n = 8$ per group) (right panel). **b**, Serum titres of indicated cytokines were measured by ELISA ($n = 10$ per group). Mice received a solvent control (black squares) or I-BET (blue triangles) 1 h before LPS injection and samples were collected at 2 h after LPS treatment. *** $P < 0.001$, ** $P < 0.01$, * $P < 0.05$ as determined by unpaired t -test.

and naI-BET genes. Following I-BET treatment, the promoter of the siBET gene *Il6* showed a marked reduction in BET recruitment and diminished levels of associated H3K4me3, P-TEFb, RNA Pol II and RNA Pol II S2 (Fig. 3b, c). In contrast to *Il6*, the naI-BET gene *Tnf* showed higher accumulation of BRD2, BRD3 and to a lesser extent BRD4, around the transcriptional start site (TSS) following I-BET treatment (Fig. 3b, c). The relatively higher BET levels at the *Tnf* locus were associated with largely unaffected levels of P-TEFb, RNA Pol II and RNA Pol II S2 (Fig. 3b, c). In support of distinct epigenetic states between siI-BET and naI-BET genes, the siI-BET gene *Il1b* had reduced BET accumulation at its TSS that resulted in a drop of P-TEFb, Pol II and Pol II S2 levels. In contrast, the epigenetic landscape of the naI-BET gene *Nfkb1a* displayed little change in response to I-BET (Supplementary Fig. 11).

The selectivity of gene responses to I-BET correlated inversely with the timing of LPS-induced gene activation. Opposite to early stimulated (primary response) naI-BET genes, the majority of siI-BET genes, with the exception of *Il1b*, belong to the category of secondary response genes (SRG) that become upregulated at later points of macrophage activation (Supplementary Fig. 12a, c). Most of the siI-BET genes, as well as *Il1b*, were characterized by low basal levels of H3ac/H4ac, H3K4me3, RNA Pol II, as well as low CpG content of their promoters (Fig. 3, Supplementary Figs 8 and 12b). The latter feature conveys higher stability to promoter-associated nucleosomes that generates a selective barrier for transcriptional activation of secondary response genes^{23,24}. It is likely that suppression of BET recruitment as well as reduction in H3ac/H4ac and H3K4me3 by I-BET aggravates the already non-permissive transcriptional state of the siI-BET genes and reduces the probability of their expression, thus defining the selectivity of I-BET.

The suppression of key inflammatory genes by I-BET suggested a potent ability of the compound to treat inflammatory conditions *in vivo*. The serum titres of intravenously (i.v.) administered I-BET remain within the effective concentrations for several hours after injection (Supplementary Fig. 13). Injection of I-BET in mice before the initiation of LPS- or heat-killed *Salmonella typhimurium*-induced

endotoxic shock was able to prevent or attenuate death of mice (Fig. 4a left and middle panel). Most promisingly for therapeutic applications, a single dose of I-BET applied at 1.5 h after LPS injection, at the time when mice started to develop symptoms of inflammatory disease, cured the mice (Fig. 4a, left panel). Furthermore, in mice that suffer from polymicrobial peritonitis and sepsis caused by caecal ligation and puncture (CLP), twice-daily injections of I-BET for 2 days protected mice against death caused by sepsis (Fig. 4a, right panel).

The marked therapeutic effect of I-BET on endotoxic shock and sepsis occurred despite unaltered serum TNF levels (Fig. 4b). As TNF is an established mediator of sepsis-associated inflammatory processes, the protective effect of I-BET on sepsis suggests the ability of I-BET to interfere not only with the expression of inflammatory proteins (Fig. 4b), but also with TNF-inducible gene expression. Indeed, treatment of BMDMs with I-BET suppressed TNF-inducible key pro-inflammatory cytokine (*Il1b*, *Il1a*) and chemokine genes (*Ccl5*, *Cxcl10*, *Cxcl2/3*) as well as vasoactive and lipid-related genes (*Pdgfb*, *Adora2b*, *Fabp3*) that contribute to sepsis pathogenesis (Supplementary Fig. 14a, b). Notably, similar to the siI-BET genes in LPS-treated BMDMs, the majority of siI-BET genes in TNF-treated cells fit into the secondary response gene category as assessed by epigenetic modifications and CpG content (Supplementary Fig. 14c).

In summary, we show the anti-inflammatory potential of the synthetic compound I-BET that, by interfering with binding of bromodomain-containing BET proteins to acetylated histones, disrupts the formation of the chromatin complexes essential for expression of inflammatory genes. The genes susceptible to I-BET share a common pattern of chromatin modifications at their promoters as well as low promoter CpG content. Suppression of inflammation by I-BET demonstrates the potential of drugs that interfere with protein binding to post-translationally modified histones to achieve a high level of selectivity and potency by exploiting the inherited epigenetic states of genes that contribute to specific physiological and pathological processes.

METHODS SUMMARY

I-BET is an optimized derivative of benzodiazepine compounds that were identified by high-throughput screening of activators of ApoA1-luciferase reporter in HepG2 cells as described in Supplementary Information. The chemical synthesis of I-BET is described in Supplementary Information. The 1.6 Å crystal structure of BRD4-BD1 with I-BET was produced by soaking apo crystals in 2 mM I-BET for 4 days. Molecular replacement using 2oss.pdb gave excellent difference density at the acetylated binding site that allowed the ligand binding to be unambiguously modelled. Methods and statistics for data collection and refined coordinates are provided in Supplementary Information and deposited in the RCSB Protein Data Bank with PDB ID code 3P5O. Bone marrow-derived macrophages (BMDMs) were differentiated from a bone marrow cell suspension obtained from C57BL/6 mice as described in supplementary information. For microarray, qPCR (quantitative PCR) and ChIP (chromatin immunoprecipitation) analyses, BMDMs were pre-incubated with 1 μM or 5 μM of I-BET, DMSO or an inactive I-BET compound for 30 min before LPS (100 ng ml⁻¹) or TNF (50 ng ml⁻¹) stimulation. Microarray experiments were performed using Illumina MouseRef-8 v2.0 expression BeadChip kits (GEO accession code GSE21764). qPCR was performed using SYBR Green (Roche Lightcycler 480). ChIP was performed as described²⁵ and detailed in supplementary information. ChIP sequencing libraries were generated as described²⁶ (GEO accession code GSE21910). For LPS-induced endotoxic shock, 5 mg per kg of LPS was injected intraperitoneally (i.p.) into age-matched C57BL/6 mice. Heat-killed *Salmonella typhimurium* (IR715; 5×10^9 per kg) was injected intravenously. Caecal ligation puncture (CLP) was performed as described²⁷. For *in vivo* experiments I-BET or a solvent control (20% beta-cyclodextrin, 2% DMSO in 0.9% saline) were given via retro-orbital or tail vein injection (CLP) at a dose of 30 mg per kg.

Received 24 May; accepted 22 October 2010.

Published online 10 November 2010.

- Medzhitov, R. & Horng, T. Transcriptional control of the inflammatory response. *Nature Rev. Immunol.* **9**, 692–703 (2009).
- Smale, S. T. Selective transcription in response to an inflammatory stimulus. *Cell* **140**, 833–844 (2010).

3. Natoli, G. Control of NF- κ B-dependent transcriptional responses by chromatin organization. *Cold Spring Harb. Perspect. Biol.* **1**, a000224 (2009).
4. Maniatis, T. & Reed, R. An extensive network of coupling among gene expression machines. *Nature* **416**, 499–506 (2002).
5. Hargreaves, D. C., Horng, T. & Medzhitov, R. Control of inducible gene expression by signal-dependent transcriptional elongation. *Cell* **138**, 129–145 (2009).
6. LeRoy, G., Rickards, B. & Flint, S. J. The double bromodomain proteins Brd2 and Brd3 couple histone acetylation to transcription. *Mol. Cell* **30**, 51–60 (2008).
7. Jang, M. K. *et al.* The bromodomain protein Brd4 is a positive regulatory component of P-TEFb and stimulates RNA polymerase II-dependent transcription. *Mol. Cell* **19**, 523–534 (2005).
8. Yang, Z. *et al.* Recruitment of P-TEFb for stimulation of transcriptional elongation by the bromodomain protein Brd4. *Mol. Cell* **19**, 535–545 (2005).
9. Taverna, S. D., Li, H., Ruthenburg, A. J., Allis, C. D. & Patel, D. J. How chromatin-binding modules interpret histone modifications: lessons from professional pocket pickers. *Nature Struct. Mol. Biol.* **14**, 1025–1040 (2007).
10. Jenuwein, T. & Allis, C. D. Translating the histone code. *Science* **293**, 1074–1080 (2001).
11. Ruthenburg, A. J., Li, H., Patel, D. J. & Allis, C. D. Multivalent engagement of chromatin modifications by linked binding modules. *Nature Rev. Mol. Cell Biol.* **8**, 983–994 (2007).
12. Huang, H. *et al.* Solution structure of the second bromodomain of Brd2 and its specific interaction with acetylated histone tails. *BMC Struct. Biol.* **7**, 57 (2007).
13. Liu, Y. *et al.* Structural basis and binding properties of the second bromodomain of Brd4 with acetylated histone tails. *Biochemistry* **47**, 6403–6417 (2008).
14. Vollmuth, F., Blankenfeldt, W. & Geyer, M. Structures of the dual bromodomains of the P-TEFb-activating protein Brd4 at atomic resolution. *J. Biol. Chem.* **284**, 36547–36556 (2009).
15. Gavrilin, M. A. *et al.* Pylrin critical to macrophage IL-1 β response to *Francisella* challenge. *J. Immunol.* **182**, 7982–7989 (2009).
16. Hagen, F. S. *et al.* Expression and characterization of recombinant human acyloxacyl hydrolase, a leukocyte enzyme that deacylates bacterial lipopolysaccharides. *Biochemistry* **30**, 8415–8423 (1991).
17. Huang, B., Yang, X. D., Zhou, M. M., Ozato, K. & Chen, L. F. Brd4 coactivates transcriptional activation of NF- κ B via specific binding to acetylated RelA. *Mol. Cell Biol.* **29**, 1375–1387 (2009).
18. Jiang, Y. W. *et al.* Mammalian mediator of transcriptional regulation and its possible role as an end-point of signal transduction pathways. *Proc. Natl Acad. Sci. USA* **95**, 8538–8543 (1998).
19. Denis, G. V. *et al.* Identification of transcription complexes that contain the double bromodomain protein Brd2 and chromatin remodeling machines. *J. Proteome Res.* **5**, 502–511 (2006).
20. Nishiyama, A., Dey, A., Miyazaki, J. & Ozato, K. Brd4 is required for recovery from antimicrotubule drug-induced mitotic arrest: preservation of acetylated chromatin. *Mol. Biol. Cell* **17**, 814–823 (2006).
21. Marshall, N. F., Peng, J., Xie, Z. & Price, D. H. Control of RNA polymerase II elongation potential by a novel carboxyl-terminal domain kinase. *J. Biol. Chem.* **271**, 27176–27183 (1996).
22. Sims, R. J. III, Belotserkovskaya, R. & Reinberg, D. Elongation by RNA polymerase II: the short and long of it. *Genes Dev.* **18**, 2437–2468 (2004).
23. Ramirez-Carrozzi, V. R. *et al.* Selective and antagonistic functions of SWI/SNF and Mi-2 β nucleosome remodeling complexes during an inflammatory response. *Genes Dev.* **20**, 282–296 (2006).
24. Ramirez-Carrozzi, V. R. *et al.* A unifying model for the selective regulation of inducible transcription by CpG islands and nucleosome remodeling. *Cell* **138**, 114–128 (2009).
25. Lee, T. I., Johnstone, S. E. & Young, R. A. Chromatin immunoprecipitation and microarray-based analysis of protein location. *Nature Protocols* **1**, 729–748 (2006).
26. Goldberg, A. D. *et al.* Distinct factors control histone variant H3.3 localization at specific genomic regions. *Cell* **140**, 678–691 (2010).
27. Rittirsch, D., Huber-Lang, M. S., Flierl, M. A. & Ward, P. A. Immunodesign of experimental sepsis by cecal ligation and puncture. *Nature Protocols* **4**, 31–36 (2008).

Supplementary Information is linked to the online version of the paper at www.nature.com/nature.

Acknowledgements We would like to acknowledge R. Grimley and C. Patel for supplying FRET data and R. Woodward, C. Delves, E. Jones and P. Holmes for protein production. J. Witherington, N. Smithers, S. Baddeley, J. Seal and L. Cutler provided compound selectivity and pharmacokinetics data. G. Krysa, O. Mirguet and R. Gosmini contributed to the discovery, development and characterization of the compound. We thank R. Anthony and S. McCleary for assistance with animal models, R. Gejman for bioinformatics analysis of gene expression kinetics and A. Santana and T. Chapman for technical assistance. We would like to thank C. Nathan, R. Medzhitov, S. Rudensky and S. Smale for helpful discussions and S. Sampath for his contribution to the concept of 'histone mimicry'. R.C. is supported by an NIH KL2 Career Development Award and I.M. is supported by the American Italian Cancer Foundation. K.L.J. is supported by the National Health and Medical Research Council of Australia and is currently a Rockefeller University Women in Science Fellow.

Author Contributions E.N. identified, characterized and optimized the compound for *in vivo* experiments; K.L.J., U.S. and S.B. contributed equally to design, execution and analysis of *in vitro* and *in vivo* experiments. S.D. performed bioinformatics analysis of ChIP sequencing data; C.-w.C. performed crystallography, ITC, SPR and thermal shift assays; R.C. performed quantitative analysis of epigenetic states of the LPS-inducible genes; I.M. optimized BRD2 and BRD3 profiling of the LPS-inducible genes; P.W. performed bioinformatics analysis of gene expression in LPS-stimulated macrophages. H.C., J.W. and J.K. discovered, characterised and optimised the compound for *in vivo* experiments. C.M.R. was involved in studies of inflammatory responses. J.M.L., R.K.P. and K.L. contributed to the initiation and development of the studies on pharmacological targeting of proteins that recognize post-translationally modified histones. A.T. conceived and supervised this study, and wrote the final manuscript.

Author Information Crystal structure of the first bromodomain of human BRD4 in complex with I-BET inhibitor was deposited in the RCSB Protein Data Bank with PDB ID code 3P50. Microarray and ChIP sequencing results were deposited in GEO with GEO accession codes GSE21764 and GSE21910, respectively. Reprints and permissions information is available at www.nature.com/reprints. The authors declare competing financial interests: details accompany the full-text HTML version of the paper at www.nature.com/nature. Readers are welcome to comment on the online version of this article at www.nature.com/nature. Correspondence and requests for materials should be addressed to A.T. (tarakho@rockefeller.edu), compound requests should go to K.L. (Kevin.2.Lee@gsk.com).

Transcriptional activation of polycomb-repressed genes by ZRF1

Holger Richly¹, Luciana Rocha-Viegas¹, Joana Domingues Ribeiro¹, Santiago Demajo¹, Gunes Gundem², Nuria Lopez-Bigas², Tekeya Nakagawa³, Sabine Rospert⁴, Takashi Ito³ & Luciano Di Croce^{1,5}

Covalent modification of histones is fundamental in orchestrating chromatin dynamics and transcription^{1–3}. One example of such an epigenetic mark is the mono-ubiquitination of histones, which mainly occurs at histone H2A and H2B^{4–6}. Ubiquitination of histone H2A has been implicated in polycomb-mediated transcriptional silencing^{7–9}. However, the precise role of the ubiquitin mark during silencing is still elusive. Here we show in human cell lines that ZRF1 (zuotin-related factor 1) is specifically recruited to histone H2A when it is ubiquitinated at Lys 119 by means of a novel ubiquitin-interacting domain that is located in the evolutionarily conserved zuotin domain. At the onset of differentiation, ZRF1 specifically displaces polycomb-repressive complex 1 (PRC1) from chromatin and facilitates transcriptional activation. A genome-wide mapping of ZRF1, RING1B and H2A-ubiquitin targets revealed its involvement in the regulation of a large set of polycomb target genes, emphasizing the key role ZRF1 has in cell fate decisions. We provide here a model of the molecular mechanism of switching polycomb-repressed genes to an active state.

To identify proteins capable of binding ubiquitinated H2A (H2Aub), we developed an affinity purification based on the expression of Flag-tagged histone H2A. Among several potential H2Aub-binding proteins (Supplementary Fig. 1A, C and Supplementary Table 1), we chose to analyse ZRF1 in more depth, as within its carboxy terminus this protein contains two SANT domains, which are often found in subunits of chromatin-remodelling complexes (Fig. 1a). Intriguingly, its yeast homologue Zuo1 is linked to the ubiquitination of histone H2B in *Saccharomyces cerevisiae*¹⁰. Moreover, ZRF1 has also been implicated in cancer and differentiation^{11–13}. It adopts an oligomeric conformation and is located in the nucleus as well as in the cytosol (Supplementary Figs 1D, E and 2A). Purification of mononucleosomes from 293T cells expressing Flag-tagged histone H2A, either wild type or mutated (KKRR) at the ubiquitination sites (K118/K119), revealed ubiquitin-specific ZRF1 binding preferentially to the wild-type mononucleosomes (Fig. 1b and Supplementary Fig. 1B, F, H, I). Corroborating this finding, we observed specific binding of ubiquitinated wild-type nucleosomes to recombinant ZRF1 (Fig. 1c). Thus, these data point to the ubiquitin mark at histone H2A as a docking site for ZRF1.

ZRF1 shares homology in the zuotin domain with its yeast orthologue Zuo1 (Fig. 1a), which is synthetically lethal with Rad6, the E2 enzyme involved in the specific ubiquitination of histone H2B¹⁰. We reasoned that the conserved zuotin domain might contain the ubiquitin-binding motif⁴. Results from pull-down experiments with a GST-ubiquitin fusion protein and different recombinant ZRF1 truncation proteins allowed us to map the ubiquitin-binding domain (UBD) to a region C-terminal of the DnaJ domain (Fig. 1d). H2A ubiquitination as well as histone H3K27me3 are marks typically located in promoter regions of polycomb-silenced genes^{15,16}. To test for ubiquitin-dependent recruitment of ZRF1 to chromatin, we established NT2 knockdown cell lines for ZRF1 or RING1B (a PRC1 subunit that is an E3 ligase; Fig. 1e). We

then analysed occupancy at several promoter regions of polycomb-repressed genes, including *PER1*, *NF1C* (Fig. 1f) and the well-characterized *HOX* genes^{15,16}. ZRF1 enrichment at the promoters clearly depended on the abundance of RING1B and on H2Aub levels (Fig. 1g, h and Supplementary Fig. 1G).

It has been shown that PRC1 is tethered to chromatin by the interaction of its subunit PC1 with a trimethyl mark on Lys 27 of histone H3 (H3K27me3)^{8,16}. Using purified mononucleosomes containing either wild-type H2A or the H2A(KKRR) mutant, we observed that co-purification of the PRC1 subunits RING1B and BMI1 depended on the ubiquitination of histone H2A (Fig. 2a). In contrast, we did not find an alteration of the H3K27 methylation levels in nucleosomes devoid of the ubiquitin mark, indicating that stable maintenance of PRC1 at chromatin depends on the ubiquitin mark (Fig. 2a and Supplementary Fig. 2J). To understand the functional relationship between ZRF1 and PRC1, we characterized further the binding affinity of RING1B towards the ubiquitin residue by GST pull-down experiments (Supplementary Fig. 2B). Furthermore, after reconstituting RING1B-containing mononucleosome complexes, RING1B was efficiently released from nucleosomes following incubation with GST-ubiquitin (Fig. 2b and Supplementary Fig. 2C). This finding indicated that ZRF1 could compete with RING1B for binding at H2Aub. Indeed, ZRF1 overexpression led to displacement of the PRC1 subunits RING1B and BMI1 from chromatin, whereas ZRF1 knockdown led to an enhanced occupancy of RING1B at chromatin that caused an increase in H2A ubiquitination (Fig. 2c, d and Supplementary Fig. 2D–H). We next performed competition assays with the GST-ubiquitin substrate. When the His-tagged RING1B concentration was maintained, we observed that increasing the His-ZRF1 concentration led to a reduction of RING1B bound to the ubiquitin substrate, emphasizing the competition for the ubiquitin residue by both proteins (Fig. 2e). We then assembled recombinant RING1B–GST-ubiquitin complexes and performed pull-down experiments after adding either bovine serum albumin (BSA) alone (lane 1) or recombinant His-UBD and BSA (lanes 2 and 3). In concordance with the previous result, we observed RING1B replaced by the UBD of ZRF1 (Fig. 2f). Similarly, on reconstituted RING1B–mononucleosome complexes, ZRF1 efficiently displaced RING1B (Fig. 2g and Supplementary Fig. 2I). Finally, chromatin immunoprecipitation (ChIP) experiments in 293T cells overexpressing either ZRF1 or only the UBD, indicated an enrichment of ZRF1 or the UBD at promoters of the *HOX* gene cluster concomitantly with the displacement of the PRC1 subunits RING1B and BMI1 (Fig. 2h–i and Supplementary Fig. 2F). In contrast, neither a ZRF1 deletion mutant devoid of the UBD nor the yeast homologue Zuo1, which shows only a weak ubiquitin-binding capacity, were recruited to chromatin or were able to displace PRC1 (Supplementary Fig. 3A–C). It has been shown that depletion of RING1B, and thus H2A ubiquitination, leads to the loss of PRC2 from chromatin¹⁷. In agreement with this previous study, we found that PRC2 levels were reduced at KKRR mutant nucleosomes.

¹Centre de Regulació Genòmica (CRG)/UPF, 08003 Barcelona, Spain. ²Department of Experimental and Health Sciences, Universitat Pompeu Fabra, 08003 Barcelona, Spain. ³Nagasaki University School of Medicine, Nagasaki 852-8523, Japan. ⁴Institut für Biochemie und Molekularbiologie (ZBMZ), Universität Freiburg, 79104 Germany. ⁵Institució Catalana de Recerca i Estudis Avançats (ICREA), Centre de Regulació Genòmica (CRG), PRBB, c/ Dr. Aiguader 88, 08003 Barcelona, Spain.

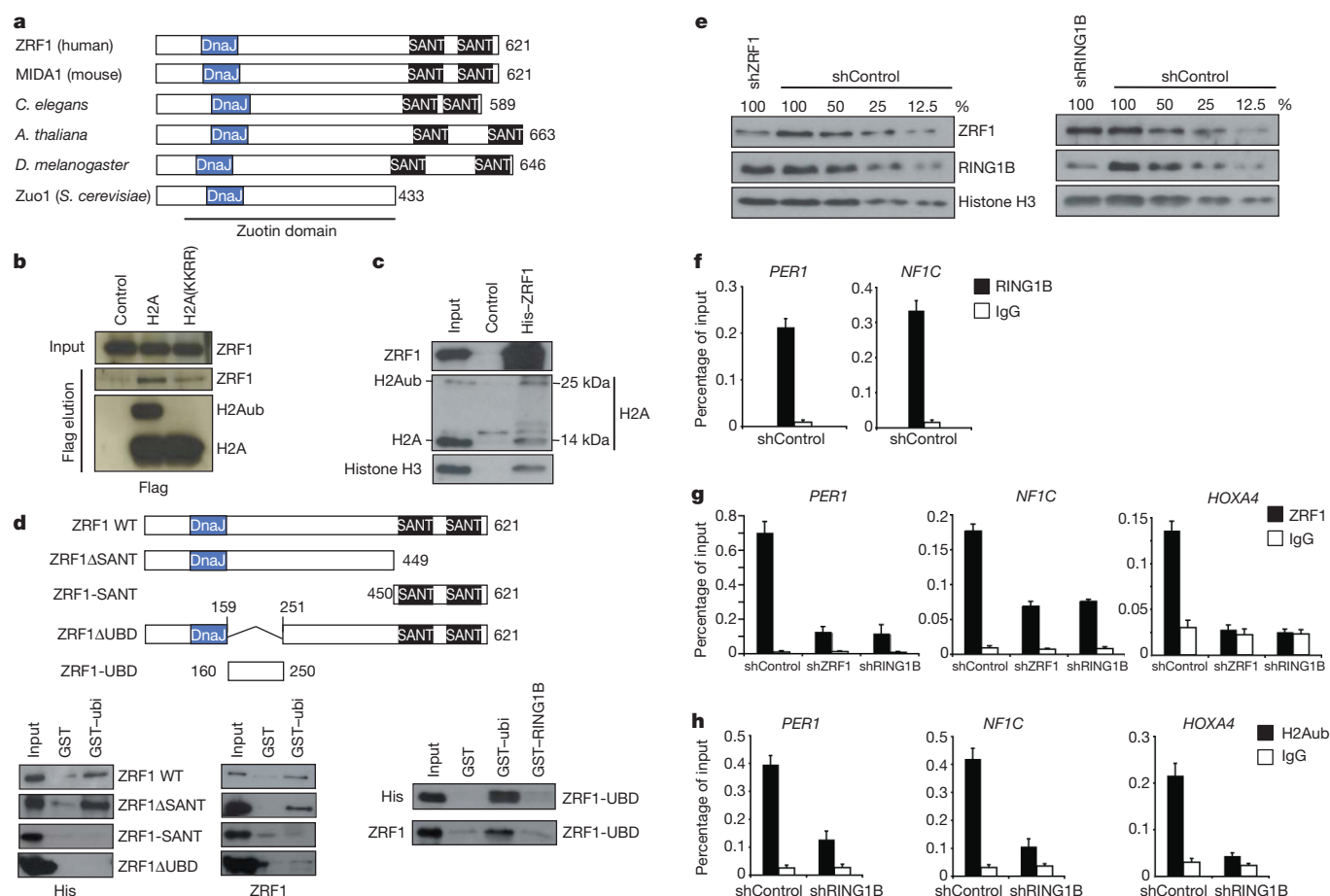


Figure 1 | ZRF1 interacts with H2Aub. **a**, Schematic diagram of ZRF1 orthologues indicating the DnaJ domain and SANT domains. The numbers along the right-hand side of panels **a** and **d** refer to the number of amino acids each of the proteins is composed of. **b**, Flag-tagged histone H2A and H2A(KKRR) were expressed in 293T cells. Mononucleosomes were purified and eluates were subjected to immunoblot analysis using ZRF1 and Flag antibodies. The inputs correspond to 3%. **c**, Nuclear protein extracts containing mononucleosomes were incubated with recombinant His-ZRF1. Precipitated ZRF1–nucleosome complexes were subjected to immunoblot analysis using the indicated antibodies. The inputs represent 5% of His-ZRF1 and 2% of the

protein extract. **d**, GST pull-downs with GST, GST-ubiquitin (GST-ubi) and GST-RING1B (right panel) and the His-tagged proteins indicated. Bound material was subjected to immunoblot analysis using His and ZRF1 antibodies. The input shown represents 2%. WT, wild type. **e**, Protein extracts of RING1B and ZRF1 knockdown cell lines were subjected to immunoblotting and probed with the antibodies indicated in the figure. **f**, ChIP experiments performed in NT2 control cells with RING1B antibodies. **g**, **h**, ChIP experiments performed in the NT2 control and knockdown cells with ZRF1 and H2Aub antibodies. The occupancy at promoters of the *PER1*, *NF1C* and *HOXA4* genes was tested by quantitative PCR. Data are represented as mean \pm s.e.m. ($n = 3$).

Similarly, PRC2 levels decreased upon binding of ZRF1 to chromatin (Supplementary Fig. 4A–C).

To globally identify ZRF1 target genes, we performed a ChIP-on-chip (see Methods) analysis in NT2 cells^{18,19}. Because our data indicate that ZRF1 might antagonize silencing by polycomb proteins, we designed an experiment that allowed us to study the occupancy of ZRF1 under conditions of retinoic-acid-induced differentiation (Fig. 3a). We found ZRF1 to be enriched in 758 (not induced), 2,295 (induced for 1 h) or 995 (induced for 3 h) genes (Fig. 3b and Supplementary Table 2). Analysis of the ZRF1 occupancy at its target genes revealed a marked increase at 1 h of induction (Fig. 3b, Supplementary Fig. 5C and Supplementary Table 2). Clustering the target genes with respect to their cellular functions indicates a role for ZRF1 in developmental processes and differentiation (Fig. 3c, d and Supplementary Fig. 5A, B). Additional ChIP-on-chip analysis indicates that RING1B and H2Aub target genes are mainly involved in developmental processes (Supplementary Figs 7A–L, 8A–J and Supplementary Tables 4 and 5), as shown in previous publications^{20,21}. The overlap of ZRF1 targets (1 h retinoic acid) with RING1B and H2Aub targets led to the identification of 1,102 common target genes (Fig. 3e, f). Moreover, comparison of ZRF1 target genes with polycomb target genes²² indicates that ZRF1 is more closely linked to PRC1 than to PRC2 (Supplementary Figs 6A, B, 8K, L). We next performed a gene

expression analysis comparing short hairpin RNA targeting ZRF1 (shZRF1) with shControl (non-specific shRNA constructs) cells, with or without retinoic-acid treatment. Interestingly, downregulated genes in shZRF1 after retinoic-acid stimulation are ZRF1 or polycomb targets, particularly for PRC1 and H2Aub (Supplementary Figs 6C, 9A–G and Supplementary Table 6). Among these genes more than a hundred are targeted by ZRF1, RING1B and H2Aub and many of these are major players in developmental pathways (Fig. 4a, b). To corroborate our findings, we performed ChIP experiments and gene expression analysis on selected ZRF1 target genes. We found that ZRF1 was significantly enriched at these genes only after stimulation with retinoic acid (Fig. 4c and Supplementary Fig. 10A). Under the same conditions, we observed transcriptional activation of the same genes in wild-type NT2 cells. However, in ZRF1 knockdown cells, we detected a decrease of the messenger RNA levels (Fig. 4d and Supplementary Fig. 10B). In sum, the data presented show a clear involvement of ZRF1 in the PRC1 pathway and, most importantly, that activation of genes targeted by PRC1 and H2Aub is facilitated by ZRF1.

Several polycomb target genes become activated during differentiation, concomitantly with the disappearance of the polycomb-dependent repressive marks^{15,16,23,24}. Analysis of two *HOXA* genes revealed that retinoic-acid-induced transcriptional activation depended on the presence of ZRF1. In contrast, RING1B knockdown caused a more robust

expression analysis comparing short hairpin RNA targeting ZRF1 (shZRF1) with shControl (non-specific shRNA constructs) cells, with or without retinoic-acid treatment. Interestingly, downregulated genes in shZRF1 after retinoic-acid stimulation are ZRF1 or polycomb targets, particularly for PRC1 and H2Aub (Supplementary Figs 6C, 9A–G and Supplementary Table 6). Among these genes more than a hundred are targeted by ZRF1, RING1B and H2Aub and many of these are major players in developmental pathways (Fig. 4a, b). To corroborate our findings, we performed ChIP experiments and gene expression analysis on selected ZRF1 target genes. We found that ZRF1 was significantly enriched at these genes only after stimulation with retinoic acid (Fig. 4c and Supplementary Fig. 10A). Under the same conditions, we observed transcriptional activation of the same genes in wild-type NT2 cells. However, in ZRF1 knockdown cells, we detected a decrease of the messenger RNA levels (Fig. 4d and Supplementary Fig. 10B). In sum, the data presented show a clear involvement of ZRF1 in the PRC1 pathway and, most importantly, that activation of genes targeted by PRC1 and H2Aub is facilitated by ZRF1.

Several polycomb target genes become activated during differentiation, concomitantly with the disappearance of the polycomb-dependent repressive marks^{15,16,23,24}. Analysis of two *HOXA* genes revealed that retinoic-acid-induced transcriptional activation depended on the presence of ZRF1. In contrast, RING1B knockdown caused a more robust

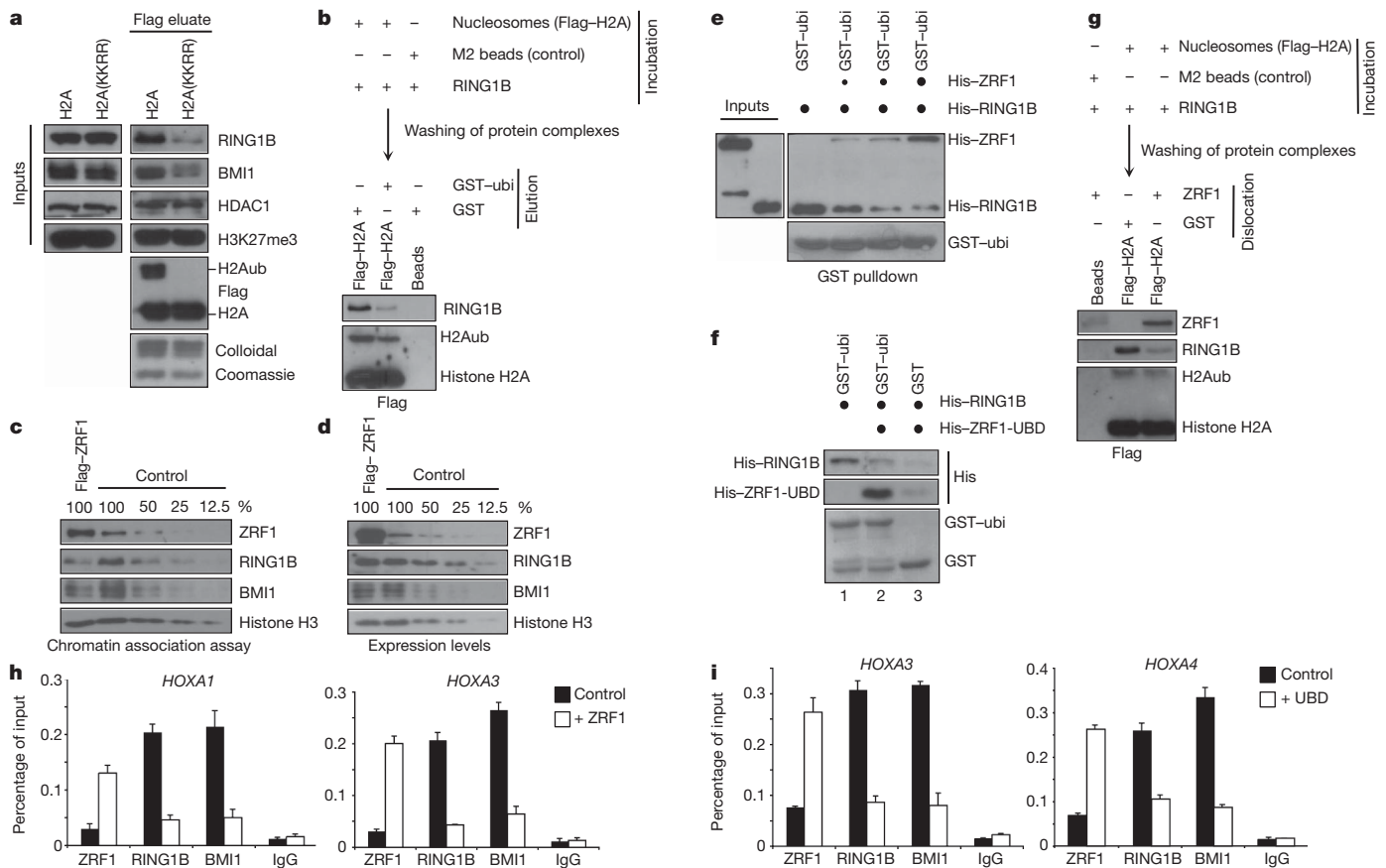


Figure 2 | ZRF1 and PRC1 compete for binding of H2Aub.

a, Mononucleosomes were purified from 293T cells expressing Flag-tagged H2A or a double mutant (KKRR). The purified material was subjected to immunoblot analysis using the indicated antibodies. The inputs represent 3%. **b**, Nucleosome-His-RING1B complexes were assembled, washed and incubated with GST (70 ng μl^{-1}) or GST-ubiquitin (70 ng μl^{-1}). Flag eluates were subjected to immunoblot analysis with the indicated antibodies. **c**, Chromatin association assay of 293T cells overexpressing ZRF1. Immunoblot analysis was performed with the indicated antibodies. **d**, Immunoblot analysis of 293T cells overexpressing ZRF1 using the indicated antibodies. **e**, GST-ubiquitin was incubated with constant amounts of His-RING1B and increasing amounts of His-ZRF1 finally reaching equimolar levels (last lane). The inputs show 10% of His-RING1B and 10% of the maximal amount of His-ZRF1.

activation of those genes, thus supporting opposing roles for PRC1 and ZRF1 in transcriptional regulation of promoters (Fig. 4e). Next we investigated the occupancy of both ZRF1 and RING1B at promoters of *HOX* genes during retinoic-acid-induced transcription. Retinoic-acid treatment led to the recruitment of ZRF1 to promoter regions with a concomitant reduction of RING1B occupancy, clearly indicating mutually exclusive binding for these proteins at chromatin (Fig. 4f, g). Accordingly, in ZRF1 knockdown cells, RING1B was not efficiently removed from chromatin after retinoic-acid induction (Fig. 4h), as supported by previous experiments (Fig. 2a–h). In related experiments (1 h retinoic acid) we found H2Aub to be slightly reduced at *HOXA* gene promoters, indicating a deletion of this histone mark shortly after the removal of PRC1 complexes (Supplementary Fig. 11A–C). A set of similar results was obtained in retinoic-acid-induced differentiation of leukaemic cells (Supplementary Fig. 10C–E)²⁴. On the basis of our results, we reasoned that ZRF1 might facilitate transcription. Recently, it has been shown that USP21-mediated H2A deubiquitination precedes gene activation²⁵. To investigate further the impact of ZRF1 on transcriptional activation, we performed *in vitro* experiments testing whether ZRF1 might act in concert with specific deubiquitinases. *In vitro* deubiquitination assays carried out with mouse liver chromatin demonstrate that ZRF1 facilitates H2A deubiquitination (Fig. 4i).

f, GST and GST-ubiquitin were incubated with RING1B, washed and incubated with His-ZRF1-UBD (see Methods). The retained material was subjected to immunoblot analysis with His antibodies. Lane 1 shows the pull-down in the presence of only BSA, lanes 2 and 3 in the presence of both BSA and His-ZRF1-UBD. **g**, Nucleosome-His-RING1B complexes were assembled and incubated with GST (100 ng μl^{-1}) or ZRF1 (100 ng μl^{-1}). After elution by Flag peptide, immunoblot analysis was performed with Flag, RING1B and ZRF1 antibodies. **h**, ChIP experiments with ZRF1, RING1B and BMI1 antibodies after overexpression of ZRF1 in 293T cells. **i**, Experiments were performed as already stated with the exception that the Flag-UBD was overexpressed instead of the full-length ZRF1. The occupancy at promoters of *HOX* genes was tested with quantitative PCR. Data are represented as mean \pm s.e.m. ($n = 3$).

Thus, these results showed that, besides its function in the displacement of PRC1 complexes, ZRF1 facilitates transcription by cooperating with deubiquitinase enzymes.

Ubiquitination of H2A has long been correlated with activation of genes²⁶. It is intriguing that ubiquitination of histone H2A not only has an effect on gene silencing but also is necessary to attract a factor that switches genes from a silenced to a transcriptionally activated state. However, it is still unclear how ZRF1 binding to chromatin is regulated (Supplementary Fig. 12A, B). One potential mode of regulating ZRF1, and thus cell differentiation, could be to mask its UBD domain. It has been shown that proteins of the ID (inhibitor of differentiation) family bind to ZRF1 in a region spanning its UBD domain¹³ (Supplementary Fig. 12C). Our data indicate that association of PRC1 with chromatin depends on the H2Aub mark, whereas H3K27me3 is not sufficient to retain PRC1 complexes and is most probably required for its initial targeting^{21,27}. RING1B/PRC1 are not as abundant as H2Aub, thus excluding a continuous binding of PRC1 complexes throughout chromatin. Yet it has been shown that during DNA damage H2A E3 ligases bind ubiquitinated H2A and propagate the initial chromatin ubiquitination marks²⁸. A similar sliding mechanism could also apply to our findings regarding RING1B, and challenge the current view of ubiquitination and deubiquitination cycles (see also Supplementary

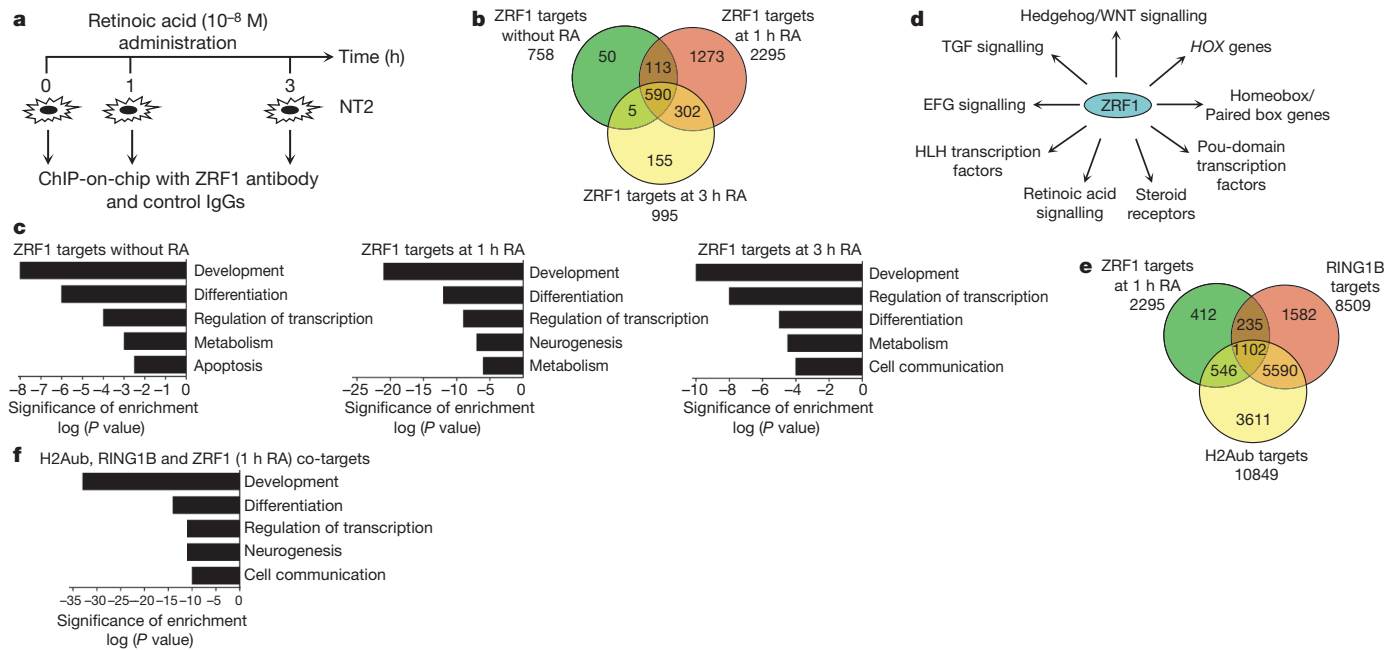


Figure 3 | Genome-wide mapping of ZRF1 target genes in NT2 cells.

a, Schematic representation of the experimental approach for the ChIP-on-chip experiment. Chromatin was subjected to triplicate ChIP experiments with ZRF1 and control antibodies. The obtained material was amplified and hybridized with Human Promoter Arrays chips from Agilent. **b**, Venn diagram of the ZRF1 target genes as obtained by Chipper analysis. **c**, Functional enrichment analysis of ZRF1 target genes at the different time points of retinoic-acid (RA) induction. **d**, A selection of ZRF1 target genes identified in

this study (induced for 1 h), focusing on those known to be involved in key pathways controlling cell fate decisions. **e**, Venn diagram showing significant overlapping between the gene lists of RING1B, H2Aub and ZRF1 (induced for 1 h) as obtained by ChIP-on-chip analysis. The *P* values after overlapping the H2Aub target genes with ZRF1 and/or RING1B targets are listed in the following: RING1B ($P = 10^{-16}$), ZRF1 (1 h; $P = 10^{-12}$) and RING1B-ZRF1 co-targets ($P = 10^{-16}$). **f**, Functional enrichment analysis of the 1,102 common ZRF1/RING1B/H2Aub target genes.

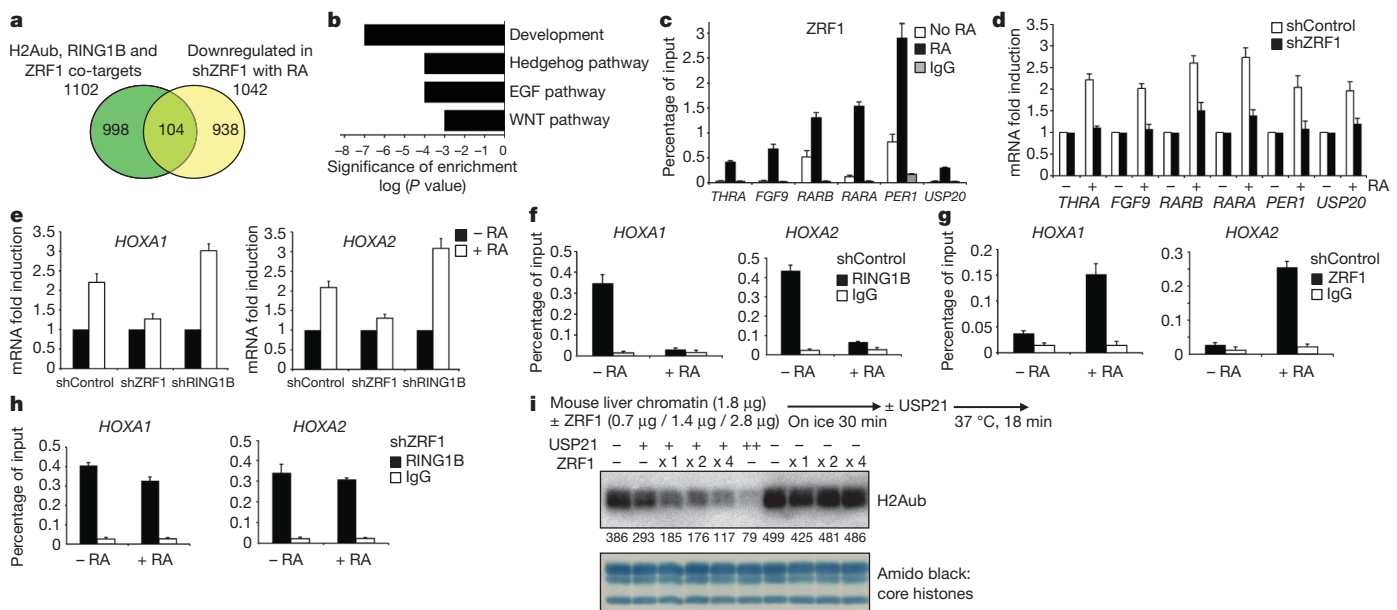


Figure 4 | ZRF1 functions in activating polycomb-repressed genes. **a**, The list of genes significantly repressed in comparison to shControl cells after stimulation with retinoic acid was overlapped with the common ZRF1/RING1B/H2Aub target genes (see also Supplementary Fig. 9). **b**, Functional enrichment analysis of the 104 common target genes downregulated in shZRF1 cells. **c**, ChIP experiments were performed with ZRF1 antibodies and chromatin obtained from NT2 induced with retinoic acid (*THRA*, *FGF9*, *RARB* and *RARA*: 1 h retinoic acid; *PER1* and *USP20*: 3 h retinoic acid). The occupancy at promoters of the aforementioned genes was tested by quantitative PCR. Data are represented as mean \pm s.e.m. ($n = 3$). **d**, The mRNA levels of the genes indicated were measured in NT2 shZRF1 and shControl cell lines after

supplementing with retinoic acid for the respective times (*THRA*, *FGF9*, *PER1* and *USP20*: 3 h retinoic acid; *RARA* and *RARB*: 2 h retinoic acid). Data are represented as mean \pm s.e.m. ($n = 3$). **e**, shControl, shZRF1 and shRING1B NT2 cells were induced for 1 h with 10^{-8} M of retinoic acid. RNA levels of the ribosomal gene *PUM1* ($n = 3$). **f–h**, shControl NT2 cells or shZRF1 knockdown cells were kept under the same conditions as in **e**, and chromatin was used in ChIP experiments with RING1B and ZRF1 antibodies. Data are represented as mean \pm s.e.m. ($n = 3$). **i**, Mouse liver chromatin was incubated with ZRF1 and USP21 (10 or 20 ng) as indicated. The H2Aub levels were quantified after detection with specific antibodies.

Discussion). However, future research will have to reveal the dynamics of PRC1-catalysed ubiquitination.

METHODS SUMMARY

Experiments were performed using human cell lines (NT2, 293T and U937) and affinity-purified or commercially available antibodies. The knockdown cells used were established by retroviral infection. ChIP experiments, mutagenesis of histone H2A, genome-wide studies and protein purification procedures are explained in Methods.

Full Methods and any associated references are available in the online version of the paper at www.nature.com/nature.

Received 12 June 2009; accepted 12 October 2010.

- Strahl, B. D. & Allis, C. D. The language of covalent histone modifications. *Nature* **403**, 41–45 (2000).
- Li, B., Carey, M. & Workman, J. L. The role of chromatin during transcription. *Cell* **128**, 707–719 (2007).
- Kouzarides, T. Chromatin modifications and their function. *Cell* **128**, 693–705 (2007).
- Goldknopf, I. L. *et al.* Isolation and characterization of protein A24, a “histone-like” non-histone chromosomal protein. *J. Biol. Chem.* **250**, 7182–7187 (1975).
- Zhu, B. *et al.* Monoubiquitination of human histone H2B: the factors involved and their roles in *HOX* gene regulation. *Mol. Cell* **20**, 601–611 (2005).
- Nickel, B. E., Allis, C. D. & Davie, J. R. Ubiquitinated histone H2B is preferentially located in transcriptionally active chromatin. *Biochemistry* **28**, 958–963 (1989).
- Wang, H. *et al.* Role of histone H2A ubiquitination in Polycomb silencing. *Nature* **431**, 873–878 (2004).
- Kuzmichev, A., Nishioka, K., Erdjument-Bromage, H., Tempst, P. & Reinberg, D. Histone methyltransferase activity associated with a human multiprotein complex containing the Enhancer of Zeste protein. *Genes Dev.* **16**, 2893–2905 (2002).
- Zhou, W. *et al.* Histone H2A monoubiquitination represses transcription by inhibiting RNA polymerase II transcriptional elongation. *Mol. Cell* **29**, 69–80 (2008).
- Pan, X. *et al.* A DNA integrity network in the yeast *Saccharomyces cerevisiae*. *Cell* **124**, 1069–1081 (2006).
- Greiner, J. *et al.* Characterization of several leukemia-associated antigens inducing humoral immune responses in acute and chronic myeloid leukemia. *Int. J. Cancer* **106**, 224–231 (2003).
- Resto, V. A. *et al.* A putative oncogenic role for MPP11 in head and neck squamous cell cancer. *Cancer Res.* **60**, 5529–5535 (2000).
- Inoue, T., Shoji, W. & Obinata, M. MIDA1, an Id-associating protein, has two distinct DNA binding activities that are converted by the association with Id1: a novel function of Id protein. *Biochem. Biophys. Res. Commun.* **266**, 147–151 (1999).
- Hicke, L., Schubert, H. L. & Hill, C. P. Ubiquitin-binding domains. *Nature Rev. Mol. Cell Biol.* **6**, 610–621 (2005).
- Bracken, A. P., Dietrich, N., Pasini, D., Hansen, K. H. & Helin, K. Genome-wide mapping of Polycomb target genes unravels their roles in cell fate transitions. *Genes Dev.* **20**, 1123–1136 (2006).
- Lee, M. G. *et al.* Demethylation of H3K27 regulates polycomb recruitment and H2A ubiquitination. *Science* **318**, 447–450 (2007).
- Saito, S. *et al.* Haptoglobin- β chain defined by monoclonal antibody RM2 as a novel serum marker for prostate cancer. *Int. J. Cancer* **123**, 633–640 (2008).
- Andrews, P. W. Retinoic acid induces neuronal differentiation of a cloned human embryonal carcinoma cell line *in vitro*. *Dev. Biol.* **103**, 285–293 (1984).
- Andrews, P. W. *et al.* Pluripotent embryonal carcinoma clones derived from the human teratocarcinoma cell line Tera-2. Differentiation *in vivo* and *in vitro*. *Lab. Invest.* **50**, 147–162 (1984).
- Boyer, L. A. *et al.* Polycomb complexes repress developmental regulators in murine embryonic stem cells. *Nature* **441**, 349–353 (2006).
- Kallin, E. M. *et al.* Genome-wide uH2A localization analysis highlights Bmi1-dependent deposition of the mark at repressed genes. *PLoS Genet.* **5**, e1000506 (2009).
- O’Geen, H. *et al.* Genome-wide analysis of KAP1 binding suggests autoregulation of KRAB-ZNFs. *PLoS Genet.* **3**, e89 (2007).
- Pasini, D., Bracken, A. P., Hansen, J. B., Capillo, M. & Helin, K. The polycomb group protein Suz12 is required for embryonic stem cell differentiation. *Mol. Cell Biol.* **27**, 3769–3779 (2007).
- Villa, R. *et al.* Role of the polycomb repressive complex 2 in acute promyelocytic leukemia. *Cancer Cell* **11**, 513–525 (2007).
- Nakagawa, T. *et al.* Deubiquitylation of histone H2A activates transcriptional initiation via trans-histone cross-talk with H3K4 di- and trimethylation. *Genes Dev.* **22**, 37–49 (2008).
- Levinger, L. & Varshavsky, A. Selective arrangement of ubiquitinated and D1 protein-containing nucleosomes within the *Drosophila* genome. *Cell* **28**, 375–385 (1982).
- Lagarou, A. *et al.* dKDM2 couples histone H2A ubiquitylation to histone H3 demethylation during Polycomb group silencing. *Genes Dev.* **22**, 2799–2810 (2008).
- Doil, C. *et al.* RNF168 binds and amplifies ubiquitin conjugates on damaged chromosomes to allow accumulation of repair proteins. *Cell* **136**, 435–446 (2009).

Supplementary Information is linked to the online version of the paper at www.nature.com/nature.

Acknowledgements We are indebted to S. Jentsch, S. Berger, K. Helin, J. Hasskarl, R. Shiekhattar, T. Zimmermann and V. Raker for antibodies and plasmids and for discussions; and to the CRG Microarray facility and Light Microscopy Facility. This work was supported by the Spanish “Ministerio de Educación y Ciencia” (BFU2007-63059), the Association for International Cancer Research (10-0177), by the AGAUR and Consolider to L.D.C., and by FOR967 to S.R.; H.R. was supported by a FEBS fellowship; J.R. by a fellowship from Fundação para a Ciência e Tecnologia; L.R.-V. by a Juan de la Cierva Fellowship; S.D. by a PFIS fellowship.

Author Contributions H.R. cloned, purified proteins and performed biochemical studies. H.R., L.R.-V., J.D.R. and S.D. performed ChIP analysis. G.G. and N.L.-B. performed genome-wide analysis. T.N. and T.J. performed *in vitro* transcription and deubiquitination experiments. S.R. provided essential tools. H.R. and L.D.C. designed the experiments, supervised the project and wrote the manuscript. All authors commented on the manuscript.

Author Information Reprints and permissions information is available at www.nature.com/reprints. The authors declare no competing financial interests. Readers are welcome to comment on the online version of this article at www.nature.com/nature. Correspondence and requests for materials should be addressed to L.D.C. (luciano.dicroce@crg.es).

METHODS

Plasmids, antibodies and cell lines. Antibodies against ZRF1 and RING1B were either previously described²⁹, or raised in rabbits against full-length protein and affinity purified. To that end, GST fusion proteins of both proteins were cross-linked to glutathione beads and packed into polystyrol mini-columns (Pierce). Antisera were repeatedly run over the columns, washed and finally eluted in Tris buffer pH 2.5. The affinity-purified antibody was finally set to pH 8.0. For Fig. 1d the ZRF1 serum against full-length protein was used to visualize the recombinant protein deletion mutants. In all other experiments the antibody purified with GST-ZRF1ΔSANT (a ZRF1 protein lacking the C-terminal SANT domains) was used. Antibodies against H2Aub, IgM conjugating antibody and H3K4 trimethyl were obtained from Upstate antibodies. Antibodies against histone H2A and the histone modification H3K4 trimethyl were purchased from Abcam. Antibodies against the His and Flag epitopes were purchased from Qiagen and SIGMA, respectively. Antibodies against EED and SUZ12 were a gift from K. Helin. Plasmids for the ectopic expression of Flag-tagged ID proteins were a gift from J. Hasskarl. For tagging proteins the pet28 (His tag, Novagen), pCMV2 (Flag, Invitrogen) and pGex (GST, Invitrogen) vector series were used. The ZRF1 specific sequences GTTATCTGATCCAGTAAAA and GATCAAAGCAGCTCATAAA were used to synthesize oligonucleotides and cloned into pRetroSuper³⁰. In the case of RING1B the specific sequences AGAACACCATGACTACAAA and TTCTAAAGCTAACCTCACA were cloned into the same vector. Mutagenesis of histone H2A was performed using the Quikchange mutagenesis kit (Stratagene) on a pCMV2b histone H2A plasmid. Information on the cloning and sequences are available upon request. The embryonic carcinoma cell line NTERA2 (NT2/D1) and HEK 293T cells were cultured in DMEM medium supplemented with 10% fetal bovine serum at 37 °C and 5% CO₂. NT2 cells were treated with retinoic acid to induce differentiation at the given concentrations for the mentioned time intervals. U937 cells were cultured in RPMI medium at 37 °C and 5% CO₂.

Purification of recombinant proteins. Proteins were purified as suggested by Qiagen (His-tagged proteins) and Amersham (GST-tagged proteins) after inducing BL21 bacterial strains transformed with the respective plasmids at an optical density of 0.5 with 0.2 mM of isopropyl-β-D-thiogalactoside either for 4 h at 37 °C or at 20 °C for 14 h.

Purification of ubiquitin-binding proteins. HEK 293T cells were transfected with pCMV2b-histone H2A or the corresponding empty vector (Control) and after 48 h mononucleosomes were purified by means of the Flag epitope as stated in Supplementary Fig. 1A, C. After harvesting by centrifugation, cells were resuspended in buffer A (10 mM HEPES pH 7.9, 1.5 mM MgCl₂, 10 mM KCl and 0.5 mM dithiothreitol (DTT), phenylmethylsulphonyl fluoride (PMSF)) and homogenized by 10 strokes in a Dounce homogenizer with a B-type pestle. After centrifugation, nuclei were resuspended in lysis buffer (137 mM NaCl, 2.7 mM KCl, 10 mM NaH₂PO₄, 2 mM KH₂PO₄, 0.1% Triton X-100, 0.5 mM DTT, PMSF) and sonified using a Diagenode Bioruptor to obtain mononucleosomes (4 °C, 4 cycles of 15 min, 'H' setting). Protein extracts were then subjected to centrifugation (16,100g, 4 °C, 30 min) to remove debris and incubated with M2-Flag Agarose beads. The bound material or the control beads (M2-beads incubated with protein extracts from control transfections) were poured in polystyrol mini-columns (Flag-H2A column and Control column), washed intensively with lysis buffer and then used subsequently in an affinity purification. To this end, a nuclear protein extract devoid of histone proteins was prepared from 293T cells as previously described³¹. In brief, nuclei were extracted by resuspension of cells in buffer A (10 mM HEPES pH 7.9, 1.5 mM MgCl₂, 10 mM KCl and 0.5 mM DTT, PMSF) and homogenized by 10 strokes in a Dounce homogenizer with a B-type pestle. The crude nuclei were resuspended in buffer C (20 mM HEPES pH 7.9, 25% (v/v) glycerol, 1.5 mM MgCl₂, 420 mM NaCl, 0.2 mM EDTA, 0.5 mM DTT and PMSF) and homogenized in a Dounce homogenizer (10 strokes, B-type pestle). The resulting protein suspension was stirred by a magnetic stirring bar for 30 min at 4 °C and then centrifuged at 25,000g in an SS34 rotor for 3 h. The resulting supernatant was dialysed against lysis buffer, and run in a loop over two polystyrol mini-columns (Flag-H2A column and Control column; see above). After intensive washing with lysis buffer the columns were incubated with a solution of lysis buffer with recombinant His-tagged ubiquitin previously purified by Ni-NTA Agarose (Qiagen) and gel filtration on a Superose 12 column. After eluting the ubiquitin-binding proteins, the columns were washed again in lysis buffer and mononucleosomes were subsequently eluted by a solution of Flag peptide in lysis buffer. Both eluates were subjected to electrophoresis, stained with colloidal coomassie, and possible interactors were subjected to MALDI-Fingerprint analysis.

Transfection and retroviral infection. Transfection of HEK 293T cells was usually performed by the calcium phosphate co-precipitation method as described²⁴. pRS-based retrovirus was produced by transfecting the GP2-293 packaging cell line (Clontech). The collected retrovirus was subsequently used to transduce NT2 or

293T cell lines by spinoculation at 900g for 90 min at 32 °C in the presence of protamine sulphate. After incubating overnight at 37 °C the protocol was repeated for two consecutive days.

M2-Flag affinity chromatography. Purification of Flag-tagged proteins from 293T cells was essentially done as described earlier. All experiments with Flag-tagged histone H2A were performed in polystyrene mini-columns (Pierce) with subsequent elution using the Flag peptide (Sigma) at a concentration of 100 µg ml⁻¹ in PBS.

ZRF1-H2Aub interaction experiments. Nuclear protein extracts were prepared as described earlier to obtain mononucleosomes. The protein extract was then incubated with or without recombinant His-ZRF1 (lanes ZRF1 and Control in Fig. 1c) for 4 h at 4 °C. Ni-NTA Agarose was added and after 2 h of incubation at 4 °C the beads were washed intensively with lysis buffer. The precipitated material was then subjected to western blotting.

Nucleosome-RING1B complexes and *in vitro* assays. Mononucleosomes were purified as described earlier, but washed with lysis buffer containing 450 mM NaCl and maintained at the Flag-M2 Agarose beads. The bound nucleosomes and empty M2 beads were subsequently incubated with bacterial extracts in lysis buffer containing recombinant His-RING1B. After 2 h of incubation at 4 °C the beads were washed in the same buffer intensively (see Supplementary Fig. 2C). The RING1B-nucleosome complexes were then incubated with equal or equimolar amounts of either GST or GST-ubiquitin (Fig. 2b) or ZRF1 (Fig. 2g) in lysis buffer. After 2 h of incubation at 4 °C the beads were packed into polystyrol columns, washed and eluted with Flag peptide at 100 µg ml⁻¹. The eluate was finally subjected to immunoblotting.

ChIP. ChIP experiments were essentially performed as described²⁴. For all experiments affinity-purified antibodies were used as described earlier. The immunoprecipitated DNA was quantified by real-time quantitative PCR (Roche Lightcycler). The primers for verifying the occupancy of the immunoprecipitated protein at chromatin are available upon request.

Genome-wide mapping of ZRF1 target genes (ChIP-on-chip). Chromatin from NT2 cells before (0 h) and after induction with retinoic acid (10⁻⁸ M) for 1 h or 3 h was subjected to ChIP experiments with ZRF1 and control antibodies. For each time-point of the ChIP experiments triplicates were carried out. The obtained material was amplified with the WGA kit (Sigma) and linear amplification of the material was tested in qPCR reactions with known ZRF1 targets. Labelling and hybridization to Agilent Human Promoter Arrays were carried out following the supplier's instructions. Analogously, chromatin from unstimulated NT2 cells was subjected to ChIP experiments with RING1B, H2Aub and the respective conjugating antibody. The obtained material was processed as described earlier.

Microarray analysis. Microarray analysis was performed after extracting a triplicate of three different biological samples of RNA from NT2 cells lines (shZRF1 and shControl) either from non-induced cells or cells induced with retinoic acid (10⁻⁸ M, 3 h). RNA was amplified, labelled and subsequently hybridized to a Human Genome Oligo Microarray (Agilent). Raw data were analysed using the Limma package.

Data analysis and statistics. Absolute foreground and background readings from channels were used as input to the chipper program. Default parameters were used as defined previously³². Chipper calculates *q* values (corrected *P* values), thus accounting for multiple testing corrections per probe. Probes with *q* values <0.05 were accepted as significant. Probes, which are significantly bound by ZRF1, were compared to those significantly bound by IgG to subtract IgG targets. ZRF1 targets were mapped to genes according to the information provided by Agilent. To study significant overlapping between genes bound by ZRF1 and genes bound by SUZ12, RING1B, H2Aub or the H3K27me3 mark, respectively, the enrichment analysis (EA) method was applied. The statistical significance (*P* value) was calculated using the binomial distribution. Significance levels were corrected for multiple comparisons with the Benjamini and Hochberg method. Functional enrichment analysis was performed with the DAVID software³³.

RNA preparation and analysis by quantitative PCR. RNA was extracted with the RNeasy mini kit (Qiagen) and transcribed to cDNA by reverse transcription using the AMV kit (Roche). The expression of the respective genes was assayed by quantitative real-time PCR (Roche Lightcycler). As a reference, the expression of GAPDH or PUM1 was measured for each experiment. The sequences of the primers are available upon request.

GST pull-down. Purified GST-proteins were bound in equimolar amounts to glutathione beads (Amersham) in binding buffer (20 mM Tris pH 8.0, 150 mM NaCl, 0.5% NP-40). Loaded beads were washed in the same buffer and used for incubation with recombinant proteins for 2 h at 4 °C. For the competition assay (Fig. 2e) with recombinant ZRF1 and RING1B, the amounts of RING1B were kept constant and the amounts of ZRF1 were increased with every consecutive pull-down until finally reaching equimolar conditions. For preassembling RING1B-ubiquitin complexes (Fig. 2f), GST and GST-ubiquitin were bound to beads,

washed and incubated with RING1B at 4 °C for 2 h. Loaded beads were then incubated with a roughly tenfold higher amount of ZRF1-UBD together with an excess of BSA—where stated—for 90 min at 4 °C. Finally, beads were washed intensively in binding buffer, denatured in SDS buffer, and subjected to electrophoresis and subsequent western blotting analysis.

Gel-filtration analysis. Gel-filtration was performed on an AEKTA-Explorer system (Amersham) using Superose12 or Superose6 columns (Amersham). After calibrating the column with specific proteins, a solution of recombinant protein in PBS was injected and the UV-elution profile was detected. To verify each volume of elution the fractions were subjected to western blotting by probing with specific antibodies.

Chromatin association assays. Cells were crosslinked with a solution of 1% formaldehyde in PBS for 10 min at 24 °C. Nuclei were prepared by resuspending the cell pellets in buffer A (100 mM Tris pH 7.5, 5 mM MgCl₂, 60 mM KCl, 0.5 mM DTT, 125 mM NaCl, 300 mM sucrose, 1% NP-40). After lysis on ice the nuclei were pelleted and resuspended in buffer B (100 mM Tris pH 7.5, 1 mM CaCl₂, 60 mM KCl, 0.5 mM DTT, 125 mM NaCl, 300 mM sucrose) and supplemented with 10 U of MNase I for 20 min at 37 °C. The reaction was stopped by adding EDTA. The chromatin was pelleted and resuspended in buffer C (1% SDS, 10 mM

EDTA, 50 mM Tris pH 8.0) overnight at 4 °C. After centrifugation (16,100g, 2 min) the supernatant was used for western blotting.

In vitro deubiquitination assays. Deubiquitination experiments were essentially performed as previously described²⁵. In short, mouse liver chromatin was incubated with no or increasing amounts of recombinant ZRF1. Subsequently USP21 was added and reactions were incubated at 37 °C for 18 min.

29. Otto, H. *et al.* The chaperones MPP11 and Hsp70L1 form the mammalian ribosome-associated complex. *Proc. Natl Acad. Sci. USA* **102**, 10064–10069 (2005).
30. Brummelkamp, T. R., Nijman, S. M., Dirac, A. M. & Bernards, R. Loss of the cylindromatosis tumour suppressor inhibits apoptosis by activating NF- κ B. *Nature* **424**, 797–801 (2003).
31. Dignani, J. D., Lebovitz, R. M. & Roeder, R. G. Accurate transcription initiation by RNA polymerase II in a soluble extract from isolated mammalian nuclei. *Nucleic Acids Res.* **11**, 1475–1489 (1983).
32. Gibbons, F. D., Proft, M., Struhl, K. & Roth, F. P. Chipper: discovering transcription-factor targets from chromatin immunoprecipitation microarrays using variance stabilization. *Genome Biol.* **6**, R96 (2005).
33. Huang, D. W., Sherman, B. T. & Lempicki, R. A. Systematic and integrative analysis of large gene lists using DAVID bioinformatics resources. *Nature Protocols* **4**, 44–57 (2009).

Neurotransmitter/sodium symporter orthologue LeuT has a single high-affinity substrate site

Chayne L. Piscitelli^{1,2*}, Harini Krishnamurthy^{2*} & Eric Gouaux^{2,3}

Neurotransmitter/sodium symporters (NSSs) couple the uptake of neurotransmitter with one or more sodium ions^{1–3}, removing neurotransmitter from the synaptic cleft. NSSs are essential to the function of chemical synapses, are associated with multiple neurological diseases and disorders⁴, and are the targets of therapeutic and illicit drugs⁵. LeuT, a prokaryotic orthologue of the NSS family, is a model transporter for understanding the relationships between molecular mechanism and atomic structure in a broad range of sodium-dependent and sodium-independent secondary transporters^{6–13}. At present there is a controversy over whether there are one or two high-affinity substrate binding sites in LeuT. The first-reported crystal structure of LeuT, together with subsequent functional and structural studies, provided direct evidence for a single, high-affinity, centrally located substrate-binding site, defined as the S1 site^{14,15}. Recent binding, flux and molecular simulation studies, however, have been interpreted in terms of a model where there are two high-affinity binding sites: the central, S1, site and a second, the S2 site, located within the extracellular vestibule¹⁶. Furthermore, it was proposed that the S1 and S2 sites are allosterically coupled such that occupancy of the S2 site is required for the cytoplasmic release of substrate from the S1 site¹⁶. Here we address this controversy by performing direct measurement of substrate binding to wild-type LeuT and to S2 site mutants using isothermal titration calorimetry, equilibrium dialysis and scintillation proximity assays. In addition, we perform uptake experiments to determine whether the proposed allosteric coupling between the putative S2 site and the S1 site manifests itself in the kinetics of substrate flux. We conclude that LeuT harbours a single, centrally located, high-affinity substrate-binding site and that transport is well described by a simple, single-substrate kinetic mechanism.

We first measured the thermodynamic response and stoichiometry of L-leucine binding to LeuT using isothermal titration calorimetry (ITC). To minimize the potential for artefacts in our binding assays arising from endogenously bound Leu co-purifying with LeuT, we extensively washed cell membranes with Na⁺-free buffer containing the Na⁺ chelator 15-crown-5¹⁷. For the wild-type LeuT–Leu interaction, ITC binding isotherms were best fitted by a single-site model with a substrate-to-LeuT stoichiometry, *N*, of 0.70 ± 0.01 and a dissociation constant, *K*_d, of 54.7 ± 1.8 nM (Fig. 1a and Supplementary Table 1). Binding of Leu to LeuT is driven by enthalpic and entropic factors with a ΔH of -3.93 ± 0.02 kcal mol⁻¹ and a $-T\Delta S$ of -6.01 ± 0.13 kcal mol⁻¹. Thermodynamic binding models of higher complexity describing two-site random- or sequential-binding modes yielded poorer fits to the data, with either high χ^2 values or non-converging parameters.

The measured stoichiometry, of 0.70, suggests that approximately 30% of LeuT in the ITC cell is unable to bind titrated substrate. This could be due to incomplete removal of endogenously bound substrate

despite extensive ‘washing’ of the membranes. To weaken substrate binding and thus diminish the relative proportion of Leu-bound LeuT, as well as to specifically probe the interaction of substrate with LeuT, we mutated Tyr 108 to Phe, thereby disrupting the hydrogen bond between the hydroxyl group of Tyr 108 and a carboxylate oxygen of substrate bound to the S1 site¹⁴. We proposed that by ablating the hydrogen bond between Tyr 108 and Leu, the Tyr 108 Phe mutation would reduce the enthalpy of Leu binding to the S1 site, thus allowing us to isolate apo-LeuT more readily.

Similar to the case for wild-type LeuT, the binding isotherm for Leu binding to the Tyr 108 Phe mutant was best fitted by a single-site

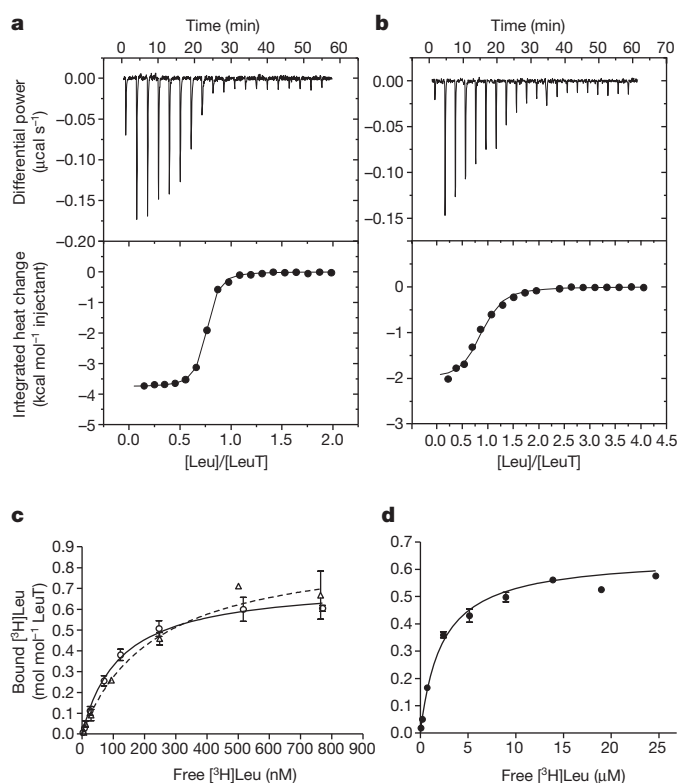


Figure 1 | Leu binding measured by ITC and equilibrium dialysis. **a, b**, ITC data for Leu binding to wild-type LeuT (**a**) and Leu binding to mutant Tyr 108 Phe–LeuT^K (see Methods) (**b**). Raw injection heats (expressed as differential power) are shown in the top panels and the corresponding specific binding isotherms (calculated from the integrated injection heats and normalized to moles of injectant) are shown in the bottom panels, determined at 25 °C and pH 7.0. Square brackets denote concentration. **c, d**, Quantitation of [³H]Leu-binding stoichiometry by equilibrium dialysis for the wild type (open circle, solid line) or the Leu 400 Ala mutant (open triangle, dashed line) (**c**), and for Tyr 108 Phe–LeuT^K (**d**). Errors bars, s.e.m.; *n* = 2.

¹Department of Biochemistry and Molecular Biology, Oregon Health and Science University, 3181 SW Sam Jackson Park Road, Portland, Oregon 97239, USA. ²Vollum Institute, Oregon Health and Science University, 3181 SW Sam Jackson Park Road, Portland, Oregon 97239, USA. ³Howard Hughes Medical Institute, Oregon Health and Science University, 3181 SW Sam Jackson Park Road, Portland, Oregon 97239, USA.

*These authors contributed equally to this work.

model (Fig. 1b). Reflecting the predicted binding-site perturbation, the dissociation constant increased to $K_d = 1.4 \pm 0.1 \mu\text{M}$; the stoichiometry parameter also increased ($N = 0.79 \pm 0.01$) relative to the wild-type transporter (Supplementary Table 1). Notably, ΔH decreased to $-1.92 \pm 0.03 \text{ kcal mol}^{-1}$, a difference of $2.01 \text{ kcal mol}^{-1}$ from wild-type LeuT and consistent with the loss of a single hydrogen bond between LeuT and a single substrate molecule bound at the S1 site.

Because the stoichiometry values from the ITC experiments ranged from 0.7 to 0.8, we were compelled to determine how much residual substrate remained bound to LeuT. To measure the amount of 'free' amino acid present in our LeuT samples, we employed quantitative amino-acid analysis (qAAA). The qAAA results (Supplementary Tables 2–7) show that the molar ratio of free Leu to LeuT is approximately 6% for Tyr 108 Phe but is negligible for the wild-type preparations. The presence of more free Leu in the Tyr 108 Phe preparations was unexpected and may be due to variations in individual membrane preparations as well as variability in qAAA determinations. Even if all of the free Leu is bound to LeuT, however, the fraction of LeuT bound with substrate does not fully account for the substoichiometric values obtained from ITC. Possible explanations for the substoichiometric binding of substrate are that the LeuT samples used in the experiments contain trace amounts of contaminating proteins, as judged by SDS-polyacrylamide gel electrophoresis (Supplementary Fig. 1), that there is a small amount of protein aggregation, as judged by fluorescence-detection size-exclusion chromatography¹⁸ (Supplementary Fig. 1), or that a fraction of LeuT is not competent to bind substrate.

To corroborate the binding parameters obtained by ITC, we used equilibrium dialysis to measure $[^3\text{H}]\text{Leu}$ binding to LeuT. Data for wild-type LeuT and the Tyr 108 Phe mutant were well fitted by a single-site binding equation (Fig. 1c, d) with respective stoichiometries of 0.73 ± 0.03 and 0.72 ± 0.02 (Supplementary Table 1). Taken together, both the ITC and the equilibrium dialysis data are consistent with there being a single substrate-binding site. The observed differences between wild-type LeuT and Tyr 108 Phe demonstrate that we can use the LeuT crystal structure to perturb binding of substrate to the S1 site both specifically and predictably.

We next probed the presence of the S2 site by asking whether mutations in this proposed site would also measurably perturb binding of substrate to LeuT. In fact, it is claimed that mutation of Leu 400 to Cys ablates Leu binding to the S2 site, reducing overall binding to LeuT by approximately one-half⁶. We therefore measured $[^3\text{H}]\text{Leu}$ binding to mutants Leu 400 Ala and Leu 400 Cys. Using equilibrium dialysis, we observed that the extent of Leu binding to Leu 400 Ala was comparable to that for the wild-type transporter (Fig. 1c and Supplementary Table 1). This conclusion was reinforced using the scintillation proximity assay (SPA) method¹⁹ to compare $[^3\text{H}]\text{Leu}$ binding with wild type, Leu 400 Ala and Leu 400 Cys (Fig. 2a). We find that neither the Leu 400 Ala nor the Leu 400 Cys mutant shows any significant change in Leu binding, as measured by maximum binding capacity or dissociation constant, relative to wild-type LeuT (Supplementary Table 1).

A limitation of the SPA method is the unreliable determination of the scintillant counting efficiency, which in turn complicates an accurate conversion of measured radioactivity in counts per minute to moles of radioligand. To circumvent the need for this transformation, we quantified the binding-site stoichiometry by titrating transporter protein at 20-fold excess over K_d with 0.06–3.0 molar equivalents of $[^3\text{H}]\text{Leu}$ ²⁰. The resulting response is initially first order with respect to Leu concentration, as binding sites are in excess over ligand. When binding reaches saturation, binding is zeroth order with respect to Leu concentration. The intersection abscissa of the first-order and zeroth-order linear regressions provides the ligand concentration equivalent to the binding-site concentration, thus defining a stoichiometric value that is independent of ordinate radioactivity conversions. Using this method, we measured $[^3\text{H}]\text{Leu}$ binding to wild-type LeuT and to the Leu 400 Ala

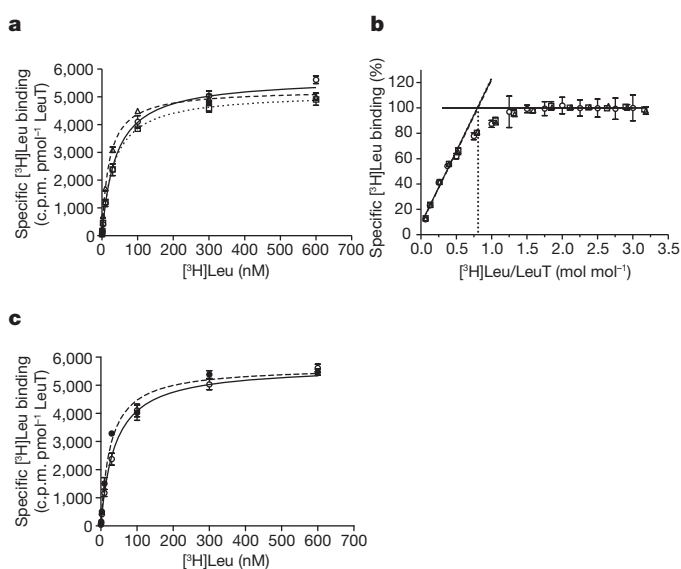


Figure 2 | Leu binding measured by scintillation proximity assays.

a, Saturation binding isotherms and nonlinear regression analysis for wild-type LeuT (open circle, solid line), Leu 400 Ala mutant (open triangle, dashed line) and Leu 400 Cys mutant (open square, dotted line). c.p.m., counts per minute. **b**, Saturation binding at high LeuT concentration ($\sim 20K_d$), quantifying substrate-binding stoichiometry. Symbols and lines are as in **a**. **c**, Saturation binding for wild-type LeuT in the absence (same data as in **a**) or presence of 1 mM clomipramine (closed circle, dashed line). Error bars, s.e.m.; $n = 2$.

and Leu 400 Cys mutants (Fig. 2b). For each of these transporters, binding-site saturation occurs at a nearly identical ligand concentration, each corresponding to a substrate-to-transporter stoichiometry of about 0.8, confirming that mutations at the Leu 400 position do not decrease the binding capacity of LeuT for Leu (Supplementary Table 1).

We performed a final saturation binding analysis to assess the effect of clomipramine, an inhibitor of LeuT transport^{21,22} that was proposed to displace Leu binding from the S2 site¹⁶. We saw no change in the binding of Leu to wild-type LeuT in the presence of 10 nM LeuT and 1 mM clomipramine, thus indicating that Leu- and clomipramine-binding sites do not overlap (Fig. 2c and Supplementary Table 1). This is consistent with previous data indicating that clomipramine is a non-competitive inhibitor of LeuT transport²¹.

To augment our assessment of binding-site stoichiometry, we next asked whether LeuT-catalysed transport is better modelled by a single-site kinetic model or one in which two substrates are bound. Previously reported flux measurements for several substrates showed that LeuT steady-state kinetics is well described by single-site Michaelis–Menten parameters. The overall slow turnover rate of LeuT under those conditions, however, may have obscured the detection of more complex kinetic behaviour. Here we sought to re-evaluate the kinetics of Ala transport under conditions tailored to promote higher turnover, to determine whether transport kinetics are better fitted by a one- or a two-site model. We first determined that uptake is more robust at low (acidic) pH values, with a maximum at pH 5, and that mutation of Lys 288, a residue protruding into the hydrophobic portion of the membrane bilayer¹⁴, to Ala (LeuT^K) further enhanced substrate flux (Supplementary Fig. 2). Steady-state kinetics for Ala uptake by LeuT^K under optimized conditions was measured in the presence of a 200 mM inward Na^+ gradient. The data well fitted the Michaelis–Menten rectangular hyperbola with a Michaelis constant of $K_m = 0.79 \pm 0.06 \mu\text{M}$ and a maximal velocity of $V_{\text{max}} = 11,006 \pm 281 \text{ pmol min}^{-1} \text{ mg}^{-1}$ (Fig. 3a). The corresponding turnover number is $k_{\text{cat}} = 0.65 \text{ min}^{-1}$, which is about sixfold higher than that measured for wild-type LeuT at pH 7 with a 100 mM Na^+ gradient¹⁵ (Supplementary Table 8).

We reasoned that transport would be further stimulated by including valinomycin. Addition of this K^+ -selective ionophore will induce a

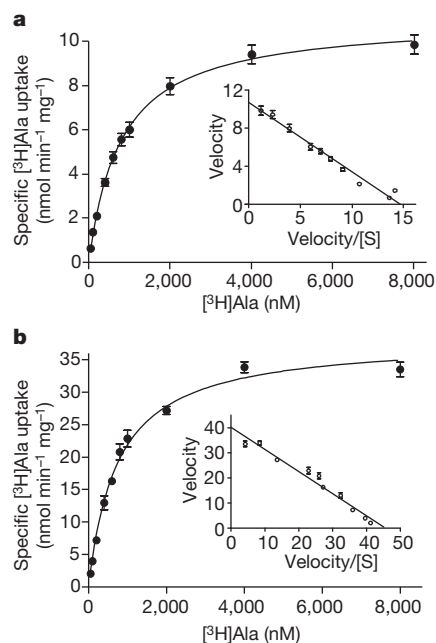


Figure 3 | Transport kinetics of $[^3\text{H}]\text{Ala}$ uptake. **a**, Steady-state Ala uptake as a function of Ala concentration at pH 5. Inset, the corresponding Eadie-Hofstee plot with linear regression ($r^2 = 0.93$). Error bars, s.e.m.; $n = 4$. **b**, Steady-state Ala uptake at pH 5 in the presence of valinomycin to induce a membrane potential. Inset, the corresponding Eadie-Hofstee plot with linear regression ($r^2 = 0.96$). Error bars, s.e.m.; $n = 2$. S, substrate.

negative-inside membrane potential and prevent the build-up of positive charge inside the liposomes during transport. With valinomycin present, k_{cat} increased to 2.3 min^{-1} yet K_{m} remained nearly unchanged at $0.75 \pm 0.06 \mu\text{M}$ (Fig. 3b and Supplementary Table 8). Similar to transport under membrane-neutral conditions, valinomycin-stimulated transport is well fitted by a single-site Michaelis-Menten kinetic model.

In conjunction with the Michaelis-Menten modelling, the steady-state kinetic data were fitted with alternative kinetic models that describe kinetic mechanisms involving two binding sites: the Hill equation²³ for a random-order, cooperative-binding response; and a two-site, ordered-binding kinetic model²⁴. Data fitted to the Hill equation converged with a Hill slope of $n_{\text{H}} = 0.96 \pm 0.03$, indicating that there are not multiple interacting substrate sites underlying the kinetic behaviour of LeuT. A two-site, ordered-binding reaction scheme, which provides explicit treatment for both singly and doubly occupied transporter complexes²⁴, was fitted to the flux data. Although V_{max} was calculated to be $10,965 \pm 308 \text{ pmol min}^{-1} \text{ mg}^{-1}$, which is nearly identical to the Michaelis-Menten model, the apparent dissociation constant, K_{S} , and the dissociation coefficient, α , converged to $6.8 \pm 22 \text{ nM}$ and 114 ± 360 , respectively, indicating that the parameters are not well fitted by the data.

In conclusion, we have examined the stoichiometry of substrate binding to LeuT using multiple methods, and find consistent evidence for a single, high-affinity substrate-binding site. We find no evidence to support the notion that mutation of Leu 400 to Ala or Cys, or the presence of clomipramine, perturbs the stoichiometry of substrate binding. Furthermore, the kinetics of substrate flux is best fitted by a single-substrate kinetic model. Taken together, these data refute the two-substrate binding model for LeuT¹⁶ and are consistent with previously determined crystallographic and functional data^{14,15,21}. The mechanistic implications of our work are that transport of substrate by LeuT occurs through a singly occupied intermediate where substrate is bound to a central, high-affinity site (the S1 site; Fig. 4). We maintain, however, that substrate may indeed transiently bind to weak, low-affinity sites as it transits from the extracellular solution to the S1 site and from the S1 site to the intracellular solution, as suggested by previous structural and computational studies^{6,15}.

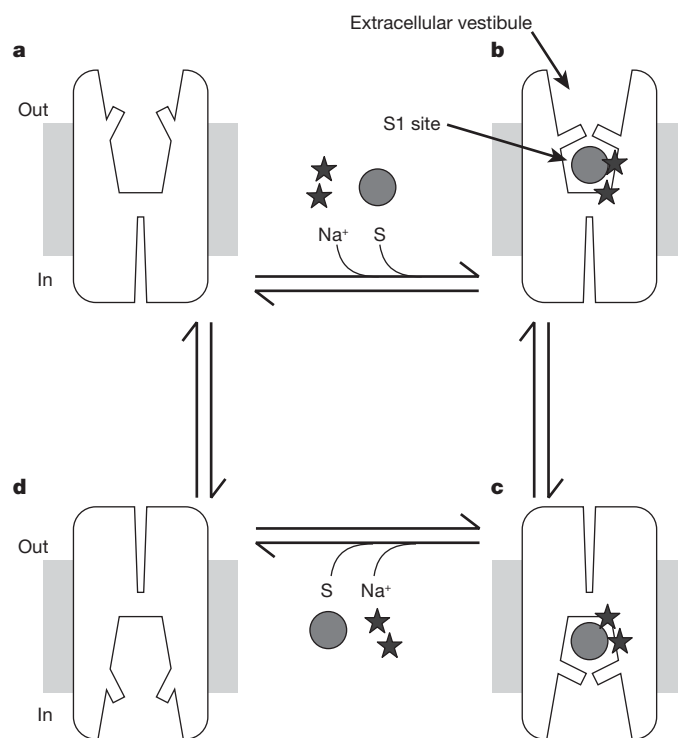


Figure 4 | LeuT mechanism. Starting from the apo transporter in an open-to-outside conformation (**a**), substrate (S) and sodium ions bind, forming the outward-facing occluded conformation (**b**) characterized by closure of a 'thin gate' over the S1 substrate-binding site². Clomipramine, which inhibits transport, binds in the extracellular vestibule^{21,22} directly above the thin gate, near the putative S2 site¹⁶. The substrate- and ion-bound transporter undergoes structural isomerization to form the inward-facing conformation (**c**), allowing release of substrate and ions to the intracellular solution, thereby generating an open-to-inside apo transporter (**d**) that isomerizes to the open-to-outside conformation (**a**).

METHODS SUMMARY

We washed membranes containing LeuT or mutants three times with buffer containing 50 mM Tris-HCl (pH 8.0) and 10 mM 1,4,7,10,13-pentaoxacyclopentadecane (15-crown-5)¹⁷, and purified them as described in either ref. 14 (ITC and equilibrium dialysis) or ref. 16 (SPA). For ITC experiments²⁵, we determined the protein and Leu concentrations and the residual free-amino-acid content of purified LeuT by qAAA (Supplementary Tables 1–6). An extinction coefficient of $136,459 \text{ cm}^{-1} \text{ M}^{-1}$ was empirically determined by qAAA measurements of LeuT. We performed ITC experiments at 25°C using an ITC₂₀₀ calorimeter (MicroCal) with either $20 \mu\text{M}$ wild-type or $30 \mu\text{M}$ Tyr 108 Phe LeuT in the cell, and titrated with $200 \mu\text{M}$ or $500 \mu\text{M}$ L-Leu, respectively. Equilibrium dialysis experiments were performed by placing $100 \mu\text{l}$ of 60 nM wild-type LeuT, 94 nM Leu 400 Ala or $5.7 \mu\text{M}$ Tyr 108 Phe in the sample chamber of a Rapid Equilibrium Dialysis Device plate (Thermo Scientific) and $300 \mu\text{l}$ of $[^3\text{H}]\text{Leu}$ at $0.3\text{--}30 \mu\text{M}$ in the buffer chamber. Saturation binding experiments using SPA were performed with 10 nM protein incubated with $2 \text{ mg ml}^{-1} \text{ Cu}^+$ -Ysi SPA beads (GE Healthcare) in the presence of $0.3\text{--}600 \text{ nM}$ $[^3\text{H}]\text{Leu}$. For measurement of binding-site concentration using SPA, we used 400 nM protein and $25\text{--}1,200 \text{ nM}$ $[^3\text{H}]\text{Leu}$. For transport assays, LeuT proteoliposomes were prepared as previously described¹⁴ in a 1:100 protein/lipid weight ratio. Transport assays were conducted at 27°C with $10 \mu\text{g ml}^{-1}$ protein. To determine steady-state kinetic parameters, we allowed reactions to proceed for 2 min and quenched, filtered and analysed them using GRAPHPAD PRISM 4 as previously described¹⁴.

Full Methods and any associated references are available in the online version of the paper at www.nature.com/nature.

Received 3 September; accepted 12 October 2010.

1. Abramson, J. & Wright, E. M. Structure and function of Na^+ -symporters with inverted repeats. *Curr. Opin. Struct. Biol.* **19**, 425–432 (2009).
2. Krishnamurthy, H., Piscitelli, C. L. & Gouaux, E. Unlocking the molecular secrets of sodium-coupled transporters. *Nature* **459**, 347–355 (2009).

3. Sobczak, I. & Lolkema, J. S. Structural and mechanistic diversity of secondary transporters. *Curr. Opin. Microbiol.* **8**, 161–167 (2005).
4. Hahn, M. K. & Blakely, R. D. Monoamine transporter gene structure and polymorphisms in relation to psychiatric and other complex disorders. *Pharmacogenomics J.* **2**, 217–235 (2002).
5. Amara, S. G. & Sonders, M. S. Neurotransmitter transporters as molecular targets for addictive drugs. *Drug Alcohol Depend.* **51**, 87–96 (1998).
6. Celik, L., Schiøtt, B. & Tajkhorshid, E. Substrate binding and formation of an occluded state in the leucine transporter. *Biophys. J.* **94**, 1600–1612 (2008).
7. Rosenberg, A. & Kanner, B. I. The substrates of the gamma-aminobutyric acid transporter GAT-1 induce structural rearrangements around the interface of transmembrane domains 1 and 6. *J. Biol. Chem.* **283**, 14376–14383 (2008).
8. Vandenberg, R. J., Shaddock, K. & Ju, P. Molecular basis for substrate discrimination by glycine transporters. *J. Biol. Chem.* **282**, 14447–14453 (2007).
9. Faham, S. *et al.* The crystal structure of a sodium galactose transporter reveals mechanistic insights into Na⁺/sugar symport. *Science* **321**, 810–814 (2008).
10. Weyand, S. *et al.* Structure and molecular mechanism of a nucleobase-cation-symport-1 family transporter. *Science* **322**, 709–713 (2008).
11. Shaffer, P. L., Goehring, A., Shankaranarayanan, A. & Gouaux, E. Structure and mechanism of a Na⁺-independent amino acid transporter. *Science* **325**, 1010–1014 (2009).
12. Gao, X. *et al.* Structure and mechanism of an amino acid antiporter. *Science* **324**, 1565–1568 (2009).
13. Fang, Y. *et al.* Structure of a prokaryotic virtual proton pump at 3.2 Å resolution. *Nature* **460**, 1040–1043 (2009).
14. Yamashita, A. *et al.* Crystal structure of a bacterial homologue of Na⁺/Cl[−]-dependent neurotransmitter transporters. *Nature* **437**, 215–223 (2005).
15. Singh, S. K., Piscitelli, C. L., Yamashita, A. & Gouaux, E. A competitive inhibitor traps LeuT in an open-to-out conformation. *Science* **322**, 1655–1661 (2008).
16. Shi, L. *et al.* The mechanism of a neurotransmitter:sodium symporter-inward release of Na⁺ and substrate is triggered by substrate in a second binding site. *Mol. Cell* **30**, 667–677 (2008).
17. Christensen, J. J., Hill, J. O. & Izatt, R. M. Ion binding by synthetic macrocyclic compounds. *Science* **174**, 459–467 (1971).
18. Kawate, T. & Gouaux, E. Fluorescence-detection size-exclusion chromatography for precrystallization screening of integral membrane proteins. *Structure* **14**, 673–681 (2006).
19. Quick, M. & Javitch, J. A. Monitoring the function of membrane transport proteins in detergent-solubilized form. *Proc. Natl Acad. Sci. USA* **104**, 3603–3608 (2007).
20. Hansen, S. B. *et al.* Tryptophan fluorescence reveals conformational changes in the acetylcholine binding protein. *J. Biol. Chem.* **277**, 41299–41302 (2002).
21. Singh, S. K., Yamashita, A. & Gouaux, E. Antidepressant binding site in a bacterial homologue of neurotransmitter transporters. *Nature* **448**, 952–956 (2007).
22. Zhou, Z. *et al.* LeuT-desipramine structure reveals how antidepressants block neurotransmitter uptake. *Science* **317**, 1390–1393 (2007).
23. Hill, A. V. The combinations of haemoglobin with oxygen and with carbon monoxide. I. *Biochem. J.* **7**, 471–480 (1913).
24. Segel, I. H. *Enzyme Kinetics: Behavior and Analysis of Rapid Equilibrium and Steady-State Enzyme Systems* 398–401 (Wiley, 1975).
25. Wiseman, T., Williston, S., Brandts, J. F. & Lin, L. N. Rapid measurement of binding constants and heats of binding using a new titration calorimeter. *Anal. Biochem.* **179**, 131–137 (1989).

Supplementary Information is linked to the online version of the paper at www.nature.com/nature.

Acknowledgements We thank T. Pan and R. Hibbs for comments and L. Vaskalis for assistance with figures. C.L.P. was supported by the ARCS foundation and NIH training grant T32 DK007680. This work was supported by the NIH. E.G. is an investigator with the Howard Hughes Medical Institute.

Author Contributions C.L.P., H.K. and E.G. designed the research; C.L.P. and H.K. performed the research and analyzed the data; and C.L.P., H.K. and E.G. wrote the paper.

Author Information Reprints and permissions information is available at www.nature.com/reprints. The authors declare no competing financial interests. Readers are welcome to comment on the online version of this article at www.nature.com/nature. Correspondence and requests for materials should be addressed to E.G. (gouauxe@ohsu.edu).

METHODS

Mutagenesis and protein purification. Site-directed mutants of LeuT were prepared using PCR. The Tyr 108 Phe mutant of LeuT was made in the background of the Lys 288 Ala mutation (Tyr 108 Phe–LeuT^K). Wild-type LeuT and mutants bearing a carboxy-terminal His₈ tag were expressed in C41 cells and purified as previously described¹⁴ with the exception that cell membranes were washed three times with 50 mM Tris-HCl (pH 8.0) supplemented with 10 mM 1,4,7,10,13-pentaazacyclopentadecane (15-crown-5)¹⁷ to facilitate the removal of bound Leu and augment the generation of apo-LeuT. Purified protein destined for equilibrium dialysis and ITC assays was concentrated to 5–30 μ M using a concentrator with a 50-kDa cut-off, and dialysed at 4 °C for 24 h against buffer I (20 mM Tris-citrate (pH 7.0), 200 mM NaCl and 1 mM dodecyl maltoside), with three buffer changes. Protein for scintillation proximity assays was purified in buffer II¹⁶ (150 mM Tris-MES (pH 7.5), 50 mM NaCl, 1 mM dodecyl maltoside and 20% glycerol). Equilibrium dialysis assays on wild-type LeuT demonstrate no notable differences using either buffer I or buffer II. Reducing conditions were maintained for preparations of the Leu 400 Cys mutant using 2 mM tris(2-carboxyethyl)phosphine (TCEP). The concentration of protein and ligand used in the ITC measurements was directly determined by qAAA on material that was subjected to overnight acid hydrolysis in 0.02 N HCl. The extent to which the purified LeuT starting material was contaminated by residual Leu was determined by qAAA of non-hydrolysed material to measure the free-amino-acid content. All qAAA measurements were performed at the Keck Biotechnology Resource Laboratory at Yale University. All other protein concentrations were estimated by absorbance spectroscopy using a molar extinction coefficient of 136,459 cm^{−1} M^{−1} at λ = 280 nm for the His-tagged protein, derived from the extinction coefficient predicted from primary sequence (ProtParam; <http://expasy.org/tools/protparam.html>) and empirically corrected by qAAA measurements of LeuT (A_{280} of unity = 0.43 mg ml^{−1}). Sample purity was assessed by SDS-polyacrylamide gel electrophoresis under reducing conditions using 12.5% Tris-Gly gels (Supplementary Fig. 1a). Protein dispersity was monitored by fluorescence-detection size-exclusion chromatography¹⁸ measuring intrinsic Trp fluorescence (Supplementary Fig. 1b).

Isothermal titration calorimetry. A solution of wild-type LeuT or Tyr 108 Phe–LeuT^K (at 20 or 30 μ M, respectively, in buffer I) was loaded into the sample cell of an ITC₂₀₀ calorimeter (MicroCal). L-Leu at 200 or 500 μ M for titrations with wild-type LeuT or Tyr 108 Phe–LeuT^K, respectively, was dissolved in buffer I and loaded into the injection syringe. Before data collection, the system was equilibrated to 25 °C with the stirring speed set to 1,000 r.p.m. Titration curves for Tyr 108 Phe–LeuT^K binding Leu were generated by five successive 1.5- μ l injections followed by fourteen 2.0- μ l injections at 180-s intervals. Titration curves for wild-type LeuT binding Leu were generated with nineteen 2.0- μ l injections at 180-s intervals. Control injections of ligand into buffer I without protein were done to determine background corrections. The integrated heats from each injection, normalized to the moles of ligand per injection, were fitted to a single-site binding isotherm²⁵ using ORIGIN 7. Final values of K_d , stoichiometry (N), ΔH and $-T\Delta S$ were determined from the average of two to four ITC runs.

Equilibrium dialysis. For each replicate, 100 μ l of either 60 nM wild-type LeuT, 94 nM Leu 400 Ala or 5.7 μ M Tyr 108 Phe–LeuT^K protein in buffer I was placed in the sample chamber of a Rapid Equilibrium Dialysis Device plate (Thermo Scientific) and 300 μ l of [³H]Leu at 0.3–30 μ M (0.27 Ci mmol^{−1}) in buffer I was placed in the buffer chamber. The unit was covered with sealing tape and incubated at room temperature (23 °C) on a shaker for 6 h. To determine the concentrations of total and free ligands, 10- μ l aliquots were removed from the sample and

buffer chambers, respectively, and added to 6 ml of Ultima Gold scintillation fluid. The concentrations of free and total Leu were calculated from the tSIE (transformed spectral index of an external standard)-corrected d.p.m. (disintegrations per minute) values measured using a liquid scintillation counter. Data were analysed as a single-site binding function. Values of K_d , B_{\max} (maximal binding) and N were determined from the average of two independent experiments, with two to four replicates each.

Scintillation proximity assays. For saturation binding analysis, 10 nM LeuT was incubated with 2 mg ml^{−1} Cu⁺-YSi SPA beads in buffer II in the presence of 0.3–600 nM [³H]Leu (10.8 Ci mmol^{−1}). The reactions were mixed on an orbital microplate shaker at room temperature. Plate readings were taken at 2, 20, 40 and 60 h using a Wallac Microbeta plate counter, although for each experiment no significant change was observed after 20 h incubation. SPA experiments to quantify the binding-site concentration in each sample were performed as described above, but using 400 nM LeuT and 25–1,200 nM [³H]Leu (10.8 Ci mmol^{−1}). For all assays, specific binding was calculated by subtracting the background radioligand binding assessed by duplicate binding measurements in the presence of 5 mM L-Ala.

Transport time course. LeuT was reconstituted into lipid vesicles as previously described¹⁴ using internal buffer appropriate for the experiment (20 mM HEPES-Tris (pH 7), 200 mM KCl or 20 mM citrate-Tris (pH 6, pH 5 or pH 4) and 200 mM KCl). Transport reactions were assembled by diluting LeuT proteoliposomes to a final protein concentration of 10 μ g ml^{−1} in external buffer (20 mM HEPES-Tris (pH 7.0), 200 mM NaCl or 20 mM citrate-Tris (pH 6.0, pH 5.0 or pH 4.0) and 200 mM NaCl) at 27 °C with 500 nM [³H]Ala (83 Ci mmol^{−1}). Uptake was followed by removing and quenching 100- μ l aliquots of the reaction in ice-cold internal buffer at various time points up to 40 min. Reactions were filtered and analysed as previously described¹⁴. Non-specific uptake was assessed by repeating the time course for the same liposome preparation under identical conditions except for the replacement of external NaCl by KCl. Non-specific uptake was then subtracted from the total uptake measured to calculate the specific uptake. Each experiment was performed in duplicate.

Steady-state kinetics. LeuT proteoliposomes at 10 μ g ml^{−1} were incubated with 0.050–8.0 μ M [³H]Ala (8.3 Ci mmol^{−1}) at 27 °C for 2 min in external buffer (20 mM citrate-Tris (pH 5.0) and 200 mM NaCl) with or without 50 nM valinomycin. Preliminary time course experiments done with 0.050, 0.40, 1.0 and 8.0 μ M [³H]Ala established that transport remained linear through the 2-min time point. Data from two to four experiments, each repeated in duplicate, were fitted to the Michaelis–Menten equation and analysed by linear regression to an Eadie–Hofstee transformation.

To test for multisite cooperative kinetics, data were modelled according to the Hill equation, $v = (V_{\max}[S]^n)/(K' + [S]^n)$, where v is the reaction velocity, n is the Hill coefficient, K' is the apparent dissociation constant, allowing the parameters n , K' and V_{\max} to float. Alternatively, data were modelled by a two-site, ordered-binding equation, $v = (V_{\max}[S]^2/\alpha K_S^2)/(1 + [S]/K_S + [S]^2/\alpha K_S^2)$, allowing the parameters α , K_S and V_{\max} to float. To compare the Michaelis–Menten model with the ordered-binding model, the F -test statistic was calculated according to the GRAPHPAD PRISM manual using the following equation: $F = ((SS_{\text{null}} - SS_{\text{alt}})/(DF_{\text{null}} - DF_{\text{alt}}))/((SS_{\text{alt}}/DF_{\text{alt}}))$, where 'null' and 'alt' refer to the Michaelis–Menten and ordered-binding models, respectively; SS is the absolute sum of squares of the variance for each model; and DF is the number of degrees of freedom for each model. For the Michaelis–Menten model, SS and DF were 3.564×10^7 and 68, respectively. For the ordered-binding model, SS and DF were 3.579×10^7 and 67, respectively.

CAREERS

EMPLOYMENT TRENDS Academia is the top destination for US PhD students **p.1135**

ONLINE Catch up on the latest Postdoc Journal entries go.nature.com/yd2cjs

NATUREJOBS For the latest career listings and advice www.naturejobs.com

G. HELLIER/ROBERT HARDING



Doha in Qatar with the Pearl Monument in the foreground. The city is host to branch campuses of renowned universities from around the world.

MIDDLE EAST

The growth of a desert jewel

Qatar's research machine is a work in progress, but its funding opportunities are already luring international scientists to its increasing number of institutions.

BY WALEED AL-SHOBAKKY

Khaled Machaca enjoys the high-risk, high-reward aspects of a start-up project. His latest is particularly demanding. Machaca has been tasked with establishing a research programme at a newly founded medical college in Qatar: a small Middle Eastern country whose science enterprise, initiated only in the past decade, is itself a start-up of sorts.

The challenges are manifold. Machaca has had to convince funders, the larger medical community and the public of the importance of his work. He has also had to source lab equipment in a place with few suppliers. To foster international collaborations, crucial to Qatari researchers' success, he has had to help craft and customize a code of research ethics, created by Qatar's Supreme Council of Health, that complies with both US and Qatari laws. And he has had to convince young scientists that they can advance their careers and conduct cutting-edge science in a country known

less for research than for hosting the news network Al-Jazeera and, as was announced this month, the 2022 soccer World Cup.

"We had serious challenges," says Machaca, who is associate research dean at Weill Cornell Medical College in Qatar (WCMC-Q), based in Doha. But he relishes the notion of building a programme from scratch. And the country has a big advantage: money. Scientists working in Qatar will find good funding and ample opportunities for big projects, but, like Machaca, they might have to deal with rigid bureaucracy, evolving research-ethics regulations and rules — on stem-cell research, for example — that could limit collaborative ventures. These trade-offs will help to determine Qatar's success as it attempts to build a sustainable science enterprise.

OASIS FOR RESEARCH

Qatar's efforts to be hospitable to science come amid a region-wide drive to engage with international — mostly Western — academia and

scientific centres. From the early 2000s to mid-2008 (when oil peaked at US\$147 a barrel), fuel prices repeatedly hit record highs, bringing a petrodollar downpour to the six oil-rich Gulf states of Saudi Arabia, Kuwait, the United Arab Emirates (UAE), Qatar, Bahrain and Oman. The revenues have driven attempts to energize ailing higher-education and research centres and to create new ones. This coincided with belt-tightening among academic and research institutions in Europe and North America — a trend that increased with the global financial crisis.

Saudi Arabia is pushing ahead with a programme that pairs international research centres such as Germany's Max Planck Institutes with domestic universities to modernize local science departments. And 2009 saw the launch of the more ambitious, more visible King Abdullah University of Science and Technology (KAUST), a graduate-level research university in Thuwal with a US\$10-billion endowment. In the UAE, Abu Dhabi campuses of major higher-education and research institutions such as ►

► as New York University and the Sorbonne University in Paris have been set up. And in 2006, Qatari emir Hamad Bin Khalifa Al-Thani pledged that 2.8% of the country's gross domestic product (which was about \$100 billion in 2008 according to the Economist Intelligence Unit in London) would be spent on scientific research.

In general, government leaders in the Gulf states are setting up multibillion-dollar research projects and high-profile partnerships not only because they can, but because they must. "The Gulf countries are in a developmental phase," says Kristin Diwan, a Gulf expert at the American University in Washington DC. They see a genuine need, she says, for the "skills and learning that are required to run their economies" and to diversify beyond the rather volatile hydrocarbon sector.

Thus far, sustained Qatari government funding has helped Machaca to increase his diabetes and obesity research programme from a handful of staff to 60 faculty members, postdoctoral fellows and research-support personnel in less than two years. He says that Qatar's research and funding environment is preferable to what many would find in the United States, given that country's recent science-funding woes.

In Qatar, the job of luring high-calibre researchers goes to the Qatar Foundation for Education, Science and Community Development and its sprawling offshoot institutions, which include branch campuses of US and European institutions, domestic research centres and the Qatar National Research Fund (QNRF). This agency aims to attract researchers from far beyond the country's borders to collaborate with Qatar-based scientists on problems that the tiny state confronts — from diabetes to network security. The main QNRF grant mechanism, the National Priorities Research Program (NPRP), has over the first three years of its existence doled out close to a quarter of a billion US dollars on 266 research projects, with participants from more than 30 countries.

That funding comes with conditions that are, at times, onerous. Collaborations must involve a Qatar-based researcher and most of the money must be spent in Qatar. The Qatar Foundation's July 2010 request for proposals states that at least half of the proposed funded research days must be spent in Qatar; and at least 65% of the total annual budget must be used there.

"We needed to make sure that international researchers collaborate with scientists based in Qatar while allowing at least 50% of the effort



"We needed international researchers to collaborate with scientists in Qatar."

Abdul Sattar Al-Taie

to be conducted inside Qatar," says Abdul Sattar Al-Taie, executive director of the QNRF. "That should contribute to our main goal of building a research environment in the country." Arguably, such provisions help to diversify Qatar's economy for the post-hydrocarbon era by transferring knowledge from foreign countries to researchers inside Qatar.

But the rules mean that Qatar's abundant funds can go only so far in attracting new research proposals — the small nation has a limited number of domestic collaborators. Eventually its science base will become "saturated," says James Holste, former associate research dean at Texas A&M University in Qatar, the Doha branch of the institution based in College Station. At that point, investments will have drastically diminished returns.

Already there are signs of strain. In the last NPRP cycle, Texas A&M in Qatar limited the number of proposals that faculty members could submit; its researchers qualify as Qatar-based, and demand for them from international institutions was so high that the school had to step in to regulate collaborations. "We were getting to the point where the labs were full and we had no place to put the people," says Holste.

Also laborious is the complex documentation required by the NPRP to detail how grant money is spent. It can be difficult, for example, to secure extra funding for a project in progress, says Bernardine Dias, a robotics researcher at Carnegie Mellon University's campuses in both Doha and Pittsburgh, Pennsylvania. Inflexibility in a funding programme, says Holste, is "a kiss of death". He advises the programme to mitigate excessive paperwork and documentation by affording its officers more discretion, according to the peculiarities of each project. One project might need more equipment; another might involve hiring postdocs to make up for the absence of PhD students (so far, no graduate programmes are offered in Qatar).

CULTURE CLASH

Machaca has experienced, first-hand, another challenge for scientists in Qatar: accommodating research practices that may contrast with those in other nations. "Most of those differences are culturally oriented," says Machaca, noting, for example, the particular importance in Qatar of involving family members during the informed-consent process.

Generally, where rules differ, researchers are expected to adopt the more stringent regulation. In such situations, the level of international collaboration may complicate matters.

The Qatar Foundation has acknowledged the need to rethink how researchers report expenses and when extra funds should be allocated. The NPRP procedures can be strict, says Amer Al Saady, science adviser to the Qatar Foundation and a member of the QNRF's steering committee. "The QNRF is being cautious, or perhaps over-cautious, in adopting this attitude," he says, emphasizing that the NPRP is only a few years

old. Complicating matters is a legacy of rare but infamous cases of plagiarism and abuse of funds. Caution will prevail, says Al Saady, until a more robust research culture has been established.

Already the QNRF is tweaking the process. "Compared with the first cycle, the QNRF has improved a lot," says Dias, who in the first NPRP cycle received funding for two proposals of about US\$750,000 each. "And what is important is that it is taking feedback from the people who are submitting proposals." The foundation has asked the outgoing dean of Carnegie Mellon's business school in Qatar to suggest ways of simplifying expenditure reporting and accommodation of unforeseen expenses.

At KAUST and the UAE's New York University Abu Dhabi Institute (NYUAD), initiatives to engage Western researchers generally entail fewer restrictions. Outside researchers who receive funding from KAUST are not required to partner with Saudi Arabia-based researchers; usually, the university just requires grant recipients to participate in a couple of seminars or workshops in the country each year, to report on their research findings and progress.

KAUST and NYUAD do have their own constraints. KAUST awards its grants to faculty members in specific institutions with which the university has signed collaboration agreements; and NYUAD bestows funds only on eligible faculty members who work full-time at New York University or NYUAD. NPRP grants are open to any researcher, from academia or industry.

Qatar's sizeable financial resources, meanwhile, allow the QNRF to fund a relatively high proportion of proposals. In the most recent cycle, for example, its success rate was 23% for



"The Qatar National Research Fund has improved a lot."

Bernardine Dias

medical and health sciences, says Al-Taie. By comparison, the US National Institutes of Health accepted approximately 20.6% of proposals. As the number of applicants to the NPRP has increased, the foundation has had to decide whether to stay on budget and turn down more proposals, or increase the budget and fund further investigators. The latter choice won out, says Al Saady.

Qatar may offer funding opportunities, but that does not guarantee top recruits. A paucity of graduate students adds to the difficulties of keeping a lab. Currently, scientists at Doha campuses get graduate students from the main campuses on short-term contracts, one or two semesters, or hire postdocs to do the work that PhD students would usually do.

Postdocs, too, may face challenges. Some principal investigators can make it difficult to

garner independence, says Rachel Jones, a postdoctoral fellow in biomedicine at the WCMC-Q. "Others give a looser rein and let their postdocs pursue their own interests as well as their supervisors," she says.

Jones credits support from her postdoc supervisor for helping her to pursue the QNRF's Young Research Scientist Experience Program, launched in May. She received an award of US\$100,000 a year for up to three years, which she views as a bridge to more substantial grants.

Many researchers would like the benefits that come with tenure, an option yet to be offered to faculty members hired at Doha branches (as opposed to those visiting from the US home campuses). This is partly explained by Gulf countries' labour and immigration laws, which frown on recruitment options implying a right of permanent residence. "Everything is set up so people who are not citizens are encouraged to leave after five or ten years," says Holste.

And Qatar and other Gulf countries rarely offer citizenship to expatriates. "A broad extension of citizenship rights to non-nationals would be extremely unpopular," says Diwan. Extensive state welfare programmes in the Gulf, along with the delicate sectarian balance to be maintained between Sunni and Shi'a Muslims, render any programme to naturalize foreigners unpalatable to most. Foreigners wishing to be hired need a Qatari sponsor (who can be an individual, a firm or a government agency). And most contracts span two to five years.

Officials at the branch campuses say that they are discussing options with the Qatar Foundation, and Al Saady notes that proposals to modernize labour laws are under way. Others in the region have proven faster than Qatar on the tenure front. The UAE, which has a thriving trade hub in Dubai, plenty of oil in Abu Dhabi and no sectarian divide, has more open labour and immigration laws than most of its neighbours.

Qatar's litany of challenges has not dissuaded enterprising researchers such as Machaca, who sees a long-term future in the small state. "As a scientist, what do I need? To do cutting-edge science, to publish it, and hopefully in the long term to be able to commercialize it. And of course you want your family to be happy," he says. "Can I do this in Doha? Absolutely." ■

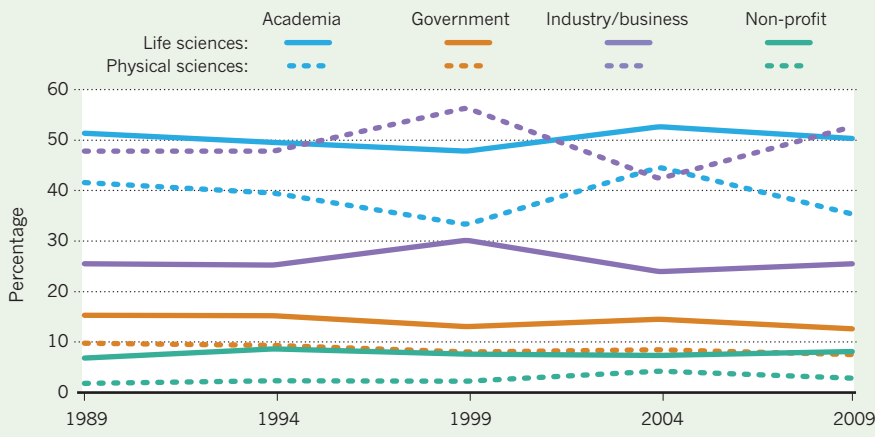
Waleed Al-Shobakky is a freelance writer based in Doha.

CORRECTION

The story 'A helping hand' (*Nature* **468**, 721–723; 2010) inadvertently implied that Anuj Kapadia is a clinical radiologist. He is an assistant professor of radiology.

DIVISION OF LABOUR

Proportion of US doctorate recipients with definite post-graduation employment commitments in the United States, by field and sector.



EMPLOYMENT TRENDS

Drawn to academia

Low salaries and elusive tenure didn't dim the appeal of self-directed research for US scientists last year.

BY KAREN KAPLAN

Despite a struggling economy, lower salaries and an increase in adjunct and contingent positions, a higher proportion of US scientists headed to academia than to any other sector in 2009, according to numbers from the US National Science Foundation (NSF). Published on 3 December, *Doctorate Recipients from US Universities: 2009* includes salary data for the first time in the annual report's 43-year history.

Even with universities offering much lower salaries than industry, half of all life-sciences PhD recipients who had secured jobs said that they were entering academic positions, according to the survey. This proportion, which has varied little since 1989, is a testament to the powerful lure of positions that enable self-directed research, say analysts. "Many scientists want the independence of working on their own research, rather than on what's handed to them," says Mark Fiegenger, an NSF programme manager based in Arlington, Virginia. The NSF received survey responses from 420 US universities and 49,562 PhD recipients.

The industrial sector proffered the highest median early-career salaries — up to US\$95,000 in some instances — in most disciplines in the physical and life sciences. The median for an academic post in biological sciences was \$45,000, compared with \$85,000 for a commercial position in the same subfield, including biochemistry, marine biology and zoology. Other fields had similar disparities.

Academia dominated life-sciences employment in 2009, but industry was stronger for physical scientists, despite changes to job numbers since 2008 that run counter to five-year trends and could be due to pharmaceutical layoffs (see 'Division of labour'). Richard Freeman, an economist at Harvard University in Cambridge, Massachusetts, attributes the five-year trend in part to hiring increases at drug-making and chemical firms. He says that mergers and layoffs will continue to slow the field down.

Industry's constraints will put pressure on academia, which is already pinched by the recession, says Marc Bousquet, an associate professor at Santa Clara University in California who is on the executive council of the American Association of University Professors. Scientists in all fields will struggle to find academic posts — and few of those available will be tenure-track, he says.

The report also uncovers significant pay differences between early-career men and women with PhDs. Men earned up to \$10,000 more than women in nearly all fields except astronomy, where they earned \$30,000 more. Joan Herbers, president of the Association for Women in Science in Alexandria, Virginia, says women need help learning to negotiate salaries and raises. "When you start out at a lower salary," she says, "that dogs you for the rest of your career."

Postdocs earned \$37,500 to \$45,000, which, given their average schedule, Freeman estimates, works out to \$12.50 to \$15 an hour. "Some of the best and brightest people in our country earn a pittance," says Freeman. ■

RECURSION¹

Worlds within worlds.

BY SIMON QUELLEN FIELD

The little man opened the door and stepped into Schmidt's office. "Who let you in here?" asked the surprised Schmidt.

"I just did," the little man said, pointing to the door.

"But that's my bathroom," Schmidt said, rising from his chair.

"No matter," said the little man. "In a moment, you won't care. Because I am about to give you the most amazing thing you have ever seen in your life."

He held out his hand, on which there sat a small blue sphere that seemed to shimmer. Schmidt was about to protest when the little man touched the sphere and pulled on it. It grew as it followed his gesture, until it was a large globe, the continents and oceans easily recognizable, clouds moving slowly across the surface. Schmidt stopped and stared. It was so lifelike. He could see three-dimensional details in the landscape, even birds and aeroplanes as the view got closer.

"We call this the Simulation," the little man said. "It's quite realistic. It uses inputs from satellites, of course, but also from all kinds of cameras all over the world, cell phones, traffic cameras, webcams, television. It's quite up-to-date. You can zoom in on anything you like."

He gestured again, and Schmidt felt a dizzy sensation as the view swooped down through clouds to view a city, and then farther down to view a street corner with busy traffic and pedestrians, all moving and in perfect 3D. He could move his head and see behind people and objects. He felt he could reach in and touch things.

"How do —?" Schmidt began.

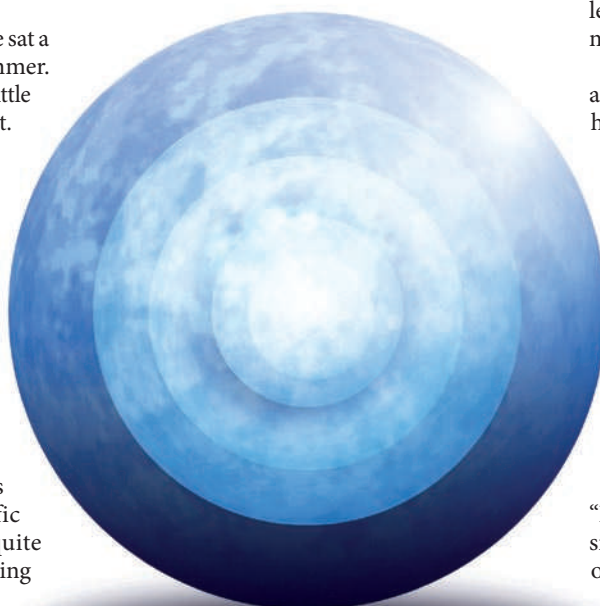
"It's a simulation," the little man said. "There's data input, but most of it is generated. Computers, you know."

The view changed as the little man made subtle movements with his hands. Schmidt seemed to fly through walls, observing people in their homes and at work, going about their routines. A woman brushing her teeth in front of a mirror. A couple arguing at a table in a café. A seductive woman trolling a bar in Paris. A fisherman struggling with a line in Australia.

"It's extremely popular where I come

from," said the little man. "People fly all around, spy on people, hang around women's locker rooms, it's highly addictive. Hardly anything else gets done. People stop talking to each other, stop going to work, they're just fascinated."

Schmidt himself was getting fascinated. It looked so real. He reached his hand out and the sphere responded, moving the scenes around as he gestured. He felt like he was flying, swooping between buildings and under bridges, peering into windows, moving



through solid walls like a ghost. He peeked into corporate boardrooms and spied on meetings in the Kremlin.

"But that's not all," the little man said. "You can go in." He zoomed in on a doorway, until the door was life-sized in front of them. "Any door you like, you just open it and walk in."

He reached for the doorknob, and turned it, pushing the door open. Schmidt looked in, and saw himself in a room that looked just like his office, standing next to a little man with a doorknob in his hand. He swung around and looked at the door to his bathroom, which was now open, and he could see himself looking back.

"How —?" he started to ask.

"Cute trick, eh?" the little man said, closing the door. "You can forget your corporate jet. Anywhere you want to go, you just open the door. That's how I got here, of course."

"That can't be real," Schmidt said, shaking his head.

"No, it isn't," the little man replied. "Like I said, it's a simulation. All done by computers. Collecting and organizing all the world's information, and presenting it in a nice three-dimensional user interface, with natural intuitive gestural inputs. Anyone can learn to use it in seconds, it needs no user manual."

"And you're giving this to me?" Schmidt asked, his gaze still held by the device, his hands still moving to direct the view.

"Free of charge," the little man said. "No catch, it's all yours."

"I can see why people get addicted to this," Schmidt said.

"Yes, that was a problem. Economy went into the crapper, people stopped having kids, food became scarce, things were really going downhill until we came up with this solution."

"What solution was that?" Schmidt asked absently, his attention still riveted on the device in his hands.

"A computer virus," the little man said. "Ingenious, really. It's called infinite recursion. Like putting two mirrors facing each other, so you get a hallway stretching on forever. We put a Simulator inside the Simulator, and the computers spend all their time simulating more simulations, until they don't have any time to do anything else. Everything grinds to a halt after a little while. The toy isn't fun anymore, and people get back to their lives."

"I'm not sure I understand," Schmidt said.

"Give it a minute or two," the little man said. He gestured, and the view zoomed in on Schmidt's office, showing the two men gazing at the sphere. Inside the sphere, two copies of the men were staring at another sphere. "It will come to you," he said. "Or maybe not." ■

Simon Quellen Field is the chief executive of Kinetic MicroScience, where he designs scientific toys and writes books about science, as well as novels in science fiction, mystery and suspense.

1. Field, S. Q. *Nature* **468**, 1138 (2010).

The assembly of a GTPase–kinase signalling complex by a bacterial catalytic scaffold

Andrey S. Selyunin¹, Sarah E. Sutton¹, Bethany A. Weigele¹, L. Evan Reddick¹, Robert C. Orchard¹, Stefan M. Bresson¹,
Diana R. Tomchick² & Neal M. Alto¹

The fidelity and specificity of information flow within a cell is controlled by scaffolding proteins that assemble and link enzymes into signalling circuits^{1,2}. These circuits can be inhibited by bacterial effector proteins that post-translationally modify individual pathway components^{3–6}. However, there is emerging evidence that pathogens directly organize higher-order signalling networks through enzyme scaffolding^{7,8}, and the identity of the effectors and their mechanisms of action are poorly understood. Here we identify the enterohaemorrhagic *Escherichia coli* O157:H7 type III effector EspG as a regulator of endomembrane trafficking using a functional screen, and report ADP-ribosylation factor (ARF) GTPases and p21-activated kinases (PAKs) as its relevant host substrates. The 2.5 Å crystal structure of EspG in complex with ARF6 shows how EspG blocks GTPase-activating-protein-assisted GTP hydrolysis, revealing a potent mechanism of GTPase signalling inhibition at organelle membranes. In addition, the 2.8 Å

crystal structure of EspG in complex with the autoinhibitory Iα3-helix of PAK2 defines a previously unknown catalytic site in EspG and provides an allosteric mechanism of kinase activation by a bacterial effector. Unexpectedly, ARF and PAKs are organized on adjacent surfaces of EspG, indicating its role as a ‘catalytic scaffold’ that effectively reprograms cellular events through the functional assembly of GTPase-kinase signalling complex.

To identify new signalling pathways targeted by bacterial pathogens, we used a human growth hormone (hGH) secretion assay⁹ to measure the ability of type III and type IV effector proteins to regulate vesicle trafficking through the general secretory pathway (Fig. 1a, b). Consecutively, each bacterial effector was tagged with enhanced green fluorescent protein (eGFP) and assessed for localization at host organelles (Fig. 1b). We noted that several type III effectors encoded by the extracellular pathogen enterohaemorrhagic *E. coli* (EHEC) O157:H7 inhibited host trafficking events, whereas effectors secreted by

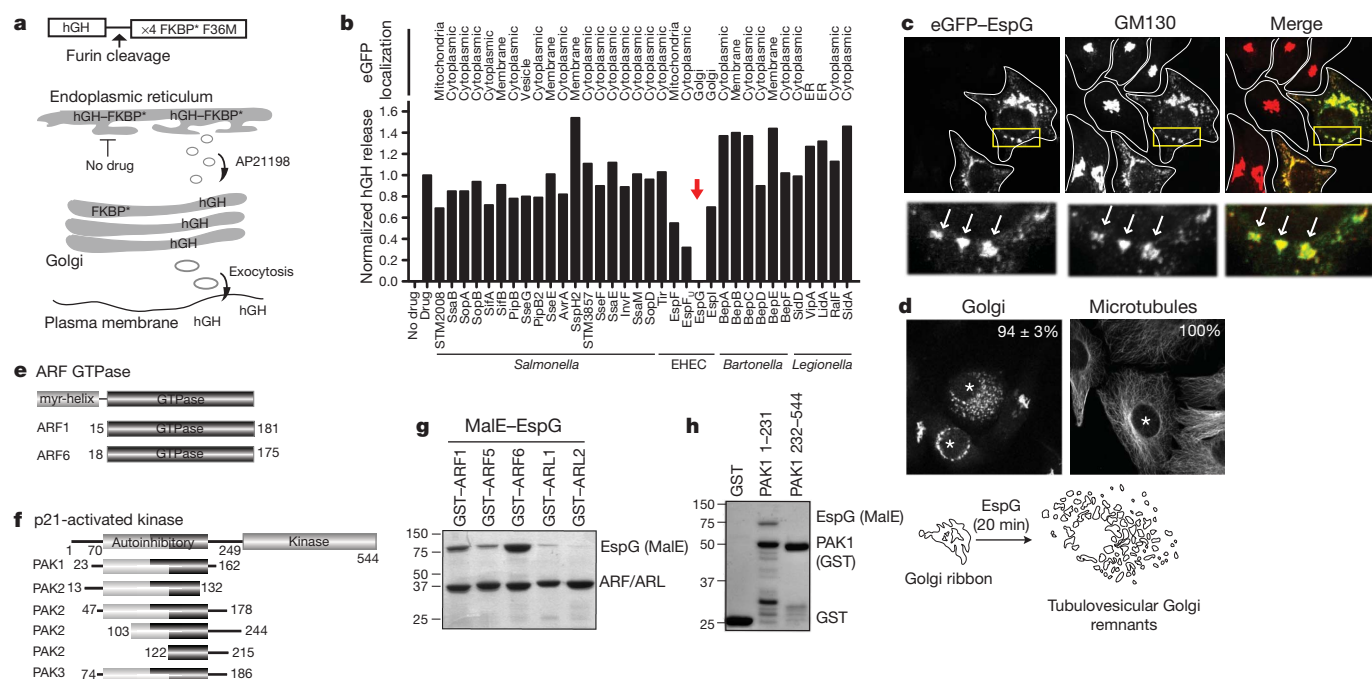


Figure 1 | EspG inhibits endomembrane trafficking and disrupts Golgi architecture. **a**, hGH trafficking assay showing how the hGH-FKBP* (Phe 36 Met mutant) aggregates in the endoplasmic reticulum until drug application (AP21998), whereby hGH enters the general secretory pathway and is secreted into the culture medium. **b**, hGH release assay showing the effects of type III and type IV effector proteins on trafficking through the general secretory pathway (Methods). hGH was quantified by enzyme-linked immunosorbent assay and normalized to GFP control (Drug) experiments. The subcellular localization of eGFP-tagged effectors is indicated.

ER, endoplasmic reticulum. **c**, Co-localization of eGFP-EspG (green) with *cis*-Golgi matrix protein GM130 (red). The Golgi in untransfected cells appears as tightly associated cisternae. **d**, Golgi and microtubule phenotypes induced by EspG protein microinjection (asterisk). The percentage of microinjected cells exhibiting each phenotype is indicated ($n = 3$, from >40 cells per experiment). **e, f**, ARF GTPase (**e**) and PAK isoforms (**f**) that interact with EspG by yeast two-hybrid. **g, h**, Glutathione pull-down of GST-ARF isoforms (**g**) and GST-PAK1 fragments (**h**) with recombinant MalE-tagged EspG.

¹Department of Microbiology, University of Texas Southwestern Medical Center, 5323 Harry Hines Boulevard, Dallas, Texas 75390-8816, USA. ²Department of Biochemistry, University of Texas Southwestern Medical Center, 5323 Harry Hines Boulevard, Dallas, Texas 75390-8816, USA.

Salmonella Typhimurium, *Legionella pneumophila* and *Bartonella henslae* showed little inhibitory functions, consistent with their intracellular life cycles (Fig. 1b). In particular, the EHEC type III effector EspG blocked exocytosis of hGH through an unknown molecular mechanism (Fig. 1b). eGFP-tagged EspG localized to the *cis*-Golgi apparatus, where it induced severe fragmentation of the organelle (Fig. 1c, d and Supplementary Fig. 1a, b). The Golgi disruption phenotype was observed when 10 nM recombinant EspG protein was microinjected into cells to mimic the protein concentration delivered by *E. coli* through the type III secretion apparatus¹⁰ (Fig. 1d). In addition, EspG disrupted the recycling endosome compartment in both transfection (Supplementary Fig. 1c, d) and microinjection experiments (data not shown). Previous genetic studies have implicated EspG^{11,12} and related *Shigella* family members¹³ in microtubule depolymerization. However, microtubules were intact in EspG microinjected cells (Fig. 1d), consistent with previous reports showing that these effectors do not disrupt cytoskeletal architectures^{14,15}. Thus, EspG represents a new class of bacterial signalling effector that functionally regulates cargo trafficking from membrane organelles.

We used a yeast two-hybrid screen to identify host enzymes targeted by EspG. The screen resulted in 26 positive interactions with multiple overlapping complementary DNA clones expressing two ARF GTPase family isoforms (ARF1 and ARF6) and three p21-activated kinase family members (PAK1, PAK2 and PAK3) (Fig. 1e, f). ARF GTPases function within a broad range of organelle systems, where they organize vesicle transport machinery, phospholipids and signalling molecules at membrane microdomains^{16,17}, whereas the PAK family of serine/threonine kinases transduce Cdc42 and Rac1 GTPase signals that establish intracellular polarity¹⁸. Direct interactions between EspG and the GTPase domain of ARF family members (Fig. 1g) and the autoinhibitory domain (AID) of PAK kinases (Fig. 1h) were shown by

in vitro binding studies using purified recombinant proteins. These findings establish two EspG substrates that are consistent with its regulatory function in host protein trafficking identified here and in bacterial infection studies conducted *in vivo*^{19,20}.

Next we crystallized EspG (residues 42–398) in complex with the GTPase domain of ARF6 (residues 13–175) and solved the structure to a resolution of 2.5 Å (Supplementary Table 1). EspG buries 602 Å² of ARF6 surface area and the complex interface is mediated by a collaboration of EspG loops (loops connecting β5 and β6, β8 and α6, and β12 and β13) that specifically engage the switch I loop of ARF6 and several residues lining the guanine-nucleotide-binding pocket (Fig. 2a and Supplementary Fig. 2a, b). The conformational state and amino-acid sequence of switch I are highly conserved between ARF family members, indicating that the EspG–ARF6 structure illustrates the nature of EspG's interaction with several ARF isoforms (Supplementary Fig. 3a, b). The importance of conserved switch I residues for binding EspG were confirmed by mutational analysis on ARF6 (Supplementary Fig. 3c).

ARF6 is GTP bound in the crystal and adopts an active-state conformation nearly identical to that of ARF6_{GTPγS} (ref. 21; Supplementary Fig. 4a). Further structural analyses revealed that switch I is inaccessible to EspG when ARF6 adopts the GDP-bound conformation (Supplementary Fig. 4a). EspG selectively bound the GTP-loaded forms of ARF1 and ARF6 but did not recognize GDP–ARF complexes (Fig. 2b). Moreover, EspG interacted with ARF6_{GTP} in its full-length myristoylated form, which was isolated from membrane fractions (Supplementary Fig. 4b). Thus, EspG preferentially targets the active ARF_{GTP} signalling molecule.

COPI coat, vesicle complex adaptors and signalling enzymes primarily associate with switch 2 and the β2/3 interswitch of ARF_{GTP} (refs 22–26; Supplementary Fig. 5a). Given the frequent occurrence of this

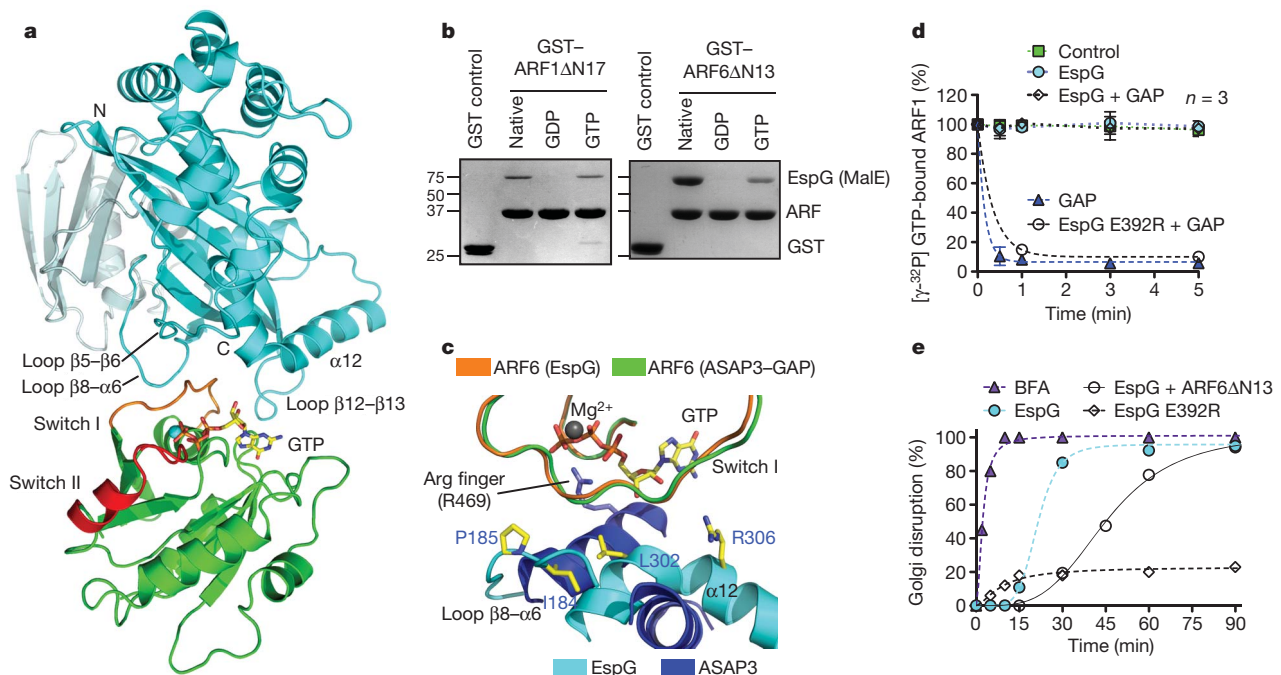


Figure 2 | The structure of EspG in complex with GTP-bound ARF6. **a**, The overall structure of EspG–ARF6_{GTP} complex. EspG is shown in cyan and ARF6 in green. Switch I and switch II on ARF6 are coloured orange and red, respectively. **b**, EspG selectively binds the GTP-loaded ARF1 and ARF6 (GST tagged) in glutathione pull-down assays. The native lane represents ARF GTPases purified from bacteria without removing or loading specific nucleotides. **c**, Structural overlay of EspG–ARF6_{GTP} and ASAP3(GAP)–ARF6_{GDP-AIFX} (Protein Data Bank ID, 3LVQ) showing how EspG sterically hinders ARF binding to ASAP3–GAP. The catalytic Arg finger of ASAP3 is labelled. **d**, GTP hydrolysis assay showing that EspG inhibits GAP-assisted

GTP hydrolysis on ARF1. The rate of $\gamma^{32}\text{P}$ [GTP] hydrolysis was measured as the percentage of $\gamma^{32}\text{P}$ [GTP] remaining on ARF1 over time. Intrinsic ARF1 GTPase activity (control, green), GAP-stimulated activity (GAP, blue triangle), and EspG inhibition of GAP activity (EspG + GAP, open diamond) or mutant EspG Glu 392 Arg (open circle) are shown. **e**, Time course of the Golgi disruption phenotype presented as the percentage of microinjected cells with altered Golgi morphology as shown in Fig. 1d. At least 45 microinjected cells were scored in each trial for a Golgi disruption phenotype, and the data are representative of three experimental trials. BFA, brefeldin A.

binding mode, we were surprised to find that EspG is rotated away from these common binding elements and is positioned directly over the guanine-nucleotide-binding pocket (Fig. 2a, c). Surprisingly, however, EspG does not function as a guanine nucleotide exchange factor (Supplementary Fig. 5b, c) or a GTPase-activating protein (GAP) (Fig. 2d, cyan circles). Rather, EspG is appropriately positioned to hinder binding of ARF-GAP and its catalytic access to the γ -phosphate of GTP (Fig. 2c). EspG completely abolished the GAP-stimulated GTPase hydrolysis on lipid-anchored ARF1 (Fig. 2d, diamonds), in comparison with the fast ARF-GAP reaction (Fig. 2d, blue triangles). The inhibition of GAP by EspG relied on a direct interaction between EspG and ARF because the binding-deficient mutant EspG Glu 392 Arg (characterized in Supplementary Fig. 6) had no effect on GAP-stimulated hydrolysis (Fig. 2d, open circles).

GTP hydrolysis and exchange on ARF is required for proper membrane transport functions, suggesting that EspG inhibits Golgi trafficking by blocking its guanine nucleotide cycle^{17,26}. Several lines of evidence support this idea. First, EspG disrupted the Golgi complex with rapid inhibitory kinetics (Fig. 2e) and a phenotype similar to the fungal toxin brefeldin A (Supplementary Fig. 7a), a potent ARF1 GTPase inhibitor that also interferes with the guanine nucleotide cycle²⁷. Second, microinjection of dominant-negative ARF protein (ARFAN13) caused a significant delay in Golgi disruption induced by EspG (Fig. 2e, open circles). Third, EspG Glu 392 Arg, a mutant that does not interact with host substrates (Supplementary Fig. 6), had no effect on Golgi morphology or trafficking function (Fig. 2e and

Supplementary Fig. 7b, c). Finally, EspG co-localized with the ARF1 effector β -COP (ref. 26) on Golgi membranes (Supplementary Fig. 1b). These combined structure and cellular studies provide a mechanism for bacterial regulation of membrane trafficking: EspG prevents vesicle transport by directly inhibiting ARF guanine nucleotide turnover on host membranes.

Having established the mechanism of ARF GTPase regulation, we next explored a second possible function of EspG: regulation of PAK family kinases. The EspG-binding site on PAK2 was defined to residues 121–136, a highly conserved sequence that encodes the $\text{I}\alpha 3$ -helix within the kinase AID (Supplementary Fig. 8). We crystallized EspG in complex with the PAK2 $\text{I}\alpha 3$ -helix fragment and solved the structure to a resolution of 2.8 Å (Supplementary Table 1). EspG recognized the initial turn of the $\text{I}\alpha 3$ -helix whereas the remainder of the peptide adopted an extended strand conformation that lies orthogonal to the EspG six-stranded β -sheet (Fig. 3a, b). EspG buries 684 Å² of the PAK2 surface area and the binding is primarily supported by a large hydrophobic interface and hydrogen bonding by residues Asn 212 and Asn 323 of EspG (Fig. 3b). This structural interface was confirmed by a series of *in vitro* binding studies and kinase assays using PAK2 and EspG mutant proteins (Supplementary Fig. 9).

To determine how EspG may regulate the kinase, we compared the peptide structure from EspG-PAK2 with the structure of $\text{I}\alpha 3$ -helix in the autoinhibited PAK1 homodimer²⁸ (Fig. 3c). In autoinhibited PAKs, the $\text{I}\alpha 3$ -helix is sandwiched between the kinase domain and the AID, where it has three autoinhibitory functions: (i) it folds onto

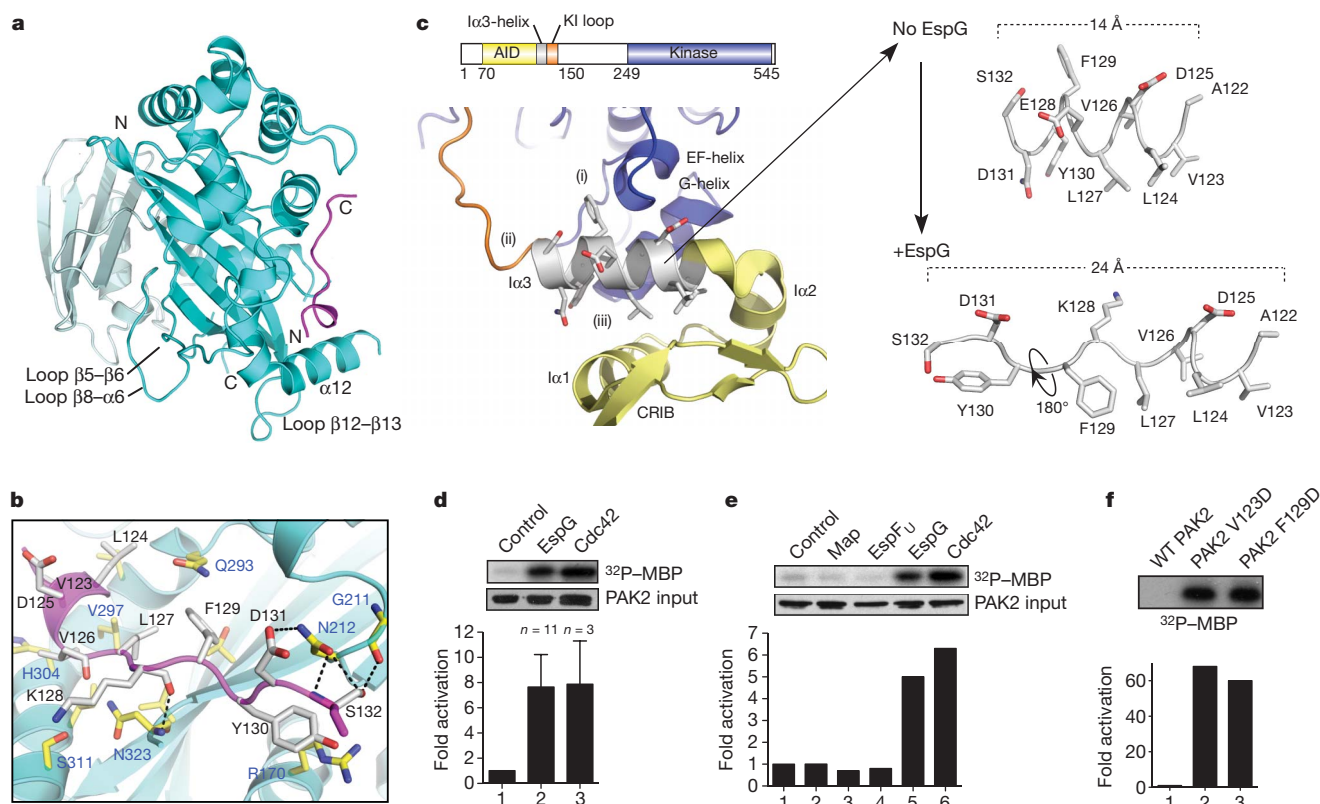


Figure 3 | The structure of EspG in complex with PAK2 $\text{I}\alpha 3$ peptide. **a**, The overall EspG-PAK2¹²³ complex with EspG oriented and coloured as in Fig. 2a. The PAK2 $\text{I}\alpha 3$ peptide (residues 123–134) are shown in magenta. **b**, Detailed interactions between EspG and PAK2¹²³. Key binding residues from EspG (blue labels) and PAK2 (black labels) are shown. **c**, Close-up view of autoinhibited PAK1 homodimer (Protein Data Bank ID, 1F3M) focused on chain B (kinase domain, blue) and chain D (autoinhibitory domain, yellow). The $\text{I}\alpha 3$ -helix inhibitory functions are labelled (i)–(iii) corresponding with those outlined in the results section. The $\text{I}\alpha 3$ -helix extracted from the PAK1 structure (numbering corresponds to PAK2 for ease of comparison) is shown at the

upper right. The corresponding PAK2 $\text{I}\alpha 3$ -helix extracted from the EspG structure (lower right) is oriented by the amino-terminal helical residues 123–127. KI loop, kinase inhibitory loop. CRIB, Cdc42/Rac1 interacting binding. **d**, **e**, PAK2 kinase assays comparing 2 μM EspG with equimolar GTP γ S-loaded Cdc42 (**d**) and the indicated EHEC type III effectors (**e**). Phosphorylation of myelin basic protein (MBP) substrate, input levels of PAK2 and quantification of each experiment are shown. **f**, PAK2 kinase assays comparing autoinhibited wild-type (WT) PAK2 with PAK2 mutants Val 123 Asp and Phe 129 Asp. Data are presented as in **d**.

the EF- and G-helices to block substrate binding; (ii) it positions the 'kinase inhibitory' loop across the enzyme catalytic cleft; and (iii) it stabilizes the AID three-helix bundle maintaining PAK homodimerization (Fig. 3c). Hence, EspG binding to the $\alpha 3$ -helix suggested a mechanism for PAK activation. EspG induced a (7.6 ± 2.5)-fold ($n = 11$) increase in PAK2 activity, a profile that is comparable to PAK stimulation by GTP γ S-loaded Cdc42 ((7.8 ± 3.4) -fold, $n = 3$) (Fig. 3d). Notably, EHEC type III effectors Map and EspF_U showed no PAK stimulatory activity, demonstrating the signalling specificity of EspG (Fig. 3e).

To gain further insight into the mechanism of kinase activation, we first examined the details of the EspG–PAK2 interface. EspG residue Asn 212 probably initiates the kinase reaction because this residue engages the surface-accessible residues Asp 131 and Ser 132 in the autoinhibited PAK homodimer (Fig. 3b and Supplementary Fig. 10). On initial recognition, EspG displaces the $\alpha 3$ -helix by reorganizing its secondary structure and by displacing side chains that normally contact the autoinhibitory interface between the kinase domain and the AID (Fig. 3c). These data suggest a novel allosteric mechanism for PAK activation. To further confirm that PAK is stimulated by local perturbations in the environment surrounding $\alpha 3$, we mutated the hydrophobic PAK2 residues Val 123 and Phe 129 that stabilize the AID and the kinase domain, respectively. Both Val 123 Asp and Phe 129 Asp resulted in a constitutively active kinase with more than 60-fold enhancement of substrate phosphorylation (Fig. 3f). We note that the mechanism of EspG binding to PAK is structurally distinct from that of Cdc42 binding²⁸, indicating that the catalytic machinery of EspG is a unique bacterial invention.

The two EspG structures reported here are nearly identical, with a root mean squared deviation of 0.612 Å over 349 C α atoms. As shown in Fig. 4a, ARF6 and PAK2 occupy distinct, non-overlapping binding sites on adjacent surfaces of EspG. Consistent with this view, EspG nucleates a trimeric complex between the kinase and GTPase in solution (Supplementary Fig. 11). This complex could also be reconstituted on Golgi mimetic liposomes (Fig. 4b). ARF1_{GTP} recruited EspG to the

artificial membrane surface (Fig. 4b, lane 4), which in turn localized PAK2 to these sites (Fig. 4b, lane 6). Notably, PAK2 localization was strictly dependent on formation of the EspG–ARF1_{GTP} complex (Fig. 4b, lanes 6–8) and ARF1 tethering to the membrane (Fig. 4b, lanes 9 and 10). As predicted by these findings, EspG co-localized with ARF1 at the Golgi (Fig. 4c). We further speculated that PAK would also be recruited to these sites. To test this hypothesis, an *in vivo* 'activity' probe was engineered by fusing the PAK2 $\alpha 3$ -helix sequence (residues 121–136) to the carboxy terminus of the mCherry fluorophore. The PAK2 probe recognized cellular EspG and was targeted to the Golgi complex in $78 \pm 5\%$ of EspG-transfected cells (Fig. 4c). By comparison, mutant EspG Asn 212 Ala that lacked all kinase stimulatory activity (Supplementary Fig. 9) localized to the Golgi complex but did not recruit PAK2 to these sites (Fig. 4c). Together, our studies support the function of EspG as a catalytic scaffold that links GTPase inhibition with kinase signal transduction pathways at membrane organelles (Fig. 4d).

EspG belongs to large family of type III effectors secreted by diverse bacterial pathogens. Our studies show that EspG has structural homology with VirA (refs 14, 15) from *Shigella flexneri*, suggesting that it too may function as an enzyme scaffold (root mean squared deviation, 3.1 Å; Z-score, 5.9) (Supplementary Fig. 12). However, a detailed structural comparison indicates that VirA is unlikely to target the same signalling pathways as EspG during *Shigella* pathogenesis (Supplementary Fig. 12). We provide mechanistic insights and structural evidence that EspG harbours two unique pathogenic activities, ARF GTPase inhibition and PAK stimulation. Moreover, EspG targets PAK to specific membrane surfaces through its association with ARFs. From a strategic point of view, the assembly of an artificial enzyme complex enables bacteria to precisely control signalling events with little competition between endogenous regulatory systems. Thus, it is intriguing to speculate that EspG organizes a higher-order signalling network to effectively subvert key cellular processes including cell polarity, adhesion, receptor trafficking and protein secretion.

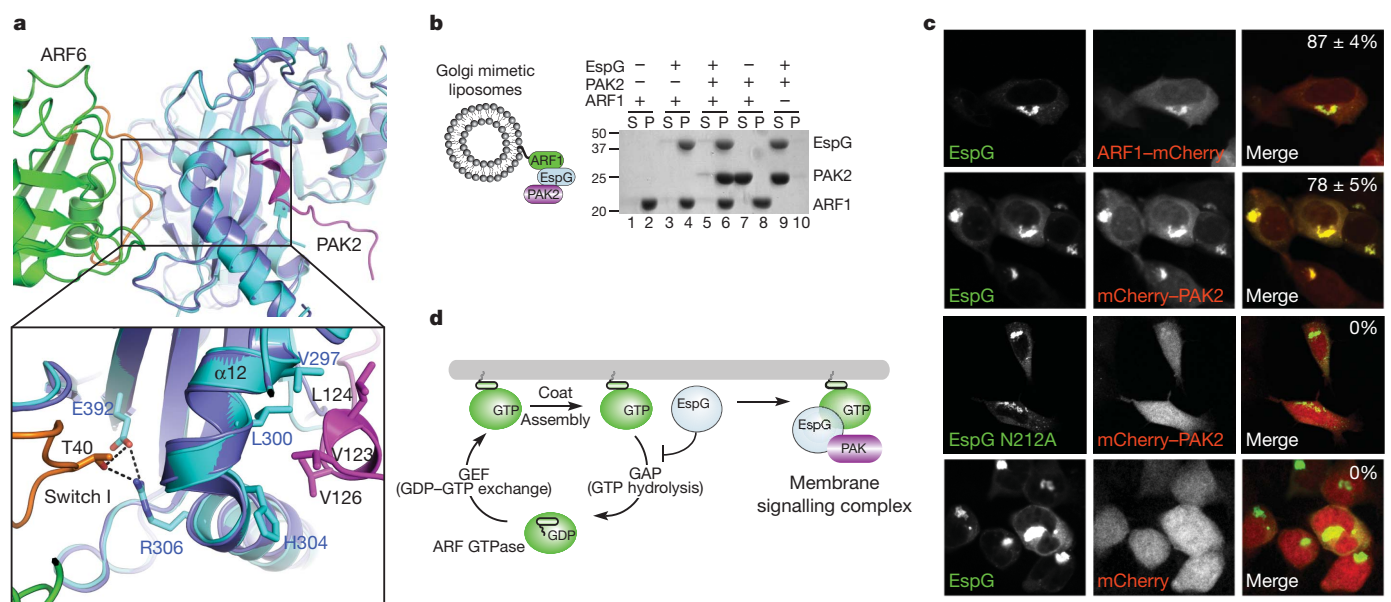


Figure 4 | EspG functions as a catalytic scaffold at membrane organelles. **a**, Structural overlay of EspG–ARF6_{GTP} and EspG–PAK2^{121–136} highlighting the close association between ARF and PAK on the surface of EspG. Colours are as in Figs 2a and 3a except that EspG from the PAK2 structure is coloured purple. **b**, Golgi-mimetic-liposome-binding assays showing that EspG nucleates a trimeric complex between ARF1 and PAK2 on membrane surfaces. After centrifugation, proteins remaining in the supernatant (S) or those associated with liposomes in the pellet (P) are indicated. **c**, HEK293A cells co-transfected

with the indicated constructs showing that eGFP–EspG co-localizes with ARF1–mCherry and recruits a PAK activity probe (mCherry–PAK2^{121–136}) to Golgi membranes. The percentage of cells exhibiting co-localized EspG with mCherry-tagged proteins ($n = 3$) is shown in the upper right of the merged micrographs. **d**, Model of the dual function of EspG as an inhibitor of membrane trafficking and as a catalytic scaffold that assembles a GTPase–kinase signalling complex at cellular membranes. GEF, guanine nucleotide exchange factor.

METHODS SUMMARY

Recombinant protein preparation and cloning were done using standard methods. In immunofluorescence experiments, we transfected cells with Eugene 200 or microinjected them with 10 nM protein, where indicated. We performed kinase assays with rabbit pEGFP-PAK2, which was immunoprecipitated from 293T cell lysates and incubated with the protein of interest in the presence of MBP, 10 μ M ATP and 5 μ Ci γ - 32 P[ATP]. Reactions were stopped by the addition of SDS buffer, separated by SDS-polyacrylamide gel electrophoresis and kinase activity was measured as 32 P counts per minute. EspG-ARF6 and EspG-PAK2-1 α 3 were purified by ion exchange and gel filtration chromatography and crystallized by the hanging-drop vapour diffusion method. We collected X-ray diffraction data at the Structural Biology Center, Advanced Photon Source, Argonne National Laboratory (USA). The structure of EspG-ARF6 was phased to a resolution of 2.5 Å by the multiwavelength anomalous dispersion method using selenomethionine-labelled EspG and ARF6 proteins. The EspG-PAK2 structure was solved to a resolution of 2.8 Å by the molecular replacement method using the EspG monomer of the EspG-ARF6 structure as the initial search model. Further details can be found in Supplementary Information.

Full Methods and any associated references are available in the online version of the paper at www.nature.com/nature.

Received 30 July; accepted 20 October 2010.

Published online 19 December 2010.

- Scott, J. D. & Pawson, T. Cell signaling in space and time: where proteins come together and when they're apart. *Science* **326**, 1220–1224 (2009).
- Lim, W. A. Designing customized cell signalling circuits. *Nature Rev. Mol. Cell Biol.* **11**, 393–403 (2010).
- Duesbery, N. S. *et al.* Proteolytic inactivation of MAP-kinase-kinase by anthrax lethal factor. *Science* **280**, 734–737 (1998).
- Yarborough, M. L. *et al.* AMPylation of Rho GTPases by *Vibrio* VopS disrupts effector binding and downstream signaling. *Science* **323**, 269–272 (2009).
- Schmidt, G. *et al.* Gln 63 of Rho is deamidated by *Escherichia coli* cytotoxic necrotizing factor-1. *Nature* **387**, 725–729 (1997).
- Li, H. *et al.* The phosphothreonine lyase activity of a bacterial type III effector family. *Science* **315**, 1000–1003 (2007).
- Alto, N. M. *et al.* The type III effector EspF coordinates membrane trafficking by the spatiotemporal activation of two eukaryotic signaling pathways. *J. Cell Biol.* **178**, 1265–1278 (2007).
- Vingadassalom, D. *et al.* Insulin receptor tyrosine kinase substrate links the *E. coli* O157:H7 actin assembly effectors Tir and EspF_U during pedestal formation. *Proc. Natl Acad. Sci. USA* **106**, 6754–6759 (2009).
- Rivera, V. M. *et al.* Regulation of protein secretion through controlled aggregation in the endoplasmic reticulum. *Science* **287**, 826–830 (2000).
- Winnen, B. *et al.* Hierarchical effector protein transport by the *Salmonella* Typhimurium SPI-1 type III secretion system. *PLoS ONE* **3**, e2178 (2008).
- Shaw, R. K. *et al.* Enteropathogenic *Escherichia coli* type III effectors EspG and EspG2 disrupt the microtubule network of intestinal epithelial cells. *Infect. Immun.* **73**, 4385–4390 (2005).
- Tomson, F. L. *et al.* Enteropathogenic *Escherichia coli* EspG disrupts microtubules and in conjunction with Orf3 enhances perturbation of the tight junction barrier. *Mol. Microbiol.* **56**, 447–464 (2005).
- Yoshida, S. *et al.* Microtubule-severing activity of *Shigella* is pivotal for intercellular spreading. *Science* **314**, 985–989 (2006).
- Germane, K. L., Ohi, R., Goldberg, M. B. & Spiller, B. W. Structural and functional studies indicate that *Shigella* VirA is not a protease and does not directly destabilize microtubules. *Biochemistry* **47**, 10241–10243 (2008).
- Davis, J. *et al.* Novel fold of VirA, a type III secretion system effector protein from *Shigella flexneri*. *Protein Sci.* **17**, 2167–2173 (2008).
- Kahn, R. A. Toward a model for Arf GTPases as regulators of traffic at the Golgi. *FEBS Lett.* **583**, 3872–3879 (2009).
- D'Souza-Schorey, C. & Chavrier, P. ARF proteins: roles in membrane traffic and beyond. *Nature Rev. Mol. Cell Biol.* **7**, 347–358 (2006).
- Bokoch, G. M. Biology of the p21-activated kinases. *Annu. Rev. Biochem.* **72**, 743–781 (2003).
- Borthakur, A. *et al.* Enteropathogenic *Escherichia coli* inhibits butyrate uptake in Caco-2 cells by altering the apical membrane MCT1 level. *Am. J. Physiol. Gastrointest. Liver Physiol.* **290**, G30–G35 (2006).
- Guttman, J. A. *et al.* Aquaporins contribute to diarrhoea caused by attaching and effacing bacterial pathogens. *Cell. Microbiol.* **9**, 131–141 (2007).
- Pasqualato, S., Menetrey, J., Franco, M. & Cherfils, J. The structural GDP/GTP cycle of human Arf6. *EMBO Rep.* **2**, 234–238 (2001).
- Hanzal-Bayer, M., Renault, L., Roversi, P., Wittinghofer, A. & Hillig, R. C. The complex of Arl2-GTP and PDE delta: from structure to function. *EMBO J.* **21**, 2095–2106 (2002).
- Isabet, T. *et al.* The structural basis of Arf effector specificity: the crystal structure of ARF6 in a complex with JIP4. *EMBO J.* **28**, 2835–2845 (2009).
- O'Neal, C. J., Jobling, M. G., Holmes, R. K. & Hol, W. G. Structural basis for the activation of cholera toxin by human ARF6-GTP. *Science* **309**, 1093–1096 (2005).
- Shiba, T. *et al.* Molecular mechanism of membrane recruitment of GGA by ARF in lysosomal protein transport. *Nature Struct. Biol.* **10**, 386–393 (2003).
- Zhao, L. *et al.* Direct and GTP-dependent interaction of ADP ribosylation factor 1 with coatomer subunit beta. *Proc. Natl Acad. Sci. USA* **94**, 4418–4423 (1997).
- Chardin, P. & McCormick, F. Brefeldin A: the advantage of being uncompetitive. *Cell* **97**, 153–155 (1999).
- Lei, M. *et al.* Structure of PAK1 in an autoinhibited conformation reveals a multistage activation switch. *Cell* **102**, 387–397 (2000).

Supplementary Information is linked to the online version of the paper at www.nature.com/nature.

Acknowledgements We would like to thank our colleagues, specifically K. Orth, M. Rosen, M. Cobb, J. Seeman, C. Brautigam and T. Fox, for helpful discussions in preparation of this manuscript, and we are particularly indebted to members of the Structural Biology Lab and mass spectrometry facilities for their efforts on this project. We would also like to thank J. Goldberg and G. Bokoch for providing valuable reagents. We would particularly like to thank J. Cherfils for providing preliminary insights into this work and for key reagents. The structure shown in this report is derived from work performed on beamlines 19-BM and 19-ID at the Structural Biology Center, Advanced Photon Source, Argonne National Laboratory. Argonne National Laboratory is operated by UChicago Argonne, LLC, for the US Department of Energy, Office of Biological and Environmental Research, under contract DE-AC02-06CH11357. R.C.O. was supported by a NIH Molecular Microbiology training grant (5T32AI007520-12). This work was supported by the Welch Foundation (#1-1704) and a grant from the NIH (NIAID; 1R01AI083359-01) to N.M.A.

Author Contributions N.M.A. and A.S.S. had the general ideas for this manuscript. A.S.S., N.M.A. and S.M.B. crystallized the protein complexes and D.R.T. solved the complex structures. N.M.A., A.S.S., S.E.S., B.A.W., L.E.R. and R.C.O. planned, performed and interpreted the experiments. N.M.A. and A.S.S. wrote the manuscript and all authors provided editorial input.

Author Information Atomic coordinates and structure factors for the reported crystal structures have been deposited with the Protein Data Bank under accession codes 3PCR and 3PCS. Reprints and permissions information is available at www.nature.com/reprints. The authors declare no competing financial interests. Readers are welcome to comment on the online version of this article at www.nature.com/nature. Correspondence and requests for materials should be addressed to N.M.A. (neal.alto@utsouthwestern.edu).

METHODS

Plasmids. The *espG* gene from EHEC O157:H7 was PCR cloned in-frame into pEGFP-C2 (Clontech) and pcDNA3.1-mCherry. For bacterial expression, 38 and 41 amino-acid N-terminal deletions (39–398 and 42–398) of EspG were PCR subcloned into pGEX-4T1 (GST-tag) (Amersham), pProEX-HTb (6xHis tag) (Novagen) and pET28b-MalE (6xHis tag, MalE-tag) vectors. EspG mutants were generated with QuickChange site-directed mutagenesis (Stratagene) following manufacturer's instructions. N-terminal deletions of ARF GTPases (ARF1Δ17, ARF5Δ17 and ARF6Δ13) and ARL proteins (ARL1Δ17 and ARL2Δ16) were PCR subcloned into pGEX-4T1 and pProEX-HTb vectors. Human PAK1 construct was obtained from Dr Gary Bockoch (TSRI, La Jolla, California), and rabbit PAK2 and PAK3 were obtained from Dr Melanie Cobb (UTSW). PCR cloning was used to generate variable-length constructs of PAK isoforms in pGEX-4T1 vector. All constructs were verified by DNA sequencing.

Yeast two-hybrid system. The yeast expression vector pLexA encoded a gene with an NH2-terminal LexA-binding domain and residues 1–398 of EHEC EspG. Day 9.5 and 10.5 mouse embryo cDNA library (250 µg) in VP16 were screened using the yeast two-hybrid system.

Protein purification for *in vitro* assays. Recombinant proteins were produced in BL21-DE3 *E. coli* strains. Protein expression was induced with 0.4 mM IPTG for 16 h at 18 °C. Bacterial pellets were lysed in either His buffer (100 mM HEPES, pH 7.5, 300 mM NaCl) or GST buffer (TBS; 50 mM Tris pH 7.5, 150 mM NaCl, 2 mM DTT) supplemented with protease cocktail (Roche). Proteins were purified with nickel agarose (Qiagen) or glutathione Sepharose (Amersham Biosciences) following manufacturer's instructions. Eluted proteins were buffer exchanged into TBS using concentration centrifugal columns (Millipore), glycerol was added to 15% and the proteins were then stored at –80 °C.

***In vitro* GST pull-downs.** Protein interactions were examined through GST pull-down assays. Unless otherwise stated, 15 µg of recombinant GST proteins immobilized to glutathione Sepharose were incubated with 20 µg of 6xHis- and/or MalE-tagged proteins for 1 h at 4 °C. Samples were washed three times in TBS supplemented with 0.5% Triton X-100. Proteins were eluted from beads with Laemmli sample buffer and were separated by SDS–polyacrylamide gel electrophoresis and stained with Coomassie blue. For nucleotide loading, ARF1Δ17 and ARF6Δ13 were incubated in nucleotide loading buffer (40 mM HEPES, 150 mM NaCl, 2 mM EDTA, 10% glycerol) with 10 µM of either GDP or GTP for 30 min at 37 °C, and then MgCl₂ was added to 10 mM and the reaction was transferred to ice after 15 min at room temperature (25 °C).

Kinase assays. To obtain full-length PAK2 kinase, 10-cm dishes with 293A cells were transfected with 5 µg rabbit PAK2 cDNA in pEGFP-C2 vector and expressed for 48 h post-transfection. Cells were broken in lysis buffer (20 mM Tris, pH 7.5, 150 mM NaCl, 5 mM EDTA, 0.5% Triton X-100). PAK2 kinase was purified by immunoprecipitation with 1:1,000 polyclonal anti-GFP antibody (Clontech) and 25 µl protein A/G slurry for 1 h at 4 °C. Beads were washed twice with lysis buffer and twice with kinase buffer (40 mM HEPES, pH 7.5, 10 mM MgCl₂). MBP (5 µg) and 2 µM activating proteins (that is, EspG or Cdc42) were added to the beads for a total volume of 30 µl. The reaction was equilibrated on ice for 30 min. The kinase activity was initiated by an addition of 10 mM ATP and 5 µCi ATPγP³². After 5 min at room temperature, the reaction was stopped with 30 µl × 2 Laemmli sample buffer. Contents were separated by SDS–polyacrylamide gel electrophoresis, transferred to nitrocellulose membrane and either analysed by western blot (1:5,000 monoclonal anti-GFP) or exposed by autoradiography. Bands were cut out and the radioactivity signal measured on a scintillation counter.

Cell microinjection, transfections and immunofluorescence microscopy. Normal rat kidney cells were microinjected with EspG proteins using a semi-automatic InjectMan NI2 micromanipulator (Eppendorf). A needle concentration of 10 nM was calculated to inject between 5,000 and 20,000 copies because we microinjected ~5% cell volume, giving a final estimated cellular concentration of 50 pM in a cell volume of 5,000 µm³. HeLa and HEK293A cells were transfected using calcium phosphate. At 16–18 h post-transfection, cells were fixed with 3.7% formaldehyde and stained with antibodies for immunofluorescence. In co-transfection experiments, equal amounts of DNA were used for each sample. Brefeldin A treatment was performed by adding 5 µg ml^{−1} of brefeldin A to the medium before fixation with formaldehyde. As a negative control, ethanol was added to the medium. All immunofluorescence images were acquired with a Zeiss LSM 5 Pascal confocal microscope. Golgi, endosomes and microtubules were detected using anti-GM130 (transduction labs), anti-EEA1 (transduction labs) and anti-α-tubulin (Sigma) antibodies, respectively.

hGH trafficking assay. hGH trafficking assays were performed as described previously⁹. Briefly, HeLa cells (50% confluence) were transfected with 1 µg of 4xKBP-hGH (Ariad Pharmaceutical, Inc.; <http://www.ariad.com/regulationkits>; source of material, David Bernstein) and either 0.5 µg eGFP–EspG or pEGFP control plasmid with Eugene6 (Roche). Sixteen hours later, the medium was

replaced with medium containing AP21998 (final concentration, 2 µM) or vehicle control. AP21998 was incubated with the cells for 2 h before the supernatant was collected. The supernatant was then diluted 100-fold and compared against a hGH standard curve (12.5–400 pg ml^{−1}) for the quantification of hGH released using an hGH enzyme-linked immunosorbent assay (Roche). For no drug controls, 100% ethanol (2 µl) was incubated with the cells for 2 h.

Liposome pull-downs and GAP assays. Liposome preparation: Lipids were purchased in powder form from Avanti Polar Lipids. Golgi mimetic liposomes were created by combining 20 mol% DOGS-NTA with DOPC, DOPE, DOPA, DOPS, PI, PI₄P and PI_{4,5}P₂ in the molar ratios reported previously²⁹. Total lipid (5 mM) was solubilized in chloroform, dried under an anhydrous nitrogen stream and further dried in a vacuum desiccator for approximately 5 h. Dried lipids were hydrated with liposome-binding buffer (20 mM Tris-HCl, pH 7.6, 50 mM NaCl, 10 mM MgCl₂) and vigorously vortexed between five freeze–thaw cycles (liquid nitrogen and 80 °C to ensure appropriate phase transition and dispersion of the various lipids), after which liposomes were generated by means of ultrasonication in a bath sonicator (Laboratory Supplies Company). Liposomes were collected from the supernatant after centrifugation (2,500g for 5 min) and used in subsequent assays.

Liposome pull-down assays: Liposomes were prepared as described above. ARF1 GTP loading was carried out by incubating purified 6xHis-tagged ARF1ΔN17 in nucleotide exchange buffer (20 mM Tris-HCl, pH 7.6, 50 mM NaCl, 5 mM EDTA, 10% glycerol, 1 mM DTT) with 100 µM GTP. After incubation at 37 °C for 30 min, 10 mM MgCl₂ was added to stabilize ARF1(GTP). The requisite volume of ARF1(GTP), GST PAK (residues 121–136) or EspG was added to bring the protein concentration to 3 µM in a 100-µl volume. Liposomes were added for a final lipid concentration of 10 µM and reactions proceeded at room temperature for 30 min. Samples were subjected to centrifugation at 100,000g in a Beckman TLA100.3 rotor and a Beckman TL100 ultracentrifuge at 4 °C for 1 h. Supernatant and pellet were separated and analysed on a 12.5% polyacrylamide gel and visualized with Coomassie blue.

GTP hydrolysis assays: ARF1 was incubated in nucleotide exchange buffer with 250 nM γ³²P[GTP] (MP Biomedical) for 30 min at 37 °C, after which 10 mM MgCl was added to stabilize ARF1(γ³²P[GTP]). ARF1(γ³²P[GTP]) was incubated with 10 µM Golgi mimetic liposomes 5 min before the addition of fivefold molar excess rat ARFGAP1 (ref. 30), EspG and EspG(E392R). In the case of hydrolytic protection assays, EspG or EspG(E392R) was added 5 min before the addition of rat ARFGAP1. Aliquots (5 µl) of the 50-µl reaction were removed at times indicated, added to 5 ml ice-cold binding buffer (TBS + 10 mM MgCl₂) and vacuum-filtered through nitrocellulose membranes. Membranes were washed three times with ice-cold binding buffer and subjected to scintillation counting. Data analysis was carried out in GRAPHPAD PRISM 5.0b.

Crystallization and structure determination. Protein expression and purification: A stable protein fragment of EspG residues 42–398 was identified by limited proteolysis and mass spectrometry. cDNA-encoding EHEC O157:H7 EspG residues 42–398 and human ARF6 residues 14–175 were synthesized by PCR and ligated into the pPRO-EX-HTb expression vector. The resulting plasmids were then transformed into the *E. coli* strain BL21-DE3. Protein expression was induced by 1 mM IPTG overnight at 16 °C and proteins were purified on Ni-NTA agarose, concentrated to 10 mg ml^{−1} in TBS buffer with 5% glycerol, snap-frozen in liquid nitrogen and stored at –80 °C. The Se-Met variant of EspG and ARF6 was expressed in methionine auxotrophic *E. coli* strain B834-DE3 and grown in minimal medium supplemented with natural amino acids and Se-Met. Expression and purification were unchanged. EspG–ARF6 complex was formed overnight at room temperature in the presence of 1:100 TEV protease to cleave the 6xHis tag. The complex was purified by successive anion exchange (Q-HP) and gel filtration (Superdex 200 GL) chromatography and concentrated to 7 mg ml^{−1} in 25 mM Tris, pH 7.5, and 50 mM NaCl. For the PAK2 crystal trials, EspG protein was expressed and purified identically to that described. However, after the anion exchange, EspG was incubated with a fivefold molar excess of PAK2 peptide (residues 121–136). The complex was purified by gel filtration as described.

Crystallization and X-ray diffraction data collection: Crystals of EspG–ARF6 were grown using the hanging-drop vapour diffusion method from drops containing 2 µl protein (7 mg ml^{−1}) and 1 µl of reservoir solution (0.1 M sodium acetate, pH 5.0, 2% PEG4000, 5% 2,3-methylpentanediol (MPD)), and equilibrated over 500 µl of reservoir solution. Bipyramid-like crystals appeared after 1 d at 20 °C and grew to their maximal extent in 2–3 d. Crystals were relatively large in all three dimensions (0.3 × 0.6 × 0.3 mm³). Cryo-protection was performed by transferring the crystals to a final solution of 37% MPD, 0.1 M sodium acetate, pH 5.0, and 2% PEG4000, increasing in 5% steps of MPD over the course of 10 min at 20 °C. Crystals were flash-frozen using liquid nitrogen. EspG–ARF6 crystals had the symmetry of space group *P*₄₃₂₁₂ with unit-cell parameters of *a* = *b* = 104.6 Å and *c* = 98.3 Å, and contained one molecule each of EspG and

ARF6 per asymmetric unit. EspG–ARF6 crystals diffracted isotropically to a d_{\min} of 2.50 Å when exposed to synchrotron radiation.

Crystals of EspG–PAK2 were grown using the hanging-drop vapour diffusion method from drops containing 1 µl protein (12 mg ml^{−1}) and 1 µl of reservoir solution (0.1 M Tris, pH 8.0, 0.25 M sodium chloride and 20% PEG4000) and equilibrated over 500 µl of reservoir solution. Plate-like crystals appeared after 2 d at 20 °C and grew to their maximal extent by 4–5 d. Crystals were large in two dimensions (0.2 × 0.5 mm²) and relatively thin (0.1 mm). Cryo-protection was performed by transferring the crystals to a final solution of 15% ethylene glycol, 22% PEG4000, 0.1 M Tris, pH 8.0, and 0.25 M sodium chloride, increasing in 5% steps of ethylene glycol over the course of 10 min at 20 °C. Crystals were flash-frozen using liquid nitrogen. EspG–PAK crystals had the symmetry of space group $P2_12_12_1$ with unit-cell parameters of $a = 86.7$ Å, $b = 104.6$ Å and $c = 192.0$ Å, and contained four molecules of EspG–PAK per asymmetric unit. EspG–PAK crystals diffracted to a d_{\min} of 2.85 Å when exposed to synchrotron radiation. Data were indexed, integrated and scaled using the HKL-3000 program package³¹. Data collection statistics are provided in Supplementary Table 1.

Phase determination and structure refinement: Phases for the EspG–ARF6 complex were obtained from a three-wavelength anomalous dispersion experiment using selenomethionyl-substituted protein with data to a d_{\min} of 2.50 Å. Fifteen selenium sites were located using the program SHELXD³²; this represented nine single-occupancy selenium sites and six half-occupancy selenium sites per EspG–ARF6 heterodimer. Phases were refined with the program MLPHARE, resulting in an overall figure of merit of 0.41 for data between 32.9 and 2.50 Å. Phases were further improved by density modification with the program DM³³, resulting in a figure of merit of 0.70. An initial model containing 97% of all EspG residues was automatically generated by alternating cycles of the programs RESOLVE³⁴ and BUCCANEER³⁵. Inspection of the electron density map revealed density for the ARF6 molecule, but the automatic model-building programs were unable to build a complete model for this protein. Placement of a model for ARF6 in the cell was performed by means of molecular replacement in the program PHASER³⁶ using the GTPγS-bound ARF6 (Protein Data Bank ID, 2J5X) as a search model.

Additional residues for EspG were manually modelled in the program O³⁷. Refinement was performed with the data collected at the selenium peak wavelength to a resolution of 2.50 Å using the program PHENIX³⁸ with a random 5% of all data set aside for an R_{free} calculation. The current model contains one EspG and one ARF6 monomer; included are residues 47–395 of EspG, residues 14–174 of ARF6, one Mg²⁺–GTP and 138 water molecules. The R_{work} value is 22.5% and the R_{free} value is 32.4%. The higher-than-average R_{free} value is probably due to the relative dearth of lattice contacts for the ARF6 molecule, as evidenced by weak electron density for the portions of ARF6 that are distal to the EspG-binding site.

The density for the portions of ARF6 (residues 20–63 and 152–170) that are proximal to EspG and to the Mg²⁺–GTP is strong and well connected. A Ramachandran plot generated with MOLPROBITY³⁹ indicated that 99.0% of all protein residues are in allowed regions.

Phases for EspG–PAK were obtained by means of molecular replacement in the program PHASER using the coordinates of EspG from the EspG–ARF6 structure as a search model. Model building and refinement was performed as described above, with the following modification: owing to the lower resolution of the data, restrained non-crystallographic symmetry was implemented during refinement. The current model contains four EspG monomers and four PAK peptides. Included are EspG residues 42–158, 163–318 and 321–397 and PAK residues 122–135, in complex A; EspG residues 43–397 and PAK residues 122–133, in complex B; EspG residues 42–158, 163–316 and 322–395 and PAK residues 123–132, in complex C; and EspG residues 42–158, 163–317 and 320–395 and PAK residues 122–134, in complex D. The R_{work} value is 20.3% and the R_{free} value is 28.6%. A Ramachandran plot generated with MOLPROBITY indicated that 99.4% of all protein residues are in allowed regions. Phasing and model refinement statistics are provided in Supplementary Table 1.

Combination models were generated by structural alignment of homologous or identical proteins from separate independent structures where applicable, using PYMOL.

29. Bremser, M. *et al.* Coupling of coat assembly and vesicle budding to packaging of putative cargo receptors. *Cell* **96**, 495–506 (1999).
30. Goldberg, J. Structural and functional analysis of the ARF1-ARFGAP complex reveals a role for coatamer in GTP hydrolysis. *Cell* **96**, 893–902 (1999).
31. Minor, W., Cymborowski, M., Otwinowski, Z. & Chruszcz, M. HKL-3000: the integration of data reduction and structure solution—from diffraction images to an initial model in minutes. *Acta Crystallogr. D* **62**, 859–866 (2006).
32. Schneider, T. R. & Sheldrick, G. M. Substructure solution with SHELXD. *Acta Crystallogr. D* **58**, 1772–1779 (2002).
33. Cowtan, K. & Main, P. Miscellaneous algorithms for density modification. *Acta Crystallogr. D* **54**, 487–493 (1998).
34. Terwilliger, T. SOLVE and RESOLVE: automated structure solution, density modification and model building. *J. Synchrotron Radiat.* **11**, 49–52 (2004).
35. Cowtan, K. The Buccaneer software for automated model building. 1. Tracing protein chains. *Acta Crystallogr. D* **62**, 1002–1011 (2006).
36. McCoy, A. J. *et al.* Phaser crystallographic software. *J. Appl. Crystallogr.* **40**, 658–674 (2007).
37. Jones, T. A., Zou, J.-Y., Cowan, S. W. & Kjeldgaard, M. Improved methods for building protein models in electron density maps and the location of errors in these models. *Acta Crystallogr. A* **47**, 110–119 (1991).
38. Adams, P. D. *et al.* PHENIX: building new software for automated crystallographic structure determination. *Acta Crystallogr. D* **58**, 1948–1954 (2002).
39. Davis, I. W. *et al.* MolProbity: all-atom contacts and structure validation for proteins and nucleic acids. *Nucleic Acids Res.* **35**, W375–W383 (2007).

Preplay of future place cell sequences by hippocampal cellular assemblies

George Dragoi¹ & Susumu Tonegawa¹

During spatial exploration, hippocampal neurons show a sequential firing pattern in which individual neurons fire specifically at particular locations along the animal's trajectory (place cells^{1,2}). According to the dominant model of hippocampal cell assembly activity, place cell firing order is established for the first time during exploration, to encode the spatial experience, and is subsequently replayed during rest^{3–6} or slow-wave sleep^{7–10} for consolidation of the encoded experience^{11,12}. Here we report that temporal sequences of firing of place cells expressed during a novel spatial experience occurred on a significant number of occasions during the resting or sleeping period preceding the experience. This phenomenon, which is called preplay, occurred in disjunction with sequences of replay of a familiar experience. These results suggest that internal neuronal dynamics during resting or sleep organize hippocampal cellular assemblies^{13–15} into temporal sequences that contribute to the encoding of a related novel experience occurring in the future.

We recorded neuronal firing sequences from the CA1 area of the mouse hippocampus (Supplementary Fig. 1) during periods of awake rest (Fam-Rest) alternating with periods of running (Fam-Run) on a familiar track (Fam session; Supplementary Fig. 2a) that preceded the exploration of a novel linear arm in contiguity with the familiar track (Contig-Run on L-shaped track; Fig. 1, Supplementary Fig. 2a and Methods). All the place cells active on the novel arm during Contig-Run, whether previously silent¹⁶ (19% in both directions and 31% in at least one direction; Methods and Supplementary Tables 1–3) or active during Fam-Run (subpanels a in Fig. 1), fired during Fam-Rest at the ends of the familiar track (range, 0.17–11.7 Hz; Supplementary Fig. 3) as part of a number of 'spiking events'. The spiking events were defined as epochs composed of multiple individual spikes from at least four different place cells active on the novel arm or familiar track, separated by less than 50 ms and flanked by at least 50 ms of silence^{3,4}. More significantly, the temporal sequence in which the cells active on the novel arm fired during Fam-Rest (subpanels b in Fig. 1) was significantly correlated with the spatial sequence in which they fired later as place cells on the novel arm during Contig-Run (subpanels c in Fig. 1), despite being uncorrelated with their spatial sequence as place cells on the familiar track during Fam-Run. This is illustrated as place cell sequences during Contig-Run (subpanels c in Fig. 1) and Fam-Run (subpanels a in Fig. 1) compared with the firing sequences of these cells within individual spiking events observed during Fam-Rest (subpanels b in Fig. 1). We refer to this process as 'preplay' of place cell sequences because the temporal sequence of firing during Fam-Rest had occurred before the actual exploration of the novel arm in the subsequent Contig-Run and was not a replay of the place cell sequences from the previous Fam-Run.

To quantify the significance of preplay and to compare it with replay, we created place cell sequence templates according to the spatial order of the peak firing of place cells^{3,4,10} on the novel arm during Contig-Run (novel arm templates; subpanels c in Fig. 1 and Methods) and on the familiar track during Fam-Run (familiar track templates) for each run direction. The spikes of all the place cells used to construct the two types

of template that were emitted during Fam-Rest were sorted by time, and spiking events were determined as explained above (subpanels b in Fig. 1). For each spiking event, we calculated a rank-order correlation between the novel arm templates and the temporal sequence of firing of the corresponding cells in the spiking events during Fam-Rest. The event correlation was considered significant if it exceeded the 97.5th percentile of a distribution of correlations resulting from randomly shuffling the order of place cells in the novel arm templates 200 times ($P < 0.025$). Forward⁴ and reverse^{3,4} preplay refers to the cases in which the sequence of place cells during Contig-Run and the firing order of the corresponding cells in Fam-Rest were in the same and opposite directions, respectively. In 91% of the preplay cases, the spiking events were correlated with the novel arm template in one direction only. The distribution of event correlation values obtained using the original novel arm templates was significantly shifted towards higher positive or negative values in comparison with the distribution of correlation values obtained using shuffled templates (Fig. 2a and Supplementary Fig. 4). Figure 2a also shows the distribution of significant preplay events (in red). Of all the spiking events detected as above and in which at least four novel arm place cells were active, 14.2% were significant preplay events for the place cell sequence on the novel arm ($P < 10^{-32}$, binomial probability test⁴) in the forward or reverse order (Fig. 2b).

The occurrence of significant preplay events was correlated with the occurrence of high-frequency ripple oscillations in CA1 (Fig. 2c). The majority of the significant preplay events (81.1%; Fig. 2d, total, blue) took place at the junction between the familiar and novel arms, and the remaining 18.9% took place at the free end of the familiar track (Fig. 2d, total, purple). The proportion of significant preplay events among the total events at each of the two track ends was higher at the junctional end (15.2%, $P < 10^{-26}$) than at the free end (8.5%, $P < 10^{-4}$) of the familiar track ($P < 0.035$, Z-test; Fig. 2d, normalized).

We found a relatively high correlation between the place field maps (Fig. 1A, B and Supplementary Fig. 5) of the familiar track before and after the novel experience (median $r = 0.66$; Fig. 2e, familiar track, blue); it was significantly higher than the correlations obtained when the cell identities were shuffled (median $r = 0.23$, $P < 10^{-4}$; Fig. 2e, familiar track, black). A similar correlation analysis showed a relatively high stability of the newly formed place fields on the novel arm from the beginning to the end of Contig-Run (median $r = 0.62$ (newly formed) versus median $r = 0.21$ (shuffled), $P < 10^{-3}$; Fig. 2e, novel arm, blue versus grey). These results suggest that preplay of the novel arm does not occur over an entirely new (that is, remapped) representation of the whole L-shaped track but rather benefits from the relative stability of the familiar track representation across sessions and perhaps facilitates the rapid, stable encoding of the novel arm experience.

Using the familiar track templates and spiking events during Fam-Rest, constructed as above, we determined that 16.2% ($P < 10^{-91}$; data not shown) were significant replay events^{3–6,17} among the spiking events in which a minimum of four familiar track place cells were active. All significant preplay events occurring during Fam-Rest ($n = 75$) were

¹The Picower Institute for Learning and Memory, RIKEN-MIT Center for Neural Circuit Genetics, Department of Biology and Department of Brain and Cognitive Sciences, Massachusetts Institute of Technology, Cambridge, Massachusetts 02139, USA.

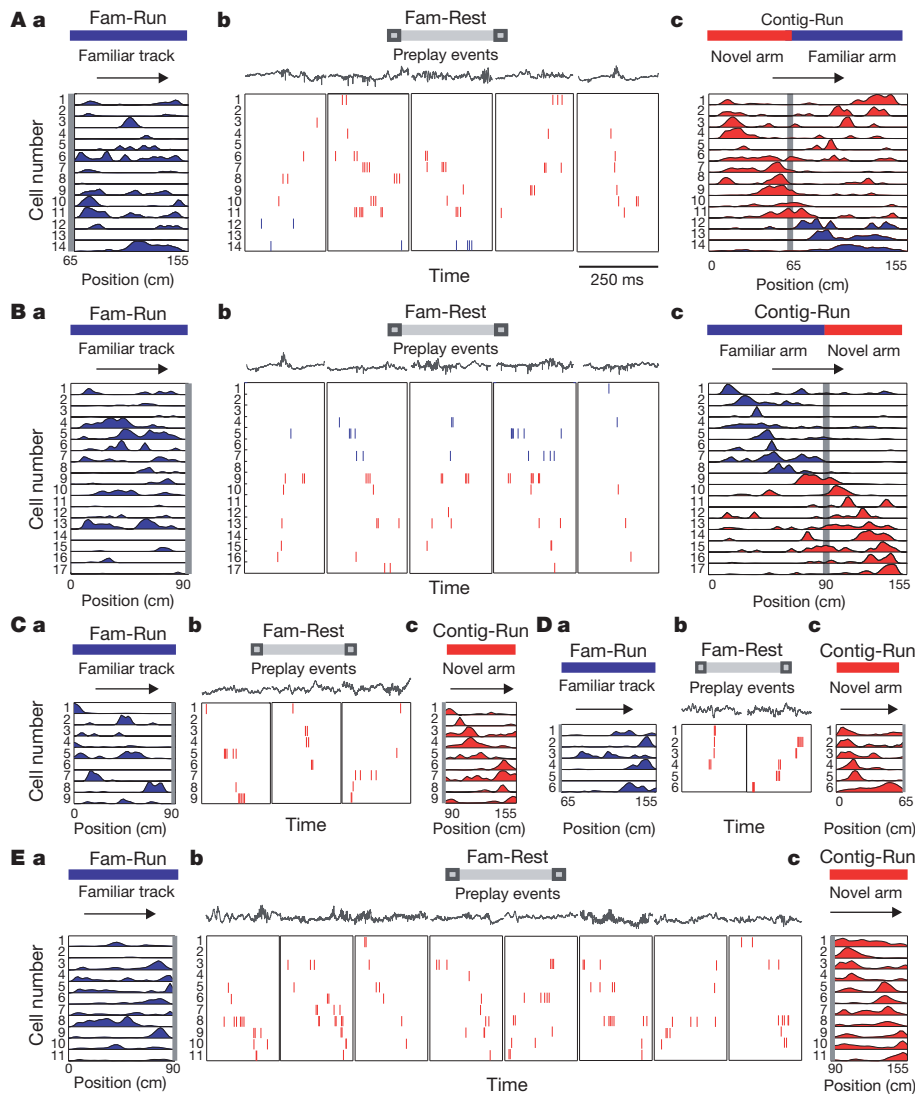


Figure 1 | Preplay of novel place cell sequences. Fam-Run and Fam-Rest respectively denote run and rest sessions on the familiar linear track before barrier removal; Contig-Run denotes run sessions on the L-shaped track after barrier removal. The L-shape track was linearized for display/analysis. **A, B, mouse 1; C, D, mouse 2; E, mouse 3.** **A–E, a,** Spatial activity on the familiar track during Fam-Run of the cells that had place fields in Contig-Run and preplayed during Fam-Rest (one cell per row); activity on the novel arm and familiar track are on the same scale. Horizontal arrows indicate run directions. Vertical grey bars indicate barrier locations during Fam-Run and Fam-Rest. **A–E, b,** Examples of representative spiking events in the forward or reverse

tested for possible replay of the familiar track spatial sequence: these spiking events were more correlated with the novel arm template (Fig. 2f, red) than the familiar track template (Fig. 2f, blue). Seventy-two percent ($n = 54$) of the significant events previously considered to be preplay had no significant correlation with the familiar track template. An additional 16% ($n = 12$) of those events were better correlated with the novel arm templates (mean absolute $r = 0.92$) than with the familiar track template (mean absolute $r = 0.67$, $P < 10^{-3}$). Together, these findings reject the hypothesis that the preplay events simply represent a replay of the familiar track activity (see additional controls in Supplementary Information). Moreover, we found that the proportion of events exclusively composed of silent cells that perfectly matched the novel arm spatial templates was 0.67 (16 of 24 triplets), which is significantly greater ($P < 0.025$) than the proportion of by-chance perfect matches (0.33).

To illustrate the distribution and relative proportions of preplay and replay events among all significant spiking events during Fam-Rest, we

calculated a ‘template specificity index’ (Fig. 2g and Methods) for each event. Pure preplay events (Fig. 2g, red) and pure replay events (Fig. 2g, blue) were segregated, and only a minority of events were significant for both preplay and replay (Fig. 2g, yellow). Consistent with this segregation of preplay and replay events, the novel arm and the ‘corresponding familiar track’ templates were not significantly correlated (Fig. 2h and Methods). The ratio between the number of pure replay events ($n = 171$) and the number of pure preplay events ($n = 54$) during Fam-Rest was about 3.1 (Fig. 2g, inset; see Supplementary Information for proportions of events). Preplay and replay events were distributed in time across Fam-Rest (Supplementary Fig. 6a–c) and their occurrences were generally uncorrelated (Supplementary Fig. 6d). The majority (79.9%) of the spiking events during Fam-Rest did not significantly correlate with either of the two templates (data not shown).

We used a Bayesian reconstruction algorithm^{2,5,6,18,19} (Methods) to decode the animals’ position from the spiking activity during Fam-Run (Fig. 3a) or Fam-Rest (Fig. 3b, c). For all original and shuffled⁴⁶

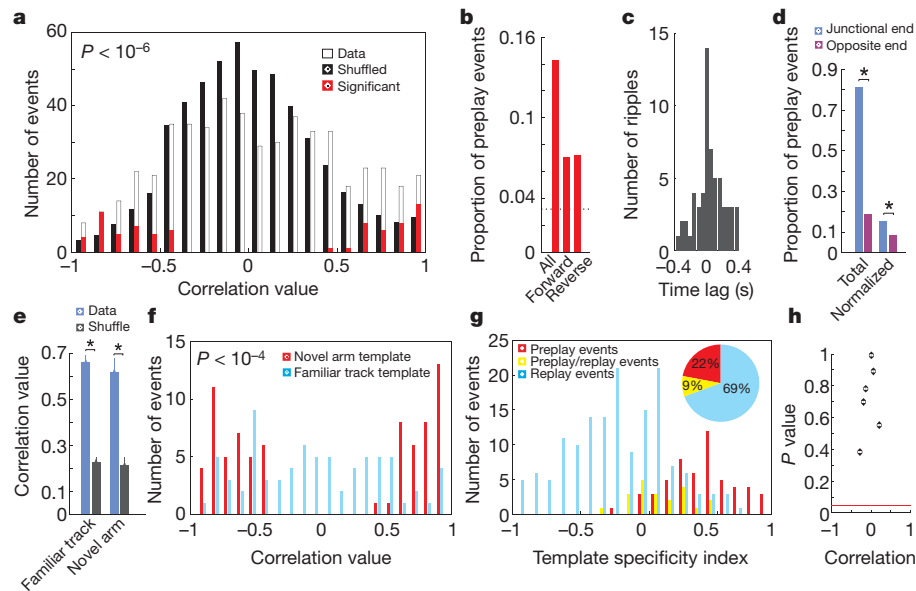


Figure 2 | Quantification of the preplay phenomenon and comparison with replay. **a**, Distribution of correlations between spiking events in Fam-Rest and spatial templates of the novel arm. Open bars indicate spiking events versus the original (unshuffled) templates; filled bars indicate spiking events versus 200 shuffled templates scaled down 200 times; red bars show the distribution of preplay (that is, significant) events. Similar distributions (not shown) of corresponding spiking events were obtained when spatial templates were constructed using all place cells active on the L-shaped track (Figs 1A, b, c and 1B, b, c; red and blue). **b**, Proportion of all, forward and reverse preplay events among the spiking events in Fam-Rest. The dotted line indicates the chance level (3.2%). **c**, Cross-correlation between preplay events and ripple epochs. **d**, Location of preplay events on the familiar track: total, proportions of preplay events at ends of the track; normalized, proportion of preplay events normalized by the number of spiking events at each end of track. Preplay events represented a trajectory running from the free end of the novel arm to the junctional end (40%) or begun near the familiar track (60%); the latter suggests that in some cases preplay events could be triggered by the activity of the familiar track place cells during Fam-Rest. **e**, Stability of place cell spatial tuning across the novel experience: familiar track, stability of the place fields active on the familiar track before (Fam-Run) versus after (Contig-Run) barrier removal; novel arm, stability of the place fields active on the novel arm at the beginning

probability distributions, a line was fitted to the data using a line-finding algorithm⁶ to represent the decoded virtual trajectory (Methods and Supplementary Information). In 16.36% of cases representing trajectories, the reconstructed trajectory during spiking events in Fam-Rest was contained within the novel arm (Fig. 3c, top), a place the animal had not yet visited (that is, trajectory preplay). Moreover, in 79.8% of the trajectory preplay cases the shuffling procedures resulted in lines that were significantly less or not at all contained within the novel arm (that is, not preplay; Supplementary Information). The remaining trajectories decoded during Fam-Rest represented replay of the familiar track (64.15%; Fig. 3c, middle) or spanned the joint familiar track/novel arm space (19.49%; Fig. 3c, bottom). Means of absolute rank-order correlations between spiking activity and novel arm templates (Fig. 2a) restricted during epochs of trajectory preplay were significantly larger than those between spiking activity and familiar track templates calculated during the same epochs (0.75 versus 0.59, $P < 10^{-4}$). Overall, these results support the existence of the preplay phenomenon.

To investigate the possibility that preplay of novel arm place cell sequences during Fam-Rest depends on the prior run experience on the familiar track, mice with no prior experience on any linear track were placed in a high-walled sleep box and recorded while resting/sleeping. The animals were then transferred to a novel isolated linear track that was in the same room but could not be seen from inside the

(first four laps of run) versus the end (last four laps) of the Contig-Run session. Data (blue), within-cell correlation of place cell spatial tuning for the corresponding track/arm; shuffle (black), cell identity shuffle (Supplementary Information). Error bars, s.e.m.; asterisks in **d** and **e** indicate significant differences. **f**, Distribution of preplay event correlations (red) versus distribution of these event correlations with the familiar track template (blue). Spiking events were detected using all place cells from the familiar track and novel arm templates (>1 Hz). Red bars are the same as in **a**. Correlation is strong with the novel arm template (preplay) and weak with the familiar arm template (replay). The P value corresponds to there being a significant difference between the two distributions. **g**, Disjunctive distribution of pure preplay (red), pure replay (blue) and preplay/replay (yellow) events during Fam-Rest over their template specificity index (Supplementary Information). Inset, proportions of pure preplay events (red), pure replay events (blue) and preplay/replay events (yellow) among all of the spiking events that were significantly correlated with at least familiar track templates or novel arm templates. **h**, Lack of correlation between the novel arm template and the corresponding familiar track template. Each of the six dots represents either a forward or a reverse run direction of one of the three mice analysed. Red horizontal line denotes a P value of 0.05. The correlation values were not significant in any of the cases (Supplementary Information).

box, and the recording continued during *de novo* formation of place cells (Supplementary Fig. 2b, *de novo* session). We found that in a relatively large proportion (16.1%) of spiking events identified during sleep/rest in the sleep box, the neuronal firing sequences were significantly correlated with the place cell sequences observed during the first run session on the novel track (Fig. 4A, B and Methods); this was the case for all four individual mice (Supplementary Fig. 7). Preplay events were associated with the ripple occurrence (Fig. 4C). The place cells established on the novel track in the *de novo* session were more dynamic (median $r = 0.42$; Fig. 4D, blue) than in Contig-Run (median $r = 0.62$, $P < 0.016$; Fig. 2e, right, blue).

We have demonstrated that a significant number of temporal firing sequences of CA1 cells during resting periods of a familiar track exploration that preceded a novel track exploration in the same general environment were correlated with the place cell sequences of the novel track rather than the familiar track. This phenomenon, preplay, is temporally opposite to the process of replay^{3–10,19,20}, when activity during rest or sleep periods recapitulates place cell sequences that have already occurred during previous explorations. Preplay differs fundamentally from replay because it occurs before exploration of novel tracks.

Although our recordings were carried out in CA1, we believe that what we observed could be a reflection of the output of the recurrent cellular assemblies from upstream regions (CA3 or entorhinal cortex).

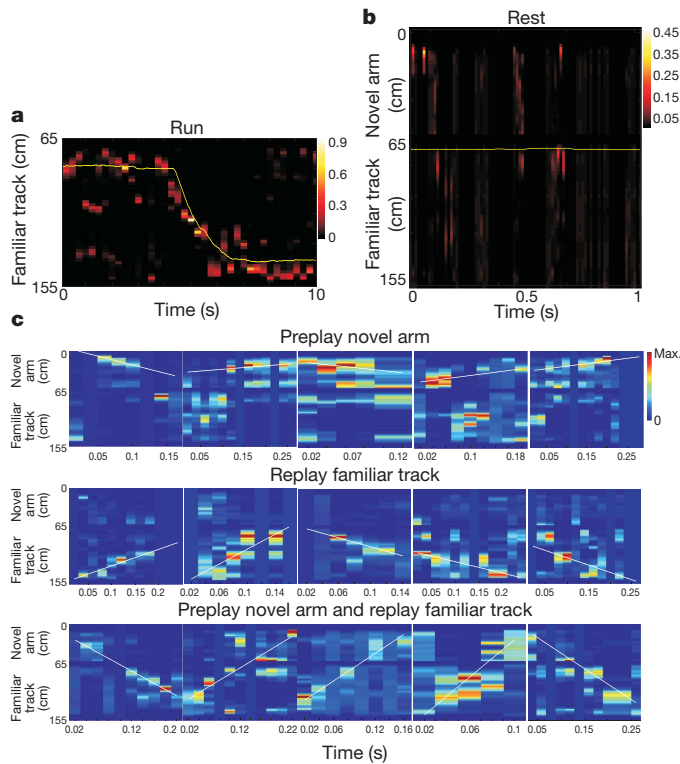


Figure 3 | Bayesian reconstruction of the animal's trajectory in the familiar track (replay) and novel arm (preplay). **a**, Position reconstruction of a one-lap run on the familiar track from the ensemble place cell activity during Fam-Run. The heat map displays the reconstructed position of the animal using ensemble place cell activity during the run (250-ms bins; animal velocity, $>5 \text{ cm s}^{-1}$). The yellow line indicates the actual trajectory of the animal during Fam-Run. **b**, Example of virtual trajectory reconstruction (familiar track and novel arm) from the ensemble place cell activity during Fam-Rest at the ends of the familiar track (20-ms bins; animal velocity, $<5 \text{ cm s}^{-1}$) before barrier removal and novel arm exploration. The yellow line reflects the spatial location of the animal in time: the animal was immobile at the junction end of the familiar track. The time-compressed ($\sim 5 \text{ m s}^{-1}$) trajectory reconstruction often 'jumps' over the barrier (top of the figure) into the novel arm area. At around 0.5 s, a preplay of the novel arm initiated from the distal (free) end of the novel arm 'propagates' towards the location of the animal. **c**, Examples of preplay of the novel arm (top), replay of the familiar track (middle) and preplay of the novel arm together with replay of the familiar track (bottom) during Fam-Rest. All conditions are the same as in **b**. The white line shows the linear fit maximizing the likelihood along the virtual trajectory. Colour bars indicate probability of trajectory reconstruction.

During running on a familiar track, some of the cells in the postulated upstream cellular assemblies fire sequentially at spatial locations while others, although connected anatomically to these cells, remain silent. The lack of expression of preplay sequences during Fam-Run may reflect their state-dependent suppression or subthreshold activation during these exploratory behaviours. Owing to increased net excitation during rest periods predominantly during ripples²¹, some of these silent cells together with some of the familiar track cells are activated above threshold and fire in a certain sequence. Their sequence of activation may be determined in part by their functional connectivity within the hippocampal formation network. Some of these sequences may in turn be activated on a novel track as place cell sequences (Supplementary Fig. 8). The activation of the novel place cell sequences during running may strengthen their pre-existing assembly organization manifested during preplay.

It could be argued that during Contig-Run the animals simply considered the novel arm to be an extension of the familiar arm and, thus, what we considered to be preplay events were replays of the previous runs on the familiar track. If this was the case, preplay events would not

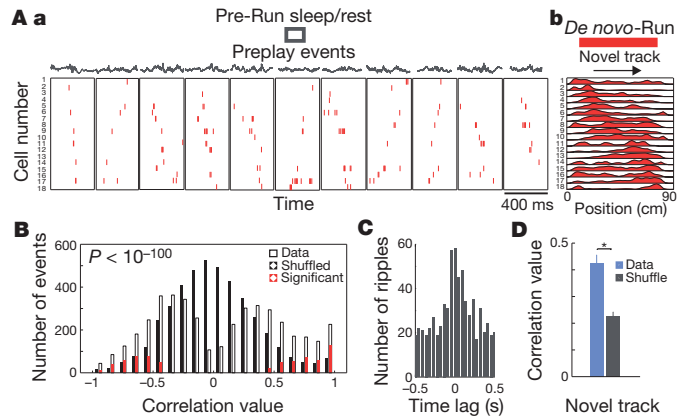


Figure 4 | Preplay of novel place cell sequences before any linear track experience. **A**, Sleep/rest session in the sleep box (Pre-Run sleep/rest) before the first run session on a linear track (*De novo*-Run). Display format is the same as in Fig. 1. **A, a**, Representative spiking events in the forward or reverse order during Pre-Run sleep/rest in 400-ms time windows. **A, b**, Place cell sequences on the novel track (red) during the *De novo*-Run session. Each row represents one cell in which the activity was normalized to the maximum firing rate. One run direction in one animal is shown. The median number of place cells active on the novel track participating in preplay events is six. **B**, Distribution of spiking events in Pre-Run sleep/rest as a function of the rank-order correlation with the place cell sequence template of the novel track. Display format is the same as in Fig. 2a. **C**, Cross-correlation between preplay events and ripple epochs during Pre-Run sleep/rest. **D**, Stability of place cell spatial tuning across the novel track experience. Display format is the same as in Fig. 2e (novel arm). Error bars, s.e.m.; asterisk indicates significant difference.

be expected to be found when the experience of the familiar track run is eliminated. This idea was refuted by the demonstration of frequent preplay events in the sleep box before the mice were transferred onto a novel linear track (*de novo* condition). Under this condition, the place cell sequences were more dynamic and a higher proportion of all spiking events correlated with the place cell sequences in these runs than in the later runs on novel linear tracks. These results suggest a shift in the relative contribution of internal^{22,23} and external drives in the formation of place cell sequences on encounter with a novel track. In the early phase, internal drives originating in the dynamic cellular assembly activities, which probably reflect numerous past experiences distinct from the current one and expressed as preplay, may have a greater role, whereas in the late phase, external drives that come from the specific set of stimuli of the current experience may dominate. Thus, place cell sequences on novel tracks seem to be products of a dynamic interplay between the internal and external drives.

Several previous studies did not reveal preplay^{7,8,10,20}. Although it is difficult to pinpoint the apparent discrepancies between these studies and the present one, we suggest that the use of insufficiently sensitive methods (pairwise correlations) by some studies^{7,8,20} and small sample sizes by others¹⁰ might have precluded detection of preplay in previous work (see Supplementary Information for details). Data from the *de novo* condition (Fig. 4), in which we observed an even higher proportion of preplay events, have not been reported previously.

Our data showed that novel preplay events coexist in disjunction with familiar replay events during the rest periods on the familiar track. This and the finding that these preplay and replay events together make up fewer than one-quarter of all detected spiking events suggest that they are part of a dynamic repertoire of temporal sequences in the hippocampus that are past-experience dependent (replay) or future-experience expectant²⁴ (preplay). Post-experience replay of place cell sequences during resting^{3–6} or slow-wave sleep^{8–10} has been proposed to have an important role in memory consolidation^{11,12}. The temporal preplay of new place cell sequences during resting or sleep is consistent with a predictive function for the hippocampal formation²⁵ and may contribute to accelerating learning²⁶

when a new experience is introduced in multiple steps of increasing novelty.

METHODS SUMMARY

We recorded place cells from the CA1 area of the hippocampus with six independently movable tetrodes in four mice during sleep/rest sessions in the sleep box before any experience on linear tracks and during the first run session on a novel track. Following familiarization with the linear track, animals were subsequently allowed to explore a continuous (L-shaped) track in which the now familiar track and a new novel arm were made contiguous. To quantify the significance of the preplay and replay processes, spiking events in which at least four cells were active were detected during sleep/rest (speed, $<1\text{ cm s}^{-1}$) periods in the sleep box or awake rest (speed, $<2\text{ cm s}^{-1}$) periods at the ends of the familiar track and novel arm, predominantly during ripple epochs.

We calculated statistical significance at the $P < 0.025$ level for each event by comparing the rank-order correlation between the event sequence and the place cell sequence (template) with the distribution of correlation values from 200 templates obtained by shuffling the original order of the place cells. Proportions of significant events were calculated as the ratio between the number of significant events and the total number of spiking events. We calculated the overall significance of preplay or replay processes by comparing the distribution of correlation values of all events with the distribution of correlation values of shuffled templates (Kolmogorov–Smirnov test). The significance of the proportion of significant events out of the total number of spiking events was determined as the binomial probability of observing the number of significant events (as successes) from the total number of spiking events (as independent trials), with a probability of success of 0.025 in any given trial. We reconstructed the position of the animal from the spiking activity emitted during resting periods using Bayesian decoding procedures⁶.

Full Methods and any associated references are available in the online version of the paper at www.nature.com/nature.

Received 4 December 2009; accepted 29 October 2010.

Published online 22 December 2010.

- O'Keefe, J. & Nadel, L. *The Hippocampus as a Cognitive Map* (Oxford Univ. Press, 1978).
- Wilson, M. A. & McNaughton, B. L. Dynamics of the hippocampal ensemble code for space. *Science* **261**, 1055–1058 (1993).
- Foster, D. J. & Wilson, M. A. Reverse replay of behavioural sequences in hippocampal place cells during the awake state. *Nature* **440**, 680–683 (2006).
- Diba, K. & Buzsáki, G. Forward and reverse hippocampal place-cell sequences during ripples. *Nature Neurosci.* **10**, 1241–1242 (2007).
- Karlsson, M. P. & Frank, L. M. Awake replay of remote experiences in the hippocampus. *Nature Neurosci.* **12**, 913–918 (2009).
- Davidson, T. J., Kloosterman, F. & Wilson, M. A. Hippocampal replay of extended experience. *Neuron* **63**, 497–507 (2009).
- Wilson, M. A. & McNaughton, B. L. Reactivation of hippocampal ensemble memories during sleep. *Science* **265**, 676–679 (1994).
- Skaggs, W. E. & McNaughton, B. L. Replay of neuronal firing sequences in rat hippocampus during sleep following spatial experience. *Science* **271**, 1870–1873 (1996).
- Nádasy, Z., Hirase, H., Czurko, A., Csicsvari, J. & Buzsáki, G. Replay and time compression of recurring spike sequences in the hippocampus. *J. Neurosci.* **19**, 9497–9507 (1999).
- Lee, A. K. & Wilson, M. A. Memory of sequential experience in the hippocampus during slow wave sleep. *Neuron* **36**, 1183–1194 (2002).
- Buzsáki, G. Two-stage model of memory trace formation: a role for “noisy” brain states. *Neuroscience* **31**, 551–570 (1989).
- Nakashiba, T., Buhl, D. L., McHugh, T. J. & Tonegawa, S. Hippocampal CA3 output is crucial for ripple-associated reactivation and consolidation of memory. *Neuron* **62**, 781–787 (2009).
- Hebb, D. O. *The Organization of Behavior: A Neuropsychological Theory* (Wiley, 1949).
- Harris, K. D., Csicsvari, J., Hirase, H., Dragoi, G. & Buzsáki, G. Organization of cell assemblies in the hippocampus. *Nature* **424**, 552–556 (2003).
- Dragoi, G. & Buzsáki, G. Temporal encoding of place sequences by hippocampal cell assemblies. *Neuron* **50**, 145–157 (2006).
- Thompson, L. T. & Best, P. J. Place cells and silent cells in the hippocampus of freely-behaving rats. *J. Neurosci.* **9**, 2382–2390 (1989).
- O'Neill, J., Senior, T. & Csicsvari, J. Place-selective firing of CA1 pyramidal cells during sharp wave/ripple network patterns in exploratory behavior. *Neuron* **49**, 143–155 (2006).
- Zhang, K., Ginzburg, I., McNaughton, B. L. & Sejnowski, T. J. Interpreting neuronal population activity by reconstruction: unified framework with application to hippocampal place cells. *J. Neurophysiol.* **79**, 1017–1044 (1998).
- Johnson, A. & Redish, A. D. Neural ensembles in CA3 transiently encode paths forward of the animal at a decision point. *J. Neurosci.* **27**, 12176–12189 (2007).
- Kudrimoti, H. S., Barnes, C. A. & McNaughton, B. L. Reactivation of hippocampal cell assemblies: effects of behavioral state, experience, and EEG dynamics. *J. Neurosci.* **19**, 4090–4101 (1999).
- Csicsvari, J., Hirase, H., Czurko, A., Mamiya, A. & Buzsáki, G. Oscillatory coupling of hippocampal pyramidal cells and interneurons in the behaving rat. *J. Neurosci.* **19**, 274–287 (1999).
- Dragoi, G., Harris, K. D. & Buzsáki, G. Place representation within hippocampal networks is modified by long-term potentiation. *Neuron* **39**, 843–853 (2003).
- Pastalkova, E., Itskov, V., Amarasingham, A. & Buzsáki, G. Internally generated cell assembly sequences in the rat hippocampus. *Science* **321**, 1322–1327 (2008).
- Black, J. E. & Greenough, W. T. *Advances in Developmental Psychology* (Lawrence Erlbaum, 1986).
- Hassabis, D., Kumaran, D., Vann, S. D. & Maguire, E. A. Patients with hippocampal amnesia cannot imagine new experiences. *Proc. Natl Acad. Sci. USA* **104**, 1726–1731 (2007).
- Tse, D. *et al.* Schemas and memory consolidation. *Science* **316**, 76–82 (2007).

Supplementary Information is linked to the online version of the paper at www.nature.com/nature.

Acknowledgements We thank M. A. Wilson for assistance with data acquisition, discussions and comments on an earlier version of the manuscript; J. O'Keefe, A. Siapas, F. Kloosterman, D. L. Buhl for comments on earlier versions of the manuscript; and F. Kloosterman for providing assistance with the line detection for the Bayesian decoding. This work was supported by NIH grants R01-MH078821 and P50-MH58880 to S.T., who was an HHMI Investigator in an earlier part of this study.

Author Contributions S.T. and G.D. conceived the project jointly. G.D. designed and performed the experiments and the analyses. G.D. and S.T. wrote the paper.

Author Information Reprints and permissions information is available at www.nature.com/reprints. The authors declare no competing financial interests. Readers are welcome to comment on the online version of this article at www.nature.com/nature. Correspondence and requests for materials should be addressed to G.D. (gdragoi@mit.edu) or S.T. (tonegawa@mit.edu).

METHODS

Surgery and experimental design. Electrophysiological recordings were performed on four C57BL/6 mice (strain NRI-floxed²⁷) with ages between 18 and 22 weeks. All animals were implanted under Avertin anaesthesia with six independently movable tetrodes aiming for the CA1 area of the right hippocampus (1.5–2 mm posterior to bregma and 1–2 mm lateral to the midline; Supplementary Fig. 1). The reference electrode was implanted posterior to lambda over the cerebellum. During the following week of recovery, the electrodes were advanced daily while animals rested in a small, walled sleeping box (12 × 20 cm², 35 cm high). The animal position was monitored by means of two infrared diodes attached to the headstage.

The experimental apparatus consisted of a 90 × 65 cm² rectangular, walled, linear track maze. All tracks were 4 cm wide at the bottom and 8–9 cm wide at the top, and all linear track walls were 10 cm high. Experimental sessions were conducted while the animals explored for chocolate sprinkle rewards placed always at the ends of the corresponding linear tracks (one sprinkle at each end of the track on each lap). Neuronal activity was recorded in naive animals (four mice) during the sleep/rest session in the sleep box immediately preceding the first experience on linear tracks, and continued (Fig. 4) during the first run session on a novel track. After familiarization with the linear track, the animals went through a recording session of 15–60 min (Fam session), and the recordings continued for the next 34–42 min (Contig session) while the animals explored an L-shaped track for the first time. In this track, the familiar arm and the novel arm were made contiguous by removing the barrier that had separated them (Fig. 1). For the purpose of analysing the recording data, the Fam session was further divided into Fam-Run, in which the animals ran through the track (velocity of animal's movement was higher than 5 cm s⁻¹), and Fam-Rest, where the animals took awake rests at the ends of the track (velocity of animal's movement was less than 2 cm s⁻¹). During resting periods, the animals consumed the chocolate sprinkle and groomed, but mostly they were still until they self-initiated the next lap of run on the linear track. After completion of the experiments, the brains of all mice were perfused, fixed, sectioned and stained using nuclear fast red (Supplementary Fig. 1) or cresyl violet for electrode track reconstruction.

Recordings and single-unit analysis. A total of 87 neurons were recorded from the CA1 area of the hippocampus in four mice during the Fam and Contig sessions (Supplementary Tables 1–3). A total of 69 CA1 neurons were recorded from the four mice in the *de novo* condition (26, 20, 10 and 13 cells, respectively). Single cells were identified and isolated using the manual clustering method Xclust² and the application of cluster quality measurements²⁸. Pyramidal cells were distinguished from interneurons on the basis of spike width, average rate and autocorrelations²².

Place fields were computed as the ratio between the number of spikes and the time spent in 2-cm bins along the track, smoothed with a Gaussian kernel with a standard deviation of 2 cm. Bins where the animal spent a total of less than 0.1 s and periods during which the animal's velocity was below 5 cm s⁻¹ were excluded. Place field length and peak rate were calculated after separating the direction of movement and linearizing the trajectory of the animal. Linearized place fields were defined as areas with a localized increase in firing rate above 1 Hz for at least five contiguous bins (10 cm). The place field peak rate and location were given by the rate and location of the bin with the highest ratio between spike counts and time spent. Place field borders were defined as the points where the firing rate became less than 10% of the peak firing rate or 1 Hz (whichever was bigger) for at least 2 cm.

Local field potential analysis. Ripple oscillations were detected during sleep/rest periods in the sleep box and during rest periods at the ends of the tracks. The electroencephalography signal was filtered (120–200 Hz) and ripple-band amplitude was computed using the Hilbert transform. Ripple epochs with maximal amplitude more than 5 s.d. above the mean, beginning and ending at 1 s.d. were detected. The time of ripple occurrence (Figs 2c and 4C) was the time of its maximal amplitude. The proportion of ripples with which cells with place fields on the novel arm of the L-shaped track fired in the preceding session (Supplementary Fig. 3) was calculated for each qualifying cell as the ratio between the number of ripples during which the cell fired at least one spike and the total number of ripples during the corresponding exploratory session.

Preplay and replay analyses. To analyse the preplay and replay processes, spiking events were detected during Pre-Run sleep/rest periods in the sleep box (*de novo* condition; velocity, <1 cm s⁻¹) or during awake rest periods at the ends of the running tracks (Contig condition; velocity, <2 cm s⁻¹). A spiking event was defined as a transient increase in the firing activity of a population of at least four different place cells within a temporal window preceded and followed by at least 50 ms of silence. Overall, similar results were obtained using 50-, 60-, 75- and 100-ms time windows. The spikes of all the place cells active on the novel track that were emitted during the Pre-Run sleep/rest in the box for the *de novo* condition as well as the spikes of all the place cells active on the familiar track or the novel arm that were

emitted during Fam-Rest session at the two ends of the familiar track for Contig condition were respectively sorted by time and further used for the detection of the spiking events.

All four animals exhibited a significant number of spiking events in the Pre-Run session of the *de novo* condition. Three of the four animals (mice 1–3) exhibited a significant number of spiking events in the Contig condition, the remaining animal (mouse 4) having a below-threshold number of simultaneously active CA1 place cells. The time of the spiking event used to compute the cross-correlation with ripple epoch occurrence (Figs 2c and 4C) was the average time of all spikes comprising the spiking event. The place cell sequences (templates) were calculated for each direction of the animal's movement and for each run session (*De novo*-Run, Fam-Run and Contig-Run) by ordering the spatial location of the place field peaks that were above 1 Hz. For place cells with multiple place fields above 1 Hz on a particular arm or track in the Contig condition (six of 52 place cells active on the novel arm in the two directions, or 12%; two for each direction in mouse 1, one in mouse 2 and one in mouse 3), only the place field corresponding to the peak firing rate of the place cell on that arm or track was considered for the construction of the template of that particular arm or track, to be consistent with all the previous studies that used spatial templates to demonstrate replay during sleep or awake rest^{3,4,10}. Place cells with fields on both the novel arm in the Contig-Run session and the familiar track in the Fam-Run session participated in the construction of both the novel arm and familiar track templates.

Statistical significance was calculated for each event by comparing the rank-order correlation between the sequence of cells' firing during the event (that is, event sequence) and the place cell sequence (template), on the one hand, and the distribution of correlation values between the event sequence and 200 surrogate templates obtained by shuffling the order of place cells, on the other⁴ (Fig. 2a). The significance level was set at 0.025 to control for multiple comparisons (two directions of run). The proportions of significant events (preplay novel track, preplay novel arm (Fig. 2b), replay novel arm and replay familiar track) were each calculated as the ratio between the number of significant events and the total number of spiking events in which at least four corresponding place cells were active⁴. Corresponding familiar track templates (Fig. 2h) were constructed by ordering the location of peak firing on the familiar track during Fam-Run (no minimum threshold of firing) of all place cells that subsequently fired on the novel arm. Cells comprising the corresponding familiar track templates are the same as those comprising the novel arm templates. We note that these corresponding familiar track templates are different from the ones used in Figs 1 and 2a–g, which were constructed by ordering the peak firing of all place cells active on the familiar track >1 Hz.

The overall significance of the preplay (Fig. 2a) or replay process was calculated by comparing the distribution of correlation values of all events relative to the original template with the distribution of correlation values relative to the shuffled surrogate templates, using the Kolmogorov–Smirnov test³. Quantification of the replay versus preplay events during the Fam-Run session (Fig. 2f, g) was performed as described above using different spatial templates for the familiar track and the novel arm. All spiking events were correlated with both the novel arm and the familiar track templates. Events significantly correlated only with familiar track or with novel arm templates were considered pure replay and pure preplay, respectively. The template specificity index was calculated for each event as the difference between the absolute value of the event's correlation with the novel arm template (preplay, high positive index) and the event's correlation with the familiar track template (replay, high negative index). For the purpose of displaying the template specificity index, events correlated with the novel arm but not with the familiar track templates were considered preplay and events correlated with the familiar track but not with the novel arm templates were considered replay (Fig. 2g). Additionally, events correlated with both the familiar track and the novel arm templates formed a third group, preplay/replay events, displayed in yellow in the inset of Fig. 2g.

Correlations between pairs of familiar track and novel arm templates (Fig. 2h) were performed using modified familiar track templates that were constructed using the location of peak firing (>0 Hz) of only those cells that had place fields on the novel arm (peak rate, >1 Hz). The lack of significant correlation in this case demonstrates that the novel arm place cell sequence is not simply a transposition of a familiar track place cell sequence on the novel arm.

We also identified neurons that did not fire during Fam-Run, that activated during Fam-Rest events and that corresponded to trajectories on the novel arm during Contig-Run (silent cells). We calculated the correlation between the order in which they fired during Fam-Rest events and their spatial sequence as new place cells on the novel arm during Contig-Run, as previously explained. Owing to the low absolute number of silent neurons, only triplets of cells were available for further analysis ($n = 24$). The proportion of events perfectly matching the spatial template was compared with the proportion of by-chance perfect matching (0.33).

Stability of place cell maps. Stabilities of place cell firing on the familiar track before and after barrier removal as well as on the novel track (*de novo* condition) and the novel arm (Contig condition) in the beginning versus the end of the run session were assessed by calculating, for each place cell and each direction, a correlation between the spatial firing in the corresponding paired situations (before versus after barrier removal for the familiar track or the first four laps versus the last four laps of the *De novo*-Run or Contig-Run session for the novel track or arm, respectively). The place cell activity was not partitioned in place fields; rather, the whole activity on the particular track or arm was considered separately for each cell and direction (average correlations are shown in Figs 2e and 4D, blue bars). In addition, we calculated the same type of correlation after shuffling the identity of the cell in one member of the correlation (once for each different cell; average correlations are in Figs 2e and 4D, black bars). Shuffle results (Figs 2e and 4D, black bars) were computed as correlation between spatial tuning of cells on the familiar track during Fam-Run and spatial tuning of all other simultaneously recorded cells on the familiar arm during Contig-Run (familiar track group; Fig. 2e, left), or correlation between spatial tuning of cells on the novel arm (or novel track) during the beginning of Contig-Run (or *De novo*-Run) and spatial tuning of all the other simultaneously recorded cells on the novel arm (or novel track) during the end of Contig-Run (novel arm group; Fig. 2e, right) or *De novo*-Run (Fig. 4D). Original and shuffled correlations were compared using the rank-sum test. The average number of laps (traversal of the novel track in both directions) per session was 20.5 in *De novo*-Run (21, 16, 27 and 18 in the four mice) and 16.3 in Contig-Run (13, 14 and 22 in the three mice).

Bayesian reconstruction of actual and virtual trajectories. For each cell, we calculated a linearized spatial tuning curve on the familiar track during the Fam-Run session and a linearized spatial tuning curve on the novel arm during the Contig-Run session. The tuning curves were constructed in 2-cm bins from spikes emitted in both run directions at velocities higher than 5 cm s^{-1} , and were smoothed with a Gaussian kernel with a standard deviation of 2 cm. We constructed a joint spatial tuning curve for each cell by juxtaposing the spatial tuning curve on the familiar track during the Fam-Run session and the spatial tuning curve on the novel arm during the Contig-Run session. We also detected for each cell all the spiking activity emitted at velocities below 5 cm s^{-1} during the Fam-Run session, where replay and preplay events where shown to occur using the rank-order correlation method. We used a Bayesian reconstruction algorithm^{6,18} to decode the virtual position of the animal from the spiking activity during Fam-Rest (Fig. 3b) in non-overlapping, 20-ms bins using the joint spatial tuning curves. We then extracted epochs of reconstructed trajectory matching the time of the spiking events as detected using multiunit activity of place cells from the familiar

track and novel arm (rank-order correlation method; see 'Preplay and replay analyses', above).

We used two shuffling procedures to measure the quality of the Bayesian decoding. In the first shuffling procedure, for each event, the original time-bin columns of the probability distribution function (PDF) were replaced with an equal number of time-bin columns randomly extracted from a pool containing the time-bin columns of all PDFs of all detected events⁶. The shuffling procedure was repeated 500 times. In the second shuffling procedure, the identity of the place cells was randomly shuffled 100 times and new PDFs were calculated for all events. For all original and shuffled PDFs, a line was fitted to the data using a previously described line-finding algorithm⁶. Lines fitted to the original and shuffled data were compared using slope, spatial extent, location on the track and probability score. We defined replay and preplay as the epochs of Fam-Rest in which the reconstructed trajectory was located on the familiar track or the novel arm, respectively. The trajectory was defined across a set of position estimates during the corresponding epoch (Fig. 3c). Only epochs that lasted at least 60 ms (three bins) and which contained reconstructed trajectories spanning at least 10 cm were considered for further analysis. Trajectories for which 75% or more of their length was located on the familiar track were considered to represent replay of an animal's trajectory on the familiar track (Fig. 3c, middle), and trajectories for which 75% or more of their length was located in the novel arm were considered to represent preplay of the animal's future trajectory on the novel arm (Fig. 3c, top). The remaining events were considered preplay-replay (Fig. 3c, bottom).

An epoch was considered significant if the new line was less than 75% contained in the familiar track for replay or novel arm for preplay in at least 95% of the shuffled cases. For each epoch that was significant for replay or preplay using the reconstruction method, we retrieved the value of the rank-order correlation between the neuronal firing sequences and the familiar track and novel arm spatial templates as calculated using the rank-order correlation method. We compared the absolute correlation values between the epoch's firing sequences and familiar track templates with the absolute correlation values between the same epoch's firing sequences and novel arm templates. We also reconstructed the trajectory of the animal on the familiar track from the spiking activity during the Fam-Run session at velocities above 5 cm s^{-1} in 250-ms bins using the spatial tuning curves on the familiar track^{6,18} (Fig. 3a) to validate the decoding procedure.

27. Tsien, J. Z., Huerta, P. T. & Tonegawa, S. The essential role of hippocampal CA1 NMDA receptor-dependent synaptic plasticity in spatial memory. *Cell* **87**, 1327–1338 (1996).
28. Schmitzer-Torbert, N., Jackson, J., Henze, D., Harris, K. & Redish, A. D. Quantitative measures of cluster quality for use in extracellular recordings. *Neuroscience* **131**, 1–11 (2005).

Evidence for a spin-aligned neutron–proton paired phase from the level structure of ^{92}Pd

B. Cederwall¹, F. Ghazi Moradi¹, T. Bäck¹, A. Johnson¹, J. Blomqvist¹, E. Clément², G. de France², R. Wadsworth³, K. Andgren¹, K. Lagergren^{1,4}, A. Dijon², G. Jaworski^{5,6}, R. Liotta¹, C. Qi¹, B. M. Nyakó⁷, J. Nyberg⁸, M. Palacz⁵, H. Al-Azri³, A. Algora⁹, G. de Angelis¹⁰, A. Atač¹¹, S. Bhattacharyya^{2†}, T. Brock³, J. R. Brown³, P. Davies³, A. Di Nitto¹², Zs. Dombrádi⁷, A. Gadea⁹, J. Gál⁷, B. Hadinia¹, F. Johnston-Theasby³, P. Joshi³, K. Juhász¹³, R. Julin¹⁴, A. Jungclaus¹⁵, G. Kalinka⁷, S. O. Kara¹¹, A. Khaplanov¹, J. Kownacki⁵, G. La Rana¹², S. M. Lenzi¹⁶, J. Molnár⁷, R. Moro¹², D. R. Napoli¹⁰, B. S. Nara Singh³, A. Persson¹, F. Recchia¹⁶, M. Sandzelius^{1†}, J.-N. Scheurer¹⁷, G. Sletten¹⁸, D. Sohler⁷, P.-A. Söderström⁸, M. J. Taylor³, J. Timár⁷, J. J. Valiente-Dobón¹⁰, E. Vardaci¹² & S. Williams¹⁹

Shell structure and magic numbers in atomic nuclei were generally explained by pioneering work¹ that introduced a strong spin-orbit interaction to the nuclear shell model potential. However, knowledge of nuclear forces and the mechanisms governing the structure of nuclei, in particular far from stability, is still incomplete. In nuclei with equal neutron and proton numbers ($N = Z$), enhanced correlations arise between neutrons and protons (two distinct types of fermions) that occupy orbitals with the same quantum numbers. Such correlations have been predicted to favour an unusual type of nuclear superfluidity, termed isoscalar neutron–proton pairing^{2–6}, in addition to normal isovector pairing. Despite many experimental efforts, these predictions have not been confirmed. Here we report the experimental observation of excited states in the $N = Z = 46$ nucleus ^{92}Pd . Gamma rays emitted following the $^{58}\text{Ni}(^{36}\text{Ar}, 2n)^{92}\text{Pd}$ fusion–evaporation reaction were identified using a combination of state-of-the-art high-resolution γ -ray, charged-particle and neutron detector systems. Our results reveal evidence for a spin-aligned, isoscalar neutron–proton coupling scheme, different from the previous prediction^{2–6}. We suggest that this coupling scheme replaces normal superfluidity (characterized by seniority coupling^{7,8}) in the ground and low-lying excited states of the heaviest $N = Z$ nuclei. Such strong, isoscalar neutron–proton correlations would have a considerable impact on the nuclear level structure and possibly influence the dynamics of rapid proton capture in stellar nucleosynthesis.

For all known nuclei, including those residing along the $N = Z$ line up to around mass 80, a detailed analysis of properties such as binding energies⁹ and the spectroscopy of excited states¹⁰ strongly suggests that normal isovector (isospin $T = 1$, see Fig. 1) pairing is dominant at low excitation energies. On the other hand, there are long-standing predictions^{2–6} for a change in the heavier $N = Z$ nuclei, from a nuclear superfluid dominated by isovector pairing to a structure where isoscalar ($T = 0$) neutron–proton (np) pairing has a major influence, as the mass number increases towards the exotic doubly magic nucleus ^{100}Sn , the heaviest $N = Z$ nucleus predicted to be bound.

Nuclei with $N = Z$ and mass number > 90 can only be produced in the laboratory with very low cross-sections. The related problems of identifying and distinguishing such reaction products and their associated

γ -rays from the vast array of $N > Z$ nuclei that are present in much greater numbers from the reactions used have prevented observation of their low-lying excited states until now. In the present work, the experimental difficulties have been overcome through the use of a highly efficient detector system and a prolonged experimental running period.

Excited states in ^{92}Pd were populated following heavy-ion fusion–evaporation reactions at GANIL (Grand Accélérateur National d'Ions Lourds), France.³⁶ Ar ions, accelerated to a kinetic energy of 111 MeV, were used to bombard an isotopically enriched (99.83%) ^{58}Ni target. Light charged particles (mainly protons and α -particles), neutrons and γ -rays emitted in the reactions were detected in coincidence. A schematic layout of the experimental set-up is shown in Fig. 2.

The two-neutron ($2n$) evaporation reaction channel following formation of the ^{94}Pd compound nucleus, leading to ^{92}Pd , was very weakly populated, with a relative yield of less than 10^{-5} of the total fusion cross-section. Gamma-rays from decays of excited states in ^{92}Pd were identified by comparing γ -ray spectra in coincidence with two emitted neutrons and no charged particles with γ -ray spectra in coincidence with other combinations of neutrons and charged particles. The typical efficiency for detecting any charged particle was 66%. This number rises to 88% or higher if more than one such particle is emitted in a particular reaction channel. The clean identification of neutrons is crucial, as scattering of neutrons from one detector segment to another can be misinterpreted as two neutrons; this would give rise to a background from the much more prolific reaction channels (where only one neutron has been emitted) in γ -ray spectra gated by two neutrons. But because neutrons have a finite velocity, the difference in detection

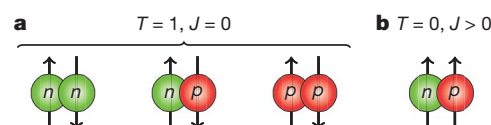


Figure 1 | Schematic illustration of the two possible pairing schemes in nuclei. **a**, The normal isospin $T = 1$ triplet. The two like-particle pairing components are responsible for most known effects of nuclear superfluidity. Within a given shell these isovector components are restricted to spin zero owing to the Pauli principle. **b**, Isoscalar $T = 0$ neutron–proton pairing. Here the Pauli principle allows only non-zero components of angular momentum.

¹Department of Physics, Royal Institute of Technology, SE-10691 Stockholm, Sweden. ²Grand Accélérateur National d'Ions Lourds (GANIL), CEA/DSM – CNRS/IN2P3, F-14076 Caen Cedex 5, France. ³Department of Physics, University of York, York YO10 5DD, UK. ⁴Joint Institute for Heavy-Ion Research, Holifield Radioactive Ion Beam Facility, Oak Ridge, Tennessee 37831, USA. ⁵Heavy Ion Laboratory, University of Warsaw, 02-093 Warsaw, Poland. ⁶Faculty of Physics, Warsaw University of Technology, Koszykowa 75, 00-662 Warsaw, Poland. ⁷Institute of Nuclear Research of the Hungarian Academy of Sciences, ATOMKI, H-4001 Debrecen, Hungary. ⁸Department of Physics and Astronomy, Uppsala University, SE-75121 Uppsala, Sweden. ⁹IFIC, CSIC, University of Valencia, E-46071 Valencia, Spain. ¹⁰Instituto Nazionale di Fisica Nucleare, Laboratori Nazionali di Legnaro, I-35020 Legnaro, Italy. ¹¹Department of Physics, Ankara University, 06100 Tandogan Ankara, Turkey. ¹²Dipartimento di Scienze Fisiche, Università di Napoli and Instituto Nazionale di Fisica Nucleare, I-80126 Napoli, Italy. ¹³Department of Information Technology, University of Debrecen, H-4010 Debrecen, Hungary. ¹⁴Department of Physics, University of Jyväskylä, FIN-40014 Jyväskylä, Finland. ¹⁵Instituto de Estructura de la Materia, CSIC, E-28006 Madrid, Spain. ¹⁶Dipartimento di Fisica dell'Università di Padova and Instituto Nazionale di Fisica Nucleare, Sezione di Padova, I-35122 Padova, Italy. ¹⁷Université Bordeaux 1, CNRS/IN2P3, Centre d'Etudes Nucléaires de Bordeaux Gradignan, F-33175 Gradignan, France. ¹⁸The Niels Bohr Institute, University of Copenhagen, 2100 Copenhagen, Denmark. ¹⁹TRIUMF, Vancouver, British Columbia V6T 2A3, Canada. [†]Present addresses: VECC, 1/AF Bidhan Nagar, Kolkata 700064, India (S.B.); Department of Physics, University of Jyväskylä, FIN-40014 Jyväskylä, Finland (M.S.).

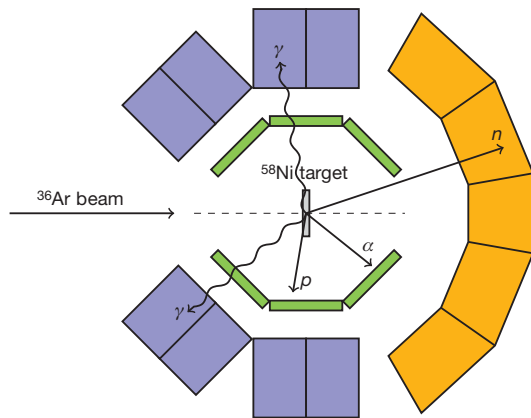


Figure 2 | Schematic illustration of the experimental set-up used to identify γ -ray transitions from excited states in ^{92}Pd . The light particles and γ -rays emitted from the $^{36}\text{Ar} + ^{58}\text{Ni}$ reaction were observed using three different detector systems. The innermost detector array, DIAMANT^{16,17} (green), which consisted of 80 CsI scintillators, was used to detect light charged particles, mainly α -particles and protons, and acted as a veto detector in the selection of events with no charged particles emitted. The Neutron Wall¹⁸ (orange), comprising 50 liquid scintillator detectors and covering a solid angle of 1π in the forward direction, was used for the detection of evaporated neutrons. It is able to discriminate between neutron and γ -ray interactions by means of a combined time-of-flight and pulse-shape analysis technique. Gamma-rays emitted from the reaction products were detected using the EXOGAM^{19,20} high-purity Ge detector system (blue). Seven segmented Ge clover detectors were placed at an angle of 90° and four detectors at an angle of 135° relative to the beam direction, leaving room for the Neutron Wall at forward angles.

time is typically smaller for interactions resulting from two separate neutrons compared to a single scattered neutron. Background contributions from neutron scattering in $2n$ -gated spectra were significantly reduced by applying a criterion to the time difference in the time-of-flight parameter, relative to the distance between the neutron detectors firing. After such corrections, the efficiency for correctly identifying both neutrons from a $2n$ -event was 3%. Figure 3a–c shows projected γ -ray spectra from the charged particle-vetoed, $2n$ -selected E_γ – E_γ coincidence matrix when γ -rays coincident with the 874 keV, 912 keV and 750 keV transitions (Fig. 3a–c, respectively) assigned to ^{92}Pd are selected. By comparing spectra with and without the charged particle veto condition applied, it is clear that these γ -rays are not associated with emission of charged particles from the compound nucleus. Figure 3d shows a plot of the intensity ratios of the 874 keV, 912 keV and 750 keV γ -rays (filled circles) in coincidence with two neutrons and one neutron, respectively, proving that the γ -rays assigned to ^{92}Pd belong to the $2n$ -evaporation reaction channel. An extensive literature search was also performed in order to exclude the possibility that the γ -rays assigned to ^{92}Pd could be due to the decay of excited states in some other nucleus. In particular, γ -rays from reactions involving possible target impurities were taken into account. See Supplementary Information for further details on the data analysis.

The three most intense γ -ray transitions assigned to ^{92}Pd (874 keV, 912 keV and 750 keV) have been ordered into a ground-state band based on their relative intensities (Fig. 3e). The uncertainties in the relative intensities of the γ -ray transitions translate into a corresponding uncertainty in their ordering, and consequently, also in the absolute positions of the 2^+ and 4^+ states. As shown in Fig. 3, these γ -rays form a mutually coincident decay sequence. Although the limited statistics precludes an accurate angular distribution analysis and hence firm spin assignments, it is likely that the 874 keV, 912 keV and 750 keV γ -ray transitions constitute a cascade of stretched $E2$ transitions depopulating the first excited 2^+ , 4^+ and 6^+ states, respectively (Fig. 3e).

Nuclei immediately below ^{100}Sn on the Segré (N, Z) chart, with $N, Z < 50$, may show special structural features, as the valence neutrons and protons here can move in identical orbits. Here, for the heaviest

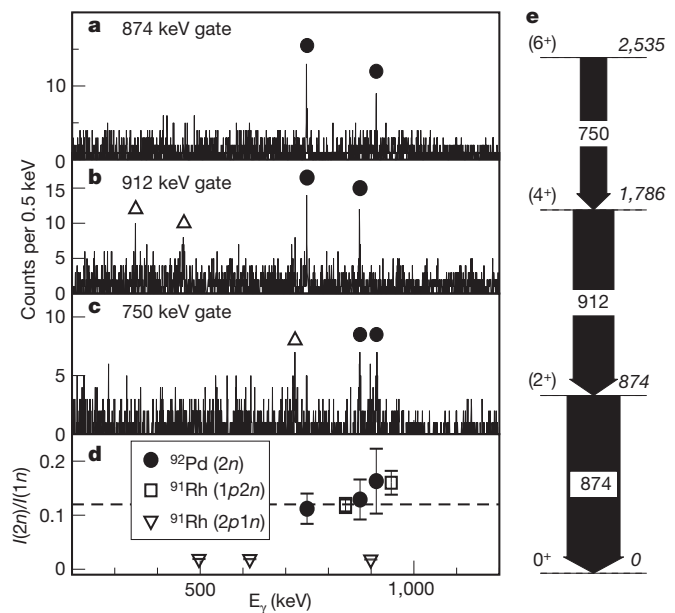


Figure 3 | Identification of γ -ray transitions in ^{92}Pd . a–c, Gamma-ray energy spectra detected in coincidence with the 874 keV, 912 keV and 750 keV γ -rays, with the additional requirement that two neutrons and no charged particle(s) were detected in coincidence. These γ -rays, assigned to depopulate the 2^+ , 4^+ and 6^+ states in ^{92}Pd , respectively, are marked by filled circles. Gamma-rays from the ^{36}Ar -induced $1p1n$ -evaporation reaction on small amounts of carbon deposited on the target during irradiation, leading to the production of ^{46}V nuclei, are visible in b and c (open triangles). These γ -rays appear in the projected spectra owing to a combined effect of the limited detection efficiency for charged particles, the finite neutron/ γ separation in the neutron detectors, the presence of γ -ray transitions at 914.9 keV and 750.7 keV in the level scheme of ^{46}V (refs 21, 22), and the fact that the reaction products from carbon contamination may recoil out of the target material, leading to Doppler broadening of such γ -rays. d, Intensity ratios of the γ -rays assigned to ^{92}Pd in coincidence with two neutrons and one neutron, respectively. The dashed line indicates the value expected for γ -rays in coincidence with two neutrons, obtained from the relative $1n$ - and $2n$ -detection efficiencies. Measured intensity ratios for γ -rays from previously known reaction products ($^{91}\text{Ru}^{23}$ and $^{91}\text{Rh}^{24}$) are included for comparison. e, Level scheme assigned to ^{92}Pd . The assigned spin-parity (left) and level energy (right, in keV) is given for each level. The energies (in keV) and relative intensities (in %, normalized to the intensity of the 874 keV transition) of the γ -ray transitions assigned to ^{92}Pd are as follows: 873.6(2), 100(8); 912.4(2), 77(5); 749.8(3), 50(6). Given uncertainties are standard (statistical) errors.

$N \approx Z$ nuclei, state-of-the-art shell model calculations predict the appearance of ground-state and low-lying yrast structures based on spin-aligned systems of np pairs, similar to a scenario proposed more than four decades ago¹¹. The np -paired ground-state configuration emanates from the strong attractive interaction between $g_{9/2}$ neutrons and protons in aligned angular momentum ($J = 9$) coupling, and is hence different from the predictions of a BCS type of isoscalar np pairing condensate in $N \approx Z$ nuclei^{2–6}. The shell model calculations were performed using empirical two-body matrix elements in the $f_{5/2} p_{3/2} p_{1/2} g_{9/2}$ model space; see Supplementary Information for details.

In Fig. 4c we show the results, compared with experimental data for ^{92}Pd (this work), ^{94}Pd (ref. 12) and ^{96}Pd (ref. 13). The level structure of the semi-magic ($N = 50$) nucleus ^{96}Pd , with four proton holes relative to the $Z = 50$ closed shell core, exhibits the typical traits of a nucleus in the normal isovector pairing phase for which the seniority coupling scheme dominates. A transition from the ground state to the first excited 2^+ state requires the breaking of one $g_{9/2}$ proton-hole pair, and therefore the energy spacing between these two levels is rather large. The distance between the subsequent levels gradually decreases as the angular momentum vectors of the $g_{9/2}$ quasiproton holes align

may influence the composition and X-ray burst profiles of accreting neutron stars, and the nucleosynthesis of neutron deficient isotopes.

Received 3 September; accepted 2 November.

Published online 22 December 2010.

1. Goeppert Mayer, M. On closed shells in nuclei. II. *Phys. Rev.* **75**, 1969–1970 (1949).
2. Engel, J., Langanke, K. & Vogel, P. Pairing and isospin symmetry in proton-rich nuclei. *Phys. Lett. B* **389**, 211–216 (1996).
3. Goodman, A. L. Restoration of axial symmetry of the equilibrium shape of ^{24}Mg by pairing correlations. *Adv. Nucl. Phys.* **11**, 260–263 (1979).
4. Engel, J. *et al.* Neutron-proton correlations in an exactly solvable model. *Phys. Rev. C* **55**, 1781–1788 (1997).
5. Satula, W. & Wyss, R. Competition between $T = 0$ and $T = 1$ pairing in proton-rich nuclei. *Phys. Lett. B* **393**, 1–6 (1997).
6. Civitarese, O., Reboiro, M. & Vogel, P. Neutron-proton pairing in the BCS approach. *Phys. Rev. C* **56**, 1840–1843 (1997).
7. Talmi, I. Generalized seniority and structure of semi-magic nuclei. *Nucl. Phys. A* **172**, 1–24 (1971).
8. Talmi, I. Generalized seniority states with definite isospin. *Nucl. Phys. A* **686**, 217–240 (2001).
9. Macchiavelli, A. O. *et al.* Is there np pairing in $N=Z$ nuclei? *Phys. Rev. C* **61**, 041303(R) (2000).
10. Afanasjev, A. & Frauendorf, S. Description of rotating $N=Z$ nuclei in terms of isovector pairing. *Phys. Rev. C* **71**, 064318 (2005).
11. Danos, M. & Gillet, V. Stretch scheme, a shell model description of deformed nuclei. *Phys. Rev.* **161**, 1034–1044 (1967).
12. Märginean, N. *et al.* Yrast isomers in ^{95}Ag , ^{95}Pd , and ^{94}Pd . *Phys. Rev. C* **67**, 061301 (2003).
13. Alber, D., Bertschat, H. H., Grawe, H., Haas, H. & Spellmeyer, B. Nuclear structure studies of the neutron deficient $N=50$ nucleus ^{96}Pd . *Z. Phys. A* **332**, 129–135 (1989).
14. Schatz, H. *et al.* End point of the rp process on accreting neutron stars. *Phys. Rev. Lett.* **86**, 3471–3474 (2001).
15. Clement, R. R. C. *et al.* New approach for measuring properties of rp-process nuclei. *Phys. Rev. Lett.* **92**, 172502 (2004).
16. Scheurer, J. N. *et al.* Improvements in the in-beam γ -ray spectroscopy provided by an ancillary detector coupled to a Ge-spectrometer: the DIAMANT-EUROGAM II example. *Nucl. Instrum. Methods Phys. Res. A* **385**, 501–510 (1997).
17. Gál, J. *et al.* The VXI electronics of the DIAMANT particle detector array. *Nucl. Instrum. Methods Phys. Res. A* **516**, 502–510 (2004).
18. Skeppstedt, Ö. *et al.* The EUROBALL neutron wall design and performance tests of neutron detectors. *Nucl. Instrum. Methods Phys. Res. A* **421**, 531–541 (1999).
19. Azaiez, F. EXOGAM: A γ -ray spectrometer for radioactive beams. *Nucl. Phys. A* **654**, 1003c–1008c (1999).
20. Simpson, J. *et al.* The EXOGAM array: a radioactive beam gamma-ray spectrometer. *Heavy Ion Phys.* **11**, 159–188 (2000); see also (<http://pro.ganil-spiral2.eu/laboratory/detectors/exogam>).
21. O'Leary, C. D. *et al.* Neutron-proton pairing, Coulomb effects and shape coexistence in odd-odd $N=Z$ ^{46}V . *Phys. Lett. B* **459**, 73–80 (1999).
22. Lenzi, S. M. *et al.* Band termination in the $N=Z$ odd-odd nucleus ^{46}V . *Phys. Rev. C* **60**, 021303(R) (1999).
23. Heese, J. *et al.* High spin states and shell model description of the neutron deficient nuclei ^{90}Ru and ^{91}Ru . *Phys. Rev. C* **49**, 1896–1903 (1994).
24. Märginean, N. *et al.* Identification of excited states and shell model description of the $N=Z+1$ nucleus ^{91}Rh . *Phys. Rev. C* **72**, 014302 (2005).

Supplementary Information is linked to the online version of the paper at www.nature.com/nature.

Acknowledgements This work was supported by the Swedish Research Council (contract nos 2007-4067 and 2008-5793), the Göran Gustafsson Foundation, the European Union Sixth Framework Programme 'Integrating Infrastructure Initiative – Transnational Access' (no. 506065; EURONS), the Hungarian Scientific Research Fund, OTKA (contract nos. K72566 and K68801), the UK Science and Technology Facilities Council (STFC), the Polish Ministry of Science and Higher Education (grant no. N N202 073935), the Spanish Ministerio de Ciencia e Innovación (contract no. FPA2007-66069), the Spanish Consolider-Ingenio 2010 Programme CPAN (CSD2007-00042), and Ankara University BIYEP project no. DPT 2005120140. We thank the EXOGAM collaboration for use of the germanium detector system, the DIAMANT collaboration for use of the charged particle detector system, the European γ -Ray Spectroscopy Pool for use of the neutron detector system, L. Einarsson and R. Seppälä for providing some of the targets used in this experiment and the GANIL staff for technical support and for providing the ^{36}Ar beam.

Author Contributions G.d.F., S.B., E.C. and A.D. were responsible for setting up the EXOGAM germanium detectors and most of the related electronics and data acquisition system. J.N. was in charge of setting up the Neutron Wall detector system with its electronics. B.M.N., A.A., J.G., K.J., G.K., J.M., J.-N.S. and J.T. were responsible for the operation of the DIAMANT charged particle detector system with its associated electronics. All authors except J.B., J.G., K.J., G.K., R.L. and C.Q. participated in the measurements. B.C., F.G.M., T.B., K.A., K.L., E.C., G.d.F., A.Jo., M.P., R.W. and H.A.-A. performed the data analysis or were involved in different aspects of it. J.B. proposed the theoretical interpretation. The shell model calculations were performed by C.Q., R.L. and J.B. The manuscript text was prepared by B.C., with contributions from R.W., J.B., T.B., A.Jo., R.L., C.Q., A.A., G.d.A., E.C., Zs.D., F.G.M., A.Ju., S.M.L., R.M., B.M.N., J.N., M.P., F.R., D.S., M.S. and J.T. T.B. prepared the figures.

Author Information Reprints and permissions information is available at www.nature.com/reprints. The authors declare no competing financial interests. Readers are welcome to comment on the online version of this article at www.nature.com/nature. Correspondence and requests for materials should be addressed to B.C. (cederwall@nuclear.kth.se).

Rapid evolutionary innovation during an Archaean genetic expansion

Lawrence A. David¹ & Eric J. Alm^{1,2,3}

The natural history of Precambrian life is still unknown because of the rarity of microbial fossils and biomarkers^{1,2}. However, the composition of modern-day genomes may bear imprints of ancient biogeochemical events^{3–6}. Here we use an explicit model of macroevolution including gene birth, transfer, duplication and loss events to map the evolutionary history of 3,983 gene families across the three domains of life onto a geological timeline. Surprisingly, we find that a brief period of genetic innovation during the Archaean eon, which coincides with a rapid diversification of bacterial lineages, gave rise to 27% of major modern gene families. A functional analysis of genes born during this Archaean expansion reveals that they are likely to be involved in electron-transport and respiratory pathways. Genes arising after this expansion show increasing use of molecular oxygen ($P = 3.4 \times 10^{-8}$) and redox-sensitive transition metals and compounds, which is consistent with an increasingly oxygenating biosphere.

Describing the emergence of life on our planet is one of the grand challenges of the biological and Earth sciences. Yet the roughly three-billion-year history of life preceding the emergence of hard-shelled metazoans remains largely unknown¹. So far, the best-understood event in early Earth history is the Great Oxidation Event, which is believed to have followed the development of oxygenic photosynthesis by ancestors of modern cyanobacteria⁷ (although the precise timeline remains controversial^{2,8}). If DNA sequences from extant organisms bear an imprint of this event, they can be used to make and test predictions; for example, genes that use molecular oxygen are more likely to appear in organisms that emerged after the Great Oxidation Event. However, the transfer of genes across species can obscure patterns of descent and disrupt our ability to correlate gene histories with the geochemical record⁹. For example, widely distributed genes may descend from a Last Universal Common Ancestor, as is widely believed to have occurred for the translational machinery¹⁰, or they may have been dispersed by horizontal gene transfer (HGT)^{11,12}, as with antibiotic resistance cassettes.

We developed a new phylogenomic method, AnGST (analyser of gene and species trees), that explicitly accounts for HGT by comparing individual gene phylogenies with the phylogeny of organisms (the 'tree of life') and generated detailed evolutionary histories for 3,983 major gene families. Gene histories reveal marked changes in the rates of gene birth, gene duplication, gene loss and HGT over geological timescales (Fig. 1), including a burst of *de novo* gene-family birth between 3.33 and 2.85 Gyr ago, which we refer to as the Archaean Expansion. This window gave rise to 26.8% of extant gene families and coincides with a rapid bacterial cladogenesis (Supplementary Fig. 15). A spike in the rate of gene loss (about 3.1 Gyr ago) follows the expansion and may represent the consolidation of newly evolved phenotypes, as ancestral genomes became specialized for emerging niches. After 2.85 Gyr ago, the rates of both gene loss and gene transfer stabilized at roughly modern-day levels. The rates of *de novo* gene birth and duplication after the Archaean Expansion seem to show opposite trends: *de novo* gene-family birth rates decrease and duplication rates increase over

time. The near absence of *de novo* birth in modern times probably reflects the fact that ORFan gene families (gene families found in only a single genome), which are widespread across all major prokaryotic groups, are not considered in this study¹³. The excess of gene duplications and ORFans in modern genomes suggests that novel genes from both sources experience high turnover. Although we did not observe changes in the rate of HGT after the Archaean Expansion, we did detect an over-representation of HGT from α -proteobacteria to ancient eukaryotes ($P = 3.3 \times 10^{-7}$, Wilcoxon rank sum test) and from cyanobacteria to plants ($P = 8.3 \times 10^{-6}$, Wilcoxon rank sum test). These patterns of HGT probably reflect the endosymbioses that gave rise to mitochondria and chloroplasts^{14,15}, and serve to validate our phylogenomic approach.

What evolutionary factors were responsible for the period of innovation marked by the Archaean Expansion? Although we cannot provide an unequivocal answer to this question with the use of gene birth dates alone, we can ask whether the functions of genes born during this time suggest plausible hypotheses. In general, birth of metabolic genes was enriched during the expansion, and especially those involved in energy production and coenzyme metabolism (Supplementary Table 2); however, further inspection also reveals an enrichment for metabolic-gene-family birth before the Archaean Expansion. To focus on specific metabolic changes linked to the Archaean Expansion we first grouped genes according to the metabolites they used, and then directly compared the occurrence of these metabolites in genes born during the Archaean Expansion with their abundance before the Archaean Expansion. The results are striking: the metabolites specific to the Archaean Expansion (positive bars in Fig. 2 inset) include most of the compounds annotated as redox/e⁻ transfer (blue bars), with Fe-S-binding, Fe-binding and O₂-binding gene families showing the most significant enrichment (false discovery rate < 5%, Fisher's exact test). Gene families that use ubiquinone and FAD (key metabolites in respiration pathways) are also enriched, albeit at slightly lower significance levels (false discovery rate < 10%). The ubiquitous NADH and NADPH are a notable exception to this trend and seem to have had a function early in life history. By contrast, enzymes linked to nucleotides (green bars) showed strong enrichment in genes of more ancient origin than the expansion.

The observed bias in metabolite use suggests that the Archaean Expansion was associated with an expansion in microbial respiratory and electron transport capabilities. Proving this association to be causal is beyond the power of our phylogenomic model. Yet this hypothesis is appealing because more efficient energy conservation pathways could increase the total free-energy budget available to the biosphere, possibly enabling the support of more complex ecosystems and a concomitant expansion of species and genetic diversity. We note, however, that although the use of oxygen as a terminal electron acceptor would have significantly increased biological energy budgets, oxygen-using genes were only enriched towards the end of the expansion (Supplementary Fig. 10). Thus, the earliest redox genes identified as part of the expansion were likely to have been used in anaerobic respiration or in oxygenic or

¹Computational & Systems Biology Initiative, Massachusetts Institute of Technology, Cambridge, Massachusetts 02139, USA. ²Departments of Biological Engineering & Civil and Environmental Engineering, Massachusetts Institute of Technology, Cambridge, Massachusetts 02139, USA. ³The Broad Institute, Cambridge, Massachusetts 02140, USA.

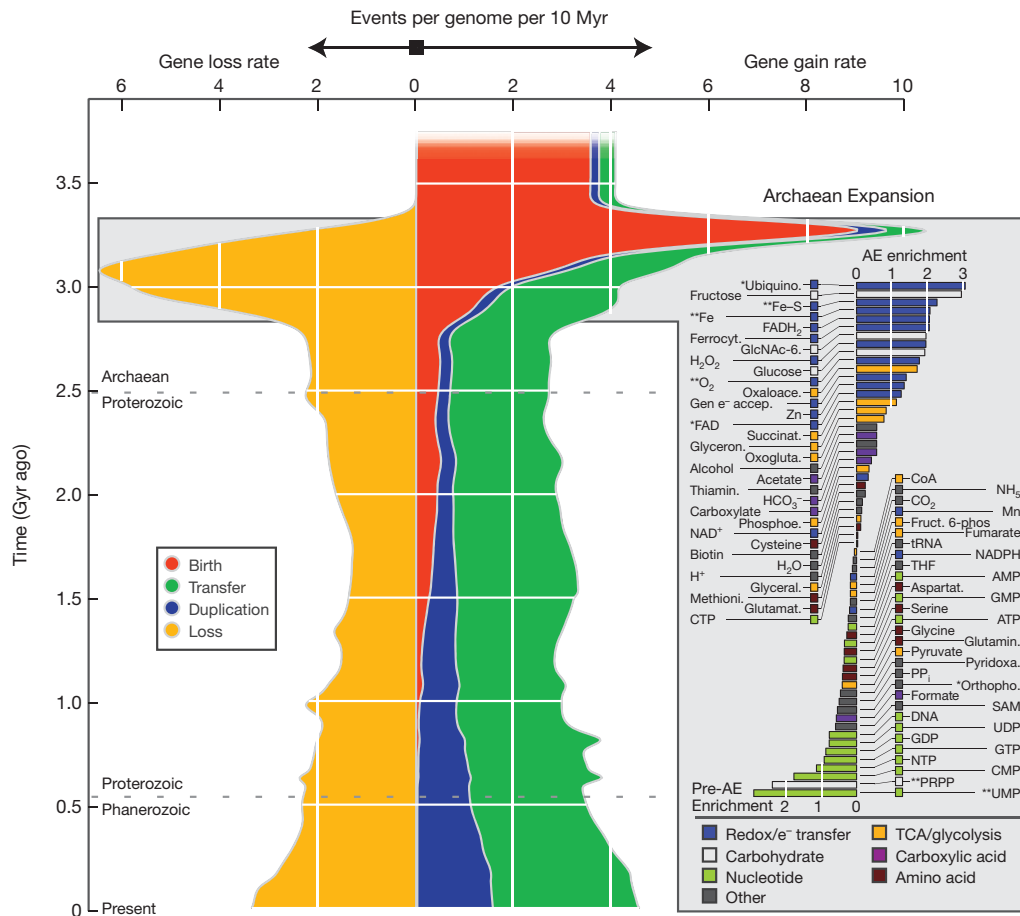


Figure 1 | Rates of macroevolutionary events over time. Average rates of gene birth (red), duplication (blue), HGT (green), and loss (yellow) per lineage (events per 10 Myr per lineage) are shown. Events that increase gene count are plotted to the right, and gene loss events are shown to the left. Genes already present at the Last Universal Common Ancestor are not included in the analysis of birth rates because the time over which those genes formed is not known. The Archaeal Expansion (AE) was also detected when 30 alternative chronograms were considered (Supplementary Fig. 9). The inset shows metabolites or classes of metabolites ordered according to the number of gene families that use them that were born during the Archaeal Expansion compared with the number born

anoxygenic photosynthesis and may have been co-opted later for use in aerobic respiration pathways.

Our metabolic analysis supports an increasingly oxygenated biosphere after the Archaeal Expansion, because the fraction of proteins using oxygen gradually increased from the expansion to the present day (Fig. 2; $P = 3.4 \times 10^{-8}$, two-sided Kolmogorov–Smirnov test). Further indirect evidence of increasing oxygen levels comes from compounds whose availability is sensitive to global redox potential. We observe significant increases over time in the use of the transition metals copper and molybdenum (Fig. 2; false discovery rate $< 5\%$, two-sided Kolmogorov–Smirnov test), which is in agreement with geochemical models of these metals' solubility in increasingly oxidizing oceans^{5,6} and with molybdenum enrichments from black shales suggesting that molybdenum began accumulating in the oceans only after the Archaeal eon¹⁶. Our prediction of a significant increase in nickel utilization accords with geochemical models that predict a tenfold increase in the concentration of dissolved nickel between the Proterozoic eon and the present day⁵ but conflicts with a recent analysis of banded iron formations that inferred monotonically decreasing maximum concentrations of dissolved nickel from the Archaeal onwards¹⁷. The abundance of enzymes using oxidized forms of nitrogen (N_2O and NO_3) also grows significantly over time, with one-third of nitrate-binding gene

families appearing at the beginning of the expansion and three-quarters of nitrous-oxide-binding gene families appearing by the end of the expansion. The timing of these gene-family births provides phylogenomic evidence for an aerobic nitrogen cycle by the Late Archaeal¹⁸. However, one striking discrepancy between our phylogenomic patterns and geochemical predictions is a modest but significant increase in iron-using genes over time (Fig. 2; false discovery rate $< 5\%$, two-sided Kolmogorov–Smirnov test). Declining iron solubility in oxygenated ocean surface waters and sulphide-mediated removal of iron from anoxic deeper waters are thought to have decreased overall iron bioavailability during the Proterozoic¹⁹. If the abundance of iron-using genes tracks iron bioavailability, we would expect these genes to decrease in abundance after the Archaeal. The conflicting phylogenomic result may reflect the confounding effect of evolutionary inertia, whereby microbes could have found more success in evolving a handful of metal-acquisition proteins (for example siderophores) rather than replacing a host of iron-binding proteins in the face of declining iron availability⁵. Alternatively, the insolubility of iron in modern oceans may be offset by large organic pools of iron.

Our chronologies of oxygen and redox-sensitive metal and compound utilization suggest ancient increases in oxygen bioavailability, as well as an Archaeal biosphere with some of the basic genetic components

before the expansion, plotted on a \log_2 scale. Metabolites whose enrichments are statistically significant at a false discovery rate of less than 10% or less than 5% (Fisher's Exact Test) are identified with one or two asterisks, respectively. Bars are coloured by functional annotation or compound type (functional annotations were assigned manually). Metabolites were obtained from the KEGG database release 51.0 (ref. 27) and associated with clusters of orthologous groups of proteins (COGs) using the MicrobesOnline September 2008 database²⁸. Metabolites associated with fewer than 20 COGs or sharing more than two-thirds of gene families with other included metabolites are omitted. Abbreviations are defined in Supplementary Table 3.

Our chronologies of oxygen and redox-sensitive metal and compound utilization suggest ancient increases in oxygen bioavailability, as well as an Archaeal biosphere with some of the basic genetic components

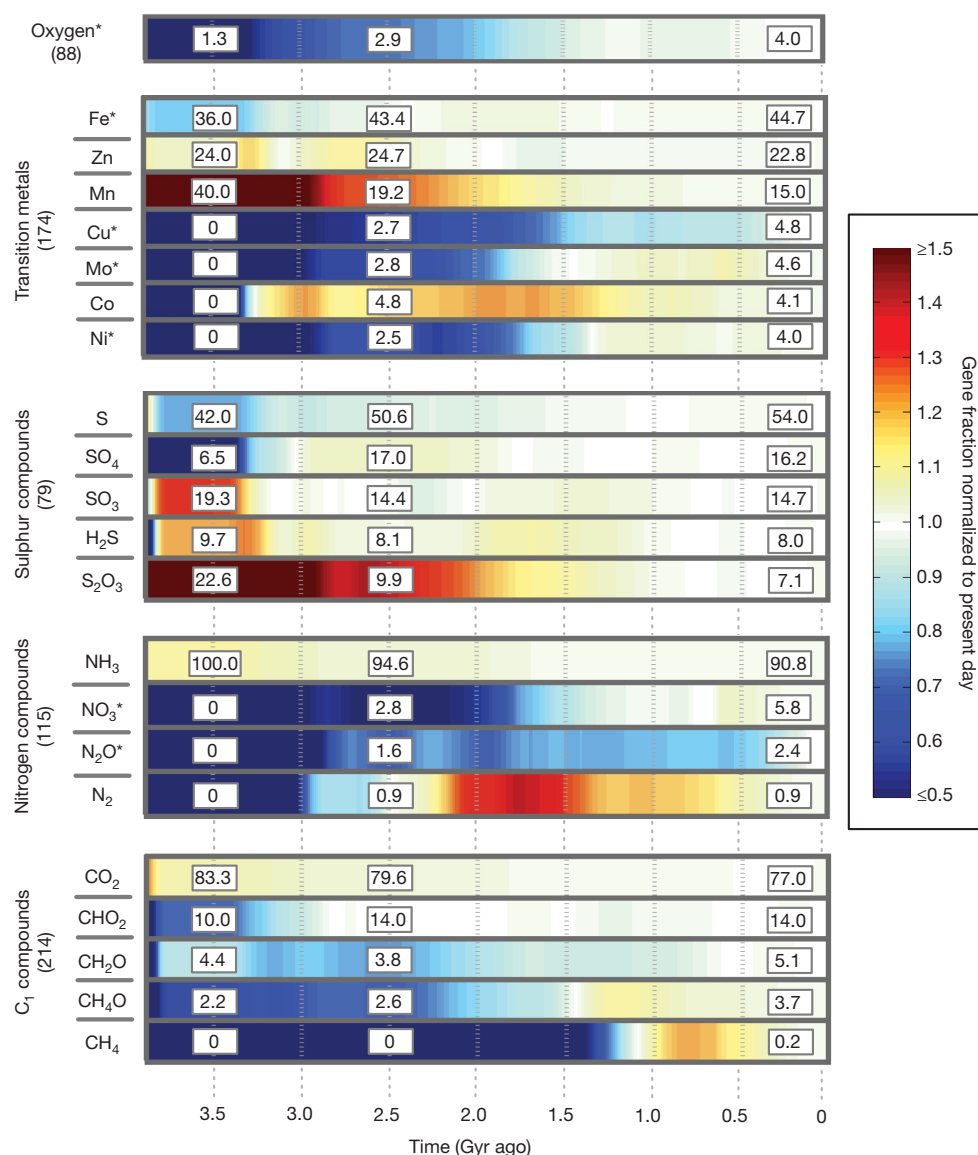


Figure 2 | Genome utilization of redox-sensitive compounds over time. The top panel illustrates a gradual increase in the fraction of enzymes that bind molecular oxygen predicted to be present over Earth history ($P = 3.4 \times 10^{-8}$, two-sided Kolmogorov–Smirnov test). Colours indicate abundance normalized to present-day values. The lower four panels group transition metals, nitrogen compounds, sulphur compounds and C₁ compounds. The fraction of each group's associated genes that bind a given compound, normalized to present-day fractions, is shown over time with a colour gradient. Enclosed boxes show raw fractional values at three time points: 3.5 Gyr ago (left), 2.5 Gyr ago (middle) and the present day (right). For example, 19.2% of

required for oxygenic photosynthesis and respiration. These results are consistent with recent biomarker-based evidence for oxygenesis preceding the Palaeoproterozoic era by hundreds of millions of years²⁰. Still, a precise timeline for the origins of oxygenesis is currently beyond the resolution of our phylogenomic model. In the results described above, we estimated lineage divergence times with PhyloBayes²¹, which enabled us to explicitly account for uncertainty in the timing of inferred events (Supplementary Fig. 13). An alternative model of evolutionary rates²² dated the rapid bacterial cladogenesis to 2.75–2.5 Gyr ago (in contrast to 3.33–2.85 Gyr for PhyloBayes) but still finds evidence for an Archaean Expansion (Supplementary Fig. 9) characterized by the emergence of electron transport genes. Uncertainty or errors in the reference tree may further decrease the power of our phylogenomic model, obscuring evidence for all except the most extreme geochemical events. Future studies that benchmark biomarker and other geochemical data against

transition-metal-binding genes are predicted to have bound Mn 2.5 Gyr ago, a value 1.28-fold the size of the present-day percentage of 15.0%. Values within parentheses give the overall number of gene families in each group. To determine which compounds showed divergent genome utilization over time, the timing of copy number changes for each compound's associated genes was compared with a background model derived from all other compounds. Compounds whose utilization significantly differs from the background model are marked with an asterisk (false discovery rate < 5%, two-sided Kolmogorov–Smirnov test). Nitrite and nitric oxide are not shown, because of their COG-binding similarity to nitrate and nitrous oxide, respectively.

the predicted age of associated gene families could be used to test and refine the 'tree of life', ultimately yielding an abundant and reliable source of Precambrian fossils: modern-day genomes.

METHODS SUMMARY

We developed AnGST to account for gene transfer, duplication, loss and *de novo* birth by comparing individual gene phylogenies with a previously described reference phylogeny²³. We refer to this process as tree reconciliation and provide a detailed description of the AnGST algorithm in Supplementary Methods. Unlike some previous methods^{24–26}, AnGST uses the topology of the gene family tree rather than just its presence or absence across genomes and can infer the direction of gene transfer in addition to gene duplication, birth and loss events. AnGST also accounts for uncertainty in gene trees by incorporating reconciliation into the tree-building process: the tree that minimizes the macroevolutionary cost function but is still supported by the sequence data is chosen as the best gene tree. To assess the sensitivity of our method to the reference tree topology, we reconciled gene families

against 30 alternative reference trees rooted on either the bacterial, archaeal or eukaryotic branches. Inferred gene-family birth ages were consistent across the ensemble of reference trees, and the Archaeal Expansion was a uniformly observed feature (Supplementary Figs 8 and 9). A conservative set of eight temporal constraints was selected from the geochemical and palaeontological literature (Supplementary Fig. 7 and Supplementary Table 1), and the PhyloBayes software package was used to infer a range of divergence times for each ancestral lineage on the reference tree²¹. We did not apply temporal constraints to lineage ages on the gene trees.

Received 15 July; accepted 27 October 2010.

Published online 19 December 2010.

- Nisbet, E. G. & Sleep, N. H. The habitat and nature of early life. *Nature* **409**, 1083–1091 (2001).
- Rasmussen, B., Fletcher, I. R., Brocks, J. J. & Kilburn, M. R. Reassessing the first appearance of eukaryotes and cyanobacteria. *Nature* **455**, 1101–1104 (2008).
- Dupont, C. L., Yang, S., Palenik, B. & Bourne, P. E. Modern proteomes contain putative imprints of ancient shifts in trace metal geochemistry. *Proc. Natl Acad. Sci. USA* **103**, 17822–17827 (2006).
- Dupont, C. L., Butcher, A., Valas, R. E., Bourne, P. E. & Caetano-Anollés, G. History of biological metal utilization inferred through phylogenomic analysis of protein structures. *Proc. Natl Acad. Sci. USA* **107**, 10567–10572 (2010).
- Saito, M. A., Sigman, D. M. & Morel, F. M. M. The bioinorganic chemistry of the ancient ocean: the co-evolution of cyanobacterial metal requirements and biogeochemical cycles at the Archean–Proterozoic boundary? *Inorg. Chim. Acta* **356**, 308–318 (2003).
- Zerkle, A. L., House, C. H. & Brantley, S. L. Biogeochemical signatures through time as inferred from whole microbial genomes. *Am. J. Sci.* **305**, 467–502 (2005).
- De Marais, D. J. When did photosynthesis emerge on Earth? *Science* **289**, 1703–1705 (2000).
- Brocks, J. J., Logan, G. A., Buick, R. & Summons, R. E. Archean molecular fossils and the early rise of eukaryotes. *Science* **285**, 1033–1036 (1999).
- Gogarten, J. P., Doolittle, W. F. & Lawrence, J. G. Prokaryotic evolution in light of gene transfer. *Mol. Biol. Evol.* **19**, 2226–2238 (2002).
- Jain, R., Rivera, M. C. & Lake, J. A. Horizontal gene transfer among genomes: the complexity hypothesis. *Proc. Natl Acad. Sci. USA* **96**, 3801–3806 (1999).
- Ragan, M. A. & Beiko, R. G. Lateral genetic transfer: open issues. *Phil. Trans. R. Soc. Lond. B* **364**, 2241–2251 (2009).
- Ochman, H., Lawrence, J. G. & Groisman, E. A. Lateral gene transfer and the nature of bacterial innovation. *Nature* **405**, 299–304 (2000).
- Fischer, D. & Eisenberg, D. Finding families for genomic ORFans. *Bioinformatics* **15**, 759–762 (1999).
- Yang, D., Oyaizu, Y., Oyaizu, H., Olsen, G. J. & Woese, C. R. Mitochondrial origins. *Proc. Natl Acad. Sci. USA* **82**, 4443–4447 (1985).
- Giovannoni, S. J. *et al.* Evolutionary relationships among cyanobacteria and green chloroplasts. *J. Bacteriol.* **170**, 3584–3592 (1988).
- Scott, C. *et al.* Tracing the stepwise oxygenation of the Proterozoic ocean. *Nature* **452**, 456–459 (2008).
- Konhauser, K. O. *et al.* Oceanic nickel depletion and a methanogen famine before the Great Oxidation Event. *Nature* **458**, 750–753 (2009).
- Garvin, J., Buick, R., Anbar, A. D., Arnold, G. L. & Kaufman, A. J. Isotopic evidence for an aerobic nitrogen cycle in the latest Archean. *Science* **323**, 1045–1048 (2009).
- Canfield, D. E. A new model for Proterozoic ocean chemistry. *Nature* **396**, 450–453 (1998).
- Waldbauer, J. R., Sherman, L. S., Sumner, D. Y. & Summons, R. E. Late Archean molecular fossils from the Transvaal Supergroup record the antiquity of microbial diversity and aerobiosis. *Precamb. Res.* **169**, 28–47 (2009).
- Lartillot, N. & Philippe, H. A Bayesian mixture model for across-site heterogeneities in the amino-acid replacement process. *Mol. Biol. Evol.* **21**, 1095–1109 (2004).
- Sanderson, M. J. r8s: inferring absolute rates of molecular evolution and divergence times in the absence of a molecular clock. *Bioinformatics* **19**, 301–302 (2003).
- Ciccarelli, F. D. *et al.* Toward automatic reconstruction of a highly resolved tree of life. *Science* **311**, 1283–1287 (2006).
- Alm, E., Huang, K. & Arkin, A. The evolution of two-component systems in bacteria reveals different strategies for niche adaptation. *PLOS Comput. Biol.* **2**, e143 (2006).
- Kunin, V. & Ouzounis, C. A. The balance of driving forces during genome evolution in prokaryotes. *Genome Res.* **13**, 1589–1594 (2003).
- Snel, B., Bork, P. & Huynen, M. A. Genomes in flux: the evolution of archaeal and proteobacterial gene content. *Genome Res.* **12**, 17–25 (2002).
- Kanehisa, M. & Goto, S. KEGG: Kyoto Encyclopedia of Genes and Genomes. *Nucleic Acids Res.* **28**, 27–30 (2000).
- Alm, E. J. *et al.* The MicrobesOnline Web site for comparative genomics. *Genome Res.* **15**, 1015–1022 (2005).

Supplementary Information is linked to the online version of the paper at www.nature.com/nature.

Acknowledgements We thank M. Polz, E. Delong, J. Waldbauer and T. Lyons for suggestions to improve this manuscript. This work is supported by the US Department of Energy ENIGMA project through contract DE-AC02-05CH11231, the National Science Foundation under an Assembling the Tree of Life Award, and a National Defense Science and Engineering Graduate Fellowship.

Author Contributions L.D. and E.A. designed the analysis. L.D. performed the analysis. L.D. and E.A. wrote the manuscript.

Author Information Reprints and permissions information is available at www.nature.com/reprints. The authors declare no competing financial interests. Readers are welcome to comment on the online version of this article at www.nature.com/nature. Correspondence and requests for materials should be addressed to E.J.A. (ejalm@mit.edu).

Oncogenically active *MYD88* mutations in human lymphoma

Vu N. Ngo^{1,†*}, Ryan M. Young^{1*}, Roland Schmitz^{1*}, Sameer Jhavar^{1*}, Wenming Xiao^{2*}, Kian-Huat Lim^{1*}, Holger Kohlhammer¹, Weihong Xu¹, Yandan Yang¹, Hong Zhao¹, Arthur L. Shaffer¹, Paul Romesser^{1,3}, George Wright⁴, John Powell², Andreas Rosenwald⁵, Hans Konrad Muller-Hermelink⁵, German Ott⁶, Randy D. Gascoyne⁷, Joseph M. Connors⁷, Lisa M. Rimsza^{8,9}, Elias Campo¹⁰, Elaine S. Jaffe¹¹, Jan Delabie¹², Erlend B. Smeland¹³, Richard I. Fisher^{9,14}, Rita M. Brazier^{9,15}, Raymond R. Tubbs^{9,16}, J. R. Cook^{9,16}, Denny D. Weisenburger¹⁷, Wing C. Chan¹⁷ & Louis M. Staudt¹

The activated B-cell-like (ABC) subtype of diffuse large B-cell lymphoma (DLBCL) remains the least curable form of this malignancy despite recent advances in therapy¹. Constitutive nuclear factor (NF)- κ B and JAK kinase signalling promotes malignant cell survival in these lymphomas, but the genetic basis for this signalling is incompletely understood. Here we describe the dependence of ABC DLBCLs on *MYD88*, an adaptor protein that mediates toll and interleukin (IL)-1 receptor signalling^{2,3}, and the discovery of highly recurrent oncogenic mutations affecting *MYD88* in ABC DLBCL tumours. RNA interference screening revealed that *MYD88* and the associated kinases *IRAK1* and *IRAK4* are essential for ABC DLBCL survival. High-throughput RNA resequencing uncovered *MYD88* mutations in ABC DLBCL lines. Notably, 29% of ABC DLBCL tumours harboured the same amino acid substitution, L265P, in the *MYD88* Toll/IL-1 receptor (TIR) domain at an evolutionarily invariant residue in its hydrophobic core. This mutation was rare or absent in other DLBCL subtypes and Burkitt's lymphoma, but was observed in 9% of mucosa-associated lymphoid tissue lymphomas. At a lower frequency, additional mutations were observed in the *MYD88* TIR domain, occurring in both the ABC and germinal centre B-cell-like (GCB) DLBCL subtypes. Survival of ABC DLBCL cells bearing the L265P mutation was sustained by the mutant but not the wild-type *MYD88* isoform, demonstrating that L265P is a gain-of-function driver mutation. The L265P mutant promoted cell survival by spontaneously assembling a protein complex containing *IRAK1* and *IRAK4*, leading to *IRAK4* kinase activity, *IRAK1* phosphorylation, NF- κ B signalling, JAK kinase activation of STAT3, and secretion of IL-6, IL-10 and interferon- β . Hence, the *MYD88* signalling pathway is integral to the pathogenesis of ABC DLBCL, supporting the development of inhibitors of *IRAK4* kinase and other components of this pathway for the treatment of tumours bearing oncogenic *MYD88* mutations.

The current molecular taxonomy of DLBCL distinguishes three main subtypes: ABC, GCB and primary mediastinal B-cell lymphoma (PMBL)⁴. Current therapy is least successful in ABC DLBCL, achieving less than a 40% cure rate¹. The anti-apoptotic NF- κ B signalling pathway is constitutively active in ABC DLBCL owing to oncogenic *CARD11* mutations or chronic active B-cell receptor signalling, augmented by inactivation of A20^{5–8}. A subset of ABC DLBCLs use JAK

kinase signalling to activate the transcription factor STAT3, a pathway that synergizes with NF- κ B in promoting cell survival^{9,10}. The oncogenic aetiology of this JAK-STAT3 signalling has not been elucidated.

We conducted an RNA interference (RNAi) screen for genes that are required for proliferation and survival of lymphoma cell lines and identified three small hairpin RNAs (shRNAs) targeting *MYD88* that were toxic to two ABC DLBCL lines but not to two GCB DLBCL lines (Supplementary Fig. 1a). During normal immune responses, *MYD88* functions as a signalling adaptor protein that activates the NF- κ B pathway after stimulation of toll-like receptors (TLRs) and receptors for IL-1 and IL-18 (refs 2, 3). *MYD88* coordinates the assembly of a multi-subunit signalling complex consisting of various members of the *IRAK* family of serine-threonine kinases¹¹. The initial RNAi screen also identified two shRNAs targeting *IRAK1* as toxic for one or both of the ABC DLBCL lines, but not for GCB DLBCL lines. A subsequent screen identified additional *MYD88* and *IRAK1* shRNAs that were toxic to all five ABC DLBCL lines tested but had little effect on GCB DLBCL, Burkitt's lymphoma, mantle cell lymphoma and multiple myeloma lines (Supplementary Fig. 1a). Using shRNAs targeting the 3' untranslated regions of *MYD88* and *IRAK1*, which reduced expression of their respective proteins (Supplementary Fig. 1c), we showed that ABC DLBCL cells could be rescued from shRNA-mediated toxicity by coexpression of coding region cDNAs (*IRAK1*, Supplementary Fig. 1d; *MYD88*, see below). *MYD88* and *IRAK1* shRNAs displayed a time-dependent toxicity for ABC DLBCL lines and induced apoptosis, but had little effect on GCB DLBCL and myeloma lines (Fig. 1 and Supplementary Fig. 1b, e). Together these data establish that *MYD88* and *IRAK1* are required to maintain the viability of ABC DLBCL cells.

To comprehensively discover somatic mutations in ABC DLBCL, we used high-throughput resequencing of mRNA to search for sequence variants in four ABC DLBCL lines. In addition to known mutations in *CARD11* and *CD79B*, we identified a single nucleotide variant that changed a leucine residue at position 265 of the *MYD88* coding region to proline (L265P) in all four ABC DLBCL lines tested. This variant resides in the *MYD88* TIR domain, which interacts with TIR domains of various receptors during innate immune responses and also mediates homotypic interactions^{12,13}.

To extend this finding, we resequenced the *MYD88* coding region in 382 lymphoma biopsy samples. The L265P mutation was by far the most

¹Metabolism Branch, Center for Cancer Research, National Cancer Institute, NIH, Bethesda, Maryland 20892, USA. ²Bioinformatics and Molecular Analysis Section, Division of Computational Bioscience, Center for Information Technology, National Institutes of Health, Bethesda, Maryland 20892, USA. ³Howard Hughes Medical Institute-National Institutes of Health Research Scholars Program, Bethesda, Maryland 20892, USA. ⁴Biometric Research Branch, DCTD, National Cancer Institute, NIH, Bethesda, Maryland 20892, USA. ⁵Department of Pathology, University of Würzburg, 97080 Würzburg, Germany. ⁶Department of Clinical Pathology, Robert-Bosch-Krankenhaus, and Dr Margarete Fischer-Bosch Institute for Clinical Pharmacology, 70376 Stuttgart, Germany. ⁷British Columbia Cancer Agency, Vancouver, British Columbia V5Z 4E6, Canada. ⁸Department of Pathology, University of Arizona, Tucson, Arizona 85724, USA. ⁹Southwest Oncology Group, 24 Frank Lloyd Wright Drive, Ann Arbor, Michigan 48106, USA. ¹⁰Hospital Clinic, University of Barcelona, 08036 Barcelona, Spain. ¹¹Laboratory of Pathology, Center for Cancer Research, National Cancer Institute, NIH, Bethesda, Maryland 20892, USA. ¹²Pathology Clinic, Rikshospitalet University Hospital, N-0310 Oslo, Norway. ¹³Institute for Cancer Research, Rikshospitalet University Hospital and Center for Cancer Biomedicine, Faculty Division of the Norwegian Radium Hospital, University of Oslo, N-0310 Oslo, Norway. ¹⁴James P. Wilmot Cancer Center, University of Rochester School of Medicine, Rochester, New York 14642, USA. ¹⁵Oregon Health and Science University, Portland, Oregon 97239, USA. ¹⁶Cleveland Clinic Pathology and Laboratory Medicine Institute, Cleveland, Ohio 44195, USA. ¹⁷Departments of Pathology and Microbiology, University of Nebraska Medical Center, Omaha, Nebraska 68198, USA. [†]Present address: Division of Hematopoietic Stem Cell and Leukemia Research, City of Hope National Medical Center, Duarte, California 91010, USA.

*These authors contributed equally to this work.

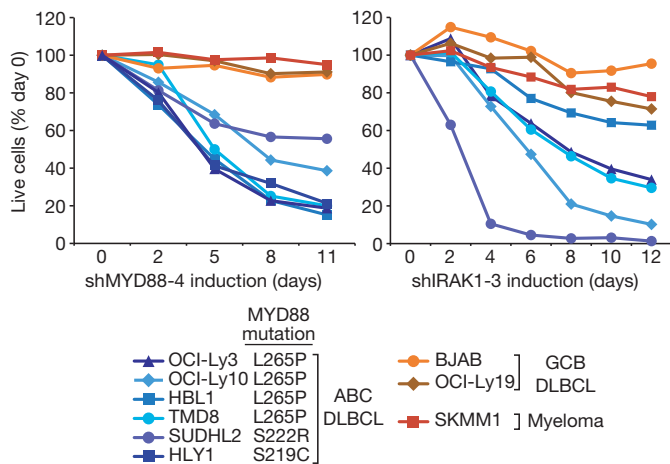


Figure 1 | **MYD88 is required for survival of ABC DLBCL cells.** *MYD88* and *IRAK1* shRNAs have selective toxicity for ABC DLBCL lines. Shown is the fraction of GFP⁺, shRNA-expressing cells relative to the GFP⁺, shRNA-negative fraction at the indicated times, normalized to the day 0 values.

common variant observed, occurring in 29% of ABC DLBCL biopsies. By contrast, this mutation was rare or absent among DLBCLs of the GCB and PMBL subtypes and among Burkitt's lymphomas (Fig. 2b). Of note, *MYD88* L265P was also observed in 9% of gastric mucosa-associated lymphoid tissue (MALT) lymphomas. Most *MYD88* L265P mutations appeared heterozygous by sequencing, but six biopsy samples and one ABC DLBCL line (OCI-Ly3) were homozygous. By array-based comparative genomic hybridization¹⁴, 56% (15 of 27) of the ABC DLBCL cases with gain or amplification of the *MYD88* locus had the L265P mutation, compared to 29% (13 of 45) with wild-type *MYD88* copy number ($P = 0.023$), indicating selection by the cancer cells for this mutant allele. A host of other, less common *MYD88* mutations were equally distributed among ABC and GCB DLBCL cases (Fig. 2a, b). Whereas most mutations were in the TIR domain, one mutation

(V52M) was in the death domain and two were between the death and TIR domains (S149G/I). Six ABC DLBCL lines had a *MYD88* mutation (Fig. 1), whereas all 14 GCB DLBCL lines tested were wild type. In 13 DLBCL cases for which matched germline DNA was available, the *MYD88* mutations (L265P, V217F, S219C, M232T, S243N, T294P) were confirmed to be somatically acquired. Overall, *MYD88* mutations were observed in 39% of ABC DLBCLs (Fig. 2b), establishing *MYD88* as among the most frequently altered genes in this malignancy.

The *MYD88* mutations partially overlapped with abnormalities in *CD79B/A*, *A20* and *CARD11* in ABC DLBCL tumours (Fig. 2c). Among cases with a *MYD88* L265P mutation, 34% had a coincident *CD79B/A* mutation whereas this overlap was significantly less common among ABC DLBCLs without a *CD79B/A* mutation (18%; $P = 0.03$). These data raise the possibility of a functional interaction between the chronic active B-cell receptor signalling that is associated with *CD79B/A* mutations⁸ and the signalling that is instigated by the *MYD88* L265P mutation. Some cases had *MYD88* L265P as well as a *CARD11* mutation, which strongly activates NF- κ B, suggesting that the *MYD88* mutation confers additional biological attributes beyond NF- κ B activation.

The location of the *MYD88* mutations within the three-dimensional structure of the *MYD88* TIR domain was both surprising and instructive (Fig. 2d). The L265P mutation occurs at a residue that is invariant in evolution and contributes to a β -sheet at the hydrophobic core of the domain. Another mutation, M232T, affects a methionine that is in an adjacent β -sheet and contacts the leucine affected by L265P. A cluster of mutations were in the 'B-B loop', an evolutionarily conserved region that mediates TIR domain interactions¹⁵. Two other mutations, S222R and S243N, alter an adjoining face of the TIR domain. Only one mutant affects the opposite side of the TIR domain (T294P), altering the conserved 'box 3' motif that is important in IL-1 signalling¹³.

To examine whether the *MYD88* mutants confer a gain or loss of function, we performed a complementation experiment in which we knocked down endogenous *MYD88* in ABC DLBCL lines and ectopically expressed wild-type or mutant *MYD88* coding regions. In ABC

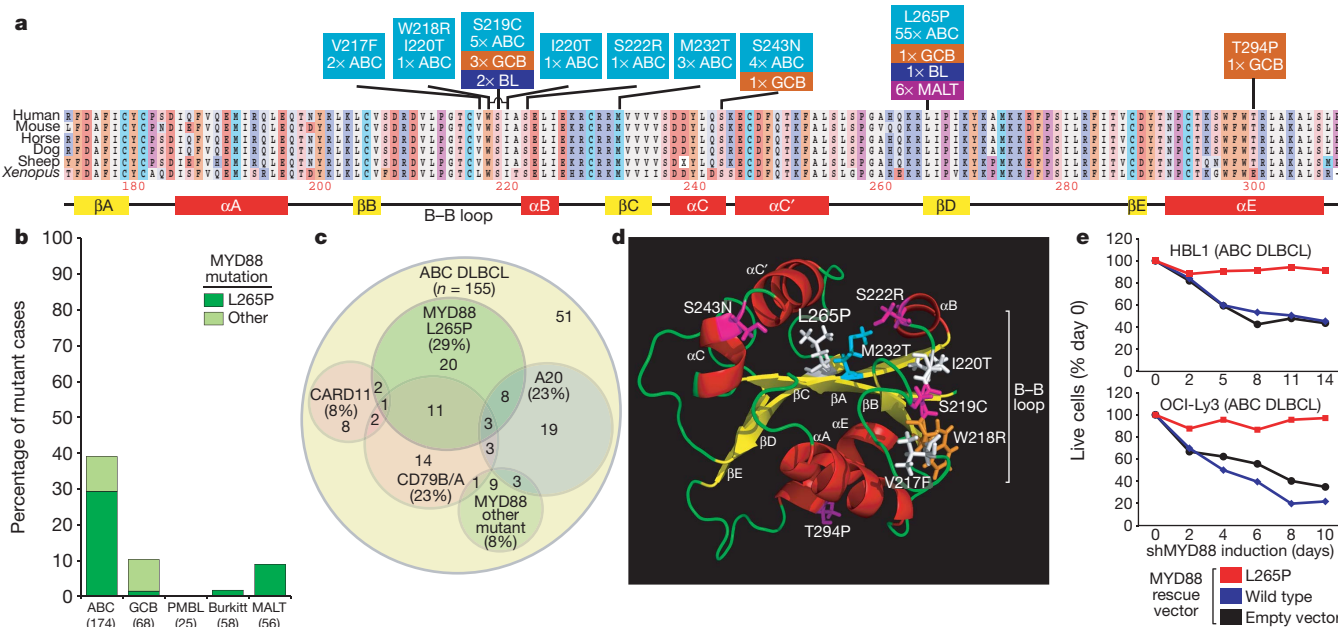


Figure 2 | **MYD88 mutations in human lymphomas.** **a**, *MYD88* missense mutations in lymphoma biopsies and cell line models of ABC DLBCL (light blue), GCB DLBCL (orange), MALT lymphoma (purple) and Burkitt's lymphoma (BL; dark blue). Amino acid positions are shown according to protein accession NP_002459. **b**, Frequencies of *MYD88* mutations in biopsy samples from different lymphoma subtypes. **c**, Overlap of *MYD88* mutations with other recurrent genetic alterations in ABC DLBCL tumour specimens. Genetic subsets were defined by somatic mutations and, in the case of the A20

subset, by homozygous deletion or epigenetic silencing. **d**, Location of *MYD88* mutations in the three-dimensional structure of the *MYD88* TIR domain.

e, Dependence of ABC DLBCLs on *MYD88* L265P. A 3'-UTR-directed *MYD88* shRNA was inducibly expressed in the indicated ABC DLBCL lines, which were stably transduced with rescue vectors expressing wild-type or L265P *MYD88* coding regions, or with an empty vector. Shown is the fraction of viable shRNA-expressing cells relative to the shRNA-negative fraction, normalized to day 0 values.

DLBCL lines harbouring an L265P mutation, *MYD88* L265P rescued the cells after *MYD88* knockdown, but wild-type *MYD88* was ineffective (Fig. 2e), although these *MYD88* isoforms were expressed equivalently (data not shown). Hence, these ABC DLBCLs are 'addicted' to the action of the L265P *MYD88* mutant, indicating that it is a gain-of-function driver mutation that confers a selective advantage during the evolution of ABC DLBCL tumours.

To assess the biochemical and functional consequences of the *MYD88* mutations, we fused green fluorescent protein (GFP) to *MYD88* and introduced the fusion proteins into DLBCL lines. Immunoprecipitation of *MYD88*-GFP with anti-GFP antibodies brought down IRAK1 and IRAK4, two kinases known to associate with *MYD88* upon TLR or IL-1 stimulation (Fig. 3a). During IL-1 signalling, IRAK1 becomes hyperphosphorylated by IRAK4, resulting in slowly migrating IRAK1 isoforms¹⁶. In cells bearing the *MYD88* L265P, a prominent, slow-migrating IRAK1 species co-immunoprecipitated with *MYD88* (Fig. 3a). By contrast, wild-type *MYD88* did not associate strongly with these IRAK1 isoforms nor did the other *MYD88* mutants tested (Fig. 3b). Treatment with λ -phosphatase collapsed the slow-migrating IRAK1 species into a single band, confirming that they are phosphorylated IRAK1 isoforms (Fig. 3c). Phosphorylation of endogenous IRAK1 was observed in an ABC DLBCL line with L265P but not in a GCB DLBCL line (Fig. 3c). Thus, the *MYD88* L265P mutant nucleates a signalling complex in ABC DLBCLs that includes phosphorylated IRAK1, consistent with a gain-of-function phenotype.

IRAK4 co-immunoprecipitated with *MYD88*, but it associated equivalently with wild-type and L265P *MYD88* (Fig. 3a). Knockdown of IRAK4 was toxic for ABC DLBCL lines but not for GCB DLBCL and myeloma lines (Fig. 3d and Supplementary Fig. 1c). Wild-type IRAK4 rescued ABC DLBCL lines after *IRAK4* shRNA induction, but a kinase-dead IRAK4 isoform could not (Fig. 3e), despite equivalent expression (data not shown). By contrast, IRAK1 kinase activity was not required for the survival of ABC DLBCL cells (Supplementary Fig. 1d). A selective small-molecule inhibitor of IRAK1 and IRAK4 kinase activity¹⁷ killed ABC DLBCL lines but not GCB DLBCL and myeloma lines (Fig. 3f). Together, these findings demonstrate that ABC DLBCLs rely upon IRAK4 kinase activity to transduce signals from *MYD88* L265P that promote survival.

To investigate signalling pathways that are engaged by *MYD88* L265P, we knocked it down in an ABC DLBCL line and profiled the ensuing gene expression changes (Supplementary Table 1 and Supplementary Fig. 2). We identified 285 genes that were down-modulated after *MYD88* knockdown, and searched for overlap between this *MYD88* signature and previously defined gene expression signatures¹⁸ (Supplementary Table 2). The most significantly enriched signature reflects NF- κ B signalling in ABC DLBCL (44 \times enrichment, $P = 2.4 \times 10^{-130}$). This signature was also inhibited after *IRAK1* knockdown (Supplementary Fig. 3), indicating that IRAK1 mediates NF- κ B activation by *MYD88* L265P. To compare the ability of wild-type and mutant *MYD88* isoforms to activate NF- κ B, we expressed them as GFP fusion proteins in a GCB DLBCL line with little endogenous NF- κ B activity. Whereas wild-type *MYD88* activated an NF- κ B-dependent reporter modestly, L265P had strong activity, as did M232T and S243N, whereas S222R and T294P had an intermediate effect (Fig. 4b). At all *MYD88* expression levels, L265P was superior to wild-type *MYD88* in upregulating CD83, a previously established NF- κ B target in this system⁵ (Fig. 4c). Other *MYD88* mutants induced CD83 to varying degrees but all were more active than wild-type *MYD88*. Thus, mutant *MYD88* isoforms can contribute to the constitutive NF- κ B activation that typifies ABC DLBCL¹⁹.

A signature of JAK kinase signalling in ABC DLBCL overlapped significantly with the *MYD88* signature (Fig. 4a; 14 \times enrichment, $P = 9.6 \times 10^{-39}$) and with IRAK1-regulated genes (Supplementary Fig. 3b). This was notable because autocrine secretion of IL-6 and IL-10 drives JAK-STAT3 signalling in a subset of ABC DLBCLs⁹. *MYD88* knockdown significantly diminished the secretion of IL-6 and

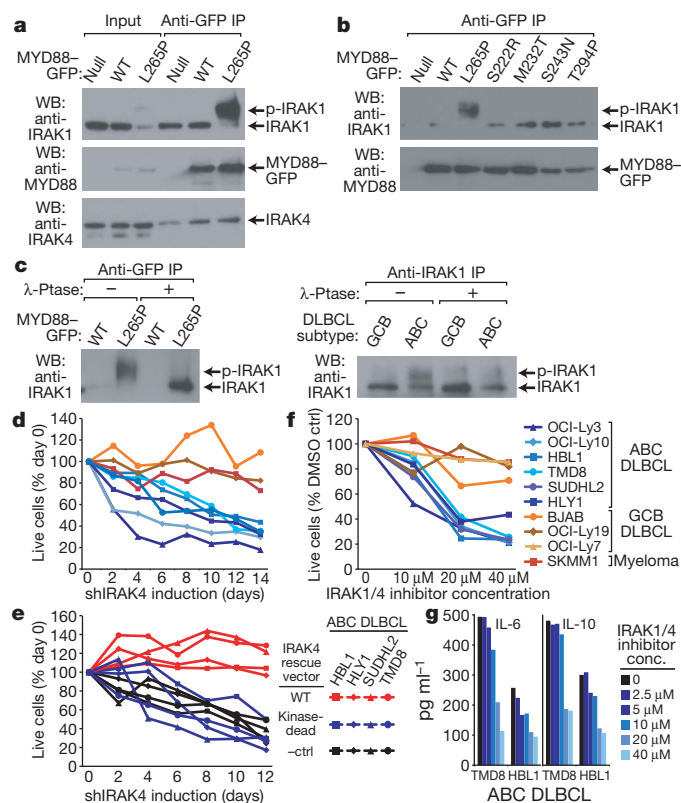
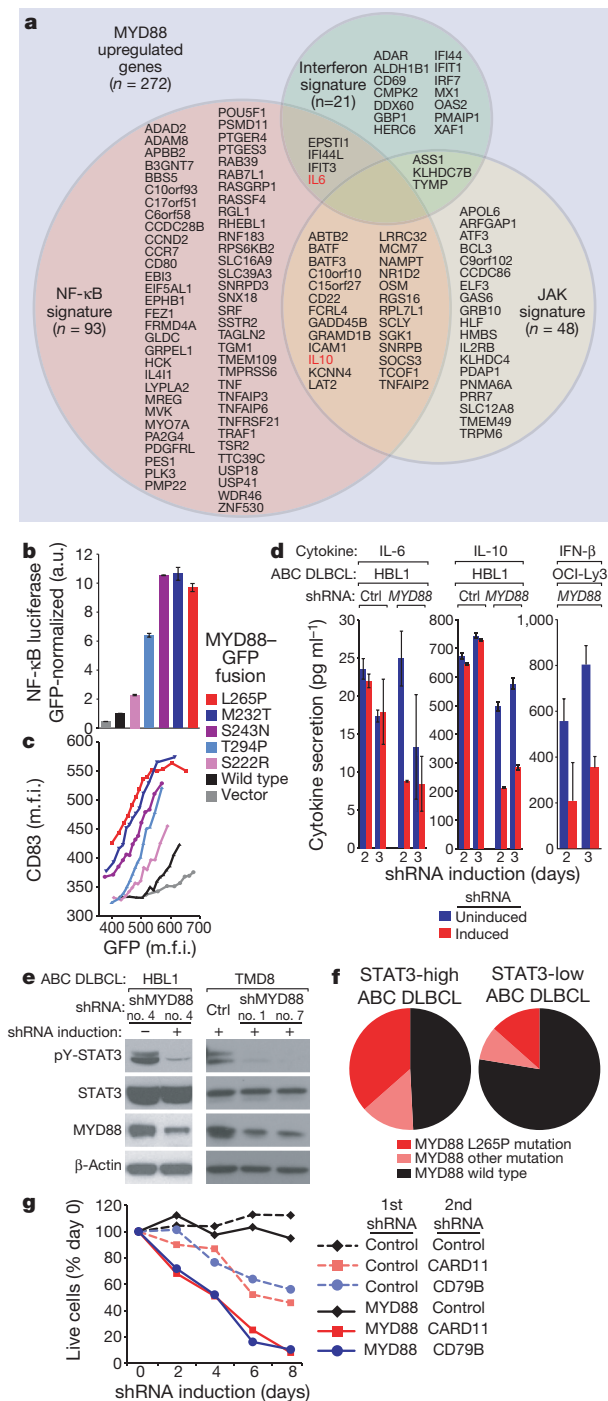


Figure 3 | *MYD88* mutations are gain-of-function. **a**, An altered IRAK1 isoform associated with *MYD88* L265P. The GCB DLBCL line BJAB was transduced with GFP-tagged wild-type (WT) or L265P *MYD88*, or with an empty vector (null). Anti-GFP immunoprecipitates (IP) and input lysates were examined by immunoblotting for IRAK1, IRAK4 and *MYD88*. **b**, Preferential association of an altered IRAK1 isoform with *MYD88* L265P. BJAB cells were transduced with the indicated GFP-tagged *MYD88* isoforms and examined as in **a**. **c**, *MYD88* L265P associates with phosphorylated IRAK1. Top panel: BJAB cells were transduced with the indicated GFP-tagged *MYD88* isoforms. Anti-GFP immunoprecipitates were treated with λ -phosphatase as indicated and examined by immunoblotting for IRAK1 or *MYD88*. Bottom panel: anti-IRAK1 immunoprecipitates from HBL1 (ABC) or BJAB (GCB) cells were treated with λ -phosphatase as indicated and examined by immunoblotting for IRAK1. **d**, Toxicity of *IRAK4* shRNAs for ABC DLBCLs. The indicated lines were transduced with retroviruses expressing *IRAK4* shRNA and the relative number of shRNA⁺ cells is plotted versus time after shRNA induction, normalized to day 0. Data are representative of experiments with three different *IRAK4* shRNAs. **e**, IRAK4 kinase activity is required for ABC DLBCL survival. The indicated ABC DLBCL lines were transduced with retroviruses expressing wild-type or kinase-dead IRAK4 isoforms, or with an empty vector (–ctrl). The survival of cells after induction of an *IRAK4* shRNA is shown. **f**, A small-molecule IRAK1/4 kinase inhibitor is selectively lethal for ABC DLBCLs. Viability of the indicated lines was measured after treatment for 3 days with various inhibitor concentrations and normalized to DMSO-treated cells. **g**, IRAK4 kinase activity regulates IL-6 and IL-10 secretion. The indicated cytokines were measured in the supernatant of ABC DLBCL lines after treatment for 24 h with various concentrations of the IRAK1/4 inhibitor.

IL-10 as well as the phosphorylation of STAT3 in several ABC DLBCL lines (Fig. 4d, e and Supplementary Fig. 1f). IL-6 and IL-10 secretion was also blocked by the IRAK1/4 kinase inhibitor, indicating that IRAK4 links *MYD88* L265 signalling to the expression of these cytokines (Fig. 3g). Previous work identified a 'STAT3-high' subgroup of ABC DLBCL tumours with autocrine IL-6/IL-10 signalling and STAT3 phosphorylation, which was missing in a 'STAT3-low' subgroup⁹. The *MYD88* L265P mutation was significantly more common in the STAT3-high subgroup (37%) than in the STAT3-low subgroup (13%) ($P = 0.0036$), and other *MYD88* mutations were modestly enriched among STAT3-high cases as well (Fig. 4f). These data indicate that



MYD88 mutations contribute to JAK–STAT3 signalling in ABC DLBCL tumours.

The MYD88 signature included a number of genes that are induced by type I interferon (Fig. 4a; 7× enrichment, $P = 4.3 \times 10^{-10}$), which is intriguing given that MYD88 signalling can induce interferon (IFN)-β production by innate immune cells. IFN-β was measurable in the supernatant of the OCI-Ly3 ABC DLBCL line, and MYD88 knockdown diminished its secretion (Fig. 4d). MYD88 knockdown decreased IFN-β mRNA levels in the HBL1 line (Supplementary Fig. 2), although IFN-β secretion was below the detection limit. Future work should address whether the secretion of immunomodulatory cytokines such as IFN-β, IL-6 and IL-10 influences immune cells in the microenvironment of ABC DLBCL tumours.

Given the pleiotropic action of MYD88 L265P, we investigated whether MYD88 signalling cooperates with B-cell receptor signalling

Figure 4 | MYD88 mutants activate NF-κB and cytokine signalling. **a**, Venn diagram of genes affected by MYD88 knockdown in the HBL1 ABC DLBCL line, grouped according to membership in gene expression signatures. **b**, MYD88 mutants constitutively activate NF-κB. BJAB cells co-expressing the indicated MYD88–GFP mutants and a NF-κB-driven luciferase reporter construct were assayed for luciferase activity, which was normalized to the expression levels of each MYD88–GFP isoform. a.u., arbitrary units. **c**, Correlation of MYD88 protein levels with CD83 expression. BJAB cells bearing GFP-tagged MYD88 isoforms were assessed for CD83 and GFP expression. Cells were assigned to equally sized bins based on their GFP levels, and the mean fluorescence intensity (m.f.i.) of CD83 in each bin was plotted. **d**, MYD88 knockdown decreases cytokine secretion in ABC DLBCL. MYD88 or control (ctrl) shRNAs were induced in ABC DLBCL lines, and the indicated cytokines were measured in the supernatant over time. **e**, STAT3 phosphorylation in ABC DLBCL depends on MYD88. MYD88 or control (ctrl) shRNAs were induced in ABC DLBCL lines, and cells were assessed by immunoblotting for phosphorylated STAT3 (pY-STAT3), total STAT3, MYD88 and β-actin. **f**, Preferential association of MYD88 mutant isoforms with the STAT3-high subgroup of ABC DLBCL tumours. See text for details. **g**, MYD88 and B-cell-receptor signalling pathways cooperate to maintain ABC DLBCL survival. OCI-Ly10 ABC DLBCL cells were first transduced with retroviruses expressing MYD88 or control shRNAs and then infected with retroviruses expressing CD79A, CARD11, or control shRNAs along with GFP. The relative viability of GFP⁺ cells is plotted, normalized to day 0 values. All error bars are s.e.m. ($n = 3$).

to maintain ABC DLBCL survival. Knockdown of MYD88 enhanced the killing of an ABC DLBCL line with chronic active BCR signalling by CD79B or CARD11 shRNAs (Fig. 4g). This finding indicates that MYD88 and B-cell receptor signalling provide non-redundant survival signals to ABC DLBCL cells, in keeping with the fact that some ABC DLBCL tumours harbour MYD88 L265P as well as CD79B or CARD11 mutations (Fig. 2c).

Our genetic and functional data establish a new oncogenic pathway in lymphomagenesis. Somatically acquired MYD88 mutations in ABC DLBCL promote NF-κB and JAK–STAT3 signalling, which mediate cell survival in this lymphoma type^{9,19}. MYD88 L265P was the most biologically potent mutant and was unique in its ability to coordinate a stable signalling complex containing phosphorylated IRAK1, which probably accounts for its high recurrence among lymphomas. MYD88 L265P also genetically links MALT lymphoma with ABC DLBCL, two lymphoma subtypes that share other oncogenic features^{7,14,20–22}. Other MYD88 mutations may also be drivers of lymphomagenesis given their recurrent nature and ability to activate NF-κB. From a therapeutic standpoint, the signalling complex coordinated by MYD88 L265P represents an enticing target. Our study also provides a genetic method to identify patients whose tumours may depend upon MYD88 signalling and who may therefore benefit from therapies targeting IRAK4 alone or in combination with agents targeting the B-cell receptor⁸, NF-κB^{23,24} or JAK–STAT3 pathways⁹.

METHODS SUMMARY

RNAi screens, doxycycline-inducible shRNA expression and shRNA toxicity assays were described previously²⁵. RNA interference screening results are listed in Supplementary Table 3. The sequences of individual shRNAs described in the figures are given in Supplementary Table 4. Gene expression profiling data have been submitted to GEO under accession number GSE22900.

Pre-treatment tumour biopsies were obtained from patients with *de novo* DLBCL, Burkitt's lymphoma and gastric MALT lymphoma. Samples were analysed as per a protocol approved by the National Cancer Institute Institutional Review Board. Assignment of DLBCL specimens to subtypes was performed as described¹. High-throughput RNA sequencing was accomplished using an Illumina GAIIX instrument.

Full Methods and any associated references are available in the online version of the paper at www.nature.com/nature.

Received 21 July; accepted 17 November 2010.

Published online 22 December 2010.

1. Lenz, G. *et al.* Stromal gene signatures in large-B-cell lymphomas. *N. Engl. J. Med.* **359**, 2313–2323 (2008).

2. Iwasaki, A. & Medzhitov, R. Regulation of adaptive immunity by the innate immune system. *Science* **327**, 291–295 (2010).
3. Ishii, K. J. & Akira, S. Innate immune recognition of, and regulation by, DNA. *Trends Immunol.* **27**, 525–532 (2006).
4. Lenz, G. & Staudt, L. M. Aggressive lymphomas. *N. Engl. J. Med.* **362**, 1417–1429 (2010).
5. Lenz, G. *et al.* Oncogenic CARD11 mutations in human diffuse large B cell lymphoma. *Science* **319**, 1676–1679 (2008).
6. Compagno, M. *et al.* Mutations of multiple genes cause deregulation of NF- κ B in diffuse large B-cell lymphoma. *Nature* **459**, 717–721 (2009).
7. Kato, M. *et al.* Frequent inactivation of A20 in B-cell lymphomas. *Nature* **459**, 712–716 (2009).
8. Davis, R. E. *et al.* Chronic active B-cell-receptor signalling in diffuse large B-cell lymphoma. *Nature* **463**, 88–92 (2010).
9. Lam, L. T. *et al.* Cooperative signaling through the signal transducer and activator of transcription 3 and nuclear factor- κ B pathways in subtypes of diffuse large B-cell lymphoma. *Blood* **111**, 3701–3713 (2008).
10. Ding, B. B. *et al.* Constitutively activated STAT3 promotes cell proliferation and survival in the activated B-cell subtype of diffuse large B-cell lymphomas. *Blood* **111**, 1515–1523 (2008).
11. Lin, S. C., Lo, Y. C. & Wu, H. Helical assembly in the MyD88–IRAK4–IRAK2 complex in TLR/IL-1R signalling. *Nature* **465**, 885–890 (2010).
12. Xu, Y. *et al.* Structural basis for signal transduction by the Toll/interleukin-1 receptor domains. *Nature* **408**, 111–115 (2000).
13. Li, C., Zienkiewicz, J. & Hawiger, J. Interactive sites in the MyD88 Toll/interleukin (IL) 1 receptor domain responsible for coupling to the IL1 β signaling pathway. *J. Biol. Chem.* **280**, 26152–26159 (2005).
14. Lenz, G. *et al.* Molecular subtypes of diffuse large B-cell lymphoma arise by distinct genetic pathways. *Proc. Natl Acad. Sci. USA* **105**, 13520–13525 (2008).
15. Jiang, Z. *et al.* Details of Toll-like receptor:adapter interaction revealed by germ-line mutagenesis. *Proc. Natl Acad. Sci. USA* **103**, 10961–10966 (2006).
16. Yamin, T. T. & Miller, D. K. The interleukin-1 receptor-associated kinase is degraded by proteasomes following its phosphorylation. *J. Biol. Chem.* **272**, 21540–21547 (1997).
17. Powers, J. P. *et al.* Discovery and initial SAR of inhibitors of interleukin-1 receptor-associated kinase-4. *Bioorg. Med. Chem. Lett.* **16**, 2842–2845 (2006).
18. Shaffer, A. L. *et al.* A library of gene expression signatures to illuminate normal and pathological lymphoid biology. *Immunol. Rev.* **210**, 67–85 (2006).
19. Davis, R. E., Brown, K. D., Siebenlist, U. & Staudt, L. M. Constitutive nuclear factor κ B activity is required for survival of activated B cell-like diffuse large B cell lymphoma cells. *J. Exp. Med.* **194**, 1861–1874 (2001).
20. Dierlamm, J. *et al.* Characteristic pattern of chromosomal gains and losses in marginal zone B cell lymphoma detected by comparative genomic hybridization. *Leukemia* **11**, 747–758 (1997).
21. Novak, U. *et al.* The NF- κ B negative regulator TNFAIP3 (A20) is inactivated by somatic mutations and genomic deletions in marginal zone B-cell lymphomas. *Blood* **113**, 4918–4921 (2009).
22. Staudt, L. M. Oncogenic activation of NF- κ B. *Cold Spring Harb. Perspect. Biol.* **2**, a000109 (2010).
23. Milhollen, M. A. *et al.* MLN4924, a NEDD8-activating enzyme inhibitor, is active in diffuse large B-cell lymphoma models: rationale for treatment of NF- κ B-dependent lymphoma. *Blood* **116**, 1515–1523 (2010).
24. Lam, L. T. *et al.* Small molecule inhibitors of I κ B kinase are selectively toxic for subgroups of diffuse large B-cell lymphoma defined by gene expression profiling. *Clin. Cancer Res.* **11**, 28–40 (2005).
25. Ngo, V. N. *et al.* A loss-of-function RNA interference screen for molecular targets in cancer. *Nature* **441**, 106–110 (2006).

Supplementary Information is linked to the online version of the paper at www.nature.com/nature.

Acknowledgements This research was supported by the Intramural Research Program of the NIH, National Cancer Institute, Center for Cancer Research, an NCI SPECS grant (U01-CA 114778), and by the Foundation for NIH, through a gift from the Richard A. Lauderbaugh Memorial Fund. This study was conducted under the auspices of the Lymphoma/Leukemia Molecular Profiling Project (LLMPP). R.S. is supported by the Dr Mildred Scheel Stiftung für Krebsforschung (Deutsche Krebshilfe). P.R. was an HHMI-NIH Research Scholar. This study used the high-performance computational capabilities of the Biowulf Linux cluster at the National Institutes of Health, Bethesda, Maryland (<http://biowulf.nih.gov>). We thank D. Staudt for discussions, K. Meyer for help with the GEO submission, and X. Li for IRAK1 plasmids. We are grateful to B. Tran and the Center for Cancer Research Sequencing Facility for implementation of next generation RNA sequencing.

Author Contributions V.N.N., R.M.Y., R.S., S.J., K.-H.L., H.K. and A.L.S. designed and performed experiments. W.X., Y.Y. and H.Z. performed experiments. W.X., G.W. and J.P. analysed data. A.R., H.K.M.-H., G.O., R.D.G., J.M.C., L.M.R., E.C., E.S.J., J.D., E.B.S., R.I.F., R.M.B., R.R.T., J.R.C., D.D.W. and W.C.C. supplied patient samples and reviewed pathological and clinical data. L.M.S. designed and supervised research and wrote the manuscript.

Author Information Gene expression profiling data have been submitted to GEO under accession number GSE22900. Reprints and permissions information is available at www.nature.com/reprints. The authors declare no competing financial interests. Readers are welcome to comment on the online version of this article at www.nature.com/nature. Correspondence and requests for materials should be addressed to L.M.S. (lstaudt@mail.nih.gov).

METHODS

Cell lines. Cell lines were cultured in RPMI 1640 medium supplemented with penicillin/streptomycin and 10% fetal bovine serum or, for the OCI series of cell lines, Iscove's medium with 20% fresh human plasma. Cells were maintained in a humidified, 5% CO₂ incubator at 37 °C. All cell lines were engineered to express an ecotropic retroviral receptor and the bacterial tetracycline repressor as previously described²⁵.

Retroviral vectors and retroviral transduction. A previously described retroviral vector, pRSMX²⁵, was used to express shRNA for the library screen. A modified version of this vector, pRSMX-PG, in which the puromycin selectable marker was fused with the green fluorescence protein (GFP), was used to co-express shRNA and GFP for shRNA toxicity assay. Retroviral transduction was performed by transfecting the retroviral vector and a mixture of helper plasmids for a mutant ecotropic envelope and *gag* and *pol* into 293T cells using Lipofectamine 2000 (Invitrogen). Retroviral supernatants were harvested 48 h after transfection and were used to transduce ecotropic receptor-expressing target cells by centrifugation at 2,500 r.p.m. for 1.5 h in the presence of 8 µg ml⁻¹ polybrene.

shRNA library screening. Pools of shRNA library were screened as previously described²⁵. Briefly, pools of roughly 1,000 shRNA expressing retroviral vectors were used to transduce target cell lines. After puromycin selection, stable integrants were induced to express shRNA by doxycycline (20 ng ml⁻¹). Parallel uninduced cultures were kept as control. After 3 weeks of shRNA induction, genomic DNA from both uninduced and induced cultures were harvested. shRNA-associated bar code sequences from the genomic DNA were PCR amplified and *in vitro* transcribed, as described²⁵. The transcribed RNA products were labelled fluorescently with either Cy5 (induced) or Cy3 (uninduced) using the Universal Linkage System (Amersham Biosciences) and hybridized onto microarrays containing DNA oligonucleotides complementary to the bar code sequences, as described²⁵. Each bar code experiment was performed in quadruplicate, and the microarray results for each bar code were averaged. The complete screening results are presented in Supplementary Table 3, which includes some data that have been previously published^{8,25}.

shRNA sequences. The shRNA sequences used in individual experiments are listed in Supplementary Table 4.

shRNA toxicity and complementation assays. shRNA toxicity was assayed as described²⁵. Briefly, the pRSMX-PG vector that co-expresses shRNA and GFP was transduced into lymphoma and multiple myeloma cell lines. Two days after retroviral transduction, doxycycline was added to induce shRNA expression. The fraction of GFP⁺, shRNA-expressing cells relative to the GFP⁺, shRNA⁻ fraction was monitored over various time points by flow cytometry and plotted against the same GFP⁺, shRNA-expressing fraction on day 0 of doxycycline induction. The reduction of the GFP⁺, shRNA-expressing fraction at later time points indicates shRNA toxicity. Complementation studies were performed in the DLBCL cell line that harbours the MYD88 L265P mutation. HBL1 cells were transduced with retroviral vectors that co-express GFP and shRNA targeting the 3' UTR of *MYD88* (or *IRAK1*). shRNA-transduced cells were subsequently infected with retroviruses co-expressing wild-type or mutant *MYD88* (or *IRAK1*) coding regions and mouse CD8 (Lyt2). The cell fraction positive for GFP and CD8 (using anti-mouse CD8a, BD Pharmingen) was monitored over time by flow cytometry as above. TMD8 and OCI-Ly3 cells were first transduced with retroviruses co-expressing wild-type or mutant *MYD88* (or *IRAK1*) coding regions and mouse CD8 (Lyt2) and enriched for Lyt2 expression with magnetic beads. Enriched cells were subsequently infected with retroviral vectors that co-express GFP and an shRNA targeting the 3' UTR of *MYD88*. The cell fraction positive for GFP and CD8 was monitored over time by flow cytometry.

For the *IRAK4* complementation assay, HBL1, HLY1, TMD8 and SUDHL2 lymphoma cell lines were first retrovirally transduced with either vLyt2 empty vector, or vLyt2 vector expressing wild-type or kinase-dead *IRAK4* (K213A/K214A). The infected cells were later enriched using the CD8 microbeads method (Miltenyi Biotec) according to manufacturer's protocol. The enriched cells were then infected with retroviral vector pRSMX-PG expressing either a control shRNA or an *IRAK4* shRNA. Doxycycline was added 2 days after infection to induce shRNA expression. The fraction of GFP-positive cells was monitored over time by FACS analysis and the decline of GFP hence shRNA expressing cells indicates toxicity.

Synergistic toxicity of MYD88 and either CARD11 or CD79A knockdown. OCI-Ly10 cells were first infected with either pRSMX-puro empty vector or pRSMX-puro vector encoding *MYD88* shRNA sequence (5'-GTACCAGTATTTATCTACTCTA-3'). Two days after infection the two cell lines were selected using 1 µg ml⁻¹ puromycin. The selected cells were then retrovirally infected with pRSMX-PG encoding either a scramble control, shRNA sequence against *CARD11* (target sequence 5'-GGGGTGTGTACCAGGCTATGA-3') or *CD79A* (target sequence 5'-GGGGCTTCCTTAGTCATATTC-3'). Doxycycline was

added 2 days after infection to induce shRNA expression. The fraction of GFP-positive cells was monitored over time by FACS analysis and the decline of GFP hence shRNA expressing cells indicates toxicity.

High-throughput RNA sequencing/PCR amplification/Sanger sequencing. The standard Illumina pipeline for RNA-seq was used, using paired-end 75-base-pair runs with each sample run in one sequencing lane, yielding ~20 million reads per sample. Sequences were mapped back to both RefSeq and Ensemble transcript models using the BWA algorithm²⁶, yielding a median resequencing coverage of 10×. Single nucleotide variants (SNVs) were reported that deviated from the human reference genome sequence, were observed in both sequencing directions, represented >20% of the resequencing coverage at a particular base pair position, and were not known SNPs in the dbSNP database of NCBI. A total of 52,160 putative SNVs was detected in the four ABC DLBCL cell lines studied. Sequences have been submitted to the NCBI short sequence archive under accession SRP003192. On the basis of the criteria above, all SNVs that are not represented in publically available databases of single nucleotide polymorphisms (SNPs) are listed in Supplementary Table 5. Except for the MYD88 mutations, other SNVs in this table have not been validated by independent means.

Sanger sequencing of MYD88 was accomplished with the following primers: MYD88-Full-F, 5'-GACCTCTCCAGATCTCAAAAGGCAGATTCC-3' (PCR amplification and sequencing, exon 1); MYD88-Full-R, 5'-GCAGAAGTACATGGACAGGCAGACAGATAC-3' (PCR amplification and sequencing, exon 5); MYD88-Seq-E1R, 5'-TCTCTCCATGGGAGACAGGATGCTG-3' (sequencing exon 1); MYD88-Seq-E2F, 5'-TGGGTAAGAGGTAGGCACTCCAG-3' (sequencing exon 2); MYD88-Seq-E2R, 5'-GCCCATCTGCTTCAACACCCATGC-3' (sequencing exon 2); MYD88-Seq-E3F, 5'-AAGCCTTCCCATGGAGCTCTGACAC-3' (sequencing exon 3); MYD88-Seq-E3R, 5'-GCTAGGAGGAGATGCCAGTATCTG-3' (sequencing exon 3); MYD88-Seq-E4F, 5'-ACTAAGTTGCACAGGACCTGCAGC-3' (sequencing exon 4); MYD88-Seq-E4R, 5'-ATCCA GAGGCCACCTACACATTC-3' (sequencing exon 4); MYD88-Seq-E5F, 5'-GTTGTTAACCTGGGGTTGAAG-3' (sequencing exon 5).

For 155 cases of ABC DLBCL, analysis of CARD11, CD79B, and A20 by Sanger sequencing was performed as described^{5,8,27}.

A20 was declared epigenetically silenced if the expression level in a case was more than 2 standard deviations below the mean of other ABC DLBCL cases, based on previous gene expression profiling data¹. Deletion of the A20 locus (*TNFAIP3*) was analysed by quantitative PCR using primers to amplify exon 3 and exon 6, as described²⁷, and compared to a reference gene, *CHMP4A*, that is not subject to copy number alterations in ABC DLBCL. A20 was declared deleted if one or both of the A20 PCR products had an estimated copy number that was more than 3 standard deviations below the average of 9 normal control DNA samples. The following quantitative PCR primers were used: CHMP4A-F, 5'-CTGAAGGGAGGAGGGGTTTCATTC-3' (qPCR control gene); CHMP4A-R, 5'-CTTGGGTGTTCTTCTGGCCAGTC-3' (qPCR control gene); A20-E3F, 5'-ACCTTTGCTGGGTCTTACATGCAG-3' (qPCR A20); A20-E3R, 5'-TATGCCACCATGGAGCTCTGTTAG-3' (qPCR A20); A20-E6F, 5'-TGAGATCTACTTACCTATGGCCTTG-3' (qPCR A20); A20-E6R, 5'-TCAGGTGGCTGAGTTAAAGACAG-3' (qPCR A20).

Expression vectors and cDNA mutagenesis. The expression vector, vLyt2-MYD88-EGFP, encoding carboxy terminus EGFP-tagged MYD88 was constructed by three-way ligation of PCR-generated MYD88 and EGFP products into the pBMN-IRES-Lyt2 vector (provided by G. Nolan). The restriction site SalI was included in the MYD88 PCR reverse primer and the EGFP PCR forward primer to facilitate the ligation between MYD88 and EGFP. MYD88 or EGFP PCR products were generated using the following primer pairs: 5'-TAGTAGGGATCCG CCGCCACCATGCGACCGACCGCGCTGA-3' (MYD88), 5'-TAGTAGGTC GAGGGCAGGGACAAGGCCTTGGC-3' (MYD88), 5'-TAGTAGGTCGACATGGTGAGCAGGCGCAGGAG-3' (EGFP), 5'-TAGTAGGCGGCCGCTTACTGTACAGCTCGTCCAT-3' (EGFP).

The expression vector vLyt2-AU1-MYD88 encoding amino terminus AU1-tagged MYD88 was constructed by inserting PCR-generated MYD88 into the pBMN-IRES-Lyt2 vector. MYD88 PCR product was generated using the following primers: 5'-TAGTAGGGATCCGCGCCGACCATGCGACACATACCGCTACA TCCGACCGACCGCGCTGAGGCT-3' and 5'-TAGTAGGCGGCCGCTCAG GCGAGGACAAGGCCTTGGC-3'.

IRAK1 expression vectors were similarly created by inserting PCR-generated *IRAK1* cDNAs (from pIND-*IRAK1* wild type and K239A kinase-dead templates, a gift from X. Li) into the pBMN-IRES-Lyt2 vector, using the following PCR primers: 5'-TAGTAGCTCGAGGCGGCCACCATGGCCGGGGGGCGGGC-3' and 5'-TAGTAGGCGGCCGCTCACTTGTATCGTCGCTCTTGTAGTCGC TCTGAAATTCATCACTTTC-3'.

IRAK4 expression vectors were generated by inserting PCR-generated *IRAK4* cDNA (from a template obtained from the Dana-Farber/Harvard Cancer Center

DNA Resource Core) into the pBMN-IRES-Lyt2 vector, using the following primers: 5'-TAGTAGGGATGGGCGCCACCATGGACACATACCGCTACATCAACAAACCCATAACACCATCA-3' and 5'-TAGTAGGCGGCGGCTCAAGAAGCTGTCATCTCTTGCAG-3'.

MYD88 mutants were created with the Phusion site-directed mutagenesis kit (New England BioLabs), using either vLyt2-MYD88-EGFP or vLyt2-AU1-MYD88 vector as templates. All cDNA inserts from PCR cloning and site-directed mutagenesis were verified by sequencing. The MYD88 mutagenesis primers used were the following: L265P forward P-CATCAGAAGCGACCGATCCCCATCAAG and L265P reverse P-GGCACCTGGAGAGAGGCTGAGTGC AAA; M232T forward P-AGGTGCCGCCGACGGTGGTGGTTGTC and M232T reverse P-CTTTTCGATGAGCTCACTAGCAATAGA; S243N forward P-GAT TACCTGCAGAACAAAGGAATGTGAC and S243N reverse P-ATCAGAGACA ACCACCACCATCCGG; T294P forward P-ACCAACCCCTGCCCCAATCT TGGTTC and T294P reverse P-GTAGTCGACAGCAGTGATGAACCTCAG; S222R forward P-GGTCTATTGCTAGGGAGCTCATCGAAA and S222R reverse P-AGACACAGGTGCCAGGCAGGACATCGC.

The IRAK4 kinase-dead mutant was generated similarly using the following mutagenesis primers: K213A/K214A forward P-ACTGTGGCAGTGGCGGCG CTTGACGAAATG and K213A/K214A reverse P-TGTGTTATTACGTAGC CTTTATATACA.

MYD88 co-immunoprecipitation. BJAB cells were retrovirally transduced with various MYD88-GFP fusion constructs co-expressing a Lyt2 surface marker. Cells were enriched for Lyt2 expression using anti-Lyt2 magnetic beads (Invitrogen, 114.47D) following the manufacturer's instructions. Enriched cells were lysed at 10^7 cells per ml in RIPA buffer (0.5% Triton X-100, 0.5% deoxycholate, 0.05% SDS, 10 mM Tris, pH 8.0, 50 mM NaCl, 10 mM EDTA, 1 mM Na_3VO_4 , 30 mM pyrophosphate, 10 mM glycerophosphate, 1 mM AEBSEF, 0.02 U ml⁻¹ aprotinin and 0.01% $\text{Na}_2\text{S}_2\text{O}_8$) for 10 min on ice. Lysates were cleared by centrifuging for 20 min at 14,000g at 4 °C. MYD88-GFP constructs were immunoprecipitated with washed anti-GFP agarose beads (Chromotek) for 30 min at 4 °C, then washed 3–4 times in 1× RIPA buffer. For λ -phosphatase treatment, the agarose beads were washed two additional times in 10 mM Tris, pH 8.0 with 50 mM NaCl to remove EDTA and phosphates inhibitors. λ -phosphatase (New England Biolabs) treatment was done according to the manufacturer's instructions. Reactions were quenched by the addition of 2× lamellae sample buffer followed by boiling. Samples were separated on 10% polyacrylamide gels and transferred to Immobilon-p PVDF membranes (Millipore) for western blot analysis. Antibodies used for immunoblotting were anti-IRAK1 rabbit polyclonal (Santa Cruz Biotech), anti-IRAK4 rabbit polyclonal (Cell Signaling Technologies) and anti-MYD88 rabbit monoclonal (Cell Signaling Technologies).

NF- κ B reporter assay. BJAB cells retrovirally expressing MYD88-GFP constructs (see above) were transduced with lentiviral particles containing a NF- κ B firefly luciferase reporter construct by following the manufacturer's instructions (SA Biosciences). Firefly luciferase activity was measured using the Dual-Luciferase Reporter Assay System (Promega) following the manufacturer's instructions. Luminescence from equivalent amounts of lysate was read in triplicate on a Microtiter Plate Luminometer (Dyn-Ex Technologies). All readings were normalized to the mean fluorescence intensity of MYD88-GFP expression for each MYD88 mutant as determined by FACS analysis on a FACScalibur flow cytometer (Becton Dickinson).

Western blotting. Cells were lysed in lysis buffer (50 mM Tris pH 7.4, 150 mM NaCl, 1% Triton X-100, 1% NP-40, 2 mM EDTA) supplemented with Complete Protease Inhibitor Cocktail Tablets (Roche) and phosphatase inhibitors (Sigma) for 30 min. Lysates were cleared by centrifugation at 15,000g at 4 °C for 10 min and protein concentrations were determined by BCA protein assay (Pierce). 80–100 μ g of lysates were subjected to electrophoresis through a 4–12% Bis-Tris gel (Invitrogen) and immobilized on the nitrocellulose membranes. Proteins were detected using the following antibodies: MYD88, IRAK4, β -actin, STAT3 and p-STAT3 (Y705) (Cell Signaling Technology).

IRAK1 immunoprecipitation. Cells were lysed at 10^7 cells per ml in RIPA buffer as described above. Lysates were pre-cleared with protein-A agarose beads (Pierce) before incubation with 1 μ g ml⁻¹ of anti-IRAK1 polyclonal antibody (Santa Cruz Biotech, H-273) for 2 h on ice. Protein-A agarose beads were added to lysates and

rotated for 1 h at 4 °C, then washed three times with 1× RIPA buffer. λ -phosphatase treatment was performed as described above. Samples were separated on 10% polyacrylamide gels and transferred to Immobilon-p PVDF membranes (Millipore) for western blot analysis.

Cytokine measurement. The culture medium of cells transduced with inducible shRNAs was replaced with fresh medium plus doxycycline, and the concentrations of IL-6, IL-10 or IFN- β in culture supernatants at the indicated times were measured by ELISA (R&D Systems). Alternatively, unmanipulated lymphoma cells lines were placed into fresh media with the addition of the IRAK1/4 inhibitor (EMD chemicals) and assessed for cytokines as above. The results were normalized to live cell numbers, and are representative of at least two independent experiments.

Apoptosis measurements. HBL1 cells were retrovirally transduced with either control or MYD88-specific shRNAs, as described above. shRNA expression was induced with doxycycline and cells were evaluated for apoptosis on 2, 3 and 4 days after induction. To measure apoptosis, cells were first fixed for 10 min with 1.5% paraformaldehyde, centrifuged and then fixed and permeabilized in cold methanol overnight. Methanol-fixed cells were washed three times with FACS buffer (PBS with 1% FBS) and stained with PE rabbit anti-active caspase 3 (BD Pharmingen) and Alexa Fluor 647 mouse anti-cleaved PARP (Asp 214) (BD Pharmingen) for 20 min at room temperature in the dark, followed by an additional wash with FACS buffer. Stained cells were subjected to FACS analysis (FACScalibur, BD) and apoptotic cells were defined as double positive for both active caspase 3 and cleaved PARP.

Cell viability assay by MTS. The described DLBCL and multiple myeloma cell lines were plated in duplicate at a density of 50,000 cells per well in 96-well plates along with DMSO as negative control, or different concentrations of IRAK1/4 inhibitor (EMD Chemicals). Cell viability at 1, 2 and 3 days after drug treatment was assayed by adding 3-(4,5-dimethylthiazol-2-yl)-5-(3-carboxymethoxyphenyl)-2-(4-sulphophenyl)-2H-tetrazolium and an electron coupling reagent (phenazine methosulphate; Promega), incubated for 3 h and measured by the amount of 490 nm absorbance using a 96-well plate reader. The presented data were derived from 3 days of drug treatment. The assay was performed twice.

MYD88 and IRAK1 signature analysis. To generate a gene expression signature of MYD88 signalling in ABC DLBCL, the HBL1 cell line was transduced with retroviral vectors expressing either shMYD88-4 or shMYD88-7. After puromycin selection, shRNA expression was induced for 24 or 48 h and gene expression was measured relative to parallel uninduced cultures using Agilent 4×44K oligonucleotide microarrays. A set of 284 MYD88 target genes was selected as those that were downregulated by 0.4 log₂ in ≥ 3 arrays. A signature of NF- κ B signalling (NF- κ B-10 signature; <http://lymphochip.nih.gov/signaturedb/>) in ABC DLBCL was generated by treating HBL1 cells with the I κ B kinase- β inhibitor MLN120B for 2 h, 3 h, 4 h, 6 h, 8 h, 12 h, 16 h and 24 h. Genes that were downregulated >0.4 log₂ in at least four arrays with a one-sided *t*-test <0.01 were chosen. A signature of JAK signalling in ABC DLBCL (JAKUp-2 signature; <http://lymphochip.nih.gov/signaturedb/>) was generated by treating HBL1 cells with JAK inhibitor I (5 μ M; Calbiochem) for 2 h, 4 h, 6 h and 8 h. Genes were chosen that were decreased in expression by >0.4 log₂ at ≥ 3 time points. A signature of IFN signalling (IFN-3; <http://lymphochip.nih.gov/signaturedb/>) was curated as the union between three published gene expression signatures of type I interferon signalling (IFN-1, IRF3-1 and Module-3.1 signatures; <http://lymphochip.nih.gov/signaturedb/>). A Fisher's exact test was used to calculate the significance of the overlap between the MYD88 signature and the other signatures.

Similar methods were used to generate a signature of IRAK1 signalling in ABC DLBCL. Two ABC DLBCL cell lines, HBL1 and TMD8, were transduced with retroviruses expressing shIRAK1-3 or a control shRNA. After puromycin selection, shRNA expression was induced for 24 h or 48 h and RNA and relative gene expression in shIRAK1 and control shRNA-expressing cells was analysed by gene expression profiling as above. A signature of 350 genes was selected as those that were downregulated by 0.4 log₂ in ≥ 3 arrays.

26. Schmidlin, H., Diehl, S. A. & Blom, B. New insights into the regulation of human B-cell differentiation. *Trends Immunol.* **30**, 277–285 (2009).
27. Schmitz, R. et al. *TNFAIP3* (A20) is a tumor suppressor gene in Hodgkin lymphoma and primary mediastinal B cell lymphoma. *J. Exp. Med.* **206**, 981–989 (2009).

Spatially asymmetric reorganization of inhibition establishes a motion-sensitive circuit

Keisuke Yonehara¹, Kamill Balint¹, Masaharu Noda^{2,3}, Georg Nagel⁴, Ernst Bamberg^{5,6} & Botond Roska¹

Spatial asymmetries in neural connectivity have an important role in creating basic building blocks of neuronal processing^{1,2}. A key circuit module of directionally selective (DS) retinal ganglion cells is a spatially asymmetric inhibitory input from starburst amacrine cells^{3–5}. It is not known how and when this circuit asymmetry is established during development. Here we photostimulate mouse starburst cells targeted with channelrhodopsin-2 (refs 6–8) while recording from a single genetically labelled type of DS cell^{9,10}. We follow the spatial distribution of synaptic strengths between starburst and DS cells during early postnatal development before these neurons can respond to a physiological light stimulus, and confirm connectivity by monosynaptically restricted trans-synaptic rabies viral tracing. We show that asymmetry develops rapidly over a 2-day period through an intermediate state in which random or symmetric synaptic connections have been established. The development of asymmetry involves the spatially selective reorganization of inhibitory synaptic inputs. Intriguingly, the spatial distribution of excitatory synaptic inputs from starburst cells is significantly more symmetric than that of the inhibitory inputs at the end of this developmental period. Our work demonstrates a rapid developmental switch from a symmetric to asymmetric input distribution for inhibition in the neural circuit of a principal cell.

DS retinal ganglion cells respond to movement in a ‘preferred’ direction with robust spiking, but show minimal response to movement in the opposite, or ‘null’, direction^{2,11–13}. DS cells receive GABAergic inhibitory inputs from starburst amacrine cell processes pointing in the null direction, but not from those pointing in the preferred direction^{3,14}. Glutamatergic excitatory input from bipolar cells is also directionally selective. Interestingly, starburst cells also communicate to DS cells using acetylcholine^{15,16}, but this excitatory connection seems to be symmetric¹⁴. Directional selectivity is present before eye opening (around postnatal day 13 (P13) in mice), as well as in dark-reared animals^{9,17–19}, indicating that the establishment of circuit asymmetry does not require visual experience. How and when such highly specific synaptic connections are established between starburst and DS cells during development remain unknown. Retinal cells do not respond to light until P10–11 in mice^{18,20}, with the exception of melanopsin-containing ganglion cells²¹, which limits the ability to follow the early development of functional connectivity. Directional selectivity may develop by the asymmetric refinement of previously formed inhibitory connections (Supplementary Fig. 1a) or, alternatively, the inhibitory synaptic inputs form asymmetrically (Supplementary Fig. 1b).

To distinguish between these possibilities, we probed the spatial distribution of synaptic strengths from starburst amacrine cells to individual ON DS cells during postnatal development. ON DS cells respond to slow movement and are critical for mediating the optokinetic reflex^{22–24}. In SPIG1–GFP (SPIG1, also known as Fstl4, locus driving green fluorescent

protein expression) knock-in mice, upward-motion-preferring ON DS cells are selectively labelled with GFP throughout development in most retinal regions^{9,10}.

To activate the starburst cells of SPIG1–GFP mice before amacrine and ganglion cells receive light-driven inputs from bipolar cells, this mouse line was crossed with another line expressing Cre recombinase specifically in starburst cells (choline acetyltransferase (ChAT)–Cre knock-in mice)²⁵. At P0, we transduced these SPIG1–GFP × ChAT–Cre mice with a Cre-recombinase-dependent adeno-associated virus (AAV) carrying a reversed and double-floxed C128T mutant channelrhodopsin-2 (ChR2c)^{6–8} followed by 2A–DsRed2 (ChR2c–2A–DsRed2, see Methods, Fig. 1a). 2A sequence codes for a *cis*-acting hydrolase element²⁶ that creates equimolar amounts of ChR2c and red-fluorescent, soluble DsRed2. A soluble marker in the cell body allowed easier quantification of fluorescence, and therefore ChR2 expression, than in a membrane-bound fusion construct. ChR2c-expressing cells are responsive to light at an intensity 50-fold lower than cells expressing wild-type ChR2 (ref. 7) and could, therefore, be activated by light patterns generated by an overhead projector.

Immunohistochemistry showed that all DsRed2-marked neurons were also positive for ChAT, a marker for starburst cells. Conversely, a substantial fraction (~60%) of starburst cells in both the ganglion cell layer (GCL) and inner nuclear layer (INL) (Fig. 1b, c) were DsRed2-labelled. Therefore, starburst cells, but no other cell type in these mice, are labelled red and express light-sensitive ChR2c, whereas upward-motion-preferring ON DS cells are labelled green (Fig. 1e). First, we characterized the light-excitability of ChR2c-positive starburst cells in intact, isolated retinas between P6 and P9. Light illumination evoked robust currents in DsRed2-expressing cells, even in the presence of glutamatergic synaptic blockers (CPP, NBQX, APB), suggesting ChR2c as the source of the currents (Fig. 1d). Increasing illumination evoked increasing membrane potential changes in starburst cells and, as expected due to the 2A element, the red fluorescence intensity of the recorded cell bodies correlated well ($R = 0.83$) with the magnitude of the membrane potential change at the stimulation intensity which is used to test the distribution of synaptic strengths in subsequent experiments (Supplementary Fig. 2).

To test whether the genetically tagged neural circuit could report the synaptic strengths from starburst to ON DS cells, we isolated excitatory and inhibitory inputs to ON DS cells at P8 while stimulating ChR2c-expressing starburst cells with light patterns (see Methods). A full-field light step elicited both inhibitory and excitatory currents in ON DS cells (Fig. 1f and Supplementary Fig. 3). The inhibitory component was blocked by the GABA receptor antagonist picrotoxin, and the excitatory input by the cholinergic receptor antagonist curare. Blocking glutamate receptors had no effect on the light-evoked currents (Fig. 1f) or on the miniature excitatory postsynaptic currents (mEPSC, Supplementary Fig. 4). mEPSCs were blocked by curare (Supplementary Fig. 4). These results confirmed that ON DS cells receive GABAergic and

¹Neural Circuit Laboratories, Friedrich Miescher Institute for Biomedical Research, 4058 Basel, Switzerland. ²Division of Molecular Neurobiology, National Institute for Basic Biology, 444-8787 Okazaki, Japan. ³School of Life Science, The Graduate University for Advanced Studies, 444-8787 Okazaki, Japan. ⁴Universität Würzburg, Botanik I, Julius-von-Sachs-Platz 2, 97082 Würzburg, Germany. ⁵Max-Planck-Institut für Biophysik, Max-von-Laue Strasse 3, 60438 Frankfurt, Germany. ⁶Johann Wolfgang Goethe-Universität, Institut für Biophysikalische Chemie, Max-von-Laue-Strasse 9, 60438 Frankfurt, Germany.

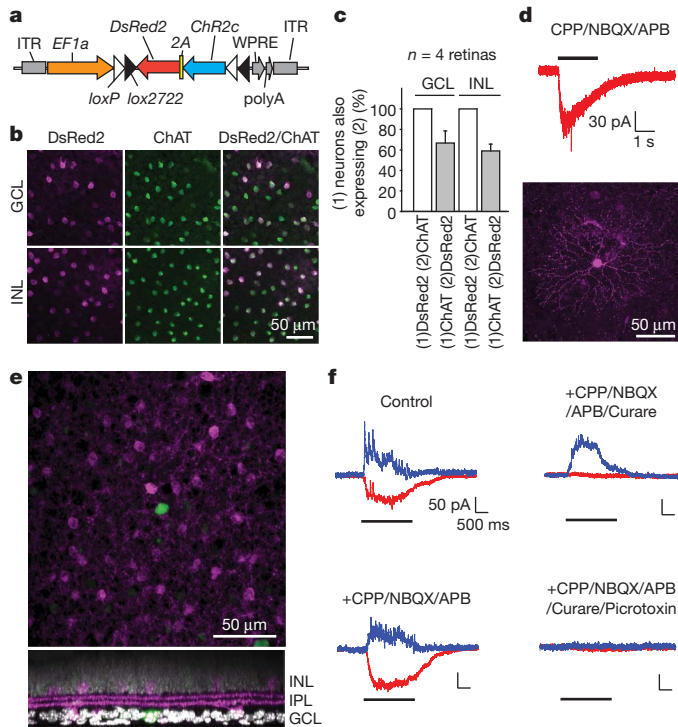


Figure 1 | Targeting of Chr2c to starburst amacrine cells at P8. **a**, AAV vector. EF1a, promoter; ITR, inverted terminal repeat; WPRE, woodchuck post-transcriptional regulatory element. **b**, Confocal images from an AAV-transduced retina. **c**, Relationship between DsRed2-expressing and ChAT-positive cells. **d**, Top, excitatory currents in an AAV-labelled starburst cell in the presence of synaptic blockers. Full-field flash stimulus. Bottom, confocal image of the recorded starburst cell. **e**, Top, confocal image of a retina in which ON DS cells are expressing GFP (green) and starburst amacrine cells are expressing Chr2c and DsRed2 (magenta). Bottom, side-view. IPL, inner plexiform layer. **f**, Synaptic currents recorded at -60 mV (red) and 20 mV (blue) holding potentials from a GFP-positive ON DS cell in response to a full-field flash. Error bars, s.d.

cholinergic synaptic inputs in response to starburst cell stimulation, but do not receive glutamatergic synaptic input from bipolar cells at this stage.

The Chr2c-assisted synaptic strength mapping depends on direct connections between starburst and ON DS cells during early postnatal development. To test whether this is the case, we performed monosynaptically restricted retrograde synaptic tracing with G-deleted rabies virus^{27,28} complemented with G-expressing herpes virus initiated from GFP-labelled ON DS cells (see Methods, Supplementary Figs 5 and 6). At P6, starburst cells were rabies-labelled around infected GFP-marked ON DS cells (Fig. 2), indicating that starburst cells are directly connected to ON DS cells at this developmental stage.

Having confirmed monosynaptic connection from starburst cells already at P6, we investigated the spatial distribution of the strength of synaptic connections by stimulating starburst cells with light steps in eight sectors surrounding the recorded ON DS cells (Fig. 3). We calculated a spatial asymmetry index (SAI) that quantified the degree of spatial asymmetry of the synaptic inputs to ON DS cells along the dorso-ventral axis (see Methods). We found that the inhibitory input was already spatially asymmetric along the dorso-ventral axis by P8; stimulation of the ventral (null) side evoked more inhibitory current than stimulation of the dorsal (preferred) side. In contrast, the excitatory input was significantly more symmetric along the same axis (Fig. 3 and Supplementary Fig. 7). To avoid potential bias due to non-uniform viral transduction we normalized the synaptic currents with either the number of DsRed2-expressing starburst cells (using a threshold) or the sum of the measured red fluorescence (which reflects the voltage change in starburst cells, as shown before, Supplementary Fig. 2) of the starburst

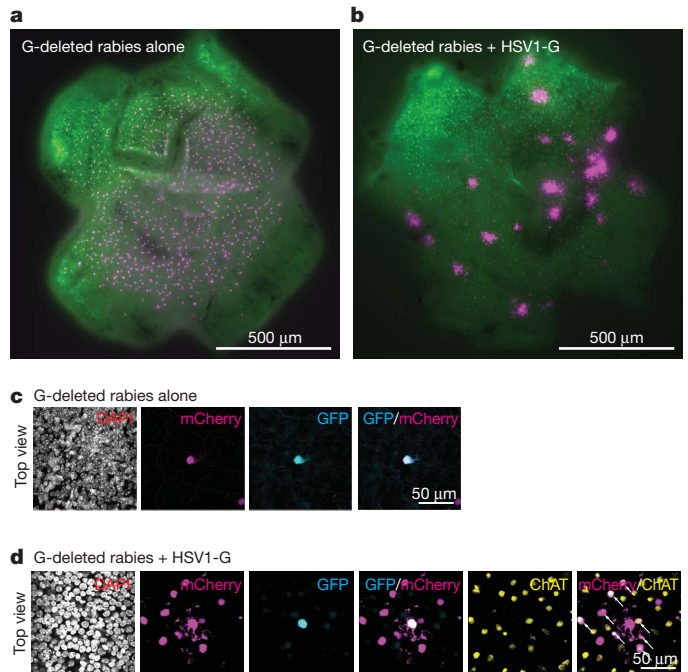


Figure 2 | Monosynaptically restricted circuit mapping initiated from ON DS cells. **a**, **b**, Live images of SPIG1-GFP retinas at P6 in which GFP-labelled ON DS cells (green) were infected with G-deleted rabies expressing mCherry (magenta) either alone (**a**) or in combination with G-encoding herpes virus (**b**). **c**, Confocal images of a GFP-labelled ON DS cell (cyan) infected with G-deleted rabies virus only (magenta). **d**, Confocal images of an ON DS cell infected with both G-deleted rabies virus and G-encoding herpes virus from **b**. Most of the labelled presynaptic cells (arrows) are ChAT-positive starburst cells (yellow) in the GCL.

cells in each of the eight sectors in which the light stimulus was presented (see Methods). The normalized responses, like the recorded raw responses, also showed asymmetric inhibition and more symmetric excitation along the dorso-ventral axis at P8 (Fig. 3, Supplementary Figs 7 and 8). In contrast to P8, the raw and normalized inhibition and excitation at P6 was symmetric along the same axis (Fig. 3, Supplementary Figs 7 and 8). The lack of asymmetry in inhibition at P6 was not due to ineffective activation of starburst cells because of low Chr2c expression level, since half-maximal activation at P9, which should be similar to maximal activation at P6 in terms of eliciting changes of membrane potential (Supplementary Fig. 2), revealed asymmetry (Supplementary Fig. 9).

Next, we investigated the emergence of asymmetry from P6 to P9 (Fig. 4). SAI of inhibition increased significantly, but there was no significant change in excitation between any pairs of days (Supplementary Fig. 8, note: the lack of stars between pairs of conditions on any of the figures means no significant change). The lack of statistically significant change in excitation was not due to saturating intensities because half-maximal activation of excitatory inputs to ON DS cells did not significantly change the SAI of excitation at P9 (Supplementary Fig. 9). The mean direction of inhibitory input of individual recorded cells, computed as the vector sum of inputs for all eight directions, was random at P6 but became confined to the ventral side by P8 (direction of red bars in Fig. 4h). Because the variation in DsRed2 expression across the eight sectors was not statistically different between P6 and P9 (Supplementary Fig. 10), the randomness at P6 is not due to greater variation in gene expression from AAV at earlier time points. We conclude that before P6 the spatial distribution of inhibitory connectivity between starburst cells and ON DS cells is either random or symmetric (with some synapses having little strength). Inhibitory connectivity rapidly reorganizes to become asymmetric along the 'preferred-null' (dorso-ventral) axis between P6 and P8, whereas excitatory cholinergic

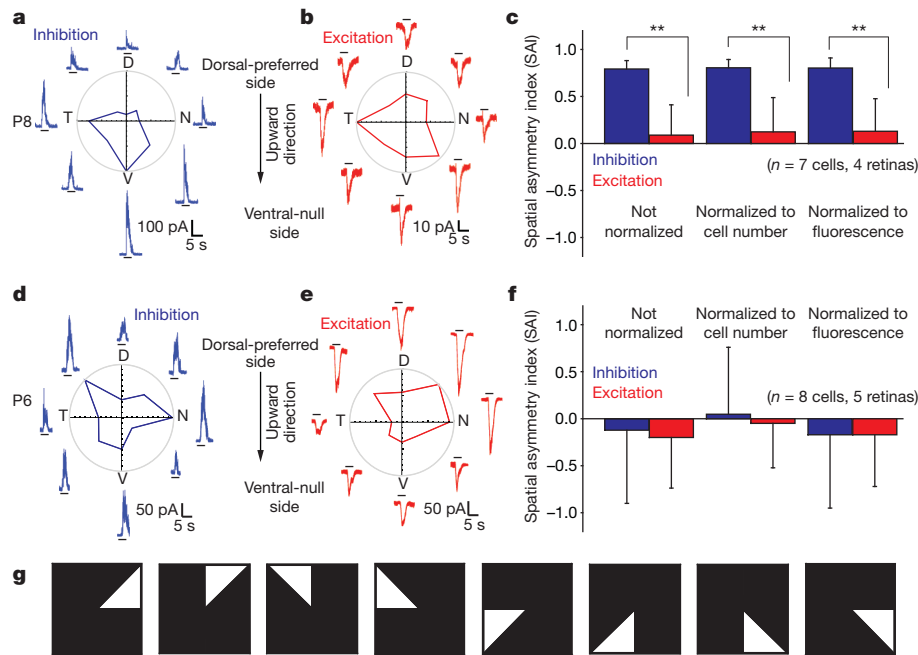


Figure 3 | ChR2c-assisted circuit mapping at P8 and P6. a–f, Recordings from ON DS cells at P8 (a–c) and P6 (d–f). Inhibitory (a, d) and excitatory (b, e) postsynaptic currents elicited in an ON DS cell by the stimulation of eight

sectors surrounding the cell. Polar plots are also shown. c, f, Spatial asymmetry index (SAI) for inhibition and excitation. g, Sketch of light patterns used to stimulate one of eight sectors around the recorded ON DS cell. Error bars, s.d.

input remains significantly more symmetric throughout this developmental period (Supplementary Fig. 1a).

Is inhibitory connectivity strengthened at the ventral ('null') and weakened at the dorsal ('preferred') side or is only one of these two mechanisms driving the development of asymmetry? Since starburst cells similarly control the strength of cholinergic excitation and GABAergic inhibition to ON DS cells (Supplementary Fig. 11) and excitation is not significantly different along the dorso-ventral axis from P6 to P9, the ratio of inhibition to excitation (neither normalized) in the dorsal and ventral sides should be a measure of the inhibitory synaptic strength that depends less on the level of ChR2c expression

(which increases over the days, Supplementary Fig. 2d) than inhibition alone. This ratio increased in the ventral (though the increase was not significant) and decreased in the dorsal side (Supplementary Fig. 12), suggesting that 'push-pull' synapse reorganization is at work.

The retinal stratum in which ON DS cells extend their dendrites embodies three different directionally selective computations that lead to preferential responses to nasal, upward and downward motion in different types of ON DS cells. We suggest that, in the physical space shared by these circuits, it is the spatially selective refinement of the distribution of inhibitory input strength to each DS ganglion cell that underlies the establishment of each directionally selective retinal circuit.

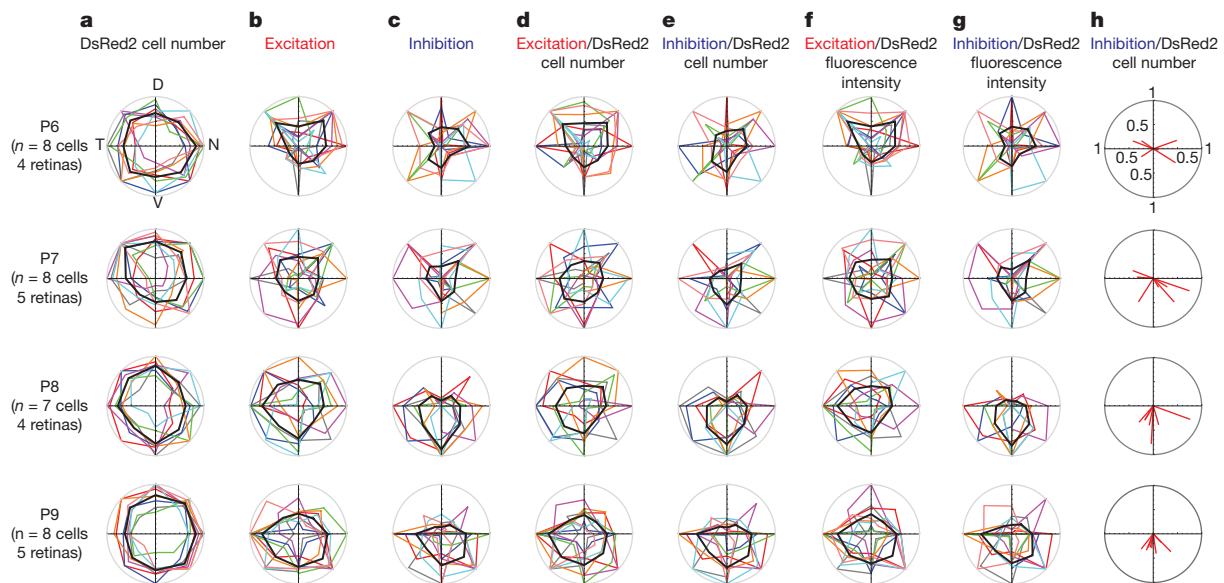


Figure 4 | Development of asymmetry. Coloured lines indicate normalized current responses from individual cells and the black line indicates the mean response of all recorded cells (or the mean cell number for a). Polar plot of the number of DsRed2-expressing cells (a), excitatory (b) and inhibitory (c) inputs, excitatory (d) and inhibitory (e) inputs normalized to the number of DsRed2

expressing cells in each sector, excitatory (f) and inhibitory (g) inputs normalized to the mean DsRed2 fluorescence intensity of cells in each sector. h, Red bars indicate the vector sum of inhibitory inputs normalized to the number of DsRed2 expressing cells in each sector.

Higher-order brain computations, for example orientation selectivity in the visual cortex, also rely on spatial circuit asymmetries. Mechanistic insights from the development of retinal directional selectivity may help to understand how asymmetry in cortical circuits is established.

METHODS SUMMARY

On the day of birth (P0) starburst amacrine cells in the progeny of a cross between mice expressing Cre in starburst amacrine cells and SPIG1–GFP mice expressing GFP in ON DS cells were labelled with Chr2c *in vivo* by transduction with a Cre-recombinase-dependent AAV. Retinas were isolated at P6 or later and GFP-labelled ON DS cells were recorded in voltage clamp at -60 mV (for excitation) or 20 mV (for inhibition)²⁹ guided by a two-photon microscope at 930 nm (ref. 30). Photostimulation was performed with white light steps (duration 2 s, inter-stimulus interval 10 s) generated by a digital light projector (PLUS Vision) and directed onto each of eight sectors surrounding the recorded cell. Stereotaxic injections of rabies and herpes viruses to the medial terminal nucleus (MTN) of SPIG1–GFP mice were performed at P1 and infected retinas were isolated at P6.

Full Methods and any associated references are available in the online version of the paper at www.nature.com/nature.

Received 24 July; accepted 2 December 2010.

Published online 19 December 2010.

- Hubel, D. H. & Wiesel, T. N. Receptive fields, binocular interaction and functional architecture in the cat's visual cortex. *J. Physiol. (Lond.)* **160**, 106–154 (1962).
- Barlow, H. B. & Hill, R. M. Selective sensitivity to direction of movement in ganglion cells of the rabbit retina. *Science* **139**, 412–414 (1963).
- Fried, S. I., Munch, T. A. & Werblin, F. S. Mechanisms and circuitry underlying directional selectivity in the retina. *Nature* **420**, 411–414 (2002).
- Euler, T., Detwiler, P. B. & Denk, W. Directionally selective calcium signals in dendrites of starburst amacrine cells. *Nature* **418**, 845–852 (2002).
- Lee, S. & Zhou, Z. J. The synaptic mechanism of direction selectivity in distal processes of starburst amacrine cells. *Neuron* **51**, 787–799 (2006).
- Bamann, C., Gueta, R., Kleinlogel, S., Nagel, G. & Bamberg, E. Structural guidance of the photocycle of channelrhodopsin-2 by an interhelical hydrogen bond. *Biochemistry* **49**, 267–278 (2010).
- Berndt, A., Yizhar, O., Gunaydin, L. A., Hegemann, P. & Deisseroth, K. Bi-stable neural state switches. *Nature Neurosci.* **12**, 229–234 (2008).
- Radu, I. *et al.* Conformational changes of channelrhodopsin-2. *J. Am. Chem. Soc.* **131**, 7313–7319 (2009).
- Yonehara, K. *et al.* Identification of retinal ganglion cells and their projections involved in central transmission of information about upward and downward image motion. *PLoS ONE* **4**, e4320 (2009).
- Yonehara, K. *et al.* Expression of SPIG1 reveals development of a retinal ganglion cell subtype projecting to the medial terminal nucleus in the mouse. *PLoS ONE* **3**, e1533 (2008).
- Vaney, D. I. & Taylor, W. R. Direction selectivity in the retina. *Curr. Opin. Neurobiol.* **12**, 405–410 (2002).
- Barlow, H. B. & Levick, W. R. The mechanism of directionally selective units in rabbit's retina. *J. Physiol. (Lond.)* **178**, 477–504 (1965).
- Demb, J. B. Cellular mechanisms for direction selectivity in the retina. *Neuron* **55**, 179–186 (2007).
- Fried, S. I., Munch, T. A. & Werblin, F. S. Directional selectivity is formed at multiple levels by laterally offset inhibition in the rabbit retina. *Neuron* **46**, 117–127 (2005).
- Ariel, M. & Daw, N. W. Pharmacological analysis of directionally sensitive rabbit retinal ganglion cells. *J. Physiol. (Lond.)* **324**, 161–185 (1982).
- Masland, R. H. & Ames, A. III. Responses to acetylcholine of ganglion cells in an isolated mammalian retina. *J. Neurophysiol.* **39**, 1220–1235 (1976).
- Chan, Y. C. & Chiao, C. C. Effect of visual experience on the maturation of ON-OFF direction selective ganglion cells in the rabbit retina. *Vision Res.* **48**, 2466–2475 (2008).
- Chen, M., Weng, S., Deng, Q., Xu, Z. & He, S. Physiological properties of direction-selective ganglion cells in early postnatal and adult mouse retina. *J. Physiol. (Lond.)* **587**, 819–828 (2009).
- Elstrott, J. *et al.* Direction selectivity in the retina is established independent of visual experience and cholinergic retinal waves. *Neuron* **58**, 499–506 (2008).
- Tian, N. & Copenhagen, D. R. Visual deprivation alters development of synaptic function in inner retina after eye opening. *Neuron* **32**, 439–449 (2001).
- Hattar, S., Liao, H. W., Takao, M., Berson, D. M. & Yau, K. W. Melanopsin-containing retinal ganglion cells: architecture, projections, and intrinsic photosensitivity. *Science* **295**, 1065–1070 (2002).
- Oyster, C. W., Takahashi, E. & Collewijn, H. Direction-selective retinal ganglion cells and control of optokinetic nystagmus in the rabbit. *Vision Res.* **12**, 183–193 (1972).
- Simpson, J. I. The accessory optic system. *Annu. Rev. Neurosci.* **7**, 13–41 (1984).
- Sun, W., Deng, Q., Levick, W. R. & He, S. ON direction-selective ganglion cells in the mouse retina. *J. Physiol. (Lond.)* **576**, 197–202 (2006).
- Ivanova, E., Hwang, G. S. & Pan, Z. H. Characterization of transgenic mouse lines expressing Cre recombinase in the retina. *Neuroscience* **165**, 233–243 (2010).
- Tang, W. *et al.* Faithful expression of multiple proteins via 2A-peptide self-processing: a versatile and reliable method for manipulating brain circuits. *J. Neurosci.* **29**, 8621–8629 (2009).
- Wickersham, I. R. *et al.* Monosynaptic restriction of transsynaptic tracing from single, genetically targeted neurons. *Neuron* **53**, 639–647 (2007).
- Stepien, A. E., Tripodi, M. & Arber, S. Monosynaptic rabies virus reveals premotor network organization and synaptic specificity of cholinergic partition cells. *Neuron* **68**, 456–472 (2010).
- Roska, B. & Werblin, F. Vertical interactions across ten parallel, stacked representations in the mammalian retina. *Nature* **410**, 583–587 (2001).
- Munch, T. A. *et al.* Approach sensitivity in the retina processed by a multifunctional neural circuit. *Nature Neurosci.* **12**, 1308–1316 (2009).

Supplementary Information is linked to the online version of the paper at www.nature.com/nature.

Acknowledgements We thank B. G. Scherf, S. Djaffer and J. Jüttner for technical assistance, T. Szikra for helping with light intensity calibration, V. Busskamp for suggesting the use of the 2A element and the cloning strategy for the 2A-based expression system, and V. Busskamp, K. Farrow, S. Oakeley and P. King for their comments on the manuscript. We thank E. Callaway for providing the rabies viruses and K. Conzelmann and S. Arber for discussion about rabies viruses. The study was supported by the Friedrich Miescher Institute for Biomedical Research, a US Office of Naval Research Naval International Cooperative Opportunities in Science and Technology Program grant, a Marie Curie Excellence grant, a National Centre of Competence in Research Frontiers in Genetics grant, an European Research Council as well as RETICIRC, TREATRUSH and OPTONEURO grants from the European Union to B.R. and an EMBO Long-Term Fellowship to K.Y.

Author Contributions K.Y. performed and designed all retinal experiments, *in vivo* injection experiments with rabies, herpes and AAV viruses, developed all plasmids, analysed data and wrote the paper. K. B. grew and titred rabies viruses. M.N. developed SPIG1–GFP mice. G.N. and E.B. developed Chr2c. B.R. designed experiments, analysed data and wrote the paper.

Author Information Reprints and permissions information is available at www.nature.com/reprints. The authors declare no competing financial interests. Readers are welcome to comment on the online version of this article at www.nature.com/nature. Correspondence and requests for materials should be addressed to B.R. (botond.roska@fmi.ch).

METHODS

Animals. ChAT-Cre mice were purchased from Jackson Laboratory (strain: B6;129S6-Chat^{tm1(Cre)Low1/J}). In ChAT-Cre mice, Cre recombinase is expressed under the control of the ChAT locus. In SPIG1-GFP mice GFP is expressed under the control of the SPIG1 locus^{9,10}. To obtain neonatal SPIG1-GFP × ChAT-Cre mice we crossed SPIG1-GFP homozygous mice with ChAT-Cre homozygous mice. All animal procedures were performed in accordance with standard ethical guidelines (European Communities Guidelines on the Care and Use of Laboratory Animals, 86/609/EEC) and were approved by the Veterinary Department of the Canton of Basel-Stadt, Switzerland.

AAV plasmids. In the present paper, we refer to the C128T mutant ChR2 (refs 6–8) as ChR2c. To obtain pAAV-EF1a-double floxed-ChR2c-2A-DsRed2-WPRE-hGHpA we linearized pAAV-EF1a-double floxed-hChR2(H134R)-EYFP-WPRE-hGHpA (provided by K. Deisseroth) using NheI/AscI. ChR2c was PCR-amplified from pGEMHE-ChR2c using a HindIII-2A-covering primer. Forward primer: 5'-GCTAGCGCTAGCCACCATGGATTATGGAGGCGCCC TG-3'. Reverse primer: 5'-TCTCCCGCAAGCTTAAGAAGGTCAAAATTCTT GCCGGTGCCCTTGTGTAC-3'. DsRed2 was PCR-amplified from pDsRed2-N1 (Clontech) using a HindIII-2A-covering primer. Forward primer: 5'-ACCTTC TTAAGCTTGCGGGAGACGTCGAGTCCAACCTGGGCCCCATGGCCTCCT CCGAGAACGTC-3'. Reverse primer: 5'-GGCGCGCGCGCGCGCCCTATC ACAGGAACAGGTGGTGGCG-3'. These two PCR products were then digested with NheI, AscI and HindIII and triple ligation was performed.

AAV production. Serotype 7 recombinant AAVs were made by Penn Vector Core. Penn Vector Core performed the genome copy (GC) number titration (titre: 5.78×10^{12} GC per ml) using real-time PCR (TaqMan reagents, Applied Biosystems).

Logic of AAV labelling. We used the viral vector AAV EF1a-double floxed-ChR2c-2A-DsRed2 to target the expression of ChR2c to starburst cells expressing Cre. In AAV EF1a-double floxed-ChR2c-2A-DsRed2, two incompatible *loxP* variants³¹, *loxP* and *lox2722*, flank an inverted version of *ChR2c* followed by the red fluorescent marker *DsRed2*. In the presence of Cre, a stochastic recombination of either *loxP* variant takes place, resulting in the inversion of *ChR2c-2A-DsRed2* into the sense direction, followed by expression of the ChR2c-2A-DsRed2. The 2A element³² codes for a *cis*-acting hydrolase element²⁶ that creates equimolar amounts of ChR2c and red-fluorescent DsRed2.

AAV injection. We injected the virus at the day of birth. SPIG1-GFP × ChAT-Cre mice were anesthetized with crushed ice. Virus ($1.5 \mu\text{l}$, 8.68×10^9 GC) was loaded into pulled glass pipettes (tip diameter, $30 \mu\text{m}$) and injected into the vitreal space of both eyes using a microinjector (Narishige). After 6 days, DsRed2 expression was brightly detectable; hence all recordings were performed on retinas at P6 or later.

Preparation of retinas. Neonatal mice were killed by decapitation. Eyes were enucleated. The retinas were isolated and the pigment epithelium removed in Ringer's medium (in mM: 110 NaCl, 2.5 KCl, 1 CaCl₂, 1.6 MgCl₂, 10 D-glucose, 22 NaHCO₃, bubbled with 5% CO₂/95% O₂, pH 7.4) and mounted ganglion-cell-side up on a filter (MF-membrane, Millipore) with a 2-mm rectangular aperture in the centre. Before starting superfusion, DsRed2-positive regions together with GFP-positive cells were located with an epifluorescence stereomicroscope (Olympus) and photographed for later determination of the average DsRed2 fluorescence intensity around recorded ON DS cells for data normalization and orientation of the retina. Only GFP cells surrounded by DsRed2 expression were chosen for the recordings. The orientation of the isolated SPIG1-GFP × ChAT-Cre retina was determined by the pattern of GFP expression. In most retinal regions, GFP is expressed exclusively in one type of ON DS cells during the developmental period. An exception is the dorsal (slightly temporal) region, where GFP is expressed in many different ganglion and amacrine cell types. A thick axon bundle in this region runs in the dorso-ventral direction towards the optic disk and can be used as a compass in isolated retinas⁹. The retinas were superfused in Ringer's medium at 35–36 °C in the microscope chamber for the duration of the experiment. In this retinal preparation, ChR2c-mediated light responses could be measured for more than 8 h.

Two-photon imaging, electrophysiology and pharmacology. Fluorescent cells were found with the help of a two-photon microscope equipped with a Mai Tai HP two-photon laser (930 or 1,010 nm) (Spectra Physics) integrated into the electrophysiological setup³⁰. Current recordings were made in whole-cell voltage clamp mode using an Axon Multiclamp 700B amplifier with borosilicate glass electrodes (BF100-50-10, Sutter Instruments) pulled to 7–9 MΩ, and filled with (in mM) 112.5 CsCH₃SO₃, 1 MgSO₄, 7.8×10^{-3} CaCl₂, 0.5 BAPTA, 10 HEPES, 4 ATP-Na₂, 0.5 GTP-Na₃, 5 lidocaine N-ethylbromide (Qx314-Br), 7.75 neurobiotin chloride, pH 7.2. Excitatory and inhibitory synaptic currents ('excitation' and 'inhibition', respectively) were separated by voltage-clamping the cell to the equilibrium potential of chloride (−60 mV) and unselective cation channels (20 mV), respectively²⁹. For

recording mEPSCs, cells were voltage-clamped at −60 mV and recorded for 3–5 min. Voltage recordings from DsRed2-positive starburst cells were made in whole-cell current clamp mode with glass electrodes pulled to 7–9 MΩ and filled with (in mM) 115 K-gluconate, 9.7 KCl, 1 MgCl₂, 0.5 CaCl₂, 1.5 EGTA, 10 HEPES, 4 ATP-Na₂, 0.5 GTP-Na₃, pH 7.2. In pharmacological experiments, agents were bath-applied at the following concentrations: 10 μM CPP ((±)-3-(2-carboxypiperazin-4-yl) propyl-1-phosphonic acid, blocking NMDA receptors), 10 μM NBQX (6-nitro-2,3-dioxo-1,4-dihydrobenzo[f]quinoxaline-7-sulfonamide, blocking AMPA and kainate receptors), 10 μM APB (L-(+)-2-amino-4-phosphonobutyric acid, blocking metabotropic glutamate receptors and therefore blocking the ON pathway), 50 μM curare (tubocurarine chloride, blocking nicotinic acetylcholine receptors), 100 μM picrotoxin (blocking GABA A and C receptors). All chemicals were obtained from Sigma, with the exception of APB (Calbiochem). Data were analysed offline with Mathematica (Wolfram Research).

Photostimulation. ChR2c was activated with light generated by a digital light projector (V-332, PLUS Vision). The stimulation was generated via custom-made software (Matlab, Mathworks; Labview, National Instruments). Light intensity was measured using a spectrometer (USB 4000, Ocean Optics) calibrated with a reference source (LS1-Cal, Ocean Optics). Light intensity was modulated by using different grey scales (0–255) combined with different neutral density filters (ND0, ND10, ND20 and ND 30). To correlate the stimulus intensity and the change in membrane potential in ChR2c-expressing starburst cells (Supplementary Fig. 2), we used full-field flash at 24 different intensities (12.08–15.86 in Log intensity photons $\text{cm}^{-2} \text{s}^{-1}$) presented for 2 s with an inter-stimulus interval of 5 s. For the stimulation of the eight sectors (Figs 3, 4), each stimulus was presented for 2 s with an inter-stimulus interval of 10 s. The eight sectors were stimulated in a random order. The light pattern was focused on the GCL. To find a 'weak light intensity' that evoked half the maximum excitatory current input to ON DS cell (Supplementary Fig. 9), full-field flash at 24 different intensities (12.08–15.86 in Log intensity photons $\text{cm}^{-2} \text{s}^{-1}$) was presented sequentially (presentation for 2 s with an inter-stimulus interval of 5 s) initially and next the retinas were then stimulated in eight sectors using the determined light intensity.

Data collection and analysis. Light stimulation of each of the eight sectors (Fig. 3g) around the recorded ON DS cell body was repeated in each recorded ON DS cell 3–10 times for both excitation and inhibition and the mean light responses were determined for all eight directions. To correct for non-uniform viral expressions in the eight sectors, we performed two different types of normalizations. In the first procedure, we normalized the current evoked in each sector by the number of DsRed2-expressing cells in the sector within 200 μm of recorded ON DS cell bodies in the GCL. Here we used an arbitrary fluorescence threshold that was constant between experiments. We choose the particular distance of 200 μm because the radius of the dendrites of ON DS cells plus the radius of the processes of starburst amacrine cells at P6 and P9 were together less than 200 μm (data not shown).

In the second procedure, we normalized each sector to the average fluorescence intensity of the starburst cells in the sector and not just the number. This was reasonable because the fluorescence intensity of the starburst cells correlated well ($R = 0.83$) with the magnitude of the voltage response of the starburst cell at the stimulation intensity used for the mapping procedure (Supplementary Fig. 2); therefore, the average fluorescence is a measure of the stimulation strength of the starburst cells in the sector.

To yield the eight quantities plotted on polar plots, these normalized (or not normalized) values were further normalized to the largest of the eight numbers (for excitation and inhibition, independently). Note that this normalization is useful for eliminating variations in synaptic currents arising from the patch-clamp technique including series resistance and leak conductance. Note that the largest value (of the eight) to which normalization is performed is a mean of a distribution since each segment was stimulated 3–10 times (see above). The direction of the tuning was determined by multiplying the eight values above with the corresponding unit vectors pointing in eight directions and then forming the vector sum. The direction of the vector sum was interpreted as the direction of tuning.

The spatial asymmetry index (SAI) was calculated as:

$$\text{SAI} = (I_{\text{ventral}} - I_{\text{dorsal}}) / (I_{\text{ventral}} + I_{\text{dorsal}})$$

where I_{ventral} and I_{dorsal} are the amplitudes of the normalized or not normalized currents evoked by the stimulation of ventral or dorsal sectors (both normalized and not normalized SAI's are shown in Fig. 3 and Supplementary Figs 7–9).

Monosynaptic restriction of circuit tracing. To create rabies G-expressing replication-defective herpes simplex virus-1 (HSV1), the GFP open reading frame (ORF) in the HSV1 vector pR19EF1a-GFP-WCm (Biovex) was replaced with that of G. First, the G ORF was amplified by PCR from pHCMV-G³³ using primers 5'-GTGTCGTGAGGAATTCGTACCGGATCCTCTAGGCCACC-3' and 5'-CC GCTTACTTGTACATTACAGTCTGGTCTACCCCCACT-3'. The GFP ORF

was removed from pR19EF1a-GFP-WCm by EcoRI/BsrGI digestion and the PCR fragment of G was recombined into EcoRI-BsrGI site using an in-fusion PCR kit (Takara-Clontech). The viral particles were produced by Biovex. G-deleted rabies virus encoding mCherry (SADΔG-mCherry)³⁴ was a gift from E. Callaway. Rabies virus expressing mCherry instead of the G glycoprotein was harvested from BHK-B19G cells (provided by E. Callaway) and centrifuged as described earlier²⁷. We performed stereotaxic surgery to label ganglion cells projecting to the medial terminal nucleus (MTN). A cocktail of 10^3 plaque-forming units of rabies virus and 6×10^4 plaque-forming units of HSV1 in 20 nl DMEM were loaded into pulled-glass pipettes (tip inner diameter of 20–30 μ m) and injected into the MTN using a microinjector (Narishige, IM-9B). For control experiments, we injected 2×10^5 plaque-forming units of rabies virus. Injections were performed with 24 mice at P1. Retinas were isolated at P6. Six well infected retinas at P6 were fixed by PFA and stained with antibodies. Brains were also isolated and the injection sites were localized. All rabies and HSV1 work was carried out under Biosafety level 2 conditions.

The key point of viral tracing was to infect with rabies and herpes viruses an upward-motion sensitive ON DS ganglion cell to initiate the retrograde passage of rabies viruses from this cell type. Because GFP exclusively labelled upward-motion sensitive ON DS cells in the ventral retina of SPIG1-GFP mice it was enough to examine the rabies-labelled cells around a GFP-labelled ganglion cell regardless of the injection site. The reason we performed the viral tracing in the SPIG1-GFP line was to have an internal control for the ganglion cell type for which we examine its local circuit. The fact that rabies did label GFP cells (in red) shows that the injection reached the MTN (because SPIG1-GFP cells exclusively target MTN^{9,10}, see also Supplementary Fig. 6). Even if by mistake we had injected these viruses also to other retinorecipient brain regions, this would not compromise our tracing results of the GFP-labelled ganglion cells provided, first, that the rabies-labelled circuits in the retina were far away so that the ganglion cell to which an amacrine cell is presynaptic to could be determined and, second, that only one ganglion cell was labelled in that local circuit. The reason we used low rabies titres for the herpes/rabies co-injections was to make sure that the circuits analysed were far away from each other in the retina (see Fig. 2b). In all circuits we analysed there was only one ganglion cell in it (which was GFP-labelled, see Fig. 2d). The definition of 'ganglion cell' was based on the existence of an axon.

Immunohistochemistry. After the experiments, retinas were fixed for 30 min in 4% (w/v) paraformaldehyde in PBS (137 mM NaCl, 2.7 mM KCl, 4.3 mM Na₂HPO₄, 1.47 mM KH₂PO₄, pH 7.4) and washed with PBS for at least 1 day at 4 °C. To aid penetration of the antibodies, retinas were frozen and thawed three times after cryoprotection with 30% (w/v) sucrose. All other procedures were carried out at room temperature. After washing in PBS, retinas were blocked for 1 h in 10% (w/v) normal donkey serum (NDS; Chemicon), 1% (w/v) bovine serum albumin (BSA), and 0.5% (v/v) Triton X-100 in PBS. Primary antibodies were incubated for 7 days in 3% (v/v) NDS, 1% (w/v) BSA, 0.02% (w/v) sodium azide and 0.5% (v/v) Triton X-100 in PBS. Secondary antibodies were incubated for 2 h in 3% (v/v) NDS, 1% (w/v) BSA, and 0.5% (v/v) Triton X-100 in PBS together with

streptavidin-Alexa Fluor 633 (Invitrogen, 1:200) and DAPI (4',6-diamidino-2-phenylindole dihydrochloride, Roche Diagnostics, 10 μ g ml⁻¹) in some experiments. Streptavidin binds to neurobiotin and thus labels neurobiotin-filled cells; DAPI binds to DNA and therefore labels nuclei. After a final wash in PBS, retinas were embedded in Prolong Gold antifade (Invitrogen).

The following set of primary and secondary antibodies combinations were used in experiments in which we recorded from SPIG1 cells while stimulating ChR2c-2A-DsRed2-expressing starburst cells: (1) Primary: goat anti-ChAT (1:200, AB144P, Chemicon). Secondary: donkey anti-goat IgG conjugated with Alexa Fluor 405 (1:200, Invitrogen). (2) Primary: rabbit anti-red fluorescent protein (RFP; 1:200, AB3216, Chemicon). This primary antibody binds to DsRed2. Secondary: donkey anti-rabbit IgG conjugated with Cy3 (1:200, Jackson). (3) Primary: rat anti-GFP (1:500, 04404-84, Nacalai). Secondary: donkey anti-rat IgG conjugated with Alexa Fluor 488 (1:200, Invitrogen). The following set of primary and secondary antibodies combinations were used for staining rabies virus-infected retinas: (1) Primary: goat anti-ChAT (1:200, AB144P, Chemicon). Secondary: donkey anti-goat IgG conjugated with Alexa Fluor 633 (1:200, Invitrogen). (2) Primary: rabbit anti-red fluorescent protein (RFP; 1:200, AB3216, Chemicon). Secondary: donkey anti-rabbit IgG conjugated with Cy3 (1:200, Jackson). (3) Primary: rat anti-GFP (1:500, 04404-84, Nacalai). Secondary: donkey anti-rat IgG conjugated with Alexa Fluor 488 (1:200, Invitrogen).

Confocal analysis. Stained retinas were analysed with a Zeiss LSM 700 confocal microscope. The DsRed2-expressing cell number was assessed from z-stack images by using a $\times 20$ lens, numerical aperture (NA) 0.7, $\times 0.5$ digital zoom. All images were recorded at the same laser power and gain control. Overall morphologies of the recorded starburst or ganglion cells were assessed using a $\times 40$ oil immersion lens, NA 1.2, $\times 0.5$ digital zoom or $\times 63$ oil immersion lens, NA 1.3, $\times 0.5$ digital zoom. The mCherry-labelled presynaptic circuits of ON DS cells were assessed from z-stack images using a $\times 63$ oil immersion lens, NA 1.3.

Statistical analysis. The non-parametric Mann-Whitney U test was used to compare data obtained from different cells on different days and the Wilcoxon signed rank test for comparing pairs of data where each pair was obtained from the same cell (excitation and inhibition). Significance is denoted by * for $P < 0.05$ and ** for $P < 0.01$. The error bars and \pm values represent standard deviations (s.d.). On each figure, the lack of stars between any pairs of data signifies $P > 0.05$ and, therefore, that the two distributions are not statistically different.

- Atasoy, D., Aponte, Y., Su, H. H. & Sternson, S. M. A. FLEX switch targets channelrhodopsin-2 to multiple cell types for imaging and long-range circuit mapping. *J. Neurosci.* **28**, 7025–7030 (2008).
- Trichas, G., Begbie, J. & Srinivas, S. Use of the viral 2A peptide for bicistronic expression in transgenic mice. *BMC Biol.* **6**, 40 (2008).
- Sena-Esteves, M., Tebbets, J. C., Steffens, S., Crombleholme, T. & Flake, A. W. Optimized large-scale production of high titer lentivirus vector pseudotypes. *J. Virol. Methods* **122**, 131–139 (2004).
- Marshall, J. H., Mori, T., Nielsen, K. J. & Callaway, E. M. Targeting single neuronal networks for gene expression and cell labeling in vivo. *Neuron* **67**, 562–574 (2010).

Cortical representations of olfactory input by trans-synaptic tracing

Kazunari Miyamichi¹, Fernando Amat², Farshid Moussavi², Chen Wang³, Ian Wickersham^{4†}, Nicholas R. Wall⁴, Hiroki Taniguchi⁵, Bosiljka Tasic¹, Z. Josh Huang⁵, Zhigang He³, Edward M. Callaway⁴, Mark A. Horowitz² & Liqun Luo¹

In the mouse, each class of olfactory receptor neurons expressing a given odorant receptor has convergent axonal projections to two specific glomeruli in the olfactory bulb, thereby creating an odour map. However, it is unclear how this map is represented in the olfactory cortex. Here we combine rabies-virus-dependent retrograde mono-trans-synaptic labelling with genetics to control the location, number and type of ‘starter’ cortical neurons, from which we trace their presynaptic neurons. We find that individual cortical neurons receive input from multiple mitral cells representing broadly distributed glomeruli. Different cortical areas represent the olfactory bulb input differently. For example, the cortical amygdala preferentially receives dorsal olfactory bulb input, whereas the piriform cortex samples the whole olfactory bulb without obvious bias. These differences probably reflect different functions of these cortical areas in mediating innate odour preference or associative memory. The trans-synaptic labelling method described here should be widely applicable to mapping connections throughout the mouse nervous system.

The functions of mammalian brains are based on the activity patterns of large numbers of interconnected neurons that form information processing circuits. Neural circuits consist of local connections—where pre- and postsynaptic partners reside within the same brain area—and long-distance connections, which link different areas. Local connections can be predicted by axon and dendrite reconstructions¹, and confirmed by physiological recording and stimulation methods². Long-distance connections are more difficult to map, as commonly used methods can only trace bulk projections with a coarse resolution. Most methods cannot distinguish axons in passing from those that form synapses, or pinpoint the neuronal types to which connections are made^{1,2}. Trans-synaptic tracers can potentially overcome these limitations². Here we combine a retrograde rabies-virus-dependent mono-trans-synaptic labelling technique³ with genetic control of the location, number and cell type of ‘starter’ neurons to trace their presynaptic partners. We systematically mapped long-distance connections between the first olfactory processing centre, the olfactory bulb, and its postsynaptic targets in the olfactory cortex including the anterior olfactory nucleus (AON), piriform cortex and amygdala (Supplementary Fig. 1).

Genetic control of trans-synaptic tracing

Rabies virus can cross synapses from postsynaptic to presynaptic neurons with high specificity⁴, without notable defects in the morphology or physiology of infected neurons for extended periods of time^{3,5}. Recent genetic modifications of rabies virus have permitted mono-trans-synaptic labelling³. Specifically, the rabies envelope glycoprotein (G) required for viral spread was replaced with a fluorescent marker⁶. Further, the virus was pseudotyped with EnvA, an avian virus envelope protein that lacks an endogenous receptor in mammals, and thus cannot infect wild-type mammalian cells. However, it can infect cells expressing the EnvA receptor TVA, and can subsequently produce infectious particles if TVA-expressing cells also

express G to complement the ΔG rabies virus (Fig. 1a, bottom). The new viral particles can cross synapses to label presynaptic partners of starter neurons. As trans-synaptically infected neurons do not express G, the modified virus cannot spread from them to other neurons. Paired recordings in cultured brain slices support the efficacy and specificity of this strategy³.

To extend this method to a limited number of starter cells of a defined type and at a precise location *in vivo*, we combined mouse genetics and viral infections (Fig. 1a, b). We created a transgenic mouse (*CAG-stop-tTA2*) that conditionally expresses the tetracycline trans-activator tTA2 under the control of a ubiquitous CAG promoter only upon Cre-mediated excision of a transcriptional stop cassette. After crossing these mice with transgenic mice expressing the tamoxifen-inducible Cre (CreER), a small fraction of CreER⁺ cells also express tTA2 following tamoxifen induction. We then used stereotactic injections to deliver into specific regions of the brain an adeno-associated virus (AAV) serotype 2 expressing three proteins: histone-GFP, TVA and G, under the control of a tetracycline-response element (TRE). Expression of TVA and G allows infected, tTA2⁺ cells to be receptive to infection by the modified rabies virus, which we injected into the same location two weeks later. We define starter cells as those infected by both AAV and rabies virus, and therefore labelled by both histone-GFP and mCherry; their presynaptic partners are infected only by rabies virus and therefore express only mCherry.

We tested our strategy by using a ubiquitously expressing *actin-CreER*⁷ in combination with *CAG-stop-tTA2* in the neocortex. Starter cells could be unambiguously identified by histone-GFP expression (Supplementary Fig. 2). In all but one case, we observed more than one starter cell (Supplementary Fig. 3 shows the example of a single starter cell). In a typical example, 35 starter cells in the motor cortex expressed histone-GFP and mCherry (Fig. 1c (3)), demonstrating that AAV and rabies virus can infect the same cells *in vivo*. In addition to many locally labelled cells (Fig. 1c (1)), mCherry⁺ cells were

¹HHMI/Department of Biology, Stanford University, Stanford, California 94305, USA. ²Department of Electrical Engineering, Stanford University, Stanford, California 94305, USA. ³Department of Neuroscience, Children's Hospital, Boston, Massachusetts 02115, USA. ⁴Systems Neurobiology Laboratory, The Salk Institute for Biological Studies and Neurosciences Graduate Program, University of California, San Diego, La Jolla, California 92037, USA. ⁵Cold Spring Harbor Laboratory, New York, New York 11724, USA. [†]Present address: HHMI/Department of Brain and Cognitive Sciences, Massachusetts Institute of Technology, Cambridge, Massachusetts 02139, USA.

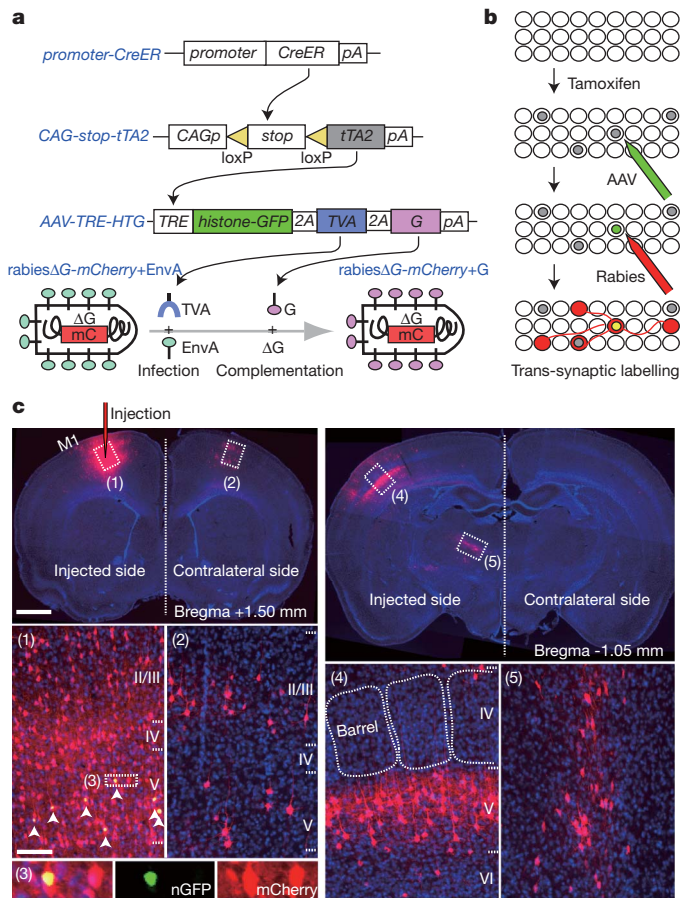


Figure 1 | Genetic control of rabies-mediated neural circuit tracing.

a, b, Schematic representation of the methodology used to control the location, number and type of starter cells for rabies-virus-mediated trans-synaptic labelling. tTA2 is expressed in a small subset of CreER⁺ cells (grey nuclei in **b**). tTA2 activates an AAV-delivered transgene to express: (1) a histone-GFP marker to label the nuclei of starter cells in green; (2) EnvA receptor (TVA) to enable subsequent infection by EnvA-pseudotyped rabies virus (rabiesΔG-mCherry+EnvA); and (3) rabies glycoprotein (G) to initiate trans-synaptic labelling. **c**, Top left, a 60-μm coronal section that includes the injection site in the motor cortex (M1). Cells labelled with both histone-GFP (nGFP) and mCherry (arrowheads in **c** (1)), magnified in **c** (3)) can be distinguished from cells labelled with mCherry alone, which are found near the injection site (**c** (1)), in the contralateral motor cortex (**c** (2)), in the somatosensory barrel cortex (top right; magnified in **c** (4)), and in the motor-specific ventrolateral nucleus of the thalamus (**c** (5)). Scale bars, 1 mm for low-magnification images at the top, 100 μm for high-magnification images at the bottom.

enriched in layers II, III and V in the contralateral motor cortex (Fig. 1c (2)), consistent with layer specificity of callosal projections⁸. mCherry⁺ cells were also found in layers III and V of the ipsilateral somatosensory cortex (Fig. 1c (4)) and in motor-specific thalamic nuclei (Fig. 1c (5)), which are known sources of monosynaptic inputs to the motor cortex⁹.

In all experiments, histone-GFP⁺ cells were found within 450 μm of the injection sites, consistent with a previous report that AAV serotype 2 predominantly infects neurons locally¹⁰. Omitting AAV or tamoxifen yielded no trans-synaptically labelled neurons (Supplementary Fig. 4). Moreover, our strategy labelled neurons only through synaptic connections but not through axons in passage (Supplementary Fig. 5). Finally, rabies virus spread was restricted to neurons directly connected to starter cells, and only in the retrograde direction (Supplementary Fig. 6). Together, these experiments validated our genetic strategy for retrograde mono-trans-synaptic labelling *in vivo*.

AON maintains the dorsal–ventral topography

In the mouse, olfactory receptor neurons that express a single type of odorant receptor send convergent axonal projections to a specific pair of glomeruli in the lateral and medial olfactory bulb^{11–13}. Odorants are detected by combinations of olfactory receptor neuron classes¹⁴, and are represented as spatiotemporal activity patterns of glomeruli¹⁵. Each mitral cell sends its apical dendrite to a single glomerulus and thus receives direct input from a single olfactory receptor neuron class. Mitral cell axons relay information to the olfactory cortex (Supplementary Fig. 1a). Previous axon tracing studies showed that individual mitral cells send axons to distinct cortical areas, and that small cortical regions receive broad input from the olfactory bulb^{16–19}. However, understanding the principles underlying odour perception and odour-mediated behaviours requires systematic and quantitative analysis of connection patterns of mitral cells with their cortical target neurons.

We first established that mitral cells throughout the olfactory bulb can be infected by rabies virus via their axons (Supplementary Fig. 7). We then applied our strategy (Fig. 1a, b) to specific areas of the AON, piriform cortex and cortical amygdala (Supplementary Fig. 1b), and examined the distribution of trans-synaptically labelled mitral cells. In a typical example, 11 clustered starter cells in the AON (Fig. 2a) resulted in 69 labelled mitral cells distributed widely across the olfactory bulb (Supplementary Fig. 8 and Supplementary Movie 1). Bright mCherry fluorescence from rabies virus allowed us to unequivocally follow the primary dendrites of the labelled mitral cells to single target glomeruli (Fig. 2b). Each mitral cell sent its apical dendrite into a single glomerulus. Four glomeruli were each innervated by two labelled mitral cells (Fig. 2b, right, and Supplementary Table 1).

To quantitatively compare the patterns of labelled glomeruli from different animals, we established a three-dimensional (3D) reconstruction protocol for the olfactory bulb, and aligned each olfactory bulb to a standard olfactory bulb model (Fig. 2c). To test the accuracy of this procedure, we reconstructed and aligned olfactory bulbs from three P2-IRES-*tauGFP* transgenic mice²⁰. These GFP-labelled glomeruli were located within a distance of a few glomeruli from each other (Supplementary Fig. 9), consistent with the natural variability of olfactory receptor neuron axon targeting²¹. This precision of our 3D reconstruction enables the comparison of olfactory bulbs from different animals.

The AON has been proposed to provide feedforward modification of information from the olfactory bulb to the piriform cortex²². Little is known about its organization except for a small and distinct AON pars externa, which maintains dorsal–ventral olfactory bulb topography^{23–25}. We injected AAV and rabies virus to different areas of the AON (Supplementary Table 1), and established an AON 3D-reconstruction protocol analogous to that for the olfactory bulb (Fig. 2c, left). Labelled glomeruli from AON injections were distributed widely in the olfactory bulb (Fig. 2c, middle). However, starter cells from the ventral and dorsal AON preferentially labelled ventral and dorsal glomeruli, respectively (Fig. 2c). To quantify the spatial distributions of starter cells in the AON and trans-synaptically labelled glomeruli in the olfactory bulb, we introduced a cylindrical coordinate system into the olfactory bulb and AON models, where *Z* represents the position along the anterior–posterior axis and *θ* represents the angle from the polar axis (Fig. 2c). No correlations were found between *Z*_{AON} and *θ*_{OB} (where OB is olfactory bulb), *Z*_{AON} and *Z*_{OB}, or *θ*_{AON} and *Z*_{OB} (Supplementary Fig. 10a). However, we found a strong positive correlation (*R*² = 0.79) between *θ*_{AON} and *θ*_{OB} (Fig. 2d), which correspond to the dorsal–ventral axes of the AON and olfactory bulb, respectively. Thus, the AON maintains the dorsal–ventral topography of the olfactory bulb.

A coarse topography exists between olfactory receptor neuron cell-body positions in the olfactory epithelium and target glomeruli in the olfactory bulb along the dorsal–ventral axis²⁶. Specifically, the olfactory cell adhesion molecule (OCAM) is expressed in a subset of olfactory receptor neurons²⁷ that project to the ventral ~55% of glomeruli in the olfactory bulb. In the olfactory bulb, ~25° clockwise rotation of the

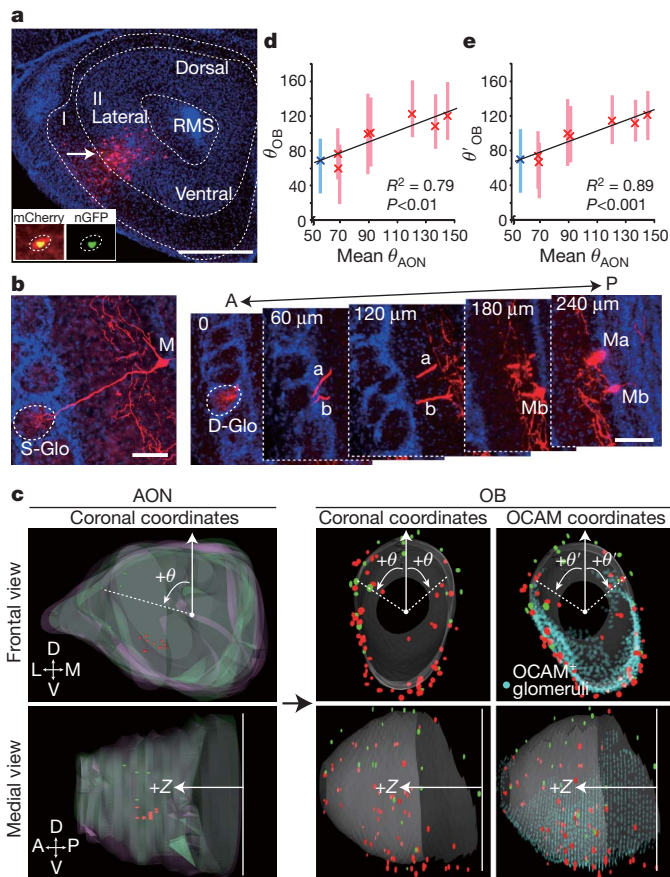


Figure 2 | The olfactory bulb to AON connections show a dorsal-ventral topography. **a**, A 60- μ m coronal section with two starter cells located in layer II of the ventrolateral AON, one of which (arrow) is magnified in the inset. RMS, rostral migratory stream. Scale bar, 500 μ m. **b**, Typical examples of trans-synaptically labelled mitral cells from cortical starter cells. Left, a 60- μ m coronal section that captures both the cell body and the apical dendrite of a mitral cell. Right, more frequently, a mitral cell apical dendrite spans several consecutive 60- μ m coronal sections. S-Glo, glomerulus innervated by a single labelled mitral cell (M). D-Glo, glomerulus innervated by two labelled mitral cells (Ma, Mb). A, anterior; P, posterior. Scale bar, 100 μ m. **c**, Superimposed 3D reconstructions of the AONs and olfactory bulbs (OBs) from two injected brains. Eleven red and four green starter cells from two AONs labelled red and green glomeruli, respectively. Light red and green, contours of two superimposed AONs. D, dorsal; L, lateral; M, medial; V, ventral. **d, e**, Correlations between θ_{AON} and θ_{OB} (**d**) and θ_{AON} and θ'_{OB} (**e**). Crosses represent mean θ_{AON} (x-axis) and mean θ_{OB} or θ'_{OB} (y-axis). Error bars represent 50% of the distribution surrounding the mean θ_{OB} or θ'_{OB} . R^2 , square of Pearson's correlation coefficient; P , statistical significance tested against the null hypothesis assuming no correlation between θ_{AON} and θ_{OB} or θ'_{OB} . Red and blue, experiments using *actin-CreER* and *CaMKII-CreER*⁴⁷, respectively.

polar axis around the z-axis maximized the separation of OCAM⁺ and OCAM⁻ glomeruli (Supplementary Fig. 11). In this new OCAM coordinate system represented by θ'_{OB} (Fig. 2c, right), the correlation coefficient between θ'_{OB} and θ_{AON} increased to $R^2 = 0.89$ (Fig. 2e), showing that adjusting the dorsal-ventral axis of the olfactory bulb according to a biological marker improved the AON and olfactory bulb topographic correspondence. Thus, the topography between the olfactory epithelium and the olfactory bulb further extends to the AON.

Dorsally biased olfactory bulb input to amygdala

Mitral cell axons project to the anterior and posterolateral cortical amygdala^{28,29}. The organization of this axonal input is unknown. We injected AAV and rabies virus to small areas within these regions, and mapped starter cells onto a common schematic drawing based on

anatomical landmarks (Fig. 3a). Trans-synaptically labelled mitral cells and glomeruli from amygdala starter cells were broadly distributed in the olfactory bulb. However, the labelled glomeruli were enriched in the dorsal olfactory bulb (Fig. 3c). For quantification, we compared the mean experimental θ'_{OB} for each injection with mean θ'_{OB} values produced by computer simulation from the same number of glomeruli distributed randomly throughout the olfactory bulb ($\text{sim}\theta'_{\text{OB}}$). For the AON experiments, the mean experimental θ'_{OB} values for the majority of the samples were significantly larger or smaller than the corresponding mean $\text{sim}\theta'_{\text{OB}}$ values (Fig. 3e, left), reflecting the dorsal-ventral topography between the olfactory bulb and the AON. By contrast, none of the mean θ'_{OB} values from the amygdala was significantly larger than the corresponding mean $\text{sim}\theta'_{\text{OB}}$ (Fig. 3e, middle). Six out of ten mean θ'_{OB} values from the cortical amygdala fell significantly below the corresponding mean $\text{sim}\theta'_{\text{OB}}$ values. For these dorsally biased samples, the density of labelled glomeruli gradually decreased along the dorsal-ventral axis without a sharp boundary (Supplementary Fig. 12). Simple spatial correspondence between starter-cell locations and the degree of dorsal bias was not evident (Supplementary Fig. 10b). In summary, the cortical amygdala overall receives biased input from the dorsal olfactory bulb.

Less organized olfactory bulb input to piriform cortex

The piriform cortex is the largest cortical area in the olfactory cortex. Recent physiological analysis^{30,31} found that neurons activated by specific odours are apparently not spatially organized; the underlying anatomical basis is unclear. We injected AAV and rabies virus into several areas in the anterior and posterior piriform cortex, and mapped starter cells from different brains onto a common schematic drawing of the entire piriform cortex based on anatomical landmarks (Fig. 3b). Labelled glomeruli were broadly distributed throughout the olfactory bulb, regardless of starter-cell locations in the piriform cortex (Fig. 3d). In sharp contrast to trans-synaptic labelling from the AON or amygdala, where different samples showed highly variable mean θ'_{OB} , mean θ'_{OB} values from the piriform cortex tracings were much less variable and closely resembled a random distribution (Fig. 3e). Only one out of ten samples had a mean θ'_{OB} slightly above the 95th percentile of the mean $\text{sim}\theta'_{\text{OB}}$. Further, no strong spatial correspondence was evident in correlation analyses of θ'_{OB} , Z_{OB} and the location of starter cells in the piriform cortex (Supplementary Fig. 10c). These data indicate that highly restricted areas of the piriform cortex receive direct mitral cell input representing glomeruli that are distributed throughout the olfactory bulb with no apparent spatial organization.

Convergence of mitral cell input

Convergent inputs from different glomeruli to individual cortical neurons could allow the olfactory cortex to integrate combinatorial odour representations in the olfactory bulb. In support of this, previous studies have shown that odour receptive ranges of AON cells are broader than those of mitral cells³², and that some piriform cortex neurons are activated by a binary odour mix but not individual components³¹. However, a large fraction of inputs in these studies could come from other cortical neurons through extensive recurrent connections (Figs 2a and 3a, b). Direct convergence of mitral cell axons onto individual cortical neurons is implied in physiological studies of piriform cortical neurons in slices^{33–35}. Our trans-synaptic labelling enabled a direct examination of mitral cell convergence to individual cortical neurons *in vivo*.

The convergence index, defined by the number of labelled mitral cells divided by the number of the starter cells in the cortex, exceeded 1 in all experiments using *actin-CreER* (Fig. 4a and Supplementary Table 1). This finding demonstrates that individual cortical neurons receive direct inputs from multiple mitral cells *in vivo*. As the vast majority of labelled mitral cells corresponded to different glomeruli (Supplementary Table 1), individual cortical neurons must receive direct inputs representing multiple glomeruli. This convergence index

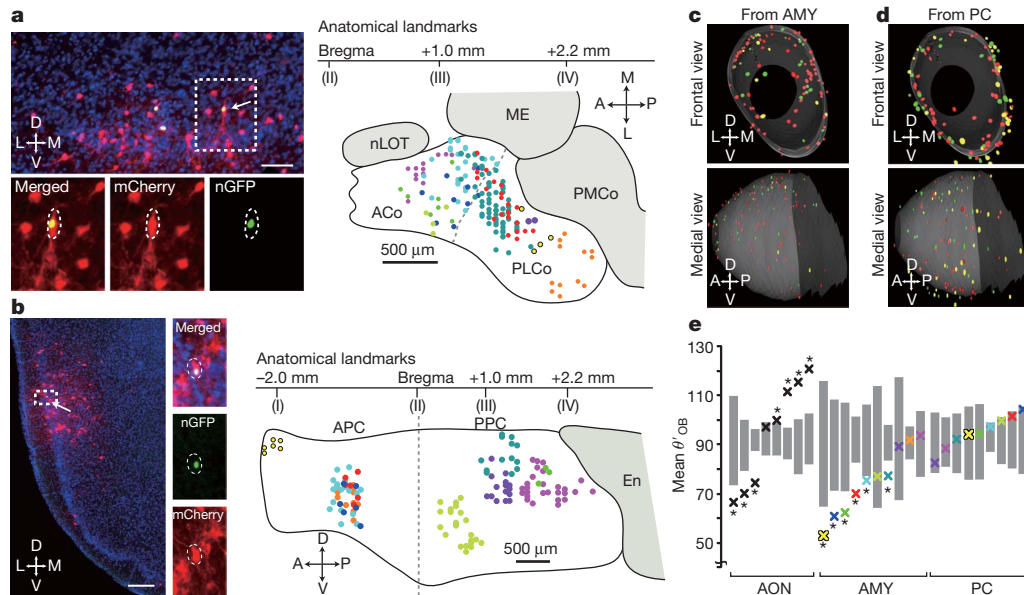


Figure 3 | Representations of olfactory bulb input in the amygdala and piriform cortex. **a, b**, Starter cells from the cortical amygdala and piriform cortex. Left, single coronal sections at the injection sites in the posterolateral cortical amygdala (**a**) and the posterior piriform cortex (**b**). Arrows point to starter cells magnified in insets. Scale bars, 100 μ m in **a**, 200 μ m in **b**. Right, schematic representations of ten independent injections each into amygdala (**a**) or piriform cortex (**b**). Starter cells from each injection are labelled with a specific colour. The dotted line denotes the rough border between the anterior cortical amygdala (ACo) and the posterolateral cortical amygdala (PLCo) based on anatomical landmarks according to a mouse brain atlas⁴⁸. APC, anterior piriform cortex; En, lateral entorhinal cortex; ME, medial amygdala; nLOT,

nucleus of lateral olfactory tract; PMCo, posteromedial cortical amygdala; PPC, posterior piriform cortex. **c, d**, Superposition of three independent 3D reconstructions of glomerular maps with starter cells from the cortical amygdala (AMY; **c**) or the piriform cortex (PC; **d**). **e**, Mean θ'_{OB} values (crosses) from each experiment are plotted in the same column with the 95% confidence intervals for corresponding θ'_{OB} values (grey bars). Samples with experimental mean θ'_{OB} outside the 95% confidence intervals are labelled with asterisks (* $P < 0.05$). Colours in **a** (scheme), **c** and **e** (amygdala) are matched to represent the same samples, and so are the colours in **b** (scheme), **d** and **e** (piriform cortex).

is probably an underestimate, as not all starter cells necessarily received direct mitral cell input (overestimation of the denominator), and not all cells presynaptic to starter cells were trans-synaptically infected by the rabies virus (underestimation of the numerator; see Supplementary Fig. 3).

The convergence indices varied widely in different experiments, and did not differ substantially in the three cortical areas we examined. However, in experiments that contained starter cells located in layer I, which is mostly composed of GABAergic local interneurons³⁶, the convergence indices were greater (Fig. 4a, red). Assuming all starter cells in a given layer contribute equally to mitral cell labelling, multiple regression analyses indicate that layer I neurons receive direct input from more mitral cells than layer II/III neurons (Fig. 4b).

To confirm the higher convergence index for layer I GABAergic neurons, we replaced the ubiquitous *actin-CreER* with *GAD2-CreER*, which is expressed only in GABAergic interneurons (Supplementary Fig. 13). We found that GABAergic neurons located in layer II or III of the piriform cortex received little direct mitral cell input, whereas those located in layer I showed a much greater convergence index (Fig. 4b, right, and Supplementary Table 1). Thus, cortical GABAergic neurons are highly diverse with respect to mitral cell innervation. These observations are in accordance with recent physiological studies^{30,34}, and suggest different physiological roles for these GABAergic neurons; layer I and deeper layer GABAergic neurons provide global feedforward and feedback inhibition to cortical pyramidal neurons, respectively.

Sister mitral cells connect independently

Each glomerulus is innervated by the apical dendrites of ~25 electrically coupled mitral cells³⁷. We refer to these cells as 'sister' mitral cells. Sister mitral cells may preferentially connect to the same cortical postsynaptic target neurons compared to 'non-sister' mitral cells that receive direct input from different glomeruli. Such an organization could increase the signal-to-noise ratio in information transmission

from mitral cells to cortical neurons. Alternatively, sister mitral cells may connect to cortical neurons independently to deliver olfactory information widely across different cortical neurons.

We used the frequency of dually labelled glomeruli from our data set and statistical simulation to distinguish between these possibilities. Dually labelled glomeruli (D) could result from a single starter cell (Ds) or two starter cells (Dt). Assuming that an individual starter cell can receive input from any of the 2,000 glomeruli, we compared the distribution of Ds derived from our data and from a simulation according to the null hypothesis that sister mitral cells connect independently with postsynaptic targets. If sister mitral cells share significantly more postsynaptic targets than at random, then the 'data Ds' distribution should be significantly higher than the simulated 'random Ds' distribution. In all but two cases, these two distributions were not statistically different (Fig. 4c). Both exceptions came from trans-synaptic labelling from the AON, which showed dorsal-ventral topography, so the original assumptions were not accurate. When we reduced the number of accessible glomeruli to 1,500, no sample showed significant differences. Thus, our analysis indicates that individual mitral cells innervating the same glomerulus act independently in making connections with their cortical targets.

Discussion

Our study revealed several general principles that define cortical representations of the olfactory bulb input. First, individual cortical neurons receive direct input from mitral cells originating from multiple glomeruli. On average, each excitatory neuron receives direct input from four mitral cells, but this number is likely to be an underestimate. Convergence of mitral cell inputs enables cortical neurons to integrate information from discrete olfactory channels. The lower bound of four already affords ~10¹² glomerular combinations for 1,000 olfactory channels, far exceeding the number of neurons in the mouse olfactory cortex. Thus, the olfactory cortical neuron repertoire samples only a

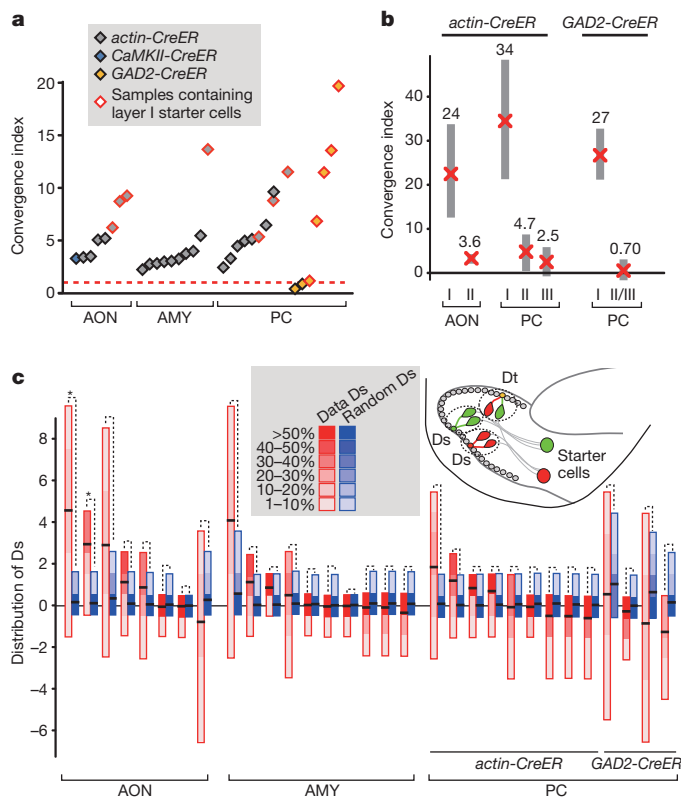


Figure 4 | Convergence and independence of mitral cell inputs.

a, Convergence index for each cortical injection experiment is represented by a diamond, with the type and layer of starter cells specified by the colour code above. AMY, amygdala; PC, piriform cortex. **b**, Multiple regression analysis to estimate the convergence indices of starter cells located in different layers of the AON and piriform cortex. Estimated mean convergence indices (red crosses) and the corresponding 95% confidence intervals (grey bars) are shown. Data from *actin-CreER* and *GAD2-CreER* were analysed separately. Injections into amygdala produced only one sample that contained layer I cells and were therefore excluded. **c**, Schematic of dually labelled glomeruli (D) resulting from two starter cells (Dt) or a single starter cell (Ds). Comparison of the distributions of Ds derived from experimentally observed frequency of D (Data Ds; red) and from simulated D based on the null hypothesis detailed in Methods (Random Ds; blue). For each sample, the distributions of 'data Ds' and 'random Ds' are shown by coloured heat maps. * $P < 0.05$.

small fraction of all possible combinations of direct olfactory bulb inputs.

Second, neurons restricted to small olfactory cortical regions receive input from glomeruli that are broadly distributed in the olfactory bulb. Although similar findings were reported previously^{16–19}, our study provides a higher resolution analysis of direct connectivity between mitral cells and cortical neurons, rather than inferring connection from the presence of axons, which could be a major caveat of previous tracing studies (see Supplementary Fig. 5). At the same time, mitral cells representing the same glomerulus connect independently to post-synaptic cortical neurons, thus maximizing the spread of olfactory information originating from individual olfactory channels. Our finding is consistent with analyses of axon arborization patterns of singly labelled mitral cells (S. Ghosh and colleagues; manuscript submitted).

Third, different cortical areas receive differentially organized olfactory bulb input (Supplementary Fig. 1c). The AON maintains a coarse topography along the dorsal–ventral axis, suggesting a pre-processing role for olfactory-bulb-derived information before sending to other cortical areas. A lack of apparent spatial organization in the piriform cortex with regard to olfactory bulb input provides an anatomical basis for recent physiological studies^{30,31}, and suggests that the piriform cortex acts as an association cortex^{31,38}. In the cortical amygdala, many neurons seem to receive strongly biased input from the dorsal olfactory bulb. Mice lacking

olfactory receptor neurons that project to the dorsal olfactory bulb lose their innate avoidance of odours from predator urine and spoiled food, despite retaining the ability to sense these odours³⁹. The cortical amygdala may preferentially process the olfactory information that directs innate behaviours. Our study is in agreement with similar findings using axon tracings from individual glomeruli (D. L. Sosulski and colleagues; manuscript submitted).

Interestingly, axonal arborization patterns of *Drosophila* olfactory projection neurons (equivalent to mitral cells) in higher olfactory centres show a similar organizational principle. Projection neuron axon arborization patterns in the lateral horn—a processing centre directing odour-mediated innate behaviour—are highly stereotyped with respect to projection neuron classes^{40,41}, and are partitioned according to the biological significance of the odorants⁴². Arborization patterns of axon collaterals of the same projection neurons in the mushroom body, an olfactory memory centre⁴³, are much less stereotyped^{40,42}, consistent with a physiological study indicating non-stereotyped connections⁴⁴. Therefore, from insects to mammals, a common theme emerges for the representations of olfactory information: more stereotyped and selective representation of odours is necessary for directing innate behaviours, whereas broader and less stereotyped sampling of the whole olfactory space is better suited for brain regions implicated in associative memories.

The genetically controlled mono-trans-synaptic tracing described here should be widely applicable for mapping neuronal circuitry throughout the mouse brain. It is currently unknown how rabies virus crosses synapses, and whether the efficiency and specificity vary with cell type, connection strength and activity^{3,5,45}. Further applications of these trans-synaptic methods to other neurons and circuits⁴⁶ will be necessary to address these questions. Nevertheless, the control experiments (Fig. 1 and Supplementary Figs 2–6) confirmed that our strategy labels neurons that are directly presynaptic to starter cells but not neurons whose axons pass through the injection sites without making synapses. Our method will be especially valuable for analysing long-distance connections that are usually refractory to physiological mapping strategies². This method can be further extended to genetic manipulation of starter cells to combine circuit tracing with genetic loss- or gain-of-function experiments. These approaches will facilitate the investigation of not only the organization of information flow within neural circuits, but also the molecular basis of neuronal connections at single-cell resolution *in vivo*.

METHODS SUMMARY

Detailed methods on the generation of *CAG-stop-tTA2* mice, viral preparations, animal surgery, tissue processing, 3D reconstruction and quantitative analyses can be found in Methods.

Full Methods and any associated references are available in the online version of the paper at www.nature.com/nature.

Received 23 August; accepted 2 December 2010.

Published online 22 December 2010.

1. Cowan, W. M. The emergence of modern neuroanatomy and developmental neurobiology. *Neuron* **20**, 413–426 (1998).
2. Luo, L., Callaway, E. M. & Svoboda, K. Genetic dissection of neural circuits. *Neuron* **57**, 634–660 (2008).
3. Wickersham, I. R. *et al.* Monosynaptic restriction of transsynaptic tracing from single, genetically targeted neurons. *Neuron* **53**, 639–647 (2007).
4. Ugolini, G. Specificity of rabies virus as a transneuronal tracer of motor networks: transfer from hypoglossal motoneurons to connected second-order and higher order central nervous system cell groups. *J. Comp. Neurol.* **356**, 457–480 (1995).
5. Ugolini, G. Advances in viral transneuronal tracing. *J. Neurosci. Methods* **194**, 2–20 (2010).
6. Wickersham, I. R., Finke, S., Conzelmann, K. K. & Callaway, E. M. Retrograde neuronal tracing with a deletion-mutant rabies virus. *Nature Methods* **4**, 47–49 (2007).
7. Guo, C., Yang, W. & Lobe, C. G. A Cre recombinase transgene with mosaic, widespread tamoxifen-inducible action. *Genesis* **32**, 8–18 (2002).
8. Wise, S. P. & Jones, E. G. The organization and postnatal development of the commissural projection of the rat somatic sensory cortex. *J. Comp. Neurol.* **168**, 313–343 (1976).

9. Iriki, A., Pavlides, C., Keller, A. & Asanuma, H. Long-term potentiation in the motor cortex. *Science* **245**, 1385–1387 (1989).
10. Taymans, J. M. *et al.* Comparative analysis of adeno-associated viral vector serotypes 1, 2, 5, 7, and 8 in mouse brain. *Hum. Gene Ther.* **18**, 195–206 (2007).
11. Vassar, R. *et al.* Topographic organization of sensory projections to the olfactory bulb. *Cell* **79**, 981–991 (1994).
12. Ressler, K. J., Sullivan, S. L. & Buck, L. B. Information coding in the olfactory system: evidence for a stereotyped and highly organized epitope map in the olfactory bulb. *Cell* **79**, 1245–1255 (1994).
13. Mombaerts, P. *et al.* Visualizing an olfactory sensory map. *Cell* **87**, 675–686 (1996).
14. Malnic, B., Hirono, J., Sato, T. & Buck, L. B. Combinatorial receptor codes for odors. *Cell* **96**, 713–723 (1999).
15. Wilson, R. I. & Mainen, Z. F. Early events in olfactory processing. *Annu. Rev. Neurosci.* **29**, 163–201 (2006).
16. Luskin, M. B. & Price, J. L. The distribution of axon collaterals from the olfactory bulb and the nucleus of the horizontal limb of the diagonal band to the olfactory cortex, demonstrated by double retrograde labeling techniques. *J. Comp. Neurol.* **209**, 249–263 (1982).
17. Scott, J. W., McBride, R. L. & Schneider, S. P. The organization of projections from the olfactory bulb to the piriform cortex and olfactory tubercle in the rat. *J. Comp. Neurol.* **194**, 519–534 (1980).
18. Shipley, M. T. & Adamek, G. D. The connections of the mouse olfactory bulb: a study using orthograde and retrograde transport of wheat germ agglutinin conjugated to horseradish peroxidase. *Brain Res. Bull.* **12**, 669–688 (1984).
19. Nevelle, K. R. & Haberly, L. B. in *The Synaptic Organization of the Brain* (ed. Shepherd, G. M.) (Oxford Univ. Press, 2004).
20. Feinstein, P. & Mombaerts, P. A contextual model for axonal sorting into glomeruli in the mouse olfactory system. *Cell* **117**, 817–831 (2004).
21. Schaefer, M. L., Finger, T. E. & Restrepo, D. Variability of position of the P2 glomerulus within a map of the mouse olfactory bulb. *J. Comp. Neurol.* **436**, 351–362 (2001).
22. Brunjes, P. C., Illig, K. R. & Meyer, E. A. A field guide to the anterior olfactory nucleus (cortex). *Brain Res. Rev.* **50**, 305–335 (2005).
23. Yan, Z. *et al.* Precise circuitry links bilaterally symmetric olfactory maps. *Neuron* **58**, 613–624 (2008).
24. Schoenfeld, T. A. & Macrides, F. Topographic organization of connections between the main olfactory bulb and pars externa of the anterior olfactory nucleus in the hamster. *J. Comp. Neurol.* **227**, 121–135 (1984).
25. Scott, J. W., Ranier, E. C., Pemberton, J. L., Orona, E. & Mouradian, L. E. Pattern of rat olfactory bulb mitral and tufted cell connections to the anterior olfactory nucleus pars externa. *J. Comp. Neurol.* **242**, 415–424 (1985).
26. Miyamichi, K., Serizawa, S., Kimura, H. M. & Sakano, H. Continuous and overlapping expression domains of odorant receptor genes in the olfactory epithelium determine the dorsal/ventral positioning of glomeruli in the olfactory bulb. *J. Neurosci.* **25**, 3586–3592 (2005).
27. Yoshihara, Y. *et al.* OCAM: a new member of the neural cell adhesion molecule family related to zone-to-zone projection of olfactory and vomeronasal axons. *J. Neurosci.* **17**, 5830–5842 (1997).
28. Swanson, L. W. & Petrovich, G. D. What is the amygdala? *Trends Neurosci.* **21**, 323–331 (1998).
29. Scalia, F. & Winans, S. S. The differential projections of the olfactory bulb and accessory olfactory bulb in mammals. *J. Comp. Neurol.* **161**, 31–55 (1975).
30. Poo, C. & Isaacson, J. S. Odor representations in olfactory cortex: “sparse” coding, global inhibition, and oscillations. *Neuron* **62**, 850–861 (2009).
31. Stettler, D. D. & Axel, R. Representations of odor in the piriform cortex. *Neuron* **63**, 854–864 (2009).
32. Lei, H., Mooney, R. & Katz, L. C. Synaptic integration of olfactory information in mouse anterior olfactory nucleus. *J. Neurosci.* **26**, 12023–12032 (2006).
33. Franks, K. M. & Isaacson, J. S. Strong single-fiber sensory inputs to olfactory cortex: implications for olfactory coding. *Neuron* **49**, 357–363 (2006).
34. Stokes, C. C. & Isaacson, J. S. From dendrite to soma: dynamic routing of inhibition by complementary interneuron microcircuits in olfactory cortex. *Neuron* **67**, 452–465 (2010).
35. Apicella, A., Yuan, Q., Scanziani, M. & Isaacson, J. S. Pyramidal cells in piriform cortex receive convergent input from distinct olfactory bulb glomeruli. *J. Neurosci.* **30**, 14255–14260 (2010).
36. Suzuki, N. & Bekkers, J. M. Inhibitory neurons in the anterior piriform cortex of the mouse: classification using molecular markers. *J. Comp. Neurol.* **518**, 1670–1687 (2010).
37. Christie, J. M. *et al.* Connexin36 mediates spike synchrony in olfactory bulb glomeruli. *Neuron* **46**, 761–772 (2005).
38. Haberly, L. B. Parallel-distributed processing in olfactory cortex: new insights from morphological and physiological analysis of neuronal circuitry. *Chem. Senses* **26**, 551–576 (2001).
39. Kobayakawa, K. *et al.* Innate versus learned odour processing in the mouse olfactory bulb. *Nature* **450**, 503–508 (2007).
40. Marin, E. C., Jefferis, G. S., Komiyama, T., Zhu, H. & Luo, L. Representation of the glomerular olfactory map in the *Drosophila* brain. *Cell* **109**, 243–255 (2002).
41. Wong, A. M., Wang, J. W. & Axel, R. Spatial representation of the glomerular map in the *Drosophila* protocerebrum. *Cell* **109**, 229–241 (2002).
42. Jefferis, G. S. *et al.* Comprehensive maps of *Drosophila* higher olfactory centers: spatially segregated fruit and pheromone representation. *Cell* **128**, 1187–1203 (2007).
43. Davis, R. L. Olfactory memory formation in *Drosophila*: from molecular to systems neuroscience. *Annu. Rev. Neurosci.* **28**, 275–302 (2005).
44. Murthy, M., Fiete, I. & Laurent, G. Testing odor response stereotypy in the *Drosophila* mushroom body. *Neuron* **59**, 1009–1023 (2008).
45. Marshel, J. H., Mori, T., Nielsen, K. J. & Callaway, E. M. Targeting single neuronal networks for gene expression and cell labeling *in vivo*. *Neuron* **67**, 562–574 (2010).
46. Stepien, A. E., Tripodi, M. & Arber, S. Monosynaptic rabies virus reveals premotor network organization and synaptic specificity of cholinergic partition cells. *Neuron* **68**, 456–472 (2010).
47. Madisen, L. *et al.* A robust and high-throughput Cre reporting and characterization system for the whole mouse brain. *Nature Neurosci.* **13**, 133–140 (2010).
48. Lein, E. S. *et al.* Genome-wide atlas of gene expression in the adult mouse brain. *Nature* **445**, 168–176 (2007).

Supplementary Information is linked to the online version of the paper at www.nature.com/nature.

Acknowledgements We thank Stanford Transgenic Facility for help in generating transgenic mice, F. Zhang and K. Deisseroth for teaching us stereotactic injection, Y. Yoshihara and H. Zeng for reagents, C. Manalac and M. Shu for technical assistance, R. Axel, L. Buck, and L. Stryer, R. Yuste and members of the L.L. laboratory for discussion and critical reading of the manuscript. K.M. was supported by the JSPS program for Research Abroad and Human Frontier Science Program. K.M. is currently a research associate and L.L. is an investigator of the Howard Hughes Medical Institute. This work was also supported by an NIH grant.

Author Contributions K.M. planned and performed all the experiments. F.A. and F.M. developed the computer programs for 3D reconstructions and statistical simulation under the supervision of M.A.H. C.W. and Z.H. performed the initial AAV production. I.W., N.R.W. and E.M.C. provided the modified rabies virus and the construct to make the AAV vector. H.T. and Z.J.H. provided the *GAD2-CreER* mice. B.T. provided DNA constructs. L.L. supervised the project. L.L. and K.M. wrote the manuscript, with contributions from B.T.

Author Information Reprints and permissions information is available at www.nature.com/reprints. The authors declare no competing financial interests. Readers are welcome to comment on the online version of this article at www.nature.com/nature. Correspondence and requests for materials should be addressed to L.L. (llu@stanford.edu).

METHODS

Generation of CAG-stop-*tTA2* Mice. The *tTA2* transactivator gene⁴⁹ was placed after the CAG promoter of plasmid *pCA-HZ2* (ref. 50) using a polymerase chain reaction (PCR)-based cloning method. A neomycin resistance (*neo*^r) gene and a transcriptional stop signal⁵¹ were flanked by *loxP* sites to create a *loxP-neo^r-stop-loxP* cassette. This cassette was then introduced between the CAG promoter and *tTA2* using PCR-based cloning. An *EcoRI* fragment obtained from *ETLpA-/LTNL*¹³, which contains the *IRES-tau-lacZ* cassette, was introduced after the *tTA2* coding sequence. The resulting cassette (*CAG-stop-tTA2-IRES-tau-lacZ*) was cloned into *pBT264* to flank the cassette with two copies of a ~250-bp β -globin *HS4* insulator sequence⁵² on each side. *pBT264 (pii-TRE-tdTomato-3Myc-ii)* was generated by inserting PCR-amplified copies of ~250-bp-long core insulator fragments (*i*) from the chicken β -globin *HS4* insulator on each side of *TRE-tdTomato-3Myc* in *pBT239*. The insulator fragments were amplified from *pJC13-1* (ref. 53). The final construct, *pKM1 (pii-CAG-stop-tTA2-IRES-tau-lacZii)*, was tested by transient co-transfection with *pBT264* into cultured HEK293 cells. When a Cre-encoding plasmid *pBT140* (cytomegalovirus (CMV) promoter driving nuclear localization signal-Cre) was further introduced into the same cell, strong tdTomato fluorescence was detected 72 h after transfection. *pKM2* was digested with restriction enzymes *SwaI* and *AscI*, the insert was gel-purified using Qiagen gel extraction kit and eluted into 10 mM Tris-HCl, pH 7.4, 0.1 mM EDTA. The purified and linearized DNA devoid of plasmid backbone was used for mouse transgenesis via standard pronuclear injection procedure. Founders were screened by PCR primers to detect the *neo^r* gene. Four independent transgenic lines were established. They were crossed with mice containing β -actin-CreER⁷ and *TRE-Bi-SG-T* reporter⁵³ to screen for functional *CAG-stop-tTA2* transgenes. Mice containing all three transgenes were injected with 1 mg of tamoxifen in corn oil at postnatal day (PD)10, and brains were collected at PD21 for the analysis. Two lines showed broad tdTomato fluorescence throughout the brain. One line (containing 2–3 copies of the transgene based on Southern blotting) was used exclusively in this study.

Virus preparations. All viral procedures followed the Biosafety Guidelines approved by the Stanford University Administrative Panel on Laboratory Animal Care (A-PLAC) and Administrative Panel of Biosafety (APB). To make the AAV containing the *TRE-HTG* cassette, which encodes histone-GFP, TVA and G linked by the 2A 'self-cleaving' peptides, the *HTG* cassette obtained from *pBOB-synP-HTB* (I.W. and E.M.C., unpublished plasmid) was placed after the *TRE-Tight* promoter in *pTRE-Tight* (Clontech), and then the entire construct was subcloned into the pAAV vector (Stratagene). Recombinant AAV serotype 2 was produced using the pAAV helper free kit (Stratagene) according to the manufacturer's instructions. AAV was also produced commercially by the Gene Therapy Center of the University of North Carolina. The AAV titre was estimated to be $\sim 4 \times 10^{12}$ viral particles ml⁻¹ based on serial dilution and blot hybridization analysis. Pseudotyped ΔG rabies virus was prepared as previously described⁵⁴. The pseudotyped rabies virus titre was estimated to be $\sim 5 \times 10^8$ infectious particles per ml based on the infections of cell line 293-TVA800 by serially diluted virus stocks.

Animal surgery. All animal procedures followed animal care guidelines approved by A-PLAC. To activate Cre in animals carrying a *CreER* transgene, we injected intraperitoneally 0.1–1 mg of tamoxifen (Sigma) dissolved in corn oil into mice around PD10. For trans-synaptic labelling, 0.1–0.3 μ l of AAV-*TRE-HTG* was injected into brain at PD21 by using a stereotactic apparatus (KOPF). During surgery, animals were anaesthetized with 65 mg kg⁻¹ ketamine and 13 mg kg⁻¹ xylazine (Ben Venue Laboratories). For motor cortex injections, the needle was placed 1.5 mm anterior and 1.5 mm lateral from the Bregma, and 0.4 mm from the brain surface. For olfactory cortex injections, see Supplementary Fig. 1b for the stereotactic parameters. After recovery, animals were housed in regular 12 h dark/light cycles with food and water *ad libitum*. Two weeks later, 0.3 μ l of pseudotyped rabies virus (ΔG -mCherry+EnvA) was injected into the same brain location under anaesthesia. After recovery, animals were housed in a biosafety room for 7 days to allow rabies virus to infect, trans-synaptically spread and express sufficient amount of mCherry to label presynaptic cells. All animals were healthy and their brain structures were normal 7 days after rabies virus infection, confirming non-pathogenicity of ΔG mutant rabies virus.

Tissue processing. Brain tissue was processed according to previously described procedures⁵⁵. To set the common coronal plane among different animals, the cerebellum was cut off and the brain was embedded in the Optimum Cutting Temperature (OCT) compound (Tissue-Tek) with the cut surface facing the bottom of the mould. The brain was adjusted to ensure that the left–right axis was parallel to the section plane. Neither mCherry nor histone-GFP required immunostaining for visualization. In some cases, brain sections were immunostained for better signal preservation according to previously published methods⁵⁶ using the following antibodies: chicken anti-GFP (1:500; Aves Labs), rabbit anti-DsRed (1:1,000; Clontech), donkey anti-chicken fluorescein isothiocyanate

(FITC) and donkey anti-rabbit Cy3 (1:200; Jackson ImmunoResearch). In most trans-synaptic labelling experiments starting from the olfactory cortex, every one of four sections of the olfactory bulb was immunostained by the free-floating method with goat anti-OCAM (1:100; R&D Systems) and donkey anti-goat Alexa488 (Invitrogen) to label OCAM⁺ olfactory receptor neuron axons. For immunostaining against GABA, 60- μ m free-floating coronal sections were treated with rabbit anti-GABA (1:2,000 in PBS with 0.3% Triton-X100; Sigma) for 48 h. GABA⁺ cells were visualized with donkey anti-rabbit Cy3 (1:200; Jackson ImmunoResearch). Sections were imaged with a Nikon CCD camera by using a 10 \times objective or by 1- μ m optical sectioning using confocal microscopy (Zeiss 510).

3D reconstruction. To compare distribution of labelled glomeruli (olfactory bulb) and starter cells (AON) across different samples, we needed to map them in a common 3D reference frame. To do this, we first saved manual annotations carried out in Adobe Illustrator in a scalable vector graphics (SVG) format. The SVG file saved all the annotations as an extensible markup language (XML) file describing the ellipses and contours (defined later), making it feasible to accurately parse the information by MATLAB scripts. In the olfactory bulb, we represented all glomeruli as ellipses. We used the centre of mass for each ellipse to define a single point, and calculated the centre of mass of all the points to define the centre of each slice. For the AON, we defined the contour as the boundary between layer I and layer II, which can be clearly distinguished by differences in the density of 4',6'-diamidino-2-phenylindole (DAPI) staining. To define the centre of mass for each contour, we replaced it with a dense series of points and used these points to calculate the centre of mass. Now, each slice is represented by a series of points and the centre of mass contained within an SVG file. To assemble the slices represented by SVG files into a 3D shape, we first aligned the centre of mass for each slice to that of the previous slice to form the cylindrical (*z*-)axis. Then, we refined the alignment by sequentially applying the iterative closest points (ICP) algorithm⁵⁶, which can identify the local rotation and translation parameters for each slice to maximize the overlap with the previous slice. Once we had aligned all the slices in a sample to generate a 3D shape, we needed to identify an orientation for the polar axis that could be most reliably identified in different 3D reconstructions. As the olfactory bulb is ellipsoidal, the principle component analysis (PCA) can reliably find a plane that contains the *z*-axis and intersects the 3D shape to maximize the surface of the intersection (plane *m*). We then defined the polar axis to be contained within the plane *m*, perpendicular to the *z*-axis, and pointing in the dorsal direction. For the AON, we approximated the contours of the most posterior slide of the AON as a triangle and calculated the rotation around the *z*-axis that minimizes the distance of the three vertices to those of a standard AON sample. We applied the same rotation to the whole 3D shape. To define the orientation of the polar axis, we used the side of the triangle that connects two of its medial vertices and points in the dorsal direction. Then we defined the polar axis as the line that is parallel to it and that intersects the *z*-axis. Finally, we calculated the volume occupied by each shape and applied a uniform scaling factor to account for different sizes of the anatomical structures in different animals.

All the steps explained earlier were implemented in MATLAB, which ran automatically without human intervention to avoid biasing the registration results. Once we had registered each shape, we used a standard algorithm to extract surfaces from two-dimensional (2D) contours⁵⁷ to transform the point cloud into a triangulated mesh that could be saved in the visualization toolkit (VTK)⁵⁸ format for visualization and analysis purposes.

We used the following landmarks to map starter cells in the amygdala and piriform cortex (Fig. 3): appearance of the olfactory tubercle (Fig. 3, I); end of the olfactory tubercle (Fig. 3, II); appearance of the hippocampus (Fig. 3, III); and appearance of the dentate gyrus of the hippocampus, on the ventral edge of the cortex (Fig. 3, IV).

Quantitative analyses. For each tracing experiment where we analysed the distribution of labelled glomeruli along the dorsal–ventral axis using mean θ'_{OB} (Fig. 3e), we generated a corresponding random distribution of simulated mean θ'_{OB} (mean θ'_{OB}^{sim}) from *M* glomeruli, where *M* is the number of labelled glomeruli in the injection. To generate this random distribution for each experiment, we randomly selected *M* glomeruli from a given 3D reconstruction model (generated from that injection) and calculated the mean θ'_{OB}^{sim} value for those randomly selected *M* glomeruli to get the mean θ'_{OB}^{sim} . We then repeated the same simulation 50,000 times to obtain mean θ'_{OB}^{sim} , mean θ'_{OB}^{sim} , and therefore to obtain the range of mean θ'_{OB}^{sim} for *M* glomeruli that are randomly distributed throughout the olfactory bulb. Once we obtained distributions for mean θ'_{OB}^{sim} that corresponded to each injection, we compared the mean θ'_{OB}^{sim} distribution with the experimental mean θ'_{OB} . If the value for the experimental mean θ'_{OB} was outside of the 95% of the mean θ'_{OB}^{sim} distribution, we considered the glomerular distribution to be non-random for that sample.

Multiple regression analysis (Fig. 4b) was conducted by using Excel (Microsoft). Data from every experiment in Supplementary Table 1 ($n = 8$ for the AON, $n = 10$ for the piriform cortex using *actin-CreER*) was used for the left part of the Fig. 4b. Data from seven experiments obtained from *GAD2-CreER* in the anterior piriform cortex were used in Fig. 4b, right. The number of labelled mitral cells in the olfactory bulb was set as a dependent variable, Y , and the number of starter cells in layer k ($k = \text{I, II, III}$) was set as an independent variable, X_k . The constant was set to zero. Excel then calculated the values of coefficients A_k (shown by red crosses in Fig. 4b) and 95% confidence intervals of A_k based on the student's t -test (shown by grey bars in Fig. 4b). R^2 values for these multiple regression assays were: 0.98 for the AON; 0.96 for the piriform cortex (*actin-CreER*); and 0.97 for the piriform cortex (*GAD2-CreER*) data sets.

To estimate the number of dually labelled glomeruli originating from single starter cells (data Ds in Fig. 4c) in our experimental data, we first simulated a hypothetical number of dually labelled glomeruli originating from single starter cells (Ds) and two independent starter cells (Dt) according to the null hypothesis that mitral cells connect randomly with postsynaptic targets. This situation can be modelled by 'balls and bins': there are 2,000 bins (a bin represents a single glomerulus) and N balls (a ball represents a single trans-synaptic labelling event). N balls were randomly thrown into 2,000 bins, and the number of bins that received more than one ball (that is, glomeruli labelled more than once) was counted. To distinguish Ds from Dt, we further introduced n different colours to the balls, where each colour represented an individual starter cell in the cortex. We assumed that an equal number of balls (N/n) were labelled with n different colours. Each ball was randomly thrown into one of 2,000 bins, and the number of bins containing more than one ball was counted. We separately counted the bins with more than one ball of an identical colour (representing Ds) and the bins with more than one ball of different colours (representing Dt). We fixed the number of bins (glomeruli) to be 2,000, while N and n corresponded to the number of labelled mitral cells and the number of starter cells, respectively, in each experiment. We repeated this simulation 100,000 times for each set of N and n to obtain the simulated distribution of Ds and Dt (we call these 'random Ds' and

'random Dt'). To estimate the Ds components in experimental data (data Ds), we assumed that individual starter cells contributed independently to the labelling (random Dt = data Dt). On the basis of the equation: D (number of observed dually labelled glomeruli) = Ds + Dt, we estimated the data Ds distribution by subtracting the random Dt from observed D (Fig. 4c). Then we determined if there was a significant difference in the distribution of data Ds and random Ds. We considered two distributions to be significantly different if the probability of data Ds > random Ds or data Ds < random Ds exceeded 0.95 (shown by asterisks in Fig. 4c). To accurately count dually labelled glomeruli, samples with more than 200 labelled mitral cells were excluded from this analysis.

49. Urlinger, S. *et al.* Exploring the sequence space for tetracycline-dependent transcriptional activators: novel mutations yield expanded range and sensitivity. *Proc. Natl Acad. Sci. USA* **97**, 7963–7968 (2000).
50. Zong, H., Espinosa, J. S., Su, H. H., Muzumdar, M. D. & Luo, L. Mosaic analysis with double markers in mice. *Cell* **121**, 479–492 (2005).
51. Muzumdar, M. D., Luo, L. & Zong, H. Modeling sporadic loss of heterozygosity in mice by using mosaic analysis with double markers (MADM). *Proc. Natl Acad. Sci. USA* **104**, 4495–4500 (2007).
52. Chung, J. H., Whiteley, M. & Felsenfeld, G. A 5' element of the chicken β -globin domain serves as an insulator in human erythroid cells and protects against position effect in *Drosophila*. *Cell* **74**, 505–514 (1993).
53. Li, L. *et al.* Visualizing the distribution of synapses from individual neurons in the mouse brain. *PLoS ONE* **5**, e11503 (2010).
54. Wickersham, I. R., Sullivan, H. A. & Seung, H. S. Production of glycoprotein-deleted rabies viruses for monosynaptic tracing and high-level gene expression in neurons. *Nature Protocols* **5**, 595–606 (2010).
55. Espinosa, J. S., Wheeler, D. G., Tsien, R. W. & Luo, L. Uncoupling dendrite growth and patterning: single-cell knockout analysis of NMDA receptor 2B. *Neuron* **62**, 205–217 (2009).
56. Zhang, Z. Iterative point matching for registration of free-form curves and surfaces. *Int. J. Comput. Vis.* **13**, 119–152 (1994).
57. Cong, G. & Parvin, B. Surface reconstruction from sparse fringe contours. *Proc. 4th IEEE Workshop Appl. Comput. Vis.* **140** (1998).
58. Schroeder, W., Martin, K. & Lorensen, B. *The Visualization Toolkit: An Object-Oriented Approach to 3-D Graphics* (Prentice Hall, 1997).

The developmental transcriptome of *Drosophila melanogaster*

Brenton R. Graveley^{1*}, Angela N. Brooks^{2*}, Joseph W. Carlson^{3*}, Michael O. Duff^{1*}, Jane M. Landolin^{3*}, Li Yang^{1*}, Carlo G. Artieri⁴, Marijke J. van Baren⁵, Nathan Boley⁶, Benjamin W. Booth³, James B. Brown⁶, Lucy Cherbas⁷, Carrie A. Davis⁸, Alex Dobin⁸, Renhua Li⁴, Wei Lin⁸, John H. Malone⁴, Nicolas R. Mattiuzzo⁴, David Miller⁹, David Sturgill⁴, Brian B. Tuch^{10,11}, Chris Zaleski⁸, Dayu Zhang⁷, Marco Blanchette^{12,13}, Sandrine Dudoit¹⁴, Brian Eads⁹, Richard E. Green¹⁵, Ann Hammonds³, Lichun Jiang⁴, Phil Kapranov⁸, Laura Langton⁵, Norbert Perrimon¹⁶, Jeremy E. Sandler³, Kenneth H. Wan³, Aaron Willingham¹⁷, Yu Zhang⁴, Yi Zou⁷, Justen Andrews⁹, Peter J. Bickel⁶, Steven E. Brenner^{2,17}, Michael R. Brent⁵, Peter Cherbas^{7,9}, Thomas R. Gingeras^{8,18}, Roger A. Hoskins³, Thomas C. Kaufman⁹, Brian Oliver⁴ & Susan E. Celniker³

***Drosophila melanogaster* is one of the most well studied genetic model organisms; nonetheless, its genome still contains unannotated coding and non-coding genes, transcripts, exons and RNA editing sites. Full discovery and annotation are pre-requisites for understanding how the regulation of transcription, splicing and RNA editing directs the development of this complex organism. Here we used RNA-Seq, tiling microarrays and cDNA sequencing to explore the transcriptome in 30 distinct developmental stages. We identified 111,195 new elements, including thousands of genes, coding and non-coding transcripts, exons, splicing and editing events, and inferred protein isoforms that previously eluded discovery using established experimental, prediction and conservation-based approaches. These data substantially expand the number of known transcribed elements in the *Drosophila* genome and provide a high-resolution view of transcriptome dynamics throughout development.**

Drosophila melanogaster is an important non-mammalian model system that has had a critical role in basic biological discoveries, such as identifying chromosomes as the carriers of genetic information¹ and uncovering the role of genes in development^{2,3}. Because it shares a substantial genic content with humans⁴, *Drosophila* is increasingly used as a translational model for human development, homeostasis and disease⁵.

High-quality maps are needed for all functional genomic elements. Previous studies demonstrated that a rich collection of genes is deployed during the life cycle of the fly^{6–8}. Although expression profiling using microarrays has revealed the expression of ~13,000 annotated genes, it is difficult to map splice junctions and individual base modifications generated by RNA editing⁹ using such approaches. Single-base resolution is essential to define precisely the elements that comprise the *Drosophila* transcriptome.

Estimates of the number of transcript isoforms are less accurate than estimates of the number of genes. Whereas ~20% of *Drosophila* genes are annotated as encoding alternatively spliced pre-mRNAs, splice-junction microarray experiments indicate that this number is at least 40% (ref. 7). Determining the diversity of mRNAs generated by alternative promoters, alternative splicing and RNA editing will substantially increase the inferred protein repertoire. Non-coding RNA genes (ncRNAs) including short interfering RNAs (siRNAs) and

microRNAs (miRNAs) (reviewed in ref. 10), and longer ncRNAs such as *bxd* (ref. 11) and *rox* (ref. 12), have important roles in gene regulation, whereas others such as small nucleolar RNAs (snoRNAs) and small nuclear RNAs (snRNAs) are important components of macromolecular machines such as the ribosome and spliceosome. The transcription and processing of these ncRNAs must also be fully documented and mapped.

As part of the modENCODE project to annotate the functional elements of the *D. melanogaster* and *Caenorhabditis elegans* genomes^{13–15}, we used RNA-Seq and tiling microarrays to sample the *Drosophila* transcriptome at unprecedented depth throughout development from early embryo to ageing male and female adults. We report on a high-resolution view of the discovery, structure and dynamic expression of the *D. melanogaster* transcriptome.

Strategy for characterization of the transcriptome

To discover new transcribed features (Supplementary Table 1) and comprehensively characterize their expression dynamics throughout development, we conducted complementary tiling microarray and RNA-Seq experiments using RNA isolated from 30 whole-animal samples representing 27 distinct stages of development (Supplementary Table 2). These included 12 embryonic samples collected at 2-h intervals for 24 h, six larval, six pupal and three sexed adult stages at 1, 5

¹Department of Genetics and Developmental Biology, University of Connecticut Health Center, 263 Farmington Avenue, Farmington, Connecticut 06030-6403, USA. ²Department of Molecular and Cell Biology, University of California, Berkeley, California 94720, USA. ³Department of Genome Dynamics, Lawrence Berkeley National Laboratory, Berkeley, California 94720, USA. ⁴Section of Developmental Genomics, Laboratory of Cellular and Developmental Biology, National Institute of Diabetes and Digestive and Kidney Diseases, National Institutes of Health, Bethesda, Maryland 20892, USA. ⁵Center for Genome Sciences and Department of Computer Science, Washington University, St. Louis, Missouri 63108, USA. ⁶Department of Statistics, University of California, Berkeley, California, 94720 USA. ⁷Center for Genomics and Bioinformatics, Indiana University, 1001 E. 3rd Street, Bloomington, Indiana 47405-7005, USA. ⁸Cold Spring Harbor Laboratory, Cold Spring Harbor, New York 11724, USA. ⁹Department of Biology, Indiana University, 1001 E. 3rd Street, Bloomington, Indiana 47405-7005, USA. ¹⁰Genetic Systems Division, Research and Development, Life Technologies, Foster City, California 94404, USA. ¹¹Genome Analysis Unit, Amgen, South San Francisco, California 94080, USA. ¹²Stowers Institute for Medical Research, 1000 East 50th street, Kansas City, Missouri 64110, USA. ¹³Department of Pathology and Laboratory Medicine, Kansas University Medical Center, 3901 Rainbow Boulevard, Kansas City, Kansas 66160, USA. ¹⁴Division of Biostatistics, School of Public Health, University of California, Berkeley, California 94720, USA. ¹⁵Department of Biomolecular Engineering, University of California, Santa Cruz, Santa Cruz, California 95064, USA. ¹⁶Department of Genetics and Howard Hughes Medical Institute, Harvard Medical School, Boston, Massachusetts 02115, USA. ¹⁷Department of Plant and Microbial Biology, University of California, Berkeley, California 94720, USA. ¹⁸Affymetrix, Santa Clara, California 95051, USA.

*These authors contributed equally to this work.

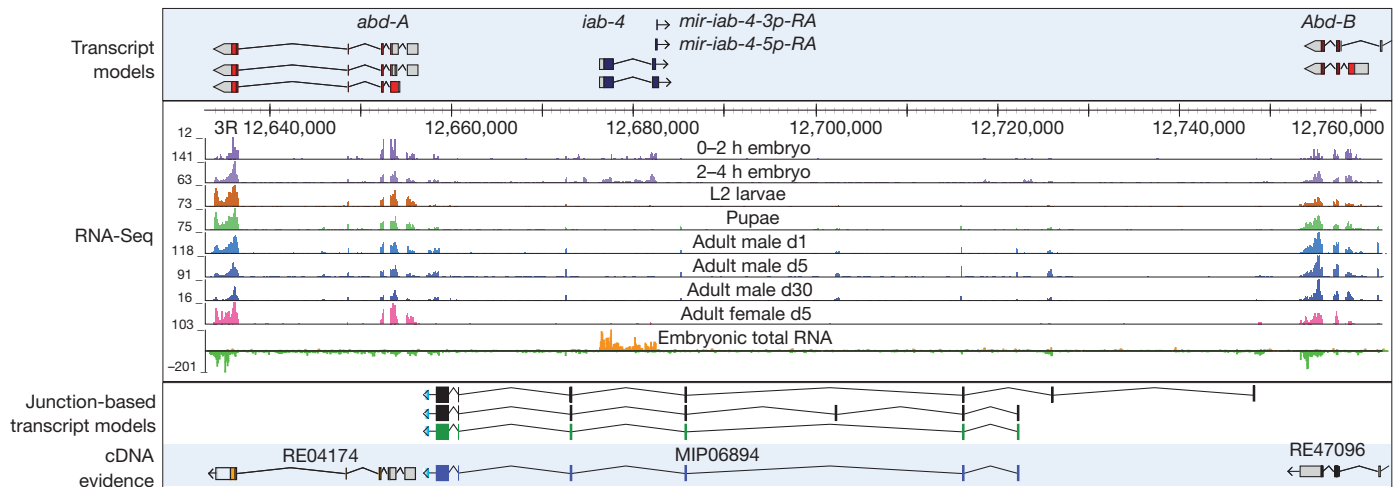


Figure 1 | Discovery of new RNAs in the Bithorax complex. Genomic organization and experimental evidence for new transcripts located between the HOX genes, *abd-A* and *Abd-B*, based on short poly(A)⁺ RNA and total RNA-Seq expression profiles. The numbers to the left of each track indicate the

maximal number of reads for that sample. Three manually curated junction-based transcript models are shown; the green transcript model was fully validated by a cDNA, MIP06894.

and 30 days after eclosion. We used 38-base-pair (bp) resolution genome tiling microarrays to analyse total RNA from all 30 biological samples and poly(A)⁺ mRNA from the 12 embryonic samples (Supplementary Fig. 1). To attain single-nucleotide resolution and to facilitate the analysis of alternative splicing and RNA editing, we performed non-strand-specific poly(A)⁺ RNA-Seq from all 30 samples generating a combination of single and paired-end ~75-bp reads on the Illumina Genome Analyser IIX platform (short poly(A)⁺ RNA-Seq) (Supplementary Table 3 and Supplementary Fig. 2). To identify primary transcripts and non-coding RNAs, the 12 embryonic time points were also interrogated with strand-specific 50-bp sequence reads from partially rRNA-depleted total RNA on the Applied Biosystems SOLiD platform (Supplementary Table 4 and Supplementary Fig. 3). To improve connectivity, mixed-stage embryos, adult males and adult females were used to generate ~250-bp reads on the Roche 454 platform (non-strand-specific long poly(A)⁺ RNA-Seq) (Supplementary Table 5). In total, we generated 176,962,906,041 bp of mapped sequence representing 1,266-fold coverage of the genome and 5,902-fold coverage of the annotated *D. melanogaster* transcriptome.

Discovery of new transcribed regions

We identified 1,938 new transcribed regions (NTRs) not linked to any annotated gene models. Herein, 'transcripts' refer to RNA molecules synthesized from a genomic locus whereas 'genes' refer to one or more transcripts that share exons in their mature spliced form. modENCODE cDNAs fully support 13% of the NTRs (Supplementary Fig. 4) and partially support 23%. Most NTRs (84%) are detected by poly(A)⁺ RNA-Seq, 44% by total RNA-Seq and 42% by tiling array. Approximately half of the NTRs are conserved in the distantly related *Drosophila pseudoobscura* and *Drosophila mojavensis* (Supplementary Fig. 4b) and 30% of these are detected by poly(A)⁺ RNA-Seq data from *D. pseudoobscura* or *D. mojavensis* adult heads (Supplementary Fig. 4c, d, Supplementary Table 6 and Supplementary Methods). The NTRs probably eluded previous detection because they are expressed at low levels, in temporally restricted patterns, and are enriched for single-exon genes. The new multi-exon gene models (48%) have fewer, shorter and less conserved exons than annotated genes.

Nearly one-third of the NTRs have a predicted open reading frame (ORF) greater than 100 amino acids. The remaining NTRs could encode small peptides but many are likely to be non-coding RNAs. A small fraction (9%) of NTRs are heterochromatic; most of these (232) have sequence similarity (greater than 100-nucleotide match and greater than 60% identity) to transposable elements (TEs) and

represent transcribed TEs or TE fragments. It remains to be determined whether these regions have any function, although recent studies describe TE-associated regions that have acquired functions^{16,17}.

Even in the well-studied Bithorax complex² we found an NTR. Known genetic breakpoints in the infra-abdominal regions *iab-3* to *iab-8*, which lie between the homeotic genes *abdominal A* (*abd-A*) and *Abdominal B* (*Abd-B*), disrupt normal male development and affect fertility^{18,19}. Within this region are regulatory elements²⁰ and evidence for long non-coding RNAs that have eluded detection for over 20 years^{21–23}. We used the RNA-Seq data to infer the structures of at least three overlapping transcripts and validated one form (Fig. 1). The RNAs are expressed in embryos and adult males but not females. On the basis of the presumed role of this new gene and spatial expression in the embryonic gonad (data not shown), we have named it *male specific abdominal* (*msa*). The cDNA contains short ORFs that are conserved in the *melanogaster* subgroup and could encode male-specific peptides. Whether they function as regulatory and/or as peptide-encoding RNAs is an important question for understanding development and segmental morphological diversity.

Discovery of small ncRNAs

We identified 37 unannotated intron-encoded and two unannotated intergenic small ncRNAs (<300 nucleotides) with an average fragments per kilobase of transcript per million fragments mapped (FPKM)²⁴ >20 from total embryonic RNA-Seq (Fig. 2 and Supplementary Table 7). Most of these ncRNAs are highly conserved in *Drosophila* sibling species²⁵. We found published but unannotated ncRNAs: a U4atac snRNA²⁶ and four small Cajal-body-specific RNAs (scaRNAs)²⁷. Of the remaining 34 ncRNAs, three are box C/D-like snoRNAs, 28 are box H/ACA-like snRNAs, one is a scaRNA-like RNA, and two are unclassified. One-third of these are located in the introns of genes encoding RNA-binding proteins, the majority of which are involved in pre-mRNA splicing (*xl6*, *SC35*, *tra2*, *Dek*, *Prp8*, *Tudor-SN*, and *pUf68*).

Discovery of microRNA primary transcripts

MicroRNAs are processed from primary microRNA transcripts (pri-miRNAs) and are either independently transcribed or embedded in the introns of protein-coding genes. We identified 23 putative independently transcribed pri-miRNAs from the total embryonic RNA-Seq and tiling array data that encode 37 annotated miRNAs (Supplementary Table 8). Only two primary transcripts were previously annotated (*bft* and *iab-4*). The pri-miRNAs range from 1 to 18 kb and terminate

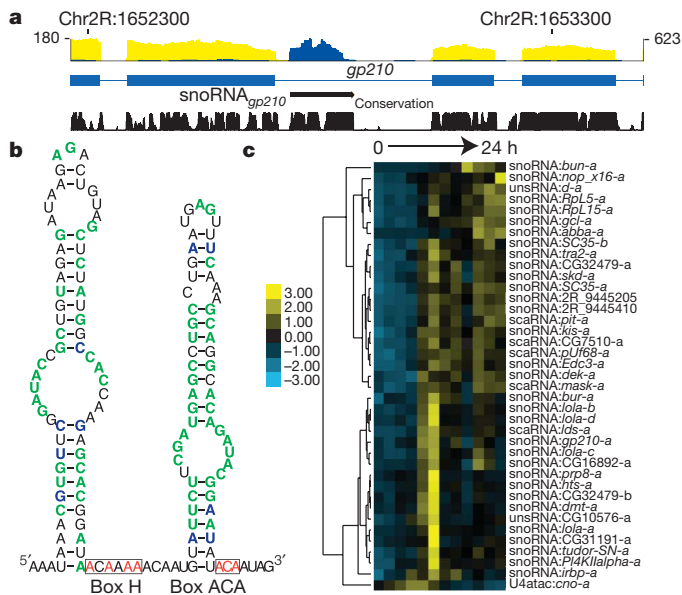


Figure 2 | Discovery of small non-coding RNAs. **a**, Poly(A)⁺ (yellow) and total RNA (blue) data from 10–12-h embryos are shown for the *gp210* gene which hosts a representative new snoRNA. The maximal number of reads in the poly(A)⁺ and total RNA-Seq data are shown on the left and right of the track, respectively. **b**, The predicted RNA secondary structure of snoRNA_{*gp210*} is characteristic of a H/ACA-box snoRNA. Nucleotides that are 100% conserved in sequence or base-pairing are indicated in green and blue, respectively. **c**, Embryonic expression of the new small RNAs. The scale bar indicates FPKM Z-scores. unsRNA, unclassified small RNA.

at the mature miRNA (*pre-mir-315*, Supplementary Fig. 5a). Twelve of the 23 precursors have cap analysis of gene expression (CAGE) peaks that map at their initiation sites²⁸. pri-miRNA expression is dynamic in embryonic development (Supplementary Fig. 5b).

Overview of the *Drosophila* transcriptome

We calculated expression levels of annotated genes, transcripts and NTRs (Supplementary Table 9) in the short poly(A)⁺ RNA-Seq and tiling array data sets. From the RNA-Seq data we detected expression of 14,862 genes (Supplementary Fig. 7a) and 36,274 transcripts (Fig. 3a) with an FPKM >1 (Supplementary Tables 9–18) of which 67% of genes and 58% of transcripts were also observed in the array data (score >300) (Supplementary Fig. 6 and Supplementary Tables 19 and 20). This includes the confirmation of 87% of annotated genes and transcripts and the discovery of 17,745 new transcripts. In addition, from the total RNA-Seq data we detected expression of 12,854 genes and 32,139 transcripts with an FPKM >1 (Supplementary Tables 12, 13, 21 and 22) of which 77% of genes and 89% of transcripts were also observed in the array data. Of the genes and transcripts observed exclusively in the total RNA-Seq data, 519 genes and 1,005 transcripts (primarily noncoding) were previously annotated and 122 genes and 1,422 transcripts are new discoveries. The genes and transcripts not detected in any data set include small genes (<200 bp), members of multi-copy gene families such as ribosomal RNAs, paralogues (expected owing to our mapping parameters), genes known to be expressed at low levels or in small numbers of cells (for example, gustatory and odorant receptor genes), and non-polyadenylated transcripts.

Expression dynamics

We examined the dynamics of gene expression throughout development using the short poly(A)⁺ RNA-Seq data. The numbers of expressed genes (FPKM >1) (Supplementary Fig. 7a) and transcripts (Fig. 3a) gradually increases, from 7,045 (0–2 h embryos) to 12,000 (adult males). Adult males express ~3,000 more genes than adult females, consistent

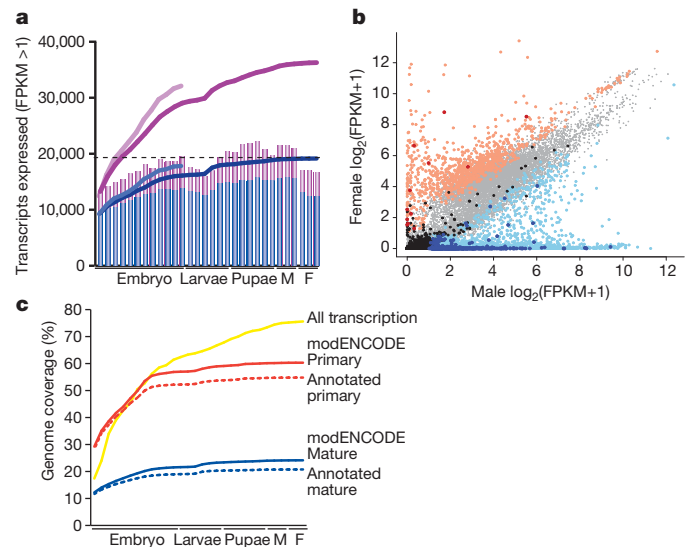


Figure 3 | Dynamics of gene expression. **a**, Transcripts expressed (FPKM >1) in the short poly(A)⁺ RNA-Seq data: FlyBase 5.12, blue; modENCODE, purple. The bar graphs indicate the number of transcripts expressed in each sample (Supplementary Table 1); the lines indicate the cumulative number of expressed transcripts. The lighter blue and purple lines indicate the cumulative number of transcripts expressed in the embryonic total RNA-Seq samples. The horizontal dotted lines indicate the number of expressed previously annotated transcripts. F, female; M, male. **b**, Scatter plot of sex-biased gene expression. Light red, female-biased annotated ($n = 960$); dark red, female-biased NTRs ($n = 12$); light blue, male-biased annotated ($n = 2,401$); dark blue, male-biased NTRs ($n = 431$); light grey, unbiased annotated ($n = 8,217$); black, unbiased NTRs ($n = 136$). **c**, Genome coverage. For each developmental sample, the short poly(A)⁺ reads were used to estimate the percentage of the genome covered using a cutoff of two reads. The mature and primary transcripts were inferred for the previously FlyBase 5.12 (dotted lines) and modENCODE (solid lines) gene models.

with the known transcriptional complexity of the testis²⁹. We observed that 40% of expressed genes are constitutively expressed in 30 samples (Supplementary Fig. 7b). We also observed developmentally regulated expression of TEs (Supplementary Materials and Supplementary Fig. 8).

We observed pronounced expression changes in over 1,500 genes in the first two third instar larval samples (Supplementary Fig. 7a, c). Expression of 1,199 genes increased at least tenfold, and 421 genes decreased at least tenfold (Supplementary Table 23). Nearly all of the upregulated genes are expressed for the first time during the third instar stage and most are poorly characterized genes.

The earliest known event in metamorphosis is the ‘mid-3rd transition’³⁰, identified by the synchronous changes in the transcription of a number of well studied genes, *Ecdysone-induced protein 28/29kD* and *Fat body protein 1* (reviewed in ref. 31), and the switch from proximal to distal promoters of *Alcohol dehydrogenase*³². These markers coincide with the surge reported here. The mid-3rd transition has no morphological or behavioural correlates and is associated with a pulse of the steroid hormone ecdysone³³ acting through a non-standard receptor³⁴. Whether the onset of testis development is a consequence of the mid-3rd transition, or whether the two events are functionally related, remains to be investigated.

Over 29% of protein-coding genes showed significant sex-biased expression in adults (false discovery rate <0.1%), with more male-biased (1,829) or male-specific genes (572) than female-biased (945) or female-specific genes (15) (Supplementary Tables 24 and 25, and Fig. 3b). Known female (*ovo* and *otu*) and male (*dj*) sex-biased genes were expressed as expected. We found that 74% of the NTRs expressed in adults were significantly male-biased whereas only 2.1% were significantly female-biased.

Table 1 | Classification of alternative splicing events

| Splicing event | Diagram | FlyBase r5.12 | modENCODE | New events | Short poly(A) ⁺ RNA-Seq | Significantly changing |
|------------------------------|---------|---------------|-----------------|-----------------|------------------------------------|------------------------|
| Cassette exons | | 793 | 2,717 | 2,014 | 2,369 | 1,539 |
| Alternative 5' splice sites | | 843 | 5,192 | 4,599 | 4,583 | 3,142 |
| Alternative 3' splice sites | | 879 | 6,253 | 5,505 | 5,579 | 3,242 |
| Mutually exclusive exons | | 229 | 251 | 123 | 228 | 226 |
| Coordinate cassette exons | | 301 | 1,227 | 979 | 992 | 467 |
| Alternative first exons | | 1,767 | 4,936 | 3,442 | 4,473 | 3,996 |
| Alternative last exons | | 227 | 604 | 432 | 553 | 471 |
| Retained/unprocessed introns | | 1,434 | 2,679 (5,667) | 1,275 (4,263) | 2,439 (35,641) | 868 (8,998) |
| Total | | 6,437 | 23,859 (26,847) | 18,369 (21,478) | 21,216 (54,418) | 13,951 (22,081) |

The number of retained/unprocessed introns in parentheses indicates the total number identified, whereas the number not in parentheses indicates the subset of identified events that have been validated by cDNA sequences or FlyBase 5.12 annotations.

Genome coverage

Mature mRNAs are encoded by 20% of the *D. melanogaster* genome and primary transcripts by 60% (Fig. 3c). An additional 15% of the genome (~75% total) is detected when considering all of the short poly(A)⁺ RNA-Seq data. However, as greater than 99% of the reads map within the bounds of the transcript models, the reads that map to intergenic regions constitute a small minority of our data. Thus, although pervasive transcription of mammalian genomes has been observed in microarray studies³⁵, we found little evidence of such ‘dark matter’³⁶ (that is, pervasive transcription) in *D. melanogaster*.

Discovery and dynamics of alternative splicing

To characterize constitutive and alternative splicing, we identified 71,316 splice junctions, of which 22,965 were new discoveries. Of the new splice junctions, 26% were supported by multiple experimental data types and 74% by only one data type, (Supplementary Fig. 9a) primarily short poly(A)⁺ RNA-Seq. Of the 20,751 new junctions from the short poly(A)⁺ RNA-Seq data, 7,833 were incorporated into new transcript models or transcribed regions (NTRs). The remaining new junctions have yet to be incorporated into transcript models.

We also identified a total of 102,026 exons (Supplementary Table 26). Of the 52,914 representing new and revised exons, 65% were validated by capture and sequencing of cDNAs and 2,586 were supported by RNA-Seq data from *D. mojavensis* and *D. pseudoobscura*. Of the new exons, 3,392 were identified from the new splice junctions but have yet to be incorporated into transcript models.

To examine splicing dynamics throughout development, we categorized all splicing events into the common types of alternative splicing events (Table 1). We identified a total of 23,859 splicing events, of which 18,369 were new or recategorized, a threefold increase from

annotated splicing events. An additional 2,988 retained/unprocessed introns were identified that were supported by only one experimental data type. In all, 7,473 genes contain at least one alternative splicing event, which is 60.7% of the 12,295 expressed multi-exon genes—also a threefold increase in the fraction of genes with alternatively spliced transcripts. Although smaller than the fraction of human genes with alternatively spliced transcripts (95%)^{37,38}, a larger proportion of *Drosophila* genes encode alternative transcripts than was previously known.

Of the new alternative exons, 8,226 were previously annotated as constitutive. As observed³⁹, annotated cassette exons, and their flanking introns, are more highly conserved than annotated constitutive exons (Fig. 4a). The newly discovered cassette exons are more highly conserved than the new constitutive exons, although both classes are less conserved than the corresponding class of annotated exons. New cassette exons that were previously annotated as constitutive exons are the most highly conserved set of exons (Fig. 4a). Annotated and new cassette exons show a strong tendency to preserve reading frame (Supplementary Fig. 9b), indicating that these transcripts increase protein diversity. Both annotated and new cassette exons tend to be shorter than their constitutive counterparts, although both sets of new exons tend to be shorter than annotated exons.

To assess the extent of splicing variation we calculated the ‘per cent spliced in’ or Ψ (ref. 38) for each splicing event in each sample as well as the switch score ($\Delta\Psi$) by determining the difference between the highest and lowest Ψ values across development ($\Delta\Psi = \Psi_{\max} - \Psi_{\min}$). This revealed a very smooth distribution of $\Delta\Psi$ among all events, indicating that the splicing of most exons is fairly constant whereas only a minority change markedly (Supplementary Fig. 9c and Supplementary Table 27). Only 831 splicing events have a Ψ value >90. Further statistical

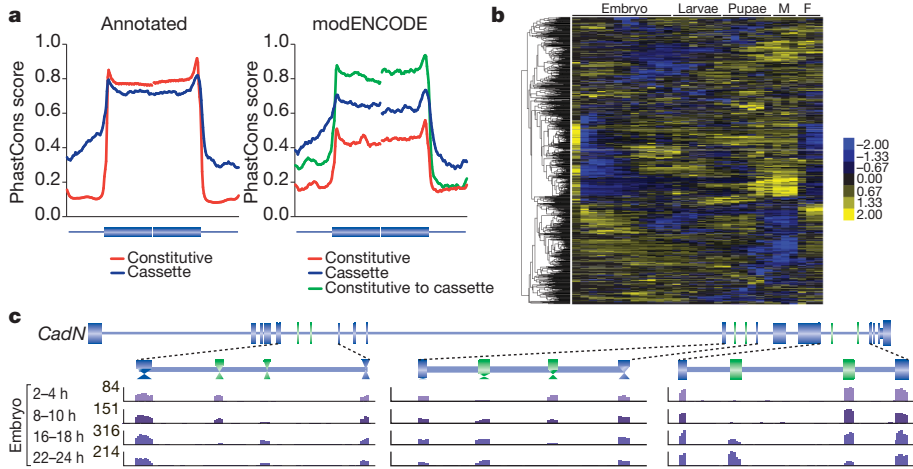


Figure 4 | Developmentally regulated splicing events. a, Conservation of internal constitutive and cassette exons >50 nucleotides that were annotated or new discoveries. (Annotated constitutive, $n = 26,127$; annotated cassette, $n = 438$; modENCODE cassette, $n = 173$; modENCODE constitutive, $n = 306$; FlyBase 5.12 constitutive to modENCODE cassette, $n = 304$.) b, Clusters of

regulated cassette exon events during development. The scale bar indicates Z-scores of Ψ . c, Regulated alternative splicing in *CadN* during embryogenesis. The maximal number of reads in the poly(A)⁺ RNA-Seq data are indicated for each track

analyses (see Supplementary Methods) identified 13,951 (66%) alternative splicing events that change significantly throughout development (Supplementary Table 28).

Hierarchical clustering of cassette exon events revealed the dynamic nature of splicing throughout development (Fig. 4b), as exemplified by *Cadherin-N* (*CadN*), a gene with three sets of mutually exclusive exons (Fig. 4c). In each set, one exon is preferentially included in early embryos, the other in late embryos, with a smooth transition between the two. Our analysis also identified groups of exons that have coordinated splicing patterns (Fig. 4b). A set of 55 genes contain exons that are preferentially included in early embryos, late larvae, early pupae and females but skipped in all other stages. Gene Ontology (GO) analysis of these genes indicates that many encode proteins involved in epithelial cell-to-cell junctions. GO analysis of genes that contain exons preferentially included during late pupal and adult stages indicates that many encode proteins that are part of neuronal synapses.

Sex-biased alternative splicing

Sex determination in *Drosophila* is mediated by a cascade of regulated alternative splicing events involving *Sex lethal* (*Sxl*), *transformer* (*tra*), *male-specific lethal 2* (*msl-2*), *doublesex* (*dsx*) and *fruitless* (*fru*) that specify nearly all physical and behavioural dimorphisms between males and females as well as X chromosome dosage compensation⁴⁰. Our RNA-Seq data confirm sex-biased ($\Delta\Psi = |\Psi_{\text{male}} - \Psi_{\text{female}}|$) splicing of *Sxl* ($\Delta\Psi = 89.6$), *tra* ($\Delta\Psi = 39.2$), *dsx* ($\Delta\Psi = 59.7$) and *fru* ($\Delta\Psi = 100$).

In addition to the canonical sex-determination cascade, we identified 119 strongly sex-biased splicing events ($\Delta\Psi > 70$) (Supplementary Fig. 9d). One striking example is *Reps*, which was annotated as containing six constitutive exons. RNA-Seq data indicate that exon five is a sex-biased alternative cassette exon ($\Delta\Psi = 73.39$) (Supplementary Fig. 10). This highly conserved exon is included in males and skipped in females. The intron upstream of this cassette exon contains conserved SXL binding sites, indicating that it is regulated by SXL and is a candidate sex differentiation gene.

Discovery of RNA editing sites

Previous studies identified 127 sites in 55 *Drosophila* genes that undergo A-to-I RNA editing⁴¹. This post-transcriptional modification is catalysed by dADAR, which is expressed at increasing levels throughout development and is thought to target products involved in nervous system function. We analysed the poly(A)⁺ RNA-Seq data to identify exonic nucleotide positions consistent with A-to-I editing and defined 972 edited positions within transcripts of 597 genes, including previously described edited sites in the transcripts of 36

genes (Supplementary Table 29). These genes include those required for rapid neurotransmission and other widely ranging functions. For most sites, the frequency of editing increases throughout development and does not correlate with overall expression levels (Fig. 5a). Editing typically begins in late pupal stages, although we find transcripts that seem to be edited in late embryogenesis. Consistent with earlier studies⁴², exons containing editing sites are more highly conserved than unedited exons. The majority of the edited positions (630) alter amino acid coding, the others are either silent (201) or within untranslated regions (141). For example, the transcripts of *quiver* (*qvr*) are edited at six positions, four that result in amino acid changes (Fig. 5b). *qvr* encodes a potassium channel subunit that modulates the function of the voltage-gated Shaker (SH) potassium channel. *Sh* transcripts are also edited at multiple positions⁴³. The combinatorial editing of both proteins probably has an important role in modulating action potentials in the arthropod nervous system and may have implications for the regulation of sleep⁴⁴. Expressed sequence tags, long poly(A)⁺ RNA-Seq and cDNAs cross-validate nearly one-quarter (214) of the newly discovered sites.

Computational analysis identified three potential editing-associated sequence motifs (Fig. 5a). We observe 381 sites with one or more motifs in close proximity to the edited nucleotide (Supplementary Table 30). Motif C, although less common than motifs A and B, is more strongly associated with the editing site. Most (93%) instances of motif C occur on the sense strand of the transcript and the A at the 3' end of the motif is the edited nucleotide. This motif is over-represented in editing events that occur early in development.

Discussion

Our interrogation of the transcriptome of *D. melanogaster* throughout development has considerably expanded the number of building blocks used to make a fly. Specifically, we identified nearly 2,000 NTRs, increased the number of alternative splicing events by threefold and the number of RNA editing sites by an order of magnitude. The resulting view of the transcriptome at single-base resolution markedly improves our understanding of expression dynamics throughout the *Drosophila* life cycle and has substantial biological implications.

The *D. melanogaster*, *C. elegans* and human genomes are organized quite differently. Specifically, 20%, 45% and 2.5% of the *D. melanogaster*, *C. elegans* and human genomes, respectively, encode exons or mature transcripts. Primary transcripts comprise a larger fraction of each genome—60%, 82% and 37%. This highlights the fact that primary transcripts and introns are much shorter in *D. melanogaster* and *C. elegans* than in human and that the *D. melanogaster* and *C. elegans* genomes are more compact than the human genome.

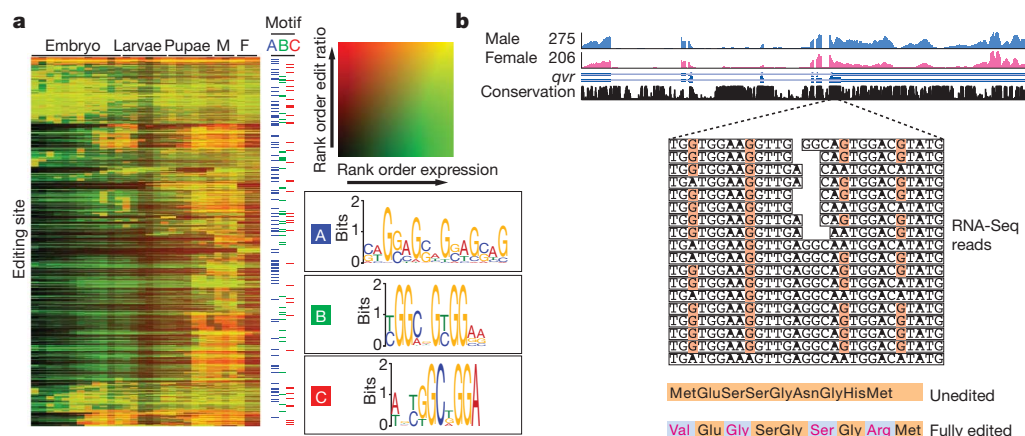


Figure 5 | Discovery of RNA editing events. **a**, Rows represent edited sites. Rank-ordered expression levels (number of reads) are shown in green and the rank-ordered editing ratios are shown in red. Pictogram representations of editing motifs A, B and C are shown. **b**, RNA editing of *qvr*. Male and female

expression and conservation tracks are shown above RNA-Seq reads from adult females that align to the edited positions (orange). Conceptual translation of the unedited and fully edited transcripts result in four amino acid changes (red) at the C terminus of QVR.

The existence of unannotated genes was indicated by microarray studies^{8,45} and conservation among *Drosophilid* genomes²⁵. However, the NTRs that we identified were not identified by comparative sequence analysis⁴⁶ as they are less conserved than most previously known genes. This emphasizes the importance of using both comparative analyses and transcriptome profiling for genome annotation.

Despite the depth of our sequencing, the annotation of the *D. melanogaster* transcriptome is not finished. We failed to detect expression of 1,488 annotated genes including members of gene families to which short reads can not be uniquely mapped and genes expressed at low levels or in spatially and temporally restricted patterns. Moreover, although we substantially increased the fraction of genes that encode alternatively spliced or edited transcripts, we again failed to detect several annotated RNA processing events. Study of more temporally and spatially restricted samples will allow deeper exploration of the *Drosophila* transcriptome, and almost certainly result in the discovery of yet additional features. Furthermore, functional studies of the new and previously unstudied elements will provide valuable insight into metazoan development.

METHODS SUMMARY

Animal staging, collection and RNA extraction. Isogenic (y^1 ; $cn\ bw^1\ sp^1$) embryos were collected at 2-h intervals for 24 h. Collection of later staged animals started with synchronized embryos and included resynchronizing with appropriate age indicators. Six larval, six pupal and three adult sexed stages, 1, 5 and 30 days, were collected. RNA was isolated using TRIzol (Invitrogen), DNase and purified on an RNeasy column (Qiagen). poly(A)⁺ RNA was prepared from an aliquot of each total RNA sample using an Oligotex kit (Qiagen).

Tiling arrays. RNAs from three biological replicates of each sample were independently hybridized on 38-bp arrays (Affymetrix GeneChip *Drosophila* Tiling 2.0R array) as described⁴⁷.

RNA-Seq. Libraries were generated and sequenced on an Illumina Genome Analyser IIx using single or paired-end chemistry and 76-bp cycles. SOLiD sequencing used total RNA treated with the RiboMinus Eukaryote Kit (Invitrogen). Samples were fragmented, adaptors ligated (Ambion) and sequenced for 50 bases using SOLiD V3 chemistry. 454 sequencing used poly(A)⁺ RNA from Oregon R adult males and females and mixed-staged y^1 ; $cn\ bw^1\ sp^1$ embryos. Sequences are available from the Short Read Archive and the modENCODE website (<http://www.modencode.org/>).

Targeted RT-PCR and cDNA isolation and sequencing. Standard procedures were used for RT-PCR and targeted cDNA isolation and sequencing.

Analysis. Cufflinks²⁴ was used to identify new transcript models and to calculate expression levels for annotated and predicted transcript models. MFold⁴⁸ was used to predict secondary structures from the new snoRNA-like RNAs. JuncBASE⁴⁹ identified alternative splicing events and calculated per cent spliced in (Ψ)³⁸. Editing sites were identified by comparing aligned reads to the reference genome.

Received 3 September; accepted 2 December 2010.

Published online 22 December 2010.

- Morgan, T. H. Sex limited inheritance in *Drosophila*. *Science* **32**, 120–122 (1910).
- Lewis, E. B. A gene complex controlling segmentation in *Drosophila*. *Nature* **276**, 565–570 (1978).
- Nüsslein-Volhard, C. & Wieschaus, E. Mutations affecting segment number and polarity in *Drosophila*. *Nature* **287**, 795–801 (1980).
- Rubin, G. M. *et al.* Comparative genomics of the eukaryotes. *Science* **287**, 2204–2215 (2000).
- Spradling, A. C. Learning the common language of genetics. *Genetics* **174**, 1–3 (2006).
- Arbeitman, M. N. *et al.* Gene expression during the life cycle of *Drosophila melanogaster*. *Science* **297**, 2270–2275 (2002).
- Stolc, V. *et al.* A gene expression map for the euchromatic genome of *Drosophila melanogaster*. *Science* **306**, 655–660 (2004).
- Manak, J. R. *et al.* Biological function of unannotated transcription during the early development of *Drosophila melanogaster*. *Nature Genet.* **38**, 1151–1158 (2006).
- Bass, B. L. *RNA Editing* (Oxford Univ. Press, 2001).
- Rana, T. M. Illuminating the silence: understanding the structure and function of small RNAs. *Nature Rev. Mol. Cell Biol.* **8**, 23–36 (2007).
- Lipshitz, H. D., Peattie, D. A. & Hogness, D. S. Novel transcripts from the *Ultrathorax* domain of the Bithorax Complex. *Genes Dev.* **1**, 307–322 (1987).
- Meller, V. H., Wu, K. H., Roman, G., Kuroda, M. I. & Davis, R. L. roX1 RNA paints the X chromosome of male *Drosophila* and is regulated by the dosage compensation system. *Cell* **88**, 445–457 (1997).
- Celniker, S. E. *et al.* Unlocking the secrets of the genome. *Nature* **459**, 927–930 (2009).
- The modENCODE Consortium *et al.* Identification of functional elements and regulatory circuits by *Drosophila* modENCODE. *Science* doi:10.1126/science.1198374 (in the press).
- Gerstein, M. B. *et al.* Integrative analysis of the *Caenorhabditis elegans* genome by the modENCODE project. *Science* doi:10.1126/science.1196914 (in the press).
- Bejerano, G. *et al.* A distal enhancer and an ultraconserved exon are derived from a novel retroposon. *Nature* **441**, 87–90 (2006).
- Xie, X., Kamal, M. & Lander, E. S. A family of conserved noncoding elements derived from an ancient transposable element. *Proc. Natl Acad. Sci. USA* **103**, 11659–11664 (2006).
- Karch, F. *et al.* The abdominal region of the Bithorax Complex. *Cell* **43**, 81–96 (1985).
- Celniker, S. E., Sharma, S., Keelan, D. & Lewis, E. B. The molecular genetics of the bithorax complex of *Drosophila* cis-regulation in the *Abdominal-B* domain. *EMBO J.* **9**, 4277–4286 (1990).
- Ho, M. C. *et al.* Functional evolution of cis-regulatory modules at a homeotic gene in *Drosophila*. *PLoS Genet.* **5**, e1000709 (2009).
- Sanchez-Herrero, E. & Akam, M. Spatially ordered transcription of regulatory DNA in the bithorax complex of *Drosophila*. *Development* **107**, 321–329 (1989).
- Bae, E., Calhoun, V. C., Levine, M., Lewis, E. B. & Drewell, R. A. Characterization of the intergenic RNA profile at abdominal-A and Abdominal-B in the *Drosophila* bithorax complex. *Proc. Natl Acad. Sci. USA* **99**, 16847–16852 (2002).
- Bender, W. MicroRNAs in the *Drosophila* bithorax complex. *Genes Dev.* **22**, 14–19 (2008).
- Trapnell, C. *et al.* Transcript assembly and quantification by RNA-Seq reveals unannotated transcripts and isoform switching during cell differentiation. *Nature Biotechnol.* **28**, 511–515 (2010).
- Clark, A. G. *et al.* Evolution of genes and genomes on the *Drosophila* phylogeny. *Nature* **450**, 203–218 (2007).
- Padgett, R. A. & Shukla, G. C. A revised model for U4atac/U6atac snRNA base pairing. *RNA* **8**, 125–128 (2002).
- Tycowski, K. T., Shu, M. D., Kukoyi, A. & Steitz, J. A. A conserved WD40 protein binds the Cajal body localization signal of scaRNP particles. *Mol. Cell* **34**, 47–57 (2009).
- Hoskins, R. A. *et al.* Genome-wide analysis of promoter architecture in *Drosophila melanogaster*. *Genome Res.* doi:10.1101/gr.112466.110 (in the press).
- Parisi, M. *et al.* A survey of ovary-, testis-, and soma-biased gene expression in *Drosophila melanogaster* adults. *Genome Biol.* **5**, R40 (2004).
- Andres, A. J. & Cherbas, P. Tissue-specific ecdysone responses: regulation of the *Drosophila* genes Eip28/29 and Eip40 during larval development. *Development* **116**, 865–876 (1992).
- Andres, A. J., Fletcher, J. C., Karim, F. D. & Thummel, C. S. Molecular analysis of the initiation of insect metamorphosis: a comparative study of *Drosophila* ecdysteroid-regulated transcription. *Dev. Biol.* **160**, 388–404 (1993).
- Lockett, T. J. & Ashburner, M. Temporal and spatial utilization of the alcohol dehydrogenase gene promoters during the development of *Drosophila melanogaster*. *Dev. Biol.* **134**, 430–437 (1989).
- Warren, J. T. *et al.* Discrete pulses of molting hormone, 20-hydroxyecdysone, during late larval development of *Drosophila melanogaster*: correlations with changes in gene activity. *Dev. Dyn.* **235**, 315–326 (2006).
- Costantino, B. F. *et al.* A novel ecdysone receptor mediates steroid-regulated developmental events during the mid-third instar of *Drosophila*. *PLoS Genet.* **4**, e1000102 (2008).
- Birney, E. *et al.* Identification and analysis of functional elements in 1% of the human genome by the ENCODE pilot project. *Nature* **447**, 799–816 (2007).
- van Bakel, H., Nislow, C., Blencowe, B. J. & Hughes, T. R. Most “dark matter” transcripts are associated with known genes. *PLoS Biol.* **8**, e1000371 (2010).
- Pan, Q., Shai, O., Lee, L. J., Frey, B. J. & Blencowe, B. J. Deep surveying of alternative splicing complexity in the human transcriptome by high-throughput sequencing. *Nature Genet.* **40**, 1413–1415 (2008).
- Wang, E. T. *et al.* Alternative isoform regulation in human tissue transcriptomes. *Nature* **456**, 470–476 (2008).
- Philipps, D. L., Park, J. W. & Graveley, B. R. A computational and experimental approach toward a priori identification of alternatively spliced exons. *RNA* **10**, 1838–1844 (2004).
- Sanchez, L. Sex-determining mechanisms in insects. *Int. J. Dev. Biol.* **52**, 837–856 (2008).
- Stapleton, M., Carlson, J. W. & Celniker, S. E. RNA editing in *Drosophila melanogaster*: New targets and functional consequences. *RNA* **12**, 1922–1932 (2006).
- Jepson, J. E. & Reenan, R. A. Genetic approaches to studying adenosine-to-inosine RNA editing. *Methods Enzymol.* **424**, 265–287 (2007).
- Hoopengardner, B., Bhalla, T., Staber, C. & Reenan, R. Nervous system targets of RNA editing identified by comparative genomics. *Science* **301**, 832–836 (2003).
- Wang, J. W. & Wu, C. F. Modulation of the frequency response of Shaker potassium channels by the quiver peptide suggesting a novel extracellular interaction mechanism. *J. Neurogenet.* **24**, 67–74 (2010).
- Hild, M. *et al.* An integrated gene annotation and transcriptional profiling approach towards the full gene content of the *Drosophila* genome. *Genome Biol.* **5**, R3 (2003).
- Stark, A. *et al.* Discovery of functional elements in 12 *Drosophila* genomes using evolutionary signatures. *Nature* **450**, 219–232 (2007).
- Cherbas, L. The transcriptional diversity of 25 *Drosophila* cell lines. *Genome Res.* doi:10.1101/gr.112961.110 (in the press).
- Zuker, M. Mfold web server for nucleic acid folding and hybridization prediction. *Nucleic Acids Res.* **31**, 3406–3415 (2003).

49. Brooks, A. N. *et al.* Conservation of an RNA regulatory map between *Drosophila* and mammals. *Genome Res.* doi:10.1101/gr.108662.110 (in the press).

Supplementary Information is linked to the online version of the paper at www.nature.com/nature.

Acknowledgements We thank C. Trapnell and L. Pachter for discussions and assistance with Cufflinks, and E. Clough for comments and feedback. A.N.B. was partially supported by an NSF graduate fellowship. This work was funded by an award from the National Human Genome Research Institute modENCODE Project (U01 HB004271) to S.E.C. (Principal Investigator) and M.R.B., P.C., T.R.G., B.R.G. and N.P. (co-Principal Investigators) under Department of Energy contract no. DE-AC02-05CH11231, and by the National Institute of Diabetes and Digestive and Kidney Diseases Intramural Research Program (B.O.).

Author Contributions J.A., M.R.B., P.C., T.R.G., B.R.G., R.A.H., T.C.K., B.O., N.P. and S.E.C. designed the project. J.A., S.E.B., M.R.B., P.C., T.R.G., B.R.G., R.A.H., B.O. and S.E.C. managed the project. D.M. prepared biological samples. T.C.K. oversaw biological sample production. D.Z. and B.E. prepared RNA samples. J.A. oversaw RNA sample production. W.L. and A.W. analysed array data. P.K. managed array data production. L.Y. prepared Illumina RNA-Seq libraries. C.A.D., L.L., J.E.S., K.H.W. and L.Y. performed Illumina sequencing. J.M.L., B.R.G. and S.E.C. managed Illumina sequencing

production. M.B. and R.E.G. performed 454 sequencing of adults. R.A.H. managed production of the embryonic SOLiD and 454 sequencing. C.A.D. managed data transfers. C.Z. managed databases and formatted array and sequence data for submission. C.G.A., P.J.B., S.E.B., A.N.B., S.D., M.O.D., B.R.G. and D.S. developed analysis methods. C.G.A., J.B.B., N.B., B.W.B., S.E.B., A.N.B., J.W.C., S.E.C., L.C., P.C., C.A.D., A.D., M.O.D., B.R.G., R.L., J.H.M., N.R.M., D.S. and Yi.Z. analysed data. B.B.T. aligned the SOLiD data. M.J.V. and J.M.L. generated annotations. C.G.A., D.S. and J.H.M. analysed species validation data. L.J., C.G.A., D.S. and N.R.M. performed species RNA-Seq quality control. Yu.Z. and J.H.M. oversaw sequencing and gathered species samples. C.G.A., A.N.B., J.W.C., L.C., P.C., A.H., D.S., J.M.L., R.L., N.R.M., J.H.M. and B.O. contributed to the text. A.H. assisted with manuscript preparation. B.R.G. and S.E.C. wrote the paper with input from all authors. All authors discussed the results and commented on the manuscript.

Author Information All sequence data have been deposited in the SRA, cDNA sequences have been deposited in GenBank, and array data deposited in GEO (see Supplementary Table 35 for all accession numbers). All data is also available at <http://www.modencode.org>. Reprints and permissions information is available at www.nature.com/reprints. The authors declare no competing financial interests. Readers are welcome to comment on the online version of this article at www.nature.com/nature. Correspondence and requests for materials should be addressed to B.R.G. (graveley@neuron.uchc.edu) or S.E.C. (celniker@fruitfly.org).

Comprehensive analysis of the chromatin landscape in *Drosophila melanogaster*

Peter V. Kharchenko^{1,2}, Artyom A. Alekseyenko^{3,4}, Yuri B. Schwartz^{5†}, Aki Minoda⁶, Nicole C. Riddle⁷, Jason Ernst^{8,9}, Peter J. Sabo¹⁰, Erica Larschan^{3,4,11}, Andrey A. Gorchakov^{3,4}, Tingting Gu⁷, Daniela Linder-Basso^{5†}, Annette Plachetka^{3,4}, Gregory Shanower^{5†}, Michael Y. Tolstorukov^{1,2}, Lovelace J. Luquette¹, Ruibin Xi¹, Youngsook L. Jung^{1,3}, Richard W. Park^{1,12}, Eric P. Bishop^{1,12}, Theresa P. Canfield¹⁰, Richard Sandstrom¹⁰, Robert E. Thurman¹⁰, David M. MacAlpine¹³, John A. Stamatoyannopoulos^{10,14}, Manolis Kellis^{8,9}, Sarah C. R. Elgin⁷, Mitzi I. Kuroda^{3,4}, Vincenzo Pirrotta⁵, Gary H. Karpen^{6*} & Peter J. Park^{1,2,3*}

Chromatin is composed of DNA and a variety of modified histones and non-histone proteins, which have an impact on cell differentiation, gene regulation and other key cellular processes. Here we present a genome-wide chromatin landscape for *Drosophila melanogaster* based on eighteen histone modifications, summarized by nine prevalent combinatorial patterns. Integrative analysis with other data (non-histone chromatin proteins, DNase I hypersensitivity, GRO-Seq reads produced by engaged polymerase, short/long RNA products) reveals discrete characteristics of chromosomes, genes, regulatory elements and other functional domains. We find that active genes display distinct chromatin signatures that are correlated with disparate gene lengths, exon patterns, regulatory functions and genomic contexts. We also demonstrate a diversity of signatures among Polycomb targets that include a subset with paused polymerase. This systematic profiling and integrative analysis of chromatin signatures provides insights into how genomic elements are regulated, and will serve as a resource for future experimental investigations of genome structure and function.

The model organism Encyclopedia of DNA Elements (modENCODE) project is generating a comprehensive map of chromatin components, transcription factors, transcripts, small RNAs and origins of replication in *Drosophila melanogaster* and *Caenorhabditis elegans*^{1,2}. *Drosophila* has been used as a model system for over a century to study chromosome structure and function, gene regulation, development and evolution. The availability of high-quality euchromatic and heterochromatic sequence assemblies^{3–5}, extensive annotation of functional elements⁶, and a vast repertoire of experimental manipulations enhance the value of epigenomic studies in *Drosophila*.

Genome-wide profiling of chromatin components provides a rich annotation of the potential functions of the underlying DNA sequences. Previous work has identified patterns of post-translational histone modifications and non-histone proteins associated with specific elements (for example, transcription start sites, enhancers), as well as delineating the transcriptional status of genes and large domains^{7,8}. Here we present a comprehensive picture of the chromatin landscape in a model eukaryotic genome. We define combinatorial chromatin ‘states’ at different levels of organization, from individual regulatory units to the chromosome level, and relate individual states to genome functions.

Combinatorial chromatin states

We performed chromatin immunoprecipitation (ChIP)-array analysis for numerous histone modifications and chromosomal proteins

(Supplementary Table 1), using antibodies tested for specificity and cross-reactivity⁹ (Supplementary Fig. 1). Here we describe analyses of cell lines S2-DRSC (S2) and ML-DmBG3-c2 (BG3), derived from late male embryonic tissues (stages 16–17) and the central nervous system of male third instar larvae, respectively (see <http://www.modencode.org> for data from other cell lines and animal stages). Analysis reveals groups of correlated features, including those associated with heterochromatic regions¹⁰, Polycomb-mediated repression¹¹, and active transcription¹² (Supplementary Fig. 2), similar to those observed in other organisms^{13,14}. This indicates that specific histone modifications work together to achieve distinct chromatin ‘states’.

We used a machine-learning approach to identify the prevalent combinatorial patterns of 18 histone modifications, capturing the overall complexity of chromatin profiles observed in S2 and BG3 cells with 9 combinatorial states (Fig. 1a, Methods). The model associates each genomic location with a particular state, generating a chromatin-centric annotation of the genome (Fig. 1b). We examined each state for enrichment in non-histone proteins (Fig. 1a and Supplementary Fig. 3) and gene elements, as well as distribution across the karyotype (Fig. 1b and Supplementary Fig. 4) and finer-scale levels (Fig. 1c–e).

Most distinct chromatin states are associated with transcriptionally active genes. Active promoter and transcription start site (TSS)-proximal regions are identified by state 1 (Fig. 1; red), marked by prominent enrichment in H3K4me3/me2 (tri/dimethylation of residue K4 of

¹Center for Biomedical Informatics, Harvard Medical School, Boston, Massachusetts 02115, USA. ²Children's Hospital Informatics Program, Boston, Massachusetts 02115, USA. ³Division of Genetics, Department of Medicine, Brigham & Women's Hospital, Boston, Massachusetts 02115, USA. ⁴Department of Genetics, Harvard Medical School, Boston, Massachusetts 02115, USA. ⁵Department of Molecular Biology and Biochemistry, Rutgers University, Piscataway, New Jersey 08854, USA. ⁶Department of Molecular and Cell Biology, University of California at Berkeley, and Department of Genome Dynamics, Lawrence Berkeley National Lab, Berkeley, California 94720, USA. ⁷Department of Biology, Washington University in St Louis, St Louis, Missouri 63130, USA. ⁸MIT Computer Science and Artificial Intelligence Laboratory, Cambridge, Massachusetts 02139, USA. ⁹Broad Institute of MIT and Harvard, Cambridge, Massachusetts 02142, USA. ¹⁰Department of Genome Sciences, University of Washington, Seattle, Washington 98195, USA. ¹¹Department of Molecular Biology, Cell Biology and Biochemistry, Brown University, Providence, Rhode Island 02906, USA. ¹²Graduate Program in Bioinformatics, Boston University, Boston, Massachusetts 02115, USA. ¹³Department of Pharmacology and Cancer Biology, Duke University Medical Center, Durham, North Carolina 27710, USA. ¹⁴Department of Medicine, University of Washington, Seattle, Washington 98195, USA. †Present addresses: Department of Molecular Biology, Umea University, 901 87 Umea, Sweden. (Y.B.S.); Department of Plant Biology and Pathology, SEBS, Rutgers University, New Brunswick, New Jersey 08901, USA (D.L.-B.); Department of Basic Sciences, The Commonwealth Medical College, Scranton, Pennsylvania 18510, USA (G.S.).

*These authors contributed equally to this work.

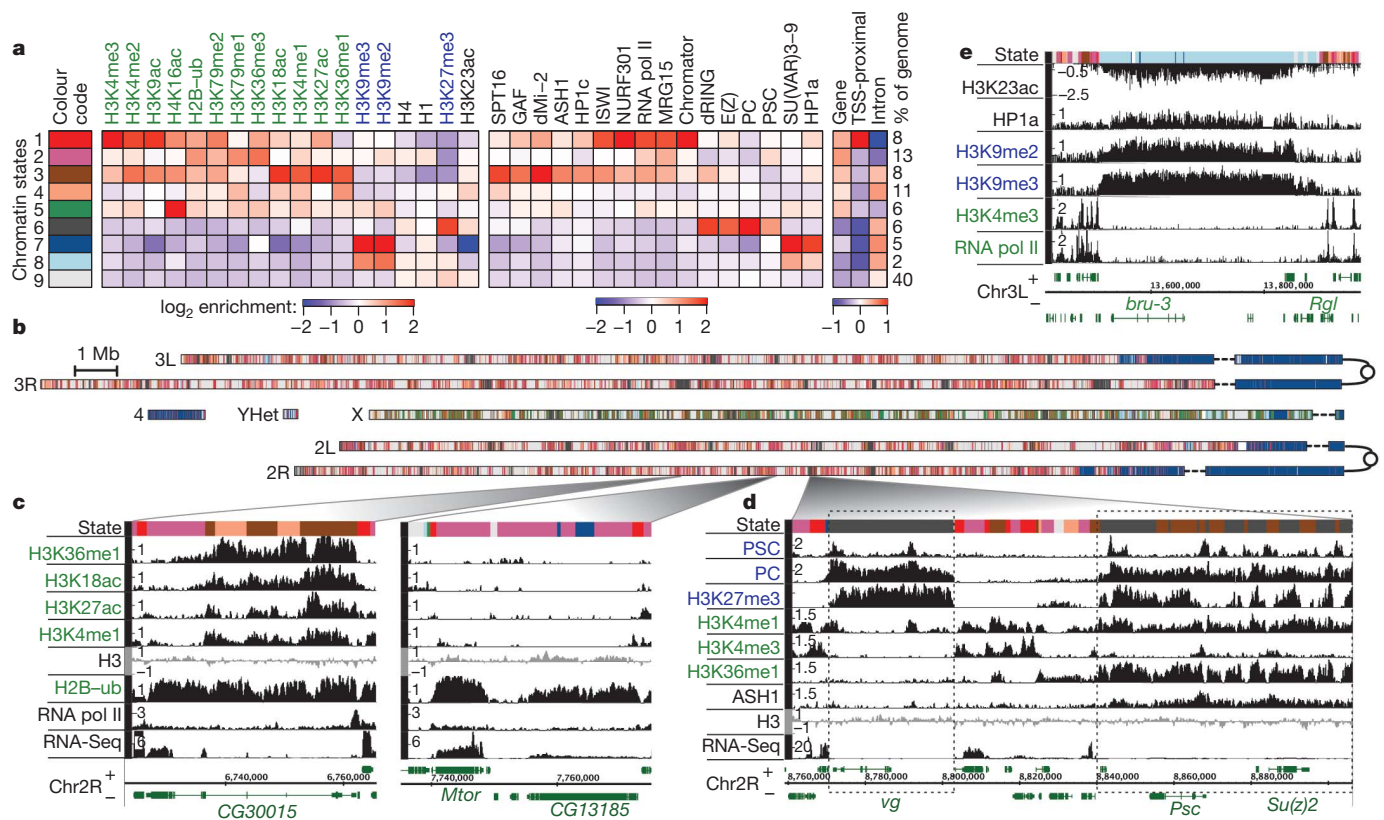


Figure 1 | Chromatin annotation of the *Drosophila melanogaster* genome. **a**, A 9-state model of prevalent chromatin states found in S2 and BG3 cells. Each chromatin state (row) is defined by a combinatorial pattern of enrichment (red) or depletion (blue) for specific chromatin marks (first panel, columns; active marks in green, repressive in blue). For instance, state 1 is distinguished by enrichment in H3K4me2/me3 and H3K9ac, typical of transcription start sites (TSS) in expressed genes. The enrichments/depletions are shown relative to chromatin input (S2 data shown, see Supplementary Fig. 3 for BG3 data and histone density normalization). The second panel shows average enrichment of chromosomal proteins. The third panel shows fold over/under-representation of genic and TSS-proximal (± 1 kb) regions relative to the entire tiled genome. The enrichment of intronic regions is relative to genic regions associated with each state. **b**, A genome-wide karyotype view of the domains defined by the 9-state model in S2 cells. Centromeres are shown as open circles, and dashed

lines span gaps in the genome assembly. Several prominent chromatin organization features are illustrated (colour code in **a**), including the extent of pericentromeric heterochromatin (state 7) and the H4K16ac-driven signature of the dosage-compensated male X chromosome (state 5). (BG3 in Supplementary Fig. 4.) **c–e**, Examples of chromatin annotation at specific loci. **c**, Two distinct chromatin signatures of transcriptionally active genes: one (left) is associated with enrichment in marks of states 3 and 4, whereas the other (right) is limited to states 1 and 2, recapitulating well established TSS and elongation signatures (note that small patches of state 7 in CG13185 illustrate H3K9me2 found at some expressed genes in S2 cells¹⁶). **d**, A locus containing two Polycomb-associated domains, silent (left) and balanced (right). **e**, A large state 8 domain located within euchromatic sequence in BG3 cells, enriched for chromatin marks typically associated with heterochromatic regions, but at lower levels than in pericentromeric heterochromatin (state 7).

histone H3) and H3K9ac (acetylation of K9 of histone H3). The transcriptional elongation signature associated with H3K36me3 enrichment is captured by state 2 (purple), found preferentially over exonic regions of transcribed genes. State 3 (brown), typically found within intronic regions, is distinguished by high enrichment in H3K27ac, H3K4me1 and H3K18ac. A related chromatin signature is captured by state 4 (coral), distinguished by enrichment of H3K36me1, but notably lacking H3K27ac. The number of genes associated with each chromatin state and the distribution of states within genes are shown in Supplementary Fig. 5.

Several aspects of large-scale organization are revealed by the karyotype view (Fig. 1b). Chromosome X is markedly enriched for state 5 (green), distinguished by high levels of H4K16ac in combination with H3K36me3 and other marks of 'elongation' state 2 (a combinatorial pattern associated with dosage compensation in male cells¹⁵). Pericentromeric heterochromatin domains and chromosome 4 are characterized by high levels of H3K9me2/me3 (state 7, dark blue)¹⁰. Finally, the model distinguishes another set of heterochromatin-like regions containing moderate levels of H3K9me2/me3 (state 8, light blue; Fig. 1e). Surprisingly, this state occupies extensive domains in autosomal euchromatic arms in BG3 cells, and in chromosome X in both cell lines¹⁶.

Further aspects of chromatin organization can be visualized by folding the chromosome using a Hilbert curve (Fig. 2a)¹⁷, which maintains the

spatial proximity of nearby elements. Thus, local patches of corresponding colours reveal the sizes and relative positions of domains associated with particular chromatin states (Fig. 2b and Supplementary Figs 6–9). For instance, specks of TSS-proximal regions (state 1) are typically contained within larger blocks of transcriptional elongation marks (state 2), which are in turn encompassed by extensive patches of H3K36me1-enriched domains (state 4) and variable-sized blocks of state 3. The clusters of open chromatin formed by these gene-centric patterns are separated by extensive silent domains (state 9) and regions of Polycomb-mediated repression (state 6). Factors responsible for domain boundaries were not identified in our analysis (Supplementary Fig. 10).

We also developed a multi-scale method to characterize chromatin organization at the spatial scale appropriate for the genome properties being investigated. For example, we observe that chromatin patterns most accurately reflect the replication timing of the S2 genome at scales of ~ 170 kb (Supplementary Information, section 1). This is consistent with size estimates of chromatin domains influencing replication timing¹⁸, and suggests that multiple replication origins are coordinately regulated by the local chromatin environment (each replicon is ~ 28 – 50 kb¹⁹).

To examine combinatorial patterns not distinguished by the simplified 9-state model, we also generated a 30-state combinatorial model that uses presence/absence probabilities of individual marks²⁰ (Supplementary

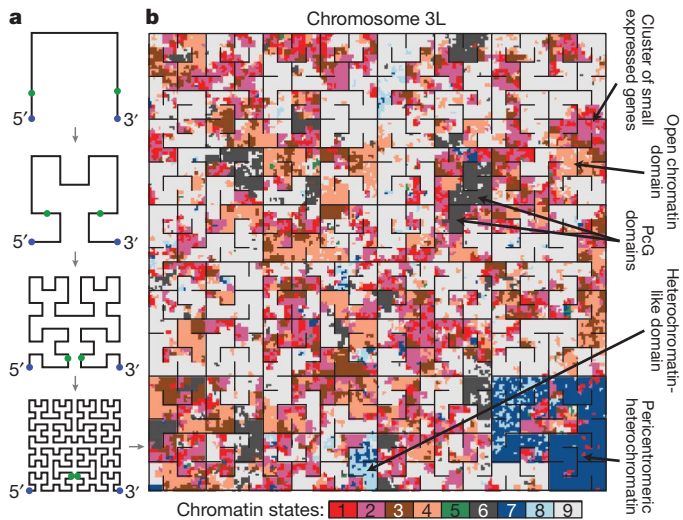


Figure 2 | Visualization of spatial scales and organization using compact folding. **a**, The chromosome is folded using a geometric pattern (Hilbert space-filling curve) that maintains spatial proximity of nearby regions. An illustration of the first four folding steps is shown. Note that although this compact curve is optimal for preserving proximity relationships, some distal sites appear adjacent along the fold axis (green dots). **b**, Chromosome 3L in S2 cells. A domain of a given chromatin state appears as a patch of uniform colour of corresponding size. Thin black lines are used to separate regions that are distant on the chromosome. The folded view illustrates chromatin organization features that are not easily discerned from a linear view: active TSSs (state 1) appear as small specks surrounded by elongation state 2, commonly next to larger regions marked by H3K36me1-driven state 4, which also contains patches of intron-associated state 3. These open chromatin regions are separated by extensive domains of state 9. See Supplementary Figs 6 and 7 for other chromosomes and BG3 data. The folded views can be browsed alongside the linear annotations and other relevant data online: <http://compbio.med.harvard.edu/flychromatin>.

Fig. 11). The increased number of states can identify finer variations that are biologically significant, for example, a signature corresponding to transcriptional elongation in heterochromatic regions¹⁶.

Chromatin state variation among genes

Active genes generally display enrichments or depletions of individual marks at specific gene segments (Fig. 3a). When classified according to their chromatin signatures (Supplementary Fig. 12), active genes fall into subclasses correlated with expression magnitude (Supplementary Information, section 2), gene structure and genomic

context (for example, heterochromatic genes combine H3K9me2/me3 with some active marks)¹⁶. Of particular interest is one class of long expressed genes, many with regulatory functions, which are enriched for H3K36me1 (cluster 2, Supplementary Fig. 12; 131 genes in S2, 202 in BG3; Supplementary Table 2).

To examine further the patterns associated with long genes, we clustered expressed autosomal genes ≥ 4 kb based on blocks of enrichment for each chromatin mark (Fig. 3b; 1,055 genes). We observe that genes with large 5'-end introns (green subtree, Fig. 3b; 552 genes) show extensive H3K27ac and H3K18ac enrichment, broader H3K9ac domains, and blocks of H3K36me1 enrichment (chromatin state 3, Fig. 3b, last column). These genes are enriched for developmental and regulatory functions (Supplementary Table 3), and are positioned within domains of Nipped-B²¹ (Fig. 3b), a cohesin-complex loading protein previously associated with transcriptionally active regions^{21,22}. In contrast, genes with more uniformly distributed coding regions (red subtree, Fig. 3b) lack most state 3 marks, and H3K9ac enrichment is restricted to the 2 kb downstream of the TSS. These differences are not explained by variation in histone density (Supplementary Fig. 13). Overall, the presence or absence of state 3 is the most common difference in the chromatin composition of expressed genes that are 1 kb and longer (Supplementary Fig. 14), and the presence of state 3 consistently correlates with a reduced fraction of coding sequence in the gene body, mainly associated with the presence of a long first intron.

State 3 domains are highly enriched for specific chromatin remodelling factors (SPT16 (also known as DRE4) and dMI-2; Supplementary Figs 15 and 16), whereas state 1 regions around active TSSs are preferentially bound by NURF301 (also called E(bx)) and MRG15. ISWI is enriched in both states 1 and 3 (Supplementary Figs 16 and 17). State 3 domains also exhibit the highest levels of nucleosome turnover²³, and show higher enrichment of the transcription-associated H3.3 histone variant²⁴ than either the TSS- or elongation-associated states 1 and 2 (Supplementary Figs 15 and 16). Consistent with earlier analyses of cohesin-bound regions²⁵, state 3 sequences tend to replicate early in G1 phase, and show abundance of early replicating origins (Supplementary Fig. 18). A regulatory role for state 3 domains is suggested by enrichment for a known enhancer binding protein (dCBP/p300²⁶) in adult flies, and for enhancers validated in transgene constructs²⁷ (Supplementary Fig. 19).

Modes of regulation in Polycomb domains

In *Drosophila*, loci repressed by Polycomb group (PcG) proteins are embedded in broad H3K27me3 domains that are regulated by Polycomb response elements (PREs) bound by E(Z), PSC and dRING (Fig. 1d)^{28,29}. We find that regions of H3K4me1 enrichment surround all

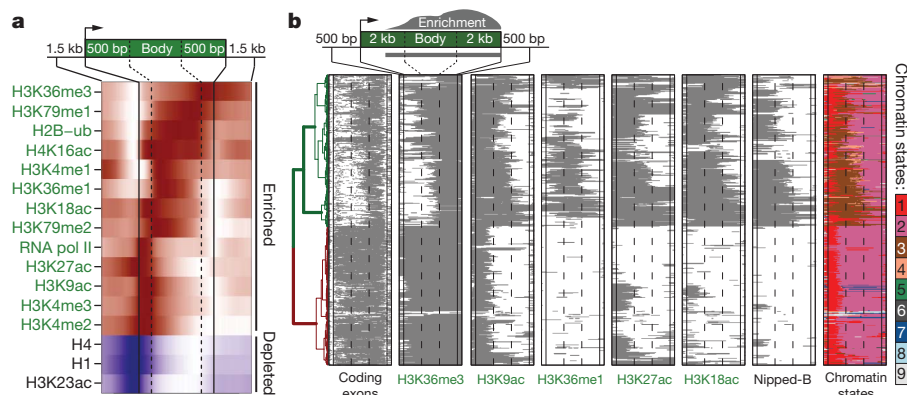


Figure 3 | Chromatin patterns associated with transcriptionally active genes. **a**, Location and extent of chromatin features relative to boundaries of expressed genes (≥ 1 kb) in BG3 cells. The colour intensity indicates the relative frequency of enrichment/depletion (red/blue) of a given mark within the gene (normalized independently for each mark). **b**, Regions enriched for 'active' chromatin marks in long transcribed genes. The plot shows the extent of regions enriched for various active marks at transcriptionally active genes (≥ 4 kb) on

BG3 autosomes. Each row represents a scaled gene. The first column illustrates coding exons; the last column shows chromatin state annotation. The clustering of the genes according to the spatial patterns of chromatin marks separates genes with a high fraction of coding sequence (red subtree, bottom) from genes containing long introns (green subtrees, top), which are associated with chromatin state 3 (last column) and binding of specific chromosomal proteins, such as Nipped-B²¹ (also see Supplementary Fig. 13).

PREs, 90% of which also display narrower peaks of H3K4me2 enrichment (Supplementary Fig. 20). Although this pattern is reminiscent of transcriptionally active promoter regions, PREs lack H3K4me3, indicating that a different mechanism of H3K4 methylation is used, perhaps involving the *Trithorax* H3K4 histone methyltransferase (HMTase) found at all PREs²⁹.

To examine chromatin states associated with PcG targets, we analysed the chromatin and transcriptional signatures of TSSs in Polycomb-bound domains (Fig. 4a and Supplementary Fig. 21). In addition to fully repressed TSSs (cluster 1, Fig. 4a), we identify TSSs maintained in the 'balanced' state²⁹ (cluster 2, Fig. 4a), distinguished by coexistence of Polycomb with active marks (including the HMTase ASH1) and production of full-length messenger RNA transcripts (for example, *Psc* domain, Fig. 1d).

TSSs in clusters 3 and 4 are distinguished by the presence of adjacent PREs (Fig. 4a). Surprisingly, 53% of the PRE-proximal TSSs produce short RNA transcripts³⁰ (cluster 3, Fig. 4a), indicating stalling of engaged RNA pol II³⁰. Using the global run-on sequencing (GRO-Seq) assay to accurately assess engaged RNA polymerases³¹, we observe that cluster 3 TSSs produce short transcripts in the sense orientation. The level of GRO⁺ signal is similar to that found at fully transcribed genes (Supplementary Fig. 22); thus, some transcription initiates in cluster 3, but elongation fails. Interestingly, these genes are enriched for regulatory and developmental functions, even more than other genes within Polycomb domains (see Supplementary Tables 4 and 5). Genes without TSS-proximal PREs generally lack short transcript signatures (for example, cluster 1 in Fig. 4a; see Supplementary Fig. 21 for exceptions). Importantly, engaged polymerases and transcripts are not a general feature of PREs; TSS-distal PREs typically lack short RNA and GRO-Seq signals (Fig. 4b and Supplementary Fig. 22) despite being similarly enriched in H3K4me1/me2. The striking link between TSS-proximal PREs and the production of short RNAs suggests a potential mechanism for control of these developmental regulatory genes, whereby the same features that recruit H3K4 methyl marks to PREs may also facilitate RNA pol II recruitment to nearby TSSs.

DHS plasticity and chromatin states

We used a DNase I hypersensitivity assay^{32,33} to examine the distributions of putative regulatory regions and their relationships with chromatin states. DNase I hypersensitivity mapping broadly identifies sites with low nucleosome density and regions bound by non-histone proteins^{34–36}. Short-read sequencing identified 8,616 high-magnitude DNase I hypersensitive sites (DHSs) in S2 cells and 6,354 in BG3 cells (and a comparable number of low-magnitude DHSs; Supplementary Fig. 23 and Methods). Approximately half of the high-magnitude DHSs are found at transcriptionally active TSSs (Supplementary Fig. 24). Thus, the chromatin context of the TSS-proximal DHSs is dominated by the features

expected for an active TSS, including RNA pol II, H3K4me3 and other state 1 marks (clusters 1, 2; Fig. 5a and Supplementary Fig. 25).

Of the 36% TSS-distal DHSs, most (60%) are positioned within annotated expressed genes (Supplementary Fig. 24). These gene-body DHSs are distinguished from TSS-proximal DHSs by low H3K4me3, higher levels of H3K4me1, H3K27ac, and other marks linked to chromatin state 3 (clusters 3, 4; Fig. 5a and Supplementary Fig. 26). An additional 20% of the TSS-distal DHSs are outside of annotated genes, but show signatures associated with active transcription starts or elongation, suggesting new alternative promoters or unannotated genes (Supplementary Figs 27 and 28). The remaining 20% of TSS-distal DHSs that appear to be intergenic (6% of all DHSs) are typically enriched for H3K4me1, but lack other active marks (cluster 5, Fig. 5a).

Most DHS positions fall into the TSS-proximal state 1 or the intron-biased state 3 (Fig. 5b). State 3 lacks H3K4me3 and is enriched for H3K4me1, H3K27ac and H3K18ac, similar to mammalian enhancer elements³⁷. Many state 3 DHS positions are occupied by known regulatory proteins: GAGA factor binds to 49% of these DHSs in S2 cells, and developmental transcription factors bind to 44% of these DHSs in embryos³⁸. Notably, we find that TSS-distal DHSs in *Drosophila* exhibit low-level bi-directional transcripts (Fig. 5a, shortRNA panel; see also Supplementary Figs 29 and 30), analogous to the enhancer RNAs (eRNAs) characterized in mice³⁹. Analysis of GRO-Seq data (Fig. 5e) indicates that eRNA-like transcripts are common to both intra- and intergenic TSS-distal DHSs in *Drosophila*, a feature that is conserved with mammals.

The association of DHSs with chromatin states 1 and 3 (Fig. 5c) persists even in chromosome 4 and pericentromeric heterochromatin, where such states are infrequent (Supplementary Fig. 31). This suggests that these chromatin states and associated remodelling factors (for example, ISWI, SPT16) provide the context necessary for non-histone chromosomal protein binding at DHSs, or are the consequence of such binding events. To investigate this interdependency, we analysed a high-confidence set of loci that exhibit DHSs in only one of the two examined cell lines (Supplementary Fig. 32). Surprisingly, although in general more DHSs are in state 1 regions, 91% of the cell-type-specific DHSs are found within state 3 domains (14-fold increase compared to state 1 DHSs; Supplementary Table 6 and Fig. 5d). Comparison with DHSs in an additional cell type (Kc167, Supplementary Fig. 33) confirms that DHSs displaying plasticity between cell types are mostly found in state 3. When DHSs are absent, the altered loci maintain chromatin state 3 in 23% of the cases (Fig. 5d), indicating that the presence of state 3 is not always dependent on the DHS. More frequently, the altered loci transition to state 4 (43% of the cases), an open chromatin state that lacks many of the histone modifications and chromatin remodellers characteristic of state 3. Although the less frequent

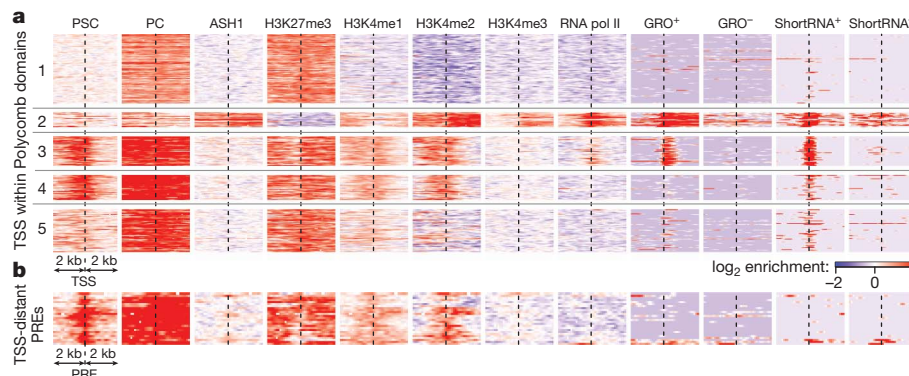


Figure 4 | Signatures of TSSs within domains of Polycomb-mediated repression. **a**, Distinct classes of TSSs in S2 cell Polycomb domains. Each row represents a TSS. Clusters 1–5 illustrate distinct TSS states (see Supplementary Fig. 21 for complete set of clusters). Cluster 1 shows fully repressed TSSs with the expected pattern of PC and H3K27me3 enrichment; cluster 2 shows 21 TSSs found within ASH1 domains, maintained in a balanced state. Clusters 3 and 4 distinguish TSSs located in the immediate proximity of Polycomb response

elements (PREs), showing the symmetrical H3K4me1/me2 enrichment typical of all PREs. Many such TSSs (cluster 3, 42 TSSs) produce short, non-polyadenylated transcripts along the sense strand (GRO⁺/shortRNA⁺ columns), indicating the presence of paused polymerase. **b**, PRE positions distant from annotated TSSs. TSS-distal PREs exhibit enrichment for H3K4me1/me2, but are not associated with GRO or shortRNA signatures.

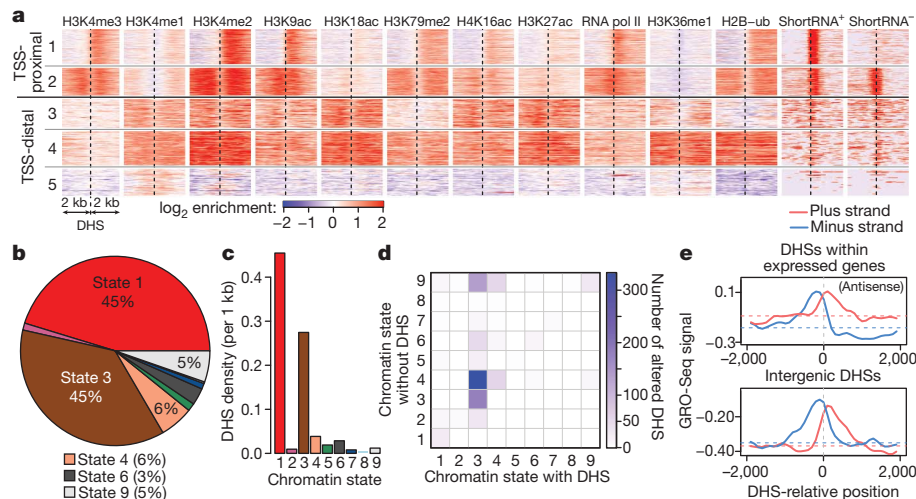


Figure 5 | Chromatin signatures of regulatory elements identified by DNase I hypersensitivity. **a**, Representative classes of high-magnitude DNase I hypersensitive sites (DHSs) and chromatin signatures in S2 cells. TSS-proximal (within 2 kb) DHSs show chromatin signatures expected of expressed gene promoters: high H3K4me3 and RNA pol II signal extending in the direction of transcription (left to right; cluster 2 groups bi-directional promoters). TSS-distal DHSs are associated with high H3K4me1 and low H3K4me3 levels. Most TSS-distal DHSs found within the bodies of expressed genes (clusters 3, 4) are associated with chromatin state 3. A cluster of rare intergenic DHSs (cluster 5) is associated with localized peaks of H3K4me1/2 (complete sets of clusters in Supplementary Figs 25, 26 and 28). **b**, Distribution of DHS positions among chromatin states. The vast majority of DHSs are found within the TSS-proximal state 1 or enhancer-like state 3 regions. **c**, States 1 and 3 exhibit the highest

density of DHSs. **d**, Cell-line-specific DHSs are positioned predominantly within the enhancer-like state 3. The transition matrix shows the chromatin state of loci containing DHSs in one cell line (*x* axis), and the state of the same locus in the other cell line where the DHS is absent (*y* axis). Most of the DHSs that differ between cell lines originate from state 3. When DHSs are absent, the loci typically transition to an open chromatin state 4 (43%), or maintain state 3 (23%). In both scenarios, most of the associated genes remain transcriptionally active (see Supplementary Fig. 34). **e**, Low levels of engaged RNA polymerase are associated with TSS-distal DHSs. The top plot shows the local increase in the antisense GRO-seq signal for DHSs located within transcribed genes; dashed lines show median levels. Intergenic DHS positions (bottom plot) also show bi-directional GRO-seq signal of comparable magnitude. See Supplementary Figs 27, 29 and 30.

transitions to the Polycomb state 6 (7%) or background state 9 (17%) typically coincide with gene silencing, most of the genes that maintain state 3 or transition to state 4 remain transcriptionally active (Supplementary Fig. 34). These observations provide further support for an enhancer-like function for state 3 DHSs, and suggest a more subtle regulatory role than simple linkage to the presence or absence of gene expression.

Chromatin annotation of genome functions

The genomic chromatin state annotation and discovery of refined chromatin signatures for chromosomes, domains, and subsets of regulatory genes demonstrate the utility of a systematic, genome-wide profiling of an organism that is already understood in considerable detail. Clearly, the definition and functional annotation of chromatin patterns will be enhanced by incorporation of data for different types of components. Five 'colours' of chromatin were recently identified in Kc167 cells using chromosomal protein maps⁴⁰. Comparison with our 9-state model shows similarities as well as differences in the ability to distinguish functional elements (Supplementary Fig. 35); thus, further integration of such data in the same cell type may resolve additional functional features. Our results illustrate the utility of integrating multiple data types (histone marks, non-histone proteins, chromatin accessibility, short RNAs and transcriptional activity) for comprehensive characterization of functional chromatin states.

An important, repeated theme is that chromatin state analysis identifies unexpected distinctions between subsets of active genes. Besides the differences linked to genomic context (for example, male X chromosome, heterochromatin), the main source of variability is the presence of the acetylation-rich state 3 (Fig. 6). Several lines of evidence suggest that the intronic positions marked by state 3 are important for gene regulation. State 3 regions show specific associations with known chromatin remodellers (SPT16, dMi-2 and ISWI) and gene regulatory proteins (for example, GAF, dCBP/p300), and the highest rates of nucleosome turnover and transcription-dependent deposition of the H3.3 variant. State 3 genes are also bound by cohesin

complex proteins, thought to associate with decondensed chromatin²¹ to promote looping interactions with promoter regions²².

A regulatory role for state 3 chromatin is further suggested by the high density of DHSs, comparable to that of active TSS state 1, and the fact that state 3 accounts for most of the DHS plasticity among cell types. The combinations of histone marks found in state 3 are similar to signatures of mammalian enhancers³⁷, which also show high variability between cell types³⁷. Furthermore, state 3 DHSs exhibit low levels of short, non-coding bidirectional transcripts reminiscent of eRNAs identified in mice³⁹. Together, these findings suggest that state 3 regions contain enhancers or other regulatory elements, and that a combination of modifications can be used to identify new elements in the genome.

Genes within repressive Polycomb domains also display several distinct combinatorial chromatin patterns (Fig. 4a), which probably represent a range of functional states: repressed, paused, or expressed genes in either balanced²⁹ or fully activated states. Alternatively, distinct signatures might mark subsets of regulatory genes that require either long-term repression or the ability to reverse functional states, depending on environmental or developmental cues. The PRE-proximal paused TSSs have some similarity to the 'bivalent' genes in mammalian cells, which also display transcriptional pausing of key regulatory and developmental genes^{41,42}. However, the mammalian 'bivalent state' is characterized by the simultaneous

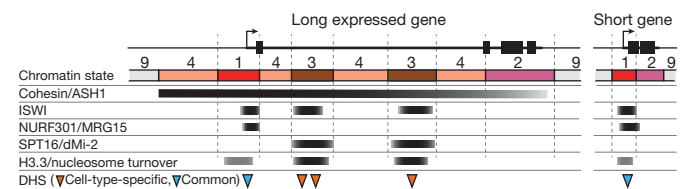


Figure 6 | Spatial arrangements of chromatin states associated with active transcription. Unlike short or exon-rich expressed genes, expressed genes with long intronic regions commonly contain one or more regions of enhancer-like state 3, associated with specific chromosomal proteins, high nucleosome turnover and DHSs displaying cell-type plasticity.

presence of PcG proteins, H3K27me3 and H3K4me3, which in *Drosophila* is found only in the fully elongating 'balanced' state^{29,43}.

Comprehensive analysis of chromatin signatures has enormous potential for annotating functional elements in both well studied and new genomes. Going forward, our systematic characterization of the epigenomic and transcriptional properties of *Drosophila* cells should spur in-depth experimental analyses of the relationship between chromatin states and genome functions, ranging from whole chromosomes down to individual regulatory elements and circuits.

METHODS SUMMARY

Histone modification and chromosomal protein antibodies were characterized for cross-reactivity. ChIP-chip was performed in duplicate, using Affymetrix *Drosophila* Tiling 2.0R Arrays. Digital DNase I-Seq assays were performed as described previously⁴⁴, and Global Run-On library (GRO-Seq) data was generated as described previously³¹. Short RNA data was generated by ref. 30, and RNA-Seq data was generated by ref. 45. See ref. 46 for other modENCODE RNA-Seq data. The chromatin state models were generated as hidden Markov models (HMMs) of different histone marks. DHSs were identified as read density peaks significantly enriched relative to the genomic DNA control. Clustering of chromatin signatures was determined using the PAM algorithm.

Full Methods and any associated references are available in the online version of the paper at www.nature.com/nature.

Received 2 September; accepted 6 December 2010.

Published online 22 December 2010.

- modENCODE. Identification of functional elements and regulatory circuits by *Drosophila* modENCODE. *Science* doi:10.1126/science.1198374 (in the press).
- Gerstein, M. B. *et al.* Integrative analysis of the *Caenorhabditis elegans* genome by the modENCODE project. *Science* doi:10.1126/science.1196914 (in the press).
- Adams, M. D. *et al.* The genome sequence of *Drosophila melanogaster*. *Science* **287**, 2185–2195 (2000).
- Clark, A. G. *et al.* Evolution of genes and genomes on the *Drosophila* phylogeny. *Nature* **450**, 203–218 (2007).
- Hoskins, R. A. *et al.* Sequence finishing and mapping of *Drosophila melanogaster* heterochromatin. *Science* **316**, 1625–1628 (2007).
- Tweedie, S. *et al.* FlyBase: enhancing *Drosophila* Gene Ontology annotations. *Nucleic Acids Res.* **37**, D555–D559 (2009).
- Felsenfeld, G. & Groudine, M. Controlling the double helix. *Nature* **421**, 448–453 (2003).
- Mendenhall, E. M. & Bernstein, B. E. Chromatin state maps: new technologies, new insights. *Curr. Opin. Genet. Dev.* **18**, 109–115 (2008).
- Egelhofer, T. A. *et al.* An assessment of histone-modification antibody quality. *Nature Struct. Mol. Biol.* doi:10.1038/nsmb.1972 (5 December 2010).
- Eissenberg, J. C. & Reuter, G. Cellular mechanism for targeting heterochromatin formation in *Drosophila*. *Int. Rev. Cell Mol. Biol.* **273**, 1–47 (2009).
- Schwartz, Y. B. & Pirrotta, V. Polycomb complexes and epigenetic states. *Curr. Opin. Cell Biol.* **20**, 266–273 (2008).
- Li, B., Carey, M. & Workman, J. L. The role of chromatin during transcription. *Cell* **128**, 707–719 (2007).
- Liu, C. L. *et al.* Single-nucleosome mapping of histone modifications in *S. cerevisiae*. *PLoS Biol.* **3**, e328 (2005).
- Barski, A. *et al.* High-resolution profiling of histone methylations in the human genome. *Cell* **129**, 823–837 (2007).
- Larschan, E. *et al.* MSL complex is attracted to genes marked by H3K36 trimethylation using a sequence-independent mechanism. *Mol. Cell* **28**, 121–133 (2007).
- Riddle, N. C. *et al.* Plasticity in patterns of histone modifications and chromosomal proteins in *Drosophila* heterochromatin. *Genome Res.* doi:10.1101/gr.110098.110 (in the press).
- Anders, S. Visualization of genomic data with the Hilbert curve. *Bioinformatics* **25**, 1231–1235 (2009).
- MacAlpine, D. M., Rodriguez, H. K. & Bell, S. P. Coordination of replication and transcription along a *Drosophila* chromosome. *Genes Dev.* **18**, 3094–3105 (2004).
- Blumenthal, A. B., Kriegstein, H. J. & Hogness, D. S. The units of DNA replication in *Drosophila melanogaster* chromosomes. *Cold Spring Harb. Symp. Quant. Biol.* **38**, 205–223 (1974).
- Ernst, J. & Kellis, M. Discovery and characterization of chromatin states for systematic annotation of the human genome. *Nature Biotechnol.* **28**, 817–825 (2010).
- Misulovin, Z. *et al.* Association of cohesin and Nipped-B with transcriptionally active regions of the *Drosophila melanogaster* genome. *Chromosoma* **117**, 89–102 (2008).
- Kagey, M. H. *et al.* Mediator and cohesin connect gene expression and chromatin architecture. *Nature* **467**, 430–435 (2010).
- Deal, R. B., Henikoff, J. G. & Henikoff, S. Genome-wide kinetics of nucleosome turnover determined by metabolic labeling of histones. *Science* **328**, 1161–1164 (2010).
- Henikoff, S., Henikoff, J. G., Sakai, A., Loeb, G. B. & Ahmad, K. Genome-wide profiling of salt fractions maps physical properties of chromatin. *Genome Res.* **19**, 460–469 (2009).
- MacAlpine, H. K., Gordan, R., Powell, S. K., Hartemink, A. J. & MacAlpine, D. M. *Drosophila* ORC localizes to open chromatin and marks sites of cohesin complex loading. *Genome Res.* **20**, 201–211 (2010).
- Visel, A. *et al.* ChIP-seq accurately predicts tissue-specific activity of enhancers. *Nature* **457**, 854–858 (2009).
- Zinzen, R. P., Girardot, C., Gagneur, J., Braun, M. & Furlong, E. E. Combinatorial binding predicts spatio-temporal cis-regulatory activity. *Nature* **462**, 65–70 (2009).
- Schwartz, Y. B. *et al.* Genome-wide analysis of Polycomb targets in *Drosophila melanogaster*. *Nature Genet.* **38**, 700–705 (2006).
- Schwartz, Y. B. *et al.* Alternative epigenetic chromatin states of Polycomb target genes. *PLoS Genet.* **6**, e1000805 (2010).
- Nechaev, S. *et al.* Global analysis of short RNAs reveals widespread promoter-proximal stalling and arrest of Pol II in *Drosophila*. *Science* **327**, 335–338 (2010).
- Core, L. J., Waterfall, J. J. & Lis, J. T. Nascent RNA sequencing reveals widespread pausing and divergent initiation at human promoters. *Science* **322**, 1845–1848 (2008).
- Wu, C. The 5' ends of *Drosophila* heat shock genes in chromatin are hypersensitive to DNase I. *Nature* **286**, 854–860 (1980).
- Wu, C., Bingham, P. M., Livak, K. J., Holmgren, R. & Elgin, S. C. The chromatin structure of specific genes: I. Evidence for higher order domains of defined DNA sequence. *Cell* **16**, 797–806 (1979).
- Elgin, S. C. The formation and function of DNase I hypersensitive sites in the process of gene activation. *J. Biol. Chem.* **263**, 19259–19262 (1988).
- Jin, C. *et al.* H3.3/H2A.Z double variant-containing nucleosomes mark 'nucleosome-free regions' of active promoters and other regulatory regions. *Nature Genet.* **41**, 941–945 (2009).
- Hesselberth, J. R. *et al.* Global mapping of protein-DNA interactions *in vivo* by digital genomic footprinting. *Nature Methods* **6**, 283–289 (2009).
- Heintzman, N. D. *et al.* Histone modifications at human enhancers reflect global cell-type-specific gene expression. *Nature* **459**, 108–112 (2009).
- MacArthur, S. *et al.* Developmental roles of 21 *Drosophila* transcription factors are determined by quantitative differences in binding to an overlapping set of thousands of genomic regions. *Genome Biol.* **10**, R80 (2009).
- Kim, T. K. *et al.* Widespread transcription at neuronal activity-regulated enhancers. *Nature* **465**, 182–187 (2010).
- Filion, G. J. *et al.* Systematic protein location mapping reveals five principal chromatin types in *Drosophila* cells. *Cell* **143**, 212–224 (2010).
- Bernstein, B. E. *et al.* A bivalent chromatin structure marks key developmental genes in embryonic stem cells. *Cell* **125**, 315–326 (2006).
- Kanhere, A. *et al.* Short RNAs are transcribed from repressed polycomb target genes and interact with polycomb repressive complex-2. *Mol. Cell* **38**, 675–688 (2010).
- Schuettengruber, B. *et al.* Functional anatomy of polycomb and trithorax chromatin landscapes in *Drosophila* embryos. *PLoS Biol.* **7**, e13 (2009).
- Sekimata, M. *et al.* CCTC-binding factor and the transcription factor T-bet orchestrate Th1 helper 1 cell-specific structure and function at the interferon- γ locus. *Immunity* **31**, 551–564 (2009).
- Cherbas, L. *et al.* The transcriptional diversity of 25 *Drosophila* cell lines. *Genome Res.* **21**, doi:10.1101/gr.112961.110 (in the press).
- Gravely, B. R. *et al.* The developmental transcriptome of *Drosophila melanogaster*. *Nature* doi:10.1038/nature09715 (this issue).

Supplementary Information is linked to the online version of the paper at www.nature.com/nature.

Acknowledgements We thank our technicians D. Acevedo, S. Gadel, C. Kennedy, O.-K. Lee, S. Marchetti, S. Vong and M. Weaver, and Rutgers BRTC. We also thank our colleagues who donated antibodies: J. Kadoonaga (H1), A. L. Greenleaf (RNA pol II), G. Reuter (SU(VAR)3-9), G. Cavalli (GAF) and I. F. Zhimulev/H. Saumweber (Chromator). The major support for this work came from the modENCODE grant U01HG004258 to G.H.K. (Principal Investigator) and S.C.R.E., M.I.K., P.J.P. and V.P. (co-Principal Investigators), administered under Department of Energy contract no. DE-AC02-05CH11231. Additional funding came from RC2 HG005639, U01 HG004279, R01 GM082798, R37 GM45744, RC1 HG005334, R01 GM071923, U54 HG004592 and NSF 0905968.

Author Contributions P.V.K. performed most bioinformatic analysis. A.A.A., Y.B.S., A.M., N.C.R., E.L., A.G.K., T.G., D.L.-B., A.P. and G.S. generated data, directed by S.C.R.E., M.I.K., V.P. and G.H.K. The 30-state analysis was performed by J.E. and M.K., whereas M.Y.T., L.J.L., R.X., Y.L.J., R.W.P. and E.P.B. performed additional bioinformatic analysis. P.J.S., T.P.C., R.S., R.E.T. and J.A.S. generated and processed DHS data. D.M.M. helped with replication analysis. P.J.P. supervised all analysis. G.H.K. coordinated the entire project. P.V.K., G.H.K. and P.J.P. wrote the manuscript, with contributions from S.C.R.E., M.I.K., V.P., Y.B.S., N.C.R., A.A.A. and A.M.

Author Information The data are available from the modENCODE site (<http://www.modencode.org>). GRO-Seq data are available from Gene Expression Omnibus (GEO, GSE25321). Reprints and permissions information is available at www.nature.com/reprints. The authors declare no competing financial interests. Readers are welcome to comment on the online version of this article at www.nature.com/nature. Correspondence and requests for materials should be addressed to P.J.P. (peter_park@harvard.edu) or G.H.K. (karpn@fruitfly.org).

METHODS

Growth conditions. ML-DmBG3-c2 cells were obtained from DGRC (<https://dgrc.cgb.indiana.edu/>), and S2-DRSC cells were from the DRSC (<http://www.flyrnai.org/>). All cell lines were grown to a density of $\sim 5 \times 10^6$ cells ml^{-1} in Schneider's media (Gibco) supplemented with 10% FCS (HyClone). 10 μg ml^{-1} insulin was added to the ML-DmBG3-c2 media.

Antibodies. Antibodies are listed in Supplementary Table 1. Commercial antibodies against modified histones were tested by western blot for the lack of cross-reactivity with the corresponding recombinant histone produced in *Escherichia coli* and non-histone proteins from embryonic nuclear extracts. Antibody specificity was further assayed by western dot/slot blot against a panel of synthetic modified histone peptides. Only antibodies that showed <50% of total signal associated with non-histone proteins, and more than fivefold higher affinity for the corresponding histone peptide, were used in ChIP experiments.

The specificity of antibodies against chromosomal proteins was tested by western blots with nuclear extracts prepared from mutant flies or S2 cells subjected to RNAi knockdown⁴⁷. An antibody was considered specific if it recognized a major band of expected mobility that was absent in the sample prepared from mutant flies, or diminished twofold or more after RNAi depletion. When possible, distributions of a chromosomal protein were mapped with two antibodies generated against different epitopes (see Supplementary Fig. 17). Data from chromatin proteins for which only one antibody was available were validated by comparison with published genomic distributions for a different component of the same complex, or to published genomic distributions generated with a different antibody.

ChIP and microarray hybridization. Crosslinked chromatin from cultured cells was prepared as described²⁸ with the following modifications. Before ultrasound shearing, cells were permeabilized with 1% SDS, and shearing was done in TE-PMSF (0.1% SDS, 10 mM Tris-HCl pH 8.0, 1 mM EDTA pH 8.0, 1 mM PMSF) using a Bioruptor (Diagenode) (2 \times 10 min, 1 \times 5 min; 30 s on, 30 s off; high power setting).

ChIP was performed as in ref. 28 and immunoprecipitated DNA was amplified using the whole genome amplification kit (WGA2, Sigma) according to the manufacturer's instructions (chemical fragmentation step was omitted). The amplified material was labelled and hybridized to *Drosophila* Tiling Arrays v2.0 (Affymetrix) as in ref. 28.

Processing of ChIP data. At least two independent biological replicates were assessed for each ChIP profile. The \log_2 intensity ratios (M values) were calculated for each replicate. The profiles were smoothed using local regression (lowess) with 500 bp bandwidth, and the genome-wide mean was subtracted. The regions of significant enrichment were determined as clusters of at least 1 kb in length, with gaps no more than 100 bp where M value exceeds a statistically significant (0.1% false discovery rate (FDR)) enrichment threshold. The set of biological replicates was deemed consistent if the enriched regions from individual experiments had a 75% reciprocal overlap, or if at least 80% of the top 40% of the regions identified in each experiment were identified in the other replicate (before comparison the replicates were size-equalized by increasing the significance threshold for a replicate with more enriched sequence). The data from individual replicates were then combined using local regression smoothing, and used for all of the presented analysis, unless noted otherwise.

DNase I hypersensitivity. Digital DNase I-Seq assays were performed as described previously⁴⁴. The sequenced reads were aligned to the Berkeley *Drosophila* Genome Project release 5 (BDGP.R5) genome assembly, recording only uniquely mappable reads. To detect DNase I hypersensitive sites, hotspot positions were identified based on a 300-bp scanning window statistic (Poisson model relative to 50 kb background density, Z -score threshold of 2), and peaks of read density were selected within the hotspots using randomization-based thresholding at 0.1% FDR. The set of high-magnitude DHSs analysed here (except for Supplementary Fig. 23) was identified as a subset of all peaks that show statistically significant enrichment

over the normalized genomic DNA read density profile (using a 300-bp window centred around the peak, binomial model, with Z -score threshold of 3). This method controls for copy number variation and sequencing/mapping biases; however, it may also reduce the sensitivity of DHS detection. In the DHS chromatin profile clustering analysis (Fig. 5a, relevant Supplementary figures), DHSs found within 1 kb of another DHS were excluded if their enrichment magnitude (relative to genomic background) was lower (to avoid showing the same region more than once).

RNA sequencing. The preparation of RNA-Seq libraries and sequencing is described in ref. 45. The sequenced reads were aligned to the BDGP.R5 genome assembly and annotated exon junctions, recording only uniquely mappable reads. The RPKM (reads per kilobase of exonic sequence per million reads mapped) was estimated for each exon. The total transcriptional output of each annotated gene was estimated based on the maximum of all exons within the gene. The presented analysis uses $\log_{10}(\text{RPKM} + 1)$ values unless otherwise noted.

GRO sequencing. Global Run-On library was prepared from S2 cells and sequenced as described³¹. The reads were aligned to the BDGP.R5 genome assembly, recording only uniquely mappable reads. The smoothed profiles of reads mapping to each strand were calculated using Gaussian smoothing ($\sigma = 100$ bp). The analysis uses $\log_{10}(d + 1)$, where d is the smoothed density value.

Short RNA data processing. The short RNA data for S2 cells was generated by ref. 30, and was aligned and processed in the same way as the GRO-Seq data.

Chromatin state models. To derive a 9-state joint chromatin state model for S2 and BG3 cells (Fig. 1a), the genome was first divided into 200-bp bins, and the average enrichment level was calculated within each bin based on unsmoothed \log_2 intensity ratio values taking into account individual replicates, using all histone enrichment profiles and PC to discount the genome-wide difference in S2 H3K27me3 profiles. The bin-average values of each mark were shifted by the genome-wide mean, scaled by the genome-wide variance, and quantile-normalized between the two cells. The hidden Markov model (HMM) with multivariate normal emission distributions was then determined from the Baum-Welch algorithm using data from both cell types, and 30 seeding configurations determined with K -means clustering. States with minor intensity variations (Euclidian distance of mean emission values <0.15) were merged. Larger models (up to 30 states) were examined, and the final number of states was chosen for optimal interpretability.

An extensive discrete chromatin state model (Supplementary Fig. 11) was calculated as described in ref. 20. The model was trained using a 200-bp grid with binary calls (enriched/not enriched). The binary calls were made based on a 5% FDR threshold determined from ten genome-wide randomizations for each mark. For H1, H4 and H3K23ac regions of significant depletion rather than enrichment were called.

Regions of enrichment for individual marks. To determine contiguous regions of enrichment for individual marks, a three-state HMM was used, with states corresponding to enriched, neutral and depleted profiles (normally-distributed emission parameters: ($\mu = [-0.5 \ 0 \ 0.5]$, $\sigma^2 = 0.3$). The enriched regions were determined from the Viterbi path. The HMM segmentation was applied to unsmoothed M value data taking into account individual biological replicates. The genes were clustered based on the combinatorial pattern of occurrence of enriched regions (coding exons and state panels were not used for clustering).

Classification of enrichment profiles. Clustering of chromatin signatures around TSSs (Fig. 4a), PREs (Fig. 4b) and DHSs (Fig. 5a and relevant Supplementary Information sections) was determined using the Partitioning Around Medoids algorithm. For clustering, each profile was summarized with average values within bins spanning ± 2 -kb regions. One-hundred-base-pair bins were used for the central ± 500 -bp region, 300-bp bins outside.

47. Clemens, J. C. *et al.* Use of double-stranded RNA interference in *Drosophila* cell lines to dissect signal transduction pathways. *Proc. Natl Acad. Sci. USA* **97**, 6499–6503 (2000).

natureOUTLOOK

NUTRIGENOMICS

23/30 December 2010 / Vol 468 / Issue No. 7327



COVER ART: NIK SPENCER

Supplements Editor
Herb Brody

Associate Editor
Michelle Grayson

Sub Editor
Tony Scully

Production Editor
Donald McDonald

Art Editor
Wes Fernandes

Picture Researcher
Madeline Hutchinson

Production Controller
Emilia Orviss

Web Production
Terhi Raukko

Sponsorship
Reya Silao, Stephen Russell, Yvette Smith, Gerard Preston

Marketing
Elena Woodstock, Hannah Phipps

Project Manager
Helen Anthony

Magazine Editor
Tim Appenzeller

Managing Editor
Nick Campbell

Editor-in-Chief
Philip Campbell

Food. Our need for it is primal, but our relationship with it is complex and ever-changing.

For many in the developed world, eating has become a leisure pursuit, and cooking a hobby. But our bodies are still hard-wired for a tougher world where food means survival. Our sense of taste, for example, evolved to be a front-line defence against toxins and a sensor to help detect the most energy-rich fare. However, our innate craving for sweets and fats now seems to be leading us down a path of bodily destruction.

Food affects people differently. Current nutritional research involves looking beyond ingredients in an attempt to understand the effects of food at genetic and epigenetic levels. From the first milk meal we take, through feast and famine; our genes influence our diet, and nutrients — or lack of them — affect gene expression.

Regional differences in food and culture have left their mark on our genome. Around the world, populations have adapted to their diet to make the most of local resources. In some instances, a foodstuff can protect against deadly infection, giving selective advantage to those who can readily digest it.

Nutrition has also directed the evolution of our species. Only *Homo sapiens* and our extinct hominin cousins have used fire to manipulate raw food, thereby creating safer, easily digestible and tastier recipes. Combined with the use of tools and an omnivorous, wide-ranging appetite, the advent of cooking increased the energy yield for metabolism and fed our enlarging brains.

Because food is packed full of complex, biologically active molecules, the fact it has an impact on our health is no surprise. Yet teasing apart the effects of each component on the body is a tall task, and one that will continue for many years to come. Some people predict an age of diets customized to individual energy needs and disease susceptibility. But no matter how good the science is, or how well we are able to exploit food as an agent of healthfulness, we will still be eating for pleasure for some time yet.

We are pleased to acknowledge the financial support of Nestlé Research Center in producing this Outlook. As always, *Nature* retains sole responsibility for all editorial content.

Michelle Grayson

Associate Editor, Nature Outlook.

CONTENTS

- S2 INTERDISCIPLINARY RESEARCH**
Big science at the table
Nutrition enters the twenty-first century
- S5 DEVELOPMENT**
Mother's milk: A rich opportunity
Breast milk research is surprising scientists
- S8 EVOLUTION**
The first supper
Did food make us what we are?
- S10 HEALTH**
Edible advice
Can diets prevent disease?
- S13 DIVERSITY**
Of beans and genes
Diet-related genes evolve along cultural lines
- S16 HISTORY**
The changing notion of food
Pioneers and breakthroughs in nutrition
- S18 TASTE**
More than meets the mouth
Beyond the flavour of food
- S20 EPIGENETICS**
Tales of adversity
Long-term effects of prenatal malnutrition
- S21 TECHNOLOGY**
A flavour of the future
Biomarkers, smart technology and social networks
- COLLECTION**
- S23 Chronic high-fat diet in fathers programs β -cell dysfunction in female rat offspring**
Sheau-Fang Ng et al.
- S27 Dairy intake associates with the IGF rs680 polymorphism to height variation in periadolescent children**
GV Dedoussis et al.
- S33 Functional genomics: Vitamin D and disease**
Mary Muers
- S34 CLOCK gene is implicated in weight reduction in obese patients participating in a dietary programme based on the Mediterranean diet**
M Garaulet et al.

Nature Outlooks are sponsored supplements that aim to stimulate interest and debate around a subject of interest to the sponsor, while satisfying the editorial values of *Nature* and our readers' expectations. The boundaries of sponsor involvement are clearly delineated in the *Nature Outlook* Editorial guidelines available at http://www.nature.com/advertising/resources/pdf/outlook_guidelines.pdf

CITING THE OUTLOOK

Cite as a supplement to *Nature*, for example, *Nature* Vol XXX, No. XXXX Suppl, Sxx–Sxx (2010). To cite previously published

articles from the collection, please use the original citation, which can be found at the start of each article.

VISIT THE OUTLOOK ONLINE

The *Nature Outlook Nutrigenomics* supplement can be found at <http://www.nature.com/nature/outlook/nutrigenomics>. All featured articles will be freely available for 6 months.

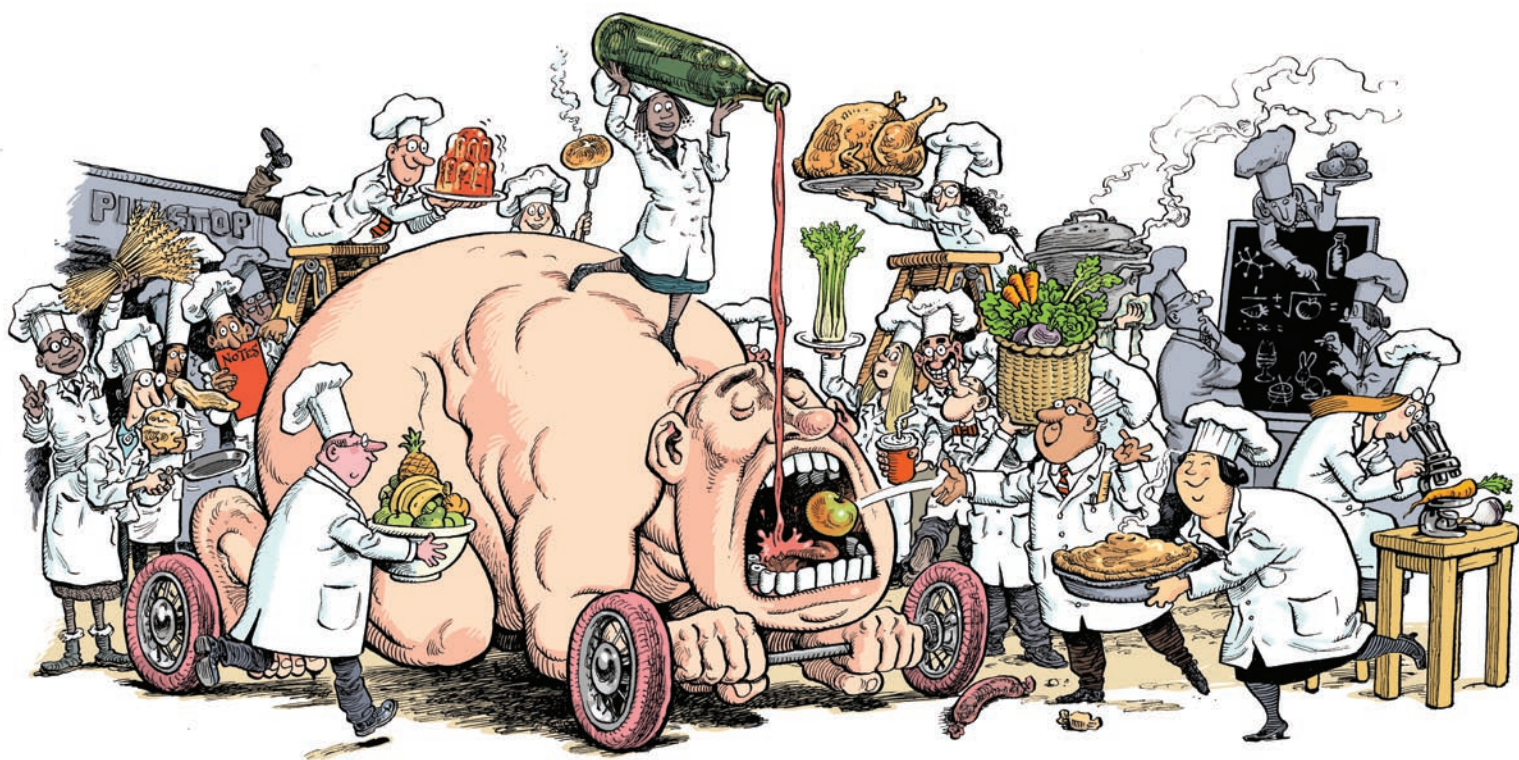
SUBSCRIPTIONS AND CUSTOMER SERVICES

For UK/Europe (excluding Japan): Nature Publishing Group, Subscriptions, Brunel Road, Basingstoke, Hants, RG21 6XS, UK.

Tel: +44 (0) 1256 329242. Subscriptions and customer services for Americas – including Canada, Latin America and the Caribbean: Nature Publishing Group, 75 Varick St, 9th floor, New York, NY 10013-1917, USA. Tel: +1 866 363 7860 (US/Canada) or +1 212 726 9223 (outside US/Canada). Japan/China/Korea: Nature Publishing Group – Asia-Pacific, Chiyoda Building 5-6th Floor, 2-37 Ichigaya Tamachi, Shinjuku-ku, Tokyo, 162-0843, Japan. Tel: +81 3 3267 8751.

CUSTOMER SERVICES

Feedback@nature.com
Copyright © 2010 Nature Publishing Group



INTERDISCIPLINARY RESEARCH

Big science at the table

Researchers are adopting the tools of bioinformatics and pharmaceuticals to study and interpret the ever-growing body of data on the interplay between diet and genes.

BY LUCAS LAURSEN

José Ordovas sips a mint tea in a languid café in Madrid, Spain. His eyes scan two mobile phones as he confirms his next appointments. In conversation, he switches effortlessly between Spanish and English to find the right expressions. If the geneticist seems to be moving on a different wavelength from the other patrons, he could blame it on the jet lag: he has just flown from Boston where it's now 5am. This is his third overseas trip this month, but Ordovas contends his frequent visits from Tufts University, where he's based, to Europe have no adverse effects. "For me the time difference doesn't matter, I'm up at 4am to make calls to Europe when I'm home anyway, and then I'm up late on calls to California," he says.

Ordovas embodies the hustle and bustle of the 'big science' approach that has changed

nutrition research in the past decade. This field, once confined to small groups of researchers studying the effects of single nutrients — such as particular vitamins or proteins — on a few dozen volunteers, is now adopting the heavy-lifting tools developed for genetics and pharmaceutical research. It also has a catchy name: nutrigenomics. And the more that researchers learn how our genes interact with our diet, the more they appreciate the deeper insight gained by an interdisciplinary approach. Such knowledge could lead to breakthroughs in our understanding of risk factors for diabetes and cardiovascular disease (see *Edible advice*, page S10) or, for example, improve the design of weight-loss diets.

Nutrigenomics is starting to reveal that a person's diet is more than the number of calories they eat or the ratio of proteins to carbohydrates or fats. Those are important, but the analogy of human metabolism as a car engine that requires

a certain type and amount of fuel does not hold up in the age of whole-genome analysis. Nutrition researchers are realizing that our diet does more than just fire our pistons. It is as if the fuel we consume can reach out from the combustion chambers in the engine — through the genetic pathways that govern our metabolism — and tune the engine mid-race.

Multiply those fine adjustments by every possible mutation in each gene of the human genome, perhaps 10 million tweaks in total, and you have an idea of the scale of Ordovas' task. "The only way to realize this concept is via big science," he says.

Ordovas studies how food influences cholesterol and other cardiovascular health indicators in large groups of people. "You take large numbers of individuals with a well-characterized

➔ **NATURE.COM**
for more on how big
science is shaping
nutrigenomics
go.nature.com/kqZpjV

ILLUSTRATIONS BY DAVID PARKINSON

diet,” says his collaborator John Mathers, a nutrition scientist at the University of Newcastle, UK, “and you do a genomic study to ask the question: how does diet interact with the genome to produce a particular phenotype?” Cardiovascular health might be nutrigenomics’ strongest application to date, Mathers says, but researchers are also beginning to study the long-term effects of nutrition on the brain and on ageing.

ADOPTING AND ADAPTING

Answering these questions requires examining how small genetic mutations, called single nucleotide polymorphisms (SNPs), affect the production of enzymes and hormones that control metabolism. There are thousands of these mutations in each individual and countless feedback loops, meaning that researchers in the emerging area of metabolomics must employ sophisticated bioinformatics models. “A lot of those tools were developed for pharmaceutical studies and now have become almost commonplace in all areas of biology, including nutrition,” says Mathers.

Progress in pharmaceutical research has stimulated improvements in microarrays, high-throughput sequencing, polymorphism identification and DNA methylation technologies, used to scan for novel receptors that might respond to potential drug molecules, says bioinformaticist Chris Evelo of Maastricht University in the Netherlands. In large clinical trials, researchers often collect information about multiple levels of an individual’s health before and after the trial in case a drug targeting the heart has an unanticipated effect on the liver, for instance. Likewise, nutrigenomics specialists are concerned with the broader effects of any experimental dietary intervention. “This

system-wide approach has been the rule in nutrigenomics research all along. There often are no clear target genes for diet changes,” says Evelos. This problem forces researchers to seek out subtle interactions among many elements of the metabolic system and related genes.

In addition to epidemiological studies, which examine global populations without interfering with anybody’s diet, many researchers in

Nutrition research has experienced the move towards more pharma-like genome-wide intervention studies.

nutrigenomics are employing intervention studies, which are more like the clinical trials used by drug and medical device makers. “In this other type of study you deliberately modify the nutritional exposure

of cells, animals or people,” explains Mathers, “and then measure the expression of genes using whole genome expression arrays to try to understand how altered nutritional exposure regulates gene expression and, ultimately, phenotype.” Nutrition researcher Lynnette Ferguson at the University of Auckland in New Zealand has experienced the move towards more pharma-like genome-wide intervention studies. She notes that, as recently as 2003, she and her colleagues were “talking about single genes, single nutrients.” Yet many promising treatments based on single molecules had clear effects in the lab but never passed animal trials. This is because, as Evelo says, “if you push the system in one place it will compensate through another mechanism and in the end the wished for effect does not occur.” Since then, rapid improvements in microarrays and

‘deep sequencing’ technologies have enabled researchers to consider the impact of food down to the level of individual SNPs. It has also given them a more objective tool to measure what volunteers are actually eating, rather than relying on self-reporting.

Adopting technology from outside traditional nutrition science means adopting new research methods. “My own advantage was that I had been part of a cancer research programme,” says Ferguson. “I’ve watched the development of pharmaceuticals, seen my colleagues work with them and seen the sorts of models they use.” Ferguson’s team used high-throughput sequencing to screen human cells for modifications to the interleukin-12/23 receptor pathway — important for bowel health — that they suspected were caused by certain foods. This work helped them develop a cellular assay for measuring the effect of particular food components on gene expression in human cells. The next step is to validate whether such nutrient-genome interactions exist in animal models, before planning human trials, just as if they were testing a new drug.

GENETIC PROFILING

These tests will not be straightforward as not all people respond to dietary changes in the same way that not all people react to a particular medicine. Identifying different populations based on their genetic responsiveness is starting to show promise, according to Ordovas. In the best case scenario, researchers would screen individuals against panels of genetic risk factors. In the case of cholesterol, Ordovas and colleagues have found specific genetic differences between people whose cholesterol levels are affected by changing their diet and those who only respond to medication. Right now, doctors try patients on multiple diets before prescribing cholesterol-reducing drugs to avoid side effects. But with a reliable genetic screening test, doctors could prescribe drugs to patients unlikely to respond to dietary changes, saving time and helping reduce the harm caused by living with elevated cholesterol levels.

The majority of dietary effects are subtle, however, and certain genetic profiles might be relatively rare and more difficult to screen. This requires large cohorts to detect and identify signals. “In any gene, there are a few key polymorphisms that we scan, but others will be less common, may not be on the chip we use, or in the specific ethnic group that we are studying, but could still cause disease,” says Ordovas. That means he may need to scan ever-larger numbers of volunteers — perhaps into the hundreds of thousands. Unlocking the massive datasets that will emerge will, of course, require dozens of researchers — outnumbering the volunteers that participated in Ordovas’ studies in the 1980s (a fact he mentions when he gives presentations about this burgeoning field).

MEETING OF MINDS

New conferences catering for nutrigenomics

4th Asia Pacific Nutrigenomics Conference

21–25 February 2010, Auckland, New Zealand
Exploring the theme of gut health as influenced by both genetics and the microbiota. Around 200 people attended from 19 countries.

7th nuGO Week

31 August – 3 September 2010, Glasgow, UK
An overarching theme of metabolic health, with sessions on biomarkers, modelling tools and personalized nutrition. Around 130 people attended.

1st International Conference on Nutrigenomics

26–29 September 2010, Sao Paulo, Brazil
Discussions centred on the interaction between diet and genes, and how this enables personalized health and disease prevention, particularly in Latin America.

1st Global HealthShare Initiative Workshop

18–20 October 2010, Davis, California
An invitation-only event that jointly addressed issues of nutrition and immunity in the developing world.

4th Congress of the International Society of Nutrigenetics/Nutrigenomics

17–20 November 2010, Pamplona, Spain
Reviewing developments in the related fields of nutrigenomics, nutrigenetics and nutriepigenomics, in disease prevention.

On top of the new mentality and tools, any new scientific discipline needs a way to share data. Through a collaboration called the European Nutrigenomics Organisation (NuGO), Ben van Ommen at the Netherlands Organisation for Applied Scientific Research (TNO) recruits contributors to the Nutritional Phenotype Database (dbNP). Its goal is to combine data from many different areas of biology, including genetics, transcription, protein production, metabolism and behavioural data. “The European Bioinformatics Institute made Array Express and the US National Center for Biotechnology Information has made Gene Expression Omnibus and they store transcriptome data,” says van Ommen. “That’s good but it’s not good enough for us. Nobody does just a transcriptome study or just a metabolomics experiment — everybody does it all together.”

Ordovas agrees: “When I began studying lipids I only looked at the biochemistry. We all used to be like rhinoceros poachers who took the horn and left the carcass, but now we have more tools and collaborators and everyone extracts information from all the data in a study.”

MAKING TEAMWORK PAY OFF

This type of ‘extensive phenotyping’, quantifying all relevant parameters, is already paying off. A NuGO study led by Gertruud Bakker found that an experimental anti-inflammatory diet in 36 healthy but overweight men increased the concentration of adiponectin, an anti-inflammatory protein, in the bloodstream. By monitoring hundreds of other metabolism-related proteins and metabolites of

blood cells and adipose tissue, the team identified more than 500 other diet-driven changes. These included improving the ratio of omega-3 to omega-6 anti-inflammatory precursors in blood plasma and lowering levels of oxidative stress-causing prostaglandin in urine. If the team had used only single-

Selecting collaborators at first was “like early dating situations”.

metabolite methods, van Ommen says, they “would only have detected an effect on adiponectin.”

Adapting pharmaceutical technologies to food isn’t the only challenge for researchers: “it’s also how you deal with all that data,” says Evolos. Some computer models aim to describe observations whereas others try to replicate or predict. “We are trying to integrate those two approaches,” says Evelo. This could help researchers working on different facets of the same problem to better understand one another’s results, forge new collaborations, and help trace biological problems from the point where food molecules interact with the transcriptome to the symptoms that are presented in a doctor’s examination room.

As a proof of principle, the NuGO team used dbNP to track the development of human-like insulin resistance. Evelo and colleagues fed mice a high-fat diet and performed genome-wide transcriptome analysis, tissue sampling, plasma sampling and proteome analysis. They observed that the first signs emerged in a type of fat tissue. This finding neatly explains previous studies that suggested the ratio of saturated to unsaturated fatty acids affects whether a person develops insulin resistance.

In addition to the database, there are a slew of new meetings (see Meeting of minds, page S4). Ferguson established an annual retreat to help New Zealand’s nutrition and genomics researchers, from academia and industry, find common ground. “I feel that the slight tension between different priorities [in these groups] has actually been a benefit,” says Ferguson. One resulting food developed from genetic research on Crohn’s disease is a bread less likely to inflame an irritable bowel.

Nutrigenomics researchers also make the most of social networking to stay in touch. One researcher uses the Twitter handle @nutrigenomics; Ordovas and Jim Kaput, head of the FDA’s personalized medicine division, often make Skype calls during the weekend. If this side of big science sounds a bit like cultivating a long-distance relationship — it is, says Ferguson. Selecting collaborators at first was “like early dating situations: did we want to work together? Did we want to work with other partners?” Now that funding is available, there are many more people expressing an interest. Ferguson and collaborators

must now ask the hard questions of ‘what’s your skill set?’ and ‘what can you contribute?’ before inviting would-be partners on board.

The near-term future of nutrigenomics is almost certain: researchers are already hustling to persuade government and funding bodies to finance follow-up studies on the latest research by asking the same questions but on a more ambitious scale — testing hypotheses derived from cell cultures in animals and humans.

LONGER TO WAIT

Some researchers question how useful individual nutrition advice will be in the near term. “Personalized nutrition advice may not be helpful to the general public if they don’t know their own genetics,” says Albert Koulman, an analytical chemist at the Medical Research Council in Cambridge, UK. But consumer genomic analysis provokes more questions, such as who pays, who gets the results and whether it affects health insurance rates. “There’s much more than just the biology, there’s the business side and the ethics. We’re still just scouting scenarios,” says van Ommen.

Commercial pet food today may be a preview of the kind of food categories humans might find in future markets, according to Kenneth Kornman, head of InterLeukin Genetics. “Pet foods I get for my dog are age-categorized, or categorized by sensitivities such as gastrointestinal problems,” he says. Dietary needs for individuals also change over the course of their lifetime and from one group of people to the next.

Food manufacturers could one day offer the same choices pet food makers do today — with the additional cost of ensuring that the food is safe for human consumption. There is a big cost to launching such a food, notes Kornman. “You’d need to have a reasonable idea that you’ll earn it back.” Yet few companies know how to market genetically customized nutrition to customers or how to successfully patent a diet consisting of widely available foods, he says.

Instead, nutrigenomics researchers face the challenge of identifying and measuring a much more subtle state than disease: health. “Optimal health is much more than the absence of disease,” says van Ommen, “so we need a different set of biomarkers, not of disease, but of health.”

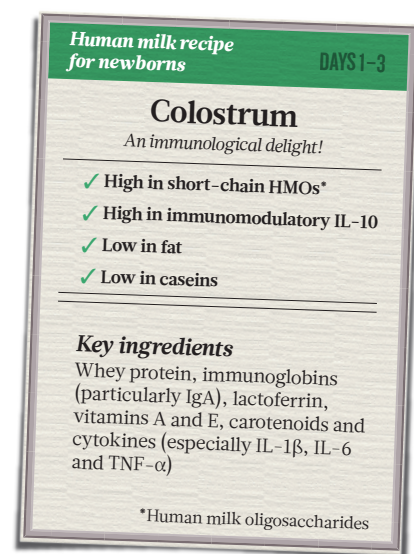
Measuring that will require understanding more than just the chemistry of our food or the on-off switches of our genes. “We’ve started to better appreciate the fact that it’s not just the diet and it’s not just the genetic factors but it is an interaction of the two that permits a metabolic change that gets translated in a complex disease over time,” says Kornman. It may be a tricky tune to follow, but nutrigenomics researchers are all ears. ■

Lucas Laursen is a journalist based in Madrid.





I. HOOTON/SCIENCE PHOTO LIBRARY



DEVELOPMENT

Mother's milk: A rich opportunity

Research on the contents of milk and how breast-feeding benefits a growing child is surprising scientists.

BY ANNA PETHERICK

Should you ever need to mix formula milk for a tamarin wallaby, you will face a complicated recipe. During its 300 days in the pouch between birth and weaning, the baby wallaby, or joey, drinks different milk almost on a weekly basis.

Early on, the joey needs colostrum, which is packed with antibodies. After 60 days, the formula should be rich in asparagine-containing peptides, which are thought to help brain development. Ninety days later, the baby wallaby will

need a dose of sulphur-containing amino acids, such as cysteine and methionine, which will cause hair follicles and nails to grow.

For healthy development, the number of calories contained in the milk must also rise, such that the joey is weaned from milk that is four and a half times as energy rich as the liquid it first drank. This compositional sequence appears to be entirely dictated by the mother's body. And, bizarrely, her teats can function independently, with each baby wallaby effectively stuck to one teat for the first 200 days in the pouch. In fact, a joey may have a pouch

mate of a different age that feeds on an adjacent teat — and which receives milk of a different composition, appropriate for its age¹.

Unlike a wallaby's, human milk does not change so radically over time because the developmental signals, which wallabies transfer in milk, can be delivered through the human placenta. The major constituents of human milk — the fat, protein and carbohydrate — vary little over the course of lactation. But a closer analysis reveals important time-dependent variation in the complement of bioactive ingredients in human milk — the molecules and cells that have biological functions beyond fuelling metabolism and providing the raw materials for infant growth. Finding what these ingredients are and what they do drives much of today's lactation research.

A MAMMALIAN MIXTURE

Until recently, the study of human lactation was conceived mainly from the perspective of public health. Now the trend is to approach the subject from an evolutionary standpoint. This perspective presumes that an infant should breastfeed as much as possible to maximize its chances of survival, whereas a mother must balance her current metabolic investment in milk production with her potential investment in future offspring.

For example, evolutionary theory suggests that mothers should invest more in feeding sons because a successful son can produce many more offspring than a daughter. Several recent studies support this view by identifying clear differences in the breast milk consumed by males and females. In humans, for example, baby boys receive milk that has substantially more fat and protein than the milk girls get².

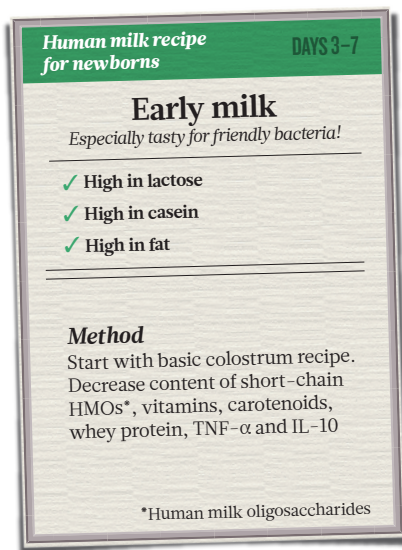
➔ NATURE.COM
more about the science behind breastfeeding
go.nature.com/95CsV7

In rhesus macaques, sons drink milk with a higher concentration of cortisol, a hormone that modulates ►

► metabolism, even though their mothers have no more cortisol circulating in their blood than when nursing a daughter. It is unclear whether this cortisol-related sex difference has a function. But there are clues: young male macaques that consume milk containing high levels of the hormone develop bold behaviour, whereas cortisol in milk appears to have no influence on female macaque infants³. Whether this has a parallel in humans is yet to be determined.

A second major shift in human lactation research entails the incorporation of new tools to answer traditional questions — such as comparing the effects of breast and formula feeding — and to grapple with evolutionary and functional issues. Human milk is dilute compared to the milk of other placental mammals, but it does contain some surprising ingredients. Advances in high-throughput mass spectrometry, for example, have revealed the existence of more than 200 human milk oligosaccharides (HMOs). Calito Lebrilla, an analytical chemist at the University of California, Davis, has found that mothers seem to produce individual complements of about 100 HMOs — but no one has figured out why different mothers produce different sets of HMOs, or even if it is the same complement of HMOs for each child.

Although they are carbohydrates, HMOs do not appear to nourish infants. Instead they feed certain gut bacteria, giving them a competitive edge over other species. “When a child is born its gut is rapidly populated by pathogenic bacteria,” says Lebrilla. “However as the child is fed human milk the population changes to beneficial



species” *Bifidobacterium infantis*, which protects against diarrhoea, is particularly efficient at metabolizing the small-mass HMOs that are abundant in early lactation⁴. So breast milk gives *B. infantis* an advantage over other species in establishing a gut population. “The mother is therefore ‘selecting’ specific bacteria to grow in the infant’s gut by her HMOs,” says Lebrilla.

Furthermore, some HMOs can inhibit harmful bacteria and viruses directly. For example, certain HMOs block the binding of *Campylobacter jejuni*, the most common cause of bacterial diarrhoea, to intestinal mucosa, and thereby inhibiting pathogenesis⁵.

Human milk also delivers some microbes directly to the gut. Breast milk is laced with several species of lactic acid bacteria from the mother’s intestine that are thought to travel to her mammary glands inside white blood cells. Most of these species inhibit pathogenic bacteria by secreting hydrogen peroxide and compounds called bacteriocins.

The past decade has seen a large extension in the list of immunological factors detected in human milk. Breast milk was long thought to provide only passive immunity to infants, through maternal antibodies in the form of secretory immunoglobulin A. However, the newly identified crop of immune-regulatory proteins could be prompting and modulating development of the infant’s own immune system. Of particular interest are cytokines, which orchestrate the immune system by signalling between its cells.

There is even evidence that breast milk influences gene expression in infant gut cells. In a pilot study, Sharon Donovan, a paediatric nutritionist at the University of Illinois, and Robert Chapkin, a biochemist at Texas A&M University, extracted RNA from exfoliated intestinal cells from several 3-month-old infants. They assessed the statistical difference in RNA expression between breast- and formula-fed infants. Several of the genes that varied were identified as putative master genes, which control the expression of other genes. Most of these genes encode transcription factors associated with angiogenesis and wound repair — including *EPAS1*, a gene that

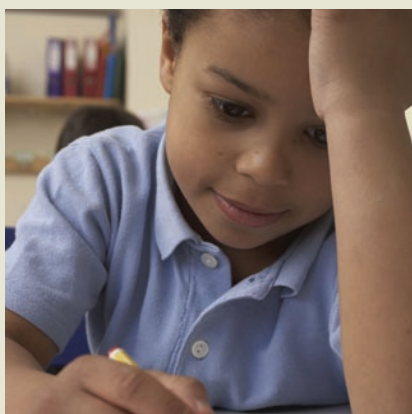
BRAINY BABIES

Does breast milk make you smarter?

Between late 2002 and the spring of 2005, 13,889 Belarusian children of about six years of age took an IQ test and had their reading and writing skills evaluated by teachers. The mothers of about half of them had been encouraged to breastfeed under a World Health Organization (WHO) programme called the Baby-Friendly Hospital Initiative. As a result, these mothers were seven times more likely to have exclusively breastfed until their child was 3-months old.

Results of this study, called Promotion of Breastfeeding Intervention Trial (PROBIT), showed that the 6-year-olds whose mothers were part of the WHO initiative had better academic ratings from their teachers and IQ scores on average 5.9 points higher¹⁰. “PROBIT found lots of health benefits in the first year of life,” says Michael Kramer, an epidemiologist at McGill University in Montreal, Canada, “but over the longer term the only difference was cognitive ability.”

No one is quite sure what causes this intelligence boost. But one 2007 study by



Tests point to higher IQ in breast-fed children.

Duke University psychologist Avshalom Caspi has identified a candidate: a gene that appears to mediate the effects of human milk on brain development¹¹. Caspi and colleagues trawled the Kyoto Encyclopaedia of Genes and Genomes (KEGG) database for genes involved in the

metabolism of long-chain polyunsaturated fatty acids. These acids are linked to several aspects of neuron development. Two such fats — docosahexaenoic acid (DHA) and arachidonic acid (AA) — are present in human breast milk, but not in cows’ milk or most infant formulas.

The KEGG search identified a gene on chromosome 11, called *FADS2*, which is both regulated by dietary AA and DHA and also encodes an enzyme that catalyses metabolism of these two acids. One specific variant of the *FADS2* gene was present in more than 90% of the cohort in the study. Researchers found that only the breastfed babies who had this specific *FADS2* variant exhibited an IQ advantage. The research implies that fatty acid metabolism could be part of the missing link between breastfeeding and IQ. This *FADS2* variant was estimated to account for a difference of 4.1 IQ points, which goes a long way towards explaining the 5.9 IQ points difference found in the PROBIT trial.

T. HALL/PHOTOLIBRARY.COM

is transcribed three times as much in the gut cells of breastfed infants⁶.

Donovan and Chapkin's study is the first evidence that breast milk — rich in natural bacteria — affects infant gene expression, and Donovan cautions about over-interpreting their findings. This is, however, likely to be an expanding area of research as probiotics become more commonly used as ingredients in formula milk. "We have no idea how these are potentially affecting gene expression," says Donovan.

Over the years, the 'breast versus formula' debate has become polarized, and several researchers contacted for this article complained that either breastfeeding advocacy groups or formula companies had exaggerated their findings in the past. Donovan's recent gene expression study was sponsored by a formula milk manufacturer, but she is applying for US National Institutes of Health funding for further studies to avoid the criticism that comes with being commercially funded.

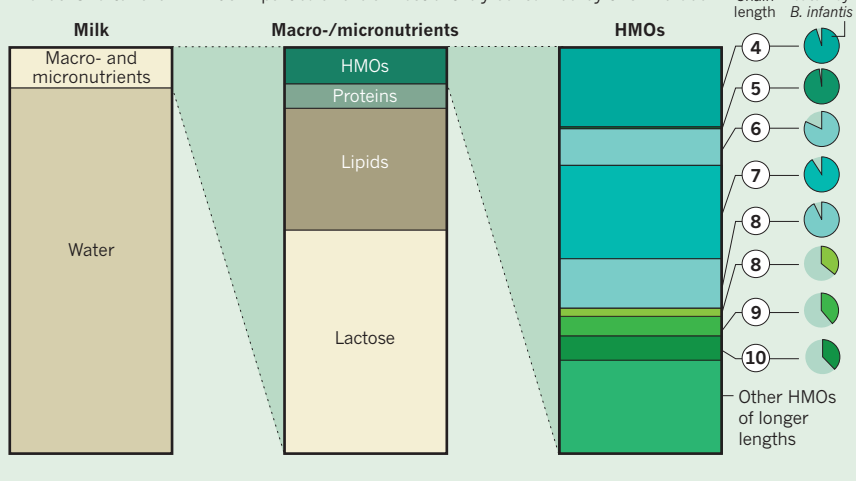
HEALTH CONTROVERSIES

Researchers have tried to disentangle the effects of feeding an infant formula rather than breast milk. "The vast majority of studies tend to gravitate towards breast milk as better, rather than equal, but the evidence varies in quality," says Jonathan Wells, who studies human ecology at University College London. "Many of the accepted benefits of human milk relate to avoiding pathogens." And while these pathogens might be less dangerous to a baby in a more medically advanced society than in a developing one, breast milk still offers advantages to all infants. Breastfeeding has consistently been found to protect against necrotizing enterocolitis (in which portions of the bowel tissue die) in pre-term infants, and against diarrhoea and ear infections in full-term infants.

Impacts on health in later life stand out less clearly in the data, although associations between formula feeding and type 2 diabetes and inflammatory bowel disease have been observed. Some meta-analyses report that breastfeeding reduces the chance that a child will be obese at school age by about 20%. But these results are not conclusive. The largest breastfeeding trial, Promotion of Breastfeeding Intervention Trial (PROBIT), found no difference in the plumpness of two groups of six-and-a-half-year-old Belarusian children, where one group had been breastfed for much longer before the introduction of formula milk⁷.

WHAT'S IN HUMAN MILK

Human milk oligosaccharides (HMOs) are food for friendly bacteria like *Bifidobacterium infantis*. Shorter chain HMOs in particular are almost entirely consumed by this microbe.



There was also no difference between these groups in the prevalence of asthma or allergies⁸. PROBIT did, however, show an intriguing link between breastfeeding and intelligence (see Brainy babies, page S6).

The breastfeeding-IQ association had been reported before, but what made PROBIT's results important was the size of its dataset. It is critical to have a very large sample size in order to eliminate confounding factors. Qualities such as obesity and IQ often vary across rich countries in similar patterns to the tendency of mothers to breastfeed. In developed countries, wealthier women are more likely to breast-feed — but they are also generally slimmer, better educated and spend more time talking to their babies.

It might be that certain ingredients in formula milk are responsible for later weight issues. Results from the European Childhood Obesity Project supports the 'early protein hypothesis', which holds that higher levels of protein found in standard infant formulas programme the body to become fatter in later years⁹. The project randomized 1,000 European infants to

receive either formula of high-protein concentration (standard formula), formula of low-protein concentration (similar to the protein content of human milk), or breast milk. The result: unlike the high-protein group, the low-protein group grew no tubbier than the breastfed control group.

The diverse ingredients of an infant's first meal have an impact on its development, and no matter how much we tinker with the composition of formula milk it will always lack many of the trace constituents of human milk. As research identifies these substances, it increasingly seems they serve a role beyond direct nutritional benefit: that of communicating information to the infant about the environment and even the social structure around the mother, which affects the richness of her diet and her level of physical activity and therefore also affects her milk.

Wells believes that very young humans should be thought of as having to adapt to the mother's surroundings, rather than to the wider world. Indeed, the fact there are so many bioactive molecules in breast milk means that breastfeeding is an activity that empowers mothers. He adds, "The more we learn about the details of breast milk the more we realize that males have a little chance to influence their offspring by non-genetic pathways. Mothers have a very rich opportunity." ■

Anna Petherick is a journalist in Buenos Aires.

1. Lefèvre C. M. et al. *Genomics and Human Genetics*, **11**, 219-238 (2010).
2. Powe C. E. et al. *Am. J. Hum. Biol.* **22**(1), 50-54 (2010).
3. Sullivan E. C. et al. *Developmental Psychology* DOI: 10.1002/dev.20483 (2010).
4. Ward R. E. et al. *Appl. Environ. Microbiol.* **72** (6), 4497-4499 (2006).
5. Ruiz-Palacios G. M. et al. *J. Biol. Chem.* **278** (16), 14112-14120 (2003).
6. Chapkin R. S. *Am. J. Physiol. Gastrointest. Liver Physiol.* **298** (5), G582-589 (2010).
7. Kramer M. S. et al. *Am. J. Clin. Nutr.* **86**, 1717-1721 (2007).
8. Kramer M. S. et al. *Brit. Med. J.* doi: 10.1136 (2007).
9. Koletzko B. et al. *Adv. Exp. Med. Biol.* **646**, 15-29 (2009).
10. Kramer, M. S. et al. *Arch. Gen. Psychiatry* **65** (5), 578-584 (2008).
11. Caspi A. et al. *Proc. Natl. Acad. Sci. USA* **104** (47), 18860-18865 (2007).

Human milk recipe for newborns

WEEK 2 ONWARDS

Mature milk

Nourishment for growth!

✓ More milk

✓ Less fat

✓ Less whey protein

Method

HMO* content should be at half initial level. IL-1B, IL-6, vitamins and carotenoids also substantially reduced

Maintain concentration of lactose, IFN-γ, and casein

*Human milk oligosaccharides



EVOLUTION

The first supper

Diet-directed evolution shaped our brains, but whether it was meat or tubers, or their preparation, that spurred our divergence from other primates remains a matter of hot debate.

BY MICHAEL EISENSTEIN

Given the millions of years since our ancestors parted ways, it's unsurprising that a chimpanzee's idea of a good meal differs from our own. "When I visited our study site in Uganda, I followed a chimp in the forest for a day and tried to eat everything it ate," recalls Svante Pääbo, an evolutionary geneticist at the Max Planck Institute in Leipzig, Germany. "It's too disgusting and not digestible — you can't really do it."

Part of the reason is genetics. In 2008, Pääbo and colleagues found evidence for accelerated evolution of both the regulatory and coding sequences of diet-related genes shared by chimpanzees and humans¹. Many anthropologists now believe that radical changes in diet may have been a major driver of hominin evolution and possibly even the primary factor that propelled our genus *Homo* forward by enabling us to survive and thrive.

One evolutionary milestone was encephalization: an enlargement of the brain estimated to have begun roughly 1.8 million years ago when *Homo habilis* transitioned to *Homo erectus*. What powered this growth spurt remains a subject of ongoing debate.

MEAT AND POTATOES

A big brain is a huge investment in metabolic terms. One model advanced in the mid-1990s, the expensive tissue hypothesis, suggests our

ancestors settled that bill by gaining access to more nutrient-rich diets, which spurred brain growth while reducing gut size. Scientists have suggested that the wealth of vitamins, proteins and fats in meat was a major boon and there is evidence our ancestors used stone tools to carve up their food as early as 2.5 million years ago. An article published in *Nature* this year reported the find of 3.4 million year-old fossil bones scarred by cutting tools, pushing the date back further still to australopithecines.

"There's fairly decent evidence that meat was likely a piece of the diet of australopithecines," says Josh Snodgrass, an anthropologist at the University of Oregon, "but they were probably eating diets that were much more plant-based." Given the richness of nutrients in meat, Snodgrass believes that even minor changes would have had a big impact on caloric intake and contends that use of more sophisticated tools may have increased consumption of meat in early hominins. "Access to high-quality animal foods was probably at least one of the major driving factors in allowing [encephalization] to happen," he says.

On the other hand, the pursuit of a steak dinner is not without hazards, according to David Braun, an archaeologist at the University of Cape Town in South Africa. "There are multiple consequences of making that shift," he says. "There are costs of predator-prey interaction, of entering into a niche that hominins

aren't necessarily all that well-adapted to, and all kinds of parasitological costs."

Dartmouth College anthropologist Nathaniel Dominy favours the view that our ancestors might have put their tools to better use in unearthing root vegetables. He has observed how modern hunter-gatherers survive in an African savannah-like environment that may not be radically dissimilar from where *H. erectus* flourished. He suggests that tubers offered an essential buffer against the vicissitudes of the hunter lifestyle. "Modern hunter-gatherers have language, technology and iron-tipped spears, yet they still struggle to get enough meat to survive," he says. "It's hard to imagine a bunch of hominins without those accoutrements getting a lot of meat." Tubers were abundant and may have provided the staple nutrients needed to make brain growth adaptive when easy access to meat was no sure thing.

However, efficient tuber digestion depends on another major technological advance — cooking. "Most tubers absolutely require roasting," says Dominy. Harvard University anthropologist Richard Wrangham believes this is not a problem. In 1999, he published a

controversial article promoting his hypothesis that controlled fire and cooking became a component of the hominin toolbox as early as two

NATURE.COM

For more on how food and fire shaped humanity see go.nature.com/fxnjfl

LOOK AND LEARN/THE BRIDGEMAN ART LIBRARY

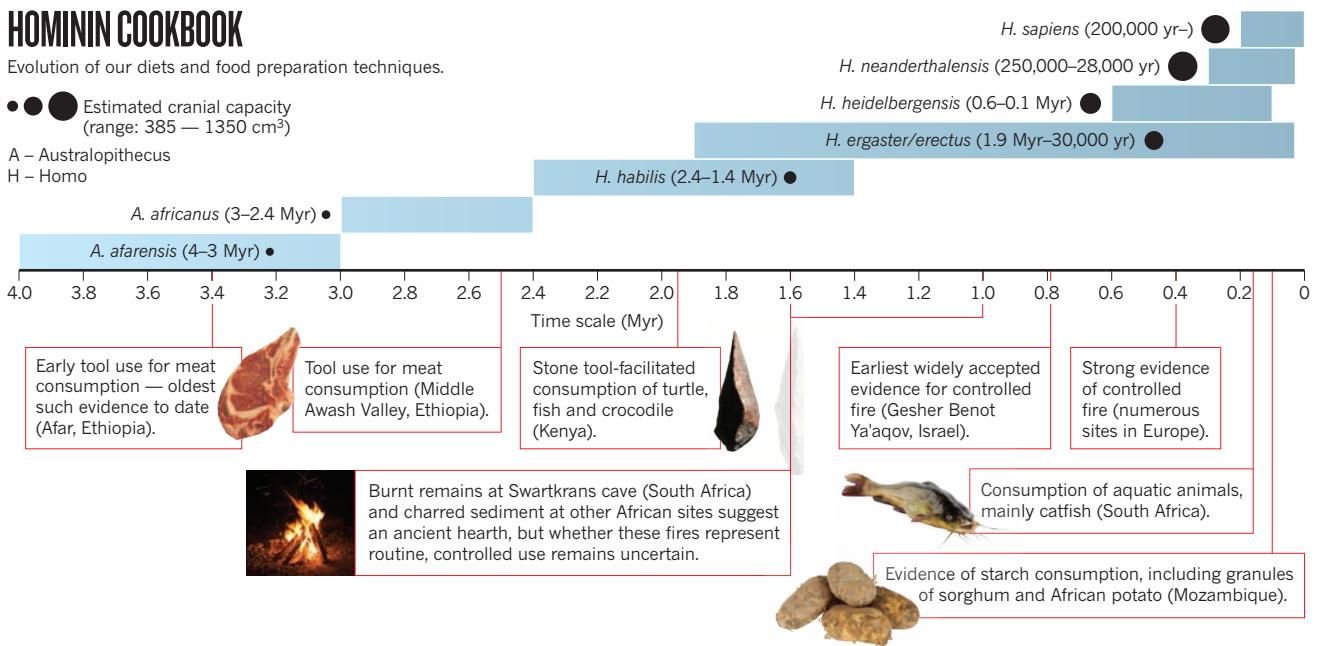
HOMININ COOKBOOK

Evolution of our diets and food preparation techniques.

● ● ● Estimated cranial capacity (range: 385 — 1350 cm³)

A – Australopithecus

H – Homo



million years ago. Wrangham has since developed this concept to explain how our ancestors maximized the nutritional benefits of tubers, meat and other foodstuffs. “It has not been appreciated by most people until recently that cooking has a large effect on net energy gain,” says Wrangham. “Normally it’s considered necessary because it enlarges the possible diet and makes food safer, but energy is such a key variable for evolutionary adaptation.”

Preliminary analyses by Wrangham and colleagues suggest that cooking may have made proteins and starches more digestible while simultaneously reducing the cost to the immune system of fending off parasites or bacterial infection.

THE HARD FACTS

Many anthropologists remain wary of the evidence gap in Wrangham’s hypothesis. The earliest sign of controlled fire comes from Israel, dating back some 800,000 years — considerably shorter than 2 million years. Nevertheless, Braun is hesitant to rule out Wrangham’s theory, pointing out that remains of cooking fires can be ephemeral. The evidence found at the Israeli site is particularly unusual. “Gesher Benot Ya’aqov is the kind of place archaeologists dream of,” he says. “Wood is preserved there, as are all kinds of activities that aren’t preserved elsewhere.”

Braun has encountered similar challenges: a recent study by his team at a 1.95 million year old site in Turkana, Kenya, found remains of bones and stone tools indicating that predecessors of *H. erectus* may have routinely eaten fish and other marine life². If this represents a true dietary pattern, then ‘brain food’ may have lived up to its name by providing an abundant source of the polyunsaturated fatty acids that fuel the growth of the cerebral cortex.

Nevertheless, an early role for aquatic animals in the hominin diet remains controversial as archaeological evidence points to seafood only becoming a regular item on the menu between 150,000 and 200,000 years ago. This could be explained by the challenges of actually finding evidence of these foods being prepared. “The preservation that happened at that particular site, I think, is unusually good,” says Braun. “We usually use marks on bone surfaces as a determining factor of whether something is part of the diet [and] those don’t preserve really well for aquatic animals.”

Unfortunately, any efforts to link food choice to human evolution will continue to depend on what can be unearthed at such sites: evidence from the genetic record is likely to be harder to find. Pääbo and colleagues assembled a draft of the Neanderthal genome³. This offers a wealth of information on human evolution over the

The pursuit of a steak dinner is not without hazards.

somewhere on this side of a million years — and it’s much more realistic to say half a million years, maximum,” says Pääbo. As such, any hope of obtaining usable genomic data from our early African ancestors is a pipe dream, and attempts to characterize hominin genetic evolution generally focus on our closest extant kin — the chimpanzee and bonobo.

Some of the best evidence might be found lining the fossilized jawbones of our ancestors. Peter Ungar, a paleoanthropologist at the University of Arkansas, has been using digital analysis to chart the ‘landscapes’ of ancient teeth down to the subtle abrasions that cover

the chewing surfaces. “Those scratches are the actual result of a hominin passing food across its teeth, and we can relate that to what the animal was adapted to doing,” he says.

Based on a growing collection of both *H. habilis* and *H. erectus* samples, Ungar sees a striking transition to teeth that are thinly enamelled and highly textured, which are clues to a diversification in diet. “If our *Homo* ancestors were processing their food outside of the mouth more with tools, then you’re not going to get the same selective pressures to maintain big, thickly enamelled, flat teeth,” he says. “Teeth with thinner enamel and more relief are actually better for shearing and grinding tougher foods, like meat and leaves.” He suggests that although individual *H. erectus* may not have necessarily indulged in a diverse diet, they developed a capacity to rely on a broad array of ‘fallback foods’ — a skill that would have proved useful in the rapidly changing climate of the early Palaeolithic, and enabled humanity to settle far beyond the continent of Africa.

Braun considers this a reasonable theory, but he also appreciates the need for further investigation into the nutritional building blocks of this increasingly diverse diet. “For every 10 years of field work, we answer one or two questions,” he says. “It’s going to require a lot more boots on the ground.” In the meantime, anthropologists and archaeologists will have to continue to content themselves with reconstructing the Palaeolithic buffet one course at a time. ■

Michael Eisenstein is a journalist in Philadelphia

1. Somel, M. *et al.* *PLOS one* **3**(1): e1504 (2008).
2. Braun, D. R. *et al.* *Proc. Natl Acad. Sci. USA* **107**(22):10002–10007 (2010).
3. Green, R. E. *et al.* *Science* **328**, 710–722 (2010).



HEALTH

Edible advice

Diet-related illnesses are some of the biggest killers today. Can we tailor our food intake to prevent these diseases? Large international projects are underway to find out.

BY FAROOQ AHMED

Too much tea can treble cancer risk in women'. 'Tea could cut risk of ovarian cancer'. Just two examples of the frequent contradictory newspaper headlines that confuse the public about the health benefits — or risks — of food and confound genuine nutrition-related research.

For some diseases such as diabetes the link with food is subtle. "Although we know that dietary factors are related to the risk of diabetes, there are a lot of inconsistencies between studies in terms of what precise micronutrients or macronutrients associate with the disease. We're quite limited in terms of the data," explains Nick Wareham, head of the epidemiology unit at the UK's Medical Research Council.

Using new tools and methodologies, ambitious projects are underway to make up this shortfall. One such effort, which Wareham coordinates, is InterAct — a multinational study to define how diet and lifestyle influence risk of type 2 diabetes. This disorder of blood glucose regulation is a growing problem in Europe, afflicting nearly 40% of the population at some point in their lifetime. InterAct estimates that the diabetes accounts for as much as 10% of health care costs in Europe.

Through endeavours such as InterAct, researchers are starting to expose the complex interplay of genetics, diet and disease, and bring order to the confusing array of nutritional information.

InterAct began in 2006 as part of the European Community's sixth Framework Programme. It has a budget of €10 million and involves more than 12,000 patients recently diagnosed with diabetes across 10 countries — nine in Europe plus India. Such a broad cohort is important. "Sometimes variation within a country is not so great," says Wareham. "International efforts give you heterogeneity in the lifestyles of patients, especially in the diet, and that's a major advantage." This diversity provides scientists with more variables to study as they attempt to untangle what factors are responsible for causing disease.

THE BIGGER THE BETTER

This research is part of the largest diet and disease study ever undertaken: the European Prospective Investigation into Cancer and Nutrition (EPIC). Initiated in 1992, EPIC has recruited more than half a million people. Participants are physically examined at one of 23 centres, complete lifestyle surveys including detailed diet questionnaires, and have their

blood tested. Their DNA is scanned for disease-related genes using techniques that can detect hundreds of thousands of genetic variants in large numbers of individuals.

"Large-scale projects can really be a catalyst to bring together multiple centres to share instruments," says Wareham. "InterAct has benefited greatly from the huge EPIC cohort and access to those technologies."

Another large-scale study, a parallel to InterAct though not part of EPIC, is Interheart — which examined the link between dietary patterns and heart-attack risk. Between 1999 and 2003, the Canadian-led study recruited 5,761 patients and 10,646 control subjects, living in 52 countries, across six continents. Using questionnaires, physical examinations, and blood analysis, the teams compiled data on people including demography, diet, anthropometric measurements such as body mass index and biomarker levels including cholesterol and lipoproteins.

Interheart researchers concluded that the globalization of a Western pattern diet — high in animal products, fried foods, and salty snacks — is responsible for a third of the risk of heart attack worldwide¹. A 'prudent' diet rich in fruits and vegetables reduced risk regardless of location. Prior to Interheart, few epidemiological studies linked dietary patterns in ethnically diverse populations and cultures to disease. Research like this "is crucial if we truly want to understand these diseases, because they manifest differently in European and other populations," says nutritional geneticist Jim Kaput, who also serves as director of the Division of Personalized Nutrition and Medicine at the US Food and Drug Administration.

CROSSED PATHWAYS

InterAct and Interheart both demonstrate that the metabolic pathways at the epicentre of dietary-related illnesses, such as diabetes and cardiovascular disease, are strongly related. Research on one can uncover clues to the other. "Factors like blood pressure, cholesterol and triglyceride levels, which are predictive of coronary heart disease, are also associated with diabetes," notes Wareham.

Leafy vegetables, such as lettuce and spinach, are core components of the prudent diet as identified by the Interheart study. These vegetables are enriched in polyunsaturated fatty acids (PUFAs) — essential macronutrients also found in some types of fishes, nuts and cheese. Two types of PUFAs in particular, omega-3 and omega-6, are powerful dietary components because they can change gene expression, both directly and indirectly. PUFAs "act more like hormones than like typical food," says nutrition scientist Donald Jump of Oregon State University, who studies these macronutrients.

For example, PUFAs have two ways to

➔ **NATURE.COM**
to see the latest
research on diet and
disease
go.nature.com/ctbpue

PETER THIEDEKE/ALAMY

modulate gene activity and lower the levels of fatty acids and triglycerides in the liver: they can bind and activate a family of transcription factors called peroxisome-proliferator-activated receptors (PPARs) to speed up the breakdown of fatty acids; PUFAs can also deplete another transcription factor, sterol regulatory element binding protein-1 — thereby curtailing fatty-acid synthesis. This two-pronged attack provides a significant health benefit. “Along with cholesterol,” explains Jump, “elevated triglycerides are a common target for the management of atherosclerosis, cardiovascular disease and stroke.”

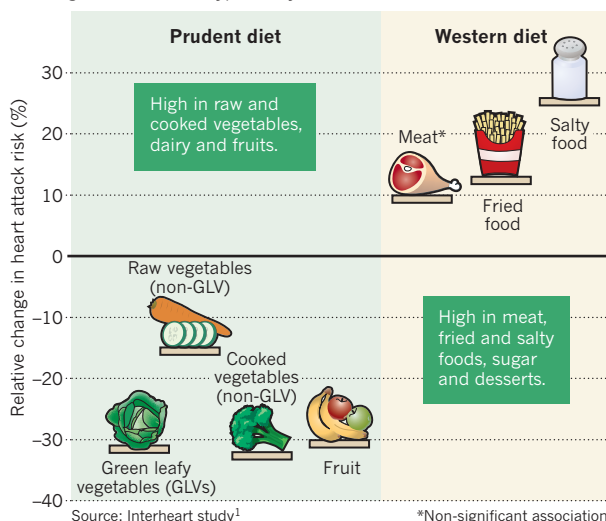
Although most research on PUFAs has focused on their connection to cardiovascular disease, by manipulating an enzyme involved in fatty-acid metabolism Jump’s team has demonstrated that PUFAs can also balance blood glucose levels, suggesting a potential treatment for type 2 diabetes².

“Dietary omega-3s are not usually thought of as a treatment for elevated blood sugar,” says Jump. Yet by studying diet and its effect on metabolic pathways, these types of links are being uncovered.

After diet and metabolism, a third element in development of diet-related disease is the genome. “In humans, genetic background plays a role in either responding well, or not, to particular nutrients,” says Jump. Adding global

RISKY FOODS

Diets high in certain food types carry an elevated risk of heart attack.



genetic diversity to the mix greatly increases the complexity of the research.

The International HapMap Project, a database of genetic variation, began in 2002 and stores data from Canada, China, Japan, Nigeria, the United Kingdom and the United States. So far, the project has identified tens of millions of single nucleotide polymorphisms (SNPs) associated with both disease and drug response. SNPs in PPAR genes that are regulated by PUFAs affect, among other things, the ability to lose weight, a crucial step to controlling diabetes. One SNP in particular has been

found to account for 7% of the variation in people’s weight loss³.

In 2010, InterAct recruited the ten-thousandth person to their search for markers that reveal the roles of obesity and exercise in the risk of developing diabetes. Analyses of their genomes will be published in 2011, and Wareham is confident this approach will uncover new interactions. “We’re using a discovery approach on a mass scale,” he says. “We don’t focus so much on the expression of particular genes, but on the interplay between innate susceptibility and dietary and lifestyle factors.”

Such a link would fill a gap in our knowledge. “Hypothetically,” muses Wareham, “the genome-wide influence of dietary and lifestyle factors may account for the heritability we

have seen in diabetes that remains unaccounted for on the basis of simple genetic variation.”

Subtle changes are lost in the background noise of standard single-gene studies. But they do have an impact — not least of all for our definition of disease and the way that clinical trials are designed. “Geneticists,” says Kaput, “have been treating all of us like coins when it comes to deciding whether we have a disease: heads or tails — are you or are you not diabetic? That’s how many studies are designed.”

There is a need for new ways to interpret disease that recognize the contribution of genes

DEVELOPING WORLD NUTRIGENOMICS

Reversing the health and nutrition relationship.

As globalization is exporting fatty fast-food diets around the world, malnutrition is rampant in many developing countries. According to Médecins Sans Frontières, malnutrition causes 60% of deaths in children under the age of five in developing nations. New technologies that provide nourishment while treating diseases could save millions of lives.

That’s the stark reality that led Raymond Rodriguez to launch the Global HealthShare Initiative (GHSI). “We started to look at health disparities in racial, ethnic and economically disadvantaged communities,” explains Rodriguez, director of the Center of Excellence for Nutritional Genomics at the University of California, Davis. “Often the people who need food and drugs the most are the last to get them.”

Lack of proper nutrition opens the door to disease. “Malnourished individuals have reduced immunity, and thus vaccines are less effective,” says Somen Nandi of



Malnutrition impairs vaccine efficacy.

GHSI. Nandi is leading efforts to develop an international network of researchers, investors, non-governmental organizations and drug makers to combat diseases with nutrition-based therapeutics. “We’re merging the concepts of nutrition and immunity,” says Nandi.

One tangible benefit of this new way of thinking is a novel rice-based matrix in

development as a delivery base for a vaccine against cholera and diarrhoea. This could help sustain the malnourished and bolster their immunity, while immunizing against the diseases.

GHSI’s vaccine development projects also recognize the economic factors involved. Rodriguez’s and Nandi’s ambitious goal is to help create sustainable economies in countries where diarrhoeal diseases are prevalent, such as Bangladesh. They hope to identify and develop sites in resource-limited countries where therapeutics can be formulated, manufactured and distributed.

“We think that GHSI will create an opportunity for the four billion people who are not a part of the global economy to enjoy better health and a better standard of living,” says Rodriguez. Thus the fruits of nutrigenomics research could not only help Westerners cope with a diet of excess, but also bring better lives to the impoverished people in developing nations.

and metabolic pathways. Metabolites are small molecules — amino acids, vitamins and other chemicals — in circulation and influenced by both genes and nutrient intake. Metabolomics, or the study of these metabolites, offers perhaps the best opportunity to observe these interactions in a minimally invasive manner.

Metabolic phenotypes can be very finely segregated, as demonstrated in an analysis of urinary metabolite patterns found in thousands of individuals in China, Japan, the United Kingdom and the United States. Not only did East Asians have a different pattern of metabolites from Western populations, but individuals from northern China could be differentiated from those in southern China. Both Chinese groups were distinct from Japanese, who were in turn different from Japanese Americans⁴. People who consumed a lot of meat, as is common in Western diets, had elevated levels of biomarkers indicative of high blood pressure compared with people who have a primarily vegetarian diet.

InterAct is also searching for novel biomarkers that accumulate as an individual's risk of diabetes rises. When combined with epidemiological studies, this type of metabolic phenotyping could lead to the identification of biological red flags for individuals, even before disease manifests. Biomarker metabolites might also be therapeutic targets one day.

BREAKING DOWN SILOS

While large-scale scientific projects such as InterAct and Interheart have had success, barriers still exist to international collaborations. Researchers occasionally encounter a lack of willingness or an inability to share information. “It has sometimes been a challenge to convince colleagues who run the individual centres that by working together we end up with better science,” says Wareham.

Kaput agrees. He suggests that biologists take a page from the physicists’ handbook. “They built the Large Hadron Collider, thereby working across disciplines”, he says, “but we still haven’t made the silos go away in the biological sciences community.”

Wareham has faith in the technology-driven approach that encourages and facilitates collaboration. These major projects, he says, can bring different disciplines closer together — as they have in the genetic HapMap project. “The ability to measure multiple SNPs at very low cost on a mass scale revolutionized that field, and I think that’s where we’re headed for other risk factors such as diet and nutrition,” contends Wareham.

Such a large-scale, system-wide approach is being used by Kaput and FDA chemist Carolyn Wise. They are considering early environmental influences, micronutrient availability, metabolic and regulatory pathways and genome-wide association maps as they try to define combined genetic–metabolic types

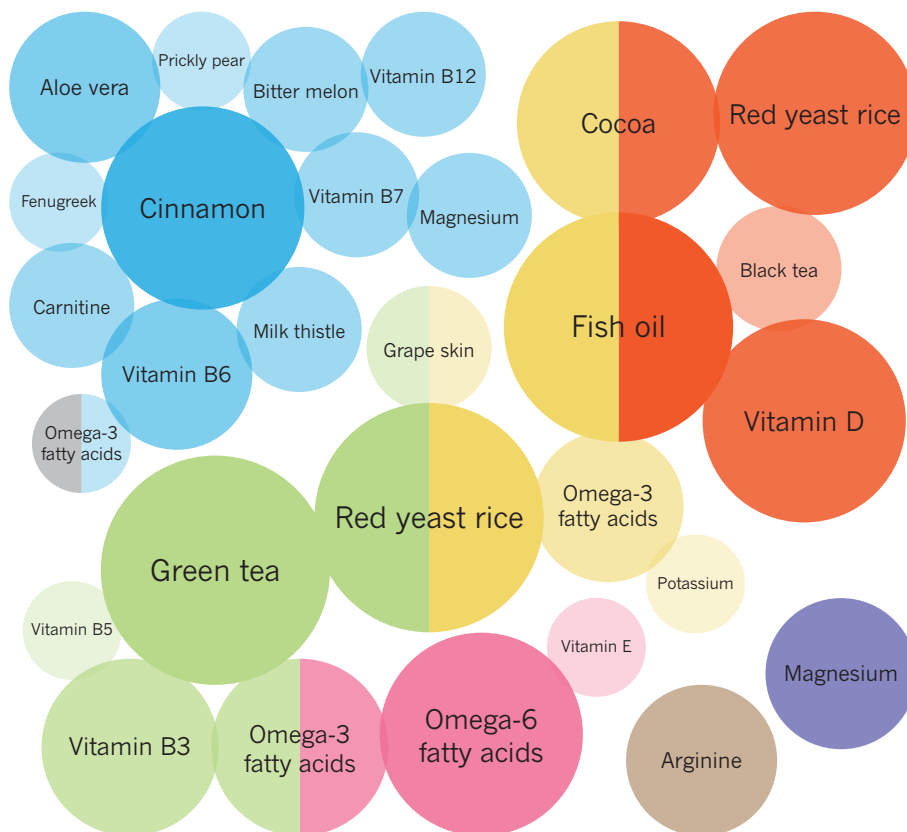
SUPPLEMENTARY ASSESSMENT

Common ingredients and nutritional supplements and their relative health benefits. Larger, darker circles indicate greater likelihood that the supplement helps.

● Blood pressure ● Heart arrhythmias ● General heart health
● Cholesterol ● Heart disease ● Hypertension
● Diabetes ● General cardiovascular health

STRENGTH OF EVIDENCE

Strong
Good
Promising
Conflicting
Slight
None



Adapted from www.informationisbeautiful.net/play/snake-oil-supplements/

for people in terms of obesity and type 2 diabetes⁵. This approach can be emulated and scaled in other studies to help researchers work together and share information as they try to make sense of huge amounts of data.

PREVENTION IS BETTER THAN CURE

As these nutrigenomic studies begin to classify individuals into specific groups based on the interplay of their lifestyle, metabolic pathways and genetic variants, tailored diets may become early therapeutic interventions. Personalized diets might even guide people genetically at risk for diabetes, but not yet in a pre-diabetic state, to help them avoid developing the disorder by fine-tuning what they eat. A well-regulated ounce of prevention could obviate the need for a cure.

However, the development of personalized diets has been prematurely promised before. In the early 2000s, a slew of companies claimed to be able to provide personalized nutritional advice based on genetic tests. An investigation by the US Government Accountability Office in 2006 found that these companies “misled consumers” and provided only generalized advice. The US Senate Special Committee

on Aging convened a hearing that further criticized these direct-to-consumer genetic tests. Unable to secure funding, several of these companies went bust.

Here, says Kaput, is where the FDA’s Division of Personalized Nutrition and Medicine is ahead of the curve. “Right now, we don’t have a product to regulate. We’re not sure where the field is going necessarily, but when products come in for possible FDA regulatory activities, we will have the research background to help the regulatory centres make their evaluation.”

Teasing out the relationship between food and disease is a tricky task, one that involves tens of thousands of people and encompasses hundreds of nutritional and genetic factors. It is not likely to provide simple or quick fixes either, meaning that for now at least the ‘tea causes cancer’ stories can safely be ignored. ■

Farooq Ahmed is a science writer in New York.

1. Iqbal, R. *et al. Circulation* **118**, 1929–1937 (2008).
2. Tripathy, S., Torres-Gonzalez, M. & Jump, D. B. *J. Lipid Res.* **9**, 2642–2654 (2010).
3. Matsuo, T. *et al. Obesity* **10**, 1924–1931 (2009).
4. Holmes, E. *Nature* **453**, 396–400 (2008).
5. Wise, C. & Kaput J. *J. Diabetes Sci. Technol.* **3**, 710–721 (2009).



DIVERSITY

Of beans and genes

Several human genes involved in digestion have diverged along cultural lines. Research suggests these adaptations influence the range of foods tolerated and even certain diseases.

BY MICHAEL EISENSTEIN

Nathaniel Dominy was surprised to find that diet-related genes, like people, sometimes simply repeat themselves to get a point across rather than change the message.

In 2007 while most evolutionary biologists were looking for evidence of selection in the form of genetic mutations, Dominy and colleagues learned that people with high-starch diets had additional copies of the gene coding salivary amylase and that these repeats increased production of the carbohydrate-processing enzyme. “Few would have expected at the time that [these repeats] could have any effect at all — and they had a big effect,” recalls Dominy, an anthropologist at Dartmouth College in New Hampshire.

This discovery also offered proof to the growing number of evolutionary geneticists who believe that culture-specific factors, such as diet, have had as powerful an effect on human evolution as more obvious externalities like climate and habitat — with some even suggesting that these factors could have accelerated the overall evolutionary pace. “I don’t think we have the data yet to make those claims,” cautions Mark Stoneking, a population geneticist at

the Max Planck Institute in Leipzig, Germany. “[But] there certainly has been recent evolution in modern humans because of responses to natural selection, and culture may very well be playing a role in a lot of those.”

THE GENETICS OF LUNCH

Even if you can enjoy a cold glass of milk without then feeling sick to your stomach, chances are you know somebody who can’t. In fact, adult lactose intolerance is the biologically ‘normal’ state of affairs. “The general pattern in mammals is to lose lactase expression after weaning,” explains Dallas Swallow, a geneticist at University College London.

Nevertheless, adults with ‘lactase persistence’ are widespread in many parts of the world. For example, lactase persistence is characteristic of 89%–96% of Scandinavian and British people, is widespread among pastoralist cultures in Africa and the Middle East, but appears in only 1% of Chinese individuals.

Although one single nucleotide polymorphism (SNP) affecting lactase gene expression accounts for the vast majority of European instances, this trait seems to have arisen independently in different regions of Africa as a result of several distinct yet tightly-clustered variations within a regulatory segment of the

lactase gene. “That’s convergent or parallel evolution,” says Swallow. “The same phenotype is being selected, with different mutations causing that phenotype.”

Each of these variants is thought to have emerged within the last 10,000 years, roughly coinciding with the emergence of agriculture and dairy farming, and conferring obvious advantages on those cultures. “Milk is nutritionally good, and if you don’t have lactase you can’t digest the main carbohydrates in it: you might get diarrhoea or flatulence, and you’ve lost a source of food, water and calcium,” says Swallow. “In the context of African tribes, the most plausible thing is that it was a source of clean, nutritious liquid.”

Most geneticists cite lactase persistence as a leading example of recent human evolution driven by shifts in culture and diet. “This happens to be a ‘low-hanging fruit,’” says Sarah Tishkoff, a geneticist at the University of Pennsylvania. “It’s a Mendelian trait and it left a really strong selection signature.” Identifying other,

equally clear examples has proven challenging, although the subsequent amylase breakthrough by Dominy and colleagues suggests that other ►

➔ **NATURE.COM**
Learn more about how
dietary adaptations
affect health
go.nature.com/6YJSUD

FLOORTJE/ISTOCKPHOTO

► such traces are there to be found.

Today, many people enjoy starch-rich diets as a matter of choice, but for early humans, tubers and other starchy plants might have been an essential staple in lean times (see The first supper, page S8). “Amylase is the only enzyme that can hydrolyze starch,” says Dominy. “If you can produce a lot of amylase, you have a big advantage in the sense that you can extract and assimilate carbohydrates almost instantaneously at the level of the mouth.”

The number of copies of the salivary amylase gene, *AMY1*, was already known to vary among individuals. In partnership with Anne Stone and then graduate student George Perry at Arizona State University, Dominy demonstrated that not only does this copy number directly correlate with enzyme levels, but the average copy number within a population also correlates with the starch content of their traditional diet. For example, the Japanese routinely consume large amounts of rice and other starch, whereas the Yakut, a Siberian hunting and fishing culture, have a diet based on fish and meat; these differences are reflected at the level of the *AMY1* gene in Japanese and Yakut populations. “Even though they are closely related genetically, and geographically not separated by a great distance, there’s a difference in the number of copies in these two populations on average,” says Dominy.

SUFFERING FOR HEALTH

The shift from an active foraging lifestyle to a more sedentary agricultural existence also appears to have introduced selective pressures, as populations struggled to survive nutritional deficiencies. Some intriguing but enigmatic signs of lifestyle-specific adaptation have been detected in the gene encoding N-acetyltransferase 2 (*NAT2*), an enzyme that is best known for its role in drug metabolism, but which also contributes to the processing of toxins ingested from plants and well-cooked meat. In a series of recent studies, geneticist Lluís Quintana-Murci of the Institut Pasteur and colleagues investigated the extent by which different populations express *NAT2* variants that acetylate — and thereby help break down — target molecules quickly or slowly. “We showed that most hunter-gatherer populations present fast-acetylation alleles,” he says, “whereas the slower acetylators are very common in farmer-descended populations, like with most Europeans and particularly in the Middle East.” *NAT2* is also associated with the metabolism of folate, the natural form of folic acid, normally obtained from leafy greens or animal liver. Quintana-Murci’s team proposed a model in which the sharp drop in folate intake associated with a shift to a grain- and cereal-rich diet favoured the emergence of alleles that suppress use of folate reserves, although he emphasizes that this is purely speculative until further data are available.

Both versions of the *NAT2* enzyme carry

certain disadvantages, as acetylation can actually enhance rather than reduce the toxicity of certain compounds: fast acetylation is linked with colon and lung cancers, whereas slow acetylation is associated with prostate and bladder cancers. Therefore, any nutritional benefits are likely to be closely balanced against the potentially harmful outcomes of *NAT2* variation.

There are a number of other instances where selective pressures appear to have resulted in a trade-off. For example, although the twenty-odd *T2R* proteins involved in bitter taste perception represent a potent early warn-

Most traits are complicated and multifactorial in nature.

ing system for harmful compounds, the genes encoding these factors also exhibit a striking level of variability (see More than meets the mouth, page S18). Unusual patterns of distribution have been observed for several variants that could alter the sensitivity of the mouth to bitter chemicals. “It’s clear that there are ethnic differences in the composition of *T2R* haplotypes,” says Wolfgang Meyerhof, a geneticist at the German Institute of Human Nutrition in Nuthetal.

In a study of taste variation in central African populations by Meyerhof and colleagues, one low-sensitivity variant of the *T2R16* bitter receptor, which normally responds to cyanogenic glycosides found in the starchy tuber cassava, was found to be unexpectedly common. These glycosides are metabolized in the gut to release toxic cyanide. The researchers speculated that the health costs of consuming potentially toxic compounds must be balanced by some sort of positive selection, perhaps arising from enhanced resistance against the malarial parasites that are widespread in this region, to sustain this allele in the population.

In fact, there are several instances where the

benefits of lowering pathogen susceptibility are apparently sufficient to select for otherwise deleterious alleles. “Infectious disease is probably one of the strongest selective forces in the past or ever,” says Tishkoff. She points to the example of glucose-6-phosphate dehydrogenase (*G6PD*) deficiency, a widespread enzymopathy associated with blood cell defects and potentially severe toxic reaction to foods including the fava bean (shown in main image, page S13). The gene variants associated with *G6PD* deficiency, also known as ‘favism’, are widespread in several ethnic groups that routinely eat these beans. Their prevalence, in spite of the near-term dietary and health costs, could result from the protection these variants confer against malaria.

As with lactase persistence, the strong adaptive advantages of this phenotype are demonstrated by its independent appearance in diverse populations; distinct *G6PD*-deficient alleles have emerged in Africa, the Mediterranean and the Middle East. More recently, Quintana-Murci and colleagues determined that an allele of this gene is prevalent in Southeast Asia, which results in only moderate enzyme deficiency, appears to protect against *Plasmodium vivax* — an unexpected finding, as *P. vivax* is seldom lethal and was presumed to represent a much less potent force for short-term human evolution than its highly dangerous relative *P. falciparum*. “It’s about the consequences,” says Quintana-Murci. “*P. vivax* could be important in childhood, or in women who are pregnant and infected — maybe they won’t die, but their babies are born with low birth weight, which eventually weakens them and raises their chances of dying.”

However, not all phenotypes can be directly linked to genetic variation. As years of genome-wide association studies have demonstrated, most traits are considerably more complicated and multifactorial in nature, and tracking

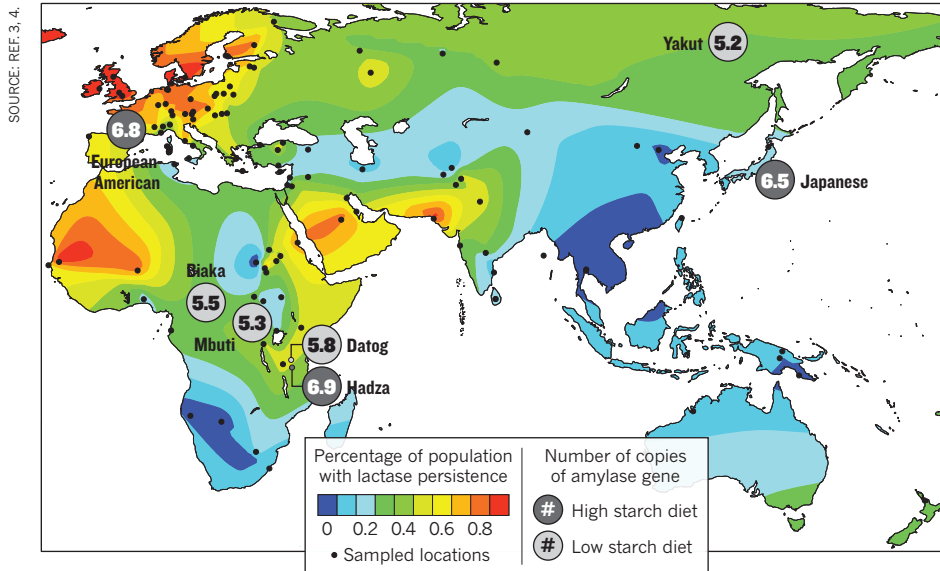


Milk provides many nutrients to those who can tolerate it (see map on opposite page).

ERNST TOBISCH/STILL PICTURES/PHOTOLIBRARY.COM

MILK AND STARCH CONSUMPTION

Global distribution of genes related to ability to digest starchy foods and lactose in milk.



components of our diet, and their metabolic products profoundly influence our physiology,” says Jeffrey Gordon, a microbiologist at Washington University in St Louis, Missouri. “It’s like bringing a set of utensils to a dinner party that the host does not have.”

Nicholson has already found some compelling evidence that genes expressed by the gut flora have effects that reach far beyond the digestive tract. “We’ve found deep compartmental connections between microbial status and bile acid metabolism,” he says, “[And] there are some staggering connectivities between blood pressure and gut microbial metabolites.”

Research from Gordon’s lab has shown there are differences in the sets of bacterial species that reside in the guts of individuals, even identical twins. “Certainly less than 10% — and it might even be less than 2% — of the bugs that are in you are also in me,” says Nicholson. Gordon and others are confident that the impact of cultural variation is at least as strong.

Our understanding of the genetic basis of even relatively well-characterized phenomena pertaining to dietary variation, like lactase persistence, could be confounded by the impact of these commensals. “There are Chinese students who come to the West who can drink quite a lot of milk even though they come from a genetic background where they’re not lactase persistent,” says Swallow. “We think that’s due to adaptation of the intestinal flora.” It also appears possible that the considerably smaller, but potentially equally diverse, microbial communities in our mouths may play an important role in the early stages of meal digestion, as indicated by a recent study that suggests oral bacteria may facilitate the processing of wheat gluten.

One of the most striking findings comes from a recent study by a team at France’s Centre National de la Recherche Scientifique, presenting strong evidence that Japanese individuals can digest seaweed carbohydrates more efficiently². This was made possible by an ancestral gene transfer event from kelp-borne bacteria that endowed their gut flora with the capacity to produce porphyranase and agarase enzymes. This adaptation is seemingly absent in North Americans who have not historically consumed raw kelp. Microbe-watchers like Nicholson suggest that this study could be a strong indicator of the future, as the research community begins to come to terms with the extent to which human genetic effects on diet might be overwhelmed by the bacteria we carry. “It’s a piece of genius,” he says. “It’s something I use in my slide presentations now to worry geneticists.” ■

Michael Eisenstein is a journalist in Philadelphia.

1. Qin, J. *et al. Nature* **464**, 59–65
2. Hehemann, J. H. *et al. Nature* **464**, 908–912 (2010).
3. Itan, Y. *et al. BMC Evolutionary Biology* **10**, 36 (2010).
4. Perry GH *et al. Nat. Genet.* **39** (10), 1256–1260 (2007).

down these complex changes will require alternative allele-hunting tactics.

A TANGLED WEB

University of Chicago geneticist Anna Di Rienzo recently tried to identify allelic variants that differ in frequency among populations residing in similar geographic regions or ecosystems but who have distinct diets or modes of subsistence, such as farming or foraging. Through this approach, her team uncovered various hints of genetic adaptation in carbohydrate metabolism and folate production, associated with the adoption of diets based on roots and tubers. Conversely, cultures with a cereal-rich diet were more likely to produce a truncated, hyperactive version of *PLPR2* — an enzyme responsible for breaking down plant glycolipids — than their non-cereal-consuming counterparts. “There is a consistent frequency shift between populations,” says Di Rienzo. “The stop codon [in *PLPR2*] occurs always at higher frequencies in populations that have a cereal-rich diet compared to populations that don’t and yet live in the same geographic region.”

Yet it remains a challenge to piece together such minor genetic variations scattered throughout the genome. “These aren’t mutations that will knock you dead,” says Di Rienzo. “They make subtle changes to gene function or expression, and detecting those subtle changes can really be quite hard.”

For more recent adaptations, the mutations can also be very rare, making it difficult to detect clear patterns. Even when the data seem to suggest the presence of selective pressure behind a given variant, it is essential to have a solid understanding of the cultural history of the region to eliminate demographic biases. “If a lot of the individuals you’ve tested have the same great-grandparents, it’s quite a

different story from if they were relatively unrelated,” explains Swallow.

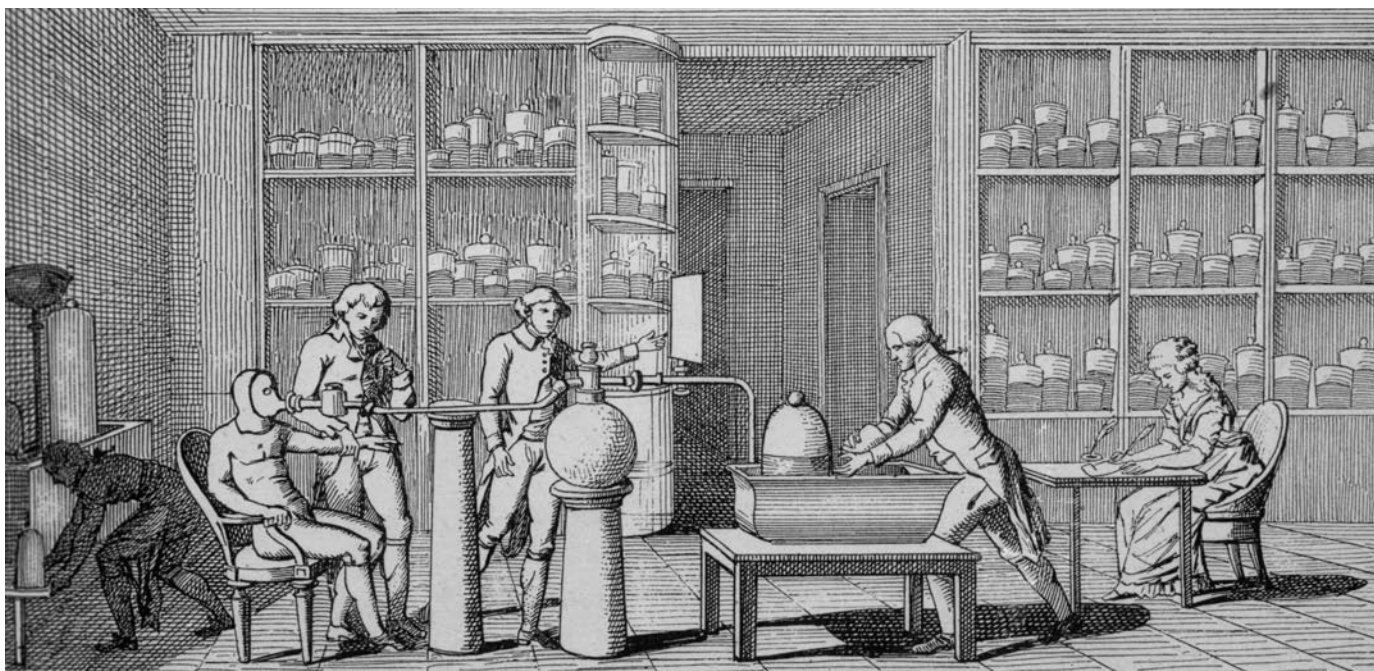
Most importantly, studies need to demonstrate clear functional contributions from a particular variant or subset of variants, and arrive at plausible reasons for why these changes are adaptive in some cases but not in others. “We want to know what the biology is that’s being affected by these unusual patterns,” says Stoneking. “How many of them are real, and how many are false positives, and what are the underlying stories? That’s sort of where the field is a bit stuck at the moment.”

IT TAKES A COMMUNITY

Clearly, scouring for signals of recent evolution amid the tens of thousands of interconnected human genes and regulatory regions can be compared to finding the proverbial needle in the haystack — but what if that haystack is far bigger than most people think?

Jeremy Nicholson, a biological chemist at Imperial College London, points out the tremendous diversity of the intestinal microbial flora, citing a report in 2010 which showed that Europeans each carry a complement of at least 160 bacterial species, with more than 536,000 bacterial genes between them — well over 20-times the human gene count¹. “It actually should be thought of as a multicellular organism with a very large genome,” he adds.

Even with our limited understanding of the microbial communities that thrive in our digestive tract and elsewhere in the body, it’s increasingly clear that their net genomic output is inextricably linked with our own metabolic function, and the composition and activity of these communities is a direct by-product of our environment, culture and diet. “The gut microbial community can be viewed as a metabolic organ — an organ within an organ; they sense, adjust to, and process



BETTMANN/CORBIS

Eighteenth century chemist Antoine Lavoisier investigates whether exhaled breath is analogous to the fumes of a combustion engine.

HISTORY

The changing notion of food

The pioneers of nutrition research determined the energy content of food and also helped to overturn misconceptions about various diseases that plagued humankind.

BY NED STAFFORD

Nutrigenomics — and the rest of modern nutrition science — stands on foundations laid in the late eighteenth century.

That is not to say that nobody had taken an interest before then in how food works. The ancient civilizations of Egypt, Greece, Rome, Persia, China and India were aware of a link between food and health. “They all had their food rules, many of which are still valid today,” says Claus Leitzmann, a human nutritionist at the University of Giessen in Germany. “The ancient Egyptians used garlic medicinally.”

Some of our food-truths hark back millennia. The ancient Greek physician Hippocrates recommended that food should be thoroughly chewed before swallowing, and consumed in moderation to maintain good health. In the Middle Ages, the German nun and Christian mystic Hildegard of Bingen “knew a lot about food”, says Leitzmann. “She made some very intelligent recommendations,” such as eating cooked rather than raw foods.

But before the eighteenth century there was little scientific investigation into the composition of food or how the body processes

it. The researchers of the time were “dependent on experimental observation”, says Leitzmann. Their method was ‘feed and watch’. It was French chemist Antoine Lavoisier, regarded as the father of modern chemistry, who first conducted the research that led to today’s science of nutrigenomics.

FOOD AS FUEL

Lavoisier was one of the first scientists to design laboratory equipment to test what happens to food after it is swallowed. Before his work, scientists knew that the weight of ingested food exceeded the weight of excreted faeces and urine. They attributed this loss to perspiration. But Lavoisier believed that food was fuel and that the body, like the fuel-burning engines being developed at the time, must expel carbon dioxide as a product of combustion. He suspected that exhaled carbon dioxide accounted for this lost matter.

To test his theory, in the early 1780s Lavoisier invented a new type of device — the ice calorimeter. It was composed of an outer shell packed with ice, to maintain a constant temperature of 0 °C, encasing a chamber housing a guinea pig. The animal’s body heat melted the ice. By weighing water flowing out of the calorimeter, Lavoisier was able to estimate

metabolic heat and compare it with the heat produced by a lit candle or burning charcoal.

His theory proved correct. Lavoisier declared: “respiratory gas exchange is a combustion like that of a candle burning.”

In today’s calorie-counting world, this does not sound like much of a revelation. But at the time it was a breakthrough. “It was theoretically important to realize that the body needed energy to function and that one major function of food is to supply it,” says Elizabeth Neswald, a science historian at Brock University in Ontario, Canada. “It was a basis for determining what someone needs to survive; what leads to weight gain, what leads to weight loss, what enables physical labour and what the relationship between food and physical labour is.”

Lavoisier’s research also emphasized the importance of food composition and of realizing that faeces, urine, perspiration and respiration are an essential part of the equation.

“These early nutrition scientists spent a large part of their time — or their assistants’ time — inspecting and analysing other

“Early nutrition scientists spent a large part of their time inspecting other people’s excrement.”

people's excrement," says Neswald. "In nutrition experiments, it was vital to assess the differences between input and output — food going in and all products coming out."

This method, known as 'balance trials,' was pioneered in the 1830s by French chemist Jean-Baptiste Boussingault. He conducted balance trials for nitrogen — a constituent element of proteins — by comparing the nitrogen content of hay, oats and potatoes fed to cows and horses with the animals' excrement and, in the case of cows, milk. He showed that animal feed contained sufficient nitrogen to meet bodily requirements, ending speculation that additional nitrogen was obtained from the atmosphere.

MACRONUTRIENT EXPLORATION

By the mid-nineteenth century, scientists had learned that the primary elements in food are carbon, nitrogen, hydrogen and oxygen, and had divided food constituents into four main types: carbohydrates, fats, protein and water. Yet the chemical make-up of the first three classes was unknown.

It was a German chemist, Justus von Liebig, who made the next leap forward. The precocious von Liebig (appointed professor at the University of Giessen at age 21) invented the 'kaliapparat', a special piece of glassware for analysis of carbon in organic compounds.

Von Liebig's laboratory, arguably the first teaching laboratory, attracted scientists from around the world. He helped train a generation of nutritional researchers whose work would carry on into the early twentieth century. In the 1860s, for example, two of von Liebig's protégés — physiologist Carl von Voit and chemist Max Joseph von Pettenkofer — obtained funding from the Bavarian government to build a state-of-the-art respiration chamber large enough to hold a person. The chamber could measure the daily balances of both carbon and nitrogen and thereby estimate human protein requirements.

Neswald notes that most of the nutrition research of this period focused not on the health of individuals, but rather on finding the cheapest, easiest methods to feed "institutionalized and impoverished populations" to prevent food riots. Von Voit, says Neswald, visited prisons and workhouses "to assess what people were fed and what their state of health was, with the aim of providing dietary guidelines".

The concept of food as fuel, which contains important dietary components, was further refined in the United States. Agricultural chemist Wilbur Olin Atwater had spent time in von Voit's laboratory as a postdoc, returning to the United States in 1871 to spearhead nutrition science. Atwater spent five years in the 1890s building a respiration calorimeter

larger than von Voit's and able to hold humans for longer than a day. His measurements were so precise that his energy equivalents for protein, fat and carbohydrate are still used today. Atwater was first to adopt the word 'calorie' as an energy unit for food. (A calorie of food energy is actually equivalent to 1000 calories of thermal energy.)

SMALLER AND SMALLER

Scientists soon began to realize that in addition to supplying energy and macronutrients, food also played a more subtle role in health and disease. Japanese physician Takaki Kanehiro, who studied in the 1870s at St Thomas's Hospital Medical School in London, was a rare exception to the nineteenth century German dominance of nutrition. "He was the first person to show that beriberi arises from malnutrition," says Katsuhiko Yokoi, a human nutritionist at Seitoku University in Japan. Previously beri-beri was thought to be an infectious disease.

By the early twentieth century, other scientists around the world had begun to explore links between nutritional deficiencies and other ailments, including rickets and

US biochemist Charles Glen King showed that scurvy was caused by a deficiency of the newly discovered vitamin C.

Animal research led to further vitamin and disease-related discoveries. US biochemist Elmer Verner McCollum learned German so he could read the works of past nutrition researchers, which inspired him to experiment on rats. At the University of Wisconsin, where McCollum initially worked, research protocols stipulated the use of cows as animal models. But McCollum convinced his superiors to let him try smaller animals. He bought 12 albino rats from a pet store and established the first colony of rats for nutritional experimentation in the United States. In 1913, his studies with these rats led him to identify the first fat-soluble vitamin, vitamin A, and later showed that it is vitamin D — and not vitamin A as some thought — that prevents rickets.

Proving the link between micronutrients and disease didn't come easily. US Public Health Service worker and epidemiologist Joseph Goldberger theorized that pellagra, then a major disease causing diarrhoea, dermatitis, dementia and death, was diet-related

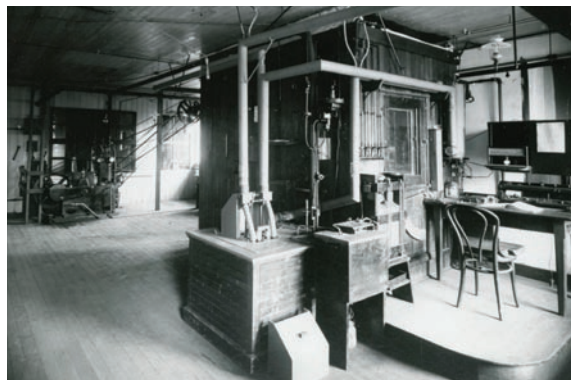
and not, as prevailing medical opinion held at the time, an infectious disease. In 1916, to prove his point, Goldberger and his assistant subjected themselves to a series of tests — they injected each other with blood from a pellagra sufferer, swabbed out the secretions of an pellagra-infected person's nose and throat and rubbed them into their own, and swallowed capsules containing scabs of pellagra sufferers' rashes. And yet despite such gross exposure, they did not develop pellagra. However, Goldberger was unable to find the diet-related cause. It was another two decades before American biochemist Conrad Elvehjem realized

that pellagra was caused by a deficiency of niacin (vitamin B3).

So many micronutrients had been discovered by 1944 that some believed the field of nutrition had been fully defined with little else to discover. But while the constituent parts of food might have been teased out, their impact on the body was only starting to be appreciated.

From Lavoisier, through von Liebig, to scientists today such as Jose Ordovas (see Big science at the table, page S2), nutrition research has focused on smaller and smaller elements. As scientists have probed deeper into biochemical mechanisms of bodily absorption and function — unlocking mysteries as they go — they have also triggered new questions, until we get to 'how do our genes interact with the food we eat?' And that's the question we are still trying to answer today. ■

Ned Stafford is a science writer in Hamburg.



Atwater-Rosa calorimeter used to measure human energy demands.

scurvy. Unable to explain these afflictions in terms of fats, protein or carbohydrates, some scientists began to suspect the existence of another class of food ingredients.

It was Polish biochemist Casimir Funk who in 1912, while studying beriberi, isolated thiamine, the nutrient that protects against this disease. He called the substance a 'vital amine', which soon became 'vitamin'.

The battle against scurvy is an example of science later refining a nutrition-related disease association. In the mid-eighteenth century, Scottish naval physician James Lind found that scurvy could be treated or prevented by eating citrus fruits. But he incorrectly thought that sea air was to blame for the disease. Other erroneous suggestions followed: in 1846, for example, Scottish toxicologist Robert Christison hypothesized that scurvy was caused by protein deficiency. Scurvy continued to be a sporadic problem into the early twentieth century. It was not until 1932 that



RADIUS IMAGES/CORBIS

TASTE

More than meets the mouth

Certain things taste differently to different people. Why is this, and does this affect our choice of food?

BY MICHAEL EISENSTEIN

Nearly 80 years after DuPont chemists stumbled across evidence of genetic variation in perception of the bitter-tasting compound phenylthiocarbamide (PTC), Danielle Reed's team at the Monell Chemical Senses Center in Philadelphia, Pennsylvania, made a similarly serendipitous discovery.

Reed was approached by a lab technician worried she made a mistake with a experimental quinine preparation. "She said, 'I think I made the solutions wrong — here, taste this,'" recalls Reed, who then tasted the bitter compound. "I'm like, 'ugh, it seems fine to me.' But she said, 'It tastes like water to me.'"

This strange observation eventually led to the discovery of a genetic locus that affects

our tongue's ability to detect bitterness in quinine — a big step on the road to understanding how people differ from one another in terms of taste, and how these differences shape what we like to eat.

A BITTER TASTE

Bitter is one of the five primary tastes — along with sweet, sour, salty and the savoury umami — that compose the gustatory system. Of these, bitter is perhaps the best characterized in terms of the influence of genetic variability on taste.

In humans, the cells responsible for bitter taste perception express 25 receptors (T2Rs) that vary in the chemicals they recognize but which appear to perform a common role in preventing people from eating toxic compounds. Accordingly, some scientists are

convinced that humans evolved taste to detect harmful substances. "A newborn baby is born loving sweet and hating bitter — no experience required," says Linda Bartoshuk, director of human research at the Center for Smell and Taste at the University of Florida.

Insensitive variants have been identified for several bitter receptor genes and are common in the general population. For example, mutations in T2R38 render individuals incapable of tasting PTC or the related compound 6-n-propylthiouracil (PROP).

Such limited sensitivity can be an asset as many nutritious vegetables, including broccoli and sprouts, also produce bitter tasting glucosinolates. These compounds include goitrin, a thyroid toxin in large doses but which may protect against cancer in lower doses.

There are obvious nutritional advantages in mitigating the urge to avoid sprouts, and the adaptive value of this reduced sensitivity allele is evident in its global distribution alongside the more common sensitive version. "The ratio of the alleles varies depending on where you go," says Paul Breslin, a taste perception researcher at Monell, "but you see that both have been maintained in almost every population you look at anywhere on Earth."

Yet efforts to firmly link individual genetic variations with altered food preferences have not been easy. Several studies have revealed geographic or ethnic differences in the distribution of taste receptor variants that may have arisen from selective pressures (see Of beans and genes, page S13), but their effects on diet — and association with overall health — are controversial. "I'm a PTC non-taster: I can't taste goitrin in vegetables very well. But I think this has very little to do with how much broccoli I choose to eat on a daily basis," says Reed.

Attempts to establish similar correlations between disease and taste have proven equally problematic. For example, there is no clear link between sensitivity to sweet tastes and predisposition to obesity, diabetes or other diseases related to excess consumption of sugars.

Some of the strongest connections identified relate to alcohol preference. In one study, Bartoshuk partnered with Yale University geneticist Ken Kidd to examine how bitter taste shapes alcohol perception within a cohort of students. "There was a clear relationship between sensitivity and whether ethanol is perceived as bitter and harsh or slightly sweet," says Kidd. "Among those who were homozygous for the high-sensitivity [bitterness allele], nobody drank very much." Other studies at Monell have hinted at a parallel role for sweetness receptor variation, where sensitivity to, and preference for,

sweet tastes is seemingly correlated with alcohol consumption. However, Kidd and others point out that this variability

➔ NATURE.COM
for more of the latest
research on our
senses
go.nature.com/BKR7ZI

must be considered alongside the numerous other brain and metabolic factors involved in drinking alcohol.

Collectively, these data raise a question: given the front-line role of taste perception in food consumption, and the clear advantages of quickly recognizing good and bad food sources, why is it so hard to associate genetic differences in taste function with dietary behaviour?

NAME THAT TASTE

A large part of this problem arises from challenges in experimentally linking the highly subjective experience of taste with biological mechanisms. But gaps also remain in our understanding of the basic machinery of taste perception. This past spring, Charles Zuker's team at Columbia University, New York, validated the involvement of epithelial sodium channel ENaC as a component of sodium chloride salt perception in mice. Other salt receptors remain at large. "People describe potassium chloride as being kind of brackish tasting, maybe kind of metallic, like a dirty salt solution. It's clearly salty," says Breslin. "That can't be through an ENaC, because those channels pass potassium ions very poorly."

Furthermore, even though researchers have known the cells responsible for sour taste since 2006, a definitive receptor has yet to be identified. This is partly because of the complex nature of oral response to acid, where taste effects overlap with somatosensory sensations, a category of perceptual information that encompasses non-taste qualities such as temperature, texture or spiciness.

Preliminary reports also hint at additional taste qualities, enabling the tongue to recognize things like fatty acids or calcium. But there is little consensus on this, in part because no dedicated taste-quality cells have been identified and also because candidate receptors only partially account for our ability to distinguish these putative tastes. Some scientists are also sceptical because humans lack a lexicon to describe these qualities. "Just take a little canola oil and taste it — it doesn't really have a taste," says Bartoshuk. "My guess is that the real sensory input from fat is tactile — fat is gooey and oily and viscous and creamy."

Most investigators remain open to the possibility that there's more to the mouth than just the 'basic five'. A 2009 study by Zuker's team identified a protein expressed in sour cells that apparently contributes — in conjunction with somatosensory receptors — to the discrimination of a 'carbonation taste', and they are on the hunt for mechanisms that monitor other undiscovered qualities. "If you take an animal and label all the sweet, sour, bitter, salty and umami cells, there are still plenty of cells left," he says. "What we're doing now is looking for

things that are uniquely found in those [other] cells."

A GUT FEELING

Taste doesn't end at the back of the tongue. Many of the same taste receptor genes expressed in taste buds are expressed throughout the digestive system and in other tissues. Preliminary investigations suggest that these non-oral receptors help regulate appetite and metabolism. "What better way to do so than having the very same receptors reporting back from the gastrointestinal tract?" asks Zuker.

There is already strong evidence that taste receptors in the mouth help steer organisms towards the nutrients that the body needs most. "If you offer malnourished kids soups that are either plain, ordinary stocks or stocks that have been fortified, they generally prefer

absorption from the blood. Munger adds that his own investigations of genes associated with diabetes among Amish people have been confounded by these gut receptors and the ambiguity of their function. "We did see an association with variation in a particular bitter receptor and the ability of non-diabetic individuals to regulate their blood glucose," he says. However, it remains unclear whether this association arises from the effects of receptor variation on tongue-level taste preference and food selection or whether the difference lies in how the gut reacts to particular foods.

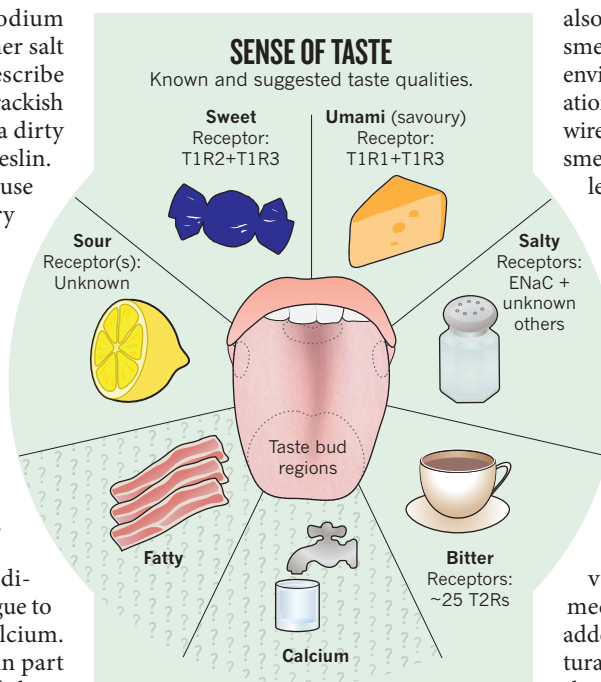
UNWIRING FLAVOUR

The biggest outstanding issue for many taste scientists is understanding how the various raw chemical sensations that transmit taste are incorporated into a more nuanced and sophisticated sense of flavour. Perception at this level also depends on signals received by sense of smell, which exhibits far greater complexity, environmental adaptability and personal variation. "You've got one sense, taste, that's hard-wired for affect," says Bartoshuk, "and another, smell, where the affect is extremely labile and learned very quickly and can also be extinguished."

Equally important is how the brain decides whether or not it likes what it senses. Alexander Bachmanov, a geneticist at Monell, cites the example of sweet-liking mice developed in his lab. "Through selective breeding, we have created mice with the same genotype for sweet taste receptors, but some are very avid consumers of sweeteners while others consume them in very modest amounts," he says, and suggests that this behaviour arises from variations in more central neurological mechanisms related to taste response. This added complexity leaves a lot of room for cultural influences and environmental factors to shape how we assign reward value to a flavour and might in turn affect the contribution of more subtle genome-level factors. As such, inherited differences in taste receptor expression or function alone are probably insufficient to explain how many of us overcome our innate aversion to bitterness and sourness to thoroughly enjoy a steaming demitasse of espresso or a bracing gin and tonic.

Nevertheless, there is evidence that genetic changes can modulate the response of this normally hard-wired sensory system. Zuker concludes that meaningful progress in untangling the neural processes behind food choice will require a solid understanding of what happens when meal meets mouth. "Before we can understand how the brain knows," he says, "we need to figure out how the tongue knows." ■

Michael Eisenstein is a journalist in Philadelphia.



soups that are amino acid-fortified over everything else, including very tasty high-calorie soups," says Breslin. "This is in young kids, who have no idea what's going on. This suggests that somehow there's this 'wisdom of the body'."

Evidence suggests that at least some of this activity may arise from metabolic signals triggered by taste receptor activation. "Taste cells express all sorts of different peptide hormones that are used in other areas of the body for regulating satiety or blood glucose," says Steven Munger, a neurobiologist at the University of Maryland.

Several studies in the past few years suggest that these receptors also direct the secretion of metabolic hormones in the lower digestive tract in response to sweet, bitter or umami stimuli; for example, intestinal sweetness receptor signalling may help regulate glucose



Children wait to be fed during the Dutch Hungerwinter of 1944–1945.

EPIGENETICS

Tales of adversity

Genetic studies of people conceived during famine reveals that prenatal malnutrition lingers long after the event.

BY FAROOQ AHMED

It is well established that a pregnant woman's habits affect the health of her unborn child, but the extent of the impact is less well known. Recent studies of tragic historical events, namely the Dutch Hungerwinter and the Great Chinese Famine, have begun to highlight the trans-generational relationship between food and genes.

The Hungerwinter (hunger winter) began late in 1944 towards the end of the Second World War. Food supplies in the northern and western regions of Nazi-occupied Holland became increasingly limited as the Germans halted overland transport of goods into Amsterdam and nearby cities.

Exacerbating this blockade, the harsh winter froze canals — cutting off a vital supply route. Rations in cities dropped to as few as 500 calories per day, less than a quarter of the recommended intake, until the country was liberated in May 1945, but not before 18,000 people starved to death.

Many children conceived during the Hungerwinter were small and underweight. What's more, certain health problems have persisted long into their adult lives. Compared to their siblings conceived before or after the famine, the Hungerwinter children are at increased risk for obesity, for example.

A propensity for obesity was also found in children of the 1968–1970 Biafra famine in a recent study in Nigeria.

The Great Chinese Famine, from 1958 to 1961, was caused by a combination of leader Mao Zedong's agricultural policies during the Great Leap Forward, widespread mismanagement and severe weather. Tens of millions of people died. Studies of Chinese born during this period link prenatal famine exposure to an increased risk of schizophrenia — a link also found in the Dutch Hungerwinter cohort.

"These extreme events offer special opportunities for research in humans that you might not otherwise have," says Lambert Lumey, an epidemiologist at Columbia University, New York, who is studying the effects of the Hungerwinter. There are obvious ethical issues and long time spans involved that make recreating the circumstances of famine impossible. "These events are crucial to helping us develop and discover underlying disease mechanisms," says Lumey.

TELL-TALE DNA

Scientists have discovered that certain genes of children conceived during a prolonged period of starvation receive special epigenetic 'tags' through a process called methylation — a gene modification that typically deactivates a

gene, but does not alter the genetic code. Methylation is part of normal development, but patterns vary across individuals.

Nearly six decades after the famine, Lumey and colleagues isolated DNA from Hungerwinter individuals. They found a below-average methylation of the insulin-like growth factor II gene (*IGF2*), which codes for a growth hormone critical to gestation. Decreasing the methylation of *IGF2* should increase the expression of the hormone. In contrast, later studies in this cohort found increased methylation of five other genes, among them genes associated with cholesterol transport and ageing, as well as the gene that produces IL-10, which has been linked with schizophrenia.

The mechanisms of these epigenetic changes and whether they have a bearing on disease remain unclear. "In humans, these are the \$100,000 questions," says epigeneticist Robert Waterland from Baylor College of Medicine in Texas.

Lumey hopes to study the children of the 'tagged' individuals to see if these changes persist into the next generation. Epigenetic information is almost fully reset in very early development, so the outcome, he says, is difficult to predict. "This is an important question regardless of what the data will later show."

Nevertheless, studies on these extreme events "provide the first convincing evidence that early nutritional exposure causes a persistent change in epigenetic regulation in humans," notes Waterland. "It's a proof of principle."

Lumey is now looking to high-throughput sequencing methods to measure genome-wide DNA methylation. "We expect that this will tell us whether there also are more epigenetic differences between prenatally exposed individuals and their unexposed siblings, than the ones we found studying candidate loci," says epigeneticist Bastiaan Heijmans of Leiden University in the Netherlands, who works with Lumey. If these modifications are indeed widespread throughout the genome, the cumulative effect of famine-induced epigenetic alterations might play a substantial role in disease progression.

Other research has shown that less-extreme diets also affect methylation patterns and disease susceptibility. For example, folic acid is an important supplement for pregnant women to help prevent neural tube defects in developing embryos. It has been shown to increase the methylation of *IGF2*, hinting that it works through an epigenetic mechanism.

Nevertheless, studying such catastrophes provides researchers with valuable information that is not otherwise available, revealing that the aftermath of famine and prenatal malnutrition lasts long after help arrives with life-saving food. ■

Farooq Ahmed is a science writer in New York.

AD WINDIG/MA/HOLLANDE HOOGTE/EYEVINE



TECHNOLOGY

A flavour of the future

Health biomarkers, smart technology and social networks are hastening an era of nutrition tailored to your individual needs but relying on information generated by the crowd.

A man steps out of a health clinic after his monthly nutritional profile. He slides a ring onto his finger and the injection-free technology transmits a read-out of his blood constituents to a central server. Skimming the data sent to his smart phone, he looks at the recommendation for his evening snack — something with a little more selenium: brazil nuts, perhaps. He considers his diet for the coming week — logged with his refrigerator — and confirms an updated home-delivery shopping list. Finally, he tots up his credits for sharing this personal health data with a population-wide genome study—redeemable against the cost of his health insurance and nutritional supplements. It's a familiar sight to his girlfriend. "We're having dinner at my parents' tomorrow. Don't you dare let the FatNav tell you what to eat, or me what to drink."

There are signs that this future is fast approaching. Domestic sleep and weight monitors can transmit results using WiFi; fridges are in development that log what you've eaten; and dinner parties are complicated by food intolerance and fad diets. Already, pin-prick blood

test results for diabetes can be uploaded online. Websites such as patientslikeme.org offer tips on drug and nutritional supplement regimens. And at SNPedia.com and DIYGenomics.org, people can share their entire genomic data to pool resources and provide more personal guidance on health issues.

Can all these platforms create genetics-based nutrition advice? Will this affect our definition of health, or the distinction between food and drugs? And how personalized will our diets become?

NOT IN SICKNESS BUT IN HEALTH

Many researchers think that personalized nutrition must begin with a new suite of biomarkers: ones that measure health rather than disease. But what does that mean? "Here we are in the twenty-first century and we don't have a definition of health other than 'the absence of disease,'" says Siân Astley, a nutrition researcher at the Institute of Food Research, UK. "Health is about much more."

Astley says that to comprehend what bio-active food compounds are doing we first have

to understand what's going on in the body before it becomes ill. "Our difficulty is that the only biomarkers we have are for when the disease process has already started."

'Omics' sciences, such as transcriptomics, proteomics and metabolomics, study many thousands of putative biomarkers in a process called 'extensive phenotyping'. "We now have examples where the protein fingerprint in tissues can indicate precancerous changes long before symptoms appear," says Astley. "The protein fingerprint offers us early diagnosis as well as an insight into potential changes that might be elicited by feeding people a different diet."

Astley also works for the Nutrigenomics Organisation (NuGO), an EU-funded project involving 23 universities and research institutes. NuGO researchers believe that to find these health biomarkers, testing conditions will need a rethink. For example, although we are all in a state of homeostatic equilibrium, the 'normal' levels of metabolites, including glucose, plasma proteins, cytokines and signalling molecules, vary from person to person. ▶

► person. Challenging that state with exercise or new foods, and then measuring changes in metabolites as the body recovers, reveals more about its reaction to bioactive compounds than simply measuring metabolites in a resting state.

THE DEVIL IN THE DETAILS

Extensive phenotyping is a big job and costs big money. Resource-limited researchers have two options: measure many people in lesser detail, or a smaller number in greater detail. Large population studies have more statistical power, but as the ultimate goal is personalized nutrition, an investigation of the individual will provide more in-depth information.

It's a conundrum facing Mike Gibney, director of University College Dublin's Institute of Food and Health. "Too many people in a study smooths out the data and is too expensive in an era when so many measurements are needed," he says. Gibney contends we are in transition towards personalized nutrition and advocates temporarily abandoning the 'individual' mantra. Instead, people should be

"Finally we have the proof in the pudding — genetic variety in dietary advice is relevant."

grouped into broader categories based on biomarkers that indicate, for example, how efficiently different sugars or proteins are metabolized. "I'm taking my research in the direction of clusters," he says. "I believe it's a half-way house." These wider groupings have the advantages of consisting of larger populations and can act as a proof of concept.

Results are emerging that support the notion of these clusters. Kenneth Kornman is founder of InterLeukin Genetics (ILG), a Massachusetts-based company developing tests for genes that affect food metabolism based on single nucleotide polymorphisms (SNPs). Kornman recently reanalysed a 2007 study by Christopher Gardner and colleagues at Stanford University. In Gardner's study, 311 women were randomized to four different diets, which varied in the content of carbohydrates. After 12 months, women on the low-carb, high-protein Atkins diet had lost the most weight.

Kornman's reanalysis involved placing 101 of the women (those available for the follow-up study) into one of three groups categorized by three SNPs related to the metabolism of dietary fats and carbohydrates. Women in the 'fat-sensitive' group shared a SNP that meant they gained more weight from a high-fat diet than did women in the 'carbohydrate-sensitive' group, and vice versa. The third group was sensitive to neither fat or carbohydrate. "Our company screened the published evidence on more than 200 SNPs and determined that these three were the only ones that met our criteria," says Kornman. The criteria were that each SNP

should have at least three validating clinical studies, should be functional (directly linked to biological or clinical effects) and linked to body weight.

Kornman found that women on a diet that matched their genotype lost two-to-three times more weight than those on an unmatched diet. The study, sponsored by ILG, was presented at the 2010 Joint Conference of the American Heart Association in San Francisco. "The scientists in the audience were shocked," recalls Ben van Ommen, director at the Netherlands Organisation for Applied Scientific Research and NuGO, who had invited Kornman to speak. Kornman, he says, "has been scrutinized by the audience and he's survived. Finally we have the proof in the pudding — genetic variety in dietary advice is relevant".

FOOD TRIBES

Moving towards the more personalized end of the nutrition spectrum will require millions more data points from many diverse groups. One way to collect information from disparate populations is to use crowd-sourcing technologies. Many people who have discovered some or all of their genetic information are sharing or offering it for analysis using websites such as SNPedia, DIYgenomics and Harvard Medical School's Personal Genome Project. As genome testing becomes cheaper, more data will become available to use in this way.

Founders of personal genome information-sharing websites, such as DIYGenomics' Melanie Swan, say they can facilitate this data-gathering process by offering a new way to conduct science that appeals to the subjects. "We aim to give individuals the opportunity to participate in citizen science research studies," says Swan. "The whole point is to experiment and find out what works best for you."

A typical experiment might investigate vitamin supplements and their precursors. Participants would consent to taking regular supplements, pay for their own genetic sequencing test, submit regular tests to an approved laboratory, and upload results to the website. Combining data from all participants paints a picture of the relationship between certain genes and the impact of a vitamin or vitamin precursor on health. DIYGenomics' first study — submitted to a peer-review journal — is a proof-of-concept, extending existing research on gene mutations and vitamin B deficiency. Another study on ageing is designed and set to recruit participants.

This new approach to research blurs the distinction between study organizer and participant. "We all design the study and we all participate. We have our own consenting process too," says Swan, adding that she sees a 'citizen ethicist' version of the Hippocratic oath

evolving to accommodate new ways of conducting research.

Some people see personal genomics as a logical follow-on to social networking and a valuable asset. "There is definitely potential in a citizen science approach," says Marina Levina, a communication researcher at The University of Memphis. Levina, however, adds a few caveats. "Citizen science implies that conventional science has failed us in some ways, whereas I would argue that guidelines and restrictions that perhaps slow down conventional science are there because of valid ethical issues."

There are other potential pitfalls. Genetic testing companies that provide genome-sharing websites have been criticized for offering inconsistent results and flimsy diagnoses regarding genetic propensity to disease. There are signs that the US Food and Drug Administration is moving to clip their wings, perhaps by enforcing tougher regulation. This echoes ongoing changes to regulation of the nutritional supplements industry in the United States and Europe, which is to be treated more like the pharmaceutical industry.

Genes are not the only important considerations when developing tailored nutritional advice. The nascent science of epigenetics, which describes how and when genes are turned on and off in the body, promises to both complicate and frustrate the road to personalized nutrition.

ILG's Kornman says epigenetics is the elephant in the room when it comes to determining optimal diet: "There is growing evidence that prenatal nutrition and environmental effects have a life long and maybe multi-generational effect in terms of fetal development and early childhood nutrition." Even if we can decode the genetic recipe of the diet-health relationship, without a greater knowledge of the epigenetic modifications put in place early in life — or in a mother's or perhaps grandmother's life — this recipe still might not taste right.

What's more, can we ever over-ride our love for sweet, fatty and salty food? "People are perverse about dietary choice," says Tom Sanders, head of nutrition and dietetics at King's College London. "They tend to offset what they perceive as good food with bad food." Put another way, we are bad at eating good food, and good at eating bad food.

Nutrigenomics may well change our definition of health and disease; blur the distinction between food and drugs; between experimenter and experimentee; and demonstrate new models of the scientific method driven by food tribes, citizen scientists and online social networks. The paradox is that as our lifestyles become ever more individualized, it could be the crowd that delivers the best advice for healthy eating. ■

Arran Frood is a freelance writer in the UK.

➔ **NATURE.COM**
more on how
technology affects
on clinical trials
go.nature.com/Q7KS5S